DENSITY MATRIX RENORMALIZATION GROUP (DMRG)-BASED APPROACHES IN COMPUTATIONAL CHEMISTRY

HAIBO MA

ULRICH SCHOLLWÖCK

ZHIGANG SHUAI

ELSEVIER

Density Matrix Renormalization Group (DMRG)-based Approaches in Computational Chemistry

Density Matrix Renormalization Group (DMRG)-based Approaches in Computational Chemistry

Haibo Ma
School of Chemistry and Chemical Engineering,
Nanjing University, Nanjing,
P.R. China

Ulrich Schollwöck
Department of Physics, Ludwig-Maximilian University of Munich,
Munich, Germany

Zhigang Shuai
Department of Chemistry, Tsinghua University, Beijing, P.R. China
School of Science and Engineering, The Chinese University of
Hong Kong, Shenzhen, P.R. China

ELSEVIER

Notices
Knowledge and best practice in this field are constantly changing. As new research and experience broaden our understanding, changes in research methods, professional practices, or medical treatment may become necessary.

Practitioners and researchers must always rely on their own experience and knowledge in evaluating and using any information, methods, compounds, or experiments described herein. In using such information or methods they should be mindful of their own safety and the safety of others, including parties for whom they have a professional responsibility.

For Information on all Elsevier publications
visit our website at https://www.elsevier.com/books-and-journals

Working together
to grow libraries in
developing countries

www.elsevier.com • www.bookaid.org

Contents

Preface

Quantum chemistry strives to solve the molecule's nonrelativistic Schrödinger equation or relativistic Dirac equation for the purpose of accurately understanding and predicting its diverse chemical and physical properties, including the structure, spectroscopy, and reactivity as well as the optoelectronic and magnetic responses. Because numerous and complicated interactions between the electrons and nuclei are involved in a molecular system, accurately solving the quantum many-body problem is still the major difficulty for quantum chemistry. In the past years, the developments of a variety of post-Hartree-Fock (HF) methods [e.g., truncated configuration interaction (CI), many-body perturbation theory (PT), and coupled cluster (CC) approaches] built on HF mean-field single-determinant reference wavefunction have enabled electronic structure calculations with chemical accuracy (~ 1 kcal/mol) for chemical systems with hundreds of weakly correlated electrons. Challenges arise however, when the traditional weak correlation assumption breaks down. In many chemical problems such as bond breaking/formation in chemical reactions and transition metal catalysis in biological photosynthesis, there are many energetically near-degenerate frontier molecular orbitals, making it impossible to approximate the electronic wavefunction by using only one leading component. In such cases, in order to describe the strong correlations therein, all possible important determinants or configuration state functions (CSFs) have to be first identified. For example, the widely used complete active space (CAS) methods expand the wavefunction using all possible determinants or CSFs within an active space constructed from a preselected set of active orbitals. Unfortunately, it is almost impossible to obtain the exact solution for large active spaces, as the dimension of the configuration space grows exponentially with the increase of the system size. Nowadays, the largest exactly solvable active space is 20 electrons in 20 orbitals (20e, 20o). This greatly hindered the simulation of many realistic chemical systems of large conjugated molecules or polynuclear transition metal complexes. For example, calculating the electronic structure of the Mn_4CaO_5 cluster in photosystem II of photosynthetic reaction or Mn_{12} single-molecule magnet requires at least 35 or 60 active orbitals, even if only Mn *3d* valence orbitals and bridging oxygen *2p* orbitals are included in the active space.

To tackle this so-called curse of dimensionality, since its invention in 1992 by White, the density matrix renormalization group (DMRG) has been widely known by the quantum physics community as the currently most powerful numerical method in the study of one-dimensional (1D) strongly correlated quantum lattices. DMRG's extraordinarily high performance can be ascribed to its efficient compression and localized representation of quantum states in its wavefunction's entangled matrix product state (MPS) formulation or the equivalent tensor train structure in mathematics language. In 1997 DMRG was for the first time introduced into theoretical chemistry community by Shuai et al., being utilized to solve the semiempirical quantum chemical Hamiltonian for studying the excited states in conjugated polymers. Later in 1999 DMRG was further applied to help the solution of ab initio quantum chemical Hamiltonians by White and Martin. It should be noted that the DMRG implementation in quantum chemistry is quite different from that in condensed matter physics. The orbitals in chemical molecular systems don't have spatial translation symmetry which is usually present in the quantum lattice sites within the condensed matter physics models. Another aspect is that the ab initio quantum chemical Hamiltonian has four-center and long-range interaction terms, whereas condensed matter physics models (like Heisenberg and Hubbard models) often have only two-center and nearest-neighbor ones. In addition, in many cases a DMRG quantum chemical calculation has to be done in momentum or energy space instead of real space, because usually there is no evident 1D spatial topology for the molecule's active orbitals. All these issues made the application of DMRG into quantum chemistry become highly nontrivial.

Fortunately, contributed by the continuous efforts of many quantum chemistry groups (including Xiang, Shuai, White, Chan, Reiher, Legeza, Zgid, Yanai, Kurashige, Wouters, Ma, et al.), DMRG has become one of the biggest breakthroughs in quantum chemistry in the last quarter century to tackle the challenge of simulating strongly correlated systems. DMRG is now widely used as a benchmark reference when testing new quantum chemical methods for strong electron correlation problems. It evolves from a purely approximate full CI solver to being fully adapted to a variety of CAS and multireference (MR) methods. Nowadays, the advanced implementation of DMRG quantum chemistry code has greatly extended the solvable active space size, from 20 orbitals by conventional CAS method to around 100 orbitals by DMRG. The development of post-DMRG methods by combining DMRG with MR-CI, MR-PT, and MR-CC as well as density functional theory can further include the dynamic electron correlation energy outside the active space, making the calculation more quantitatively accurate for realistic molecules. The incorporation of gradient and response theory also greatly expands the application toolbox for chemical problems, capable of describing various geometrical and spectroscopy properties. Encouragingly, in the past few years, time-dependent DMRG (TD-DMRG) was also successfully used

and further developed by quantum chemists to simulate the real-time nonadiabatic quantum dynamics in many chemical problems, ranging from modeling exciton dynamics in photovoltaic and photosynthetic systems to simulating vibrationally resolved 1D and two-dimensional electronic spectroscopy in molecular aggregates and to handling complex problem such as carrier and spin transport in molecular materials. Of course, DMRG quantum chemistry still has plenty of room for development before being a robust, user-friendly, and multifunctional method for popularizing its applications. These include, but are not limited to, designing new post-DMRG approaches to account dynamic correlations without using high-order n-electron reduced density matrices, embedding DMRG, or TD-DMRG in larger chemical environments and implementing massively parallel DMRG calculations.

Aiming to present a comprehensive review and summary of the outstanding progress in the rapidly developing DMRG quantum chemistry field in the last quarter century and inspire new ideas for describing strongly correlated systems, this book explores the fundamental theories and algorithms of DMRG-based quantum chemistry approaches, detailing recent ideas and key developments and providing an up-to-date view of the current understanding. We notice that DMRG method was originated in solid-state physics and only later has been transferred to quantum chemistry. For research scientists by conventional quantum chemistry training, language and concepts of DMRG are usually not familiar, so there is certain learning barrier. Therefore, we try to organize the book in a pedagogical manner to facilitate the study by graduate students, to grasp the important concepts like the relationship between DMRG algorithm and MPS formulation, etc. We expect this book will be useful for graduate students and researchers who are interested in developing DMRG-based methods for quantum many-body problems in chemistry or those who are interested in using the state-of-the-art DMRG method to deal with challenging chemical problems of electronic structure and dynamics.

In this book, Chapters 1 and 2 introduce the fundamentals and concepts of DMRG, MPS, matrix product operator (MPO), and tensor network state as well as their relationship with quantum information theory. Most of the techniques have been developed by quantum physicists with the special problems of quantum many-body theory in mind, which differ from those in quantum chemistry. We point out and highlight the differences for quantum chemists, paving the way for the more chemistry-oriented expositions in later chapters.

In Chapters 3 and 4 the implementation schemes of DMRG for semiempirical and ab initio quantum chemical Hamiltonians, the related technical details for treating MPO constructions, implementation of symmetry, as well as selecting and ordering active orbitals are described. As a preparation for later chapters, we also discuss how to perform wavefunction component analysis and compute one- and many-body RDMs.

In Chapter 5 we introduce the methods of DMRG self-consistent field, in which the DMRG basis (i.e., molecular orbitals) is further iteratively and variationally optimized in a molecular environment. The algorithms for calculating the gradients and the geometry and spectroscopy properties as well as the excited states are also unraveled. Chapter 6 covers the descriptions for various ab initio post-DMRG (DMRG-MR-CI, DMRG-MR-PT, DMRG-MR-CC, etc.) approaches to further account for dynamic electron correlations. The techniques to incorporate environmental effects are also briefly discussed.

Chapters 7 and 8 discuss the DMRG methods for dynamical and real-time properties in the frequency domain and time domain. In Chapter 7 we will introduce the frequency-domain DMRG methods for the dynamical response properties, including the Lanczos-DMRG, correction vector DMRG, dynamical DMRG, and Chebyshev matrix product state. In Chapter 8 the time-domain TD-DMRG methods for nonadiabatic quantum dynamics are introduced. The commonly used time evolution schemes are described. The algorithms to incorporate temperature effect, including thermo field dynamics and minimally entangled typical thermal state, are also presented. In both chapters, several applications ranging from pure electron dynamics to vibronic dynamics are covered.

We owe a great debt of gratitude to numerous collaborators, colleagues, and students who have helped to shape our thinking and who have provided advices in the preparation of this book. We cannot list all their names here because they are numerous and we are sure to miss some. But we are truly grateful to them as some of their sights have percolated their way into this book. A special thank should be given to Dr. Jiajun Ren, Dr. Zhen Luo, Dr. Luis Carlos Vasquez Cardenas, Tong Jiang, Weitang Li, and Yifan Cheng for having read various parts of the book and providing inputs. We would be grateful to receive errata and will maintain an up-to-date list of errata on our websites. Please feel free to contact any of the authors: haibo@nju.edu.cn (HM), schollwoeck@lmu.de (US), or zgshuai@tsinghua.edu.cn (ZS).

Haibo Ma
Ulrich Schollwöck
Zhigang Shuai

Chapter 1

Density matrix renormalization group

1.1 Introduction

The density matrix renormalization group (DMRG) has its origin in the field of strongly correlated quantum systems as they appear in condensed-matter physics. We will set out by discussing its general framework from this perspective; this will allow us to understand more clearly, what makes "original" DMRG somewhat different from DMRG as adapted to be useful for problems in quantum chemistry. This should make the language of most seminal DMRG papers in physics more accessible to the reader with a chemistry background; numerous parallel developments seem to have happened in condensed-matter physics and quantum chemistry that could have been more mutually fruitful if a common language existed.

In the case of DMRG, there has been a change in the way it is represented and thought about within physics itself; roughly speaking, a point of view anchored in statistical physics and renormalization group theory (as indicated by the name) has given way to thinking of DMRG as predominantly (but not exclusively) a variational method. In condensed-matter physics, the associated change of notations and codes is comparatively easy and has been largely achieved. It has opened the way to important new algorithmic developments, with DMRG being (only) one of a group of algorithms. In quantum chemistry, this transition turns out to be more complicated. The reformulation is underway, but a lot of the relevant literature is in the old language. The foundations of this new approach will be covered in Chapter 2.

We set out from the N-particle time-independent Schrödinger equation $\hat{H}\psi = E\psi$. In first quantization and real-space representation, the wave function depends on $3N$ coordinates in space, $\psi(\mathbf{r}_1, \ldots, \mathbf{r}_N)$, and the Hamiltonian reads

$$\hat{H} = -\sum_{i=1}^{N} \frac{\hbar^2}{2m_i} \nabla_i^2 + \frac{1}{2}\sum_{i \neq j}^{N} V(\mathbf{r}_i, \mathbf{r}_j). \tag{1.1}$$

The first term, where the operator ∇_i acts on coordinate $\mathbf{r}_i$, contains kinetic energy, which we take to be nonrelativistic. We assume that the particles

interact through a two-body interaction V that only depends on positions. The N particles are supposed to be electrons, identical fermions, such that the wave function must meet the fermionic antisymmetrization requirement

$$\psi(\ldots, \mathbf{r}_i, \ldots, \mathbf{r}_j, \ldots) = -\psi(\ldots, \mathbf{r}_j, \ldots, \mathbf{r}_i, \ldots). \tag{1.2}$$

Note that we ignore spin for the moment where we are just interested in the general structure of the problem. In order to solve the Schrödinger equation for Hamiltonian (Eq. 1.1), we start from the single-particle Hilbert-space $\mathcal{H}^1$. The N-particle Hilbert-space $\mathcal{H}^N$ is then the tensor product of N single-particle Hilbert-spaces $\mathcal{H}^1$,

$$\mathcal{H}^N = \otimes_{i=1}^{N} \mathcal{H}_i^1. \tag{1.3}$$

In order to proceed, we have to give bases to these spaces. In the real-space representation, we choose a single-particle basis $\{\phi_k(\mathbf{r})\}$ of $\mathcal{H}^1$, a countably infinite set of square-integrable functions. No numerical approach can handle this infinity, and we have to invoke a basis set truncation to B basis states ($B \geq N$ for N fermionic particles). The truncated basis then induces a basis of $\mathcal{H}^N$ as the products $\{\phi_{k_1}(\mathbf{r}_1)\phi_{k_2}(\mathbf{r}_2)\ldots\phi_{k_N}(\mathbf{r}_N)\}$. The most general N-particle wave function takes the form

$$\psi(\mathbf{r}_1, \ldots, \mathbf{r}_N) = \sum_{k_1\ldots k_N} c_{k_1\ldots k_N}\phi_{k_1}(\mathbf{r}_1)\ldots\phi_{k_N}(\mathbf{r}_N) \tag{1.4}$$

which, in general, will not be antisymmetric. Antisymmetrization is imposed in the first quantization by the introduction of Slater determinants: we choose N out of B basis functions, indexed $(k_1, \ldots, k_N)$ where $k_1 < k_2 < \ldots < k_N$. Then

$$S_{(k_1,\ldots,k_N)}(\mathbf{r}_1, \ldots, \mathbf{r}_N) = \begin{vmatrix} \phi_{k_1}(\mathbf{r}_1) & \ldots & \phi_{k_1}(\mathbf{r}_N) \\ \vdots & & \vdots \\ \phi_{k_N}(\mathbf{r}_1) & \ldots & \phi_{k_N}(\mathbf{r}_N) \end{vmatrix} \tag{1.5}$$

and the N-particle wave function takes the form

$$\psi(\mathbf{r}_1, \ldots, \mathbf{r}_N) = \sum_{(k_1\ldots k_N)} c_{(k_1\ldots k_N)} S_{(k_1,\ldots,k_N)}(\mathbf{r}_1, \ldots, \mathbf{r}_N) \tag{1.6}$$

where the sum now only runs over the ordered N-tuples $(k_1, \ldots, k_N)$. This approach, also extended to include spins, is covered extensively in all quantum chemistry literature, for instance, Szabo and Ostlund (1996). It is useful as long as N is small and we can truncate the basis to some small B. Ultimately, the limitation rests in the number of Slater determinants that have nonnegligible coefficients in Eq. (1.6).

In condensed-matter physics, first quantization is often replaced by the language of second quantization, and most of, if not all of, the literature on DMRG uses it. This is simply because in the bulk matter $N \sim 10^{23}$, and second quantization is often a very convenient way to work around this problem.

We still have single-particle and N-particle Hilbert-spaces, but now we also introduced the Fock space, the direct sum of all N-particle Hilbert-spaces,

$$\mathcal{F} = \oplus_{N=0}^{\infty} \mathcal{H}^N. \tag{1.7}$$

(We will discuss $\mathcal{H}^0$ in a second.) Again, we start from a single-particle basis $\phi_{k\sigma}(\mathbf{r})$, where now we have introduced a spin-degree of freedom σ. In the physics of strongly correlated systems, where DMRG originated, the usual choice is Wannier functions $\phi_{in\sigma}(\mathbf{r}) = \phi_{n\sigma}(\mathbf{r} - \mathbf{r}_i)$: assume we have a (say, cubic) lattice with lattice sites i, then one can construct orthonormal functions $\phi_{n\sigma}$, which are repeated identically on each lattice site. The construction, whose details will not be used here, ensures that

$$\int d^3 \mathbf{r} \phi_{in\sigma}^*(\mathbf{r}) \phi_{i'n'\sigma}(\mathbf{r}) = \delta_{ii'} \delta_{nn'}. \tag{1.8}$$

A basis truncation is again required, and n is limited to some small number. In many DMRG applications, like for the single-band Hubbard model, we have a single $\phi(\mathbf{r})$, the same for spin-up and spin-down, to which we attach spin and repeat it on lattice sites, leading to $\phi_{i\uparrow}$ and $\phi_{i\downarrow}$ on-site i, which formally corresponds to an orbital in chemistry, which can accommodate one spin-up and one spin-down electron.

We now construct the basis of the Fock space $\mathcal{F}$ from this single-particle basis. Assume we have L lattice sites, so if we take one spin-up and one spin-down Wannier function, we have $2L$ orthonormal basis functions and can, therefore, accommodate up to $2L$ particles. We now introduce (going to the abstract ket-notation) occupation number basis states $|n_{1\uparrow}n_{1\downarrow}\ldots n_{L\uparrow}n_{L\downarrow}\rangle$, indexing site (orbital) number and spin orientation; the n give the number of electrons in these orbitals, so all $n_{i\sigma} \in 0, 1$. The corresponding first-quantized representation would be a Slater determinant. The most general quantum state then reads

$$|\psi\rangle = \sum_{n_{1\uparrow}n_{1\downarrow}\ldots n_{L\uparrow}n_{L\downarrow}} c_{n_{1\uparrow}n_{1\downarrow}\ldots n_{L\uparrow}n_{L\downarrow}} |n_{1\uparrow}n_{1\downarrow}\ldots n_{L\uparrow}n_{L\downarrow}\rangle \tag{1.9}$$

without fixing particle number N at the moment. Antisymmetrization is now introduced at the level of operators, namely the creation and annihilation operators $\hat{c}_{i,\sigma}^\dagger$ and $\hat{c}_{i,\sigma}$: they create or annihilate an electron with spin orientation σ at site i. Antisymmetrization is ensured by ordering the orbitals (sites) arbitrarily and defining the action of the operators as

$$\hat{c}_{i,\sigma}^\dagger |n_{1\uparrow}, n_{1\downarrow}, \ldots, n_{i\sigma}, \ldots, n_{N\uparrow}, n_{N\downarrow}\rangle$$
$$= (-1)^{n^<} |n_{1\uparrow}, n_{1\downarrow}, \ldots, n_{i\sigma} + 1, \ldots, n_{N\uparrow}, n_{N\downarrow}\rangle \tag{1.10}$$

$$\hat{c}_{i,\sigma} |n_{1\uparrow}, n_{1\downarrow}, \ldots, n_{i\sigma}, \ldots, n_{N\uparrow}, n_{N\downarrow}\rangle$$
$$= (-1)^{n^<} |n_{1\uparrow}, n_{1\downarrow}, \ldots, n_{i\sigma} - 1, \ldots, n_{N\uparrow}, n_{N\downarrow}\rangle \tag{1.11}$$

where $n_<$ is the sum over all n "before" $n_{i\sigma}$ in the ordered occupation number state. The result is taken to be 0 if the new occupation number $n_{i\sigma} \notin \{0, 1\}$. (We will not prove the claims made here, but refer to any number of excellent text-books such as Fetter and Walecka (2003) or Bruus and Flensberg (2004)).

If we define a vacuum state $|\varnothing\rangle = |0, 0, 0, \ldots\rangle$, which is in fact the only element of $\mathcal{H}^0$, any state $|n_{1\uparrow} n_{1\downarrow} \ldots n_{L\uparrow} n_{L\downarrow}\rangle$ is created from it as

$$
\begin{aligned}
&|n_{1\uparrow} n_{1\downarrow} \ldots n_{L\uparrow} n_{L\downarrow}\rangle \\
&= \left(\hat{c}_{1\uparrow}^{\dagger}\right)^{n_{1\uparrow}} \left(\hat{c}_{1\downarrow}^{\dagger}\right)^{n_{1\downarrow}} \ldots \left(\hat{c}_{L\uparrow}^{\dagger}\right)^{n_{L\uparrow}} \left(\hat{c}_{L\downarrow}^{\dagger}\right)^{n_{L\downarrow}} |\varnothing\rangle
\end{aligned}
\tag{1.12}
$$

(In fact, one could also start from the filled Fermi sea as reference state. It only matters to have the signs correct and relative to each other, as global phases do not matter.) The reason why second quantization is very attractive is that the Hamiltonians, expressed in creation and annihilation operators, become quite simple and fermionic antisymmetrization is taken care of automatically: the kinetic energy term becomes a sum of terms where an electron hops from site (orbital) j to site (orbital) i with some amplitude T_{ij}; in the language of operators, it is annihilated on site j and created on site i. Similarly, two-body interactions, which we may think of as two electrons being scattered out of their original states into two new ones, become sums over two creation and two annihilation operators,

$$
\hat{H} = \sum_{ij,\sigma} T_{ij} \hat{c}_{i,\sigma}^{\dagger} \hat{c}_{j,\sigma} + \frac{1}{2} \sum_{ijkl,\sigma\sigma'} V_{ijkl} \hat{c}_{i,\sigma}^{\dagger} \hat{c}_{j\sigma'}^{\dagger} \hat{c}_{l\sigma'} \hat{c}_{k,\sigma},
\tag{1.13}
$$

where V_{ijkl} is also a paramater for describing interaction strengths (assuming that the single-particle wave functions do not depend on spin, but the generalization is simple).

As interaction, we assumed the Coulomb interaction, but this is of course more general. In addition, note the reversed order of indices in the two annihilation operators in (13).

DMRG deals with states and operators in this form. Many of its applications concern variants of the Heisenberg model (only localized spin degrees of freedom where the problem of antisymmetrization disappears) and the Hubbard model, but many other Hamiltonians have been studied. Let us, therefore, introduce a more generic notation: We consider a system of L sites (orbitals) (Fig. 1.1), which have d local degrees of freedom; the states are

1 L
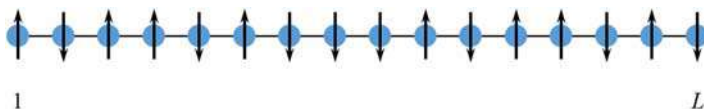
FIGURE 1.1 Our toy model: a chain of length L with open ends, where a spin-$\frac{1}{2}$ sits on each site and interacts with its nearest neighbors.

denoted $|\sigma\rangle$ (in general, σ will, therefore, label more than just spin). For a chain of L spins $\frac{1}{2}$, $d = 2$, and $|\sigma\rangle \in \{|\uparrow\rangle, |\downarrow\rangle\}$. The prototypical Heisenberg Hamiltonian reads

$$\hat{H}_{\text{Heisenberg}} = \sum_{i=1}^{L-1} \frac{J}{2} \left(\hat{S}_i^+ \hat{S}_{i+1}^- + \hat{S}_i^- \hat{S}_{i+1}^+ \right) + J_z \hat{S}_i^z \hat{S}_{i+1}^z \tag{1.14}$$

in one dimension. In a single-band Hubbard model with nearest-neighbor hopping and on-site Coulomb repulsion, we consider (instead of one spin-up and one spin-down orbital) a single spatial orbital that can accommodate up to 2 electrons. Its $d = 4$ states are denoted by $|0\rangle$, $|\uparrow\rangle$, $|\downarrow\rangle$, $|\uparrow\downarrow\rangle$, empty, with one spin-up or spin-down electron, or with one each for both spin orientations. The Hamiltonian reads

$$\hat{H}_{\text{Hubbard}} = -t \sum_{i=1}^{L-1} \sum_{\sigma} \left(\hat{c}_{i,\sigma}^\dagger \hat{c}_{i+1,\sigma} + \text{H.c.} \right) + U \sum_{i=1}^{L} \hat{n}_{i\uparrow} \hat{n}_{i\downarrow}. \tag{1.15}$$

In general, with the exception of bosonic (in physics, mainly phononic; in chemistry, mainly vibrational) modes, d is a small number; the bosonic case requires special attention; ultimately, the bosonic occupation numbers have to be limited to some maximum and convergence of results under changes of this maximum checked. Our computational basis is then formed by the tensor product of the L local bases of dimension d each,

$$|\sigma_1 \sigma_2 \ldots \sigma_L\rangle = |\sigma_1\rangle \otimes |\sigma_2\rangle \otimes \ldots \otimes |\sigma_L\rangle. \tag{1.16}$$

It is an orthonormal basis,

$$\langle \sigma_1' \ldots \sigma_L' | \sigma_1 \ldots \sigma_L\rangle = \delta_{\sigma_1', \sigma_1} \cdot \ldots \cdot \delta_{\sigma_N', \sigma_N} \tag{1.17}$$

where the local basis states are orthogonal between sites, $\langle \sigma_i | \sigma_j \rangle = 0$ for $i \neq j$. The most general quantum state now reads

$$|\psi\rangle = \sum_{\sigma_1 \sigma_2 \ldots \sigma_L} c_{\sigma_1 \sigma_2 \ldots \sigma_L} |\sigma_1\rangle \otimes |\sigma_2\rangle \otimes \ldots \otimes |\sigma_L\rangle. \tag{1.18}$$

As antisymmetrization is taken care of at the level of operators, except for global normalization there is no constraint on the coefficients $c_{\sigma_1 \sigma_2 \ldots \sigma_L}$.

The obvious problem (both in first and second quantization, which is just smart book-keeping) is the exponentially large number of expansion coefficients $c_{\sigma_1 \sigma_2 \ldots \sigma_L}$; here d^L. One idea of tackling this issue is to decimate the basis in such a way that only those degrees of freedom that are relevant to the problem at hand are kept. This is the fundamental idea of the renormalization group method, which achieves this choice iteratively. During these iterations, a sequence of effective Hamiltonians is generated by projecting onto the reduced state space. The basis states of the reduced state spaces will in general be complicated superpositions of the original computational basis

states such that operators (local operators, n-point correlators, and so forth) have to be transformed and projected as well. Rescaling and renormalizing are further important steps which are, however, not important in our context. But how do we choose the degrees of freedom to be retained?

A key renormalization group method is the numerical renormalization group (NRG) of Wilson (1975), which is very performant in the study of the Kondo effect for magnetic impurities in conductors and more generally of the physics very close to the Fermi surface of solids. (The application to electronic problems is introduced in Krishna-murthy et al. (1980) and an excellent more recent review is Bulla et al. (2008)). Without going into the details, NRG discretizes the electronic conduction band, which contains the Fermi surface logarithmically in energy space by grouping together all of the (dense) energy levels of the band within some energy interval with an exponentially fine resolution close to the Fermi energy: the width of the intervals becomes exponentially small. Each of the band intervals is then associated with exactly one Hubbard-like orbital, which can contain up to two electrons and represents all the energy levels of the band interval within appropriate approximations: After a sequence of astute simplifications, one finally arrives at an infinitely long chain of Hubbard-like orbitals with exponentially decreasing nearest-neighbor single-particle hopping as in the Hubbard model, where the hopping is, however, constant. Those close to the left end are close to the Fermi energy, and further away if we move right. The electrons in the orbitals on sites $i > 1$ do not interact: they represent the effectively free electrons of a conductor. There is, however, a Hubbard-type U-interaction on-site $i = 1$, which represents the magnetic impurity because electrons at this impurity are strongly localized and, therefore, "see" each other.

NRG now considers the Hilbert-space formed by the left-most sites, which have a joint computational basis $|m_\ell\rangle$ of dimension D, which we take to be some small, manageable power of $d = 4$ ($D = 4096 = d^6$ or so is not untypical) such that we begin with $\ell = \log_d D$ sites, 6 in our example. We call these six sites together with a block. Now we add one (seventh) site, $\ell + 1$, with basis states $|\sigma_{\ell+1}\rangle$. Now the (old) block plus the added site is taken to be the (new) block, with a computational basis $\{|m_\ell\rangle \otimes |\sigma_{\ell+1}\rangle\}$. In this vein, we can add site after site, but then the basis explodes exponentially. NRG introduces a truncation prescription to obtain a reduced D-dimensional basis $\{|m_{\ell+1}\rangle\}$ also for the new block, that is, one in d states is retained. The choice is given by diagonalizing the Hamiltonian on the block of $\ell + 1$ sites and retaining the D lowest-energy eigenstates (more precisely: those closest to the Fermi energy; in suitable mappings, these are those lowest in energy). In the new basis, creation and annihilation operators take new forms, so the Hamiltonian has to be transformed (and projected) as well; as we have discarded basis state, the projection onto the new basis involves a loss of information. (NRG has important additional scaling steps, which need not concern us here.)

NRG solved the Kondo problem, which had been one of the big myster-
ies of condensed-matter physics (with hindsight, not surprisingly so: it is
inaccessible to perturbative approaches) and was one of the reasons for
Wilson's Nobel prize in 1982. Not surprisingly, it was attempted to apply
the same procedure of iterative growth of blocks of sites and decimation by
a low-energy prescription to find the ground states of one-dimensional quan-
tum systems such as the Heisenberg or Hubbard chains. This did not work
despite the superficial similarity. The logarithmic discretization procedure of
NRG, which results in exponentially decaying scales in the hopping ele-
ments, leads to an exponential separation of energy scales as one increases
the block, which makes the iterative approach possible. Both the Hubbard
and Heisenberg chain are translationally invariant, and contributions from
"further down the chain" will continue to be of the same size. DMRG grew
out of this dilemma and provided a very powerful solution.

This prehistory explains some aspects of the original formulation of
DMRG (White, 1992), which consists of two subsequent steps, the infinite-
system DMRG, which is formally quite similar to NRG (though conceptually
very different), and the finite-system DMRG, which was considered a required
add-on to improve numerical precision, but somehow not the essence of the
method (for more details see, e.g., White (1993) or Schollwöck (2005)). In the
later formulations of Chapter 2, the emphasis is completely reversed: infinite-
system DMRG is one of several conceivable warm-up procedures, while the
finite-system DMRG, with some minor modifications, is recognized to be a
variational state optimization within a constrained state space. DMRG turns
out to be highly successful for one-dimensional quantum systems, so let us
focus in the following on a one-dimensional Hubbard or Heisenberg model,
that is, electrons or spins on a chain of lattice sites.

1.2 Infinite-system density matrix renormalization group

Infinite-system DMRG starts exactly like NRG by considering an (initially)
small old block of ℓ sites to which one site is added, forming the new block,
truncating the basis. What is changed is the decimation procedure. In NRG,
one could ignore "what comes later" because of the separation of energy
scales. Here, in a typically translationally invariant Hubbard or Heisenberg
chain, we have to imagine that the old block plus one site is part of a
thermodynamically large chain. Note right away that typical problems of
quantum chemistry say the electronic structure of a molecule do not have
this important simplifying aspect. Both T_{ij} and V_{ijkl} are in general very com-
plicated. In thermodynamic language, the entire chain is the universe, the
block plus site the system S, and the rest of the chain the environment E. A
complete description of the system as embedded in the universe is provided
by the reduced density operator $\hat{\rho}_S = \mathrm{tr}_E |\psi\rangle\langle\psi|$, where $|\psi\rangle$ is the state of the
universe. Diagonalization of the reduced density operator provides a basis

for the system. The importance of the basis states is given by the associated eigenvalues of the reduced density operator, which suggests a truncation scheme: keep those states as new basis states, which have the largest weight.

The problem is, of course, that we do not know $|\psi\rangle$ and that the environment is thermodynamically large. We simulate it now by the best approximation we have, namely using the block and site also as the environment. Calling the left and right blocks A and B, we obtain a (small) universe or superblock A••B, where the bullets stand for the individual sites. It is a chain of length $2\ell + 2$ for blocks of length ℓ. Of course, we can imagine this procedure also for chains where the left and right blocks are different, for instance, because the Hamiltonian is not translationally invariant. We grow both at the same time, one acting as the environment for the other one.

In general, states of the superblock A••B read

$$|\psi\rangle = \sum_{m_A \sigma_A \sigma_B m_B} \psi_{m_A \sigma_A \sigma_B m_B} |m_A\rangle |\sigma_A\rangle |\sigma_B\rangle |m_B\rangle \equiv \sum_{i_A j_B} \psi_{i_A j_B} |i_A\rangle |i_B\rangle, \qquad (1.19)$$

where $\{|\sigma_A\rangle\}$ are the states of the left single-site and $\{|\sigma_B\rangle\}$ those of the right one.

Let us assume that we are looking for the ground state of our universe. We approximate it by the ground state of the superblock, the nearest we get to the universe. Ground state $|\psi\rangle$ minimizes the energy

$$E = \frac{\langle\psi|\hat{H}_{A\bullet\bullet B}|\psi\rangle}{\langle\psi|\psi\rangle} \qquad (1.20)$$

with respect to the Hamiltonian of the superblock. By implementing the normalization via a Lagrangian multiplier, this minimization problem is turned into an eigenvalue problem

$$\hat{H}_{A\bullet\bullet B}|\psi\rangle - E_0|\psi\rangle = 0, \qquad (1.21)$$

where the Lagrangian multiplier E_0 is then the ground state energy of the superblock.

This is a large eigenvalue problem: in many cases, $D \approx 1000$, $d = 4$, and the vector dimension is $D^2 d^2 = 16 \times 10^6$ in this case. There is no way to solve it by one of the usual "direct" algorithms, which can deal with, say, up to dimension 10^5. In such a case, the only way of finding the ground state and its energy is via an iterative sparse matrix eigensolver, that is, the Lanczos or Jacobi-Davidson algorithms. This requires that the Hamiltonian $\hat{H}_{A\bullet\bullet B}$ can indeed be brought into sparse form, that is, if expressed as a matrix, only a very small fraction of the matrix elements are nonzero and we know their position. This then allows to carry out the basic and most costly operation of iterative sparse eigensolvers, the matrix-vector multiplication $\hat{H}_{A\bullet\bullet B}|\phi\rangle$ effectively. We will show that this is the case in a moment, and take it for granted now.

The reduced D-dimensional basis $\{|m_{A\bullet}\rangle\}$ of the new block A$\bullet$ is now determined by minimizing the distance between $|\psi\rangle$ and $|\tilde{\psi}\rangle$, the state $|\psi\rangle$ projected onto the new basis, in the 2-norm. One finds a result that can also be understood intuitively: we form the reduced density operator for A$\bullet$,

$$\hat{\rho}_{A\bullet} = \text{tr}_{\bullet B}|\psi\rangle\langle\psi|, \tag{1.22}$$

which in the untruncated product basis of A$\bullet$ has the matrix elements $(\rho_{A\bullet})_{ii'} = \sum_j \psi_{ij}\psi_{i'j}^*$. The reduced density matrix is hermitian, and can be diagonalized with real nonnegative eigenvalues, which sum to 1 for normalized $|\psi\rangle$; the eigenvectors form an orthonormal basis. The D retained basis vectors for A$\bullet$ are simply those eigenvectors that have the largest eigenvalues; in other words, we keep the states with the largest statistical weight. From a statistical physics perspective, this is very natural. B is grown at the same time by using the same procedure. Operators have to be transformed (approximately) into the new basis (bases), a point we will return to. This growth procedure is repeated until the superblock has reached the final size L, giving us an approximation to the ground state. Of course, L cannot reach the thermodynamic limit, but usually the relevant information can already be obtained from quite small L, say a (few) hundred sites.

Take $L = 100$ Hubbard sites. Then the complete basis has dimension $4^{100} \approx 1.6 \times 10^{60}$. If $D = 1000$, our final basis has dimension 1.6×10^7, about 10^{53} smaller. Why is DMRG so successful? One observes that, at least for one-dimensional translationally invariant chains, even for moderate D (say, a few hundred) the truncation error ε, the sum of the statistical weights of the discarded states is only 10^{-10} or even less at each growth step, such that the final wave function is indeed an excellent approximation to the true one. This is a consequence of the typically low entanglement of ground states of one-dimensional quantum systems, which we will briefly discuss in Chapter 2. In fact, it is numerically advantageous, perhaps a little bit more complicated to implement, not to use D in order to control the approximation, but rather to fix a small maximally allowed ε and choose D dynamically to meet this requirement. This ensures a more evenly distributed quality of local quantities and simplifies extrapolations in $\varepsilon \to 0$, the exact limit, if we run several DMRG runs at different ε. Most quantities can be extrapolated easily in $\varepsilon \to 0$ but not in D (where $D \to \infty$ would be exact).

Let us now look at the implementation of operators, in particular, also the Hamiltonian. For the moment, we ignore that the fermionic creation and annihilation operators carry a nontrivial sign that depends on the occupation of other sites and consider an operator $\hat{O}$ acting purely locally on site ℓ, with matrix elements $O^{\sigma_\ell, \sigma'_\ell} = \langle\sigma_\ell|\hat{O}_\ell|\sigma'_\ell\rangle$. ℓ is the site just being added into block A. When block A grows from $\ell - 1 \to \ell$ its matrix elements read in the new block basis

$$\langle m_\ell|\hat{O}|m'_\ell\rangle = \sum_{m_{\ell-1}, \sigma_\ell, \sigma'_\ell} \langle m_\ell|m_{\ell-1}\sigma_\ell\rangle\langle\sigma_\ell|\hat{O}|\sigma'_\ell\rangle\langle m_{\ell-1}\sigma'_\ell|m'_\ell\rangle. \tag{1.23}$$

Here, $\{|m_\ell\rangle\}$ and $\{|m_{\ell-1}\rangle\}$ are orthonormal bases of the blocks of length ℓ and $\ell-1$. Operators that were already part of block A, also need to be transformed:

$$\langle m_{\ell+1}|\hat{O}|m'_{\ell+1}\rangle = \sum_{m_\ell,m'_\ell\sigma_{\ell+1}} (\langle m_{\ell+1}|m_\ell\sigma_{\ell+1}\rangle$$
$$\times \langle m_\ell|\hat{O}|m'_\ell\rangle\langle m'_\ell\sigma_{\ell+1}|m'_{\ell+1}\rangle). \tag{1.24}$$

It is important to realize that the sum in Eq. (1.24) must be split as

$$\sum_{m_\ell\sigma_{\ell+1}} \left[\langle m_{\ell+1}|m_\ell\sigma_{\ell+1}\rangle \times \left(\sum_{m'_\ell} \langle m_\ell|\hat{O}|m'_\ell\rangle\langle m'_\ell\sigma_{\ell+1}|m'_{\ell+1}\rangle \right) \right], \tag{1.25}$$

reducing the calculational load from $O(D^4d)$ to $2O(D^3d)$. This is also typical of many other calculations in DMRG.

While the operators already in some block can be highly delocalized (in fact, the block basis is delocalized and the notion of locality becomes meaningless), the initial step presupposed a local operator acting on just one site (the site being added).

In Hamiltonians, operator products $\hat{O}\hat{P}$ occur, for instance, $\hat{c}^\dagger_{\uparrow i}\hat{c}_{i+1\uparrow}$ for the nearest-neighbor hopping of an up-spin electron. We can also imagine a longer-range term. Let us assume that i and $i+1$ will ultimately both be in block A. Let us ignore the fermionic sign for the moment. Then the correct way is to obtain a block expression for $\hat{c}^\dagger_{\uparrow i}$ as for the $\hat{O}$ discussed previously. When block A has incorporated site i, we have in the current block basis the matrix elements

$$\langle m_i|\hat{c}^\dagger_{\uparrow i}|m'_i\rangle \tag{1.26}$$

We now reach site $i+1$ at the next step (or after some steps in the case of a longer-ranged interaction). In the block-site basis $\hat{c}^\dagger_{i\uparrow}\hat{c}_{i+1\uparrow}$ is a product of matrix elements, which become, in the (new) block basis

$$\langle m_{i+1}|\hat{c}^\dagger_{i\uparrow}\hat{c}_{i+1\uparrow}|m'_{i+1}\rangle = \sum_{m_i,m'_i,\sigma_{i+1},\sigma'_{i+1}} (\langle m_{i+1}|m_i\sigma_{i+1}\rangle\langle m_i|\hat{c}^\dagger_{i\uparrow}|m'_i\rangle$$
$$\times \langle \sigma_{i+1}|\hat{c}_{i+1\uparrow}|\sigma'_{i+1}\rangle\langle m'_i\sigma'_{i+1}|m'_{i+1}\rangle). \tag{1.27}$$

In all further steps, this compound operator looks like a single-site operator. All this looks quite cumbersome, and the notation in the MPS language of Chapter 2 will be much simpler when being used to it.

For typical nearest-neighbor hopping/interaction Hamiltonians of condensed-matter physics, the Hamiltonian will then always be of the form

$$\hat{H} = \hat{H}_A + \hat{H}_{A\bullet} + \hat{H}_{\bullet\bullet} + \hat{H}_{\bullet B} + \hat{H}_B. \tag{1.28}$$

We see a first simplification, highly important for the use of the sparse matrix algorithms. Naively, with a vector dimension D^2d^2, a matrix-vector

multiplication would scale as the dimension squared, that is, D^4d^4. If we apply $\hat{H}$ in the form just given, it is in fact largely diagonal. The most expensive terms are the terms $\hat{H}_{A\bullet}$ and $\hat{H}_{\bullet B}$, which, however, are diagonal in the other block and site, respectively, such that the multiplication cost is only D^3d^3. Given that Dd is often a few thousand, this speed-up is already drastic. Even for next-nearest-neighbor hoppings/interactions, the cost remains the same. But we can do even better, by suitable bracketing of the multiplications as before, to turn this into two operations of cost D^3d^2 (which usually dominates) and D^2d^3.

In quantum chemistry (and of course in some applications in condensed-matter physics), we have much longer-ranged hoppings, for instance, due to two-operator terms $T_{ij}\hat{c}^\dagger_{is}\hat{c}_{js}$, where s gives the magnetization (spin). In this case, the matrix element can still be done as

$$\langle m_A\sigma_A\sigma_B m_B|\widehat{h}_{AB}|\psi\rangle = T_{ij}\sum_{m'_A}[\langle m_A|\widehat{c}^\dagger_{is}|m'_A\rangle$$
$$\times\left(\sum_{m'_B}\langle m_B|\widehat{c}_{js}|m'_B\rangle\langle m'_A\sigma_A\sigma_B m'_B|\psi\rangle\right)], \quad (1.29)$$

which is a sequence of two $O(D^3d^2)$ multiplications (instead of one naive $O(D^4d^2)$ calculation).

More complicatedly, we also have to consider terms like $V_{ijlk}\hat{c}^\dagger_{is}\hat{c}^\dagger_{js'}\hat{c}_{ks'}\hat{c}_{ls}$, which in condensed-matter physics usually show up when going to momentum space (with a suitable interpretation of the labels). In quantum chemistry, these terms are frequent and numerous (of the order L^4). There are, therefore, two questions: What is the cost of the "worst" contribution? Can we reduce the number of terms? Again, suitable bracketing of the sums along the lines given above reduces the cost to operations, which at worst scale as D^3d^2 (assuming $D\gg d$). The issue of reducing their number is somewhat trickier. The key idea was developed by Xiang (1996) in the context of momentum-space DMRG, but from a purely formal point of view (and ignoring the simplifications in a momentum-space Hamiltonian that come from momentum conservation) the challenge is the same as in quantum chemistry. We will postpone its discussion to the finite-system DMRG algorithm to put it into the most general perspective, but it will turn out that a factor L^2 can be gained.

In any case, the ultimate evaluation of expectation values is given at the end of the growth procedure as

$$\langle\psi|\hat{O}|\psi\rangle = \sum_{m_A m'_A \sigma_A\sigma_B m_B}\left(\langle\psi|m_A\sigma_A\sigma_B m_B\rangle\times\langle m_A|\hat{O}|m'_A\rangle\langle m'_A\sigma_A\sigma_B m_B|\psi\rangle\right). \quad (1.30)$$

Bracketing turns this into an operation of order $O(D^3d^2)$. Local operators that happen to be on one of the sites $\bullet$ can be evaluated even more efficiently (cost D^2d^3, with $D\gg d$).

Two very important aspects of practical implementations are still unresolved, but they are actually closely related: the use of quantum symmetries and the correct implementation of the fermionic signs. Typical symmetries are, apart from the spatial point groups (not so important in condensed-matter applications of DMRG) and mirror symmetries, mainly the Abelian $U(1)$ symmetries reflecting the conservation of total particle number and magnetization. In some cases, there is also non-Abelian $SU(2)$ spin symmetry, but its implementation is comparatively complicated; consult the specialist literature, such as Sierra and Nishino (1997), McCulloch and Gulacsi (2000, 2001, 2002), and Weichselbaum (2012). A huge range of these symmetries has been used successfully in numerous applications, with the most common ones being the two $U(1)$ symmetries of charge and magnetization conservation. In any case, the outcome is that the Hamiltonian matrixes will decompose into blocks with nonzero elements; the remaining parts can then be ignored in matrix-vector multiplications. The typical speed-up is another order of magnitude or even more; in the case of non-Abelian symmetries there are also important savings in the value of D (think about a $(2l + 1)$-fold degenerate angular momentum l, where instead of $2l + 1$ states $|l, m\rangle$ only one representative will suffice; in practice we find that D shrinks by a factor of 4 or 5 for systems with spin-$1/2$ electrons).

Let us discuss particle numbers, because they will lead us directly to the implementation of the fermionic sign. Because of their conservation, the total particle number, $\hat{N} = \sum_i \hat{n}_i$, commutes with the Hamiltonian, $[\hat{H}, \hat{N}] = 0$, such that eigenstates of $\hat{H}$ can be chosen to be eigenstates of $\hat{N}$. Assume we have N_ℓ particles in the chain when blocks are of size ℓ. If we manage to have that the block and site basis states have well-defined particle numbers (which we we show how to do further below), then $\psi_{m_A \sigma_A \sigma_B m_B} \neq 0$ only if $N(|m_A\rangle) + N(|\sigma_A\rangle) + N(|\sigma_B\rangle) + N(|m_B\rangle) = N_\ell$, as promised above, also leading to savings in memory.

Can this be achieved? In fact, this can be shown by recursion. Our computational basis states are eigenstates of particle number; hence we can build initial blocks A with basis states that are also such eigenstates. The block-site basis of A• has the same property, and we have to show that this also holds for the reduced basis formed from the eigenstates of the reduced density operator $\hat{\rho}_{A\bullet}$. If this is so, this property will hold throughout our calculations. We can show this by demonstrating that the reduced density matrix decomposes into blocks where all states in a block have the same particle number. As the blocks are diagonalized separately, the eigenstates will also have the (same) well-defined particle number. To see this, we consider $(\rho_{A\bullet})_{ii'} = \sum_j \psi_{ij} \psi_{i'j}^*$. The states $|i_A\rangle$ and $|j_B\rangle$ are particle number eigenstates, hence $N(|i_A\rangle) + N(|j_B\rangle) = N_\ell = N(|i_A'\rangle) + N(|j_B\rangle)$ or $N(|i_A\rangle) = N(|i_A'\rangle)$. Note that it may be convenient to let N_ℓ grow with ℓ, to maintain (for instance) half-filling.

So, when adding a site • to a block A, we can immediately give the correct fermionic sign to any local creation and annihilation operators, because for each state $|m_A\sigma_A\rangle$ we can say how many fermions come "before" the position on which the operators act, thus fix the sign. (Of course, if we have spin-up and spin-down locally on a single-site, we have to define an order of spin-up and spin-down as well, also influencing the fermionic sign).

1.3 Finite-system density matrix renormalization group

It is obvious that the idea of a small block modeling a thermodynamic embedding has its limitations, in particular, if the Hamiltonian is not translationally invariant (so that the superblock cannot "know" what will happen when it grows and "unexpected" new terms show up in the Hamiltonian, as will be the case in quantum chemistry) and/or if there is a competition between energetically close states such that there is a possibility that we start out with the wrong state and remain trapped there. Finite-system DMRG allows to improve the outcome of infinite-system DMRG iteratively, where the environment is now in all cases the true environment, if we take the chain of final size L to be the universe.

Finite-system DMRG (Fig. 1.2) continues the growth process of one of the two blocks (say block B) at the expense of the other block (here, then, block A) based on the same procedure: the ground state of the superblock (now asymmetric) gives the reduced density operator for •B, such that we can determine the truncated basis for the new block B by retaining the dominant eigenstates. At the same time, one site is peeled off block A (at its right end), such that block A becomes shorter. In the infinite-system algorithm, we have already determined a truncated basis for this smaller block, which
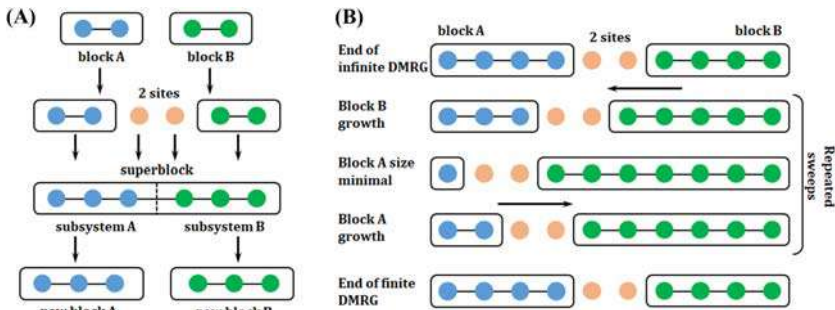
FIGURE 1.2 The left (A) and right (B) half of the figure present the iterations taken in the infinite-system and finite-system DMRG procedures respectively. In both cases, new blocks are formed from integrating a site into a block, with a state space truncation according to the density matrix prescription of DMRG. Whereas in the infinite-system version this growth happens on both sides of the chain, leading to chain growth, in the finite-system algorithm it happens only for one side at the expense of the other, leading to constant chain length.

we reuse. B grows at the expense of A until the left end of the chain is reached, where the growth direction is reversed: A now grows at the expense of B, and we reuse the earlier bases of the shrinking block B. When we reach the right end, the direction is reversed again. One pass through the chain is called a sweep. During the sweeping, we monitor convergence and stop when the energy converges or the changes in the wave function drop below some threshold. The reason why energy converges to a better value is that during sweeps we determine the bases of blocks A and B embedded in continuously improving environments (in fact, convergence analysis becomes much clearer in the MPS language).

In practice, the number of growth steps in the sweeps will always substantially exceed the number of growth steps in the infinite-system part, such that any improvement in performance is rewarding. As the large sparse eigensolver is particularly time-consuming, but iterative in nature, it is advantageous to have a good initial guess for the new ground state, following White (1996). In the finite-system algorithm, the ground states change during the sweeps, but not that much, in particular in the last sweeps before convergence. We can, therefore, use the result of the last step in a sweep as input for the next step. Of course, due to the shifted block-site-site-block structure, the last ground state must first be brought into the new basis. This is approximate in two ways: on the one hand, block plus site on the growing side are replaced by a block, on the other hand, on the shrinking side, we only have the states spanned by the old block, less than the site-block states after undoing a truncation. The approximate transformation of the result of the last step into the shifted A••B configuration is given for a sweep to the right A•→A and B→•B by the following transformations: With

$$
|\psi\rangle = \sum_{m_\ell \sigma_{\ell+1} \sigma_{\ell+2} m_{\ell+2}} \left(\psi_{m_\ell \sigma_{\ell+1} \sigma_{\ell+2} m_{\ell+2}} \times |m_\ell\rangle_A |\sigma_{\ell+1}\rangle |\sigma_{\ell+2}\rangle |m_{\ell+2}\rangle_B \right), \quad (1.31)
$$

where $|m_\ell\rangle_A$ and $|m_{\ell+2}\rangle_B$ are the block states for block A comprising sites 1 through ℓ and block B comprising sites $\ell + 3$ through L (the label of the block states is taken from the label of the bond their ends cut, labeling the bonds 1 through $L - 1$ from left to right) and a double insertion of an approximate identity $\hat{I} = \sum_{m_{\ell+1}} |m_{\ell+1}\rangle_{AA}\langle m_{\ell+1}|$ and $\hat{I} = \sum_{\sigma_{\ell+3} m_{\ell+3}} |\sigma_{\ell+3}\rangle |m_{\ell+3}\rangle_{BB}\langle m_{\ell+3}|\langle \sigma_{\ell+3}|$ we get

$$
|\psi\rangle = \sum_{m_{\ell+1} \sigma_{\ell+2} \sigma_{\ell+3} m_{\ell+3}} \left(\psi_{m_{\ell+1} \sigma_{\ell+2} \sigma_{\ell+3} m_{\ell+3}} \times |m_{\ell+1}\rangle_A |\sigma_{\ell+2}\rangle |\sigma_{\ell+3}\rangle |m_{\ell+3}\rangle_B \right), \quad (1.32)
$$

with

$$
\psi_{m_{\ell+1} \sigma_{\ell+2} \sigma_{\ell+3} m_{\ell+3}} = \sum_{m_\ell \sigma_{\ell+1} m_{\ell+2}} \left(\psi_{m_\ell \sigma_{\ell+1} \sigma_{\ell+2} m_{\ell+2}} \times \langle m_{\ell+1}| a_\ell \sigma_{\ell+1}\rangle \langle m_{\ell+3} \sigma_{\ell+3}| m_{\ell+2}\rangle \right).
$$

$$(1.33)$$

The basis transformations required in the last equation are all available from previous steps in the DMRG procedure. A similar operation can be carried out for a sweep to the left.

Another possible speed-up, which combines nicely with the prediction presented here, is to start with a relatively small basis dimension D and increase it during sweeps (or similarly, reduce the tolerated truncated weight ε). Then the algorithm does not spend too much time in those sweeps where the state is not yet very good and changes a lot, and goes to large bond dimensions for the almost converged states. When this prediction was invented, it took some ingenuity; as we will see, it is already present within the MPS formalism of Chapter 2. This is one example where a more adequate notation does a lot of work for us.

At this point, let us return to the issue of an efficient construction of an Hamiltonian. We already discussed how two-site operators such as in hopping terms can be built "on the fly" and also updated during the building of new blocks. During the finite-system DMRG, we also shrink blocks; as we do not want to (and need not to) reconstruct the expressions for the two-site operators for the shrunken blocks, we store them when they are built for a given block, to be reused later when a block shrinks back to that size. This means that we will store $O(L)$ versions of each (two-site) operator. In the most general case of long-range hopping (as is the case in quantum chemistry), where there are $O(L^2)$ two-site operators, this means storing $O(L^3)$ operators. This problem becomes even more pressing in the case of four-site operators as they appear in quantum chemistry: we have to store $O(L)$ versions of $O(L^4)$ such operators, that is, a staggering $O(L^5)$ such operators. For a matrix dimension D, total memory consumption would be $O(L^5 D^2)$ on disk for all blocks and $O(L^4 D^2)$ in RAM for the current block. At the same time, for each of the L steps of a sweep, calculation time would be of order $O(L^4 D^3)$, or $O(L^5 D^3)$ for the entire calculation, as each of these operators has to be applied to the state when calculating $H|\psi\rangle$. This sounds forbidding. Memory consumption as well as the associated calculation time can, however, be reduced drastically using a book-keeping first put forward by Xiang (1996) in the context of momentum-space DMRG where, formally, a short-ranged Hamiltonian in real-space becomes "long-ranged" in momentum space and contains numerous four-"site" operators. Let us consider the three possible operator distributions on blocks A and B (ignoring the somewhat simpler cases where up to two of the four operators sit on the sites ●●, but the procedure described below generalizes and becomes simpler in those cases):

(a) Four operators in one block (say 4 in A): Terms $V_{ijkl}\hat{c}_i^\dagger\hat{c}_j^\dagger\hat{c}_l\hat{c}_k$ (spin indices are absorbed into the notation, they do not change anything to the argument) are absorbed into a single block Hamiltonian operator during block growth. Assuming i, j, l are in the previous block and site k is added to form the current block, a representation of $\hat{c}_i^\dagger\hat{c}_j^\dagger\hat{c}_l$ in the previous block

basis allows to form $V_{ijkl} \times \hat{c}_i^\dagger \hat{c}_j^\dagger \hat{c}_l \times \hat{c}_k$ in the block plus site product basis, which is then transformed into the basis of the current block and added into the single block Hamiltonian operator. For L blocks, $O(L^3)$ representations each of $\hat{c}_i^\dagger \hat{c}_j^\dagger \hat{c}_l$ are necessary. These, in turn (and this is the important step) can be compounded into *complementary operators*

$$\hat{O}_k = \sum_{ijl} V_{ijkl} \hat{c}_i^\dagger \hat{c}_j^\dagger \hat{c}_l, \tag{1.34}$$

so that

$$\sum_{ijkl} V_{ijkl} \hat{c}_i^\dagger \hat{c}_j^\dagger \hat{c}_l \hat{c}_k \rightarrow \sum_k \hat{O}_k \hat{c}_k. \tag{1.35}$$

The complementary operators (effectively three-site operators) can be constructed as discussed for two-site operators, assuming the knowledge of two-operator terms $\hat{c}_i^\dagger \hat{c}_j^\dagger$. For L blocks, $O(L^2)$ of those exist, leading to memory consumption $O(L^3 D^2)$ on disk and $O(L^2 D^2)$ in RAM at each step.

(b) Three operators in one block, one in the other (say 3 in A, 1 in B): One applies the strategy of Eqs. (1.34) and (1.35), with $\hat{O}_l$ and $\hat{c}_l$ acting on different blocks.

(c) Two operators in a block, two in the other one: Again, the complementary operator technique can be applied, with the modification that each complementary operator living on block A has now *two* matching operators in B. A further class of complementary operators

$$\hat{O}_{kl} = \sum_{ij} V_{ijkl} \hat{c}_i^\dagger \hat{c}_j^\dagger \tag{1.36}$$

allows the simplification

$$\sum_{ijkl} V_{ijkl} \hat{c}_i^\dagger \hat{c}_j^\dagger \hat{c}_l \hat{c}_k \rightarrow \sum_{kl} \hat{O}_{kl} \hat{c}_l \hat{c}_k. \tag{1.37}$$

Memory consumption for the second type of complementary operator is $O(L^3 D^2)$ on disk and $O(L^2 D^2)$ in RAM. Taking all operator combinations together, global memory consumption is to leading order $O(L^3 D^2)$ on disk and $O(L^2 D^2)$ in RAM, which is a reduction by L^2 compared to the naive estimate in the beginning.

Using the complementary operator technique, calculation times are dominated by the terms under (c). In analogy to the construction of (a)-terms "on the fly" by generating the new terms of the sum, transforming them and adding them into the operator, the O_{kl} can be constructed at a computational expense of $O(L^3 D^2)$ for generating the L new terms to be added to each of the L^2 complementary operators with M^2 matrix elements each and $O(L^2 D^3)$ for transforming the L^2 operators into the current basis. Multiplying the

Hamiltonian to the state vector costs $O(L^2 D^3)$ time at each step (by arranging it as a sequence of two multiplications as in Eq. (1.29)) or $O(L^3 D^3)$ per sweep. Global calculation time per sweep is thus $O(L^3 D^3) + O(L^4 D^2)$, a reduction by L^2 for the dominant first term (typically, $D \gg L$ for the relevant DMRG applications). These reductions are absolutely crucial in making DMRG work for quantum chemistry problems; even with them, they present the major bottleneck in DMRG applications: L, the number of orbitals, will due to this bottleneck typically only be in the two-digit range, whereas L can easily be taken to 1000 or so for the short-ranged Hamiltonians of condensed-matter physics.

Let us conclude by reconsidering the growth and sweeping procedures. It is, of course, suggestive to use the maximum environment (a block plus a site), as we did (adding further single sites is numerically just very costly and takes us down the exponential road toward exact diagonalization)—but why should we not go the other way and reduce the number of sites from two to one (so we get A•B both in the growth and sweeping part)? In terms of statistical physics, the environment would be somewhat smaller, but on the other hand the numerical cost would go down by a factor of d (mainly in the large sparse eigensolver; for example, the application of $\hat{h}$ to a state in Eq. (1.29) would then lead to $O(D^3 d)$ operations), which for the Hubbard model would be 4. Algorithmically, this so-called *single-site DMRG* algorithm requires only minor modifications to the procedures just described. In fact, the single-site DMRG algorithm is the natural algorithm to emerge in the following Chapter, which presents algorithms based on matrix-product states. There are, however, obvious disadvantages to it, which is why it is not used in an unmodified form in the case of matrix-product states, either. In the infinite-system algorithm an obvious disadvantage is that superblock lengths oscillate between odd and even, which affects ground state properties in many translationally invariant condensed-matter Hamiltonians (but this would not matter so much in quantum chemistry); in the finite-system algorithm the question of the relative merits is much more interesting and will be discussed in the next Chapter. It will turn out that, if unmodified, the single-site algorithm prevents DMRG from finding the optimal distribution of the D block eigenstates among the total magnetization or number of particles of block states, such that the ground state search will not end up in the global minimum.

The preceding discussion has highlighted the fundamental ideas of DMRG, set up the basic algorithms for the search of ground states, and discussed where condensed-matter and quantum chemistry applications differ most in how they use DMRG. Of course, there are many details left out and the experience gained from by now certainly many thousands of papers using DMRG. For more on this, we refer to the comprehensive reviews of Schollwöck (2005) and Schollwöck (2011).

References

Bruus, H., Flensberg, K., 2004. Many-Body Quantum Theory in Condensed Matter Physics. Oxford University Press, Oxford.

Bulla, R., Costi, T.A., Pruschke, T., 2008. Numerical renormalization-group method for quantum impurity systems. Rev. Mod. Phys. 80, 395. Available from: https://doi.org/10.1103/RevModPhys.80.395.

Fetter, A.L., Walecka, J.D., 2003. Quantum theory of many-particle systems. Dover, Mineola, NY.

Krishna-murthy, H.R., Wilkins, J.W., Wilson, K.G., 1980. Renormalization-group approach to the Anderson model of dilute magnetic alloys. I. Static properties for the symmetric case. Phys. Rev. B 21, 1003. Available from: https://doi.org/10.1103/PhysRevB.21.1003.

McCulloch, I.P., Gulacsi, M., 2000. Density matrix renormalisation group method and symmetries of the Hamiltonian. Aust. J. Phys. 53, 597. Available from: https://doi.org/10.1071/PH00023.

McCulloch, I.P., Gulacsi, M., 2001. Total spin in the density matrix renormalization-group algorithm. Philos. Mag. Lett. 81, 447. Available from: https://doi.org/10.1080/09500830110040009.

McCulloch, I.P., Gulacsi, M., 2002. The non-Abelian density matrix renormalization-group algorithm. Europhys. Lett. 57, 852. Available from: https://doi.org/10.1209/epl/i2002-00393-0.

Schollwöck, U., 2005. The density-matrix renormalization-group. Rev. Mod. Phys. 77, 259. Available from: https://doi.org/10.1103/RevModPhys.77.259.

Schollwöck, U., 2011. The density-matrix renormalization-group in the age of matrix-product states. Ann. Phys. 326, 96. Available from: https://doi.org/10.1016/j.aop.2010.09.012.

Sierra, G., Nishino, T., 1997. The density matrix renormalization-group method applied to interaction round a face Hamiltonians. Nucl. Phys. B 495, 505. Available from: https://doi.org/10.1016/S0550-3213(97)00217-4.

Szabo, A., Ostlund, N.S., 1996. Modern quantum chemistry. Place: Dover, Mineola, NY.

Weichselbaum, A., 2012. Non-abelian symmetries in tensor networks: A quantum symmetry space approach. Ann. Phys. 327, 2972. Available from: https://doi.org/10.1016/j.aop.2012.07.009.

White, S.R., 1992. Density matrix formulation for quantum renormalization-groups. Phys. Rev. Lett. 69, 2863. Available from: https://doi.org/10.1103/PhysRevLett.69.2863.

White, S.R., 1993. Density-matrix algorithms for quantum renormalization-groups. Phys. Rev. B 48, 10345. Available from: https://doi.org/10.1103/PhysRevB.48.10345.

White, S.R., 1996. Spin Gaps in a Frustrated Heisenberg Model for CaV_4O_9. Phys. Rev. Lett. 77, 3633. Available from: https://doi.org/10.1103/PhysRevLett.77.3633.

Wilson, K.G., 1975. The renormalization group: Critical phenomena and the Kondo problem. Rev. Mod. Phys. 47, 773. Available from: https://doi.org/10.1103/RevModPhys.47.773.

Xiang, T., 1996. Density-matrix renormalization-group in momentum space. Phys. Rev. B 53, 10445. Available from: https://doi.org/10.1103/PhysRevB.53.R10445.

Chapter 2

Tensor network states: matrix product states and relatives

As in the previous chapter, let us look at wavefunctions of the type

$$|\psi\rangle = \sum_{\sigma_1 \sigma_2 \ldots \sigma_L} c_{\sigma_1 \sigma_2 \ldots \sigma_L} |\sigma_1\rangle \otimes |\sigma_2\rangle \otimes \ldots \otimes |\sigma_L\rangle \qquad (2.1)$$

in second quantization. At the moment, we make no assumption about an underlying structure, such as a specific lattice, we just have degrees of freedom. These might be localized electronic states on a lattice in condensed matter physics or delocalized orbitals in quantum chemistry. Again, we assume that $|\sigma_i\rangle$ is one of d different states (so we have d degrees of freedom). The exponential complexity of the many-body quantum state is hidden in the coefficients $c_{\sigma_1 \sigma_2 \ldots \sigma_L}$, of which there are d^L. One approach to make this problem tractable is to read the coefficients $c_{\sigma_1 \sigma_2 \ldots \sigma_L}$ as the entries of a a tensor of rank L, represented as in Fig. 2.1, and to decompose this high-rank tensor into low-rank tensors. (Historically this approach has been taken up much more in quantum chemisty than in physics.) The point of a decomposition into lower-rank tensors is that contraction schemes scale with the tensor ranks. For instance, the contraction of two vectors (rank 1) scales as d, when the indices run from 1 through d. The contraction of two matrices (rank 2) scales as d^3, if we contract over one index (i.e., perform a matrix multiplication). Ultimately, we want to replace a high-rank tensor by a number of (cheaper) contractions over many low-rank tensors. Yet, as such, this
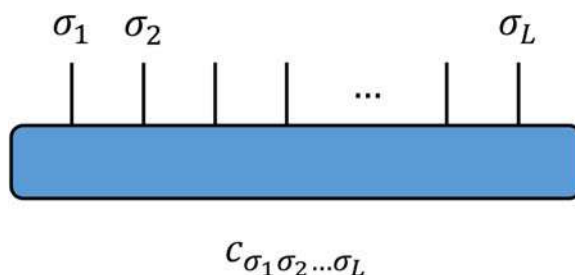
FIGURE 2.1   A high-rank tensor $c_{\sigma_1 \sigma_2 \ldots \sigma_L}$.

approach does not yet offer any computational advantage because such decompositions involves contractions over new indices which connect the various tensors, and these indices may run over very large ranges; it has to be combined with suitable approximation schemes, which curtail these ranges. We will proceed in two steps, first, we will discuss the possible decomposition schemes and second, we discuss the possible approximation schemes, which we work out for the most widely used (and least complex) decomposition scheme.

2.1 Tensor decompositions

A very simple approach is to think of the coefficients $c_{\sigma_1 \sigma_2 \ldots \sigma_L}$ as the entries of a (rectangular, not necessarily quadratic) matrix Ψ. Assuming that the $(\sigma_1 \ldots \sigma_\ell)$ and $(\sigma_{\ell+1} \ldots \sigma_L)$ are the multiindices of the rows and columns of Ψ, we can invoke a *singular value decomposition (SVD)* to replace the initial tensor by two tensors of lower rank.

2.1.1 Singular value decomposition

Singular value decompositions (SVDs) are among the most versatile tools of linear algebra. For an arbitrary matrix M of dimensions $(N_A \times N_B)$ SVD provides us with a decomposition

$$M = USV^\dagger, \tag{2.2}$$

where

- U is of dimension $(N_A \times \min(N_A, N_B))$ and has orthonormal columns (the *left singular vectors*), that is, $U^\dagger U = I$; if $N_A \leq N_B$, U is unitary, hence also $UU^\dagger = I$.
- S is of dimension $(\min(N_A, N_B) \times \min(N_A, N_B))$, diagonal with non-negative entries $S_{aa} \equiv s_a$. These are the so-called *singular values*. The number r of nonzero singular values is the *(Schmidt) rank* of M. In the following, we assume descending order: $s_1 \geq s_2 \geq \ldots \geq s_r > 0$.
- $V^\dagger$ is of dimension $(\min(N_A, N_B) \times N_B)$ and has orthonormal rows (the *right singular vectors*), that is, $V^\dagger V = I$. If $N_A \geq N_B$, V is unitary and also $VV^\dagger = I$.

This is schematically shown in Fig. 2.2.

FIGURE 2.2 Resulting matrix shapes from a singular value decomposition (SVD), corresponding to the two rectangular shapes that can occur. The singular value diagonal serves as a reminder that in $M = USV^\dagger$ S is purely non-negative diagonal.
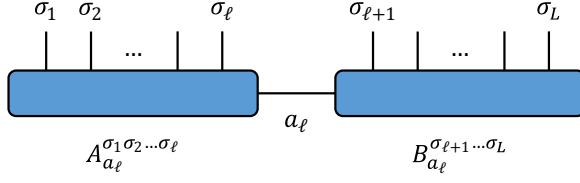
FIGURE 2.3 Decomposition of the high-rank tensor $c_{\sigma_1 \sigma_2 \dots \sigma_L}$ into two lower-rank tensors $A_{a_\ell}^{\sigma_1 \sigma_2 \dots \sigma_\ell}$ and $B_{a_\ell}^{\sigma_{\ell+1} \sigma_{\ell+2} \dots \sigma_L}$, which are contracted over the index a_ℓ. The decomposition is achieved by an SVD.

Applied to ψ, we obtain

$$\psi_{(\sigma_1 \dots \sigma_\ell),(\sigma_{\ell+1} \dots \sigma_L)} = \sum_{a_\ell} A_{a_\ell}^{\sigma_1 \dots \sigma_\ell} s_{a_\ell} \tilde{B}_{a_\ell}^{\sigma_{\ell+1} \dots \sigma_L} \equiv A_{a_\ell}^{\sigma_1 \dots \sigma_\ell} B_{a_\ell}^{\sigma_{\ell+1} \dots \sigma_L}, \qquad (2.3)$$

that is, two tensors of rank $\ell + 1$ and $L + 1 - \ell$ each, which are contracted over the "bond index" or "auxiliary index" a_ℓ. We have arbitrarily multiplied the singular values into the right tensor, but this is not mandatory. Note that the superscript vs. subscript notation does *not* imply contra- or covariant transformation properties. We just keep auxiliary "bond" indices as subscripts and physical indices as superscripts to keep them distinct. Graphically, we can represent the decomposition as in Fig. 2.3.

If we look at Eq. (2.3), we see that we have not really gained anything, as was already hinted at above: as the result of an SVD, a_ℓ runs over the same number of values as the smaller of the two multiindices. If we set $\ell = L/2$, we see that a_ℓ runs over $d^{L/2}$, that is, exponentially many values. *For a tensor decomposition to be useful, there must be a physical argument why we can restrict ourselves to a much smaller number of values and a method for identifying them.*

2.1.2 Frequently encountered tensor decompositions

Before we look at this problem, let us consider further tensor decompositions for a quantum state. Generically, they (or the states represented in this form) are called tensor network states (TNSs). In practice, they are not obtained by SVDs or higher-order generalizations. One rather writes down (often graphically) a structure that one believes to be relevant, uses this as an ansatz employed in some algorithm (like a ground-state search for a given Hamiltonian, or a time-evolution based on some Hamiltonian), which then determines the tensors.

A first class of such decompositions is shown in Fig. 2.4 (top); the first one (which can be obtained by a sequence of SVDs, chopping off one index after another starting with σ_1) provides us with a sequence of matrices $M_{a_{i-1} a_i}^{\sigma_i}$ (in reality rank-3 tensors, but we read the physical index as a matrix
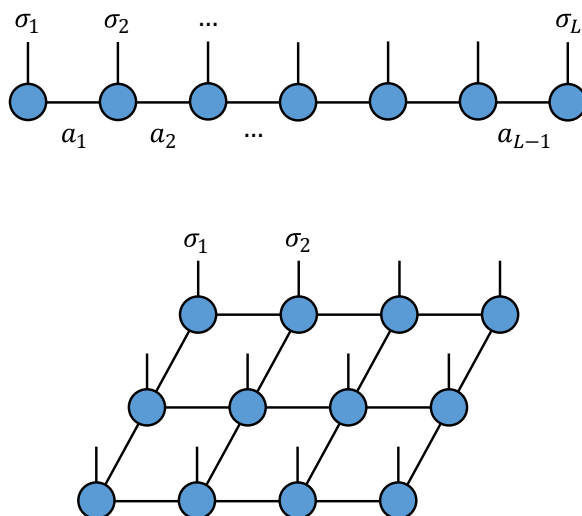
FIGURE 2.4 Frequently used decompositions of wave function coefficients I. *Top:* matrix product state (MPS), *bottom:* projected entangled-pair state (PEPS). Vertical legs correspond to physical degrees of freedom.

label), which are contracted over the bond indices a_i to give the coefficients of a quantum state. The convention is to draw the bonds horizontally and the physical indices vertically. This decomposition is called a matrix product state (MPS) and is the simplest and most widely used one. While the tensor networks discussed in the following all share the same type of operations carried out on them, they find there simplest and least cumbersome implementation for the MPS, which is why will focus on them later. The generalizations are usually conceptually straightforward, but much harder to implement from a purely practical perspective. MPS has a very long history in physics; after a long prehistory in statistical physics (Baxter (1982)'s well-known book on exactly solved models in statistical mechanics is essentially couched in terms of MPS-like structures; for early work see also, for instance, Baxter (1968)), they entered quantum physics through the work on the Affleck−Kennedy−Lieb−Tasaki model (Affleck et al., 1987, 1988) and its extensions (for important early work see, for instance, Fannes et al., 1989, 1992; Klümper et al., 1993). Their relationship to DMRG as invented by White (1992, 1993) was recognized early on by Ostlund and Rommer (1995), Nishino (1995), Dukelsky et al. (1998) and Takasaki et al. (1999). The insight that MPS opens the way to more powerful algorithms than DMRG because of some conceptual differences and clear notational advantages took hold around 2004, mainly in the context of the development of time-evolution methods (Vidal, 2003, 2004; Daley et al., 2004; Verstraete et al., 2004), see also Schollwöck (2005), and by the end of the first decade

of this millennium a panoply of algorithms for ground state searches, time evolution, and thermal physics had been developed, see Schollwöck (2011) and Paeckel et al. (2019) for reviews. The same mathematical structure was reinvented under the name of tensor trains (TTs) by Oseledets (2011) by which it seems to be more widely known in quantum chemistry.

The MPS decomposition is very reminiscent of a one-dimensional lattice where each $M^{\sigma_i}_{a_{i-1}a_i}$ corresponds to a local description of the wave function. This immediately suggests higher-dimensional generalizations adapted to the lattice structure. The second decomposition in Fig. 2.4 shows a PEPS (projected entangled-pair state) for a two-dimensional square lattice as introduced by Verstraete and Cirac (2004) (see also earlier work by Nishino et al. (2001), which at its time found not as much resonance). Further generalizations are immediately obvious; the rank of the tensors is $z + 1$, where z is the coordination number of the lattice; for the square lattice it is $4 + 1$. In quantum chemisty, PEPS-like decompositions are of reduced importance, because quantum chemistry problems usually are not blessed by the simple neighborhood notions of condensed matter problems.

Of more relevance in quantum chemistry is another decomposition, a TTNS (tree tensor network state), shown in Fig. 2.5 (top). Each tensor has
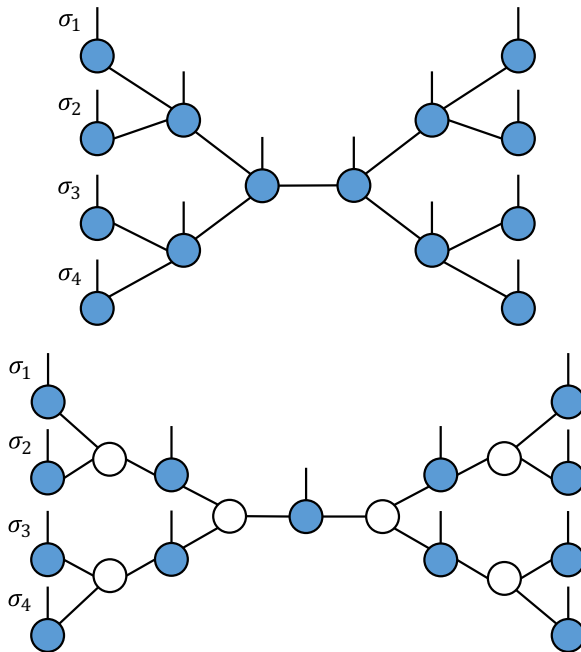
FIGURE 2.5 Frequently used decompositions of wave function coefficients II. *Top:* tree tensor network state (TTNS), *bottom:* three-legged tree tensor network state (T3NS). Vertical legs correspond to physical degrees of freedom.

one physical and three non-physical legs, formally a coodination number $z = 3$, which is between a one-dimensional and a two-dimensional system, but there is no clear interpretation of the structure as a lattice. These structures were pioneered by Shi et al. (2006) and Murg et al. (2010). We will return to discuss why this might be an interesting tensor network.

One can consider even more general tensor network states where some tensors contain *no* physical leg, as shown in Fig. 2.5 (bottom). This network is an extension of the TTNS: at the price of (roughly) doubling the number of tensors, the number of legs per tensor has gone down to three, either three auxiliary ones for auxiliary tensors (empty circles) or two auxiliary and a physical one for physical tensors (full circles), as before. This is, of course, motivated by the hope to trade expenses in contraction (which goes with the number of legs) for the number of tensors. This ansatz introduced by Gunst et al. (2018) is referred to as a three-legged tree tensor network state (T3NS).

We may wonder: (1) MPSs provide the simplest structure and are perfectly capable of representing any quantum state. Indeed, they are the most widely used TNSs; one can even identify the optimal contraction scheme. Why not just use them for any problem? The answer to this question is intimately related to quantum entanglement, which will also point us to a truncation scheme to reduce the index range of the bond indices. (2) Also, why might it make sense to propose a TTNS or T3NS which does not even match a lattice structure? The answer to this question points to subtle issues of numerical stability and conditioning (and algorithmic scaling).

2.2 Schmidt decomposition and quantum entanglement

We reconsider the application of a SVD to a pure quantum state $|\psi\rangle$ of the beginning of this Chapter. Let us group the sites (or orbitals) into two groups A and B. Typically, the sites of a group will be chosen to be adjacent in some sense, but there is no need for that. State $|\psi\rangle$ on AB can then be written as

$$|\psi\rangle = \sum_{ij} \psi_{ij} |i\rangle_A |j\rangle_B, \tag{2.4}$$

where $\{|i\rangle_A\}$ and $\{|j\rangle_B\}$ are arbitrary orthonormal bases of A and B with dimension N_A and N_B respectively. We call them *block bases* to distinguish them from the specific bases formed by the tensor products of the local bases. Again, we read the coefficients as entries of a matrix Ψ. From this representation we can derive the reduced density operators $\hat{\rho}_A = \text{tr}_B |\psi\rangle\langle\psi|$ and $\hat{\rho}_B = \text{tr}_A |\psi\rangle\langle\psi|$, which expressed with respect to the block bases take the matrix form

$$\rho_A = \Psi\Psi^\dagger, \quad \rho_B = \Psi^\dagger\Psi. \tag{2.5}$$

They can be diagonalized. Their eigenvalues are the weights given to the projectors on the associated eigenstates in the mixed state that describes the

state of A and B; in fact, this takes us directly back to the density matrix renormalization group. If we carry out instead an SVD of matrix $\Psi = USV^{\dagger}$ in Eq. (2.4), we obtain

$$
\begin{aligned}
|\psi\rangle &= \sum_{ij} \sum_{a=1}^{\min\,(N_A,N_B)} U_{ia}S_{aa}V_{ja}^{*}|i\rangle_A|j\rangle_B \\
&= \sum_{a=1}^{\min\,(N_A,N_B)} \left(\sum_i U_{ia}|i\rangle_A\right)s_a\left(\sum_j V_{ja}^{*}|j\rangle_B\right) \\
&= \sum_{a=1}^{\min(N_A,N_B)} s_a|a\rangle_A|a\rangle_B.
\end{aligned}
\tag{2.6}
$$

Due to the orthonormality properties of U and $V^{\dagger}$, the sets $\{|a\rangle_A\}$ and $\{|a\rangle_B\}$ are orthonormal and can be extended to be (new) orthonormal bases of A and B. Without any approximation, we can restrict the sum to run only over the $r \le \min\,(N_A, N_B)$ positive nonzero singular values. This yields the *Schmidt decomposition*

$$
|\psi\rangle = \sum_{a=1}^{r} s_a|a\rangle_A|a\rangle_B
\tag{2.7}
$$

which can be formulated for any state; no assumption was made. The s_a are then called the Schmidt coefficients. The Schmidt decomposition allows to read off explicit expressions for the reduced density operators for A and B introduced above very conveniently: carrying out the partial traces, one finds

$$
\hat{\rho}_A = \sum_{a=1}^{r} s_a^2|a\rangle_{A\,A}\langle a|, \qquad \hat{\rho}_B = \sum_{a=1}^{r} s_a^2|a\rangle_{B\,B}\langle a|,
\tag{2.8}
$$

showing that they share the non-vanishing part of the spectrum, but not the eigenstates (which makes sense, A and B are different parts of the system). The density matrix eigenvalues are the squares of the singular values, $w_a = s_a^2$, the respective eigenvectors are the left and right singular vectors.

We now look at the Schmidt decomposition in two different ways. It is a simple property of an SVD that the optimal approximation of a matrix $M = USV^{\dagger}$ (rank r) by a matrix M' (with rank $r' < r$) in the Frobenius norm $\|M\|_F^2 = \sum_{ij}|M_{ij}|^2$ (induced by the inner product $\langle M|N\rangle = \mathrm{tr}M^{\dagger}N$) is given by

$$
M' = US'V^{\dagger} \quad \text{with} \quad S' = \mathrm{diag}\,(s_1, s_2, \ldots, s_{r'}, 0, \ldots),
\tag{2.9}
$$

that is, one sets all but the first r' singular values in the SVD of M to be zero (and in numerical practice, will shrink the column dimension of U and the row dimension of $V^{\dagger}$ accordingly to r'). Now the distance between two matrices in the Frobenius norm corresponds to the distance between two

quantum states $|\psi\rangle$, $|\psi'\rangle$ in the 2-norm if we organize the state coefficients into matrices Ψ, Ψ' as before:

$$\| \, |\psi\rangle \, \|_2^2 = \sum_{ij} |\Psi_{ij}|^2 = \|\Psi\|_F^2. \tag{2.10}$$

(Note that this holds if and only if the sets $\{|i\rangle\}$ and $\{|j\rangle\}$ are orthonormal, which is the case here.) The optimal approximation to a quantum state $|\psi\rangle$ with r Schmidt coefficients by an (unnormalized) quantum state $|\psi'\rangle$ with r' Schmidt coefficients is therefore given by taking the Schmidt decomposition of $|\psi\rangle$, and only keep the r' largest singular values, setting the rest to zero,

$$| \, \tilde{\psi} \, \rangle = \sum_{a=1}^{r'} s_a |a\rangle_A |a\rangle_B, \tag{2.11}$$

$|\tilde{\psi}\rangle$ is then normalized to yield $|\psi'\rangle$. The corresponding restriction of the basis sizes for A and B makes this a numerically useful approximation. This truncation prescription (keep the largest singular values) is exactly equivalent to the DMRG truncation prescription (keep the largest density matrix eigenvalues).

An alternative way of looking at the Schmidt decomposition is to observe that the von Neumann entropy of the mixed states on A and B, well-known from statistical physics, can be read off directly from it,

$$\begin{aligned} S_A(|\psi\rangle) &= -\operatorname{tr}\hat{\rho}_A \log_2 \hat{\rho}_A \\ &= -\sum_{a=1}^{r} s_a^2 \log_2 s_a^2 \\ &= -\operatorname{tr}\hat{\rho}_B \log_2 \hat{\rho}_B = S_B(|\psi\rangle). \end{aligned} \tag{2.12}$$

Note that they are the same, whatever A and B are, because the von Neumann entropy only uses the squared singular values (density matrix eigenvalues). One possible way of quantifying quantum entanglement is now given by the "von Neumann entropy of entanglement", which is defined to be the usual statistical entropy of the subsystems A and B entangled with each other,

$$S_{A|B}(|\psi\rangle) = -\operatorname{tr}\hat{\rho}_A \log_2 \hat{\rho}_A = -\sum_{a=1}^{r} s_a^2 \log_2 s_a^2. \tag{2.13}$$

It is obvious that $r = 1$ corresponds to product states $|i\rangle_A |j\rangle_B$ (which also results from a single-determinant Hartree-Fock calculation) and $r > 1$ to entangled states. Entangled states, in the quantum chemistry language, are "beyond Hartree-Fock" and therefore of decisive interest.

A state can be well approximated if the spectrum $\{s_a\}$ decays rapidly, that is, if there are only very few singular values of appreciable size, so that the rest can be dismissed. This information is not so easily obtained and depends

on details. On the other hand, the von Neumann entropy of entanglement will also be low if the spectrum $\{s_a\}$ decays rapidly; so we can take entanglement as a proxy for the approximability of a quantum state in a restricted basis. (While this is not an exact statement, see Schuch et al. (2008), it is true for practical purposes; in quantum chemistry, only few of the mathematical statements derived rigorously in quantum physics are relevant, as they are not sufficiently generic.) In physics, a large number of results have been obtained on the entanglement in typical states. If we consider a bipartitioning A | B where AB is in the thermodynamic limit and A of size L^D, with D the spatial dimension, the so-called *area laws* (see Bekenstein, 1973; Srednicki, 1993; Callan and Wilczek, 1994; Plenio et al., 2005; Eisert et al., 2010) predict that for ground states of *short-ranged* Hamiltonians with a gap to excitations entanglement entropy is not extensive, but proportional to the surface, that is, $S(A|B) \sim L^{D-1}$, as opposed to thermal entropy. This implies $S \sim$ cst. in one dimension and $S \sim L$ in two dimensions. At criticality, a much richer structure emerges: in one dimension, $S = \frac{c+\bar{c}}{6}\log_2 L + k$, where c and $\bar{c}$ are the (an)holonomic central charges from conformal field theory (Vidal et al., 2003; Latorre et al., 2004); in two dimensions, bosonic systems seem to be insensitive to criticality (i.e., $S \propto L$), see Srednicki (1993) and Barthel et al. (2006), whereas fermionic systems get a logarithmic correction $S \propto L\log_2 L$ for a one-dimensional Fermi surface (with a prefactor proportional to its size), but seem to grow only sublogarithmically if the Fermi surface consists of points (Barthel et al., 2006; Gioev and Klich, 2006). It should be emphasized that these properties of ground states are highly unusual: in the thermodynamic limit, a random state out of Hilbert space will indeed show extensive entanglement entropy with probability 1. Between two D-dimensional state spaces for A and B, the maximal entanglement is $\log_2 D$ in the case where all eigenvalues of ρ_A are identical and D^{-1} (such that ρ_A is maximally mixed); meaning that one needs a state of dimension 2^S and more to encode entanglement S properly. This implies that for gapped systems in one dimension an increase in system size will not lead to a strong increase in the required D; in two dimensions, $D \sim 2^L$, such that the compression of a quantum state as indicated by an SVD will fail even for relatively small system sizes, as resources have to grow exponentially (this however does not exclude very precise results for small two-dimensional clusters or quite large stripes). Obviously, this argument implicitly makes the cavalier assumption that the eigenvalue spectrum is close to flat, which leads to maximal entanglement, such that an approximate estimation of D can be made. In practice, the spectrum is dictated by the problem and indeed far from flat: it is in fact usually exponentially decaying. But numerically, it turns out that for standard problems in physics the scaling of the resource D is predicted correctly on the qualitative level.

From the perspective of quantum chemistry, the discussion of entanglement presents itself in a different way. First, quantum chemistry Hamiltonians are usually inherently long-ranged in the sense that the underlying basis states of

chemistry are often highly delocalized which means that the Coulomb interaction makes all orbitals "talk" to all other ones. Unlike in a crystalline solid, there is no obvious notion of neighborhood. This means that most of the physicists' insights about entanglement are not very relevant as they rely on short-rangedness. Second, there is a different notion of neighborhood which is somehow implicit in physics and which was first put to use by Legeza and Solyom (2003) [for many illustrative examples, see also Szalay et al. (2015)]: one considers single orbitals i, j as A (and all $L - 1$ other orbitals as B), such that one can define entanglement entropies S_i and S_j. Considering both orbitals i and j together as A (and all $L - 2$ other orbitals as B), gives an entanglement entropy S_{ij}. The *mutual information* $I_{ij} := S_i + S_j - S_{ij}$ is then a measure how close neighbors i and j are in terms of the quantum state considered. Numerically, it turns out to be advantageous to keep such orbitals close to each other, so that no cut A|B leads to more entanglement than necessary. In physics, this is simply done by mapping the lattice to the graph of the tensor network. In quantum chemistry, the mutual information between pairs of orbitals usually generates a much more complex pattern of connectivity, and one can use elaborate schemes, for instance the analysis of the Fiedler vector, to reorder orbitals such that it is as localized as possible (see Legeza and Solyom, 2003). This approach of course requires that a low-accuracy calculation (in a sense to be explained below) at low cost gives us the necessary information to carry out the expensive high-accuracy calculation with optimally arranged orbitals. Finally, the fact that quantum chemistry Hamiltonians are usually much more complex than those of condensed matter physics means that quite a lot of algorithmic complication comes from the expensive representation of the Hamiltonian in tensor network language, rather than the state itself.

2.3 Matrix product state

2.3.1 Building matrix product state

The generic form of a matrix product state, as shown in Fig. 2.4, is

$$|\psi\rangle = \sum_{\sigma_1 \ldots \sigma_L} M_{1,a_1}^{\sigma_1} \ldots M_{a_{L-1},1}^{\sigma_L} |\sigma_1\rangle \otimes \ldots \otimes |\sigma_L\rangle \qquad (2.14)$$

The tensors are contracted over all auxiliary legs.

Even an approximate MPS is still a linear combination of all states of the Hilbert space, no product basis state has been discarded. The limiting constraint is rather on the form of the linear combinations: instead of d^L coefficients, dL matrices of dimension $(D \times D)$ with a matrix-valued normalization constraint that gives LD^2 scalar constraints have $(d-1)LD^2$ independent parameters only, generating interdependencies of the coefficients of the state. (Note that we ignore that the first and last matrix are in fact vectors, as they have only one auxiliary leg to the right or left.) The quality of the optimal

approximation of any quantum state by an MPS with fixed matrix dimensions ($D \times D$) will improve monotonically with D: take $D < D'$, then the best approximation possible for D can be written as an MPS with D' with ($D \times D$) submatrices in the ($D' \times D'$) matrices and all additional rows and columns zero. They give further parameters for improvement of the state approximation.

Given $|\psi\rangle$ via coefficients $c^{\sigma_1 \sigma_2 \cdots \sigma_L}$, the exact representation of $|\psi\rangle$ by an MPS is not unique. There are multiple gauge degrees of freedom in this representation, for each pair of sets of adjacent matrices independently. Consider two such sets $\{M^{\sigma_i}\}$ and $\{M^{\sigma_{i+1}}\}$. They must have the same number D of columns (for site i) and rows (for site $i + 1$) respectively. Take now *any* invertible ($D \times D$)-dimensional matrix X and insert $1 = XX^{-1}$ at the link between sites i and $i + 1$. The state is unchanged, and you can absorb X into the matrices as

$$M^{\sigma_i} \to M^{\sigma_i} X, \quad M^{\sigma_{i+1}} \to X^{-1} M^{\sigma_{i+1}} \tag{2.15}$$

The gauge degrees of freedom are crucially important, mainly for two reasons. (1) Certain iterative procedures to build MPS automatically choose a particular choice of gauge (or, in fact, one out of two), which we will call left-canonical and right-canonical. (2) These particular gauges present huge numerical advantages in actual computations so are always enforced.

Imagine you are considering a polymer, modeled by a Pariser-Parr-Pople (PPP) model. We have a one-dimensional sequence of building units (which we call sites); each of them has the same d electronic degrees of freedom. If we increase the polymer length by one site, $\ell - 1 \to \ell$, as illustrated in Fig. 2.6, the Hilbert space grows by a factor of d, which leads to the well-known exponential growth. Imagine now that some insight has provided you with a Hilbert space of dimension D which contains the relevant degrees of freedom for describing the polymer of length $\ell - 1$ - we call this polymer "left block A" to connect to our language used above. The orthonormal basis states are $\{|a_{\ell-1}\rangle_A\}$; hence there is a Dd-dimensional basis of the polymer of length ℓ, $\{|a_{\ell-1}\rangle_A \otimes |\sigma_\ell\rangle\}$. Now imagine once again that there is some insight which allows you to truncate this basis to only D states $\{|a_\ell\rangle_A\}$. Entirely independent of the insight, we have

$$|a_\ell\rangle_A = \sum_{a_{\ell-1}\sigma_\ell} {}_A\langle a_{\ell-1}\sigma_\ell | a_\ell\rangle_A |a_{\ell-1}\rangle_A |\sigma_\ell\rangle \tag{2.16}$$
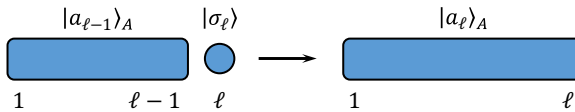
FIGURE 2.6 A block of length $\ell - 1$ is grown towards the right to a block of length ℓ by adding a site ℓ.

for these states. To make contact to the MPS notation, we introduce at site ℓ d matrices A^{σ_ℓ} of dimension $(D \times D)$ each, one for each possible local state $|\sigma_\ell\rangle$, such that Eq. (2.16) becomes

$$|a_\ell\rangle_A = \sum_{a_{\ell-1}\sigma_\ell} A^{\sigma_\ell}_{a_{\ell-1},a_\ell} |a_{\ell-1}\rangle_A |\sigma_\ell\rangle \qquad (2.17)$$

where the elements of the matrices A^{σ_ℓ} are given by (see Fig. 2.7).

$$A^{\sigma_\ell}_{a_{\ell-1},a_\ell} \equiv {}_A\langle a_{\ell-1}\sigma_\ell|a_\ell\rangle_A. \qquad (2.18)$$

Now the $\{|a_{\ell-1}\rangle_A\}$ can be expressed in the same way by the $\{|a_{\ell-2}\rangle_A\}$ and $|\sigma_{\ell-1}\rangle$. Going all the way back to a polymer of length 1, we have

$$|a_\ell\rangle_A = \sum_{a_1,a_2,\ldots,a_{\ell-1}} \sum_{\sigma_1,\sigma_2,\ldots,\sigma_\ell} A^{\sigma_1}_{1,a_1} A^{\sigma_2}_{a_1,a_2} \ldots A^{\sigma_\ell}_{a_{\ell-1},a_\ell} |\sigma_1\rangle|\sigma_2\rangle \ldots |\sigma_\ell\rangle$$

$$= \sum_{\sigma_i \in A} (A^{\sigma_1} A^{\sigma_2} \ldots A^{\sigma_\ell})_{1,a_\ell} |\sigma_1\rangle|\sigma_2\rangle \ldots |\sigma_\ell\rangle, \qquad (2.19)$$

where i runs through all the sites of block A. This construction looks as in Fig. 2.8 with the rule that all connected legs are summed over (contracted).

Similarly, we can build blocks (which we call B) to grow towards the left instead of to the right (Fig. 2.9). Ultimately we get

$$|a_\ell\rangle_B = \sum_{\sigma_i \in B} (B^{\sigma_{\ell+1}} \ldots B^{\sigma_L})_{a_{\ell+1},1} |\sigma_{\ell+1}\rangle \ldots |\sigma_L\rangle, \qquad (2.20)$$

where i runs from $\ell + 1$ to L, the sites of block B. (Note that we label block states according to the bond at which they terminate: bond ℓ connects sites ℓ and $\ell + 1$, where block B contains site $\ell + 1$.)
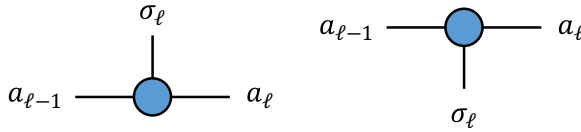
FIGURE 2.7   Graphical representation of general MPS-matrices M: the left diagram represents $M^{\sigma_\ell}_{a_{\ell-1},a_\ell}$, the right diagram the *conjugate* $M^{\sigma_\ell*}_{a_{\ell-1},a_\ell}$. The solid circle represents the lattice sites, the vertical line the physical index, the horizontal lines the matrix indices.
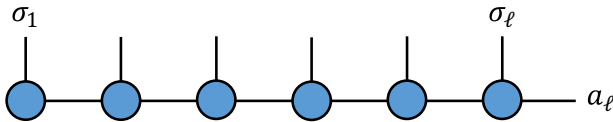
FIGURE 2.8   Graphical representation of the recursive construction of a state $|a_\ell\rangle$ by contraction (multiplication) of A-matrices. Contractions run over all connected legs.
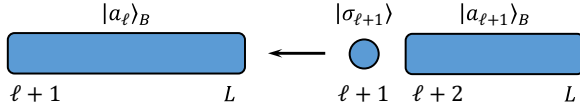
FIGURE 2.9 A block B of length $L - \ell - 1$ is grown towards the left to a block B of length $L - \ell$ by adding site $\ell + 1$.
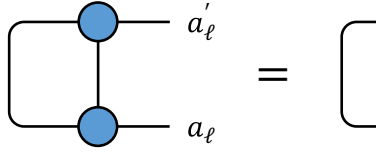
FIGURE 2.10 If two *left*-normalized *A*-matrices are contracted over their *left* index and the physical indices, a $\delta_{a'_\ell,a_\ell}$ line results. Similarly, if two *right*-normalized *B*-matrices are contracted over their *right* index and the physical indices, a $\delta_{a'_\ell,a_\ell}$ line results (no picture).

As we demand that all bases are orthonormal bases, the construction imposes conditions on the *A*- and *B*-matrices, namely

$$\sum_\sigma A^{\sigma\dagger} A^\sigma = I \qquad (\text{left} - \text{normalized}) \qquad (2.21)$$

and

$$\sum_\sigma B^\sigma B^{\sigma\dagger} = I \qquad (\text{right} - \text{normalized}) \qquad (2.22)$$

This follows from Eq. (2.17)

$$
\begin{aligned}
\delta_{a'_\ell,a_\ell} &= {}_A\langle a'_\ell | a_\ell \rangle_A \\
&= \sum_{\sigma'_\ell,\sigma_\ell} \sum_{a'_{\ell-1},a_{\ell-1}} A^{\sigma'_\ell *}_{a'_{\ell-1},a'_\ell} A^{\sigma_\ell}_{a_{\ell-1},a_\ell} \quad {}_A\langle a'_{\ell-1}\sigma'_\ell | a_{\ell-1}\sigma_\ell \rangle_A \\
&= \sum_{\sigma_\ell} \sum_{a_{\ell-1}} A^{\sigma_\ell\dagger}_{a'_\ell,a_{\ell-1}} A^{\sigma_\ell}_{a_{\ell-1},a_\ell} \\
&= \sum_{\sigma_\ell} (A^{\sigma_\ell\dagger} A^{\sigma_\ell})_{a'_\ell,a_\ell}.
\end{aligned}
\qquad (2.23)
$$

A graphical representation is provided in Fig. 2.10. The multiplication can also be interpreted as the contraction of *A* (*B*) and *A** (*B**) over both σ and their left (right) index.

If we put together a polymer of length *L* from a block A of length ℓ (units 1 to ℓ) and a block B of length $L - \ell$ (units $\ell + 1$ to *L*), within our basis

truncations the most general state reads

$$
\begin{aligned}
|\psi\rangle &= \sum_{a_\ell, a'_\ell} \psi_{a_\ell, a'_\ell} |a_\ell\rangle_A |a'_\ell\rangle_B \\
&= \sum_\sigma (A^{\sigma_1} \dots A^{\sigma_\ell})_{1, a_\ell} \psi_{a_\ell, a'_\ell} (B^{\sigma_{\ell+1}} \dots B^{\sigma_L})_{a'_\ell, 1} |\sigma\rangle
\end{aligned}
\tag{2.24}
$$

with $|\sigma\rangle \equiv |\sigma_1, \sigma_2, \dots, \sigma_L\rangle$ or even simpler

$$
|\psi\rangle = \sum_\sigma A^{\sigma_1} \dots A^{\sigma_\ell} \Psi B^{\sigma_{\ell+1}} \dots B^{\sigma_L} |\sigma\rangle.
\tag{2.25}
$$

If we multiply Ψ either into the adjacent A- or B-matrices, we arrive at an MPS as introduced before, but in a somewhat peculiar form, a so-called *mixed-canonical MPS*,

$$
|\psi\rangle = \sum_\sigma A^{\sigma_1} \dots A^{\sigma_\ell} M^{\sigma_{\ell+1}} B^{\sigma_{\ell+2}} \dots B^{\sigma_L} |\sigma\rangle.
\tag{2.26}
$$

where here Ψ has been multiplied to the adjacent B-matrices. In a mixed-canonical MPS, we have a sequence of A-matrices, then on one site, which is called the *orthogonality center*, a general M-matrix, followed by a sequence of B-matrices. This concoction looks a bit weird (why not make all matrices of the A- or B-type?) but in fact is the numerically useful and practical one.

One advantage of this representation is that we can immediately relate to our earlier discussion of the Schmidt decomposition. In Eq. (2.25), carrying out the sums over all σ^i and multiplying all matrices together, except the two multiplications involving Ψ, gives a state

$$
|\psi\rangle = \sum_{a_\ell, a'_\ell} \Psi_{a_\ell, a'_\ell} |a_\ell\rangle_A |a'_\ell\rangle_B,
\tag{2.27}
$$

where the states on the right form orthonormal sets. An SVD on $\Psi_{a_\ell, a'_\ell} = USV^\dagger$ puts this into the form of a Schmidt decomposition; multiplying U and $V^\dagger$ into the adjacent A and B-matrices does not change orthonormality. We can therefore immediately identify the best truncation of matrix dimensions at bond ℓ from S, and also identify the size of the error incurred. This argument can in fact be generalized from the approximation incurred by a single truncation to that incurred by $L-1$ truncations, one at each bond, to reveal that the error is at worst (Verstraete and Cirac, 2006).

$$
\| |\psi\rangle - |\psi_{\text{trunc}}\rangle \|_2^2 \leq 2 \sum_{i=1}^{L} \varepsilon_i(D),
\tag{2.28}
$$

where $\varepsilon_i(D)$ is the truncation error (sum of discarded squared singular values) at bond i incurred by truncating down to the leading D singular values from an exact representation of the state.

2.3.2 Overlaps, expectation values and matrix elements

Let us now turn to operations with MPS, beginning with the calculation of overlaps and expectation values. We consider an overlap between states $|\psi\rangle$ and $|\phi\rangle$, described by matrices M and $\tilde{M}$, and focus on open boundary conditions.

Taking the adjoint of $|\phi\rangle$, and considering that the wave function coefficients are scalars, the overlap reads

$$\langle\phi|\psi\rangle = \sum_\sigma \tilde{M}^{\sigma_1*}\dots\tilde{M}^{\sigma_L*}M^{\sigma_1}\dots M^{\sigma_L}. \tag{2.29}$$

Transposing the scalar formed from the $\tilde{M}\dots\tilde{M}$ (which is the identity operation), we arrive at adjoints with reversed ordering:

$$\langle\phi|\psi\rangle = \sum_\sigma \tilde{M}^{\sigma_L\dagger}\dots\tilde{M}^{\sigma_1\dagger}M^{\sigma_1}\dots M^{\sigma_L}. \tag{2.30}$$

In a pictorial representation (Fig. 2.11), this calculation becomes much simpler, if we follow the rule that all bond lines are summed over. To evaluate the above expressions most efficiently we arrange them as

$$\langle\phi|\psi\rangle = \sum_{\sigma_L}\tilde{M}^{\sigma_L\dagger}\left(\dots\left(\sum_{\sigma_1}\tilde{M}^{\sigma_1\dagger}M^{\sigma_1}\right)\dots\right)M^{\sigma_L} \tag{2.31}$$

which we evaluate from inside to outside. From the second step onwards the complexity does not grow anymore. Matrix multiplications ABC are done efficiently as $(AB)C$ or $A(BC)$. Then we are carrying out $(2L-1)d$ multiplications, each of which is of complexity $O(D^3)$. The total operation count is weakly polynomially complex, namely $O(LD^3d)$. One can show that fully left- or right-normalized states are automatically normalized to 1.

Consider $\langle\phi|\otimes_i\hat{O}^{[i]}|\psi\rangle$, tensored operators acting on individual sites i. In practice, all except one or two of these operators will be identity operators,
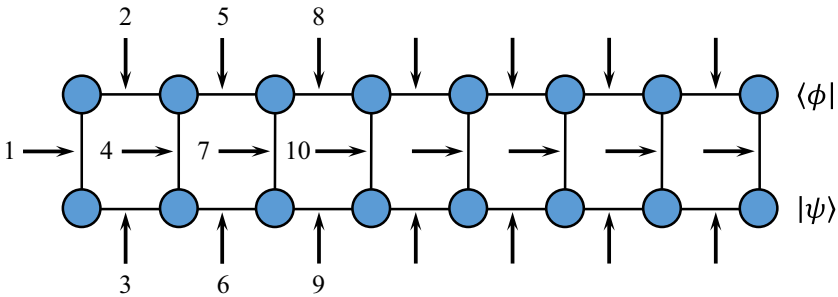
FIGURE 2.11 Overlap between two states $|\phi\rangle$ and $|\psi\rangle$ with indication of the optimal sequence of contractions, running like a zipper through the chain.
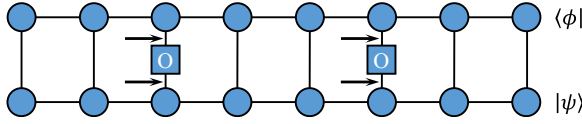
FIGURE 2.12 Matrix elements between two states $|\phi\rangle$ and $|\psi\rangle$ are calculated like the overlap, with the operators inserted at the right places, generating a double sum of physical indices there, as indicated by the arrows.

as one is mainly concerned with the calculation of local expectation values or two-site correlators. We adapt the previous calculation of overlaps of inserting the operators at the appropriate places and turn the single sums over σ_i into double sums over σ_i, σ_i' where there is no identity:

$$\sum_{\sigma,\sigma'} \tilde{M}^{\sigma_1*} \ldots \tilde{M}^{\sigma_L*} O^{\sigma_1,\sigma_1'} \cdots O^{\sigma_L,\sigma_L'} M^{\sigma_1'} \ldots M^{\sigma_L'}$$

$$= \sum_{\sigma_L,\sigma_L'} O^{\sigma_L,\sigma_L'} \tilde{M}^{\sigma_L \dagger} \left(\cdots \left(\sum_{\sigma_1,\sigma_1'} O^{\sigma_1,\sigma_1'} \tilde{M}^{\sigma_1 \dagger} M^{\sigma_1'} \right) \cdots \right) M^{\sigma_L'}$$

This amounts to the same calculation as for the overlap, with the exception that formally the single sum over the physical index turns into a double sum (Fig. 2.12). The operational count is then roughly $O(LD^3 d)$ again, because operations $O(d^2)$ occur only on the one or two sites with a non-trivial operator.

2.3.3 Adding two matrix product states

For MPSs

$$|\psi\rangle = \sum_{\sigma} M^{\sigma_1} \ldots M^{\sigma_L} |\sigma\rangle, \quad |\phi\rangle = \sum_{\sigma} \tilde{M}^{\sigma_1} \ldots \tilde{M}^{\sigma_L} |\sigma\rangle \qquad (2.32)$$

we can write down

$$|\psi\rangle + |\phi\rangle = \sum_{\sigma} N^{\sigma_1} \ldots N^{\sigma_L} |\sigma\rangle \qquad (2.33)$$

where

$$N^{\sigma_i} = M^{\sigma_i} \oplus \tilde{M}^{\sigma_i}. \qquad (2.34)$$

except on sites 1 and L, where the matrices degenerate into row and column vectors. They are correctly treated by forming a row vector $[M \ \tilde{M}]$ and a column vector $[M \ \tilde{M}]^T$ on the last sites, from the row and column vectors of the original states. Addition of MPS leads to new matrices with dimension $D_N = D_M + D_{\tilde{M}}$, such that MPS of a certain dimension are not closed under addition. Often the increase in matrix size is wasteful, as the states may share local basis states. So after additions it is worthwhile to consider *compressing* the MPS again to some lower dimension, at possibly very little loss of information.

2.3.4 Bringing a matrix product state into canonical form

For a general matrix product state, no particular demands are placed on the matrices M^{σ_i} except that their dimensions must match appropriately. Certain classes of matrices are to be preferred, namely left- and right-normalized matrices, leading to left- and right-canonical MPS: certain contractions become trivial, orthonormal reduced bases are generated automatically.

In order to bring an arbitrary MPS to canonical form we exploit that SVD generates either unitary matrices or matrices with orthonormal rows and columns which can be shown to obey the left- or right normalization condition.

2.3.4.1 Generation of a left-canonical MPS

Setting out from a general MPS, without normalization assumption, making the contractions explicit,

$$|\psi\rangle = \sum_\sigma \sum_{a_1,\ldots} M^{\sigma_1}_{1,a_1} M^{\sigma_2}_{a_1,a_2} M^{\sigma_3}_{a_2,a_3} \ldots |\sigma\rangle \tag{2.35}$$

we reshape $M^{\sigma_1}_{1,a_1}$ by grouping physical and left (row) index to carry out an SVD on the new M, yielding $M = ASV^\dagger$:

$$\sum_\sigma \sum_{a_1,\ldots} M_{(\sigma_1,1),a_1} M^{\sigma_2}_{a_1,a_2} M^{\sigma_3}_{a_2,a_3} \ldots |\sigma\rangle$$

$$= \sum_\sigma \sum_{a_1,\ldots} \sum_{s_1} A_{(\sigma_1,1),s_1} S_{s_1,s_1} V^\dagger_{s_1,a_1} M^{\sigma_2}_{a_1,a_2} \ldots |\sigma\rangle$$

$$= \sum_\sigma \sum_{a_2,\ldots} \sum_{s_1} A^{\sigma_1}_{1,s_1} \left(\sum_{a_1} S_{s_1,s_1} V^\dagger_{s_1,a_1} M^{\sigma_2}_{a_1,a_2} \right) M^{\sigma_3}_{a_2,a_3} \ldots |\sigma\rangle$$

$$= \sum_\sigma \sum_{a_2,\ldots} \sum_{s_1} A^{\sigma_1}_{1,s_1} \tilde{M}^{\sigma_2}_{s_1,a_2} M^{\sigma_3}_{a_2,a_3} \ldots |\sigma\rangle. \tag{2.36}$$

As $A^\dagger A = I$ due to SVD, after reshaping to A^{σ_1}, left-normalization holds for A^{σ_1}. The remaining two matrices of the SVD are multiplied into M^{σ_2}, such that a new MPS with $\tilde{M}^{\sigma_2}_{s_1,a_2} = \sum_{a_1} S_{s_1,s_1} V^\dagger_{s_1,a_1} M^{\sigma_2}_{a_1,a_2}$ is generated.

Now the procedure can be iterated: $\tilde{M}^{\sigma_2}_{s_1,a_2}$ is reshaped to $\tilde{M}_{(\sigma_2,s_1),a_2}$ (Fig. 2.13), singular value decomposed as $ASV^\dagger$, generating $A_{(\sigma_2,s_1),s_2}$, reshaped to a left-normalized $A^{\sigma_2}_{s_1,s_2}$. The right two matrices of the SVD are again multiplied into the
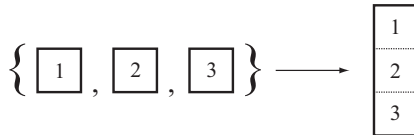
FIGURE 2.13 For canonization, sets of matrices on a given site are brought together in a single matrix.

next ansatz matrix, and so forth. After the last step, left-normalized matrices $A_{s_{i-1},s_i}^{\sigma_i}$ live on all sites. $S_{1,1}(V^\dagger)_{1,1}$, a scalar as A^{σ_L} is a column vector, survive at the last site, but this scalar is nothing but the norm of $|\psi\rangle$. We may keep it separately if we want to work with non-normalized states.

The same argumentation holds also for the generation of a right-canonical MPS, where we start from the right. We observe that if we have, say, a right-canonical MPS *BBBBBBBBB* and start to turn it into a left-canonical one starting from the left end, we have at all times a mixed-canonical MPS *AAAAMBBBB*, depending on how far we have progressed. Each iteration of the procedure shifts the orthogonality center by one, which will be a very useful building block for the ground state search algorithm.

2.3.5 Approximate compression of an MPS

Many operations on MPS (like applying operators) may lead to a (substantial) increase in MPS matrix dimensions, so it becomes necessary to approximate optimally a given MPS with matrix dimensions ($D_i' \times D_{i+1}'$) by another MPS with matrix dimensions ($D_i \times D_{i+1}$), where $D_i < D_i'$. (In practice, one often rather keeps the D_i variable and imposes an acceptable loss of accuracy which determines their value, and has to terminate the calculation if this implies matrix dimensions that can no longer be handled efficiently.) Two standard procedures are available, compression by SVD and variational compression. Compression by SVD is very simple: while bringing a state into canonical form, as described above, we move through a sequence of Schmidt decompositions of the quantum state, which allows us to truncate matrices by retaining only the D_i largest singular values. For small degrees of compression, $D \sim D'$, SVD is fast, but it is never optimal; it becomes very slow if $D' \gg D$, as follows from a detailed count of operations. It is non-optimal because a one-sided interdependence of truncations occurs: as we walk through the chain, for each SVD decomposition truncations of the *A*- and *B*-matrices affect the orthonormal systems, but the dependence is one-sided and "unbalanced": if we move through the state from right to left, for instance, truncations further to the left depend on those to the right, but not vice versa. If the truncation is small, the introduced additional inaccuracy is minor; problems arise for cases where large truncations may occur.

Variational compression is optimal, but depends on a reasonably good trial compressed state to be efficient. Generally, issues of getting stuck in a non-optimal compression may arise in the variational ansatz. For details, see Schollwöck (2011) and references therein; the fundamental idea is to minimize $\||\psi\rangle - |\tilde{\psi}\rangle\|^2 = \langle\psi|\psi\rangle - \langle\tilde{\psi}|\psi\rangle - \langle\psi|\tilde{\psi}\rangle + \langle\tilde{\psi}|\tilde{\psi}\rangle$ with respect to $|\tilde{\psi}\rangle$, the trial compressed state. This is done iteratively by moving through the matrices $\tilde{M}^{\sigma_i}$ site by site, optimizing them (to minimize the distance) while

keeping all others constant. Minimizing the distance becomes quite easy when the states are always kept in the mixed-canonical form with the orthogonality center being the site on which one currently optimizes the matrices; this effectively avoids the solution of a large sparse linear equation system which would otherwise arise.

After moving back and forth through all matrices several times, the procedure converges to the optimal compressed state. In order to assess convergence, we can monitor at each step $\||\psi\rangle - |\tilde{\psi}\rangle\|^2$, and observe the convergence of this value; if necessary, D has to be increased. The calculation of the norm distance may seem costly, but isn't. If we keep $|\tilde{\psi}\rangle$ in proper mixed canonical form, one finds, due to the left- and right-normalization properties of A- and B-matrices, that

$$\||\psi\rangle - |\tilde{\psi}\rangle\|^2 = 1 - \sum_{\sigma_i} \text{tr}\,(\tilde{M}^{\sigma_i\dagger}\tilde{M}^{\sigma_i}), \qquad (2.37)$$

which is easy to calculate. The subtracted sum is just $\langle\tilde{\psi}|\tilde{\psi}\rangle$; at the end, this allows us to normalize the state $|\tilde{\psi}\rangle$ by simple rescaling. The danger that variational compression gets stuck in a non-global minimum is often (but not always) successfully dealt with by considering two sites (and the associated matrices) at the same time, by analogy to two-site DMRG, for optimization. This is somewhat slower and not absolutely optimal, but exactly for that reason the algorithm is less likely to get stuck.

2.3.6 Good quantum numbers

Finally, let us discuss how a matrix product state can exploit good quantum numbers. Let us focus on magnetization and assume that the global state has magnetization M. This Abelian quantum number is additive, $M = \sum_i M_i$. We choose local bases $\{\sigma_i\}$ whose states are eigenstates of local magnetization. Consider now the growth process from the left. If we choose the states $|a_1\rangle$ to be eigenstates of local magnetization (e.g., by taking just the $|\sigma_1\rangle$), then Eq. (2.16) allows us to construct by induction states $|a_\ell\rangle$ that are eigenstates of magnetization, provided the matrices $A^{\sigma_\ell}_{a_{\ell-1},a_\ell}$ obtain a block structure such that for each nonzero matrix element

$$M(|a_{\ell-1}\rangle) + M(|\sigma_\ell\rangle) = M(|a_\ell\rangle) \qquad (2.38)$$

holds. This can be represented graphically easily by giving directions to the lines of the graphical representation (Fig. 2.14), with ingoing and outgoing arrows. The rule is then simply that the sum of the magnetizations on the ingoing lines equals that on the outgoing lines. In order to enforce some global magnetization M, we may simply give magnetization values 0 and M to the ingoing and outgoing dummy bonds before the first and after the last site. We may envisage that the indices of the MPS matrices are multiindices for a given magnetization allowing degeneracy, leading to elegant
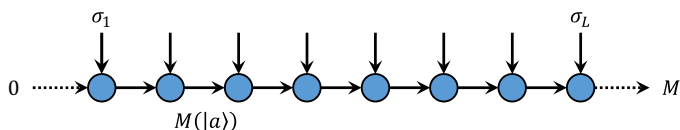
FIGURE 2.14 Representation of an open boundary condition MPS with good (additive) quantum numbers. Physical states and bonds become directed, such that the quantum numbers on the ingoing lines equal those on the outgoing lines. For the dummy bonds before the first and after the last site we set suitable values to fix the global good quantum number.

coding representation. An inversion of the bond arrows would directly tie in with the structure of B-matrices from the growth from the right, but proper book-keeping gives us lots of freedom for the arrows: an inversion means that the sign has to be reversed.

In order to use good quantum numbers in practice, they have to survive under the typical operations we carry out on matrix product states. It turns out that all operations that are not obviously unproblematic and maintain good quantum numbers can be expressed by SVDs. An SVD will be applied to matrices like $A_{(a_{i-1}\sigma_i),a_i}$. If we group states $|a_{i-1}\sigma_i\rangle$ and $|a_i\rangle$ according to their good quantum number, A will consist of blocks; if we rearrange labels appropriately, we can write $A = A_1 \oplus A_2 \oplus \ldots = U_1 S_1 V_1^\dagger \oplus U_2 S_2 V_2^\dagger \oplus \ldots$ or $A = USV^\dagger$ where $U = U_1 \oplus U_2 \oplus \ldots$ and so forth. But this means that the new states generated from $|a_{i-1}\sigma_i\rangle$ via U will also have good quantum numbers. When the need for truncation arises, this property of course still holds for the retained states.

This discussion can be extended to the substantially more difficult non-Abelian case, where the *SU(2)* group is the most relevant one. Pioneered in the DMRG case by Sierra and Nishino (1997) and McCulloch and Gulacsi (2000, 2001, 2002), it was extended to the MPS formalism by several groups, for instance McCulloch (2007) and Weichselbaum (2012).

2.4 Matrix product operator

If we consider the form of an MPS, it is a natural generalization to write general operators as

$$\hat{O} = \sum_{\sigma, \sigma'} W^{\sigma_1 \sigma'_1} W^{\sigma_2 \sigma'_2} \ldots W^{\sigma_L \sigma'_L} |\sigma\rangle\langle\sigma'|, \qquad (2.39)$$

where we now have ingoing and outgoing physical legs. We represent MPOs like MPSs, but we now have two vertical lines, one down, one up, for the ingoing and outgoing physical state in W (Fig. 2.15). The complete MPO itself then looks as in Fig. 2.16. If we want to use good quantum numbers, the methods for MPS translate directly. As for MPS, that the total sum of ingoing and outgoing quantum numbers must be equal, or
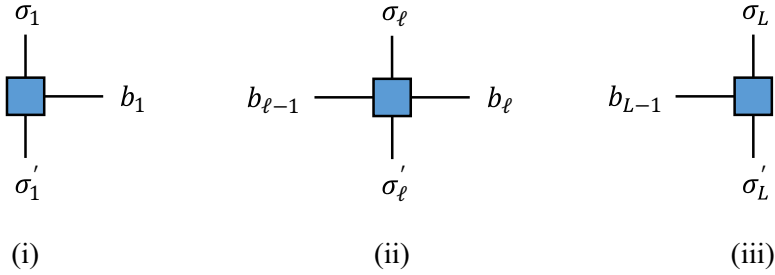
FIGURE 2.15 Elements of a matrix product operator: (i) a corner matrix operator $W^{\sigma_1 \sigma'_1}_{1,b_1}$ at the left end of the chain; (ii) a bulk matrix operator $W^{\sigma_\ell \sigma'_\ell}_{b_{\ell-1},b_\ell}$; (iii) a corner operator $W^{\sigma_L \sigma'_L}_{b_{L-1},1}$ at the right end: the physical indices points up and down, the matrix indices are represented by horizontal lines.
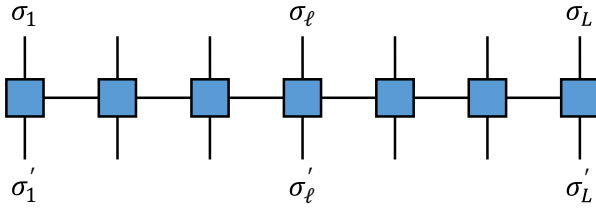
FIGURE 2.16 A matrix product operator acting on an entire chain: the horizontal matrix indices are contracted, and the MPO is ready to be applied to an MPS by simple contraction of vertical (physical) indices.

$M(|\sigma_i\rangle) + M(|b_{i-1}\rangle) = M(|\sigma'_i\rangle) + M(|b_i\rangle)$, where we interpret the bond labels as states for the notation.

By analogy to states, *any* operator can be brought into the form of Eq. (2.39), because it can be written as

$$
\begin{aligned}
\hat{O} &= \sum_{\substack{\sigma_1,\ldots,\sigma_L \\ \sigma'_1,\ldots,\sigma'_L}} c^{(\sigma_1\ldots\sigma_L)(\sigma'_1\ldots\sigma'_L)} |\sigma_1,\ldots,\sigma_L\rangle\langle\sigma'_1,\ldots,\sigma'_L| \\
&= \sum_{\substack{\sigma_1,\ldots,\sigma_L \\ \sigma'_1,\ldots,\sigma'_L}} c^{(\sigma_1\sigma'_1)\ldots(\sigma_L\sigma'_L)} |\sigma_1,\ldots,\sigma_L\rangle\langle\sigma'_1,\ldots,\sigma'_L|
\end{aligned}
\tag{2.40}
$$

which is like a state, but with a double index $\sigma_i\sigma'_i$ instead of σ_i.

As for MPS, we have to ask how we operate with them and how they can be constructed in practice. As it turns out, most operations run in perfect analogy to the MPS case. The construction will be exemplified by the Hamiltonian, which represents the most complex case.
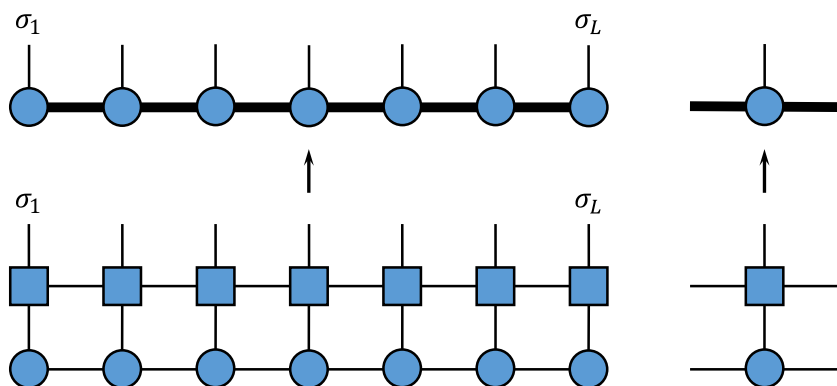
FIGURE 2.17 A matrix product operator acting on a matrix product state: matching physical (vertical) indices are contracted, a new matrix product state emerges, with multiplied matrix dimensions and product structure in its matrices.

2.4.1 Applying an MPO to an MPS

The application of a matrix product operator to a matrix product state runs as

$$\hat{O}|\psi\rangle = \sum_{\sigma,\sigma'}(W^{\sigma_1,\sigma'_1}W^{\sigma_2,\sigma'_2}\ldots)(M^{\sigma'_1}M^{\sigma'_2}\ldots)|\sigma\rangle = \sum_{\sigma}N^{\sigma_1}N^{\sigma_2}\ldots|\sigma\rangle$$

where

$$N^{\sigma_i}_{(b_{i-1},a_{i-1}),(b_i,a_i)} = \sum_{\sigma'_i}W^{\sigma_i\sigma'_i}_{b_{i-1}b_i}M^{\sigma'_i}_{a_{i-1}a_i}. \qquad (2.41)$$

This can be shown by making the matrix-matrix multiplication explicit and rearranging the sums. The application of an MPO to an MPS leaves the form of the MPS invariant, at the prize of an increase in matrix size: the new MPS dimension is the product of that of the original MPS and that of the MPO (Fig. 2.17). This typically requires a subsequent compression, using the methods previously discussed. As shown by Stoudenmire and White (2010), some practical advantages can be gained by compressing at the same time as applying the MPO.

2.4.2 Adding and multiplying MPOs

Operations with MPOs follow very much the lines of MPS. If we consider the addition of two operators, $\hat{O}$ and $\hat{P}$, that have MPO representations $W^{\sigma_i\sigma'_i}$ and $\tilde{W}^{\sigma_i\sigma'_i}$, then the resulting MPO is formed exactly as in the case of MPS, by the direct sum $W^{\sigma_i\sigma'_i} \oplus \tilde{W}^{\sigma_i\sigma'_i}$ for all sites $1 < i < L$, with the same special rules for sites 1 and L. In essence, we (again) just have to consider σ_i and σ'_i as one "big" physical index.

The "multiplication" of two operators, $\hat{Q} = \hat{P}\hat{O}$, can be read off directly from the graphical representation: we contract over the outgoing leg of $\hat{O}$ and the ingoing leg of $\hat{P}$; as in the case of the application of an MPO to an MPS, the dimension of the auxiliary legs (the matrix dimensions) multiply: if we label the matrices of the operators by Q, P and O, the rule is

$$Q^{\sigma_i \sigma'_i}_{(\tilde{b}_{i-1} b_{i-1}), (\tilde{b}_i b_i)} = \sum_{\sigma''_i} P^{\sigma_i \sigma''_i}_{\tilde{b}_{i-1} \tilde{b}_i} O^{\sigma''_i \sigma'_i}_{b_{i-1} b_i}. \tag{2.42}$$

Hence, MPO dimensions simply multiply as for tensors. If we consider an MPS as an MPO with dummy indices in one physical direction, the rule for applying an MPO to an MPS follow as a special case.

2.5 Ground state calculations with MPS

2.5.1 The basic algorithm

The ground state $|\psi_0\rangle$ of some Hamiltonian $\hat{H}$ minimizes

$$E = \frac{\langle \psi | \hat{H} | \psi \rangle}{\langle \psi | \psi \rangle} \tag{2.43}$$

with ground state energy E_0. The required energy minimization (44) can be turned into a Lagrangian multiplier problem, where the expression to be minimized is

$$\langle \psi | \hat{H} | \psi \rangle - \lambda \langle \psi | \psi \rangle; \tag{2.44}$$

the Lagrangian multiplier λ enforces normalization. Minimization in $\langle \psi |$ leads to

$$\hat{H} | \psi \rangle - \lambda | \psi \rangle \stackrel{!}{=} 0, \tag{2.45}$$

an eigenvalue problem where the lowest eigenvalue λ is the ground state energy E_0 and the associated eigenstate the ground state $|\psi_0\rangle$. We want to find the optimal approximation to this state in the form of an MPS where the largest allowed matrix dimension is D (and of course we want to know E_0). This is most efficiently done by a variational optimization of a trial MPS. This requires the representation of $\hat{H}$ as an MPO; let us assume for the moment we have it in the form

$$\hat{H} = \sum_{\sigma, \sigma'} W^{\sigma_1 \sigma'_1} W^{\sigma_2 \sigma'_2} \ldots W^{\sigma_L \sigma'_L} |\sigma\rangle\langle\sigma'|. \tag{2.46}$$

We start with an initial guess for the MPS representation of the ground state (for the moment think about it as a normalized random MPS with suitable matrix dimensions. The expression in Eq. (2.44) can be represented graphically as in Fig. 2.18. Minimization with respect to $\langle \psi |$ is replaced by minimization with respect to the *MMMMMMM* structure of the MPS. Now
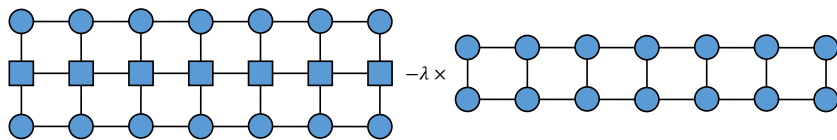
FIGURE 2.18   Network to be contracted to obtain the functional to be extremized to find the ground state and its energy. The left-hand side represents the term $\langle\psi|\hat{H}|\psi\rangle$, the right-hand side the squared norm $\langle\psi|\psi\rangle$.

the matrices (and their unknown elements) are multiplied together, yielding a multi-linear optimization problem. It is a standard procedure to formulate this as a sequence of linear optimization problems. We keep the matrices on all sites but one (ℓ) constant and consider only the matrix entries $M^{\sigma_\ell}_{a_{\ell-1}a_\ell}$ on site ℓ as variables. Then the variables appear in Eq. (2.44) only in quadratic form; the determination of the extremum becomes a linear algebra problem. The new choice of the $M^{\sigma_\ell}_{a_{\ell-1}a_\ell}$ will lower the energy, and yield a variationally better state, but of course not the optimal one. Now one continues to vary the matrix elements on another site for finding a state again lower in energy, moving through all sites multiple times, until the energy does not improve anymore. The question is, of course: do we pick the matrices randomly? How often do we have to revisit each matrix until we have found the variational optimum, that is, the MPS ground state approximation?

The answer to the first question is: we move back and forth through the sequence of matrices, and throughout the procedure always keep the MPS in a mixed-canonical representation, where the orthogonality center is chosen to be the site ℓ where the matrix sits, which is currently being optimized.

Let us work out the contractions of Eq. (2.44) expressed by MPS and first consider the calculation of the overlap, while keeping the chosen M^{σ_ℓ} in the MPS explicit. We find

$$\langle\psi|\psi\rangle = \sum_{\sigma_\ell}\sum_{a_{\ell-1}a_\ell}\sum_{a'_{\ell-1}a'_\ell}\Psi^A_{a_{\ell-1},a'_{\ell-1}}M^{\sigma_\ell*}_{a_{\ell-1},a_\ell}M^{\sigma_\ell}_{a'_{\ell-1},a'_\ell}\Psi^B_{a_\ell,a_{\ell'}}, \tag{2.47}$$

where

$$\Psi^A_{a_{\ell-1},a'_{\ell-1}} = \sum_{\sigma_1...\sigma_{\ell-1}}(M^{\sigma_{\ell-1}\dagger}...M^{\sigma_1\dagger}M^{\sigma_1}...M^{\sigma_{\ell-1}})_{a_{\ell-1},a'_{\ell-1}} \tag{2.48}$$

$$\Psi^B_{a_\ell,a'_\ell} = \sum_{\sigma_{\ell+1}...\sigma_L}(M^{\sigma_{\ell+1}}...M^{\sigma_L}M^{\sigma_L\dagger}...M^{\sigma_{\ell+1}\dagger})_{a'_\ell,a_\ell}. \tag{2.49}$$

In the case where sites 1 through $\ell-1$ are left-normalized and sites $\ell+1$ through L right-normalized, which is the case if we maintain the appropriate mixed-canonical representation with the orthogonality center at site ℓ the normalization conditions lead to a further simplification, namely

$$\Psi^A_{a_{\ell-1},a'_{\ell-1}} = \delta_{a_{\ell-1},a'_{\ell-1}}, \qquad \Psi^B_{a_\ell a'_\ell} = \delta_{a_\ell a'_\ell} \tag{2.50}$$
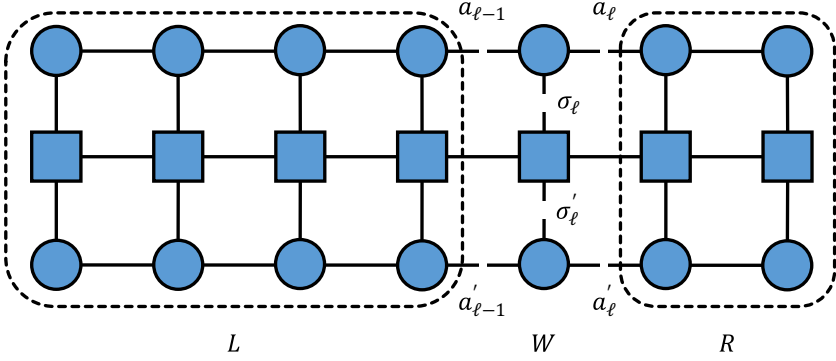
FIGURE 2.19 Network to be contracted for $\langle\psi|\hat{H}|\psi\rangle$. The network decomposes into parts L, R, W, and two M-matrices.

and the overlap calculation collapses to

$$\langle\psi|\psi\rangle = \sum_{\sigma_\ell} \sum_{a_{\ell-1}a_\ell} M^{\sigma_\ell *}_{a_{\ell-1},a_\ell} M^{\sigma_\ell}_{a_{\ell-1},a_\ell}. \tag{2.51}$$

Let us now consider $\langle\psi|\hat{H}|\psi\rangle$, with $\hat{H}$ in MPO language. We can immediately write

$$\langle\psi|\hat{H}|\psi\rangle = \sum_{\sigma_\ell,\sigma'_\ell} \sum_{a'_{\ell-1}a'_\ell} \sum_{a_{\ell-1}a_\ell} \sum_{b_{\ell-1},b_\ell} L^{a_{\ell-1},a'_{\ell-1}}_{b_{\ell-1}} W^{\sigma_\ell,\sigma'_\ell}_{b_{\ell-1},b_\ell} R^{a_\ell,a'_\ell}_{b_\ell} M^{\sigma_\ell *}_{a_{\ell-1},a_\ell} M^{\sigma'_\ell}_{a'_{\ell-1},a'_\ell} \tag{2.52}$$

where L and R are the contractions over the objects shown in Fig. 2.19. These contractions can be evaluated efficiently just as for any expectation value of a product of operators acting on all sites, moving through the graph vertical slice by vertical slice from left to right for L and from right to left for R. The contraction of three tensors is, as always, most efficiently organized as a sequence of two contractions. Now we can of course rebuild L and R for each choice of site ℓ. This involves an enormous amount of unnecessary work if we choose the sites ℓ randomly. If, instead, we move through the chain of sites one by one from right to left or vice versa, we can use (let us concentrate on the case where we move from left to right) that the M-matrices changed in the following way when we were at site $\ell - 1$ in the step before:

- The matrices on sites 1 through $\ell - 2$ do not change at all.
- The matrices on site $\ell - 1$ change.
- The matrices on sites ℓ through L do not change at all.

If, from a previous sweep through the chain from right to left, we have stored all the R for the contractions on the right, we can reuse them now. The underlying objects have not changed in the intermediate steps up to now. As far as L is concerned, the L for site ℓ is the L for site $\ell - 1$,
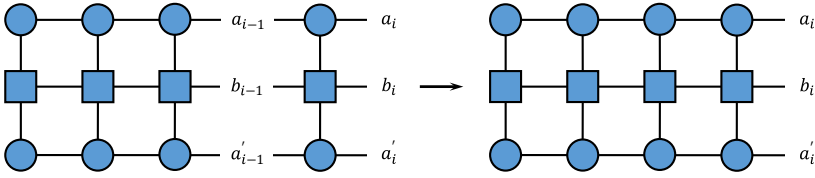
FIGURE 2.20 Update of L by contracting L of the previous step with $A^{\sigma_i *}$, $W^{\sigma_i,\sigma_i'}$ and $A^{\sigma_i'}$.
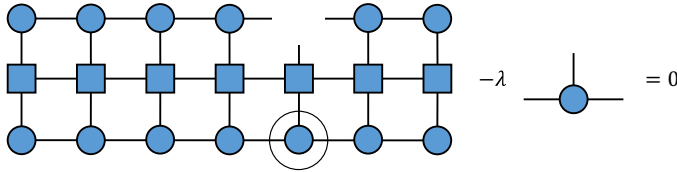
FIGURE 2.21 Eigenvalue problem for the optimization of $M^{\sigma_\ell}_{a_{\ell-1},a_\ell}$. The unknown matrix is circled on the left network.

involving sites 1 through $\ell - 2$, contracted with an additional vertical slice of three tensors at site $\ell - 1$; this will be a comparatively cheap contraction, see Fig. 2.20. We store all the L contractions, because they will retrieved once the direction of the sweep changes to right to left.

If we now take the extremum of Eq. (2.44), expressed in MPS language, with respect to $M^{\sigma_\ell *}_{a_{\ell-1},a_\ell}$ we find

$$\sum_{\sigma_\ell'} \sum_{a_{\ell-1}' a_\ell'} \sum_{b_{\ell-1},b_\ell} L^{a_{\ell-1},a_{\ell-1}'}_{b_{\ell-1}} W^{\sigma_\ell,\sigma_\ell'}_{b_{\ell-1},b_\ell} R^{a_\ell,a_\ell'}_{b_\ell} M^{\sigma_\ell'}_{a_{\ell-1}',a_\ell'} - \lambda M^{\sigma_\ell}_{a_{\ell-1},a_\ell} = 0. \qquad (2.53)$$

which in graphical representation looks as in Fig. 2.21. This is in fact a very simple eigenvalue equation; if we introduce matrix H by reshaping $H_{(\sigma_\ell a_{\ell-1} a_\ell),(\sigma_\ell' a_{\ell-1}' a_\ell')} = \sum_{b_{\ell-1},b_\ell} L^{a_{\ell-1},a_{\ell-1}'}_{b_{\ell-1}} W^{\sigma_\ell,\sigma_\ell'}_{b_{\ell-1},b_\ell} R^{a_\ell,a_\ell'}_{b_\ell}$ and a vector v with $v_{\sigma_\ell a_{\ell-1} a_\ell} = M^{\sigma_\ell}_{a_{\ell-1},a_\ell}$, we arrive at an *eigenvalue problem* of matrix dimension $(dD^2 \times dD^2)$,

$$Hv - \lambda v = 0, \qquad (2.54)$$

Solving for the lowest eigenvalue λ_0 gives us a $v^0_{\sigma_\ell a_{\ell-1} a_\ell}$, which is reshaped back to $M^{\sigma_\ell}_{a_{\ell-1} a_\ell}$, λ_0 being the current ground state energy estimate. Note that if we had not achieved the simplified overlap due to the mixed-canonical representation, we would have (a potentially much harder, because potentially ill-conditioned) *generalized* eigenvalue problem, $Hv - \lambda Nv = 0$. Staying in a mixed-canonical representation with orthogonality center site ℓ is easiest if we sweep, as this means that only a single step of the procedure that brings a state into mixed-canonical form has to be carried out, which shifts the orthogonality center by one site. This is as cheap as it can possibly be. This is another

instance where we see the importance of the mixed-canonical representation of a state. But this requires a notion of left and right, which exists for MPS, TTNS, and T3NS, but not for PEPS. For PEPS, therefore, we do not have a simple equivalent notion, making calculations at many places less stable and more tedious. This is another reason why quantum chemists have a strong preference for MPS and tree states, because they are usually not concerned with regular lattices.

In general, dD^2 is too large for an exact diagonalization, but as we are only interested in the lowest eigenvalue and eigenstate, an iterative eigensolver that aims for the ends of the spectrum will do. Typical methods are the Lanczos or Jacobi-Davidson large sparse matrix solvers. The speed of convergence of such methods ultimately rests on the quality of the initial starting or guess vector. As this eigenproblem is part of an iterative approach to the ground state, the current M^{σ_ℓ} is a valid guess that will dramatically speed up calculations close to convergence.

We summarize the resulting algorithm:

- Start from some initial guess for $|\psi\rangle$, which is right-normalized, that is, consists of B-matrices only.
- Calculate the R-expressions iteratively for all site positions $L-1$ through 1 iteratively.
- *Right sweep:* Starting from site $\ell = 1$ through site $L-1$, sweep through the lattice to the right as follows: solve the standard eigenproblem by an iterative eigensolver for M^{σ_ℓ}, taking its current value as starting point. Once the solution is obtained, left-normalize M^{σ_ℓ} into A^{σ_ℓ} by SVD to maintain the desired normalization structure. The remaining matrices of the SVD are multiplied to the $M^{\sigma_{\ell+1}}$ to the right, which will be the starting guess for the eigensolver for the next site. Build iteratively the L expression by adding one more site. Move on by one site, $\ell \to \ell + 1$, and repeat.
- *Left sweep:* Starting from site $\ell = L$ through site 2, sweep through the lattice to the left as follows: solve the standard eigenproblem by an iterative eigensolver for M^{σ_ℓ}, taking its current value as starting point. Once the solution is obtained, right-normalize M^{σ_ℓ} into B^{σ_ℓ} by SVD to maintain the desired normalization structure. The remaining matrices of the SVD are multiplied to the $M^{\sigma_{\ell-1}}$ to the left, which will be the starting guess for the eigensolver for the next site. Build iteratively the R expression by adding one more site. Move on by one site, $\ell \to \ell - 1$, and repeat.
- Repeat right and left sweeps, until convergence is achieved. Convergence is achieved if energy converges, but the best test is (using MPO) to consider $\langle\psi|\hat{H}^2|\psi\rangle - (\langle\psi|\hat{H}|\psi\rangle)^2$ to see whether an eigenstate has been reached; this expression should approach 0 as closely as possible.

The convergence control of the algorithm by means of the variance is actually not easy in quantum chemistry or any other situation where the dimension of the Hamiltonian MPO is large. As each application of $\hat{H}$

multiplies the MPS dimensions by the MPO dimension, the MPS dimensions grow by a factor identical to the square of the MPO dimension. This means that in between some truncation has to be introduced which of course invalidates the variance as a convergence control. A possible way out has been introduced by Hubig et al. (2018): it replaces the true variance by a so-called two-site variance. It can be calculated easily, without truncation, but captures the variance only of Hamiltonians with up to nearest-neighbor terms. While this is of course not the situation relevant in quantum chemistry, the two-site variance empirically scales with the true variance and therefore allows extrapolations into the exact limit.

In this iterative process, the energy can only go down, as we continuously improve by varying the parameters. Two problems occur: starting from a random state, the guesses for the M^{σ_ℓ} in the iterative eigensolvers will be very bad in the initial sweeps, leading to large iteration numbers and bad performance. Moreover, we cannot guarantee that the global minimum is actually reached by this procedure instead of being stuck in a non-global minimum (and the variance will not be indicative of a problem, if we simply get stuck in an excited eigenstate).

One way of addressing the first issue is to start out with infinite-system DMRG to produce an initial guess; an optimal MPS version of infinite-system DMRG is discussed in Schollwöck (2011). While this initial guess may be far from the true solution, it will usually fare much better than a random starting state. Moreover, one can try to balance the number of iterations (high in the first sweeps) by starting with small D, converge in that ansatz class, enlarge D and add zeros in the new matrix entries, converge again, and so on. When D gets large, the guess states will hopefully be so close to the final state that only very few iterations will be needed. It turns out, however, that starting with too small D may land us in a non-global minimum that we will not get out of upon increasing D. Quite generally, as in DMRG, one should never calculate results for just a single D, but increase it in various runs until results converge (they are guaranteed to be exact in the $D \to \infty$ limit).

2.5.2 Excitations

If we are looking for low-lying excited states instead of a ground state, two typical situations occur: (1) The excited state is known to be the ground state of another sector of the Hilbert space decomposed according to some good quantum number. Then the calculation is just a ground state calculation in that different sector. (2) The excited state is the first, second, or higher excitation in the sector of the ground state. Then we have to calculate these excitations iteratively, and orthonormalize the state with respect to the lower-lying states already identified; this clearly limits the approach to a few low-lying excitations. The place where the algorithm is to be modified is in the iterative eigensolver; for example, in the Lanczos iterations, the next Lanczos state

generated is orthonormalized not only with respect to the previous Lanczos states, but also already constructed eigenstates of the Hamiltonian. This is a standard extension of the Lanczos algorithm.

2.5.3 "Single site" vs "two site"

The variational MPS algorithm just introduced is quite prone to getting stuck. Let us consider the (typical) case of a Hamiltonian with good quantum numbers that are incorporated into the algorithm, such that the state is characterized by specific quantum numbers. Let us think of the total magnetization, which takes a value $\tilde{M}$. For any Schmidt decomposition $|\psi\rangle = \sum_{a_\ell} s_{a_\ell} |a_\ell\rangle_A |a_\ell\rangle_B$, each of the states on block A and B will have a good quantum number, namely m_a^A and m_a^B such that $m_a^A + m_a^B = \tilde{M}$. Because magnetization fluctuates on the blocks (due to hopping electrons, if we think of a PPP model), the values of, say, m_a^B will be distributed over some range, say 1 state with magnetization m, 3 states with magnetization m', 5 states with magnetization m'' and so forth. This distribution depends on how we generated the initial state, because, as I will show next, this distribution stays *fixed* in further sweeps. This means that if it does not correspond to the distribution that the variationally optimal state would yield, it can never reach that state! As the initial states of variational MPS algorithms are usually quite far from the unknown variationally optimal state, the likelihood to hit the right distribution is very small, and we have a serious problem.

The reason why the distribution stays fixed can be seen from the SVD of $M_{a_{\ell-1},a_\ell}^{\sigma_\ell}$ to carry out one (for example) left-normalization step: reshaping matrices M^{σ_ℓ} into some Ψ and applying an SVD gives at most D non-vanishing singular values; the right-singular vectors in $V^\dagger$ are nothing but the eigenvectors of $\Psi^\dagger\Psi$, which is block-diagonal because the states $|a_\ell\rangle_B$ have good quantum numbers. The right singular vectors (eigenvectors) therefore encode a basis transformation within blocks of the same quantum number, hence the number of states with a given quantum number remains the same, and so does the number of states with a given quantum number in the other part of the system because of the matching of quantum numbers required in the Schmidt decomposition.

Various ways of getting out of this potential trap have been proposed. The first one is to modify the algorithm to consider and optimize the MPS matrices on two adjacent sites at the same time, just as in conventional (two-site) DMRG. While this approach is slower (roughly by a factor of d), it offers a slightly enlarged ansatz space with a subsequent truncation that allows the algorithm to be more robust against the danger of getting stuck in local energy minima in ground state searches. In particular, the enlarged ansatz space of the two-site algorithm allows a reshuffling of the quantum number distribution due to the truncation. Once this is converged, one may switch to the faster single-site algorithm, as proposed by Takasaki et al.

(1999), although it is not at all clear that this leads strictly to the optimal outcome. Alternatively, there is a procedure by White (2005) that protects reasonably against trapping and ensures reshuffling while staying in the variational MPS (or single-site DMRG, which is the same, see below) approach. It starts from the observation that quantum numbers of a subsystem A are changed by quantum fluctuations due to those parts of the Hamiltonian that connect A to the rest of the system, and accounts for them in the determination of improved M-matrices. The arguably most performant and stable approach to this problem is at the moment provided by the subspace expansion method proposed by Hubig et al. (2015).

2.5.4 MPO representation of Hamiltonians

This task turns out to be not so trivial for the Hamiltonians of quantum chemistry with their numerous four-operator terms. In the DMRG case, the Hamiltonians were built iteratively by adding in parts of the Hamiltonian sequentially and only keep sums of operator terms, always expressed in the current block bases. It turned out that the $O(L^4)$ four-operator terms could be organized into $O(L^2)$ terms with some book-keeping. In the MPS/MPO formulation, all this is somewhat more complicated and quite subtle. We therefore discuss here only the construction of the MPO of a relatively simple Hamiltonian (PPP model), which will exemplify the idea of a finite state machine, one of the approaches that can be generalized to quantum chemical Hamiltonians.

We consider

$$\hat{H} = -t \sum_{i=1}^{L-1} \sum_{\tau} (\hat{c}^{\dagger}_{i,\tau} \hat{c}_{i+1,\tau} + \hat{c}^{\dagger}_{i+1,\tau} \hat{c}_{i,\tau}) + U \sum_{i} \hat{n}_{i,\uparrow} \hat{n}_{i,\downarrow}. \tag{2.55}$$

τ runs over the two magnetization values of an electronic spin; this unusual notation is to avoid confusion with σ in the MPOs and MPSs. In order to express this sum of tensor products in MPO form, we consider the building block $W^{\sigma\sigma'}_{bb'}$ combined with its associated projector $|\sigma\rangle\langle\sigma'|$ to become an operator-valued matrix $\hat{W}_{bb'} = \sum_{\sigma\sigma'} W^{\sigma\sigma'}_{bb'} |\sigma\rangle\langle\sigma'|$ (McCulloch, 2007) such that the MPO takes the simple form

$$\hat{H} = \hat{W}^{[1]} \hat{W}^{[2]} \dots \hat{W}^{[L]}. \tag{2.56}$$

Each $\hat{W}^{[i]}$ acts on a different local Hilbert space at site i.

To build the $\hat{W}^{[i]}$, we move through an arbitrary operator string appearing in $\hat{H}$: starting from the right end, the string contains unit operators, until at one point we encounter one of (in our example) 5 non-trivial operators (there are 4 different hopping terms because of the spin degree of freedom). For the interaction operator, the string part further to the left may only contain unit operators; for the hopping operator pairs, the complementary operator

must follow immediately to complete the hopping term, to be continued by unit operators further to the left. For book-keeping, we introduce 6 corresponding internal states of the string at some given bond. *They are not to be confused with any quantum state!* Internal state 1: there are only units to the right, internal states 2,3,4,5: one $\hat{c}_\uparrow$, $\hat{c}_\uparrow^\dagger$, $\hat{c}_\downarrow$, $\hat{c}_\downarrow^\dagger$ just to the right, internal state 6: completed interaction or hopping term somewhere to the right. Comparing the state of a string left and right of one site, only a few state transitions are allowed: $1\to1$ by the unit operator $\hat{I}$, $1\to2$ by $\hat{c}_\uparrow$, $1\to3$ by $\hat{c}_\uparrow^\dagger$, $1\to4$ by $\hat{c}_\downarrow$, $1\to5$ by $\hat{c}_\downarrow^\dagger$ and finally $1\to6$ by $U\hat{n}_\uparrow\hat{n}_\downarrow$. Furthermore $2\to6$ by $-t\hat{c}_\uparrow^\dagger$, $3\to6$ by $-t\hat{c}_\uparrow$, $4\to6$ by $-t\hat{c}_\downarrow^\dagger$, $5\to6$ by $-t\hat{c}_\downarrow$, to complete the hopping term, and $6\to6$ for a completed interaction by the unit operator $\hat{I}$. Furthermore all string states must start at 1 to the right of the last site and end at 6 (i.e., the dimension D_W of the MPO to be) to the left of the first site. This can now be encoded by the following operator-valued matrices:

$$\hat{W}^{[i]} = \begin{bmatrix} \hat{I} & 0 & 0 & 0 & 0 & 0 \\ \hat{c}_\uparrow & 0 & 0 & 0 & 0 & 0 \\ \hat{c}_\uparrow^\dagger & 0 & 0 & 0 & 0 & 0 \\ \hat{c}_\downarrow & 0 & 0 & 0 & 0 & 0 \\ \hat{c}_\downarrow^\dagger & 0 & 0 & 0 & 0 & 0 \\ U\hat{n}_\uparrow\hat{n}_\downarrow & -t\hat{c}_\uparrow^\dagger & -t\hat{c}_\uparrow & -t\hat{c}_\downarrow^\dagger & -t\hat{c}_\downarrow & \hat{I} \end{bmatrix} \tag{2.57}$$

and on the first and last sites

$$W^{[1]} = \begin{bmatrix} U\hat{n}_\uparrow\hat{n}_\downarrow & -t\hat{c}_\uparrow^\dagger & -t\hat{c}_\uparrow & -t\hat{c}_\downarrow^\dagger & -t\hat{c}_\downarrow & \hat{I} \end{bmatrix}, \quad \hat{W}^{[L]} = \begin{bmatrix} \hat{I} \\ \hat{c}_\uparrow \\ \hat{c}_\uparrow^\dagger \\ \hat{c}_\downarrow \\ \hat{c}_\downarrow^\dagger \\ U\hat{n}_\uparrow\hat{n}_\downarrow \end{bmatrix}. \tag{2.58}$$

Note that the creation and annihilation operators have to be implemented such that the correct fermionic sign emerges; as they act on neighboring sites here, this can be done easily by proper choices of signs by hand; for longer-ranged hoppings, one can use parity operators $(-1)^{\hat{n}_i}$ instead of identity operators between the pairs of creation and annihilation operators. Other equally viable book-keeping options exist.

A simple multiplication shows how the Hamiltonian emerges; a graphical representation is provided in Fig. 2.22. Inserting the explicit operator representations gives the desired $W^{\sigma\sigma'}$-matrices for the MPO. This construction can be extended quite easily to include, say, next-nearest neighbor hopping, by the introduction of additional internal states. It is therefore possible to express Hamiltonians exactly in a very compact MPO form; a similar set of rules leading to the same result has been given by Crosswhite et al. (2008).
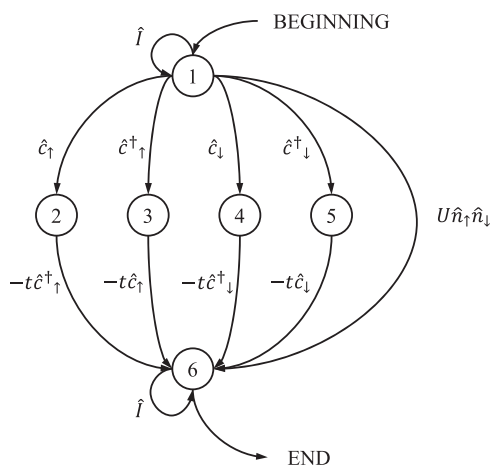
FIGURE 2.22 Graphical representation of the finite state machine that builds exactly all allowed terms in a PPP Hamiltonian.

Extensions to efficiently building the more complicated Hamiltonians of quantum chemistry can be found in (Keller et al., 2015; Chan et al., 2016; Hubig et al., 2017).

2.5.5 Comparing DMRG to variational MPS ground state searches

Expressed simply, the variational MPS ground state search is identical to the finite-system part of DMRG, up to one big modification, namely that we either switch from a two-site to a single-site DMRG algorithm, that is, consider a block-site-block configuration A•B instead of a block-site-site-block configuration A••B. Alternatively, we can take the variational MPS ground state search and optimize the contraction of the M-matrices on two neighboring sites (and decompose the result by an SVD into suitably normalized matrices on two sites).

Before we show and discuss this, let us first consider the role of the infinite-system part of DMRG: if finite-system DMRG (up to the two-site vs. single-site modification) is a variational method, the role of the infinite-system part is merely to provide a not too bad trial state. For a translationally invariant system, as mostly studied in condensed matter physics, this is certainly much better than a random initialization. In applications for quantum chemistry, building the Hamiltonian iteratively by adding orbital after orbital in an imitation of the infinite-system system is probably almost always not leading to a good initial state; a random state might be almost as good.

A useful procedure (which can actually be used both in the DMRG and the MPS framework), which is used extensively, is to observe that the cost

of sweeps scales as D^3. At the same time, if the initial guess states in the iterative eigensolvers are bad they are slowly converging and therefore particularly expensive. If the ground state is approaching convergence, the current ground state is already a very good initial guess, so the iterative eigensolvers will be quite performant. The idea is now to combine badly converging eigensolvers with cheap calculations and start with *very small D*, perhaps a random initial guess or a Hartree-Fock like product state or some improvement of it, to sweep a few times, then increase D (simply by not truncating as much), continue sweeping, increase D again and so forth. It takes some experience to find a good protocol: sweeping too often at low D will not improve the state a lot, increasing D too rapidly will leave us with a costly bad approximation of the ground state in the expensive sweeps.

The fundamental observation in comparing DMRG and variational MPS is contained in the observation that the A-matrices (and B-matrices) of an MPS in mixed-canonical representation can be obtained from the operation of building a truncated orthonormal block plus site basis from an effective block basis and a single-site basis as done in DMRG. That the MPS matrices are indeed exactly the same, follows from the observation that both DMRG and MPS look at the same optimization procedure: minimize the energy of the state given the Hamiltonian. As the eigenvalues of the reduced density matrices which give the DMRG selection criterion are nothing but the squares of the singular values appearing in MPS, which give the selection criterion for MPS, the two selection principles are identical. What we call number of states in DMRG, is the matrix dimension in MPS. The translation rule between the DMRG state and the MPS reads

$$
\begin{aligned}
|\psi\rangle &= \sum_{a_{\ell-1}\sigma_\ell\sigma_{\ell+1}a_{\ell+1}} \Psi^{\sigma_\ell\sigma_{\ell+1}}_{a_{\ell-1},a_{\ell+1}} |a_{\ell-1}\rangle_A |\sigma_\ell\rangle |\sigma_{\ell+1}\rangle |a_{\ell+1}\rangle_B \\
&= \sum_\sigma A^{\sigma_1}\ldots A^{\sigma_{\ell-1}} \Psi^{\sigma_\ell\sigma_{\ell+1}} B^{\sigma_{\ell+2}}\ldots B^{\sigma_L} |\sigma\rangle,
\end{aligned}
\tag{2.59}
$$

where the "standard" MPS would be achieved by a further SVD on $\Psi^{\sigma_\ell\sigma_{\ell+1}}$, which generates an A-matrix, a B-matrix, and a singular value matrix S in between, which can be multiplied into either the A- or B-matrix, putting the orthogonality center on site ℓ or $\ell+1$.

If we consider operators in the DMRG and MPS framework, they are identical, too: in DMRG they are expressed explicitly when the site where they act is explicit and not part of a block, and then subjected to (incomplete) basis transformations when the block grows and absorbs the site. In the MPS framework, they are kept explicitly all the time and only evaluated when sandwiched between two MPS. As long as the two MPS are the same (as is the case for expectation values), the contraction of an operator with a number of A (or B)-matrices is nothing but the execution of the sequence of block basis transformations of DMRG. Ultimately, therefore, the large sparse eigenproblems of DMRG and MPS are identical.

The growth and shrinking of left and right blocks in DMRG is the one-to-one equivalent of the shift of the orthogonality center in the mixed-canonical representation of MPS.

It remains to show that the Hamiltonians are identical, too. Strictly speaking, this is not the case: The MPO representation of $\hat{H}$ we just used is clearly exact. On the other hand, the representation of $\hat{H}$ in DMRG contains a series of reduced basis transformations, hence is inherently inexact. So, the two representations seem unrelated, with an advantage on the MPO side because it is exact. But a more careful analysis reveals that on the level of calculating expectation values $\langle\psi|\hat{H}|\psi\rangle$ as they appear in MPS and DMRG ground state searches both representations give identical results (they are not identical for higher moments, such as $\langle\psi|\hat{H}^2|\psi\rangle$, where the MPO representation is demonstrably more accurate at a numerical cost, see below).

Minimization of ground state energy is, as we have seen, a costly large sparse matrix problem. As the methods are iterative, a good initial guess is desirable. White (1996) has provided a powerful "state prediction" for DMRG. In fact, it turns out that the result of the prediction is just what one gets naturally in variational MPS language without the intellectual effort involved to find state prediction.

While this clarifies the relationship between variational MPS, single-site DMRG (the same) and two-site DMRG (different), it is important to note that the different ways of storing information more implicitly or more explicitly implies differences even if the algorithms are strictly speaking identical —the fact that in one formulation prediction is trivial and in the other is not gives us an example. But there is more.

(1) In DMRG, the effective bases for representing the states and the Hamiltonian or other operators are tied up. This is why concepts such as targetting multiple states arise, if we consider several different states like the ground state and the first excited state at the same time. One then considers mixed reduced density operators

$$\hat{\rho}_A = \sum_i \alpha_i \text{tr}_B |\psi_i\rangle\langle\psi_i| \tag{2.60}$$

with $|\psi_i\rangle$ the target states and $0 < \alpha_i \leq 1$, $\sum_i \alpha_i = 1$, to give a joint set of basis states for all states of interest. This can of course only be done at a certain loss of accuracy for given numerical resources and for a few states only. At the price of calculating the contractions anew for each state, in the MPO/MPS formulation, the state bases are only tied up at the level of the exact full basis. MPO/MPS formulations therefore acquire their full potential vs conventional DMRG language once multiple states get involved.

(2) Another instance where the MPO/MPS formulation is superior, albeit at elevated numerical cost, is the calculation of the expression $\langle\psi|\hat{H}^2|\psi\rangle$, which is interesting, for example, in the context of estimating how accurately a ground state has been obtained. In the MPO formalism, it can be done exactly

up to the inherent approximations to $|\psi\rangle$ by sandwiching the Hamiltonian MPO twice between the bra and ket. It would of course be most economical for the programmer to calculate $\hat{H}|\psi\rangle$ and take the norm, two operations which at this stage he has at hand. The operational cost of this would be $O(LD^2 D_W^2 d^2)$ for the action of the MPO and $O(LD^3 D_W^3 d)$ for the norm calculation. The latter is very costly, hence it is more efficient to do an iterative construction as done for $\langle\psi|\hat{H}|\psi\rangle$. Let me make the important remark that dimension D_W^2 is only the worst case for $\hat{H}^2$ (see Fröwis et al., 2010): Writing out the square and introducing rules for the expression leads to more efficient MPOs, whose optimality can be checked numerically by doing an SVD compression and looking for singular values that are zero. Our anisotropic Heisenberg Hamiltonian takes $D_W = 9$ instead of 25 for $\hat{H}^2$. For higher powers, the gains are even more impressive, and can be obtained numerically by compressing an explicit MPO for $\hat{H}^n$ with discarding only zeros among the singular values. (In quantum chemistry applications the Hamiltonian MPO is usually so big that such tricks do not really work.) In a DMRG calculation, there would be a sequence $\hat{H}(\hat{H}|\psi\rangle)$ in the DMRG block-site basis. The point is that before the second application of $\hat{H}$, a projection onto the reduced block bases happens (because of the DMRG-specific truncated form of $\hat{H}$), which is not the identity and loses information.

What does the comparison of MPS and DMRG imply algorithmically? First of all, the truncation error of conventional DMRG, which has emerged as a highly reliable tool for gauging the quality of results, is nothing but an artefact of the somewhat anomalous two-site setup. In variational MPS or single-site DMRG it has to be replaced by some other criterion; we proposed the variance of the energy. Second, while all the approaches are variational in the sense that they are looking for the lowest energy that can be achieved in a given type of ansatz, the ansatz varies from site to site in two-site DMRG (because of the $\Psi^{\sigma\sigma}$ anomaly in the ansatz), the ansatz stays the same all the time in single-site DMRG, which is conceptually nicer. That this comes at the expense of potential trapping which needs clever counter-strategies serves as a reminder that the mathematically most beautiful does not have to be the most practical.

References

Affleck, I., Kennedy, T., Lieb, E., Tasaki, H., 1987. Rigorous results on valence-bond ground states in antiferromagnets. Phys. Rev. Lett. 59, 799. Available from: https://doi.org/10.1103/PhysRevLett.59.799.

Affleck, I., Kennedy, T., Lieb, E., Tasaki, H., 1988. Valence bond ground states in isotropic quantum antiferromagnets. Comm. Math. Phys. 115, 477. Available from: https://doi.org/10.1007/BF01218021.

Barthel, T., Chung, C.M., Schollwöck, U., 2006. Entanglement scaling in critical two-dimensional fermionic and bosonic systems. Phys. Rev. A 74, 022329. Available from: https://doi.org/10.1103/PhysRevA.74.022329.

Baxter, R., 1968. Dimers on a rectangular lattice. J. Math. Phys. 9, 650. Available from: https://doi.org/10.1063/1.1664623.

Baxter, R., 1982. Exactly Solved Models in Statistical Mechanics. Academic Press.

Bekenstein, J., 1973. Black holes and entropy. Phys. Rev. D 7, 2333. Available from: https://doi.org/10.1103/PhysRevD.7.2333.

Callan, C., Wilczek, F., 1994. On geometric entropy. Phys. Lett. B 333, 55. Available from: https://doi.org/10.1016/0370-2693(94)91007-3.

Chan, G.L., Keselman, A., Nakatani, N., Li, Z., White, S., 2016. Matrix product operators, matrix product states, and ab initio density matrix renormalization group algorithms. J. Chem. Phys. 145, 014102. Available from: https://doi.org/10.1063/1.4955108.

Crosswhite, G., Doherty, A., Vidal, G., 2008. Applying matrix product operators to model systems with long-range interactions. Phys. Rev. B 78, 035116. Available from: https://doi.org/10.1103/PhysRevB.78.035116.

Daley, A., Kollath, C., Schollwöck, U., Vidal, G., 2004. Time-dependent density-matrix renormalization-group using adaptive effective hilbert spaces. J. Stat. Mech.: Th. Exp. 04005. Available from: https://doi.org/10.1088/1742-5468/2004/04/P04005.

Dukelsky, J., Martín-Delgado, M., Nishino, T., Sierra, G., 1998. Equivalence of the variational matrix product method and the density matrix renormalization group applied to spin chains. Europhys. Lett. 43, 457. Available from: https://doi.org/10.1209/epl/i1998-00381-x.

Eisert, J., Cramer, M., Plenio, M., 2010. Area laws for the entanglement entropy. Rev. Mod. Phys. 82, 277. Available from: https://doi.org/10.1103/RevModPhys.82.277.

Fannes, M., Nachtergaele, B., Werner, R., 1989. Exact antiferromagnetic ground states of quantum spin chains. Europhys. Lett. 10, 633. Available from: https://doi.org/10.1209/0295-5075/10/7/005.

Fannes, M., Nachtergaele, B., Werner, R., 1992. Finitely correlated states on quantum spin chains. Comm. Math. Phys. 144, 443. Available from: https://doi.org/10.1007/BF02099178.

Fröwis, F., Nebendahl, V., Dür, W., 2010. Tensor operators: Constructions and applications for long-range interaction systems. Phys. Rev. A 81, 062337. Available from: https://doi.org/10.1103/PhysRevA.81.062337.

Gioev, D., Klich, I., 2006. Entanglement entropy of fermions in any dimension and the widom conjecture. Phys. Rev. Lett. 96, 100503. Available from: https://doi.org/10.1103/PhysRevLett.96.100503.

Gunst, K., Verstraete, F., Wouters, S., Legeza, Ö., Van Neck, D., 2018. T3NS: three-legged tree tensor network states. J. Chem. Theo. Comp. 14. Available from: https://doi.org/10.1021/acs.jctc.8b00098.

Hubig, C., McCulloch, I.P., Schollwöck, U., Wolf, F.A., 2015. A strictly single-site dmrg algorithm with subspace expansion. Phys. Rev. B 91, 155115. Available from: https://doi.org/10.1103/PhysRevB.91.155115.

Hubig, C., McCulloch, I.P., Schollwöck, U., 2017. Generic construction of efficient matrix product operators. Phys. Rev. B 95, 035129. Available from: https://doi.org/10.1103/PhysRevB.95.035129.

Hubig, C., Haegeman, J., Schollwöck, U., 2018. Error estimates for extrapolations with matrix product states. Phys. Rev. B 97, 045125. Available from: https://doi.org/10.1103/PhysRevB.97.045125.

Keller, S., Dolfi, M., Troyer, M., Reiher, M., 2015. An efficient matrix product operator representation of the quantum chemical hamiltonian. J. Chem. Phys. 143, 244118. Available from: https://doi.org/10.1063/1.4939000.

Klümper, A., Schadschneider, A., Zittartz, J., 1993. Matrix-product-groundstates for one-dimensional spin-1 quantum antiferromagnets. Europhys. Lett. 24, 293. Available from: https://doi.org/10.1209/0295-5075/24/4/010.

Latorre, J., Rico, E., Vidal, G., 2004. Ground state entanglement in quantum spin chains. Quant. Inf. Comp 4, 48. Available from: https://doi.org/10.26421/QIC4.1-4.

Legeza, Ö., Solyom, J., 2003. Optimizing the density-matrix renormalization group method using quantum information entropy. Phys. Rev. B 68, 195116. Available from: https://doi.org/10.1103/PhysRevB.68.195116.

McCulloch, I.P., 2007. From density-matrix renormalization group to matrix product states. J. Stat. Mech.: Theor. Exp. 10014. Available from: https://doi.org/10.1088/1742-5468/2007/10/P10014.

McCulloch, I.P., Gulacsi, M., 2000. Density matrix renormalisation group method and symmetries of the Hamiltonian. Aust. J. Phys. 53, 597. Available from: https://doi.org/10.1071/PH00023.

McCulloch, I.P., Gulacsi, M., 2001. Total spin in the density matrix renormalization group algorithm. Philos. Mag. Lett. 81, 447. Available from: https://doi.org/10.1080/09500830110040009.

McCulloch, I.P., Gulacsi, M., 2002. The non-abelian density matrix renormalization group algorithm. Europhys. Lett. 57, 852. Available from: https://doi.org/10.1209/epl/i2002-00393-0.

Murg, V., Verstraete, F., Legeza, Ö., Noack, R.M., 2010. Simulating strongly correlated quantum systems with tree tensor networks. Phys. Rev. B 82, 205105. Available from: https://doi.org/10.1103/PhysRevB.82.205105.

Nishino, T., 1995. Density matrix renormalization group method for 2d classical models. J. Phys. Soc. Jpn. 64, 3598. Available from: https://doi.org/10.1143/JPSJ.64.3598.

Nishino, T., Hieida, Y., Okunishi, K., Maeshima, N., Akutsu, Y., Gendiar, A., 2001. Two-dimensional tensor product variational formulation. Prog. Theor. Phys. 105, 409. Available from: https://doi.org/10.1143/PTP.105.409.

Oseledets, I., 2011. Tensor-train decomposition. SIAM J. Sci. Comp. 33, 2295. Available from: https://doi.org/10.1137/090752286.

Ostlund, S., Rommer, S., 1995. Thermodynamic limit of density matrix renormalization. Phys. Rev. Lett. 75, 3537. Available from: https://doi.org/10.1103/PhysRevLett.75.3537.

Paeckel, S., Köhler, T., Swoboda, A., Manmana, S.R., Schollwöck, U., Hubig, C., 2019. Time-evolution methods for matrix-product states. Ann. Phys. 411, 167998. Available from: https://doi.org/10.1016/j.aop.2019.167998.

Plenio, M., Eisert, J., Dreissig, J., Cramer, M., 2005. Entropy, entanglement, and area: Analytical results for harmonic lattice systems. Phys. Rev. Lett. 94, 060503. Available from: https://doi.org/10.1103/PhysRevLett.94.060503.

Schollwöck, U., 2005. The density-matrix renormalization-group. Rev. Mod. Phys. 77, 259. Available from: https://doi.org/10.1103/RevModPhys.77.259.

Schollwöck, U., 2011. The density-matrix renormalization-group in the age of matrix-product states. Ann. Phys. 326, 96. Available from: https://doi.org/10.1016/j.aop.2010.09.012.

Schuch, N., Wolf, M., Verstraete, F., Cirac, J., 2008. Entropy scaling and simulability by matrix product states. Phys. Rev. Lett. 100, 030504. Available from: https://doi.org/10.1103/PhysRevLett.100.030504.

Shi, Y., Duan, L., Vidal, G., 2006. Classical simulation of quantum many-body systems with a tree tensor network. Phys. Rev. A 74, 022320. Available from: https://doi.org/10.1103/PhysRevA.74.022320.

Sierra, G., Nishino, T., 1997. The density matrix renormalization group method applied to interaction round a face Hamiltonians. Nucl. Phys. B 495, 505. Available from: https://doi.org/10.1016/S0550-3213(97)00217-4.

Srednicki, M., 1993. Entropy and area. Phys. Rev. Lett. 71, 666. Available from: https://doi.org/10.1103/PhysRevLett.71.666.

Stoudenmire, E., White, S., 2010. Minimally entangled typical thermal state algorithms. New J. Phys. 12, 055026. Available from: https://doi.org/10.1088/1367-2630/12/5/055026.

Szalay, S., Pfeffer, M., Murg, V., Barcza, G., Verstraete, F., Schneider, R., et al., 2015. Tensor product methods and entanglement optimization for ab initio quantum chemistry. Int. J. Quant. Chem. 115, 1342. Available from: https://doi.org/10.1002/qua.24898.

Takasaki, H., Hikihara, T., Nishino, T., 1999. Fixed point of the finite system DMRG. J. Phys. Soc. Jpn. 68, 1537. Available from: https://doi.org/10.1143/JPSJ.68.1537.

Verstraete, F., Cirac, J., 2004. Renormalization algorithms for quantum-many body systems in two and higher dimensions. arXiv:cond-mat/0407066.

Verstraete, F., Cirac, J., 2006. Matrix product states represent ground states faithfully. Phys. Rev. B 73, 094423. Available from: https://doi.org/10.1103/PhysRevB.73.094423.

Verstraete, F., Garcia-Ripoll, J., Cirac, J., 2004. Matrix product density operators: simulation of finite-temperature and dissipative systems. Phys. Rev. Lett. 93, 207204. Available from: https://doi.org/10.1103/PhysRevLett.93.207204.

Vidal, G., 2003. Efficient classical simulation of slightly entangled quantum computations. Phys. Rev. Lett. 91, 147902. Available from: https://doi.org/10.1103/PhysRevLett.91.147902.

Vidal, G., 2004. Efficient simulation of one-dimensional quantum many-body systems. Phys. Rev. Lett. 93, 040502. Available from: https://doi.org/10.1103/PhysRevLett.93.040502.

Vidal, G., Latorre, J., Rico, E., Kitaev, A., 2003. Entanglement in quantum critical phenomena. Phys. Rev. Lett. 90, 227902. Available from: https://doi.org/10.1103/PhysRevLett.90.227902.

Weichselbaum, A., 2012. Non-abelian symmetries in tensor networks: A quantum symmetry space approach. Ann. Phys. 327, 2972. Available from: https://doi.org/10.1016/j.aop.2012.07.009.

White, S.R., 1992. Density matrix formulation for quantum renormalization groups. Phys. Rev. Lett. 69, 2863. Available from: https://doi.org/10.1103/PhysRevLett.69.2863.

White, S.R., 1993. Density-matrix algorithms for quantum renormalization groups. Phys. Rev. B 48, 10345. Available from: https://doi.org/10.1103/PhysRevB.48.10345.

White, S.R., 1996. Spin gaps in a frustrated heisenberg model for CaV_4O_9. Phys. Rev. Lett. 77, 3633. Available from: https://doi.org/10.1103/PhysRevLett.77.3633.

White, S.R., 2005. Density matrix renormalization group algorithms with a single center site. Phys. Rev. B 72, 180403. Available from: https://doi.org/10.1103/PhysRevB.72.180403.

Chapter 3

Density matrix renormalization group for semiempirical quantum chemistry

3.1 Introduction

Density matrix renormalization group (DMRG) for quantum chemistry has been quickly developed starting with the investigation of the electronic structure of conjugated oligomers and polymers in the late 1990s with semiempirical Hamiltonian, namely, from the original Hubbard model to models with additional long-range Coulomb potential such as the Pariser−Parr−Pople (PPP) model Hamiltonian (Anusooya et al., 1997; Fano et al., 1998; Ramasesha et al., 2000; Shuai et al., 1997b; Yaron et al., 1998). In fact, in the early 1990s, there existed hot debates over the role of electron correlation effects in conjugated polymers. The most prominent model for conjugated polymer has been Su−Schrieffer−Heeger (SSH) Hamiltonian, a one-electron model featuring electron−phonon interaction (Su et al., 1979, 1980). It was generally believed the electron correlation in polymer could be treated as weak perturbation and the overall behavior of electronic structure should be one-electron bandlike. Under such approximation, (1) there would be no excitonic effect since electron and hole become free carriers, but experimentalists reported excitonic binding energy ranging from less than k_BT (~ 0.026 eV) to 1 eV; (2) the cation spin density would distribute only on even sites and vanishes on odd sites. However, a number of experimental observations indicated that there exists negative spin density on odd sites, which can only be predicted from a correlated electron model; (3) the existence of bond alternation in polyacetylene is originated from electron−phonon coupling (Peierls transition), while correlated electron model would predict Mott-type insulator. Density functional theory (DFT) at the local density approximation level will simply predict vanishing bond-alternation. Such a chaotic situation called for an accurate method for extended systems with correlation effects. In fact, quantum chemistry at the configuration interaction single and double excitation (CISD) level had long predicted the even parity excited state ($2A_g$ symmetry) lying below the odd parity $1B_u$ state, in sharp contrast to the one-electron

molecular orbital picture (Schulten and Karplus, 1972). Furthermore, one-electron theory for evaluating the third-harmonic generation spectrum predicted a vanishing two-photon absorption (TPA) around $E_g/2$ position due to symmetry reason. Correlated electron system can give rise to TPA peak (so-called mA_g state) close to mid-gap (Shuai et al., 1998a). Such a picture had changed the scope for ultrafast spectroscopy for conjugated polymers.

In conjugated polymers, the π-orbitals are energetically well separated from the σ-orbitals and hence the bonding and antibonding molecular orbitals composed of the π-orbitals in the large conjugated systems are located close to the frontier orbitals, leading to rather strong static correlation. Compared to the ground state, the excited states of conjugated polymer show a more significant electron correlation effect. The first conducting polymer, polyacetylene (Fig. 3.1), is not fluorescent in experiments due to the long-known fact that the lowest excited state is of even parity A_g state instead of the odd parity B_u state predicted by the one-electron picture: the explanation from the latter is due to the dissociative nature for the photoexcited soliton−anitsoliton pair. The conventional quantum chemistry methods beyond the mean-field approximation, such as the configuration interaction (CI) and coupled cluster (CC) methods, both have the limitation in system size to describe the electronic structure of conjugated oligomers/polymers. Because of the exponential computational cost, the full CI (FCI) method is limited to 20 electrons/20 orbitals and thus is not scalable to larger systems. The multireference CI (MRCI) is accurate to describe the excited states of short polyene, but it is hard to correctly deal with the long polyenes because the truncated CI method (commonly with singles and doubles excitation, MRCISD) lacks size-consistency. In order to predict the properties of long oligomers or even the properties in the thermodynamic limit which is far beyond the computational capability, in practice, one often resorts to extrapolating properties computed for short oligomers. The absence of size-consistency of MRCI then would make this extrapolation hazardous even for the low-lying excitations. The single-reference CC method is also difficult to capture the strong correlation in the excited states of polyene correctly. It was demonstrated that the equation-of-motion CCSD predicted wrong excited states ordering of polyenes longer than 20 π-electrons (Shuai and Brédas, 2000). At that time, the multireference CC method was far from being mature. Besides the wavefunction theory, the time-dependent DFT (TDDFT) with common functionals always predicts the lowest excited state to be of B_u symmetry, similar to the one-electron model (Jiang et al., 2012). Therefore, during the 1990s, it was urgent to call for a novel electronic structure theory beyond the conventional quantum chemistry theories to solve the

FIGURE 3.1 The chemical structure of *trans*-polyacetylene.

electronic structure of conjugated polymers. It was natural and ideal to apply DMRG to the conjugated polymer which can be modeled as a one-dimensional fermion chain.

Ever since White invented DMRG in 1992, DMRG has been proven to have exceptionally high accuracy to calculate the electronic structure of the strongly correlated one-dimensional lattice model with only nearest-neighbor interactions, such as the Hubbard model and Heisenberg model (White, 1993, 1992). The success of DMRG is due to the fact that the entanglement is independent of the system size for the one-dimensional gapped system with only nearest-neighbor interactions, as predicted by the area law (Eisert et al., 2010). However, it is generally believed that the accuracy of DMRG drastically decreases for long-range interactions. For example, the accuracy is no more guaranteed for the two-dimensional Hubbard model, which is mapped to a one-dimensional chain with artificial long-range hopping terms (Nishimoto et al., 2002). For the same reason, the accuracy of DMRG for quantum chemistry Hamiltonian with long-range Coulomb interaction is unclear. In the late 1990s Shuai, Ramasesha, and Fano et al. firstly applied DMRG to solve the electronic structure of semiempirical quantum chemistry Hamiltonian, successfully demonstrating that in the (quasi-)one-dimensional polymer, even with the long-range density−density (diagonal) Coulomb interaction, the high accuracy of DMRG still holds (Fano et al., 1998; Shuai et al., 1997a; Yaron et al., 1998). Especially, Shuai et al. first applied DMRG for the exciton binding energy (Shuai et al., 1997c, 1998b). They demonstrated that the famous Hubbard model always gives rise to zero binding energy, a very much surprising while fully justified result: exciton binding stems from long-range Coulomb interaction, and only considering Hubbard U is not enough. Long-range potential is necessary for exciton to be bound. Then, they looked at the orderings for the lowest-lying excited states, (Shuai et al., 1997a,b) decisive for light-emitting property: according to Kasha's rule, the molecular luminescence is determined by the nature of the lowest-lying excited state, (Kasha, 1950) very sensitive to the level of methodology with electron correlation. Along this line, linear and nonlinear spectroscopies have been investigated (Shuai et al., 1998a). These works have been regarded as the start of quantum chemistry DMRG. Soon after, Daul et al. (2000), Mitrushenkov et al. (2001), White and Martin (1999) and Chan and Head-Gordon (2002) developed DMRG algorithms for ab initio quantum chemistry Hamiltonian, where a numerical renormalization scheme for the auxiliary developed by Xiang for momentum-space DMRG was employed (Xiang, 1996). Although DMRG for general molecules with three-dimension nature is not as accurate as for the one-dimensional models, it is still a state-of-the-art quantum chemistry method nowadays for systems with a large active space containing more than 20 active orbitals (Chapter 4). Moreover, it turns out to be especially powerful when combined with the conventional multireference methods to further account for the dynamic electron correlation (Chapter 6).

Most of the interesting properties of conjugated polymers involve excited states. With the state-averaged DMRG algorithm, not only the ground state but also the lowest several excited states can be accurately obtained (White, 1993). The originally proposed DMRG algorithm also considered the symmetry of the systems, (White, 1993) such as the conservation of the total particle number N_{tot} and the z-component of the total spin S_z. By restricting the system to a specific symmetric subspace, it is easy to target an excited state with the same algorithm for the ground state. For example, the lowest triplet state can be targeted in the subspace $S_z = 1$. However, the excited states of conjugated polymer are much more complicated in that between the ground state and the excited state of optical interest, there exist a number of irrelevant intruder states, which deteriorate the accuracy in the state-averaged calculation. To overcome this difficulty, the development of symmetrized DMRG algorithm, including additional electron-hole symmetry, spin-flip symmetry, and C_{2h} point group symmetry, made a great advance (Ramasesha et al., 1996). With the symmetrized DMRG algorithm, the exciton binding energy, ordering of excited states, and linear and nonlinear optical (NLO) response of conjugated polymer have been successfully investigated by Shuai et al. (Shuai and Peng, 2014, 2017).

The electron−phonon interaction is very important for organic systems because organic systems are more flexible than inorganic systems. One classic example is the Peierls instability which predicts that a one-dimensional equally spaced chain with one electron per site is unstable and thus it prefers to dimerize at half-filling to lower the total energy. Polyene with single/double bond alternation is a real-world system exhibiting Peierls instability. It was also found that the bond alternation has a large effect on the ordering of the excited states of polyene (Soos et al., 1993). In practice, one would add empirical electron−lattice interaction in the model Hamiltonian (called the Peierls term) to investigate the effect of chemical structure on the electronic structure. Besides the static electronic structure, the phonon will also affect the dynamical properties. By combining the time-dependent formulation of DMRG with molecular dynamics, soliton and polaron transport in the conjugated polymer has been investigated under the semiempirical model Hamiltonian (Ma and Schollwöck, 2010, 2009, 2008; Yao et al., 2008; Zhao et al., 2009, 2008).

The remaining of this chapter is arranged as follows: In Section 3.2, we give a brief introduction to the model Hamiltonians that have been largely employed in the study of conjugated molecules; in Section 3.3, the symmetrized DMRG algorithm, including the electron-hole symmetry, spin-flip symmetry, and C_{2h} point group symmetry, is described; in Section 3.4, several applications of DMRG in the study of the electronic structures of conjugated oligomer and polymer are reviewed, including the electronic structure of ground state and excited states, the exciton binding energy, the linear and nonlinear optical properties, and the effect of electron−lattice interaction on the electronic structure.

3.2 Semiempirical model Hamiltonian

In history, the semiempirical model Hamiltonian has been widely used to study the electronic structure of conjugated polymers. Since the separability of σ- and π-orbitals is generally found to be valid for low-energy excitations in the conjugated systems because the frontier orbitals mainly consist of π orbitals, the model Hamiltonian introduced in this section is only composed of π-orbitals. More specifically, each conjugated carbon atom contributes one $2p_z$ orbital and one electron if the system is neutral. In addition, the real-space p_z atomic orbitals are assumed to be orthonormal.

$$\langle \phi_i | \phi_j \rangle = \delta_{ij} \tag{3.1}$$

For simplicity, we will only give the one-dimensional model Hamiltonian for polyacetylene, the simplest conjugated polymer (Fig. 3.1). For neutral polyacetylene, the number of orbitals and the number of electrons are equal, that is, the half-filling case. The extension to a more general conjugated topology is fairly straightforward.

The minimal model considering the effect of electron correlation is the Hubbard model, which is one of the most famous models in theoretical physics. Hubbard model has been used extensively in studying the electronic structure of conjugated polymers.

$$\hat{H}_{\text{Hubbard}} = \sum_{i\sigma} \alpha_i \hat{a}_{i\sigma}^\dagger \hat{a}_{i\sigma} + \sum_{i\sigma} t_i \left(\hat{a}_{i\sigma}^\dagger \hat{a}_{i+1\sigma} + \hat{a}_{i+1\sigma}^\dagger \hat{a}_{i\sigma} \right) + \sum_i U_i \hat{n}_{i\uparrow} \hat{n}_{i\downarrow} \tag{3.2}$$

$$\hat{n}_{i\sigma} = \hat{a}_{i\sigma}^\dagger \hat{a}_{i\sigma} \tag{3.3}$$

The first two terms in Hubbard model are one-electron terms and the third term is a two-electron term. i is the index of p_z orbital. σ is the spin index. α_i is the energy of the p_z orbital, also called site energy or Coulomb integral. t_i is the hopping integral between the neighboring orbitals, also called transfer integral or resonance integral. The physical meaning of Hubbard U is the on-site Coulomb repulsion of two electrons occupying the same site. The Hubbard model in one dimension is exactly solvable with the Bethe ansatz (Lieb and Wu, 1968), but not in two dimensions.

For the Hubbard model, it can be discussed in two limiting cases separately depending on the parameter U/t. When $U/t << 1$ (weak correlation limit), the first two one-electron terms will dominate. In this case, the zeroth-order approximation of Hubbard model becomes Hückel model, which is the earliest π-electron model.

$$\hat{H}_{\text{Hückel}} = \sum_{i\sigma} \alpha_i \hat{a}_{i\sigma}^\dagger \hat{a}_{i\sigma} + \sum_{i\sigma} t_i \left(\hat{a}_{i\sigma}^\dagger \hat{a}_{i+1\sigma} + \hat{a}_{i+1\sigma}^\dagger \hat{a}_{i\sigma} \right) \tag{3.4}$$

Since the Hückel model is a one-electron Hamiltonian with no explicit electron correlation, it can be solved exactly with molecular orbital theory.

For an infinite-sized homogeneous chain with $\alpha_i = \alpha$, $t_i = t$ (without loss of generality, α is set to 0), the molecular orbitals form a free-electron band in the momentum space with dispersion relation $E = 2t\cos(k)(-\pi < k < \pi)$. Therefore, at half-filling, the energy gap predicted by the homogeneous Hückel model is 0. In the other limit with $U/t \gg 1$ (strong correlation limit), the third term in Eq. 3.2 can be regarded as the zeroth-order Hamiltonian. Because of the large U penalty, the electrons prefer to occupy different orbitals. Therefore, for a homogeneous chain at half-filling, the lowest zeroth-order wavefunction is a singly occupied spin chain with $E_0 = 0$. In addition, the degeneracy is 2^N (2 stands for two spin states and N is the total number of orbitals). According to the Rayleigh Schrödinger perturbation theory, the first-order energy is zero, which can not lift the degeneracy. We have to resort to the second order. After considering the second-order correction, the effective Hamiltonian becomes the spin-1/2 Heisenberg model (Eq. 3.5), which is also called the classical valence bond model. The coupling constant J is equal to $2t^2/U$. For more details about the derivation, please refer to Cleveland and Medina (1976).

$$\hat{H}_{\text{Heisenberg}} = \sum_i J\left(2\hat{S}_i\hat{S}_{i+1} - \frac{1}{2}\right) \qquad (3.5)$$

As $J > 0$, the spins tend to be oriented antiparallel between neighboring sites, leading to an antiferromagnetic order. This classical valence bond model and the extended nonempirical valence bond model have been solved by Jiang et al. using the DMRG method to investigate the electronic structures of the ground and excited states of polyacenes, polyphenanthrenes, and a series of high-spin organic π-conjugated polyradicals (Gao et al., 2002; Ma et al., 2007; Qu et al., 2009).

Since Hubbard model only has local Coulomb interaction, it is not able to describe the physics of exciton, which is a bound state of an electron and a hole attracted to each other by the Coulomb interaction. Hence, the minimal model to describe exciton in the conjugated polymer is the extended-Hubbard model, including the nearest-neighbor density−density Coulomb interaction.

$$\hat{H}_{\text{extended}-\text{Hubbard}} = \hat{H}_{\text{Hubbard}} + \sum_i V_i(\hat{n}_i - z_i)(\hat{n}_{i+1} - z_{i+1}) \qquad (3.6)$$

z_i represents the effective nuclear charge of the ith atom, which is 1 for carbon. Starting with the configuration in which one electron occupies one orbital, if one electron at the ith site hops to the next site upon excitation ($n_i = 0$, $n_{i+1} = 2$), the extended-Hubbard model will gain an electron-hole binding energy V_i, while the standard Hubbard model will not. A more general description of the Coulomb interaction is to include the long-range interactions, such as the PPP model. Historically, PPP model is a semiempirical quantum chemistry model invented even before the Hubbard model in

physics (Pariser and Parr, 1953; Pople, 1953). It stems from the widely known complete neglect of differential overlap (CNDO) approximation, but for conjugated π systems. In CNDO, in addition to the simplification that the overlap matrix of atomic orbitals is identity as Eq. (3.1), the two-electron integrals are simplified as

$$(ij|kl) = \delta_{ij}\delta_{kl}(ii|kk) \tag{3.7}$$

Here, we use the chemist's notation for the two-electron integral. Therefore the PPP model Hamiltonian can be written as

$$\hat{H}_{\text{PPP}} = \hat{H}_{\text{Hubbard}} + \sum_{i>j} V_{ij}(\hat{n}_i - z_i)(\hat{n}_j - z_j) \tag{3.8}$$

The long-range Coulomb interaction V_{ij} is empirically interpolated smoothly between U for zero intersite separation and e^2/r_{12} for the intersite separation tending to infinity. There are two widely used interpolation formulas given by Klopman (1964), Ohno (1964), and Mataga and Nishimoto (1957).

$$V_{ij}^{\text{Ohno-Klopman}} = \frac{1}{\sqrt{4/\left(U_i + U_j\right)^2 + R_{ij}^2}} \tag{3.9}$$

$$V_{ij}^{\text{Mataga-Nishimoto}} = \frac{1}{2/\left(U_i + U_j\right) + R_{ij}} \tag{3.10}$$

where R_{ij} is the real-space distance between site i and j. Comparing these two formulas, the potential given by Mataga−Nishimoto formula decays more rapidly than that of Ohno−Klopman formula. Compared to the (extended) Hubbard model with only nearest-neighbor interactions, the chemical models such as PPP model which have couplings with intermediate strengths and long-range interactions are much more difficult to handle.

The chemical structure of polyacetylene has alternating single bonds and double bonds. To incorporate this chemical structure in a model study, the simplest way is to modify the transfer integral with the bond alternation parameter δ.

$$t_i = t\left(1 + (-1)^i\delta\right) \tag{3.11}$$

The δ-related hopping term is called the Peierls term. The importance of this bond alternation parameter to the electronic structure of polyacetylene has been emphasized by Soos et al. (1993) and will be shown in Section 3.4. If the lattice distortion is also considered to be influenced by the electronic structure, the PPP−Peierls (or called PPP−SSH model) Hamiltonian, including the strain energy of lattice distortion, can be solved self-consistently.

$$\hat{H}_{\text{PPP-Peierls}} = \hat{H}_{\text{PPP}} + \sum_{i\sigma} \gamma_i d_i \left(\hat{a}_{i\sigma}^\dagger \hat{a}_{i+1\sigma} + \hat{a}_{i+1\sigma}^\dagger \hat{a}_{i\sigma}\right) + \frac{1}{2}\sum_i K_i d_i^2 \tag{3.12}$$

Here, d_i denotes the change of bond length $d_i = u_{i+1} - u_i$. u_i is the displacement of atom i. γ denotes the linear electron−phonon coupling parameter. K is the force constant of each bond. The PPP−Peierls model has been used to investigate the structure of polaron, soliton, and excited states in conjugated polymers under the interplay of electron−electron correlation and electron−phonon correlation (Barford, 2013; Bursill and Barford, 1999; Ma et al., 2006, 2005, 2004).

3.3 Symmetrized density matrix renormalization group algorithm

As introduced in Section 3.1, in conjugated polymers, there are many optically irrelevant states between the ground state and the lowest optically accessible excited states. For example, below the optically allowed $1B_u$ state, there will be more and more dark states when the system size increases. The state-averaged DMRG algorithm introduced in Chapter 5 could target the lowest several energy states together. However, the accuracy will deteriorate when the number of averaged states becomes larger and larger unless the bond dimension of DMRG wavefunction is increased at the same time. (White, 1993) Fortunately, the model to describe the conjugated oligomers and polymers in Section 3.2 possesses a number of symmetries. With symmetry restrictions, a lot of intruder states can be excluded during the renormalization procedures.

3.3.1 Particle number N_{tot} and S_z symmetry

The total particle number N_{tot} and the z-component of total spin S_z of a nonrelativistic closed system are conserved. These two U(1) symmetries are easy to implement in DMRG. Each renormalized state in the L- or R-block possesses good quantum number n and s_z. The quantum number of the wavefunction formed by the direct product of the L- and R-block renormalized states is

$$N_{tot} = n_L + n_R \tag{3.13}$$

$$S_z = s_{z,L} + s_{z,R} \tag{3.14}$$

The reduced density matrix of L-block is block-diagonal with respect to the quantum number $(n_L, s_{z,L})$ by tracing out the R-block basis. Hence, the new renormalized basis is still the eigenstates of $\hat{N}$ and $\hat{S}_z$.

3.3.2 Spin-flip symmetry

For the nonrelativistic Hamiltonians, besides that S_z is conserved, the total spin S is also conserved. However, the SU(2) spin symmetry is not an

Abelian group. For example, if the renormalized basis of L-block has spin S_1, in order to construct a state of spin S in the superblock, the spin of the renormalized basis of R-block S_2 could be $|S - S_1|, \cdots, |S + S_1|$. Hence, the reduced density matrix of R-block is not block-diagonal as the case of N_{tot} and S_z symmetry and then the eigenbasis will mix the basis of different S_2. The fully spin-adapted DMRG algorithm was proposed by McCulloch et al. by using a quasi-reduced density matrix to ensure that the renormalized basis are eigenfunctions of $\hat{S}^2$ (McCulloch and Gulácsi, 2001; Sharma and Chan, 2012). See Chapter 4 for more details on the implementation of a non-Abelian group in ab initio quantum chemistry DMRG. Before that, the spin-flip symmetry was first implemented which can distinguish the even ("e") total spin ($S = 0,2,4,\ldots$) and odd ("o") total spin ($S = 1,3,5,\ldots$) (Ramasesha et al., 1996). This symmetry can only be employed in $S_z = 0$ subspace because flipping the spin will map the S_z space to -S_z space. The spin-flip operator $\hat{P}_i$ acting on the Fock space of a single site is $\hat{P}_i|0\rangle = |0\rangle$, $\hat{P}_i|\uparrow\rangle = |\downarrow\rangle$, $\hat{P}_i|\downarrow\rangle = |\uparrow\rangle$, $\hat{P}_i|\uparrow\downarrow\rangle = -|\uparrow\downarrow\rangle$. The full operator of the system is the direct product of the single-site operator

$$\hat{P} = \prod_i \hat{P}_i \tag{3.15}$$

3.3.3 Spatial symmetry

Fig. 3.1 shows that trans-polyacetylene possesses C_{2h} point group symmetry. The principal axis is a twofold axis through the center and normal to the conjugated plane. There are four irreducible representations A_g, A_u, B_g, and B_u in C_{2h} point group, but the π-orbitals all belong to B_g and A_u. The product table of B_g and A_u is given in Table 3.1.

Therefore the excited states within the π-space only can be A_g or B_u symmetry. In addition, because of the restriction of π-orbitals, we can just use the subgroup C_2 to distinguish these two irreducible representations, denoted as A and B. If the symmetry adapted atomic orbitals or canonical molecular orbitals are adopted to rewrite the Hamiltonian, the Abelian point group symmetry can be treated with the same algorithm as particle number. However, DMRG is

TABLE 3.1 The product table of B_g, A_u irreducible representations of C_{2h} point group.

	B_g	A_u
B_g	A_g	B_u
A_u	B_u	A_g

known to be more accurate when working in real space, especially for the one-dimensional chain. Hence, the model Hamiltonians above are commonly solved in real space. In the real space, the C_{2h} symmetry is only ensured when sweeping to the middle of the DMRG chain. For example, sweeping from the left to the right, the renormalized basis for the L-block is $|\mu_L, \sigma_L\rangle$. Since the system has C_{2h} symmetry, the renormalized basis for the R-block should be a copy of the L-block. The matrix representation of $\hat{C}_2$ operator is

$$
\begin{aligned}
\hat{C}_2|\mu_L, \sigma_L, \mu'_R, \sigma'_R\rangle &= |\mu_R, \sigma_R, \mu'_L, \sigma'_L\rangle \\
&= (-1)^{(n_\mu + n_\sigma)(n_{\mu'} + n_{\sigma'})}|\mu'_L, \sigma'_L, \mu_R, \sigma_R\rangle
\end{aligned}
\tag{3.16}
$$

where n is the number of electrons in each block.

3.3.4 Electron-hole symmetry

The semiempirical models introduced above have a special symmetry called electron-hole (or called charge-conjugation) symmetry. Though this symmetry does not strictly hold in the ab initio Hamiltonian of conjugated polymers, the deviation is small and thus the electron-hole symmetry could help to understand and explain the experiments and computational results. A system has electron-hole symmetry if the Hamiltonian is invariant under the transformation of a particle into a hole (Surján, 2012). The symmetry exists in a system composed of two sublattices and at half-filling. The transformation relation is

$$
a_i^\dagger \to \tilde{a}_i^\dagger = (-1)^{\eta_i} a_i
\tag{3.17}
$$

η_i is zero for sites of one sublattice and one for sites of the other sublattice. It is obvious that the transformed operators still fulfill the anticommutation relation of fermion. After the electron-hole transformation,

$$
\begin{aligned}
\hat{\tilde{H}}_{PPP} &= \sum_{i\sigma} \alpha_i \hat{a}_{i\sigma} \hat{a}_{i\sigma}^\dagger + \sum_{i\sigma} t_i \left(-\hat{a}_{i\sigma} \hat{a}_{i+1\sigma}^\dagger - \hat{a}_{i+1\sigma} \hat{a}_{i\sigma}^\dagger \right) + \sum_i U_i \hat{a}_{i\uparrow} \hat{a}_{i\uparrow}^\dagger \hat{a}_{i\downarrow} \hat{a}_{i\downarrow}^\dagger \\
&\quad + \sum_{i>j} V_{ij} \left(\hat{a}_{i\uparrow} \hat{a}_{i\uparrow}^\dagger + \hat{a}_{i\downarrow} \hat{a}_{i\downarrow}^\dagger - 1 \right) \left(\hat{a}_{j\uparrow} \hat{a}_{j\uparrow}^\dagger + \hat{a}_{j\downarrow} \hat{a}_{j\downarrow}^\dagger - 1 \right) \\
&= \left(\sum_i 2\alpha_i - \sum_{i\sigma} \alpha_i \hat{a}_{i\sigma}^\dagger \hat{a}_{i\sigma} \right) + \sum_{i\sigma} t_i \left(\hat{a}_{i\sigma}^\dagger \hat{a}_{i+1\sigma} + \hat{a}_{i+1\sigma}^\dagger \hat{a}_{i\sigma} \right) \\
&\quad + \left(\sum_i U_i - \sum_i U_i \hat{n}_i + \sum_i U_i \hat{n}_{i\uparrow} \hat{n}_{i\downarrow} \right) + \sum_{i>j} V_{ij}(1 - \hat{n}_i)(1 - \hat{n}_j)
\end{aligned}
\tag{3.18}
$$

Compared to $\hat{H}_{PPP}$ in Eq. (3.8), the difference is

$$
\Delta = \sum_i 2\alpha_i - \sum_i 2\alpha_i \hat{n}_i + \sum_i U_i - \sum_i U_i \hat{n}_i
\tag{3.19}
$$
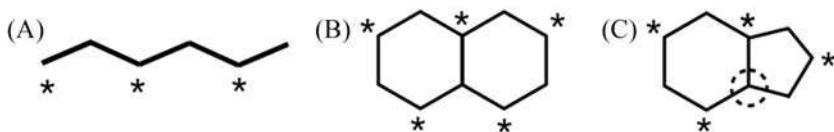
FIGURE 3.2 The electron-hole symmetry exists in (A) and (B) but not (C). The site with/without asterisk represents two different sublattices.

Therefore the electron-hole symmetry only exists in the half-filled systems, in which $\sum_i n_i = N$ (N is the total number of sites) and thus $\Delta = 0$. It doesn't have to be a one-dimensional system to have electron-hole symmetry. The key is the hopping part of the Hamiltonian. If the hopping terms only exist between the two sublattices, the hopping term is invariant after the electron-hole transformation in Eq. (3.17). Hence, the molecules in Fig. 3.2A and B have electron-hole symmetry, while the molecule in Fig. 3.2C does not. The electron-hole transformation operator acting on the Fock space of a single site is $\hat{J}_i|0\rangle = |\uparrow\downarrow\rangle$, $\hat{J}_i|\uparrow\rangle = (-1)^{\eta_i}|\uparrow\rangle$, $\hat{J}_i|\downarrow\rangle = (-1)^{\eta_i}|\downarrow\rangle$, $\hat{J}_i|\uparrow\downarrow\rangle = -|0\rangle$ (Ramasesha et al., 1996). The full electron-hole transformation operator is also given by the direct product of the single-site operators,

$$\hat{J} = \prod_i \hat{J}_i \tag{3.20}$$

The symmetry operators $\hat{P}$, $\hat{C}_2$, $\hat{J}$ commute with each other and form an Abelian group, which divides the space into eight irreducible representations— $^eA_+$, $^eA_-$, $^oA_+$, $^oA_-$, $^eB_+$, $^eB_-$, $^oB_+$, $^oB_-$. " $+$ " and " $-$ " denotes the two subspaces distinguished by the electron-hole symmetry, called "covalent" and "ionic" subspace. The symmetrization process is especially useful when discussing the optical excitation because the electric dipole operator $\mu = -e\sum_i x_i n_i$ is antisymmetric under $\hat{C}_2$, $\hat{J}$ and thus the selection rule ensures that the transition is only allowed between $^eA_+$ and $^eB_-$ (the ground state commonly belongs to $^eA_+$). To construct the symmetry adapted basis, the projector operator is

$$\hat{P}_\Gamma = \frac{1}{h}\sum_{\hat{R}} \chi_\Gamma(\hat{R})\hat{R} \tag{3.21}$$

where $\hat{R}$ is the symmetry operator, $\chi_\Gamma(\hat{R})$ is the character of $\hat{R}$ of irreducible representation Γ and $h = 8$ is the order of the group. After applying the projector operator to each direct product basis, the basis belonging to a particular irreducible representation is projected out. However, they are linear-dependent. To eliminate this linear dependency, the Gram−Schmidt orthogonalization algorithm is used. After that, the symmetry-adapted transformation matrix S is constructed (Ramasesha et al., 1996). To abandon the costly Gram−Schmidt algorithm, the transformation matrix S could also be constructed by tracking the symmetric connections of each renormalized

basis (Prodhan and Ramasesha, 2018). The effective Hamiltonian projected into a specific subspace is

$$\tilde{H} = S_\Gamma^\dagger H S_\Gamma \tag{3.22}$$

3.4 Applications

3.4.1 The electronic structure of the ground state of cyclic polyene

The ground-state electronic structure of cyclic polyene $(CH)_N$ (Fig. 3.3) has been studied by unrestricted Hartree−Fock (UHF), CC methods, etc. (Bendazzoli and Evangelisti, 1991; Bendazzoli et al., 1994; Fukutome, 1968; Paldus and Piecuch, 1992). The UHF solution of PPP model Hamiltonian predicted that there are spin density wave and charge density wave in the system. However, since UHF is not accurate for strongly correlated systems, it is interesting to check the results with DMRG. Fano et al. first applied DMRG to study the ground-state electronic structure of cyclic polyene $(CH)_N$ under homogeneous PPP model with Mataga−Nishimoto's formula of long-range Coulomb interaction (Fano et al., 1998). Table 3.2 shows the ground-state energy of cyclic polyene with the number of sites N ranging from 6 to 34 calculated by restricted Hartree-Fock (RHF), UHF, CC doubles (Bendazzoli et al., 1994), approximate coupled pair theory with quadruples and with triples and quadruples (Paldus and Piecuch, 1992), DMRG, and FCI. With $N \le 18$, the FCI calculation is still affordable, which could be used to assess the accuracy of the other approximate methods. The DMRG results are very close to FCI with only bond dimension $m = 512$. The error of $N = 18$ is only 5.7×10^{-4} eV. Even compared to the sophisticated CC methods, DMRG is still much more accurate. The results demonstrate the high accuracy of DMRG in one-dimensional semiempirical quantum chemistry Hamiltonian with long-range Coulomb interaction.
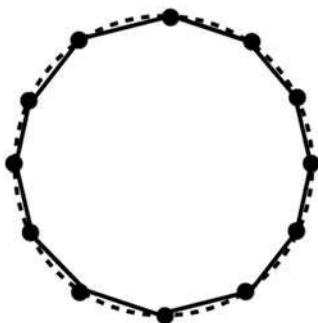
FIGURE 3.3 The topological structure of cyclic polyene $(CH)_N$.

TABLE 3.2 The energies (in eV) of cyclic polyene $(CH)_N$ calculated by restricted Hartree−Fock (RHF), unrestricted Hartree−Fock (UHF), coupled cluster doubles (CCD) (Bendazzoli et al., 1994), approximate coupled pair theory with quadruples (ACPQ), approximate coupled pair theory with triples and quadruples (ACPTQ) (Paldus and Piecuch, 1992), density matrix renormalization group (DMRG), and full configuration interaction (FCI) (Bendazzoli and Evangelisti, 1991; Bendazzoli et al., 1994) are compared for the different number of sites N.

N	RHF	UHF	CCD	ACPQ	ACPTQ	DMRG	FCI
6	− 11.358325	− 11.358325	− 12.703501	− 12.7011	− 12.7101	− 12.722032	− 12.722033
10	− 17.441467	− 17.910422	− 19.928697	− 19.9565	− 20.0185	− 20.060503	− 20.060503
14	− 23.731302	− 24.924267	− 27.326180	− 27.4399	− 27.5981	− 27.671333	− 27.671391
18	− 30.101389	− 32.007998	−	− 34.9974	− 35.2980	− 35.384861	− 35.385430
22	− 36.513220	− 39.105943	−	− 42.5918	− 43.1000	− 43.145027	−
26	− 42.950070	− 46.207715	−	−	− −	− 50.928028	−
30	− 49.403281	− 53.310920	−	−	−	− 58.715323	−
34	− 55.867856	− 60.414852	−	−	−	− 66.509902	−

FIGURE 3.4 (A) The spin−spin correlation function $S(i-j) = \langle S_z(i)S_z(j) \rangle$ and (B) density−density correlation function $R(i,j) = \langle n(i)n(j) \rangle - \langle n(i) \rangle \langle n(j) \rangle$ of cyclic polyene $(CH)_N$ calculated by DMRG. *DMRG*, Density matrix renormalization group. *Reproduced from Fano, G., Ortolani, F., Ziosi, L., 1998. The density matrix renormalization group method: application to the PPP model of a cyclic polyene chain. J. Chem. Phys. 108, 9246−9252.* https://doi.org/10.1063/1.476379, *with permission from American Institute of Physics.*

The spin−spin correlation function and the density−density correlation function $R(i,j) = \langle n(i)n(j) \rangle - \langle n(i) \rangle \langle n(j) \rangle$ of the ground state were also calculated by DMRG. Fig. 3.4A shows that there is indeed spin density wave in the cyclic polyene, but contrary to the results of UHF, there is only short-range antiferromagnetic ordering instead of long-range antiferromagnetic ordering. Fig. 3.4B shows that there is no charge density wave.

3.4.2 The excited states ordering, exciton binding, and optical properties of polyene

According to Kasha's rule, photon emission mostly occurs from the lowest electronic excited state of molecules (Kasha, 1950). Thus molecules or polymers with a dipole-forbidden lowest excited state deem to be nonemissive. The lowest excited state of short linear polyenes is a dipole-forbidden dark state with A_g symmetry instead of dipole allowed B_u state as a result of strong electron correlation (Schulten and Karplus, 1972; Tavan and Schulten, 1987). It is intriguing to reveal the excited state ordering for long polyenes or even for polyacetylene. In the independent electron limit, the $2A_g$ state corresponds to a mix of single excitation from HOMO to LUMO + 1, HOMO-1 to LUMO, and double excitation from HOMO to LUMO, while $1B_u$ state is a HOMO to LUMO single excitation. Thus, for short-chain polyene, the $2A_g$ excited state energy is significantly higher than that of $1B_u$ excited state due to the discreteness of the molecular orbital energy spectrum. When the electron correlation Hubbard U is turned on, the gap between the ground state and the $2A_g$ state narrows (In the infinite U limit, the $2A_g$ state becomes a covalent spin excitation), while the gap to the $1B_u$ state increases. The energy of states will thus cross at a given Hubbard U, which is called the "U-crossover". However, for an infinite chain, the $2A_g$

and $1B_u$ states both occur at the same energy in the Hückel limit ($U = 0$). If the $2A_g$ and $1B_u$ states evolve in the same manner as the short chains, these states would never cross with increasing U. Thus, for a given U, there must occur a crossover when the chain length increases, which is called the "N-crossover." Soos et al. (1993) found a crossover occurred with a variation of the bond-alternation parameter δ from exact diagonalization studies of short chains, which is referred to as the "δ-crossover". These three different types of crossover in polyene, U-crossover, N-crossover, and δ-crossover, have been studied thoroughly by symmetrized DMRG (Shuai et al., 1997b).

As introduced in Section 3.2, the extended-Hubbard−Peierls model is the minimal model to consider the exciton effect. Fig. 3.5 shows the "U-crossover" for short ($N = 8$) and long ($N = 80$) chains for fixed alternation $\delta = 0.07$ and $V = 0.4U$. The DMRG cutoff has been chosen between $m = 100$ and $m = 150$, depending on the necessity of numerical convergence at about 10^{-5}. This V/U relation belongs to the meaningful phase corresponding to the bond-order wave (BOW) regime ($V < U/2$). The critical correlation strength, U_c, at which the crossover occurs, is nearly independent of the chain length N. In both $N = 8$ and $N = 80$ cases, U is around $2.5t$. It is well known that the electron correlation tends to increase the energy of the ionic excitation (the U penalty) and stabilize the covalent excitation. Especially in the strong correlation limit, the $2A_g$ state becomes a covalent spin excitation
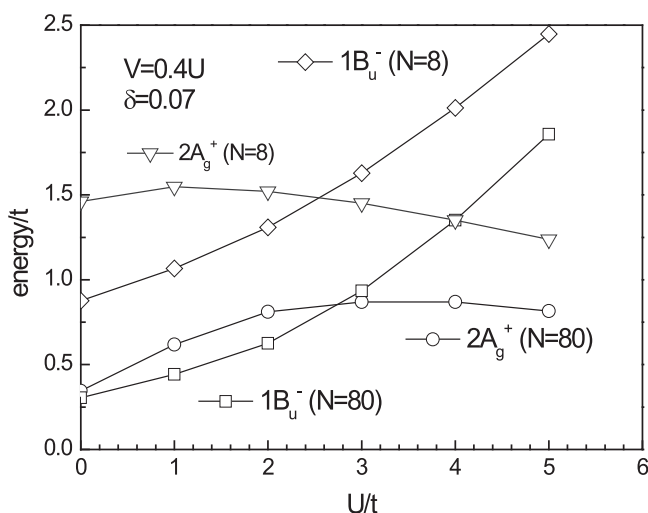
FIGURE 3.5 Crossover on U for $N = 8$ and $N = 80$ of extended-Hubbard model calculated by DMRG. *DMRG*, Density matrix renormalization group. *Reproduced from Shuai, Z., Bredas, J.-L., Pati, S.K., Ramasesha, S., 1997b. Quantum confinement effects on the ordering of the lowest-lying excited states in conjugated polymers, in: Optical Probes of Conjugated Polymers. International Society for Optics and Photonics, pp. 293−302.* https://doi.org/10.1117/12.279282, *with permission from International Society for Optical Engineering.*

which is gapless when $V = 0$, $\delta = 0$ and this state is composed of two triplets, suggested by Tavan and Schulten (1987). Thus an increase in correlation strength would lead to a decrease in the $2A_g$ energy. However, in the $N = 8$ chain, the energy of $2A_g$ state remains nearly constant before decreasing for values of U/t larger than 2.0. In longer chains, the $2A_g$ energy increases even more rapidly than the $1B_u$ energy as the correlation strength increases when $U/t < 2$. This implies a substantial ionic contribution to the $2A_g$ state in long chains when U is small besides the covalent triplet−triplet contribution.

Fig. 3.6 shows the δ-crossover and N-crossover in extended-Hubbard model. Fig. 3.6B shows that for short-chain at $U/t = 4$, $\delta = 0.27$, $2A_g$ is below $1B_u$. Upon elongating the chain length, the $1B_u$ state becomes lower than $2A_g$ state. This is because that $2A_g$ can be mainly regarded as two trip-let states, which is repulsive when the chain is too short. But when space is allowed, the $2A_g$ state saturates since triplets are much more localized than $1B_u$ state. This is a direct theoretical observation of quantum confinement-induced crossover. It should be mentioned that this behavior can only exist for intermediate correlation strength: for weak correlation, there does not exist any crossover and $2A_g$ lies above the $1B_u$ state for all chain lengths as seen from the left half of Fig. 3.5; at large values of U/t in the atomic limit, the crossover is also not expected as $2A_g$ always lies below the $1B_u$ state (the right half of Fig. 3.5). It has been widely accepted that the conjugated
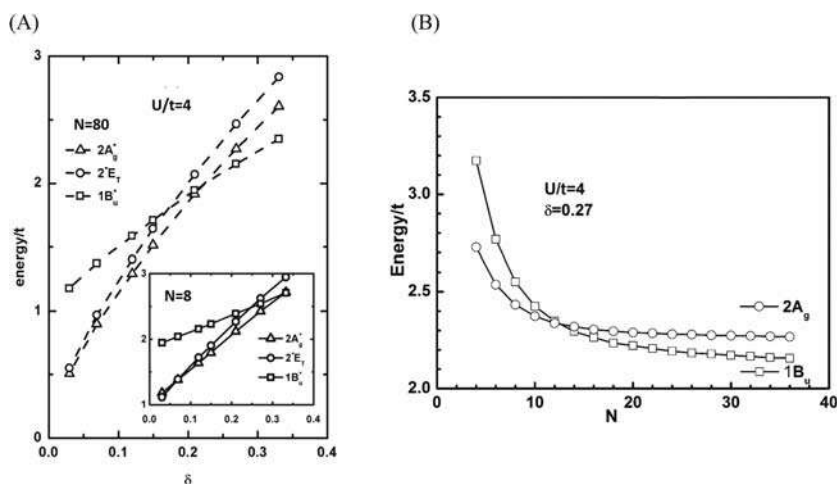
FIGURE 3.6 Crossover on (A) bond length alternation parameter δ (B) chain length N of extended-Hubbard model calculated by DMRG. *DMRG*, Density matrix renormalization group. *Reproduced from Shuai, Z., Bredas, J.-L., Pati, S.K., Ramasesha, S., 1997b. Quantum confine-ment effects on the ordering of the lowest-lying excited states in conjugated polymers, in: Optical Probes of Conjugated Polymers. International Society for Optics and Photonics, pp. 293−302. https://doi.org/10.1117/12.279282, with permission from International Society for Optical Engineering.*

molecules fall in the intermediate correlation regime. Thus the confinement-induced crossover is realistic. Beyond the extended-Hubbard model with only nearest-neighbor Coulomb interaction, PPP model with Ohno−Klopman formula of long-range Coulomb interaction has also been further investigated (Shuai et al., 1997b). For the chosen set of parameters ($U = 11.26$ eV, $t = 2.4$ eV, $\delta = 0.07$), DMRG can still be considered nearly accurate in the sense that (1) the total ground-state energy per electron is reduced by only 10^{-3} eV when increasing the bond dimension m from 100 to 120, and (2) for $m = 100$, the difference between the sum of the kept eigenvalues of the density matrices and 1 is less than 10^{-5}, which is widely considered as a criterion for the accuracy of DMRG. Fig. 3.7 shows that there does not exist any N-crossover (the $2A_g$ state of $N = 2$ is an exception because the state is not of double triplets character). For all chain lengths, the covalent $2A_g$ state is always below $1B_u$ state. In addition, the energy of $2A_g$ state is almost twice that of T_1 state.

Organic materials usually have quite a small dielectric constant ($\sim 2-3$), in contrast to inorganic semiconductors (> 10). Thus the Coulomb interaction cannot be well-screened, which leads to a much more pronounced electron-hole binding, or excitonic effect (Shuai et al., 1998b, 1997c; Yaron et al., 1998). However, the value of the exciton binding energy of conjugated polymer is a hotly debated issue——the binding energy ranging from 0.025 to
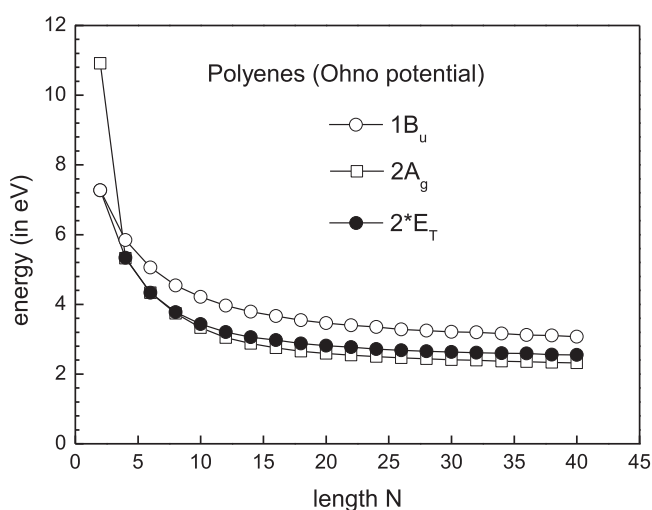
FIGURE 3.7 Excited states energies of polyenes under PPP model. *PPP*, Pariser−Parr−Pople. *Reproduced from Shuai, Z., Bredas, J.-L., Pati, S.K., Ramasesha, S., 1997b. Quantum confinement effects on the ordering of the lowest-lying excited states in conjugated polymers, in: Optical Probes of Conjugated Polymers. International Society for Optics and Photonics, pp. 293−302. https://doi.org/10.1117/12.279282, with permission from International Society for Optical Engineering.*

1 eV has been proposed in different studies. Some early results of quantum chemistry calculations showed that the exciton binding energy is extremely sensitive to both the level at which electron correlation effects are treated and the size of basis set, and usually provided too large a binding energy in comparison to the experiment. The exciton binding energy is defined as the difference between the charge excitation gap (bandgap) E_g and optical gap $E(1B_u)$. The bandgap is defined as $E_g = E(N-1) + E(N+1) - 2E(N)$ which constitutes the continuum band edge and corresponds to a well-separated pair of quasi-electron and hole ($E(N)$ is the energy of N electron system). Thus the exciton binding energy is defined as $E_b = E_g - E(1B_u)$. For the extended Hubbard–Peierls model, the excited states were calculated (Shuai et al., 1998b, 1997c). Fig. 3.8A shows that for $\delta = 0$ and $U = 5$, V does not induce any binding in the BOW phase ($V < U/2$). V lowers both the bandgap and the $1B_u$ excitation energy, see inset in Fig. 3.8A. For fixed $\delta = 0.2$, small V values hardly enhance E_b; however, a larger V strongly enhances E_b. Hence, exciton is bound only when V is large enough relative to U. Fig. 3.8B shows that for fixed electron correlation strength, E_b increases as δ increases. This implies that the larger the δ value, the more excitonic like the lowest charge excitation. From Fig. 3.8C, it is clearly seen that the δ dependence of E_b is strongly suppressed by U. Interestingly, the behavior that the Hubbard U drastically decreases the $1B_u$ exciton binding energy is rather counter-intuitive: since exciton binding is a correlation effect, the Hubbard U would be expected to increase E_b.
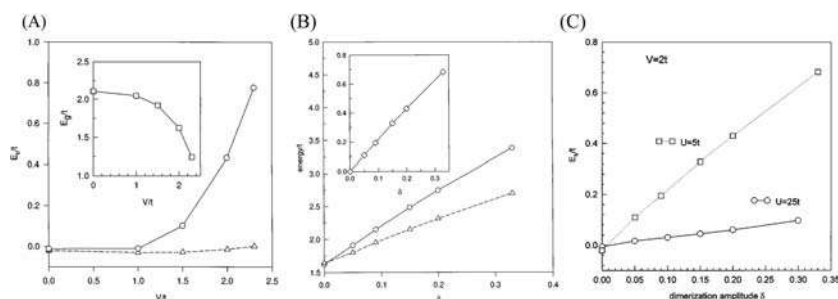
FIGURE 3.8 (A) Dependence of the binding energy E_b of $1B_u$ state on V/t for $U/t = 5$. Circles represent $\delta = 0.2$ and triangles $\delta = 0$. The inset shows the dependence of band gap E_g on V/t for $\delta = 0$. (B) Dependence of bandgap (circles) and $1B_u$ exciton energy (triangles) on alternation parameter δ for $U/t = 5$, $V/t = 2$. The inset shows E_b as a function of δ. (C) Dependence of the $1B_u$ exciton binding energy on δ with $V = 2t$: solid line for $U = 25t$ and dotted line for $U = 5t$. *Reproduced from Shuai, Z., Pati, S.K., Su, W., Brédas, J., Ramasesha, S., 1997c. Binding energy of 1 B u singlet excitons in the one-dimensional extended Hubbard-Peierls model. Phys. Rev. B. 55, 15368. https://doi.org/10.1103/PhysRevB.55.15368; Shuai, Z., Brédas, J.-L., Pati, S., Ramasesha, S., 1998b. Exciton binding energy in the strong correlation limit of conjugated chains. Phys. Rev. B. 58, 15329. https://doi.org/10.1103/PhysRevB.58.15329, with permission from American Physical Society.*

There is major interest in studying the linear and nonlinear optical responses of conjugated molecules and polymers. The response properties can be calculated with the sum-of-states (SOS) approach or the correction vector (CV) approach (introduced in Chapter 7 in detail). Ramasesha et al. and Shuai et al. first combined DMRG and these two approaches to investigate the response properties of conjugated polymers (Pati et al., 1999, p. 199; Ramasesha et al., 1997; Shuai et al., 1998a). As the dipole moment operator only couples the A_g and B_u subspace, the third-order polarizability can be expressed by time-dependent perturbation theory as

$$\gamma(-\omega_\sigma; \omega_1, \omega_2, \omega_3) =$$
$$P_{123\sigma} \sum_{lmn} \frac{\langle 1A_g|\mu|lB_u\rangle\langle lB_u|\mu|mA_g\rangle\langle mA_g|\mu|nB_u\rangle\langle nB_u|\mu|1A_g\rangle}{(\omega_{lB_u} - \omega_\sigma)(\omega_{mA_g} - \omega_1)(\omega_{nB_u} - \omega_2)} \quad (3.23)$$

where $\omega_\sigma = \omega_1 + \omega_2 + \omega_3$; $P_{123\sigma}$ represents a summation over the 24 terms of the permutations over $(-\omega_\sigma; \omega_1, \omega_2, \omega_3)$. In the SOS approach, the intermediate state nB_u and mA_g are calculated explicitly. The key aspect of SOS approach is that the summation should be converged with a few lowest excited states otherwise the approach is inefficient. In the CV approach (Ramasesha et al., 1997), only the CV $\left|\phi_i^{(1)}(\omega_1)\right\rangle$ and $\left|\phi_{ij}^{(2)}(\omega_1, \omega_2)\right\rangle$ should be calculated as

$$(H - E_0 + \omega_1 + i\varepsilon)\left|\phi_i^{(1)}(\omega_1)\right\rangle = \mu_i|1A_g\rangle \quad (3.24)$$

$$(H - E_0 + \omega_2 + i\varepsilon)\left|\phi_{ij}^{(2)}(\omega_1, \omega_2)\right\rangle = \mu_i\left|\phi_i^{(1)}(\omega_1)\right\rangle \quad (3.25)$$

The subscript i, j denote the direction of external field. With the CV, the linear polarizability α_{ij} and the third-order polarizability γ_{ijkl} could be calculated as

$$\alpha_{ij}(\omega) = \langle\phi_i^{(1)}(\omega)|\mu_j|1A_g\rangle + \langle\phi_i^{(1)}(-\omega)|\mu_j|1A_g\rangle \quad (3.26)$$

$$\gamma_{ijkl}(-\omega_\sigma; \omega_1, \omega_2, \omega_3) = P_{123\sigma}\left\langle\phi_i^{(1)}(\omega_\sigma)|\mu_j|\phi_{kl}^{(2)}(\omega_{12}, -\omega_1)\right\rangle \quad (3.27)$$

Table 3.3 shows the comparison of linear and third-order polarizabilities of Hubbard model and extended-Hubbard model calculated by CV-DMRG and exact diagonalization (Ramasesha et al., 1997). The DMRG results agree very well with the exact ones, demonstrating its high accuracy.

In Fig. 3.9A, the TPA spectra represented by the dipole transitions between the A_g excited states and the $1B_u$ state are shown (Shuai et al., 1998a). Kohler and Terpougov (1996) measured the higher A_g states of trans-octatetraene by two-photon fluorescence excitation spectroscopy (upper panel of Fig. 3.9B). There are four distinct features in the experimental two-photon fluorescence excitation spectrum at 5.54, 5.81, 5.96, and 6.18 eV.

TABLE 3.3 The linear and third-order polarizability of Hubbard and extended-Hubbard model with 12 sites calculated by correction vector-Density matrix renormalization group (CV-DMRG) ($m = 100$) and exact diagonalization. The trans-polyene geometry is used with all bond length equal to 1 Å. α values are in units of 10^{-24} esu. γ values are in units of 10^{-36} esu.

Polarizability	$U = 3t,\ V = 0$		$U = 3t,\ V = 1.5t$		$U = 3t,\ V = 2.0t$	
	Exact	DMRG	Exact	DMRG	Exact	DMRG
α_{xx}	42.61	42.57	152.12	152.05	997.90	997.72
α_{xy}	2.95	2.91	35.45	35.38	383.11	382.99
α_{yy}	1.52	1.44	14.20	14.06	154.73	154.41
γ_{xxxx}	26571	26566	51380	51374	−32929131	−32929014
γ_{xxyy}	113.8	109.1	2637.7	2628.6	−4915213	−4915102
γ_{yyyy}	1.24	1.22	189.9	186.0	−736663	−736556
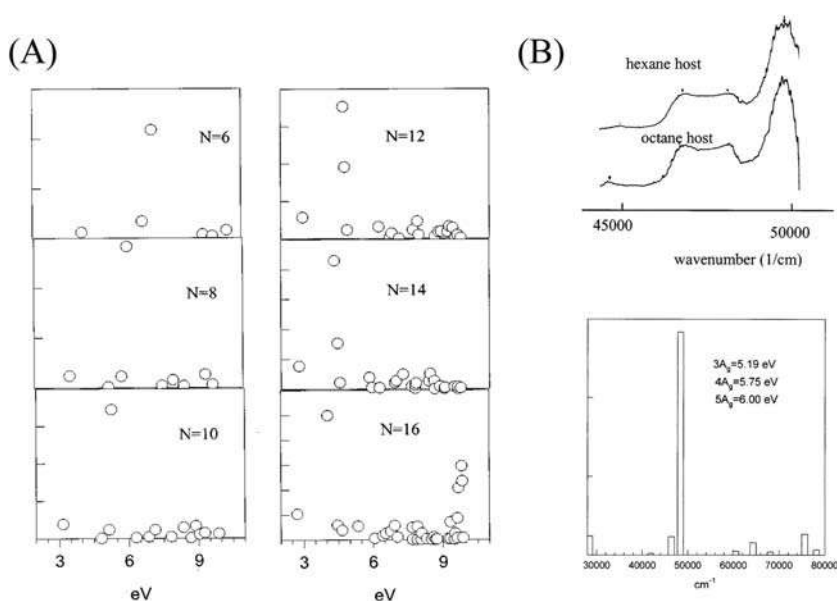
FIGURE 3.9 (A) Two-photon absorption spectra for chain length $N = 6-16$. (B) The comparison of experimental two-photon fluorescence excitation spectrum (upper panel) with DMRG results (lower panel) for octatetraene ($N = 8$). *DMRG*, Density matrix renormalization group. *Reproduced from Shuai, Z., Brédas, J., Saxena, A., Bishop, A., 1998a. Linear and nonlinear optical response of polyenes: a density matrix renormalization group study. J. Chem. Phys. 109, 2549−2555. https://doi.org/10.1063/1.476827. With permission from American Institute of Physics.*

The theoretical spectrum in the same energy window gives three features at 5.19 ($3A_g$), 5.75 ($4A_g$), and 6.00 eV ($5A_g$). Both the calculated relative intensities and positions are in good agreement with the experiment. The middle two peaks in the experiment probably have the same electronic origin——the $4A_g$ state and its vibronic band.

3.4.3 Soliton structure of excited states of polyene

The electron−lattice interaction has an important effect on the electronic structure of conjugated polymers. The famous SSH model, which is a one-electron model, has been well investigated to study the self-trapping structure of polaron and soliton on polyene (Su et al., 1979, 1980). In the presence of realistic electron correlations, Ramasesha et al. (2000) and Bursill and Barford (1999) have studied the equilibrium geometries of excitations in the PPP−Peierls model. The energy of PPP−Peierls model in Eq. 3.12 can be minimized iteratively under the constraint that the total length of the system is

unchanged. Thus the objective functional is defined as

$$\mathcal{L}(\{d_i\}, \Psi) = \langle \Psi | \hat{H} | \Psi \rangle + \eta \sum_i d_i \tag{3.28}$$

where η is the Lagrange multiplier.

$$\frac{\delta \mathcal{L}}{\delta \eta} = \sum_i d_i = 0 \tag{3.29}$$

With the Hellmann−Feynman theorem,

$$\frac{\delta \mathcal{L}}{\delta d_i} = \gamma_i \left\langle \Psi \left| \widehat{T}_i \right| \Psi \right\rangle + K_i d_i + \eta = 0 \tag{3.30}$$

$$\widehat{T}_i = \sum_\sigma a_{i\sigma}^\dagger a_{i+1\sigma} + a_{i+1\sigma}^\dagger a_{i\sigma} \tag{3.31}$$

Assuming $\gamma_i = \gamma$, $K_i = K$ and summing up all the $\delta \mathcal{L}/\delta d_i$, then

$$\eta = -\gamma \langle \Psi | \sum_i \widehat{T}_i | \Psi \rangle \tag{3.32}$$

Therefore

$$d_i = \frac{\gamma}{K} \left(\langle \Psi | \sum_j \widehat{T}_j | \Psi \rangle - \langle \Psi | \widehat{T}_i | \Psi \rangle \right) \tag{3.33}$$

Since Ψ depends on d_i, the optimization should be solved self-consistently. For polyene, the hopping integral is $t_0 = -2.539$ eV and the Hubbard U is $U = 10.06$ eV. The force constant is 46 eV/Å^2. The initial C−C bond length is 1.46 Å for the single bond and 1.35 Å for the double bond. The bond angle is fixed to be 120 degrees. The Ohno−Klopman long-range Coulomb potential is used. The electron−phonon coupling is $\gamma = 4.593$ eVÅ^{-1} (Bursill and Barford, 1999). Fig. 3.10 shows the vertical excitation energy at the equilibrium ground state geometry and 0−0 excitation energy of $2^1A_g^+$, $1^1B_u^-$ states and triplet $1^3B_u^+$ state with different chain lengths (Bursill and Barford, 1999). At the equilibrium ground state geometry, the energies of $2^1A_g^+$ and $1^1B_u^-$ are very close to each other. In addition, there is one crossover in the short chain and one crossover in the long chain. In the thermodynamic limit, the optical allowed $1^1B_u^-$ state is below the dark $2^1A_g^+$ state, same as Fig. 3.6B. After geometry optimization, the relaxation energy of $1^1B_u^-$ state is about 0.3 eV, while the relaxation energies of $2^1A_g^+$ and $1^3B_u^+$ are more substantial, about 1.0 and 0.5 eV, respectively. Hence, the $2^1A_g^+$ state is well below the $1^1B_u^-$ state after relaxation.

Fig. 3.11 plots the bond length parameter defined as $\delta_i = (-1)^i (t_i - \bar{t})/\bar{t}$ of different states with $N = 102$ after relaxation, where t_i is the hopping integral
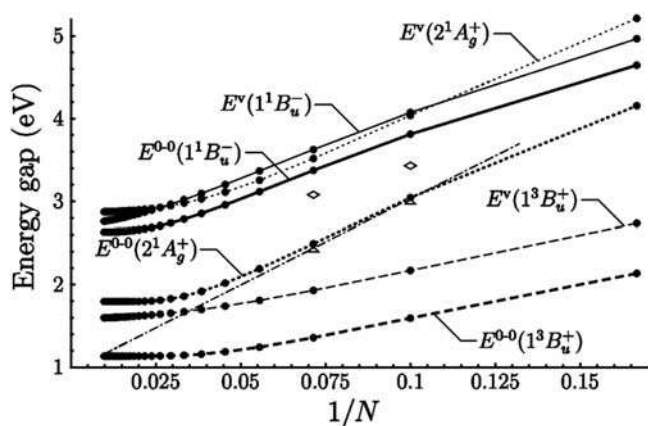
FIGURE 3.10 The vertical excitation energy at the equilibrium ground state geometry and 0−0 excitation energy of $2^1A_g^+$, $1^1B_u^-$ states and triplet $1^3B_u^+$ state with different chain lengths. *Reproduced from Bursill, R.J., Barford, W., 1999. Electron-lattice relaxation, and soliton structures and their interactions in polyenes. Phys. Rev. Lett. 82, 1514. https://doi.org/10.1103/ PhysRevLett.82.1514. With permission from American Physical Society.*
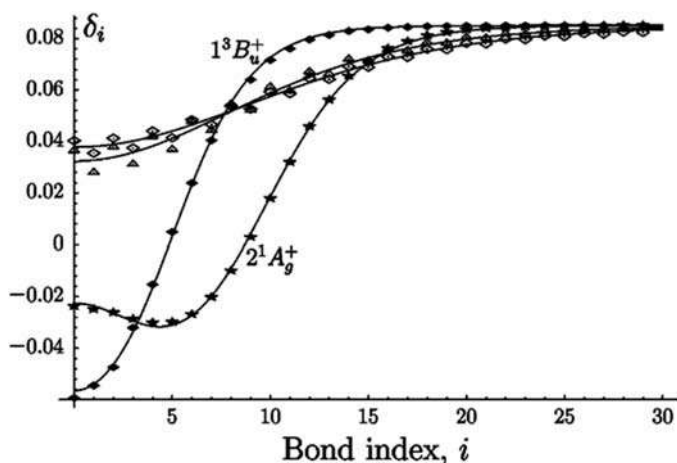
FIGURE 3.11 The bond length parameter of different excited states near the center of the chain ($N = 102$). The markers are the numerical results. The solid lines are the fit with 2-soliton (for $1^1B_u^-$ and $1^3B_u^+$ states) and 4-soliton formula (for $2^1A_g^+$ state). *Reproduced from Bursill, R.J., Barford, W., 1999. Electron-lattice relaxation, and soliton structures and their interactions in polyenes. Phys. Rev. Lett. 82, 1514. https://doi.org/10.1103/PhysRevLett.82.1514. With permission from American Physical Society.*

of the ith bond after optimization and $\bar{t}$ is the average hopping integral. The markers are the numerical results. The solid line is the 2-soliton fit for $1^1B_u^-$ and $1^3B_u^+$ states and 4-soliton fit (Su, 1995) for $2^1A_g^+$ state. Fig. 3.11 shows that $1^3B_u^+$ and $2^1A_g^+$ undergo a substantial bond distortion, while $1^1B_u^-$ only has weak distortion. This is consistent with the different behaviors of relaxation energy. The good fit of soliton's hyperbolic tangent formula indicates that the $1^3B_u^+$ state and $1^1B_u^-$ states are one soliton−antisoliton pair and the $2^1A_g^+$ state is composed of two soliton−antisoliton pairs. The 4-soliton character of the $2^1A_g^+$ state also demonstrates the fact that it has a considerable triplet−triplet character.

3.4.4 Intramolecular singlet fission in donor−acceptor type conjugated copolymer

Singlet fission (SF), a photophysical process occurring in organic conjugated molecules, such as tetracene and pentacene, has received a lot of attention from both experimentalists and theoreticians in the last decade (Smith and Michl, 2010). The basic microscopic process of SF is that the system absorbs a photon to become a singlet exciton, which then splits into two triplet excitons. According to the coupling rule of spin, two triplet states with $S = 1$ can be coupled into a singlet state with $S = 0$. Therefore the SF process is a spin-allowed process unlike the intersystem crossing. Scientists are interested in the SF process because with SF material it is possible to break the Shockley−Queisser limit for a single junction solar cell. In 2015 Busby et al. first reported that $PBTDO_1$ (benzodithiophene (B)-thiophene-1,1-dioxide (TDO)), a copolymer composed of strong donor−acceptor (DA) units, exhibits intramolecular SF (iSF) with high quantum efficiency ($\sim 170\%$) (Busby et al., 2015b). Before that, only high-efficiency intermolecular SF (xSF) was observed. Compared to xSF, iSF in DA-copolymer has the advantage that it is not sensitive to intermolecular packing and thus is more promising in practical applications. However, the microscopic mechanism of iSF is not very clear. Among the low-lying excited states, one double excitation state with triplet−triplet pair character plays the role of intermediate state, which is called $^1(TT)$ state. Some studies suggested that the $2A_g$ state is a coupled triplet−triplet state as polyacetylene discussed above (Aryanpour et al., 2015; Tavan and Schulten, 1987). By contrast, other studies suggested that $2A_g$ is destructive as a nonradiative decay pathway in competition with SF process (Busby et al., 2015a). Since $^1(TT)$ state is a double excitation state, the conventional single excitation methods will fail to correctly describe this state. Therefore it is necessary to use DMRG to study the low-lying states of the iSF system.

$$S_1 \rightleftharpoons {}^1(TT) \rightleftharpoons T_1 + T_1 \qquad (3.34)$$

The PPP model Hamiltonian is adopted to describe the conjugated backbone of DA-copolymer (Ren et al., 2017). To incorporate the electronic
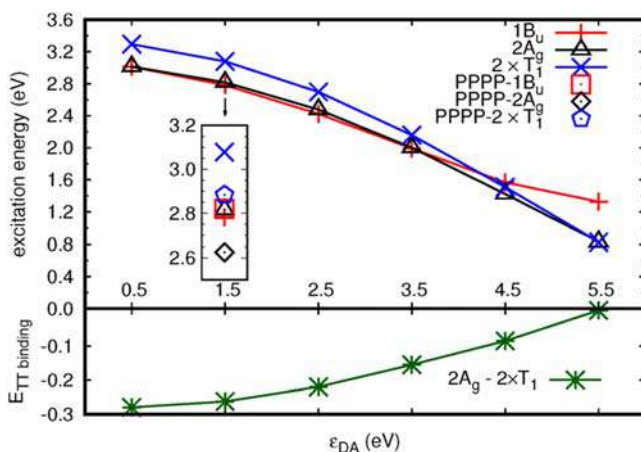
FIGURE 3.12 Excitation energies of the $1B_u$, $2A_g$ and twice T_1 states of PBTDO$_1$/ADADADA oligomer as a function of DA strength. The inset figure also plots the energy after PPP−Peierls optimization on the $2A_g$ state at $\varepsilon_{DA} = 1.5$ eV. The triplet pair binding energy $E_b = E_{2A_g} - 2 \times E_{T_1}$ is shown on the bottom panel. *Reproduced from Ren, J., Peng, Q., Zhang, X., Yi, Y., Shuai, Z., 2017. Role of the dark 2Ag state in donor−acceptor copolymers as a pathway for singlet fission: a DMRG study. J. Phys. Chem. Lett. 8, 2175−2181. https://doi.org/10.1021/acs.jpclett.7b00656, with permission from American Chemical Society.*

push−pull effect between donor and acceptor, a site energy difference ε_{DA} is introduced into the model. In Fig. 3.12, the excitation energies of the lowest three excited states, $1B_u$, $2A_g$, and twice T_1 of PBTDO$_1$/ADADADA oligomer as a function of the DA strength ε_{DA} are plotted. The energies of the $1B_u$ and $2A_g$ states are nearly degenerate (~ 20 meV) when ε_{DA} is less than 3.5 eV, indicating that a very fast internal conversion would happen from the bright $1B_u$ state to the dark $2A_g$ state. The natural transition orbital (NTO) analysis is used to identify the excitation character of the $2A_g$ and $1B_u$ states. In the configuration interaction singles (CIS) or TDDFT calculations, the sum of the square of each NTO pair singular value γ_s is exactly 1. If the excited state is a correlated many-body wavefunction, assuming that the ground state is mainly a HF configuration, $\sum_s \gamma_s^2$ could represent the proportion of single excitation components in the excited state. It is found that the $2A_g$ and $1B_u$ states have different excitation characters. For example, when $\varepsilon_{DA} = 1.5$ eV, $\sum_s \gamma_s^2$ of the $1B_u$ state is 0.766, while $\sum_s \gamma_s^2$ of the $2A_g$ state is only 0.242. Therefore, the $1B_u$ state is mainly a single excitation state, while the $2A_g$ state is mainly a double excitation state.

The local spin analysis method is also used to identify the ^{1}(TT) state, since each triplet component occupies a different position in the real space. If the local spin of half of the system is equal to 1, the state is a pure ^{1}(TT) state (Clark and Davidson, 2001). At different DA strengths ε_{DA}, the local spin $\langle S_{half}^2 \rangle$ of the $2A_g$ state is larger than 1.2, while that of $1A_g$ and $1B_u$
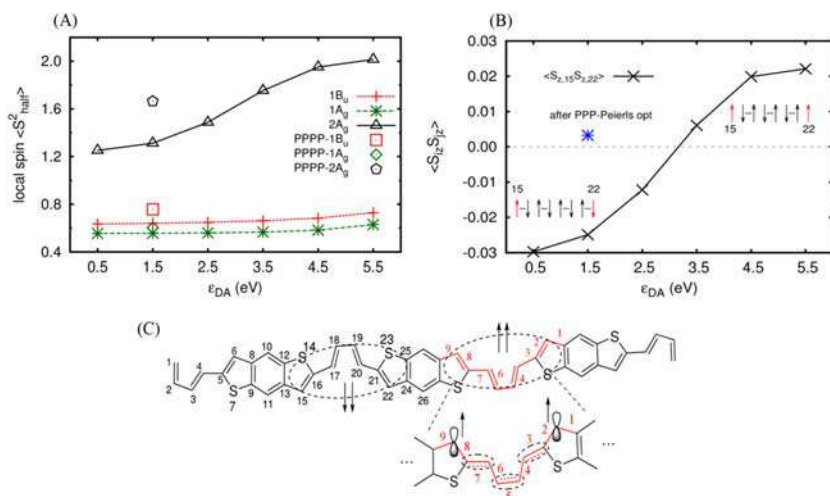
FIGURE 3.13 (A) Local spin of half the PBTDO$_1$/ADADADA oligomer [fragment from site 1 to 26 shown in (C)] in the 1A$_g$, 2A$_g$, and 1B$_u$ states as a function of DA strength ε_{DA}. The spin−spin correlation function pattern between sites 15 and 22 at different DA strengths (B). The schematic spin diagram is included. (C) Schematic representation of ^{1}(TT) structure of the 2A$_g$ state in PBTDO$_1$/ADADADA oligomer. *Reproduced from Ren, J., Peng, Q., Zhang, X., Yi, Y., Shuai, Z., 2017. Role of the dark 2Ag state in donor−acceptor copolymers as a pathway for singlet fission: a DMRG study. J. Phys. Chem. Lett. 8, 2175−2181. https://doi.org/10.1021/acs.jpclett.7b00656, with permission from American Chemical Society.*

states are always near 0.6 (Fig. 3.13). With the increase of ε_{DA}, $\left\langle S^2_{half} \right\rangle$ of the 2A$_g$ state is approaching 2.0. That is to say, larger DA strength increases the percentage of TT configuration in the 2A$_g$ wave function. Furthermore, PPP−Peierls model is used to optimize the structure on 2A$_g$ state at $\varepsilon_{DA} = 1.5$ eV. The local spin $\left\langle S^2_{half} \right\rangle$ of the 2A$_g$ state increases from 1.31 to 1.66, indicating that the relaxed structure of the 2A$_g$ state can stabilize the TT component.

The spin−spin correlation function $\left\langle \hat{S}_{iz}\hat{S}_{jz} \right\rangle$ is calculated to show the correlation of spin alignment in the real space. In the ground state, the spins tend to be oriented antiparallel between neighboring sites, and the spin−spin correlation function alternates between positive and negative along a conjugated chain. While in the 2A$_g$ state, the pattern of spin−spin correlation function is different. Take site 15 and site 22 as an example, it obeys the antiparallel rule like the ground state when ε_{DA} is small. As ε_{DA} increases, the correlation function becomes positive, which means that the electrons on sites 15 and site 22 are spin parallel, indicating a triplet configuration. Hence, the TT character of 2A$_g$ is enhanced when DA strength increases. Similar to the local spin analysis, after PPP−Peierls optimization on the 2A$_g$ state when $\varepsilon_{DA} = 1.5$ eV, $\left\langle \hat{S}_{15z}\hat{S}_{22z} \right\rangle$ changes from negative to positive, further indicating that the 2A$_g$ optimized structure would stabilize the triplet

configuration. The binding energy E_b of the triplet pair state is defined as the energy difference between the adiabatic coupled ^{1}(TT) state and two independent T_1 states. E_b is considered as the minimum energy to be overcome for the coupled ^{1}(TT) state to separate. Fig. 3.12 shows that E_b is negative and decreases (absolute value) when DA strength increases. From the thermodynamics point of view, larger DA strength favors the separation. Based on this analysis, a model to explain the mechanism of iSF in such a DA-copolymer is proposed: after photoexcitation, a quick internal conversion process occurs from the bright $1B_u$ state to the dark $2A_g$ state as a result of near degeneracy. And then, the $2A_g$ state, with a large ^{1}(TT) component would split into two uncoupled triplets. This model for DA-copolymer is consistent with the former understanding of the $2A_g$ state in polyene.

3.4.5 Pariser−Parr−Pople density matrix renormalization group for systems beyond one-dimension

In addition to one-dimensional polymers and oligomers, DMRG combined with PPP model Hamiltonian has also been used to solve the static electronic structures of ground and excited states and linear and nonlinear optical response properties for conjugated systems with other topologies, such as dendrimers (Mukhopadhyay and Ramasesha, 2009), porphyrins (Kumar et al., 2012; Thomas et al., 2013), graphene nanoribbons (GNR) (Goli et al., 2016), perylenes, (Prodhan and Ramasesha, 2018), coronene (Prodhan et al., 2019), etc. (Kumar and Ramasesha, 2010). It is more challenging for DMRG to handle systems beyond one-dimension.

In this subsection, we take the GNRs as an example. GNRs are quasi-one-dimensional forms of graphene, the properties of which depend crucially on the geometry of the edges of the ribbons, that is, zigzag (Z) and armchair (A) types. The confinement quasi-one-dimensional geometry will enhance the electronic correlation effect, making the properties of GNR quite different from what the common tight-binding model predicts. The GW method combined with Bethe−Salpeter equation can take into account the one electron−one hole interaction beyond the single-particle description, successfully predicting the quasiparticle bandgap and excitonic character of the lowest optical absorption (Spataru et al., 2004; Yang et al., 2007). However, the high-order electronic correlation effect is still lacking in these calculations, which may also be important to the properties of GNR. Ramasesha et al. have used DMRG combined with PPP model to study the electronic structures of three different structures of GNR in detail, which is 3-zigzag GNR (ZGNR), 6-/5-armchair GNR (AGNR) shown in Fig. 3.14 (Goli et al., 2016).

Although DMRG will not handle these GNRs as accurately as it does one-dimensional systems introduced above, it has been found that bond dimension $m = 750$ is still adequate to converge the one-photon gap and two-photon gap. In all the three systems, the charge gap (bandgap) is larger
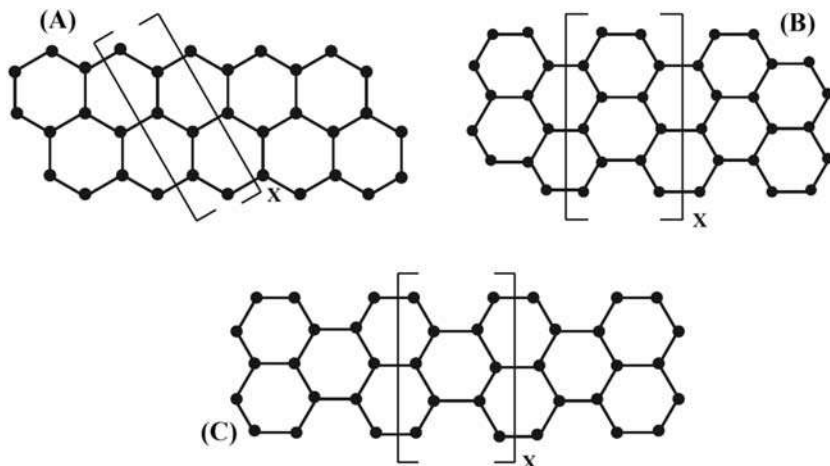
FIGURE 3.14 Molecular structures of (A) 3-ZGNR, (B) 6-AGNR, and (C) 5-AGNR. The number in the name characterizes the width of the GNR (graphene nanoribbons). *Reproduced from Goli, V.M.L.D.P., Prodhan, S., Mazumdar, S., Ramasesha, S., 2016. Correlated electronic properties of some graphene nanoribbons: a DMRG study. Phys. Rev. B. 94, 035139. https://doi.org/ 10.1103/PhysRevB.94.035139, with permission from American Physical Society.*

than 0 in the thermodynamic limit, indicating that both of them are semiconductors. Compared to the results from tight-binding model, it can be further identified that 3-ZGNB and 5-AGNR are Mott−Hubbard semiconductors, while 6-AGNR is a band semiconductor. Through calculating the spin gap, it was found that as the length of GNR increases, the ground state of the 3-ZGNR is a high-spin ferromagnetic state, while the ground state of the 6-AGNR and 5-AGNR systems is a singlet state with a finite spin gap even in the thermodynamic limit. On the contrary, 5-AGNR was predicted to be metallic without a spin gap by the tight-binding theory, which indicates the importance of electron correlation effect. Furthermore, the one-photon and two-photon gaps were calculated for all three systems. Since the ground state of 3-ZGNR gradually becomes the spin state as the length increases, Fig. 3.15 shows the results of 3-ZGNR within two spin manifolds ($S = 0$ and $S = 1$, the actual crossover occurs at $N = 14$). It was found that in 3-ZGNR, the lowest two-photon state appears above the lowest one-photon state for systems up to 3 units, but this ordering is reversed in larger systems. This size-dependent ordering behavior is quite similar to polyene introduced in the former sections. In addition, the two-photon gap extrapolates to zero in the thermodynamic limit, while the extrapolated value of the optical gap is 2.25 eV. In the case of 6-AGNR, the optical one-photon state is always below the two-photon state for all system sizes, suggesting these systems will be fluorescent. On the contrary, in 5-AGNR, the optical state is always
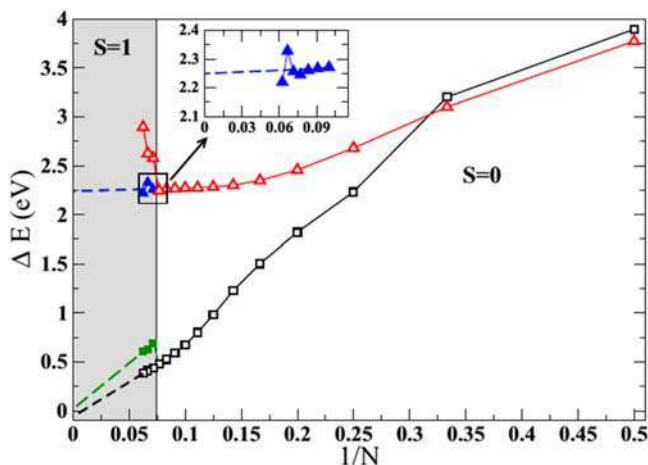
FIGURE 3.15 Lowest optical one-photon and two-photon gaps in 3-ZGNR versus the inverse of the number of unit cells: the lowest optical gap in singlet space (open triangle) and in triplet space (close triangle); the lowest two-photon gap in singlet space (open square) and in triplet space (close square). *Reproduced from Goli, V.M.L.D.P., Prodhan, S., Mazumdar, S., Ramasesha, S., 2016. Correlated electronic properties of some graphene nanoribbons: a DMRG study. Phys. Rev. B. 94, 035139. https://doi.org/10.1103/PhysRevB.94.035139, with permission from American Physical Society.*

higher than the lowest two-photon state. In both 5-AGNR and 6-AGNR, the one-photon and two-photons gaps are finite in the thermodynamic limit.

3.5   Summary

The development of DMRG in quantum chemistry began with great success in the treatment of semiempirical model Hamiltonian with both short-range and long-range Coulomb potentials. With the symmetrized DMRG algorithm, the pioneers calculated the electronic structures of the ground and excited states of polyenes longer than 100 carbon atoms as well as other more complex conjugated polymers by DMRG with unprecedented accuracy, successfully solving problems including the excited states ordering, exciton binding energies, and linear and nonlinear spectroscopy in these systems. Before that, no methods can handle such a large system accurately. The successful application of DMRG to these chemical problems has inspired the subsequent researchers to further develop DMRG for the more general ab initio Hamiltonian. The following three chapters will introduce these new developments of DMRG for ab initio Hamiltonian. After two decades of effort, DMRG nowadays has become one of the state-of-the-art methods to deal with the strong correlation problem in quantum chemistry.

Acknowledgments

References

Anusooya, Y., Pati, S.K., Ramasesha, S., 1997. Symmetrized density matrix renormalization group studies of the properties of low-lying states of the poly-para-phenylene system. J. Chem. Phys. 106, 10230−10237. Available from: https://doi.org/10.1063/1.474076.

Aryanpour, K., Dutta, T., Huynh, U.N., Vardeny, Z.V., Mazumdar, S., 2015. Theory of primary photoexcitations in donor-acceptor copolymers. Phys. Rev. Lett. 115, 267401. Available from: https://doi.org/10.1103/PhysRevLett.115.267401.

Barford, W., 2013. Electronic and Optical Properties of Conjugated Polymers. Oxford University Press.

Bendazzoli, G., Evangelisti, S., 1991. Full-CI calculations of alternant cyclic polyenes (CH) N, N = 2, 4, 6, f 18, in the PPP approximation. Chem. Phys. Lett. 185, 125−130. Available from: https://doi.org/10.1016/0009-2614(91)80152-N.

Bendazzoli, G.L., Evangelisti, S., Gagliardi, L., 1994. Full configuration interaction study of the ground state of closed-shell cyclic ppp polyenes. Int. J. Quantum. Chem. 51, 13−25. Available from: https://doi.org/10.1002/qua.560510104.

Bursill, R.J., Barford, W., 1999. Electron-lattice relaxation, and soliton structures and their inter-actions in polyenes. Phys. Rev. Lett. 82, 1514. Available from: https://doi.org/10.1103/PhysRevLett.82.1514.

Busby, E., Xia, J., Low, J.Z., Wu, Q., Hoy, J., Campos, L.M., Sfeir, M.Y., 2015a. Fast singlet exciton decay in push−pull molecules containing oxidized thiophenes. J. Phys. Chem. B. 119, 7644−7650. Available from: https://doi.org/10.1021/jp511704r.

Busby, E., Xia, J., Wu, Q., Low, J.Z., Song, R., Miller, J.R., Zhu, X., Campos, L.M., Sfeir, M. Y., 2015b. A design strategy for intramolecular singlet fission mediated by charge-transfer states in donor−acceptor organic materials. Nat. Mater. 14, 426−433. Available from: https://doi.org/10.1038/nmat4175.

Chan, G.K.-L., Head-Gordon, M., 2002. Highly correlated calculations with a polynomial cost algorithm: A study of the density matrix renormalization group. J. Chem. Phys. 116, 4462−4476. Available from: https://doi.org/10.1063/1.1449459.

Clark, A.E., Davidson, E.R., 2001. Local spin. J. Chem. Phys. 115, 7382−7392. Available from: https://doi.org/10.1063/1.1407276.

Cleveland, C.L., Medina, A.R., 1976. Obtaining a Heisenberg Hamiltonian from the Hubbard model. Am. J. Phys. 44, 44−46. Available from: https://doi.org/10.1119/1.10537.

Daul, S., Ciofini, I., Daul, C., White, S.R., 2000. Full-CI quantum chemistry using the density matrix renormalization group. Int. J. Quantum. Chem. 79, 331−342. Available from: http://doi.org/10.1002/1097-461X(2000)79:6 < 331::AID-QUA1 > 3.0.CO;2-Y.

Eisert, J., Cramer, M., Plenio, M.B., 2010. Colloquium: area laws for the entanglement entropy. Rev. Mod. Pys. 82, 277. Available from: https://doi.org/10.1103/RevModPhys.82.277.

Fano, G., Ortolani, F., Ziosi, L., 1998. The density matrix renormalization group method: application to the PPP model of a cyclic polyene chain. J. Chem. Phys. 108, 9246−9252. Available from: https://doi.org/10.1063/1.476379.

Fukutome, H., 1968. Spin density wave and charge transfer wave in long conjugated molecules. Prog. Theor. Phys. 40, 998−1012. Available from: https://doi.org/10.1143/PTP.40.998.

Gao, Y., Liu, C.-G., Jiang, Y.-S., 2002. The valence bond study for benzenoid hydrocarbons of medium to infinite sizes. J. Phys. Chem. A. 106, 2592−2597. Available from: https://doi.org/10.1021/jp012057t.

Goli, V.M.L.D.P., Prodhan, S., Mazumdar, S., Ramasesha, S., 2016. Correlated electronic properties of some graphene nanoribbons: a DMRG study. Phys. Rev. B 94, 035139. Available from: https://doi.org/10.1103/PhysRevB.94.035139.

Jiang, Y., Peng, Q., Gao, X., Shuai, Z., Niu, Y., Lin, S.H., 2012. Theoretical design of polythienylenevinylene derivatives for improvements of light-emitting and photovoltaic performances. J. Mater. Chem. 22, 4491−4501. Available from: https://doi.org/10.1039/c1jm14956c.

Kasha, M., 1950. Characterization of electronic transitions in complex molecules. Discuss. Faraday. Soc. 9, 14−19. Available from: https://doi.org/10.1039/df9500900014.

Klopman, G., 1964. A semiempirical treatment of molecular structures. II. Molecular terms and application to diatomic molecules. J. Am. Chem. Soc. 86, 4550−4557. Available from: https://doi.org/10.1021/ja01075a008.

Kohler, B.E., Terpougov, V., 1996. Octatetraene m 1 A g states: two-photon fluorescence excitation spectrum from 28 000 to 50 000 cm- 1. J. Chem. Phys. 104, 9297−9303. Available from: https://doi.org/10.1063/1.471675.

Kumar, M., Ramasesha, S., 2010. Low-lying states of transverse substituted trans -polyacetylene and trans -polyacetylene: a comparative DMRG study. Phys. Rev. B 81, 035115. Available from: https://doi.org/10.1103/PhysRevB.81.035115.

Kumar, M., Pati, Y.A., Ramasesha, S., 2012. A density matrix renormalization group method study of optical properties of porphines and metalloporphines. J. Chem. Phys. 136, 014112. Available from: https://doi.org/10.1063/1.3671946.

Lieb, E., Wu, F., 1968. Absence of Mott transition in the 1D Hubbard model. Phys. Rev. Lett. 20, 1445−1449. Available from: https://doi.org/10.1103/PhysRevLett.20.1445.

Ma, H., Liu, C., Jiang, Y., 2004. Triplet-excited region" in polyene oligomers revisited: Pariser−Parr−Pople model studied with the density matrix renormalization group method. J. Chem. Phys. 120, 9316−9320. Available from: https://doi.org/10.1063/1.1710010.

Ma, H., Cai, F., Liu, C., Jiang, Y., 2005. Spin distribution in neutral polyene radicals: Pariser−Parr−Pople model studied with the density matrix renormalization group method. J. Chem. Phys. 122, 104909. Available from: https://doi.org/10.1063/1.1861875.

Ma, H., Liu, C., Jiang, Y., 2006. Theoretical investigation of static characterization on nonlinear elementary excitations in trans-polyacetylene. J. Phys. Chem. B. 110, 26488−26496. Available from: https://doi.org/10.1021/jp0602528.

Ma, H., Schollwöck, U., 2008. Dynamical simulations of charged soliton transport in conjugated polymers with the inclusion of electron-electron interactions. J. Chem. Phys. 129, 244705. Available from: https://doi.org/10.1063/1.3046738.

Ma, H., Schollwöck, U., 2009. Dynamical simulations of polaron transport in conjugated polymers with the inclusion of electron- electron interactions. J. Phys. Chem. A. 113, 1360−1367. Available from: https://doi.org/10.1021/jp809045r.

Ma, H., Schollwöck, U., 2010. Effect of electron-electron interactions on the charge carrier transitions in trans-polyacetylene. J. Phys. Chem. A. 114, 5439−5444. Available from: https://doi.org/10.1021/jp9098039.

Ma, H., Liu, C., Zhang, C., Jiang, Y., 2007. Theoretical study of very high spin organic π-conjugated polyradicals. J. Phys. Chem. A. 111, 9471−9478. Available from: https://doi.org/10.1021/jp073300c.

Mataga, N., Nishimoto, K., 1957. Electronic structure and spectra of nitrogen heterocycles. Z. Phys. Chem. 13, 140−157. Available from: https://doi.org/10.1524/zpch.1957.13.3_4.140.

McCulloch, I.P., Gulácsi, M., 2001. Total spin in the density matrix renormalization group algorithm. Phil. Mag. Lett. 81, 447−453. Available from: https://doi.org/10.1080/09500830110040009.

Mitrushenkov, A.O., Fano, G., Ortolani, F., Linguerri, R., Palmieri, P., 2001. Quantum chemistry using the density matrix renormalization group. J. Chem. Phys. 115, 6815−6821. Available from: https://doi.org/10.1063/1.1389475.

Mukhopadhyay, S., Ramasesha, S., 2009. Study of linear and nonlinear optical properties of dendrimers using density matrix renormalization group method. J. Chem. Phys. 131, 074111. Available from: https://doi.org/10.1063/1.3202437.

Nishimoto, S., Jeckelmann, E., Gebhard, F., Noack, R.M., 2002. Application of the density matrix renormalization group in momentum space. Phys. Rev. B 65, 165114. Available from: https://doi.org/10.1103/PhysRevB.65.165114.

Ohno, K., 1964. Some remarks on the Pariser-Parr-Pople method. Theor. Chimica. Acta 2, 219−227. Available from: https://doi.org/10.1007/BF00528281.

Paldus, J., Piecuch, P., 1992. Electron correlation in one dimension: coupled cluster approaches to cyclic polyene π-electron models. Int. J. Quantum. Chem. 42, 135−164. Available from: https://doi.org/10.1002/qua.560420110.

Pariser, R., Parr, R.G., 1953. A semi-empirical theory of the electronic spectra and electronic structure of complex unsaturated molecules. I. J. Chem. Phys. 21, 466−471. Available from: https://doi.org/10.1063/1.1698929.

Pati, S.K., Ramasesha, S., Shuai, Z., Brédas, J.-L., 1999. Dynamical nonlinear optical coefficients from the symmetrized density-matrix renormalization-group method. Phys. Rev. B 59, 14827. Available from: https://doi.org/10.1103/PhysRevB.59.14827.

Pople, J.A., 1953. Electron interaction in unsaturated hydrocarbons. T. Faraday. Soc. 49, 1375−1385. Available from: https://doi.org/10.1039/tf9534901375.

Prodhan, S., Ramasesha, S., 2018. Symmetrized density matrix renormalization group algorithm for low-lying excited states of conjugated carbon systems: application to 1,12-benzoperylene and polychrysene. Phys. Rev. B. 97, 195125. Available from: https://doi.org/10.1103/PhysRevB.97.195125.

Prodhan, S., Mazumdar, S., Ramasesha, S., 2019. Correlated electronic properties of a graphene nanoflake: coronene. Molecules. 24, 730. Available from: https://doi.org/10.3390/molecules24040730.

Qu, Z., Zhang, D., Liu, C., Jiang, Y., 2009. Open-shell ground state of polyacenes: a valence bond study. J. Phys. Chem. A. 113, 7909−7914. Available from: https://doi.org/10.1021/jp9015728.

Ramasesha, S., Pati, S.K., Krishnamurthy, H., Shuai, Z., Brédas, J., 1996. Symmetrized density-matrix renormalization-group method for excited states of Hubbard models. Phys. Rev. B 54, 7598. Available from: https://doi.org/10.1103/PhysRevB.54.7598.

Ramasesha, S., Pati, S.K., Krishnamurthy, H., Shuai, Z., Brédas, J., 1997. Low-lying electronic excitations and nonlinear optic properties of polymers via symmetrized density matrix renormalization group method. Synthetic. Met. 85, 1019−1022. Available from: https://doi.org/10.1016/S0379-6779(97)80136-1.

Ramasesha, S., Pati, S.K., Shuai, Z., Brédas, J.-L., 2000. The density matrix renormalization group method: application to the low-lying electronic states in conjugated polymers. Available from: https://doi.org/10.1016/S0065-3276(00)38004-2.

Ren, J., Peng, Q., Zhang, X., Yi, Y., Shuai, Z., 2017. Role of the dark 2Ag state in donor−acceptor copolymers as a pathway for singlet fission: A DMRG study. J. Phys. Chem. Lett. 8, 2175−2181. Available from: https://doi.org/10.1021/acs.jpclett.7b00656.

Schulten, K., Karplus, M., 1972. On the origin of a low-lying forbidden transition in polyenes and related molecules. Chem. Phys. Lett. 14, 305−309. Available from: https://doi.org/10.1016/0009-2614(72)80120-9.

Sharma, S., Chan, G.K.-L., 2012. Spin-adapted density matrix renormalization group algorithms for quantum chemistry. J. Chem. Phys. 136, 124121. Available from: https://doi.org/10.1063/1.3695642.

Shuai, Z., Brédas, J.-L., 2000. Coupled-cluster approach for studying the electronic and nonlinear optical properties of conjugated molecules. Phys. Rev. B. 62, 15452. Available from: https://doi.org/10.1103/PhysRevB.62.15452.

Shuai, Z., Peng, Q., 2014. Excited states structure and processes: understanding organic light-emitting diodes at the molecular level. Phys. Rep. 537, 123−156. Available from: https://doi.org/10.1016/j.physrep.2013.12.002.

Shuai, Z., Peng, Q., 2017. Organic light-emitting diodes: theoretical understanding of highly efficient materials and development of computational methodology. Natl. Sci. Rev. 4, 224−239. Available from: https://doi.org/10.1093/nsr/nww024.

Shuai, Z., Brédas, J.-L., Pati, S., Ramasesha, S., 1997a. Quantum-confinement effects on the ordering of the lowest-lying excited states in conjugated chains. Phys. Rev. B. 56, 9298. Available from: https://doi.org/10.1103/PhysRevB.56.9298.

Shuai, Z., Bredas, J.-L., Pati, S.K., Ramasesha, S., 1997b. Quantum confinement effects on the ordering of the lowest-lying excited states in conjugated polymers, in: Optical Probes of Conjugated Polymers. International Society for Optics and Photonics, pp. 293−302. Available from: https://doi.org/10.1117/12.279282.

Shuai, Z., Pati, S.K., Su, W., Brédas, J., Ramasesha, S., 1997c. Binding energy of 1 B u singlet excitons in the one-dimensional extended Hubbard-Peierls model. Phys. Rev. B. 55, 15368. Available from: https://doi.org/10.1103/PhysRevB.55.15368.

Shuai, Z., Brédas, J., Saxena, A., Bishop, A., 1998a. Linear and nonlinear optical response of polyenes: a density matrix renormalization group study. J. Chem. Phys. 109, 2549−2555. Available from: https://doi.org/10.1063/1.476827.

Shuai, Z., Brédas, J.-L., Pati, S., Ramasesha, S., 1998b. Exciton binding energy in the strong correlation limit of conjugated chains. Phys. Rev. B 58, 15329. Available from: https://doi.org/10.1103/PhysRevB.58.15329.

Smith, M.B., Michl, J., 2010. Singlet fission. Chem. Rev. 110, 6891−6936. Available from: https://doi.org/10.1021/cr1002613.

Soos, Z., Ramasesha, S., Galvao, D., 1993. Band to correlated crossover in alternating Hubbard and Pariser-Parr-Pople chains: nature of the lowest singlet excitation of conjugated polymers. Phys. Rev. Lett. 71, 1609. Available from: https://doi.org/10.1103/PhysRevLett.71.1609.

Spataru, C.D., Ismail-Beigi, S., Benedict, L.X., Louie, S.G., 2004. Excitonic effects and optical spectra of single-walled carbon nanotubes. Phys. Rev. Lett. 92, 077402. Available from: https://doi.org/10.1103/PhysRevLett.92.077402.

Su, W., 1995. Lattice relaxation of even-parity singlet excited states in polyacetylene and four-soliton bound state. Phys. Rev. Lett. 74, 1167. Available from: https://doi.org/10.1103/PhysRevLett.74.1167.

Su, W., Schrieffer, J., Heeger, A.J., 1979. Solitons in polyacetylene. Phys. Rev. Lett. 42, 1698. Available from: https://doi.org/10.1103/PhysRevLett.42.1698.

Su, W.P., Schrieffer, J.R., Heeger, A.J., 1980. Soliton excitations in polyacetylene. Phys. Rev. B 22, 2099−2111. Available from: https://doi.org/10.1103/PhysRevB.22.2099.

Surján, P.R., 2012. Second Quantized Approach to Quantum Chemistry: an Elementary Introduction. Springer Science & Business Media.

Tavan, P., Schulten, K., 1987. Electronic excitations in finite and infinite polyenes. Phys. Rev. B 36, 4337. Available from: https://doi.org/10.1103/PhysRevB.36.4337.

Thomas, S., Pati, Y.A., Ramasesha, S., 2013. Linear and nonlinear optical properties of expanded porphyrins: a DMRG study. J. Phys. Chem. A. 117, 7804−7809. Available from: https://doi.org/10.1021/jp4052352.

White, S.R., 1992. Density matrix formulation for quantum renormalization groups. Phys. Rev. Lett. 69, 2863. Available from: https://doi.org/10.1103/PhysRevLett.69.2863.

White, S.R., 1993. Density-matrix algorithms for quantum renormalization groups. Phys. Rev. B 48, 10345. Available from: https://doi.org/10.1103/PhysRevB.48.10345.

White, S.R., Martin, R.L., 1999. Ab initio quantum chemistry using the density matrix renormalization group. J. Chem. Phys. 110, 4127−4130. Available from: https://doi.org/10.1063/1.478295.

Xiang, T., 1996. Density-matrix renormalization-group method in momentum space. Phys. Rev. B 53, R10445. Available from: https://doi.org/10.1103/PhysRevB.53.R10445.

Yang, L., Park, C.-H., Son, Y.-W., Cohen, M.L., Louie, S.G., 2007. Quasiparticle energies and band gaps in graphene nanoribbons. Phys. Rev. Lett. 99, 186801. Available from: https://doi.org/10.1103/PhysRevLett.99.186801.

Yao, Y., Zhao, H., Moore, J.E., Wu, C.-Q., 2008. Controllable spin-current blockade in a Hubbard chain. Phys. Rev. B 78, 193105. Available from: https://doi.org/10.1103/PhysRevB.78.193105.

Yaron, D., Moore, E.E., Shuai, Z., Brédas, J., 1998. Comparison of density matrix renormalization group calculations with electron-hole models of exciton binding in conjugated polymers. J. Chem. Phys. 108, 7451−7458. Available from: https://doi.org/10.1063/1.476165.

Zhao, H., Yao, Y., An, Z., Wu, C.-Q., 2008. Dynamics of polarons in conjugated polymers: An adaptive time-dependent density-matrix renormalization-group study. Phys. Rev. B 78, 035209. Available from: https://doi.org/10.1103/PhysRevB.78.035209.

Zhao, H., Chen, Y.-G., Zhang, X.-M., An, Z., Wu, C.-Q., 2009. Correlation effects on the dynamics of bipolarons in nondegenerate conjugated polymers. J. Chem. Phys. 130, 234908. Available from: https://doi.org/10.1063/1.3155207.

Chapter 4

Density matrix renormalization group for ab initio quantum chemistry Hamiltonian

Ab initio quantum chemistry methods are a class of computational chemistry methods based on the principles of quantum mechanics. The term "ab initio" indicates that the calculation is from first principles and that no empirical parameters are used. Therefore they are usually more accurate, robust, and general than their semiempirical counterparts, what have made them become dominant in the current quantum chemistry field.

In this chapter, we will introduce the basic algorithms of using density matrix renormalization group (DMRG) to solve the many-electron Schrödinger equation with an ab initio electronic Hamiltonian in its second-quantized form

$$\hat{H} = \sum_{ij,\sigma} t_{ij}\hat{a}_{i\sigma}^{\dagger}\hat{a}_{j\sigma} + \frac{1}{2}\sum_{ijkl,\sigma\tau} g_{ijkl}\hat{a}_{i\sigma}^{\dagger}\hat{a}_{k\tau}^{\dagger}\hat{a}_{l\tau}\hat{a}_{j\sigma}, \tag{4.1}$$

in which i, j, k, and l are the electrons' spatial orbitals; the subscript σ and τ denote the spin of the electrons; $\hat{a}_{i\sigma}^{\dagger}$ is the electron creation operator acting on the ith orbital with spin σ and $\hat{a}_{i\sigma}$ is the conjugated annihilation operator. t_{ij} and g_{ijkl} are the one- and two-electron integrals, respectively,

$$t_{ij} = \int \phi_i^*(\boldsymbol{r})\hat{h}\phi_j(\boldsymbol{r})\mathrm{d}\boldsymbol{r}, \tag{4.2}$$

$$g_{ijkl} = \int \phi_i^*(\boldsymbol{r}_1)\phi_k^*(\boldsymbol{r}_2)\hat{g}\phi_j(\boldsymbol{r}_1)\phi_l(\boldsymbol{r}_2)\mathrm{d}\boldsymbol{r}_1\mathrm{d}\boldsymbol{r}_2 \tag{4.3}$$

where $\hat{h}$ and $\hat{g}$ are the one- and two-electron operators. The one-electron operator (in atomic units)

$$\hat{h} = -\frac{1}{2}\sum_i \nabla_i^2 - \sum_{a,i} \frac{Z_a}{r_{ai}} \tag{4.4}$$

contains the kinetic energy operator of the electrons and the attraction operator between electrons and nuclei, and the two-electron operator (in atomic units)

$$\hat{g} = \sum_{i<j} \frac{1}{r_{ij}} \tag{4.5}$$

evaluates the electronic repulsion. Here Z_a, r_{ai}, and r_{ij} are the nuclear charges, electron-nucleus distances, and electron−electron distances, respectively. In practice, the number of unique orbital integrals can be significantly reduced by using the permutation symmetries, as

$$t_{ij} = t_{ji}, \tag{4.6}$$

$$g_{ijkl} = g_{jikl} = g_{ijlk} = g_{jilk} = g_{klij} = g_{lkij} = g_{klji} = g_{lkji}. \tag{4.7}$$

In ab initio DMRG calculations, orbitals i, j, k, and l are usually taken as a set of orthogonal molecular orbitals (MOs) from a priori Hartree−Fock self-consistent field (SCF) or other inexpensive quantum chemical calculations. The electronic Hamiltonian in Eq. 4.1 relies on both the nonrelativistic approximation and the Born−Oppenheimer approximation, which are widely applicable for most molecules. The consideration of the relativistic effect and non-Born−Oppenheimer effect in DMRG will be discussed in Section 4.11 and Section 5.7, respectively.

4.1   Renormalized operator-based density matrix renormalization group implementation

Since White and Martin (1999) made the first implementation of DMRG calculations for ab initio quantum chemistry Hamiltonian, a quick development of ab initio DMRG quantum chemistry has been witnessed in the last two decades. (see review papers of Chan and Sharma, 2011; Kurashige, 2014; Wouters and Van Neck, 2014; Baiardi and Reiher, 2020; Freitag and Reiher, 2021) As we have introduced in Chapters 1 and 2, DMRG calculations can be performed by two superficially different languages: an older language of the renormalization group and renormalized operators and a more recent language of matrix product state (MPS) and matrix product operator (MPO). Most of the earlier ab initio DMRG works (e.g., White and Martin, 1999; Daul et al., 2000; Mitrushenkov et al., 2001; Chan and Head-Gordon, 2002; Chan and Head-Gordon, 2003; Mitrushenkov et al., 2003; Legeza et al., 2003a Legeza and Sólyom, 2003) employed the older formulation, which is sometimes also called first-generation DMRG algorithm. Here, we briefly introduce the methodology fundamentals therein.

In the first-generation DMRG methods, the whole system is partitioned into two subsets, that is, the left block and right block. Then, the key step in

ab initio DMRG is to identify and construct efficiently the appropriate renormalized operators as one proceeds through the DMRG sweep. Here the renormalized operators mean expressing the operator matrices with the preserved effective bases of the left or right block after truncation.

As shown in Eq. 4.1, the local state on an MO could be one of the four possible occupation states: the doubly occupied configuration $|\uparrow\downarrow\rangle$, the spin-up singly-occupied configuration $|\uparrow\rangle$, the spin-down singly-occupied configuration $|\downarrow\rangle$, and the unoccupied configuration $|-\rangle$. Thus we can write the single-site operators (SSOs) as matrices, for example, the spin-up and spin-down creation operators can be written as

$$\hat{a}_u^\dagger = \begin{pmatrix} 0 & 0 & 1 & 0 \\ 0 & 0 & 0 & 1 \\ 0 & 0 & 0 & 0 \\ 0 & 0 & 0 & 0 \end{pmatrix}, \hat{a}_d^\dagger = \begin{pmatrix} 0 & -1 & 0 & 0 \\ 0 & 0 & 0 & 0 \\ 0 & 0 & 0 & 1 \\ 0 & 0 & 0 & 0 \end{pmatrix}, \tag{4.8}$$

and the related annihilation operators and other SSOs could be derived from the creators, for example, the spin-up annihilation and particle number operators are

$$\hat{a}_u = \left(\hat{a}_u^\dagger\right)^\dagger = \begin{pmatrix} 0 & 0 & 0 & 0 \\ 0 & 0 & 0 & 0 \\ 1 & 0 & 0 & 0 \\ 0 & 1 & 0 & 0 \end{pmatrix}, \tag{4.9}$$

$$\hat{n}_u = \hat{a}_u^\dagger \hat{a}_u = \begin{pmatrix} 1 & 0 & 0 & 0 \\ 0 & 1 & 0 & 0 \\ 0 & 0 & 0 & 0 \\ 0 & 0 & 0 & 0 \end{pmatrix}. \tag{4.10}$$

The definition of the spin-down creation operator $\hat{a}_d^\dagger$ contains a minus sign, because we usually order the spin-up electron before the spin-down one on a single spatial orbital. The spin-down creator with a minus sign makes $\hat{a}_d^\dagger|\uparrow\rangle = -|\uparrow\downarrow\rangle$ to fulfill the antisymmetric requirement of the fermionic wave function. The total Hamiltonian, as well as other global operators acting on the total wave function, can be expressed as the sum of a series of operator terms, which are the product of several SSOs. From the perspective of the traditional DMRG algorithm, the fundamental problem that needs to be solved in order to implement the ab initio DMRG is embedding such operator terms into the left-right DMRG framework.

According to the left-right partition in the traditional DMRG, the N active MOs are rearranged as a one-dimensional (1D) chain and can be split into four blocks L, n_l, n_r, and R (see Fig. 1.2). In normal cases of two-site DMRG calculations, n_l and n_r are two active sites. For each block, the Hamiltonian takes the same form as the ab initio Hamiltonian in Eq. 4.1, where the orbital

indices are only restricted to the orbitals within the block. The Hamiltonian of the superblock $L' = L + n_l$ can be obtained by combining the Hamiltonians of the subblocks L and n_l, as well as all the interactions between the two subblocks, that means

$$\hat{H}_{L'} = \hat{H}_L + \hat{H}_{n_l} + \sum_{IJ} v_{IJ} \hat{I}_L \hat{J}_{n_l}, \tag{4.11}$$

in which $\hat{I}$ is the renormalized operator of the subblock L and $\hat{J}$ is the SSO of site n_l, respectively. Therefore the dimensions of these matrices are usually 4×4 (for $\boldsymbol{H}_{n_l}$ and $\boldsymbol{J}_{n_l}$), $m \times m$ (for $\boldsymbol{H}_L$ and $\boldsymbol{I}_L$), and $4m \times 4m$ (for $\boldsymbol{H}_{L'}$), where m is the number of preserved effective bases in subblock L.

The term $\sum_{IJ} v_{IJ} \hat{I}_L \hat{J}_{n_l}$ describes the interactions between blocks L and n_l. In this case, the Hamiltonian of the superblock L' is

$$
\begin{aligned}
\hat{H}_{L'} = \hat{H}_L + \hat{H}_{n_l} &+ \sum_{i \in n_l, j \in L} \sum_{\sigma} t_{ij} \left(\hat{a}_{i\sigma}^\dagger \hat{a}_{j\sigma} + h.c. \right) \\
&+ \sum_{i \in n_l, jkl \in L} \sum_{\sigma\tau} g_{ijkl} \left(\hat{a}_{i\sigma}^\dagger \hat{a}_{k\tau}^\dagger \hat{a}_{l\tau} \hat{a}_{j\sigma} + h.c. \right) \\
&+ \sum_{i \in L, jkl \in n_l} \sum_{\sigma\tau} g_{ijkl} \left(\hat{a}_{i\sigma}^\dagger \hat{a}_{k\tau}^\dagger \hat{a}_{l\tau} \hat{a}_{j\sigma} + h.c. \right) \\
&+ \frac{1}{2} \sum_{ik \in n_l, jl \in L} \sum_{\sigma\tau} g_{ijkl} \left(\hat{a}_{i\sigma}^\dagger \hat{a}_{k\tau}^\dagger \hat{a}_{l\tau} \hat{a}_{j\sigma} + h.c. \right) \\
&+ \sum_{ij \in n_l, kl \in L} \sum_{\sigma\tau} \left(g_{ijkl} \hat{a}_{i\sigma}^\dagger \hat{a}_{k\tau}^\dagger \hat{a}_{l\tau} \hat{a}_{j\sigma} + g_{kjil} \hat{a}_{i\sigma}^\dagger \hat{a}_{k\tau}^\dagger \hat{a}_{j\tau} \hat{a}_{l\sigma} \right)
\end{aligned}
\tag{4.12}
$$

The construction of the $\hat{H}_{L'}$ Hamiltonian is performed in the DMRG sweep process and is usually called *blocking*.

For the superblock $R' = n_r + R$ on the right side, we can build the Hamiltonian similarly. In fact, Eq. (4.12) can be applied to any two-part system as long as the interaction term can be precisely constructed. We can decompose a global operator acting on the whole wave function as a sum-of-products (SOP),

$$\hat{O} = \hat{O}^{L_k} \otimes \hat{1}^{R_k} + \hat{1}^{L_k} \otimes \hat{O}^{R_k} + \sum_{b_k} \hat{o}_{b_k}^{L_k} \hat{o}_{b_k}^{R_k}, \tag{4.13}$$

in which we have introduced three kinds of left and right operator terms: (1) the identity operators $\hat{1}^{L_k}$ and $\hat{1}^{R_k}$; (2) the operators $\hat{O}^{L_k}$ and $\hat{O}^{R_k}$, respectively, acting on the left and right blocks containing sites $1, 2, \ldots, k$ and $k+1, \ldots, N$, respectively; and (3) the terms $\hat{o}_{b_k}^{L_k} \hat{o}_{b_k}^{R_k}$ denoting their interactions. Following this idea, we can write down a left-right decomposition of the total Hamiltonian into the so-called normal/complementary (N/C)

operator (Xiang, 1996) as

$$\hat{H} = \hat{H}^{L_k} \otimes \hat{1}^{R_k} + \hat{1}^{L_k} \otimes \hat{H}^{R_k} + \left(\sum_{\sigma} \sum_{i \in L_k} \hat{a}_{i\sigma}^{\dagger} \hat{S}_{i\sigma}^{R_k} + \sum_{\sigma} \sum_{i \in R_k} \hat{a}_{i\sigma}^{\dagger} \hat{S}_{i\sigma}^{L_k} + h.c. \right)$$

$$+ \frac{1}{2} \left(\sum_{\sigma\tau} \sum_{ik \in L_k} \hat{A}_{i\sigma k\tau}^{L_k} \hat{P}_{i\sigma k\tau}^{R_k} + h.c. \right) + \left(\sum_{\sigma} \sum_{ij \in L_k} \hat{B}_{i\sigma j\sigma}^{L_k} \hat{Q}_{i\sigma j\sigma}^{R_k} + h.c. \right)$$

$$- \left(\sum_{\sigma\tau} \sum_{ij \in L_k} \hat{C}_{i\sigma j\tau}^{L_k} \hat{R}_{i\sigma j\tau}^{R_k} + h.c. \right),$$

(4.14)

where

$$\hat{A}_{i\sigma k\tau} = \hat{a}_{i\sigma}^{\dagger} \hat{a}_{k\tau}^{\dagger}, \tag{4.15}$$

$$\hat{B}_{i\sigma j\sigma} = \hat{a}_{i\sigma}^{\dagger} \hat{a}_{j\sigma}, \tag{4.16}$$

$$\hat{C}_{i\sigma j\tau} = \hat{a}_{i\sigma}^{\dagger} \hat{a}_{j\tau}, \tag{4.17}$$

and various complementary operators are defined as

$$\hat{S}_{i\sigma}^{L_k} = \sum_{j \in L_k} t_{ij} \hat{a}_{j\sigma} + \sum_{\tau} \sum_{jkl \in L_k} g_{ijkl} \hat{a}_{k\tau}^{\dagger} \hat{a}_{l\tau} \hat{a}_{j\sigma}, \tag{4.18}$$

$$\hat{S}_{i\sigma}^{R_k} = \sum_{\tau} \sum_{jkl \in R_k} g_{ijkl} \hat{a}_{k\tau}^{\dagger} \hat{a}_{l\tau} \hat{a}_{j\sigma} \tag{4.19}$$

$$\hat{P}_{i\sigma k\tau}^{R_k} = \sum_{jl \in R_k} g_{ijkl} \hat{a}_{l\tau} \hat{a}_{j\sigma}, \tag{4.20}$$

$$\hat{Q}_{i\sigma j\sigma}^{R_k} = \sum_{\tau} \sum_{kl \in R_k} g_{ijkl} \hat{a}_{k\tau}^{\dagger} \hat{a}_{l\tau}, \tag{4.21}$$

$$\hat{R}_{i\sigma j\tau}^{R_k} = \sum_{kl \in R_k} g_{kjil} \hat{a}_{k\tau}^{\dagger} \hat{a}_{l\sigma}. \tag{4.22}$$

Note that the above decomposition is not symmetrical with respect to L' and R'; one superblock carries uncontracted operators such as $\hat{A}_{ik}$ and $\hat{B}_{ij}$, $\hat{C}_{ij}$ (normal operators), while the other carries only the complementary operators, such as $\hat{P}_{ik}^{R_k}$ and $\hat{Q}_{ij}^{R_k}$, $\hat{R}_{ij}^{R_k}$ (although $\hat{S}_i$ is carried for both superblocks). The two-index complementary operators can be chosen to be defined within the left or right block and the choice will change the total number of SOP terms in Eq. 4.1. For simplicity, here we only show one of the two possibilities which define the two-index complementary operators within the right block. In such cases, the number of SOP terms will increase during a DMRG

half-sweep as the active site k is moved from the left-end (the left-most site) to the right, and the size of the L_k block increases. Therefore it is usual to keep the two-index complementary operators within the right block when $k < N/2$ and keep them within the left block when $k \geq N/2$. Finally, a simple flow table of renormalized operator-based DMRG implementation for ab initio Hamiltonian is shown in Algorithm 4.1.

Algorithm 4.1: Renormalized operator-based DMRG implementation for ab initio Hamiltonian. *DMRG*, Density matrix renormalization group.

1: **procedure** Prepare(coordination, basis, ...)
2:   $\{t_{pq}\}, \{g_{pqrs}\} \longleftarrow$ Hartree−Fock or other low-level calculation
3:   Select active MOs
4:   **return** $\{t_{pq}\}, \{g_{pqrs}\}$ and other prerequisites
5: **end procedure**
6: **procedure** OrbitalOrder ($\{t_{pq}\}, \{g_{pqrs}\}$)
7:   Optimize MO order on a 1D chain **//** see Section 4.6
8: **end procedure**
9: **procedure** sweepL2R($\{t_{pq}\}, \{g_{pqrs}\}$)
10:   **for** k **in** $[1, N-1]$
11:     Build $\hat{H}_{L'}, \hat{H}_{R'}, \{\hat{O}_{L'}\}, \{\hat{O}_{R'}\}$
// see Eqs. 4.12 and 4.15−4.22
12:       construct $\hat{H}$ via Eq. 4.14
13:       $E, \psi \leftarrow$ Diagonalize($\hat{H}$) **//** Lanczos or Davidson
14:       $U, S, V^T \leftarrow$ SVD($\psi_{l'r'}$)
15:       $\hat{O}_{L'} \leftarrow$ Transform ($\hat{O}_{L'}, U$) **//** $\hat{O}_{L'}^{\text{new}} = U^T \hat{O}_{L'}^{\text{old}} U$
16: **end for**
17: **end procedure**
18: **procedure** SweepR2L($\{t_{pq}\}, \{g_{pqrs}\}$)
19:   **for** k **in** $[N, 2]$
20:     Build $\hat{H}_{L'}, \hat{H}_{R'}, \{\hat{O}_{L'}\}, \{\hat{O}_{R'}\}$
// see Eqs. 4.12 and 4.15−4.22
21:       construct $\hat{H}$ via Eq. 4.14
22:       $E, \psi \leftarrow$ Diagonalize($\hat{H}$) **//** Lanczos or Davidson
23:       $U, S, V^T \leftarrow$ SVD($\psi_{l'r'}$)
24:       $\hat{O}_{R'} \leftarrow$ Transform($\hat{O}_{R'}, V$) **//** $\hat{O}_{R'}^{\text{new}} = VT\hat{O}_{R'}^{\text{old}} V$
25:   **end for**
26:   **if** not converged **then**
27:       Go back to step 9 with updated $\{\hat{O}_{R'}\}$
28:   **end if**
29:   **return** E, ψ
30: **end procedure**

Now let's present a brief analysis of the computational costs in renormalized operator-based ab initio DMRG. (Chan and Head-Gordon, 2002; Wouters and Van Neck, 2014) The left-right decomposition is not symmetrical with respect to the left and right blocks, because one block carries uncontracted normal operators such as $\hat{a}_i \hat{a}_j$ while the other carries only the complementary operators, such as $\hat{P}_{ij}$ and $\hat{Q}_{ij}, \hat{R}_{ij}$. In the block configuration,

each block L and R carries $O(N^2)$ normal operators with memory storage of $O(N^2 m^2)$ if there are at most m DMRG states reserved in sweeps. The most expensive part of blocking is consequently the formation of the two-site complementary operators $\hat{P}_{ij}$ and $\hat{Q}_{ij}$, $\hat{R}_{ij}$, which requires $O(N^2 m^2)$ time and $O(N^2 m^2)$ storage per operator. There are $O(N^2)$ such operators, and a naive implementation would hence result in a computational time cost of $O(N^4 m^2)$ per microiteration. However, this summation needs to be performed only once per sweep for each operator, at the moment when the second-quantized operator is added. Thereon, this operator can be transformed successively. The total computational time cost per microiteration is hence reduced to $O(N^3 m^2)$ for the summation and $O(N^2 m^3)$ for the transformation (there are $O(N^2)$ operators to be transformed).

In a left-to-right sweep, after we have performed the blockings $L^{'} = L + n_l$ and $R^{'} = n_r + R$, the next stage is to truncate $L^{'}$. We have to construct the on-site effective Hamiltonian and use the iterative Davidson or Lanczos procedure to find the ground-state wave function. The key step in these iterative eigensolvers is the construction of

$$\mathbf{v}_{L'R'} = \mathbf{H}_{L'R'} \mathbf{c}_{L'R'}, \qquad (4.23)$$

in which the $\mathbf{c}_{L'R'}$ is the trial wave function vector and its dimension is the number of states in the superblock $L^{'} + R^{'}$, which is $O(16 m^2)$. By using the left-right decomposition of the total Hamiltonian as shown in Eqs. 4.11, 4.12, and 4.14, the operators $\hat{O}^{L_k}$ and $\hat{O}^{R_k}$ in the left and right blocks with a dimension $\sim 4\, m$ can be applied successively onto the trial wave function vector $\mathbf{c}_{L'R'}$. The cost for each matrix-vector multiplication is then $O(m^3)$ times the number of operator pairs in the left and right blocks, which yields an $O(N^2 m^3)$ cost per multiplication. Subsequently, a singular value decomposition (SVD) of the ground-state wave function or the equivalent diagonalization of subsystems' reduced density matrix (RDM) with time costs of $O(m^3)$ is performed to obtain the lowest m eigenvectors as the later updated basis set of the superblock $L^{'}$. The operators of $L^{'}$ are then rotated in $O(N^2 m^3)$ time. These operators, together with the wave function and transformation matrix, are saved to disk for use in the subsequent sweep iteration or renormalization transform. Overall, on each site, the most expensive parts of the renormalization transform are the blocking, diagonalization, and truncation steps, which cost $O(N^3 m^2) + O(N^2 m^3)$, $O(N^2 m^3)$, and $O(N^2 m^3)$ time, respectively. As these procedures must be applied on each site, in DMRG calculations these procedures have to be executed $O(N)$ times, leading the total time cost of the DMRG algorithm to $(N^4 m^2) + O(N^3 m^3)$, as shown in Table 4.1.

Due to the sparsity of the two-electron integrals, the number of nonzero effective operator terms in the total Hamiltonian is normally much smaller than N^4. How to decompose these terms into normal and complementary operators becomes highly nontrivial, because there are no rigorous rules to guarantee the minimum of SOP terms. The optimal decomposition choices will be discussed in Section 4.3.

TABLE 4.1 The computational cost per sweep in ab initio density matrix renormalization group algorithm.

Task	Time	Memory
Diagonalization of effective Hamiltonian	$O(N^3 m^3)$	$O(m^2)$
Singular value decomposition	$O(Nm^3)$	$O(m^2)$
Constructing normal operators	$O(N^3 m^3)$	$O(N^2 m^2)$
Constructing complementary operators	$O(N^4 m^2) + O(N^3 m^3)$	$O(N^2 m^2)$
Total	$O(N^4 m^2) + O(N^3 m^3)$	$O(N^2 m^2)$

4.2 Matrix product operator-based density matrix renormalization group implementation

As we have introduced in Chapter 2, the modern formulation of the DMRG method based on MPS and MPO, sometimes called the second-generation DMRG algorithm, is nowadays also popular in ab initio DMRG (e.g., Keller et al., 2015b; Keller and Reiher, 2016). In the MPO-based DMRG implementation, the multiconfigurational wave function is transformed as a product of rank-3 MPS tensors and the Hamiltonian as a product of rank-4 MPO tensors. Instead of performing the left-right partition in renormalized operator-based ab initio DMRG, here the Hamiltonian is completely decomposed into a series of single tensors on each orbital, rather than renormalized blocks on multiple orbitals. Thus we only have to decompose the total Hamiltonian completely before starting any DMRG sweep, and no blocking procedures but tensor contractions are essential in the sweeps.

In MPO constructions, we should use not only the nontrivial SSOs, but also the identity operator $\hat{I}$ and the parity operator $\hat{P}$. For example, for a system with $N = 6$ orbitals, one of the operator terms might be

$$t_{24}\hat{a}^{\dagger}_{2u}\hat{a}_{4u} = t_{24}\hat{I}_1\hat{a}^{\dagger}_{2u}\hat{P}_2\hat{P}_3\hat{a}_{4u}\hat{I}_5\hat{I}_6. \tag{4.24}$$

There are one creator and one annihilator operator explicitly shown in this equation, whereas on the other orbitals, an identity $\hat{I}$ or a parity operator $\hat{P}$ is implicitly included, defined as

$$\hat{I} = \begin{pmatrix} 1 & 0 & 0 & 0 \\ 0 & 1 & 0 & 0 \\ 0 & 0 & 1 & 0 \\ 0 & 0 & 0 & 1 \end{pmatrix}, \quad \hat{P} = \begin{pmatrix} 1 & 0 & 0 & 0 \\ 0 & -1 & 0 & 0 \\ 0 & 0 & -1 & 0 \\ 0 & 0 & 0 & 1 \end{pmatrix}. \tag{4.25}$$

The parity operator $\hat{P}$ is introduced to maintain the anticommutation relations between the fermionic operators $\hat{a}^{\dagger}$ and $\hat{a}$. The operator term in

Eq. (4.23) can be constructed in two steps, by applying the two nontrivial SSOs successively, as

$$\hat{P}_1 \hat{a}_{2u}^\dagger \hat{I}_3 \hat{I}_4 \hat{I}_5 \hat{I}_6,$$

and

$$\hat{P}_1 \hat{P}_2 \hat{P}_3 \hat{a}_{4u} \hat{I}_5 \hat{I}_6.$$

As $\hat{P}_i \hat{P}_i = \hat{I}_i$, we can merge these two steps and multiply the corresponding MO integral to get the complete operator term.

After splitting the total Hamiltonian in Eq. 4.1 into a series of operator terms, we need to decompose these terms and put the SSOs on their corresponding sites and positions to construct the Hamiltonian MPO tensors. An MPO tensor can be regarded as an operator valued two-dimensional matrix rather than a four-dimensional tensor. In this case, the elements in the MPO matrix are SSOs, which are two-dimensional matrices themselves. Now, the crucial part for a second-generation ab initio DMRG algorithm is to construct operator tensors, such as the Hamiltonian, in an efficient manner.

A most straightforward and naive way to build the MPO form of the Hamiltonian is to write the MPOs at different lattice sites as diagonal matrices, in which the diagonal elements are the SSOs acting on the current site. Using this naive idea, on any general site (except the first and the last sites), the MPO tensor is a $N_t \times N_t$ diagonal matrix

$$\hat{W}_i = \begin{pmatrix} \hat{O}_i^1 & 0 & \cdots & 0 \\ 0 & \hat{O}_i^2 & \cdots & 0 \\ \vdots & \vdots & \ddots & \vdots \\ 0 & 0 & \cdots & \hat{O}_i^{N_t} \end{pmatrix}, \tag{4.26}$$

in which $\hat{O}_i^k$ is the SSO acting on the ith site in the kth operator term. The dimension size N_t of the MPO matrices equals the number of operator terms. When transforming the ab initio quantum chemistry Hamiltonian in Eq. 4.1, the number of operator terms could be as large as $O(N^4)$. For $N = 30$ orbitals there would be more than 10^5 operator terms. Therefore the naive diagonal MPO tensors are not practical for large chemical systems. The optimal compact construction for ab initio MPOs and the computational scaling for MPO-based ab initio DMRG will be discussed in the next section.

With the constructed MPO representations, DMRG sweeping for the optimization of MPS will become straightforward as discussed in Chapter 2. A simple flow table of MPO-based DMRG implementation for ab initio quantum chemistry is illustrated in Algorithm 4.2.

Algorithm 4.2: MPO-based two-site DMRG implementation for ab initio Hamiltonian. *DMRG*, Density matrix renormalization group; *MPO*, matrix product operator.

1: **procedure** Prepare(coordination, basis, ...)

2: $\{t_{pq}\}, \{g_{pqrs}\} \longleftarrow$ Hartree−Fock or other low-level calculation

3:    Select active MOs

4:    **return** $\{t_{pq}\}, \{g_{pqrs}\}$ and other prerequisites

5: **end procedure**

6: **procedure** OrbitalOrder($\{t_{pq}\}, \{g_{pqrs}\}$)

7:    Optimize MO order on a 1D chain **//** see Section 4.6

8: **end procedure**

9: **procedure** MPOWithMPS($\{t_{pq}\}, \{g_{pqrs}\}$)

10:    $\left\{ \boldsymbol{M}^{n_k}_{a_{k-1}a_k} \right\} \leftarrow$ InitializeMPS()

11:    $\left\{ \boldsymbol{W}^{n_k n_k^*}_{b_{k-1}b_k} \right\} \leftarrow$ ConstructMPO($\{t_{pq}\}, \{g_{pqrs}\}$)

12: **end procedure**

13: **procedure** PrepareBlocks($\left\{ \boldsymbol{M}^{n_k}_{a_{k-1}a_k} \right\}, \left\{ \boldsymbol{W}^{n_k n_k^*}_{b_{k-1}b_k} \right\}$)

14:    **for** $k \in [1, N]$

15:      $\boldsymbol{L}^{b_k}_{a_k^*, a_k} = \sum \boldsymbol{L}^{b_{k-1}}_{a_{k-1}^*, a_{k-1}} \boldsymbol{M}^{n_k}_{a_{k-1}a_k} \boldsymbol{M}^{n_k^*}_{a_{k-1}^* a_k^*} \boldsymbol{W}^{n_k n_k^*}_{b_{k-1}b_k}$

16:      $\boldsymbol{R}^{b_{k-1}}_{a_{k-1}^*, a_{k-1}} = \sum \boldsymbol{R}^{b_k}_{a_k^*, a_k} \boldsymbol{M}^{n_k}_{a_{k-1}a_k} \boldsymbol{M}^{n_k^*}_{a_{k-1}^* a_k^*} \boldsymbol{W}^{n_k n_k^*}_{b_{k-1}b_k}$

17:    **end for**

18: **end procedure**

19: **procedure** SweepL2R($\{t_{pq}\}, \{g_{pqrs}\}$)

20:    **for** k in $[1, N-1]$

21:    $\boldsymbol{H}^{n_k^* n_{k+1}^* n_k n_{k+1}}_{a_{k-1}^* a_{k+1}^*, a_{k-1} a_{k+1}} = \sum \boldsymbol{L}^{b_{k-1}} \boldsymbol{R}^{b_{k+1}} \boldsymbol{W}^{n_k n_k^*} \boldsymbol{W}^{n_{k+1} n_{k+1}^*}$

22:    $E, \tilde{\boldsymbol{M}}^{n_k n_{k+1}}_{a_{k-1} a_{k+1}} \leftarrow$ Diagonalize $\boldsymbol{H}^{n_k^* n_{k+1}^* n_k n_{k+1}}_{a_{k-1}^* a_{k+1}^*, a_{k-1} a_{k+1}}$

23:    $\boldsymbol{U}_{a_{k-1}n_k, m}, \boldsymbol{S}_{m,m}, \left(\boldsymbol{V}^\dagger \right)_{m, n_{k+1} a_{k+1}} \leftarrow$ SVD$\left(\tilde{\boldsymbol{M}}^{n_k n_{k+1}}_{a_{k-1} a_{k+1}} \right)$

24:    $\left(\boldsymbol{M}^{n_k}_{a_{k-1}a_k} \right)^{\text{new}} = \boldsymbol{U}_{a_{k-1}n_k, m}, \left(\boldsymbol{M}^{n_{k+1}}_{a_k a_{k+1}} \right)^{\text{new}} = \sum_m \boldsymbol{S}_{m,m} \left(\boldsymbol{V}^\dagger \right)_{m, n_{k+1} a_{k+1}}$

25:    Update $\boldsymbol{L}^{b_k}_{a_k^*, a_k}$ with $\left(\boldsymbol{M}^{n_k}_{a_{k-1}a_k} \right)^{\text{new}}, \boldsymbol{L}^{b_{k-1}}_{a_{k-1}^*, a_{k-1}}$

26:    **end for**

27: **end procedure**

28: **procedure** SweepR2L($\{t_{pq}\}, \{g_{pqrs}\}$)

29:    **for** k in $[N, 2]$

30:    $\boldsymbol{H}^{n_{k-1}^* n_k^* n_{k-1} n_k}_{a_{k-2}^* a_k^*, a_{k-2} a_k} = \sum \boldsymbol{L}^{b_{k-2}} \boldsymbol{R}^{b_k} \boldsymbol{W}^{n_{k-1} n_{k-1}^*} \boldsymbol{W}^{n_k n_k^*}$

31:    $E, \boldsymbol{M}^{n_{k-1} n_k}_{a_{k-2} a_k} \leftarrow$ Diagonalize $\boldsymbol{H}^{n_{k-1}^* n_k^* n_{k-1} n_k}_{a_{k-2}^* a_k^*, a_{k-2} a_k}$

32:    $\boldsymbol{U}_{a_{k-2}n_{k-1}, m}, \boldsymbol{S}_{m,m}, \left(\boldsymbol{V}^\dagger \right)_{m, n_k a_k} \leftarrow$ SVD($\boldsymbol{M}^{n_{k-1} n_k}_{a_{k-2} a_k}$)

33:    $\left(\boldsymbol{M}^{n_{k-1}}_{a_{k-2}a_{k-1}} \right)^{\text{new}} = \sum_m \boldsymbol{U}_{a_{k-2}n_{k-1}, m}, \boldsymbol{S}_{m,m}, \left(\boldsymbol{M}^{n_k}_{a_{k-1}a_k} \right)^{\text{new}} = \left(\boldsymbol{V}^\dagger \right)_{m, n_k a_k}$

34:    Update $\boldsymbol{R}^{b_{k-1}}_{a_{k-1}^*, a_{k-1}}$ with $\left(\boldsymbol{M}^{n_k}_{a_{k-1}a_k} \right)^{\text{new}}, \boldsymbol{R}^{b_k}_{a_k^*, a_k}$

35:    **end for**

36:    **if** not converged **then**

37:      Go back to step 18 with updated $\{\boldsymbol{R}^{b_k}_{a_k^*, a_k}\}$

38:    **end if**

39:    **return** $E, \left\{ \boldsymbol{M}^{n_k}_{a_{k-1}a_k} \right\}$

40: **end procedure**

4.3   Optimal construction for matrix product operators

To construct the MPO tensors compactly, Keller et al. (2015b) proposed an efficient approach, using the so-called *fork* and *merge* operations. If two or more operator terms are identical on sites 1 through k, the common substrings can be collapsed into one single substring up to site k, which is then forked into new strings on site $k + 1$, splitting the common left part into the unique right remainders and constructing complementary operators. Because each operator on the site of the fork will be multiplied by the shared left part upon matrix−matrix multiplication, the redundant substrings can be safely removed. The second operation is to merge strings that match on sites l through L into a common right substring. If the ab initio Hamiltonian operator is constructed in this fashion, there will also be strings with identical subsections in the middle of the lattice of sites. To compact the $\hat{W}$ matrices, one can collapse strings from both sides of the orbital-chain lattice simultaneously. For general term $g_{ijkl}\hat{a}_{i\sigma}^{\dagger}\hat{a}_{k\tau}^{\dagger}\hat{a}_{l\tau}\hat{a}_{j\sigma}$ $(i < k < l < j)$, the four nontrivial SSOs divide the string running over all sites into five substrings $1 - i$, $i - k$, $k - l$, $l - j$, and $j - N$. Because one always begins with fork from the left and merges from the right, one only needs to focus on the three substrings in the center. Considering the connectivity types of the labels for these substrings, there are two possible combinations for the compact MPO representations: *fork-fork-merge* and *fork-merge-merge*.

   The above method can be easily understood as a simpler way of utilizing matrix multiplication by tracking the row and column indices of each SSO $\hat{O}_i^I$. In the matrix multiplication operation

$$C_{ij} = \sum_k A_{ik} B_{kj},$$

the element B_{kj} in the kth row of the matrix $\boldsymbol{B}$ must be multiplied by the element A_{ik} in the matrix $\boldsymbol{A}$ on B_{kj}'s left. It implies that if A_{ik} holds the common substring of multiple operator terms, all of the various remainders should be placed in the kth row of the neighboring $\boldsymbol{B}$ matrix. In practice, the matrices $\boldsymbol{A}$ and $\boldsymbol{B}$ here are two MPO tensors $\hat{W}_i$ and $\hat{W}_{i+1}$ adjacent to each other. For the general operator term

$$\hat{O}_1 \hat{O}_2 \cdots \hat{O}_N,$$

as the first tensor $\hat{W}_1$ is considered as a row-vector, the row index r_1 of the first SSO $\hat{O}_1$ is 0, and its column index c_1 can be obtained by sorting all the SSOs in this row in a certain order. For the second SSO $\hat{O}_2$, its row index r_2 in the matrix $\hat{W}_2$ must be equal to c_1, and we can get its column index c_2 by sorting all of the SSOs in this row. We can do such operations on each $\hat{W}_i$ matrices except the last one, on which the row index r_N of the last SSO $\hat{O}_N$ in column vector $\hat{W}_N$ is equal to c_{N-1} and the column index c_N is 0.

While sorting the SSOs, we can merge the common left substrings if two terms share the same part on the left. Between each pair of sites, all identical operators can be collapsed into a single bond to obtain a compact representation of the Hamiltonian. Note that the identical operators must be the same kind of SSO and share the same left/right basis. Because most elementary operators have some identity operators on the left, and the left and right bases of these identities are both vacuum states, we can always get some common left substrings consisting of identity operators, which is very helpful for reducing the dimensions of the MPO matrices.

Here we take a Hamiltonian containing four operator terms of a $N = 4$ system as a simple example:

$$\hat{H} = \hat{t}_1 + \hat{t}_2 + \hat{t}_3 + \hat{t}_4, \tag{4.27}$$

with

$$\hat{t}_1 = \hat{a}_{1u}^\dagger \hat{a}_{2u}^\dagger \hat{a}_{3u} \hat{a}_{4u}, \tag{4.28}$$

$$\hat{t}_2 = \hat{a}_{1u}^\dagger \hat{a}_{2d}^\dagger \hat{a}_{3u} \hat{a}_{3d}, \tag{4.29}$$

$$\hat{t}_3 = \hat{a}_{1u}^\dagger \hat{a}_{2d}^\dagger \hat{a}_{4u} \hat{a}_{4d}, \tag{4.30}$$

$$\hat{t}_4 = \hat{a}_{2u}^\dagger \hat{a}_{2d}^\dagger \hat{a}_{4u} \hat{a}_{4d}, \tag{4.31}$$

and the scaling factors (e.g., the MO integrals) are temporarily omitted for convenience. The four terms can be completed by adding the identity and parity operators as

$$\hat{t}_1 = \hat{a}_{1u}^\dagger \hat{P}_1 \hat{a}_{2u}^\dagger \hat{a}_{3u} \hat{P}_3 \hat{a}_{4u}, \tag{4.32}$$

$$\hat{t}_2 = \hat{a}_{1u}^\dagger \hat{P}_1 \hat{a}_{2d}^\dagger \hat{a}_{3u} \hat{a}_{3d} \hat{I}_4, \tag{4.33}$$

$$\hat{t}_3 = \hat{a}_{1u}^\dagger \hat{P}_1 \hat{a}_{2d}^\dagger \hat{I}_3 \hat{a}_{4u} \hat{a}_{4d}, \tag{4.34}$$

$$\hat{t}_4 = \hat{I}_1 \hat{a}_{2u}^\dagger \hat{a}_{2d}^\dagger \hat{I}_3 \hat{a}_{4u} \hat{a}_{4d}, \tag{4.35}$$

and the naively constructed diagonal MPO matrices and vectors are

$$\hat{W}_1 = \begin{pmatrix} \hat{a}_{1u}^\dagger \hat{P}_1 & \hat{a}_{1u}^\dagger \hat{P}_1 & \hat{a}_{1u}^\dagger \hat{P}_1 & \hat{I}_1 \end{pmatrix}, \tag{4.36}$$

$$\hat{W}_2 = \begin{pmatrix} \hat{a}_{2u}^\dagger & 0 & 0 & 0 \\ 0 & \hat{a}_{2d}^\dagger & 0 & 0 \\ 0 & 0 & \hat{a}_{2d}^\dagger & 0 \\ 0 & 0 & 0 & \hat{a}_{2u}^\dagger \hat{a}_{2d}^\dagger \end{pmatrix}, \tag{4.37}$$

$$\hat{W}_3 = \begin{pmatrix} \hat{a}_{3u}\hat{P}_3 & 0 & 0 & 0 \\ 0 & \hat{a}_{3u}\hat{a}_{3d} & 0 & 0 \\ 0 & 0 & \hat{I}_3 & 0 \\ 0 & 0 & 0 & \hat{I}_3 \end{pmatrix}, \tag{4.38}$$

$$\hat{W}_4 = \begin{pmatrix} \hat{a}_{4u} \\ \hat{I}_4 \\ \hat{a}_{4u}\hat{a}_{4d} \\ \hat{a}_{4u}\hat{a}_{4d} \end{pmatrix}. \tag{4.39}$$

It is easy to prove that

$$\hat{W}_1\hat{W}_2\hat{W}_3\hat{W}_4 = \hat{t}_1 + \hat{t}_2 + \hat{t}_3 + \hat{t}_4. \tag{4.40}$$

To reduce the size of the MPO tensors, we start from the left-most site, reorder all of the SSOs in the row-vector $\hat{W}_1$ and eventually merge the duplicate ones. We can put the identity operator $\hat{I}_1$ in the head of the vector by reordering the operator terms as

$$\hat{t}_1 \rightarrow \hat{t}_2, \ \hat{t}_2 \rightarrow \hat{t}_3, \ \hat{t}_3 \rightarrow \hat{t}_4, \ \hat{t}_4 \rightarrow \hat{t}_1.$$

Forthwith, we merge the three $\hat{a}_{u,1}^\dagger\hat{P}_1$ operators in $\hat{W}_1$ and obtain the compact MPO as

$$\hat{W}_1 = \begin{pmatrix} \hat{I}_1 & \hat{a}_{1u}^\dagger\hat{P}_1 \end{pmatrix}. \tag{4.41}$$

The next MPO tensor $\hat{W}_2$ are transformed to a 2×4 matrix as

$$\hat{W}_2 = \begin{pmatrix} \hat{a}_{2u}^\dagger\hat{a}_{2d}^\dagger & 0 & 0 & 0 \\ 0 & \hat{a}_{2u}^\dagger & \hat{a}_{2d}^\dagger & \hat{a}_{2d}^\dagger \end{pmatrix}. \tag{4.42}$$

The nonzero elements in $\hat{W}_3$ and $\hat{W}_4$ are reordered as well, thereby we have

$$\hat{W}_3 = \begin{pmatrix} \hat{I}_3 & 0 & 0 & 0 \\ 0 & \hat{a}_{3u}\hat{P}_3 & 0 & 0 \\ 0 & 0 & \hat{a}_{3u}\hat{a}_{3d} & 0 \\ 0 & 0 & 0 & \hat{I}_3 \end{pmatrix}, \tag{4.43}$$

$$\hat{W}_4 = \begin{pmatrix} \hat{a}_{4u}\hat{a}_{4d} \\ \hat{a}_{4u} \\ \hat{I}_4 \\ \hat{a}_{4u}\hat{a}_{4d} \end{pmatrix}. \tag{4.44}$$

We can easily find that the two $\hat{a}_{d,2}^{\dagger}$ operators in the second row of $\hat{W}_2$ can be merged. The final compact MPO tensors in this simple example are

$$\hat{W}_1 = \begin{pmatrix} \hat{I}_1 & \hat{a}_{1u}^{\dagger}\hat{P}_1 \end{pmatrix}, \tag{4.45}$$

$$\hat{W}_2 = \begin{pmatrix} \hat{a}_{2u}^{\dagger}\hat{a}_{2d}^{\dagger} & 0 & 0 \\ 0 & \hat{a}_{2u}^{\dagger} & \hat{a}_{2d}^{\dagger} \end{pmatrix}, \tag{4.46}$$

$$\hat{W}_3 = \begin{pmatrix} \hat{I}_3 & 0 & 0 & 0 \\ 0 & \hat{a}_{3u}\hat{P}_3 & 0 & 0 \\ 0 & 0 & \hat{a}_{3u}\hat{a}_{3d} & \hat{I}_3 \end{pmatrix}, \tag{4.47}$$

$$\hat{W}_4 = \begin{pmatrix} \hat{a}_{4u}\hat{a}_{4d} \\ \hat{a}_{4u} \\ \hat{I}_4 \\ \hat{a}_{4u}\hat{a}_{4d} \end{pmatrix}. \tag{4.48}$$

Accordingly, the product of these compact MPOs is still equal to the original Hamiltonian. Since the scaling factors are generally irreducible, they can be multiplied by the first unmerged SSOs in the corresponding operator terms, for example, the SSOs in the above matrix $\hat{W}_3$.

The relationship between the first-generation renormalized operator-based ab initio DMRG and second-generation MPO-based ab initio DMRG has been carefully examined by Chan et al. (2016). It was demonstrated that the so-called *fork-fork-merge* or *fork-merge-merge* operations in the latter's MPO compaction are completely equivalent to use $\hat{P}$ and $\hat{Q}$, $\hat{R}$ complementary operators in the right or left block in the former. Therefore, by using the compact MPO construction, MPO-based ab initio DMRG also has the same computational scaling of $(N^4m^2) + O(N^3m^3)$ as renormalized operator-based ab initio DMRG. Nevertheless, the MPO formulation is a more flexible framework to apply DMRG for higher dimensions and complex Hamiltonians, especially when containing long-range interactions. Another main advantage of MPS is that they encode wave functions as stand-alone objects that can directly be manipulated arithmetically as a whole for subsequent calculations of higher excited states or dynamic correlations and evaluating the overlaps between different states. In contrast, for traditional DMRG a series of complicated and tedious reduced basis transformations are needed.

One important fact of the optimal MPO construction is that both the so-called complementary operator technique in the first-generation renormalized operator-based DMRG algorithm and the equivalent Keller et al.'s approach for the second-generation MPO-based DMRG algorithm are not automatic and cannot guarantee the minimization of the number of SOP terms. A possible solution is to naively construct the MPO and then compress it by SVD or removing the linearly dependent terms (Hubig et al., 2017).
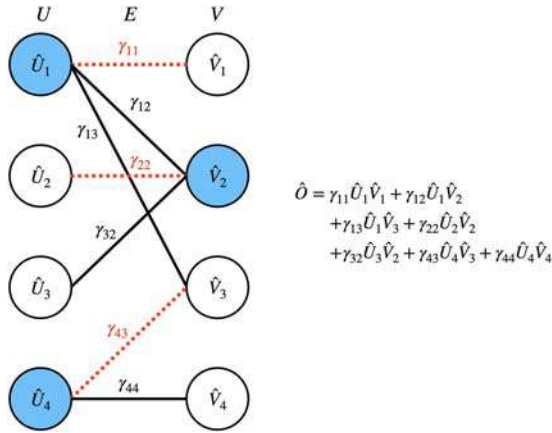
FIGURE 4.1 An example of mapping the operator $\mathcal{O}$ to a bipartite graph $G = G(U, V, E)$. The vertices represent the nonredundant operators in the left and right blocks. The edges represent the interactions with a nonzero prefactor. The filled vertices in blue form a minimum vertex cover, while the dash edges in red form a maximum matching. *Reproduced from Ren, J., Li, W., Jiang, T., Shuai, Z., 2020. A general automatic method for optimal construction of matrix product operators using bipartite graph theory. J. Chem. Phys. 153, 084118.* https://doi.org/10.1063/5.0018149, *with permission from American Institute of Physics.*

This scheme is fully generic and automatic for different operators, but a numerical SVD truncation error is introduced and it is infeasible to quantify its effect on the following DMRG calculations in advance. In addition, the numerical compression may be computational costly when the number of SOP terms in the Hamiltonian is large.

To globally minimize the number of SOP terms and eliminate the numerical errors in MPO construction, Ren et al. (2020) proposed a generic method to automatically determine the most efficient operator decomposition by virtue of using bipartite graph theory. Describing the nonredundant operators in the left and right blocks as vertices $\{U\}$ and $\{V\}$ and the interactions (MO integrals) with a nonzero prefactor as edges $\{E\}$, a global operator can be transformed to a bipartite graph $G = (U, V, E)$, as shown in Fig. 4.1. The optimal compression/decomposition problem of the operator terms at each bond can be interpreted as a minimum vertex cover problem in the graph G, which is to determine a subset of the vertices which covers all edges such that the number of the vertices in the subset is minimized. For the bipartite graph described here, the König theorem (König, 1931) proves that the number of vertices in the minimum vertex cover is equal to the number of edges in the maximum matching. A matching is an edge set in which any two edges do not share one vertex. The maximum matching shown in red in Fig. 4.1 is the matching having the maximal number of edges, which could be solved efficiently by Hungarian algorithm (Kuhn, 1955) or the Hopcroft–Karp algorithm (Hopcroft and Karp, 1973). Once the maximum matching is found, the vertices in the

minimum vertex cover could be obtained easily, and the retained operators are optimally selected.

4.4 Symmetries and spin adaption

In expensive quantum chemistry calculations, it is usually desirable to exploit symmetries to reduce memory storage, shorten computation time, and to thin out Hilbert space by decomposing it into a sum of smaller sectors. It is also crucial to utilize the symmetrical constraints to correctly identify and target the electronic state. Symmetries often used in ab initio DMRG fall into two categories, Abelian or non-Abelian.

The most frequently implemented symmetries in DMRG are the Abelian $U(1)$ symmetries, leading to total magnetization S_{tot}^z and total particle number N_{tot} as good conserved quantum numbers. In the traditional DMRG formulation with left-right partition, as the total quantum number

$$T = T_L + T_R, \ T = S_{\text{tot}}^z \text{ or } N_{\text{tot}}$$

is fixed, only a small portion of the vectors $|L_\mu\rangle$ and $|R_\nu\rangle$ can be blocked according to the specified T_L and $T - T_L$. Thus all operators used in DMRG can be expressed in a matrix representation as dense blocks of nonzero matrix elements with all other matrix elements equal to zero. Abelian molecular point group symmetries P with real-valued character tables $P \in \{C_1, C_i, C_2, C_s, D_2, C_{2v}, C_{2h}, D_{2h}\}$ and other discrete symmetries (e.g., spin-flip, particle-hole) can be also easily incorporated by using symmetrized DMRG (see Section 3.3).

The total spin $\hat{S}^2$ requires a non-Abelian Lie group $SU(2)$ symmetry in ab initio quantum chemical Hamiltonian. Since Zgid and Nooijen (2008a) proposed a first spin-adapted ab initio DMRG implementation, a variety of algorithms (Sharma and Chan, 2012; Wouters et al., 2012; Keller and Reiher, 2016; Li and Chan, 2017) have been developed to account for $U(1) \otimes SU(2) \otimes P$ symmetry, in both renormalized operator-based and MPO-based DMRG formulations.

Let us first introduce the MPO-based spin-adaption scheme proposed by Keller and Reiher (2016). Using symmetries in the MPS/MPO, the DMRG method naturally leads to the symmetry-protected tensor implementation. In the $U(1) \otimes SU(2) \otimes P$ symmetry, the local state on a certain orbital could be

$$|N, S, I\rangle \in \left\{ \left|2, 0, A_g\right\rangle, \ \left|1, \frac{1}{2}, I\right\rangle, \ \left|0, 0, A_g\right\rangle \right\}, \tag{4.49}$$

in which I denotes the irreducible representation of the point group P and A_g is the totally symmetric representation. The most complicated problem arises from the multiplicity of the total spin. With the Clebsch−Gordan expansion,

a composite system consisting of the two representations $D(N_1, S_1, I_1)$ and $D(N_2, S_2, I_2)$ can be decomposed as

$$
\begin{aligned}
&D(N_1, I_1) \otimes D(N_2, S_2, I_2) \\
&= \bigoplus_{S=|S_1-S_2|}^{S_1+S_2} D(N_1 + N_2, S, I_1 \otimes I_2).
\end{aligned}
\tag{4.50}
$$

The direct sum of multiple representations on the right side of Eq. (4.50) implies a block-sparse implementation in the spin-adapted DMRG method (Wouters and Van Neck, 2014). Because MPSs and MPOs behave as rank-k tensor operators, the Wigner–Eckart theorem is the fundamental equation to exploit spin symmetry. This states that the matrix element of the Mth component $T_M^{[k]}$ of a rank-k tensor operator $\boldsymbol{T}^{[k]}$ is generated from a reduced matrix element multiplied by the Clebsch–Gordan coefficient

$$
\langle j'm'|T_M^{[k]}|jm\rangle = \langle j' \| \boldsymbol{T}^{[k]} \| j\rangle C_{mMm'}^{jkj'}.
\tag{4.51}
$$

The double vertical line denotes Condon and Shortley's notation for a reduced matrix element, which is independent of any projection quantum number. In Eq. (4.51), j and j' refer to a spin quantum number [an irreducible $SU(2)$ representation, e.g., the total spin S]; m, m', and M are projection quantum numbers such as the z-component of spin if the z-axis is chosen as the axis of quantization. As the multiplet $M = -k, \cdots, k$ is determined by a single reduced matrix element, the Wigner–Eckart theorem entails information compression, thus allowing an efficient operators storage. As the total Hamiltonian $\hat{H}$ is a spin-zero operator, the feasibility of using the spin symmetry is based on the fact that the Hamiltonian $\hat{H}$ is invariant under the symmetric rotations. When solving the Schrödinger equation with spin symmetry, we can work with multiplets as a single entity, rather than individual states.

Henceforth, till the end of the section, bold symbols are used to represent the reduced tensors in $SU(2)$ symmetry. According to Eq. (4.51), these tensors are constructed from a series of tensor blocks, each of which is labeled with the quantum number of a certain irrep of the symmetry. Following the ideas of Keller and Reiher (2016), we associate the a-index of each MPS tensor $\boldsymbol{M}_{a_{i-1}a_i}^{n_i}$ with a quantum number

$$
q_i = (N_i, S_i, I_i),
\tag{4.52}
$$

to partition the MPS tensor into symmetry blocks. The MPS tensor $\boldsymbol{M}_{q_{i-1}a_{i-1};q_ia_i}^{n_i}$ will then be characterized by the symmetry constraint

$$
q_i \in q_{i-1} \otimes n_i,
\tag{4.53}
$$

which implies that the MPS tensor $\boldsymbol{M}_{q_{i-1}a_{i-1};q_ia_i}^{n_i}$ on site i is in fact an operator that maps states from the subsystem spanning sites 1 to $i-1$ to the

subsystem enlarged to site i, and q_{i-1}, q_i, and n_i are input, output, and operator quantum numbers, respectively.

In DMRG calculations, the MPS tensors are constructed site by site from the vacuum state. Consequently, the quantum numbers appearing in the MPS tensors on opposite ends are also the vacuum state. As we usually start the construction of the MPS/MPO tensors from left to right, in the first MPS tensor $M^{n_1}_{q_0 a_0; q_1 a_1}$, the tensor blocks are

$$q_1 : a_1 = \{(2, 0, A_g) : 1,$$
$$\left(1, \frac{1}{2}, I_1\right) : 1, \tag{4.54}$$
$$(0, 0, A_g) : 1\},$$

with the vacuum state on the a_0 bond denoted by a size-1 block $q_0{:}a_0 = \{(0, 0, A_g){:}1\}$. The tensor $M^{n_1}_{q_0 a_0; q_1 a_1}$ on site 1 consists of three 1×1 blocks. Since the three tensor blocks in Eq. 4.54 also constitute the local state n_i, the MPS tensor $M^{n_2}_{q_1 a_1; q_2 a_2}$ on site 2 shares $q_1{:}a_1$ with $M^{n_1}_{q_0 a_0; q_1 a_1}$ and the output quantum numbers are

$$q_2{:}a_2 = \left\{ \begin{array}{l} (4, 0, A_g){:}1, \left(3, \frac{1}{2}, I_1\right){:}1, \left(3, \frac{1}{2}, I_2\right){:}1, \\ (2, 1, I_1 \otimes I_2){:}1, (2, 0, I_1 \otimes I_2){:}1, (2, 0, A_g){:}2, \\ \left(1, \frac{1}{2}, I_1\right){:}1, \left(1, \frac{1}{2}, I_2\right){:}1, (0, 0, A_g){:}1 \end{array} \right\}, \tag{4.55}$$

in which the output quantum number $q_2 = (2, 0, A_g)$ appears twice in the combination of the input quantum numbers q_1 with the local site basis n_2, namely,

$$q_1 \otimes n_2 = (0, 0, A_g) \otimes (2, 0, A_g), \tag{4.56}$$

and

$$q_1 \otimes n_2 = (2, 0, A_g) \otimes (0, 0, A_g). \tag{4.57}$$

This indicates that there are two different $(2, 0, A_g)$ states defined on sites 1 and 2, corresponding to a 1×2 tensor block. The total MPS wave function can be constructed by continuing this scheme toward the right-most site, while only those tensor blocks which lead to the vacuum target state are reserved.

The most complicated process in the implementation of the spin-adapted quantum chemistry DMRG method is still the construction of MPO tensors. To those SSOs that transform according to an irreducible $SU(2)$ representation, we may apply the Wigner−Eckart theorem. The pairs $\hat{a}^{\dagger}_u$, $\hat{a}^{\dagger}_d$ and $\hat{a}_u$, $\hat{a}_d$,

for instance, each form the two components of a rank-$\frac{1}{2}$ tensor operator with reduced matrix elements

$$\hat{a}^\dagger = \begin{pmatrix} 0 & -\sqrt{2} & 0 \\ 0 & 0 & 1 \\ 0 & 0 & 0 \end{pmatrix}, \tag{4.58}$$

while in this case, the annihilation operator is no longer a simple conjugate transpose of the creation operator

$$\hat{a} = \begin{pmatrix} 0 & 0 & 0 \\ 1 & 0 & 0 \\ 0 & \sqrt{2} & 0 \end{pmatrix}. \tag{4.59}$$

The $\sqrt{2}$ values in the above matrices imply the Clebsch−Gordan coefficients. The other SSOs, such as the particle number operator $\hat{n}$, the spin-flip operator $\hat{a}^\dagger \hat{a}$, and the empty-to-double operator $\hat{d}^\dagger$, can be constructed as

$$\hat{n} = \begin{pmatrix} 2 & 0 & 0 \\ 0 & 1 & 0 \\ 0 & 0 & 0 \end{pmatrix}, \tag{4.60}$$

$$(\hat{a}^\dagger \hat{a})^{[1]} = \begin{pmatrix} 0 & 0 & 0 \\ 0 & \sqrt{3/2} & 0 \\ 0 & 0 & 0 \end{pmatrix}, \tag{4.61}$$

$$\hat{a}^\dagger \hat{n} = \begin{pmatrix} 0 & -\sqrt{2} & 0 \\ 0 & 0 & 0 \\ 0 & 0 & 0 \end{pmatrix}, \tag{4.62}$$

$$\hat{n}\hat{a} = \begin{pmatrix} 0 & 0 & 0 \\ 1 & 0 & 0 \\ 0 & 0 & 0 \end{pmatrix}, \tag{4.63}$$

$$\hat{d}^\dagger = \begin{pmatrix} 0 & 0 & 1 \\ 0 & 0 & 0 \\ 0 & 0 & 0 \end{pmatrix}, \tag{4.64}$$

$$\hat{d} = \begin{pmatrix} 0 & 0 & 0 \\ 0 & 0 & 0 \\ 1 & 0 & 0 \end{pmatrix}. \tag{4.65}$$

Note that the spin-flip operator $\hat{a}^\dagger \hat{a}$ changes the spin on a singly occupied orbital and we use its spin-1 component in Table 4.2, while the empty-to-double operator $\hat{d}^\dagger$ creates a pair of electrons on an empty orbital.

Similar to the previous sections, to implement the spin-adapted DMRG algorithm for ab initio quantum chemistry, first we need to find all the

TABLE 4.2 Terms of the Hamiltonian partitioned into one- and two-electron equivalence classes in $2U(1)$ and $SU(2)$ formulations.

Integral	$2U(1)$ Terms	$SU(2)$ Terms
t_{ii}	$\sum_\sigma \hat{n}_{i\sigma}$	$\hat{n}_i$
t_{ij}	$\sum_\sigma \left(\hat{a}_{i\sigma}^\dagger \hat{a}_{j\sigma} - \hat{a}_{i\sigma} \hat{a}_{j\sigma}^\dagger \right)$	$\sqrt{2}\left(\hat{a}_i^\dagger \hat{a}_j + \hat{a}_i \hat{a}_j^\dagger \right)$
g_{iiii}	$\hat{f}_i = \hat{n}_{iu} \hat{n}_{id}$	$\hat{f}_i$
g_{iijj}	$\sum_{\sigma \neq \tau} \left(\hat{a}_{i\sigma}^\dagger \hat{a}_{j\sigma} \hat{n}_{j\tau} - \hat{a}_{i\sigma} \hat{a}_{j\sigma}^\dagger \hat{n}_{j\tau} \right)$	$\sqrt{2}\left[\hat{a}_i^\dagger (\hat{n}\hat{a})_j + \hat{a}_i \left(\hat{a}^\dagger \hat{n} \right)_j \right]$
g_{iijj}	$(\hat{n}_{iu} + \hat{n}_{id})(\hat{n}_{ju} + \hat{n}_{jd})$	$\hat{n}_i \hat{n}_j$
g_{ijij}	$\hat{a}_{iu}^\dagger \hat{a}_{id}^\dagger \hat{a}_{jd} \hat{a}_{ju} + \hat{a}_{ju}^\dagger \hat{a}_{jd}^\dagger \hat{a}_{id} \hat{a}_{iu} - \hat{n}_{iu} \hat{n}_{ju} - \hat{n}_{id} \hat{n}_{jd} - \hat{a}_{iu}^\dagger \hat{a}_{id} \hat{a}_{jd}^\dagger \hat{a}_{ju} - \hat{a}_{ju}^\dagger \hat{a}_{jd} \hat{a}_{id}^\dagger \hat{a}_{iu}$	$\hat{d}_i^\dagger \hat{d}_j + \hat{d}_i \hat{d}_j^\dagger - \frac{1}{2}\hat{n}_i \hat{n}_j + \sqrt{3}\left(\hat{a}^\dagger \hat{a} \right)_i^{[1]} \left(\hat{a}^\dagger \hat{a} \right)_j^{[1]}$
g_{iikl}	$\sum_{\sigma\tau} \hat{n}_{i\sigma} \left(\hat{a}_{k\tau}^\dagger \hat{a}_{l\tau} - \hat{a}_{k\tau} \hat{a}_{l\tau}^\dagger \right)$	$\sqrt{2}\hat{n}_i \hat{a}_k^\dagger \hat{a}_l + \sqrt{2}\hat{n}_i \hat{a}_k \hat{a}_l^\dagger$
g_{ijil}	$\hat{a}_{iu}^\dagger \hat{a}_{id}^\dagger \left(\hat{a}_{jd} \hat{a}_{lu} + \hat{a}_{ld} \hat{a}_{ju} \right) + \hat{a}_{id} \hat{a}_{iu} \left(\hat{a}_{ju}^\dagger \hat{a}_{ld}^\dagger + \hat{a}_{lu}^\dagger \hat{a}_{jd}^\dagger \right) - \left(\hat{a}_{ju}^\dagger \hat{a}_{lu} + \hat{a}_{lu}^\dagger \hat{a}_{ju} \right) \hat{n}_{iu}$ $- \left(\hat{a}_{jd}^\dagger \hat{a}_{ld} + \hat{a}_{ld}^\dagger \hat{a}_{jd} \right) \hat{n}_{id} - \hat{a}_{iu}^\dagger \hat{a}_{id} \left(\hat{a}_{jd}^\dagger \hat{a}_{lu} + \hat{a}_{ld}^\dagger \hat{a}_{ju} \right) - \hat{a}_{id}^\dagger \hat{a}_{iu} \left(\hat{a}_{ju}^\dagger \hat{a}_{ld} + \hat{a}_{lu}^\dagger \hat{a}_{jd} \right)$	$-\sqrt{2}\hat{d}_i^\dagger \hat{a}_j \hat{a}_l + \sqrt{2}\hat{d}_i \hat{a}_j^\dagger \hat{a}_l^\dagger - \frac{\sqrt{2}}{2}\hat{n}_i \hat{a}_j^\dagger \hat{a}_l - \frac{\sqrt{2}}{2}\hat{n}_i \hat{a}_j \hat{a}_l^\dagger$ $+ \sqrt{3}\left(\hat{a}^\dagger \hat{a} \right)_i^{[1]} \hat{a}_j^\dagger \hat{a}_l - \sqrt{3}\left(\hat{a}^\dagger \hat{a} \right)_i^{[1]} \hat{a}_j \hat{a}_l^\dagger$

| g_{ijkl} | $\sum_{\sigma\tau}\hat{a}_{i\sigma}^{\dagger}\hat{a}_{k\tau}^{\dagger}\hat{a}_{l\tau}\hat{a}_{j\sigma} + \sum_{\sigma\tau}\hat{a}_{i\sigma}^{\dagger}\hat{a}_{l\tau}^{\dagger}\hat{a}_{k\tau}\hat{a}_{j\sigma} + \sum_{\sigma\tau}\hat{a}_{j\sigma}^{\dagger}\hat{a}_{k\tau}^{\dagger}\hat{a}_{l\tau}\hat{a}_{i\sigma} + \sum_{\sigma\tau}\hat{a}_{j\sigma}^{\dagger}\hat{a}_{l\tau}^{\dagger}\hat{a}_{k\tau}\hat{a}_{i\sigma}$ | $i<k<l<j, \alpha=\sqrt{3}, \beta=-1$ $$\left[\alpha\left(\hat{a}_i^{\dagger}\hat{a}_k^{\dagger}\right)^{[1]}\hat{a}_l\hat{a}_j + \beta\left(\hat{a}_i^{\dagger}\hat{a}_k^{\dagger}\right)^{[0]}\hat{a}_l\hat{a}_j\right]$$ $$+\left[\alpha\left(\hat{a}_i^{\dagger}\hat{a}_k\right)^{[1]}\hat{a}_l^{\dagger}\hat{a}_j + \beta\left(\hat{a}_i^{\dagger}\hat{a}_k\right)^{[0]}\hat{a}_l^{\dagger}\hat{a}_j\right]$$ $$+\left[\alpha\left(\hat{a}_i\hat{a}_k^{\dagger}\right)^{[1]}\hat{a}_l\hat{a}_j^{\dagger} + \beta\left(\hat{a}_i\hat{a}_k^{\dagger}\right)^{[0]}\hat{a}_l\hat{a}_j^{\dagger}\right]$$ $$+\left[\alpha(\hat{a}_i\hat{a}_k)^{[1]}\hat{a}_l^{\dagger}\hat{a}_j^{\dagger} + \beta(\hat{a}_i\hat{a}_k)^{[0]}\hat{a}_l^{\dagger}\hat{a}_j^{\dagger}\right]$$ $i<k<j<l, \alpha=-\sqrt{3}, \beta=-1$ $$\left[\alpha\left(\hat{a}_i^{\dagger}\hat{a}_k^{\dagger}\right)^{[1]}\hat{a}_j\hat{a}_l + \beta\left(\hat{a}_i^{\dagger}\hat{a}_k^{\dagger}\right)^{[0]}\hat{a}_j\hat{a}_l\right]$$ $$+\left[\alpha\left(\hat{a}_i^{\dagger}\hat{a}_k\right)^{[1]}\hat{a}_j\hat{a}_l^{\dagger} + \beta\left(\hat{a}_i^{\dagger}\hat{a}_k\right)^{[0]}\hat{a}_j\hat{a}_l^{\dagger}\right]$$ $$+\left[\alpha\left(\hat{a}_i\hat{a}_k^{\dagger}\right)^{[1]}\hat{a}_j^{\dagger}\hat{a}_l + \beta\left(\hat{a}_i\hat{a}_k^{\dagger}\right)^{[0]}\hat{a}_j^{\dagger}\hat{a}_l\right]$$ $$+\left[\alpha(\hat{a}_i\hat{a}_k)^{[1]}\hat{a}_j^{\dagger}\hat{a}_l^{\dagger} + \beta(\hat{a}_i\hat{a}_k)^{[0]}\hat{a}_j^{\dagger}\hat{a}_l^{\dagger}\right]$$ $i<j<k<l, \alpha=0, \beta=2$ $$\beta\left[\left(\hat{a}_i^{\dagger}\hat{a}_j\right)^{[0]}\hat{a}_k^{\dagger}\hat{a}_l + \left(\hat{a}_i^{\dagger}\hat{a}_j\right)^{[0]}\hat{a}_k\hat{a}_l^{\dagger} + \left(\hat{a}_i\hat{a}_j^{\dagger}\right)^{[0]}\hat{a}_k^{\dagger}\hat{a}_l + \left(\hat{a}_i\hat{a}_j^{\dagger}\right)^{[0]}\hat{a}_k\hat{a}_l^{\dagger}\right]$$ |

operator terms in the spin-adapted Hamiltonian and thenceforth use the MPO construction algorithm mentioned in the previous section to obtain the compact MPO tensors. The spin-adapted operator terms are listed in Table 4.2. Note that an eightfold permutation symmetry of the two-electron integrals (Eq. 4.7) is used therein.

In the traditional renormalized operator-based DMRG, it is much less complicated to embed spin adaption because usually only left and right blocks are considered. One must keep in mind that in this case, all the tensor operators labeled by spin S are associated with a manifold of $2S + 1$ operators that transform amongst each other under some $SU(2)$ rotation. As introduced by Sharma and Chan (2012), the spin-adapted complementary operator $\hat{B}$ can be defined as

$$B_{ij}^{0,0} = \frac{1}{\sqrt{2}} \left(\hat{a}_{iu}^{\dagger} \hat{a}_{ju} + \hat{a}_{id}^{\dagger} \hat{a}_{jd} \right) \tag{4.66}$$

for $S = 0$ singlet operator and

$$B_{ij}^{1,-1} = \hat{a}_{id}^{\dagger} \hat{a}_{ju} \tag{4.67}$$

$$B_{ij}^{1,0} = \frac{1}{\sqrt{2}} \left(\hat{a}_{iu}^{\dagger} \hat{a}_{ju} - \hat{a}_{id}^{\dagger} \hat{a}_{jd} \right) \tag{4.68}$$

$$B_{ij}^{1,1} = - \hat{a}_{iu}^{\dagger} \hat{a}_{jd} \tag{4.69}$$

for $S = 1$ triplet operators. All of the tensor operators used in the spin-adapted renormalized operator-based ab initio DMRG algorithm can be summarized in Table 4.3.

When constructing the total Hamiltonian, one must find all nontensor analogs for all possible partitions. Because the Hamiltonian $\hat{H}$ is a spin-0 operator, we can write the Hamiltonian of the left superblock $A = L + n_l$ as

$$
\begin{aligned}
\hat{H}^0[A] = {} & \hat{H}^0[L] \otimes_0 \hat{1}^0[n_l] + \hat{1}^0[L] \otimes_0 \hat{H}^0[n_l] \\
& + 2 \sum_{i \in L} \left(\hat{a}_i^{1/2}[L] \otimes_0 \hat{R}_i^{1/2\ddagger}[n_l] + \hat{a}_i^{1/2\ddagger}[L] \otimes_0 \hat{R}_i^{1/2}[n_l] \right) \\
& + 2 \sum_{i \in n_l} \left(\hat{a}_i^{1/2}[n_l] \otimes_0 \hat{R}_i^{1/2\ddagger}[L] + \hat{a}_i^{1/2\ddagger}[n_l] \otimes_0 \hat{R}_i^{1/2}[L] \right) \\
& + \sum_{ij \in n_l} \left(-\sqrt{3} \hat{B}_{ij}^1[n_l] \otimes_0 \hat{Q}_{ij}^1[L] + \hat{B}_{ij}^0[n_l] \otimes_0 \hat{Q}_{ij}^0[L] \right) \\
& + \frac{\sqrt{3}}{2} \sum_{ij \in n_l} \left(\hat{A}_{ij}^1[n_l] \otimes_0 \hat{P}_{ij}^1[L] + \hat{A}_{ij}^{1\ddagger}[n_l] \otimes_0 \hat{P}_{ij}^{1\ddagger}[L] \right) \\
& + \frac{1}{2} \sum_{ij \in n_l} \left(\hat{A}_{ij}^0[n_l] \otimes_0 \hat{P}_{ij}^0[L] + \hat{A}_{ij}^{0\ddagger}[n_l] \otimes_0 \hat{P}_{ij}^{0\ddagger}[L] \right),
\end{aligned}
\tag{4.70}
$$

TABLE 4.3 Definitions of the operators used in the spin-adapted renormalized operator-based ab initio DMRG. The indices in this table refer to spatial indices rather than spin indices.

	Components	Definition
$\hat{a}_i^{1/2}$	$\hat{a}_i^{1/2,-1/2}$	$\hat{a}_{id}^\dagger$
	$\hat{a}_i^{1/2,1/2}$	$\hat{a}_{iu}^\dagger$
$\hat{R}_k^{1/2}$	$\hat{R}_k^{1/2,-1/2}$	$\frac{1}{\sqrt{2}}\sum_{ijl} g_{ikjl}\left(\hat{a}_{iu}^\dagger \hat{a}_{ju}^\dagger \hat{a}_{lu} + \hat{a}_{iu}^\dagger \hat{a}_{jd}^\dagger \hat{a}_{ld}\right)$
	$\hat{R}_k^{1/2,1/2}$	$\frac{1}{\sqrt{2}}\sum_{ijl} g_{ikjl}\left(\hat{a}_{id}^\dagger \hat{a}_{ju}^\dagger \hat{a}_{lu} + \hat{a}_{id}^\dagger \hat{a}_{jd}^\dagger \hat{a}_{ld}\right)$
$\hat{A}_{ij}^0$	$\hat{A}_{ij}^{0,0}$	$\frac{1}{\sqrt{2}}\left(\hat{a}_{iu}^\dagger \hat{a}_{jd}^\dagger - \hat{a}_{id}^\dagger \hat{a}_{ju}^\dagger\right)$
$\hat{A}_{ij}^1$	$\hat{A}_{ij}^{1,-1}$	$\hat{a}_{id}^\dagger \hat{a}_{jd}^\dagger$
	$\hat{A}_{ij}^{1,0}$	$\frac{1}{\sqrt{2}}\left(\hat{a}_{iu}^\dagger \hat{a}_{jd}^\dagger + \hat{a}_{id}^\dagger \hat{a}_{ju}^\dagger\right)$
	$\hat{A}_{ij}^{1,1}$	$\hat{a}_{iu}^\dagger \hat{a}_{ju}^\dagger$
$\hat{B}_{ij}^0$	$\hat{B}_{ij}^{0,0}$	$\frac{1}{\sqrt{2}}\left(\hat{a}_{iu}^\dagger \hat{a}_{ju} + \hat{a}_{id}^\dagger \hat{a}_{jd}\right)$
$\hat{B}_{ij}^1$	$\hat{B}_{ij}^{1,-1}$	$\hat{a}_{id}^\dagger \hat{a}_{ju}$
	$\hat{B}_{ij}^{1,0}$	$\frac{1}{\sqrt{2}}\left(\hat{a}_{iu}^\dagger \hat{a}_{ju} - \hat{a}_{id}^\dagger \hat{a}_{jd}\right)$
	$\hat{B}_{ij}^{1,1}$	$-\hat{a}_{iu}^\dagger \hat{a}_{jd}$
$\hat{P}_{ij}^0$	$\hat{P}_{ij}^{0,0}$	$-\frac{1}{\sqrt{2}}\sum_{kl} g_{ikjl}(-\hat{a}_{lu}\hat{a}_{kd} + \hat{a}_{ld}\hat{a}_{ku})$
$\hat{P}_{ij}^1$	$\hat{P}_{ij}^{1,-1}$	$\sum_{kl} g_{ikjl}\hat{a}_{lu}\hat{a}_{ku}$
	$\hat{P}_{ij}^{1,0}$	$-\frac{1}{\sqrt{2}}\sum_{kl} g_{ikjl}(-\hat{a}_{lu}\hat{a}_{kd} - \hat{a}_{ld}\hat{a}_{ku})$
	$\hat{P}_{ij}^{1,1}$	$\sum_{kl} g_{ikjl}\hat{a}_{ld}\hat{a}_{kd}$
$\hat{Q}_{ij}^0$	$\hat{Q}_{ij}^{0,0}$	$\frac{1}{\sqrt{2}}\sum_{kl}\left(2g_{ijkl} - g_{ilkj}\right)\left(\hat{a}_{ku}^\dagger \hat{a}_{lu} + \hat{a}_{kd}^\dagger \hat{a}_{ld}\right)$
$\hat{Q}_{ij}^1$	$\hat{Q}_{ij}^{1,-1}$	$-\sum_{kl} g_{ilkj}\hat{a}_{kd}^\dagger \hat{a}_{lu}$
	$\hat{Q}_{ij}^{1,0}$	$-\frac{1}{\sqrt{2}}\sum_{kl} g_{ilkj}\left(\hat{a}_{ku}^\dagger \hat{a}_{lu} - \hat{a}_{kd}^\dagger \hat{a}_{ld}\right)$
	$\hat{Q}_{ij}^{1,1}$	$\sum_{kl} g_{ilkj}\hat{a}_{ku}^\dagger \hat{a}_{ld}$

in which the spin-adapted tensor product $\otimes_S$ is defined as

$$\hat{X}_1^{S_1} \otimes_S \hat{X}_2^{S_2} = \left(\hat{X}_1^{S_1} \hat{X}_2^{S_2}\right)^S, \tag{4.71}$$

and the symbol ‡ denotes the adjoint with an additional sign factor to preserve the Condon−Shortley phase convention used in the angular momentum ladder operators, as

$$\hat{X}^{S,m\ddagger} = (-1)^{S+m} \hat{X}^{S,-m\dagger}. \tag{4.72}$$

Similarly, one can construct the right superblock Hamiltonian and also the total one.

An important issue in spin-adapted DMRG is to find a proper way to determine the spin-adapted renormalized DMRG basis in both left and right blocks. In general, the density matrix of a subsystem does not commute with the total spin operator of the subsystem, thus the usual DMRG prescription, in which the density matrix eigenvectors are used as the many-body basis, is incompatible with spin adaptation. McCulloch and Gulácsi (2000, 2002) showed that the best states to retain in the decimation step of the DMRG are eigenvectors of a quasi-density matrix which commutes with the $\hat{S}^2$ operator. The quasi-density matrix is obtained from the usual density matrix by setting off-diagonal blocks, which couple states of different spins, to zero.

We can see clearly from Tables 4.2 and 4.3 that there are much fewer operators in the spin-adapted DMRG method than in the simpler $U(1) \otimes U(1)$ non-spin-adapted implementation. In fact, the total number of operators stored in the spin-adapted DMRG is approximately half that in the non-spin-adapted DMRG. (Sharma and Chan, 2012) However, there are certain disadvantages when using the spin-adapted DMRG algorithm in the study of high-spin states. The most serious one is that the eigenvalues of the quasi-density matrix of the left and right blocks are not equivalent for nonsinglet states. This non-equivalence means that discarded weights obtained during the forward and backward sweeps of a calculation (which respectively arise from quasi-density matrices of the left and right blocks) are different, and this makes DMRG energy extrapolation using discarded weights ambiguous. Sharma and Chan (2012) used the singlet embedding method (Tatsuaki, 2000) to overcome these disadvantages by adding a set of auxiliary noninteracting orbitals to the end of the lattice, which couple to the physical orbitals to overall yield a singlet state. Thus the wave function $|\tilde{\psi}\rangle$ of the combined physical and auxiliary orbitals is

$$\left|\tilde{\psi}_{S=0}\right\rangle = |\psi_S\rangle |\phi_S\rangle, \tag{4.73}$$

in which $|\phi_S\rangle$ is the state of the auxiliary noninteracting orbitals and does not energetically couple to the physical system.

Another way to embed spin symmetry into the DMRG method is using the spin-projected MPS (Li and Chan, 2017; Larsson, et al., 2020). The

spin-projected MPS can be obtained by applying a projection operator on the non-spin-adapted MPS

$$\left|\psi_{\text{SP−MPS}}^{(N,S,M)}\right\rangle = \hat{\mathcal{P}}_S \left|\psi_{\text{MPS}}^{(N,M)}\right\rangle, \tag{4.74}$$

in which $\hat{\mathcal{P}}_S$ is the spin projector for the total spin S and $\left|\psi_{\text{MPS}}^{(N,M)}\right\rangle$ is an MPS wave function with a given particle number N and spin projection M (e.g., the z-component of the total spin). The energy to be variationally optimized can then be considered as a functional of the underlying MPS $\left|\psi_{\text{MPS}}^{(N,M)}\right\rangle$, and its explicit functional form reads as

$$
\begin{aligned}
E\left[\left|\psi_{SP-MPS}^{(N,S,M)}\right\rangle\right] = E\left[\left|\psi_{MPS}^{(N,M)}\right\rangle\right] &= \frac{\left\langle\psi_{\text{SP−MPS}}^{(N,S,M)}\left|\hat{H}\right|\psi_{\text{SP−MPS}}^{(N,S,M)}\right\rangle}{\left\langle\psi_{\text{SP−MPS}}^{(N,S,M)}\middle|\psi_{\text{SP−MPS}}^{(N,S,M)}\right\rangle} \\
&= \frac{\left\langle\psi_{\text{MPS}}^{(N,M)}\left|\hat{\mathcal{P}}_{M,M}^{S}\hat{H}\hat{\mathcal{P}}_{M,M}^{S}\right|\psi_{\text{MPS}}^{(N,M)}\right\rangle}{\left\langle\psi_{\text{MPS}}^{(N,M)}\left|\hat{\mathcal{P}}_{M,M}^{S}\right|\psi_{\text{MPS}}^{(N,M)}\right\rangle}.
\end{aligned}
\tag{4.75}
$$

There are various choices for the spin projector $\hat{\mathcal{P}}_S$ in Eq. (4.75) and the works by Li and Chan (2017) and Larsson, et al. (2020) adopted a group theoretical projector in integral form (Percus and Rotenberg, 1962)

$$\hat{\mathcal{P}}_{M,M'}^{S} = \frac{2S+1}{8\pi^2}\int d\Omega D_{M,M'}^{S*}(\Omega)\hat{R}(\Omega),$$

$$\hat{R}(\Omega) = \exp\left(-i\alpha\hat{S}_z\right)\exp\left(-i\beta\hat{S}_y\right)\exp\left(-i\gamma\hat{S}_z\right). \tag{4.76}$$

Here $\Omega = (\alpha, \beta, \gamma)$ are the Euler angles; $\hat{R}(\Omega)$ is the rotation operator; and $D_{M,M'}^{S}(\Omega) = \exp(-iM\alpha)d_{M,M'}^{S}(\beta)\exp(-iM'\gamma)$ is the Wigner D-matrix, and $d_{M,M'}^{S}(\beta)$ is an element of the Wigner's small d matrix. The integration can be evaluated via Gauß − Legendre quadrature and results in a real-valued sum of terms.

Compared with the method to explicitly incorporate the non-Abelian $SU(2)$ symmetry into DMRG, the spin-projection scheme provides a simpler formulation to achieve spin adaptation. Besides, since the underlying state $|\psi_{\text{MPS}}^{(N,M)}\rangle$ in the SP-MPS uses only Abelian symmetries, one does not need the singlet embedding scheme for nonsinglet states to achieve a single consistent variationally optimized state. SP-MPS's another important feature is the close connection to traditional "broken-symmetry" determinants, widely used in quantum chemistry. This gives the ability to seed SP-MPS from initial broken-symmetry configurations built upon chemical intuitions, opening the possibility to fully map out the low-energy landscape of competing spin states in finite chemical systems, in particular the polymetallic

transition metal compounds. However, one may also notice that the spin-projected DMRG method is usually more computationally expensive than the non-spin-adapted approach, because there are much more tensor contractions, as shown in Eq. 4.75, than in standard non-spin-adapted DMRG processes.

Before the end of this section, we should also note that the algorithm for treating spin-adapted $SU(2)$ symmetry in DMRG can be also adopted for describing general non-Abelian point group symmetries. Sharma (2015) used the resulting implementation to calculate the ground-state and excited-state potential energy curves of the C_2 molecule with a cc-pVQZ basis set (and frozen core) to an unprecedented (near-exact) accuracy.

4.5 Reduced density matrix

In previous sections, we have shown that DMRG serves as a powerful technique for accurately calculating the many-electron wave function within a large active space. In quantum chemical computations of energies and properties of large molecular systems, because of the two-body nature of electronic interactions, it is usually more convenient to use the n-electron RDM (n-RDM) instead of the many-electron wave function expanded to an astronomical number of configurations, especially for large systems. For example, one-electron RDM (1-RDM) can be used for population analysis, e.g., calculating the charge and spin densities (Boguslawski et al., 2012a) at different atoms. The ground-state energy of a many-electron system can be also described by using the electron integrals and 1-RDM as well as two-electron RDM (2-RDM) as,

$$E = \sum_{ij} t_{ij} D_j^i + \frac{1}{2} \sum_{ijkl} g_{ikjl} D_{kl}^{ij}. \tag{4.77}$$

Here the 1- and 2-RDMs are defined as

$$D_j^i = \sum_{\sigma} \left\langle \psi \middle| \hat{a}_{i\sigma}^\dagger \hat{a}_{j\sigma} \middle| \psi \right\rangle, \tag{4.78}$$

$$D_{kl}^{ij} = \sum_{\sigma\tau} \left\langle \psi \middle| \hat{a}_{i\sigma}^\dagger \hat{a}_{j\tau}^\dagger \hat{a}_{l\tau} \hat{a}_{k\sigma} \middle| \psi \right\rangle, \tag{4.79}$$

where $|\psi\rangle$ is the ground-state many-electron wave function. Orbital optimizations in the multiconfigurational SCF method, which will be introduced in the next chapter, also require the assistance of 1- and 2-RDMs within the active space. In Chapter 6, we will know that the incorporation of

further dynamic correlation may also require additional three-electron and four-electron RDMs (3- and 4-RDMs),

$$D_{ghi}^{jkl} = \sum_{\sigma\tau\mu} \left\langle \psi \middle| \hat{a}_{j\sigma}^{\dagger} \hat{a}_{k\tau}^{\dagger} \hat{a}_{l\mu}^{\dagger} \hat{a}_{i\mu} \hat{a}_{h\tau} \hat{a}_{g\sigma} \middle| \psi \right\rangle, \tag{4.80}$$

$$D_{ghij}^{klmn} = \sum_{\sigma\tau\mu\nu} \left\langle \psi \middle| \hat{a}_{k\sigma}^{\dagger} \hat{a}_{l\tau}^{\dagger} \hat{a}_{m\mu}^{\dagger} \hat{a}_{n\nu}^{\dagger} \hat{a}_{j\nu} \hat{a}_{i\mu} \hat{a}_{h\tau} \hat{a}_{g\sigma} \middle| \psi \right\rangle, \tag{4.81}$$

which involve 6 and 8 orbital indices, respectively. Therefore, for the purpose of evaluating further energy and wave function properties, it is highly necessary to develop efficient algorithms to compute n-RDMs from a DMRG many-electron wave function.

In ab initio DMRG, the 1-RDM and 2-RDM can be in principle calculated simultaneously with the converged MPS wave function. The 1-RDM can be calculated easily within the DMRG scheme since all the matrix representations of a small number of second-quantized operators required are readily available at every step of the DMRG algorithm. However, there are N^4 elements for 2-RDM of a system with N MOs, which means that in DMRG calculations we need to perform N^4 MPS-MPO-MPS contraction operations to obtain all 2-RDM entries. This is always extremely difficult, because the system size N is usually large in DMRG calculations.

Zgid and Nooijen (2008b) proposed an effective algorithm to compute the 2-RDM effectively without performing lots of tensor contractions. Their approach assumes that different elements of the 2-RDM can be evaluated at different site steps of a sweep in renormalized operator-based DMRG. Hence, the wave function at the convergence shouldn't change during a sweep, which can be achieved by using one-site DMRG algorithm (see Chapter 1). Then 2-RDM can be easily obtained as a by-product of the DMRG sweeps. Following the ideas of left-right DMRG decomposition, the four orbital labels i, j, k, and l in D_{kl}^{ij} can be distributed between the left and right orbital subspaces. For example, to evaluate the element D_{kl}^{ij} ($i < j < k < l$) of the 2-RDM, one can use a block configuration where the indices i, j belong to the left block L, $k \in n_l$, and l in the right block R. Therefore the number of the additional two-index operators is at most of order $O(N^2)$ and accordingly the memory cost will be of order $O(m^2 N^2)$, which is the same as for the DMRG sweep algorithm. Indeed, for most elements in 2-RDM, we can find a corresponding block configuration where no more than two indices are present on any of the blocks. The exception is for the cases when more than two indices refer to the same spatial orbital, but these do not contribute to the leading cost of the computation. In the spin-adapted DMRG method, the 1-RDM and 2-RDM can be evaluated similarly, except for the multiplicity caused by blocking the operator

terms and multiplying the Clebsch−Gordan coefficients (Sharma and Chan, 2012).

It is much more complicated and expensive to compute higher order RDMs. Saitow et al. (2013) introduced an approximation to high-order RDM by using a cumulant reconstruction from lower-order RDMs. The concept of cumulant expansion is originally used in statistical mechanics to provide hierarchical relationships among different orders of correlation functions. This concept has been later extended to the quantum mechanics of fermionic many-body systems for evaluations of high-order RDMs. The cumulant decomposition of n-RDM ($n = 1, 2, 3, 4$) can be written using the antisymmetrized products among the k-RDMs ($k = 1, 2, \cdots n - 1$) along with the n-rank cumulant (Δ) as follows:

$$D_i^j = \Delta_i^j, \tag{4.82}$$

$$D_{gh}^{ij} = \Delta_{gh}^{ij} + 4D_g^i \wedge D_h^j, \tag{4.83}$$

$$D_{ghi}^{jkl} = \Delta_{ghi}^{jkl} + 9D_{gh}^{jk} \wedge D_i^l - 12D_g^j \wedge D_h^k \wedge D_i^l, \tag{4.84}$$

$$D_{ghij}^{klmn} = \Delta_{ghij}^{klmn} + 16D_{ghi}^{klm} \wedge D_j^n + 18D_{gh}^{kl} \wedge D_{ij}^{mn}$$

$$- 144D_{gh}^{kl} \wedge D_i^m \wedge D_j^n + 96D_g^l \wedge D_h^k \wedge D_i^m \wedge D_j^n, \tag{4.85}$$

where $\Delta_{\cdots}^{\cdots}$ refers to the fully-connected cumulant and is regarded as perturbative in the cumulant approximation, and the label D with n indices refer to the n-order RDM. The wedge symbol $\wedge$ represents the antisymmetrized products, as

$$(X_n \wedge Y_m)_{j_1, \cdots, j_{n+m}}^{i_1, \cdots, i_{n+m}} = \left(\frac{1}{(n+m)!}\right)^2$$

$$\times \sum_{\pi\sigma} \epsilon(\pi)\epsilon(\sigma)\pi\sigma X_{j_1, \cdots, j_n}^{i_1, \cdots, i_n} Y_{j_{n+1}, \cdots, j_{n+m}}^{i_{n+1}, \cdots, i_{n+m}} \tag{4.86}$$

where X and Y are tensors with ranks as n and m; π and σ permute all of the upper and lower indices, respectively; ϵ returns the corresponding sign change to the given permutation. Neglect of three-particle cumulant Δ_{ghi}^{jkl} in Eq. (4.84) and four-particle cumulant Δ_{ghij}^{klmn} in Eq. (4.85) allows for avoiding the costly rigorous evaluation of 3-RDM and 4-RDM in the DMRG calculation, which have a high computational scaling of N^6 and N^8, respectively. However, it introduces approximation errors (so-called cumulant errors) in the resultant 3-RDM and 4-RDM.

Algorithm 4.3: Calculating n-RDM $(n = 1, 2, 3, 4)$ from a DMRG wave function. *DMRG*, density matrix renormalization group. *n-RDM*, *n*-electron reduced density matrix.

1: **procedure** 1-RDM($|\psi\rangle$)

2:   $D_j^i = \sum_\sigma \langle \psi | \hat{a}_{i\sigma}^\dagger \hat{a}_{j\sigma} | \psi \rangle$

3:   **return** $\left\{ D_j^i \right\}$

4: **end procedure**

5: **procedure** 2-RDM($|\psi\rangle$)

6:   $D_{kl}^{ij} = \sum_{\sigma\tau} \langle \psi | \hat{a}_{i\sigma}^\dagger \hat{a}_{j\tau}^\dagger \hat{a}_{l\tau} \hat{a}_{k\sigma} | \psi \rangle$ // Zgid and Nooijen (2008b)

7:   **return** $\left\{ D_{kl}^{ij} \right\}$

8: **end procedure**

9: **procedure** Approximate3-RDM($\{D_j^i\}$, $\left\{ D_{kl}^{ij} \right\}$)

10:   $D_{ghi}^{jkl} \approx 9 D_{gh}^{jk} \wedge D_i^l - 12 D_g^j \wedge D_h^k \wedge D_i^l$

11:   **return** $\left\{ D_{ghi}^{jkl} \right\}$

12: **end procedure**

13: **procedure** Approximate4-RDM($\{D_j^i\}$, $\left\{ D_{kl}^{ij} \right\}$, $\left\{ D_{lmn}^{ijk} \right\}$)

14:   $D_{ghij}^{klmn} \approx 16 D_{ghi}^{klm} \wedge D_j^n + 18 D_{gh}^{kl} \wedge D_{ij}^{mn} - 144 D_{gh}^{kl} \wedge D_i^m \wedge D_j^n + 96 D_g^l \wedge D_h^k \wedge D_i^m \wedge D_j^n$

15:   **return** $\left\{ D_{ghij}^{klmn} \right\}$

16: **end procedure**

4.6 Orbital selection and ordering

Although DMRG method can realize the nearly exact diagonalization for up to ~ 100 MOs (Hachmann et al., 2006; Zhai and Chan, 2021), it is still impossible to take all MOs (with a number of a few hundreds or thousands) into DMRG consideration in practical calculations due to its polynomial computational scaling $O(m^2 N^4 + m^3 N^3)$. Therefore usually only a small number of most strongly correlated MOs and electrons are selected to form a complete active space (CAS), in which all possible electronic configurations are considered and solved exactly by full configuration interaction (FCI) or DMRG. In the CAS model, the entire MO space is usually divided into three subspaces: core, active, and external, as shown in Fig. 4.2. The complete configuration space $\mathcal{H}_{\text{total}}$ in the CAS method can be accordingly also expressed as a direct product of these three parts,

$$\mathcal{H}_{\text{total}} = \mathcal{H}_{\text{core}} \otimes \mathcal{H}_{\text{active}} \otimes \mathcal{H}_{\text{external}}. \tag{4.87}$$

Within this model, all of the MOs in the core space are doubly occupied and the energy is evaluated at the Hartree−Fock level, while the orbitals in
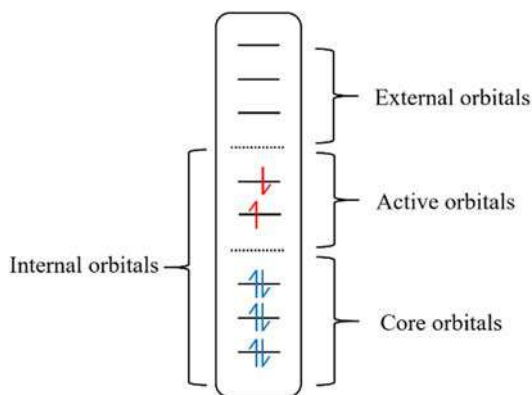
FIGURE 4.2 Division of the MO space into different subspaces. *MO*, Molecular orbital.

the external space are completely empty and do not contribute to the total energy. Electron correlations are precisely evaluated only within the active space, and the active electrons interact with the inactive electrons through an effective one-electron Hamiltonian. Therefore the choice of active orbital is obviously crucial for the accuracy of complete active space configuration interaction (CASCI)/complete active space SCF and DMRG methods: a reasonable active space must be able to contain the most entangled part of the electronic structure of the system.

Currently, the active orbitals are generally selected by using a try-and-error method, which depends to a large extent on personal experience and chemical intuition. This is, however, quite tedious and unreliable for MR calculations with large active spaces. In recent years, there have been increasing efforts to develop strategies for the selection of active orbitals. Most of them constitute the initial active space on the basis of the natural orbitals (NOs) and the associated fractional occupancies (e.g., between 0.02 and 1.98), which come from either unrestricted Hartree−Fock or inexpensive electron-correlation calculations (e.g., single-reference perturbation theory and truncated configuration interaction methods) on a large number of orbitals (e.g., Mitrushenkov et al., 2003; Ma and Ma, 2013; Keller et al., 2015a). Grimme and Hansen (2015) also introduced the fractional occupation number weighted density (FOD) obtained from finite temperature density functional theory (DFT) as measure for selecting a proper active space. Recently, low-level MR methods such as strongly contracted *n*-electron valence perturbation theory on top of a minimal active space calculation, multiconfigurational general valence bond, and DMRG with a small bond dimension are also used to produce NOs or orbital entanglement information to construct the active space (Ma and Ma, 2013; Stein and Reiher, 2016; Khedkar and Roemelt, 2019; Khedkar and Roemelt, 2020; Zou et al., 2020). Although a few tens of candidate orbitals can be explored in a preliminary low-level

DMRG calculation, its automatic selection for molecules with very large valence spaces is still expensive and challenging. This limit can be partly circumvented through preselecting orbitals either by manual inspection or by imposing constraints such as maximum distance from a reactive center. Stein and Reiher (2019) proposed a new protocol for large systems by splitting the large active space into several smaller feasible subsets in a localized basis and analyzed the entanglement entropies of these subsets in order to identify the pairwise interactions.

In addition, chemical intuition-based strategies have been recently generalized to the automatic construction of active space. Sayfutyarova, et al. (2017) proposed an atomic valence active space scheme, which automatically selects the active space based on the projection of occupied and virtual MOs, onto the target valence atomic orbitals. However, projecting the MOs onto all valence atomic orbitals of the target atoms may generate a very large active space beyond the capability of current MR calculations. For the case of conjugated π systems, Sayfutyarova and Hammes-Schiffer (2019) further developed an automated π-orbital space (PiOS) method utilizing algebraic transformations of a single-reference wave function and the Hückel theory to construct small but effective active spaces. The iCAS method proposed by Lei et al. (2021) also transforms a priori selected set of occupied/virtual atomic or fragmental orbitals to an equivalent set of localized occupied/virtual prelocalized MOs, which can then be taken as probes to select the same number of maximally matching localized occupied/virtual Hartree−Fock orbitals as the initial local orbitals spanning the desired CAS. The machine learning technique has been also adopted by Jeong, et al. (2020) and Golub, et al. (2021) to automatically select active spaces for main group diatomic molecules and transition metal complexes.

Unlike many other common wave function methods, an MPS is not orbital-invariant within the active space, except at extremely large m values. Therefore the DMRG convergence (and energy), of course, also depends on the kind of orbitals employed in the calculation. In molecular systems, canonical orbitals and NOs, as well as localized or split-localized orbitals, are often used. Recently, plane wave-based Kohn−Sham orbitals were also adopted in ab initio DMRG, paving the way toward applying the DMRG method in periodic correlated solid-state systems. (Barcza et al., 2021)

The DMRG convergence is also largely affected by the orbital ordering, due to the sequential nature of the sweeping optimization of MPS local tensors. Orbital reordering can be viewed as a kind of orbital rotation. Although the DMRG calculation becomes less sensitive to these choices as m increases, at fixed m, a good choice of orbital ordering greatly improves the accuracy and efficiency of a DMRG calculation. In principle, the best ordering of orbitals minimizes the total energy and the maximum entanglement at any cut of the 1D DMRG orbital lattice. Unfortunately, we can hardly obtain the optimal orbital ordering in the DMRG calculations in advance, as it cannot be derived

analytically from DMRG theory. For a lattice consisting of N orbitals, there are $N!$ different possibilities to arrange these orbitals. Moritz et al. (2005a) suggested to utilize the genetic algorithm (GA) to optimize the ordering with respect to a sufficiently low total electronic energy, obtained at a predefined stage of the DMRG algorithm with a fixed number of reserved states. As the DMRG method is variational, which means the full-CI energy is the lower limit of the DMRG result, for a fixed m value, the lower DMRG energy always comes together with a more reasonable ordering. However, one has to perform a huge number of DMRG calculations if we use this GA-based method to determine the optimal orbital ordering, which is usually too expensive in ab initio quantum chemistry calculations.

In the early ab initio DMRG implementations, a widely used orbital ordering approach was to utilize the reverse Cuthill−McKee (RCM) algorithm (Cuthill and McKee, 1969) reordering sparse matrices by permutating rows and columns to minimize the maximum bandwidth of MO integrals. Within the reordering procedure above, the matrix elements which have nonzero values are placed near the diagonal. Because the RCM algorithm discriminates the values only between zero and nonzero, one has to define a threshold for the values of the integrals in such a way that matrix elements with values below this threshold are set to zero. Chan and Head-Gordon (2002) as well as Moritz et al. (2005a) have explored RCM schemes in ab initio DMRG calculations by using one-electron integrals t_{ij} and two-electron exchange integral matrices $K_{ij} = g_{ijji}$ as approximations of the orbital correlation strengths, respectively.

Recently, a Fiedler vector (Fiedler, 1973)-based method is becoming more popular in ab initio DMRG implementations. The Fiedler vector is a graph theoretic technique which provides good approximations to the spectral graph partitioning problem, and a detailed study of the Fiedler vector in DMRG was first presented by Barcza et al. (2011). Here we briefly introduce the process of MO reordering using exchange integrals and the Fiedler vector method. Since the exchange integrals can be used to quantify the correlations between orbitals approximately, the orbitals $i, j, \cdots$ and the absolute values of the exchange integrals $\{|K_{ij}|\}$ constitute a weighted undirected graph G. The adjacency matrix of this graph can be regarded as

$$A_{ij} = |K_{ij}| = |g_{ijji}|. \tag{4.88}$$

The Laplacian matrix is accordingly defined as

$$\boldsymbol{L} = \boldsymbol{D} - \boldsymbol{A}, \tag{4.89}$$

in which $D_{ii} = \sum_j A_{ij}$ is the degree matrix. The Fiedler vector of this graph is the second-lowest eigenvector of the Laplacian matrix $\boldsymbol{L}$. Sorting the values of the vector coordinates then gives the Fiedler ordering. A naive example of a six-site system is shown in Fig. 4.3. The advantage of this method is that it
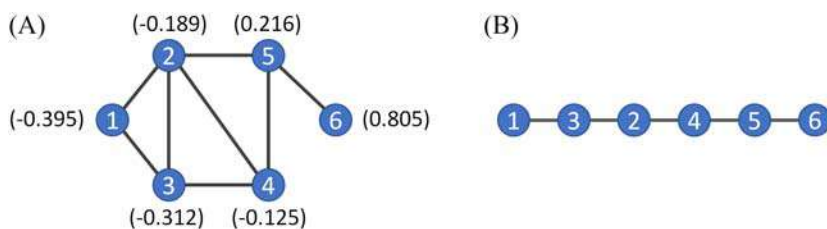
FIGURE 4.3   Schematic illustration of the Fiedler-vector-based method for orbital ordering. In (A), all existing connections are set to 1.0 and denoted as black lines. The corresponding value of one site in the Fiedler vector is marked next to it. Sorting the sites (or MOs in this chapter) in the order of the corresponding values from small to large leads to the optimized orbital ordering in (B). *MOs*, Molecular orbitals.

is trivial to be implemented from a small matrix diagonalization, and since our optimization matrix $|K_{ij}|$ is in any case approximate, it is not necessary to resolve the true global optimum (Olivares-Amaya, et al., 2015).

In the past years, the orbital entanglement entropy concepts in quantum information theory (QIT) have been also adopted for the orbital selection and ordering in ab initio DMRG and will be discussed in Section 4.9.

4.7   Error estimation

The computation cost of the DMRG method is controlled by adjusting the number of bond dimension (m) to be kept in the sweeps. The larger the number of bond dimensions is, the closer the energy is to the exact full-CI (energy). We can consider the result of a DMRG algorithm as an analytical function of an adjustable parameter like m. Consequently, it is possible to probe this analytical function by performing calculations for a few different numbers of renormalized DMRG basis states. None of these calculations has to actually provide the desired accuracy, but after one has collected enough information about the function's behavior, one can represent it by an analytic rational function that may then be used to extrapolate to the converged energy.

The detailed numerical behavior of the DMRG algorithm is still imperfectly understood. Chan and Head-Gordon (2002) analyzed the error in the energy for given m in quantum chemistry DMRG calculations and proved that under fairly general conditions the thermal density matrix eigenvalues decay asymptotically like

$$w_i \propto \mathrm{const} \times e^{-\kappa(\ln i)^{\alpha}}, \tag{4.90}$$

where $\alpha \sim 2$ and constant κ is model specific and proportional to the one-particle level density.

In an early study of the algorithm accuracy for the Ising model, Legeza and Fáth (1996) demonstrated that the error in the energy for a given m is

roughly proportional to the sum of the weights discarded during decimation. More strictly,

$$\left| E(m) - E_0 \right| \sim \text{const} \times \sum_{i > m} w_i + C. \tag{4.91}$$

The linear relationship arises simply from the boundedness of the Hamiltonian and is because the energy is a linear functional of the density matrix. From Eqs. 4.90 and 4.91, the error in the energy should asymptotically converge like

$$|\delta E| = \text{const} \times \frac{e^{-\kappa(\ln m)^2} + \ln m}{\ln m}. \tag{4.92}$$

Taking logarithms on both sides, we find that the leading term gives

$$\ln|\delta E| \cong -\kappa(\ln m)^2. \tag{4.93}$$

On the basis of the above extrapolation, Mitrushenkov et al. (2003) increased the flexibility of Eq. 4.93 and accordingly suggested another energy extrapolation scheme in terms of the incremental energies

$$\delta E_m = E_m - E_{m-1} \tag{4.94}$$

to the asymptotic value within the appropriate range of m by the following formula,

$$\lim_{m \to \overline{m}} \delta E_m = \lim_{m \to \overline{m}} \frac{c + dE_m}{f_m} = 0 \tag{4.95}$$

with

$$f_m \sim \sqrt{m^2 N^3 + 2m^3 N^2} \tag{4.96}$$

and the parameters c and d are determined by a fit to the calculated DMRG data.

Instead of using a fixed m value in the DMRG sweeps, Legeza et al. (2003b) suggested a dynamic block state selection (DBSS) protocol based on a fixed truncation error

$$\varepsilon = 1 - \sum_{\alpha=1}^{m} w_\alpha \tag{4.97}$$

of the subsystem's RDM, which can automatically adapt the bond dimension at different sites. For methylene with a (6e, 13o) CAS, a linear relationship was found between the truncation error ε and the absolute error in the energy which led to an extrapolation formula of the form

$$\ln \frac{E_{\text{DMRG}} - E_{\text{FCI}}}{E_{\text{FCI}}} = a\ln\varepsilon + b, \tag{4.98}$$

where E_{FCI}, a, and b are parameters determined from the fit of the numerical result. In contrast, Mitrushenkov et al. (2003) found another extrapolation formula

$$E_{DMRG} - E_{FCI} = A\exp\left(-B\varepsilon^{-1/2}\right), \tag{4.99}$$

to be adequate in the DMRG calculation of HF molecule, where A and B are parameters.

In order to make the extrapolations on the fly to detect when to stop the DMRG iterations, Marti and Reiher (2010) investigated an automated DMRG error protocol, which extrapolates the electronic energy using Richardson's deferred approach to the limit. In a Richardson-type algorithm, the extrapolation is performed using rational functions, which overcomes the constraint of the power series and its limited radius of convergence. The rational functions used in this approach can be written as

$$E^{(\mu\nu)}(\varepsilon) = \frac{P_\mu(\varepsilon)}{Q_\nu(\varepsilon)} = \frac{p_0 + p_1\varepsilon + \cdots + p_\mu\varepsilon^\mu}{q_0 + q_1\varepsilon + \cdots + q_\nu\varepsilon^\nu}, \tag{4.100}$$

where μ and ν are the orders of the polynomials in the denominator and in the numerator, respectively, and are determined by the number of data points. Such an error control facility was considered to provide a feasibility to perform practical DMRG calculations, at a low number m of DMRG basis states for larger systems without the need of having fully converged absolute energies.

4.8 Component analysis of density matrix renormalization group wave function

It is obvious that the DMRG wave functions based on both the left-right decomposition and MPS are intuitively quite different from the traditional many-electron wave functions based on CI configurations. Moritz and Reiher (2007) rationalized the equivalent relationship between the MPS and its CASCI formulation using Slater-determinant (SD) basis. It is now clear that the CI coefficients can be reconstructed by contracting all of the MPS local tensors, as

$$c_{n_1 n_2 \cdots n_N} = \sum_{a_1 a_2 \cdots a_{L-1}} M_{1a_1}^{n_1} M_{a_1 a_2}^{n_2} \cdots M_{a_{N-1} 1}^{n_N} \tag{4.101}$$

It should be noted that the computation of the CI coefficient for a specified SD ($|n_1 n_2 \cdots n_L\rangle$) is very straightforward and efficient, which requires only $\sim (N-1)$ matrix multiplications of $(m \times m)$-sized matrices (m usually being a few hundreds to thousands). However, the full CI expansion for a DMRG wave function in a large active space with more than 20 active

orbitals would be prohibitive, because the total number of SDs would be easily larger than 10^{10}. Totally transforming the DMRG wave function to a multiconfigurational CI-type wave function is still challenging.

Since the number of SDs in a DMRG active space is extremely large, one could learn the ideas from the recently revived selected-CI theory. For most molecules, the exact energy and properties could be described with a limited number of important electronic configurations rather than the full-CI wave function containing even more than billions of configurations. There are usually a few dominant configurations contributing a fairly large proportion of the quadratic sum of CI coefficients. These configurations are expected to provide a good approximation of the original DMRG wave functions and characterize properties of the states.

Boguslawski et al. (2011) proposed a Monte Carlo-based sampling-reconstructed CAS (SR-CAS) algorithm for reconstructing CASCI-type wave functions from a DMRG ansatz elegantly. The application to 1,3-dimethyl Arduengo carbene in their work suggests that only a comparatively small amount of SDs within the entire large active space has to be considered to construct an efficient CASCI-type wave function, and the small amount of SDs could already represent the main feature for a specific electronic state. Within the SR-CAS framework, a predefined reference (usually the HF determinant) is used to generate the trial determinants in the given active space. However, the single determinant may not be adequate or very efficient as the reference for the molecule that owns strong multiconfigurational character.

Luo et al. (2017) later developed an entanglement-driven GA (EDGA), in which the multiple SDs can be used as the reference and where the "crossover" process is employed, rather than Monte Carlo process, for generating new SDs. In addition, inspired by QIT, in which orbital interactions are quantitatively evaluated, MO entanglement entropies (see Section 4.9) were also embedded into the "mutation" process to generate more likely SD excitations. It is shown that the efficiency of determinants' reconstruction can be improved by using the sampling/evolutionary direction guided by the MO entanglement entropy.

By extracting CI expansion coefficients and collecting important determinants, one can explore the compressibility of wave functions of strongly correlated systems in CI space. Most of the configurations in the FCI space almost do not contribute to the whole wave function as they have very small CI coefficients, close to 0. Accordingly, the SR-CAS and EDGA methods are effective in practice to collect only those important configurations with large CI coefficients and construct a well-approximated multiconfigurational CI-type wave function, which can be used for further selected-CI or post-DMRG references. Such sampling algorithms have been used by Ren et al. (2021) to analyze the dominant final vibrational states in a vibronic wave function that contribute the most to the excited-state radiationless decay rate.

Wang et al. (2020) further reported the massively parallel expansions of SR-CAS and EDGA using the Charm + + parallel framework. The parallel variants can drastically enhance the efficiency in reconstructing the reference wavefunction.

Algorithm 4.4: Reconstruction of a CASCI-type wave function from MPS by EDGA. *CASCI*, Complete active space configuration interaction; *EDGA*, entanglement-driven genetic algorithm; *MPS*, matrix product state.

1: **function** initialize(n)
2:   Randomly generating n initial SDs in G
3:   **return** G
4: **end function**
5: **function** MPS2CI(Φ_i)
6:   $c_i = \langle \Phi_i | \psi \rangle = M_{1a_1}^{n_1} M_{a_1 a_2}^{n_2} \cdots M_{a_{N-1} 1}^{n_N}$
7:   **return** c_i
8: **end function**
9: **procedure** EDGA
10:   $G \leftarrow$ initialize(n)
11:   $\{c_1, c_2, \ldots c_n\} \leftarrow$ MPS2CI
12:   **if** $1 - \sum_i^{record} c_i^2 >$ rang; 10^{-k} **then**
13:      Do "crossover" and "mutation" to generate new configurations
      // refer to Luo et al. (2017)
14:      Go back to step 11
15:   **end if**
16:   **return** collected configurations $\{|\phi_0\rangle, |\phi_1\rangle, \ldots, |\phi_n\rangle\}$
17: **end procedure**

To simulate finite temperature quantum systems efficiently, White and Stoudenmire proposed a method to sample minimally entangled typical thermal states (White, 2009; Stoudenmire and White, 2010). They suggested that at a nonzero temperature β, a set of states $\{|\phi_i\rangle\}$ with minimal entropies could be selected according to

$$\sum_i P_i |\phi_i\rangle \langle \phi_i| = e^{-\beta \hat{H}}, \tag{4.102}$$

in which the unnormalized probabilities P_i could be evaluated as

$$P_i = \langle i | e^{-\beta \hat{H}} | i \rangle, \tag{4.103}$$

and the product state $|i\rangle$ could be any complete orthonormal basis of the system. Their ideas inspired Guo et al. (2018b) on the importance sampling of determinants in the zeroth-order wave function $|\psi^{(0)}\rangle$ in the perturbative DMRG (p-DMRG) method (see Section 4.10). In their implementation, a determinant $|\phi_i\rangle = |n_1 n_2 \cdots n_N\rangle$ can be sampled according to the probability

$P_i = |\langle \psi^{(0)}|\phi_i \rangle|^2$ in a single sweep site by site from left to right. With the right canonical MPS

$$\left|\psi^{(0)}\right\rangle = \sum_{n_1 \cdots n_N} M^{n_1} \cdots M^{n_N} |n_1 \cdots n_N\rangle, \tag{4.104}$$

the generation probability for n_k with given $n_1 \cdots n_{k-1}$ can be evaluated as

$$p_k(n_k|n_1 \cdots n_{k-1}) = \frac{1}{N_k} \sum_{a_k} \left|\left(M^{n_1} \cdots M^{n_k}\right)_{a_k}\right|^2 \tag{4.105}$$

with

$$N_k = p_{k-1}(n_{k-1}|n_1 \cdots n_{k-2}). \tag{4.106}$$

Thereby, the total generation probability is

$$\begin{aligned} P_i &= p_1(n_1) \cdots p_N(n_N|n_1 \cdots n_{N-1}) \\ &= |M^{n_1} \cdots M^{n_N}|^2 \\ &= |\langle \psi^{(0)}|\phi_i \rangle|^2, \end{aligned} \tag{4.107}$$

which is exactly the target distribution.

4.9   Quantum information theory analysis

As we have discussed in Chapter 2, the success of DMRG truncation in 1D strongly correlated chain can be understood in the language of QIT as preserving the maximum entanglement between system and environment as measured by the von Neumann entropy of entanglement,

$$S = -\operatorname{Tr}\hat{\rho}\ln\hat{\rho} = -\sum_\alpha w_\alpha \ln w_\alpha. \tag{4.108}$$

The concepts from QIT, like the von Neumann entropy or the mutual information, were also recently utilized to understand the electronic structure features of strongly correlated molecules and optimize the ab initio DMRG parameters in quantum chemistry.

It was suggested by Legeza and Sólyom (2004) to evaluate the total quantum information encoded in a wave function from the sum of entropies at different sites. Later, Rissler, et al. (2006) generalize Eq. 4.108 to arbitrary subsystems (e.g., one orbital or two orbitals), and defined the single-orbital von Neumann entropy $S_i^{(1)}$ of the ith orbital

$$S_i^{(1)} = -\sum_{\sigma=1}^{4} w_{\sigma,i} \ln w_{\sigma,i}, \tag{4.109}$$

with $w_{\sigma,i}$ being the eigenvalues of the (4×4)-dimensional one-orbital RDM

$$\rho_{ii'}^{(1)} = \sum_n \langle n | \langle i | \psi \rangle \langle \psi | i' \rangle | n \rangle. \tag{4.110}$$

Similarly, the two-orbital entropy $S_{ij}^{(2)}$ is obtained from the eigenvalues $w_{\tau,ij}$ of the (16×16)-dimensional two-orbital RDM

$$S_{ij}^{(2)} = -\sum_{\tau=1}^{16} w_{\tau,ij} \ln w_{\tau,ij}. \tag{4.111}$$

Furthermore, they defined orbital mutual information I_{ij} by the subtraction of the entanglement of two orbitals taken together with the rest of the system from the sum of the entanglement of two individual orbitals with the rest of the system,

$$I_{ij} = \frac{1}{2} \left(S_i^{(1)} + S_j^{(1)} - S_{ij}^{(2)} \right) \left(1 - \delta_{ij} \right). \tag{4.112}$$

The mutual information I_{ij}, also known as the orbital entanglement entropy, can be therefore obtained from a converged DMRG wave function. Although it is a quantitative description of the orbital correlation, we cannot get its precise values to determine the accurate orbital ordering before doing an accurate DMRG calculation, which also depends on the accurate orbital ordering. In practice, some rough DMRG calculations are often performed preliminarily to obtain reasonable orbital entanglement entropies at a low computational cost. Legeza and Sólyom (2003) suggested to place the strongly correlated orbitals next to each other and toward the middle of the lattice to achieve a faster DMRG convergence. Instead of using NO occupation number (NOON) as a selection criterion for active space, Stein and Reiher (2016) proposed to only consider orbitals with single-orbital entropy $S_i^{(1)}$ higher than a fraction of the maximum value found for one of the $S_i^{(1)}$ in a preliminary large-scale but low-level electron-correlation calculation. Discouraged by the computational cost, King and Gagliardi (2021) suggested an "approximate pair coefficient" method, attempting to estimate the entropy in a physically motivated fashion from orbital energies and features of the HF exchange matrix in a pair-interaction framework.

The concepts of single-orbital and two-orbital entropies, as well as orbital mutual information, have been also recently used as new orbital entanglement measures to evaluate the SR and MR character of molecular bonding structures and chemical reactions in a given orbital basis set. (Barcza et al., 2011; Boguslawski et al., 2012b; Duperrouzel et al., 2015). For instance, Duperrouzel et al. (2015) dissect bond-formation processes in metal-driven catalysis using concepts from QIT. Fig. 4.4 shows that the total quantum information increases gradually when the nickel atom and ethene molecule are pulled apart, up to a nickel−ethene distance of 2.4 Å. Beyond this point,
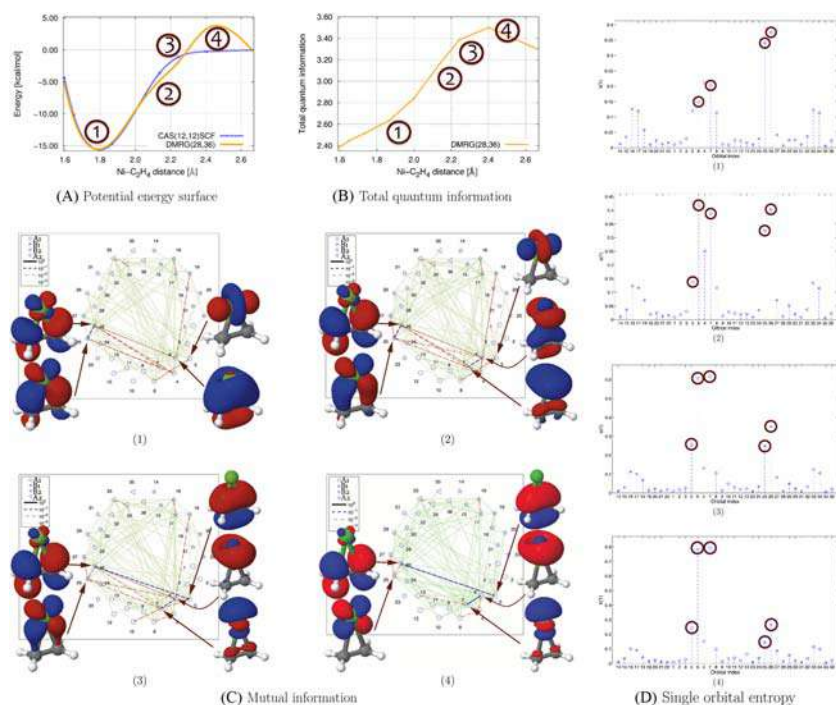
FIGURE 4.4 (A) Potential energy surface and (B−D) quantum information analysis of nickel−ethene complexation with respect to selected nickel−ethene distances. Note that the nickel−ethene distances are measured from the nickel atom to the middle of the carbon-carbon bond. The chosen distances (1−4) are marked in (A) and cover the transition state (1), and the equilibrium distance (4). MOs are marked by different symbols (according to their irreducible representation) in the mutual information and single orbital entropy diagrams. Highly correlated/entangled orbitals are highlighted in (C) and (D). *MOs*, Molecular orbitals. *Reproduced from Duperrouzel, C., Tecmer, P., Boguslawski, K., Barcza, G., Legeza, Ö., Ayers, P.W., 2015. A quantum informational approach for dissecting chemical reactions. Chem. Phys. Lett. 621, 160−164. https://doi.org/10.1016/j.cplett.2015.01.005, with permission from Elsevier.*

the total quantum information decreases indicating the transition state in which the wave function has a strong multireference character. Stein and Reiher (2016) concluded that a conservative global threshold of $\left(S_i^{(1)}\right)_{max} \approx 0.14$ for at least one orbital indicates the MR character of a wave function. The orbital mutual information I_{ij} was also used as the selection weights in the mutation process of changing the orbital occupation status in a GA for sampling the important configuration states in a large active space (Luo et al., 2017). Compared to other widely used MR diagnostic variables like NOON and configuration coefficient, QIT features of single-orbital entropy and orbital mutual information can give more informative and straightforward illustrations of electron correlations between specified

orbital pairs. Furthermore, the static and dynamic contributions to the correlation energy can be also distinguished by examining the entanglement patterns of orbitals (Boguslawski et al., 2012b).

Moreover, it has been argued that the mutual information does not really quantify the entanglement since it includes both quantum and classical correlations (Henderson and Vedral, 2000). Considering that entanglement is an important resource for realizing quantum cryptography, superdense coding, and possibly even quantum computing, recently Schilling and coworkers has proposed a new scheme to separate the total correlation into classical and quantum parts and implement their quantification in an operationally meaningful way (Ding et al., 2021).

4.10 Density matrix renormalization group for larger active spaces

DMRG's main strength lies in treating large 1D quantum lattices where all the sites are extremely strongly interacting. However, the orbitals in molecular systems usually have different chemical environments and don't have spatial translational symmetry which is present in condensed phase physics models. Therefore the mix of different correlation characters in a number of active orbitals and the presence of long-range interactions decrease the computation efficiency of ab initio DMRG and consequently hinders its application to larger systems. In recent years, a few new algorithms have been proposed to treat larger active spaces in DMRG quantum chemistry (Parker and Shiozaki, 2014; Ma et al., 2015; Ren et al., 2016; Guo et al., 2018a,b).

One of the most straightforward ideas to reduce the computation cost and apply DMRG methods on larger molecules can be addressed to reducing the number N of MPS tensor sites and using a smaller m value. With this aim, Parker and Shiozaki (2014) proposed to combine DMRG with the active space decomposition (ASD) method (Parker et al., 2013) to describe the electronic structure of molecular aggregates. In ASD-DMRG (Fig. 4.5), they chose each site to be the CAS or RAS wave function of a single molecule or fragment instead of the one-electron orbital in usual ab initio DMRG. As a consequence, the dimensionality of the single site, d, is much larger in ASD-DMRG than in conventional approaches. However, its key benefit is that this makes N much smaller and allows m to be very small, with a numerical test on a benzene pentamer and a perylene diimide trimer. Recently, Larsson et al. (2022) performed a detailed investigation on the computational costs on such cluster MPS methods which group clusters of related orbitals into large "sites." In systems with nearly constant entanglement across the lattice, a cluster MPS is found to be unlikely to reduce computational cost for the same accuracy. On the contrary, the cluster MPS is advantageous for an MPS with highly nonuniform bond dimensions, large within a cluster of sites and very small between clusters. Larsson et al. (2022) further suggested to
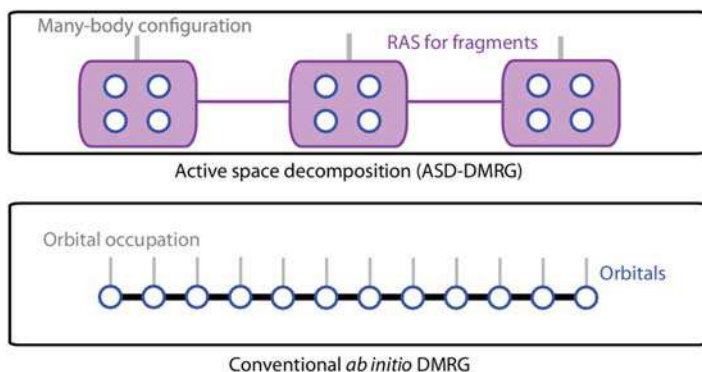
FIGURE 4.5 Comparison of wave functions in ASD-DMRG and in conventional ab initio DMRG. *ASD*, Active space decomposition; *DMRG*, density matrix renormalization group. *Reproduced from Parker, S.M., Shiozaki, T., 2014. Communication: active space decomposition with multiple sites: density matrix renormalization group algorithm. J. Chem. Phys. 141, 211102. https://doi.org/10.1063/1.4902991, with permission from American Institute of Physics.*

put large cluster sites at either end of the MPS, because now each large site only has a single boundary (and does not have a boundary with another large site), and when combined with a configuration selection of the large site Hilbert space, there is a large regime of computational advantage.

Ma et al. (2015) presented a DMRG algorithm with a multilevel (ML) control of the active space based on chemical intuition-based hierarchical orbital ordering, also called ML-DMRG, or ML-DMRG-SCF in its SCF variant. With examples of H_2O, N_2, indole, and Cr_2, ML-DMRG calculations were shown to achieve a noticeable computational efficiency gain with a little price of energy inaccuracy (normally few mHartrees) in contrast to those standard DMRG calculations with fixed m values. It is also shown that the orbital reordering based on hierarchical multiple active subspaces may be beneficial for reducing computational time, not only for ML-DMRG calculations, but also for standard DMRG ones with fixed m values.

Ren et al. (2016) proposed a new formulation called DMRG inner space perturbation theory (DMRG-isPT) to replace the expensive exact diagonalization procedure in each local matrix optimization step in order to achieve high efficiency and maintain accuracy at the same time. In the DMRG-isPT method, "small space diagonalization + large space perturbation" algorithm is adopted, in which only a smaller effective Hamiltonian (with a dimension of $16 \times m_0^2$, $m_0 \ll m$) is exactly diagonalized and then use Rayleigh–Schrodinger perturbation theory (RSPT) to calculate the first-order wave function $|\psi^{(1)}\rangle$ (with a larger dimension of $16 \times m^2$) and the second-order energy $E_2 = \langle\psi^{(1)}|\hat{Q}\hat{V}|\psi^{(0)}\rangle$. The first-order wave function $|\psi^{(1)}\rangle$ can be obtained by

solving the equation

$$\left(\hat{H}_0 - E_0\right)\left|\psi^{(1)}\right\rangle = -\,\hat{Q}\hat{H}\left|\psi^{(0)}\right\rangle, \tag{4.113}$$

in which $\hat{P} = \left|\psi^{(0)}\right\rangle\left\langle\psi^{(0)}\right|$ and $\hat{Q} = 1 - \hat{P}$ are projectors.

Using the approach similar to "small space diagonalization + large space perturbation", Guo et al. (2018a) developed a p-DMRG algorithm. The main difference between DMRG-isPT and p-DMRG is that the former uses perturbation theory at each DMRG sweeping step to approximate the local MPS tensor, while the latter applies perturbation theory on a globally converged MPS wave function with a small bond dimension. For solving the first-order equation, $\left|\psi^{(1)}\right\rangle$ in p-DMRG is achieved by minimizing the Hylleraas functional through DMRG sweeps using the MPS-PT algorithm (Sharma and Chan, 2014), which will be introduced in Section 6.3. Because this MPS-PT will require a much larger bond dimension m_1 ($m_1 \gg m_0$) for p-DMRG, a significant cost in both computation and storage becomes a bottleneck for very large active spaces with $50-100$ orbitals. To further speed up the computational efficiency, later Guo et al. (2018b) proposed a stochastic p-DMRG algorithm to avoid solving the first-order equation deterministically, through using an importance sampling algorithm over the determinant space (see Section 4.8).

4.11 Relativistic density matrix renormalization group

As we have mentioned in the beginning of this chapter, the relativistic effect is not considered in the Schrödinger equation. The term "relativistic effect" refers to any difference between the Dirac and Schrödinger models of electronic structure. In other words, it refers to any difference arising from the finite and infinite speeds of light. Relativistic quantum chemistry has witnessed fast development, especially in the last 20 years, and it can be envisaged that relativistic quantum chemistry will play an increasingly important role in the exploration of molecular science. (Reiher and Wolf, 2014; Liu, 2016; Liu, 2017; Liu, 2020)

Relativistic effect is strong for heavy and super-heavy elements as well as their compounds, which usually also exhibit strong electron correlations caused by the large number of near-degenerate d and f orbitals. Hence, the coupling of electron-correlation and relativistic effects is in general best described using relativistic multiconfigurational WFT methods. The relativistic effect has two primary origins, (1) the scalar relativistic effects of the radial contraction and energetic stabilization for s and p states and the radial expansion and energetic destabilization for outer d and f shells and (2) spin−orbit coupling effect on the splitting of shells of nonzero angular momenta (p, d, f, ...). The scalar relativistic and spin−orbit coupling effects can be treated separately or synergistically by relativistic quantum chemistry methods.

For technique details of relativistic quantum chemistry, we refer the readers to the recent books by Reiher and Wolf (2014) and Liu (2017). Here we just briefly introduce its basic ideas. Relativistic quantum chemistry starts from the Dirac equation, the relativistic quantum mechanical description of a one-electron system in the nuclear attraction potential V,

$$\hat{H}_D|\Psi\rangle = \left[c\boldsymbol{\alpha}\cdot\boldsymbol{p} + (\boldsymbol{\beta} - 1)m_ec^2 + V\right]|\Psi\rangle = E|\Psi\rangle. \qquad (4.114)$$

Here m_e is the mass of electron and c is the speed of light. The rest mass energy m_ec^2 of the electron has been subtracted in the equation. $\boldsymbol{\alpha}$ and $\boldsymbol{\beta}$ are the 4×4 Dirac matrices,

$$\boldsymbol{\alpha} = \begin{pmatrix} 0 & \boldsymbol{\sigma} \\ \boldsymbol{\sigma} & 0 \end{pmatrix}, \boldsymbol{\beta} = \begin{pmatrix} \boldsymbol{I}_2 & 0 \\ 0 & -\boldsymbol{I}_2 \end{pmatrix}, \qquad (4.115)$$

with $\boldsymbol{\sigma}$ being the vector of the 2×2 Pauli spin matrices,

$$\sigma_x = \begin{pmatrix} 0 & 1 \\ 1 & 0 \end{pmatrix}, \sigma_y = \begin{pmatrix} 0 & -i \\ i & 0 \end{pmatrix}, \sigma_z = \begin{pmatrix} 1 & 0 \\ 0 & -1 \end{pmatrix}. \qquad (4.116)$$

The eigenfunction $|\psi\rangle$ is a bispinor with four components (4C) vector containing two "large" and two "small" components ψ^L and ψ^S, respectively.

$$|\psi\rangle = \begin{pmatrix} \psi^L \\ \psi^S \end{pmatrix} = \begin{pmatrix} \psi_1^L \\ \psi_2^L \\ \psi_1^S \\ \psi_2^S \end{pmatrix}. \qquad (4.117)$$

The large and small components, respectively, originate from the electronic and positronic degrees of freedom. In the nonrelativistic limit $c \to \infty$ the small components vanish, while the large components correspond to the nonrelativistic wave functions for α and β electron spin.

There is no unique derivation for a molecular many-electron analog to the Dirac equation. In many cases, the Dirac-Coulomb (DC) or Dirac-Coulomb-Breit Hamiltonian is used in practice. Due to the expensive computational costs of 4C calculations, approximate two-component (A2C) approaches can be derived by removing the small component of the four spinors. To achieve an efficient elimination, zeroth- and first-order regular approximations and the method of normalized elimination of the small component (NESC) can be used. In addition, transformation techniques such as Douglas−Kroll (DK) or Douglas−Kroll−Hess (DKH) aim at a unitary transformation of the Dirac Hamiltonian to block-diagonal form such that ψ^L and ψ^S (in an eigenspinor basis of $\hat{H}_D$) are decoupled. A scalar approximation will be obtained if such kind of transformations are applied to the one-electron operators only, with spin-dependent terms discarded. Therefore scalar relativistic calculations are fully compatible with conventional multiconfigurational WFT code since only the one-electron integrals are affected.

Recent attention was also paid to the so-called exact two-component and quasi four-component methods, which involve no additional approximations beyond the no-pair approximation at the one-electron level. That is, results of the one-electron Dirac equation can be reproduced to machine accuracy, while substantially reducing the computational effort compared to the full 4C treatment.

In recent years, relativistic effects have been also successfully incorporated in DMRG calculations by using different relativistic models. Moritz et al. (2005b) implemented the first scalar relativistic DMRG calculation with an example of the cesium hydride molecule, in which the generalized arbitrary-order DKH protocol up to tenth order was used for a complete decoupling of the Dirac Hamiltonian. The first implementation of the A2C- and 4C-DMRG based on the four-component DC Hamiltonian was reported by Knecht et al. (2014) with a benchmark test on thallium hydride. Later, such 4C-DMRG implementation was reformulated using MPS and MPO language and its capabilities were further illustrated by studying the ground-state magnetization, as well as current density of a paramagnetic f^9 dysprosium complex (Battaglia et al., 2018). Moreover, the combination of DMRG-tailored coupled cluster (see Section 6.4) with 4C DC Hamiltonian was also accomplished by Brandejs et al. (2020) with demonstrations on the system of TlH, AsH, and SbH. The relativistic DMRG calculations have been also successfully applied to the computation of electron paramagnetic resonance spectra parameters such as g-tensor and hyperfine coupling constants (HFCCs) at different approximation levels. (Lan et al., 2015; Knecht et al., 2016; Sayfutyarova and Chan, 2018)

4.12 High-performance ab initio density matrix renormalization group

Although the DMRG method is recognized by its ability for reducing the computational costs and make many complex problems solvable, in many chemical systems, the computational costs are still very expensive. Therefore it is highly desired to apply high-performance computing technology to accelerate DMRG calculations. The most important technique for modern processors architecture is parallelization, as the main stream central processing units (CPUs) are all multicore processors nowadays. Many parallelization methods of the DMRG method have been developed and reported by previous researches. Zhai and Chan (2021) summarized the existing parallelization methods in their article and classified them into five levels from the most fine-grained level to the most coarse-grained level. These five levels are: (1) parallelism within dense matrix multiplications, (2) parallelism over symmetry sectors, (3) parallelism over normal and complementary operators, (4) parallelism over a sum of sub-Hamiltonians, and (5) parallelism over sites.

Parallelism within dense matrix multiplications is the most fine-grained parallelism. In DMRG procedure, the matrix−matrix multiplications (BLAS DGEMM) and matrix-vector multiplications (MVM) are frequently applied. Hager et al. (2004) discussed the parallelization strategies of these two major operations on shared-memory systems. Nowadays, many math libraries, like BLAS or Intel MKL, provided highly efficient implementations of these two operations. So, this parallelism can be easily acquired by linking to existing math libraries.

When the DMRG is implemented with symmetry restrictions, the operator matrix is block-sparse matrix. Therefore it can be further decomposed into several dense matrices which would been processed simultaneously. This pattern is well described by Levy et al. (2020) as shown in Fig. 4.6. Kurashige and Yanai (2009) introduced their parallelization method over symmetry sectors. By applying this strategy, they conducted a DMRG calculation for Cr_2 molecule with a (24e, 30o) active space. The energies are demonstrated to be accurate to 0.6 mE_h when the DMRG bond dimension of m as large as 10000. This parallelism was also applied by Levy et al. (2020) on distributed-memory systems. They implemented this parallelism for the two-dimensional $J_1 - J_2$ Heisenberg model at $J_2/J_1 = 0.5$ and the triangular Hubbard model, and achieved up to 256 nodes parallelism with $m = 32768$.

The parallelism over normal and complementary operators is often considered the largest source of parallelism for typical ab initio problems. As we introduced in Section 4.1, the left-right decomposition of the Hamiltonian can be written as a summation of normal and complementary operators, which is referred as the normal/complementary (NC) partition for the right block, and the complementary/normal (CN) partition for the left block. So,
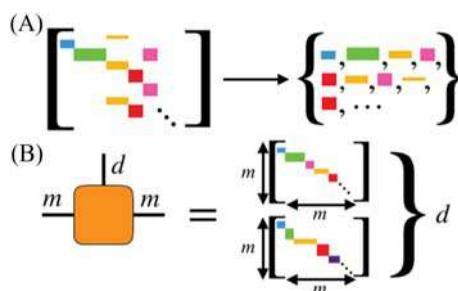
FIGURE 4.6 Cartoon of the tensor quantum block structure. (A) The block-sparse matrix was reorganized into a list of dense matrices. (B) Each tensor in an MPS has a special block-diagonal structure, where the blocks form $dm \times m$ matrices. *MPS*, Matrix product states. *Reproduced from Levy, R., Solomonik, E., Clark, B.K., 2020. Distributed-memory DMRG via sparse and dense parallel tensor contractions. In: SC '20: Proc.eedings of the International Conference for High Performance Computing, Networking, Storage and Analysis. https://doi. org/10.5555/3433701.3433732, with permission from Institute of Electrical and Electronics Engineers.*

the splitted operators can be assigned to different threads and processors. By benchmarking with a water molecule, correlating 10 electrons in 82 orbitals in C1 symmetry, keeping $m = 1000$ states, a speedup of 45 was achieved with 64 processors by Chan (2004), showing good near-linear parallelism.

Chan et al. (2016) suggested a new parallelization strategy for ab initio DMRG method. By applying the Hamiltonian compression, and an SOP representation (see Section 4.1), they achieved good computational parallelism. An important advantage of the SOP formulation is that each sub-Hamiltonian term can be manipulated completely independently of any other term. Thus the construction of sub-Hamiltonian term, the associated renormalized operators, and renormalized operator matrices for each sub-Hamiltonian term can be carried out independently. This leads to a different organization of the parallelization of the DMRG algorithm, which is highly scalable. This parallelism is coarse-grained with a very low communication cost and is easy to express in an MPO description.

The most coarse-grained parallelism is the parallelism over the sites which was firstly proposed by Stoudenmire and White (2013). In this work, the DMRG lattice was separated equally into several fragments, and several DMRG sweeps were conducted on corresponding fragments simultaneously. The sweeping pattern of this parallelism strategy is described in Fig. 4.7, in which one fragment was assigned to one computational node. When the sweep of one fragment comes to the boundary, it will wait for the neighbor to come and then communicate to each other. This strategy was then applied by
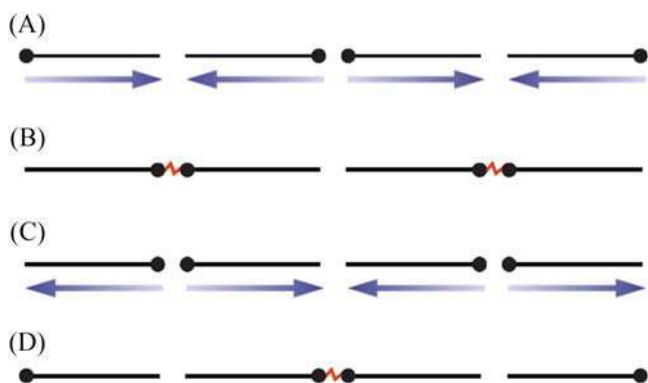
FIGURE 4.7 Sweeping pattern for one full sweep of the parallel DMRG algorithm split over four computational nodes. First, (A) the nodes are positioned in a spatially staggered pattern and sweep to the other end of their block. (B) When the nodes reach the end of their block they wait for their neighboring node to arrive, then communicate. (C) Finally, the nodes sweep back to their starting positions and (D) communicate with their other neighbor. *DMRG*, Density matrix renormalization group. *Reproduced from Stoudenmire, E.M., White, S.R., 2013. Real-space parallel density matrix renormalization group. Phys. Rev. B 87, 155137. https://doi.org/10.1103/PhysRevB.87.155137, with permission from American Physical Society.*

Secular et al. (2020) for time-dependent variational principle algorithm. Chen et al. (2021) further developed an adaptive boundary strategy for lattice sites parallelism and successfully reduced the load imbalance between nodes.

It is clear that these parallelization strategies can be employed together to develop a ML parallelization method. Brabec et al. (2020) reported a massively parallel implementation of DMRG using both strategies (2) and (3) and achieved parallelism up to 2496 CPU cores on the largest benchmark system (FeMo-cofactor cluster system with a CAS(113e, 76o) by using $m = 6000$). By identifying these five parallelization levels, Zhai and Chan (2021) implemented a low communication high-performance ab initio DMRG algorithm, applying all of the five parallelisms. They introduced a reformulated strategy (3) for a distributed-memory model using the sum of sub-Hamiltonian language. And by taking this demonstrates, a low communication version of strategy (3) can also be viewed as a variant of strategy (4). The strategy (4) and strategy (5) are implemented with distributed-memory model, and the strategy (1) and strategy (2) are implemented with shared-memory model. They benchmarked their strategies on a benzene molecule in an (30e, 108o) active space and achieved a parallelism of up to 2800 CPU cores with $m = 6000$. And they suggested that the combination of different DMRG parallelism strategies using both distributed and shared-memory models was essential to achieve near-ideal speed-ups.

In recent years, the graphic processing unit (GPU) was introduced to accelerate quantum chemistry algorithms and achieved great success. For DMRG calculations, the cuBLAS library, a GPU version of BLAS library integrated in Nvidia CUDA toolkit, implemented the matrix multiplications operations on GPU, providing a powerful tool for the most fine-grained parallelism. Based on this, Chen et al. (2020) implemented a CPU−GPU hybrid parallel method for DMRG calculations. In their strategy, both the diagonalization and the truncation procedure are optimized, and these optimizations effectively reduced the total computational time. Li et al. (2020) developed a GPU accelerated time-dependent DMRG time evolution scheme. The cuBLAS library was also applied in their implementation. Nemes et al. (2014) also introduced a hybrid CPU−GPU implementation of DMRG method. In their implementation, a new CUDA kernel was developed, as the MKL and cuBLAS libraries give poor performance. They also discussed the limitation of another widely used acceleration device, the field-programmable gate array (FPGA). As they stated, the FPGA chips have lower operating frequencies than in case of GPU architectures. And the FPGA chips are hard for programming.

To our best knowledge, the largest ab initio DMRG parallelism on CPU cores was achieved by Zhai and Chan (2021) for the (30e, 108o) benzene system, which applied up to 2800 CPU cores. We notice that other one-body-like quantum chemistry methods may achieve up to millions of CPU cores. For example, a parallelism of 8,519,680 cores for discontinuous

Galerkin DFT calculations was achieved by Hu et al. (2021). However, unlike the DFT method usually implemented with grid-based numerical integrations, many WFT methods like DMRG are more challenging to be parallelized efficiently because of tight dependence between their inner procedures, which brings more data synchronization requirements in parallelized implementations. In many-body quantum chemistry cases like ab initio DMRG, the evaluations and operations of tremendous matrices take much greater efforts, growing as a higher order polynomial with the increasing number of electrons and orbitals. It usually demands immense amounts of physical memory as well as fast and efficient input/output storage. The enormous amount of data synchronization severely restricts the parallel efficiency of many-body quantum chemistry methods. The parallelism of many-body quantum chemistry calculations is therefore significantly limited by internode communications. The internode imbalance becomes a big concern for massive parallelism that remains an unsolved problem for future work. By applying the machine learning method for workload arrangement, the internode imbalance may be able to be reduced. For large system DMRG calculations, the Davidson procedure is the most time-consuming step. It may take several iterations when the strength of correlation is large. The machine learning methods may also be able to help accelerate the Davidson diagonalization procedure by estimating a better initial guess.

4.13   Tensor network states

Before finishing, we should notice that the linear nature of the MPS is far from ideal for the entanglement structure of most chemical molecules. In the DMRG framework, we consider the actual three-dimensional MOs with long-range interactions as one-dimensional chains, which causes an unbalanced loss of correlations between MOs and accordingly requires a much larger m value. An intuitive improvement is to increase the dimension of the MPS tensors, leading to the quickly developing tensor network state (TNS) methods, as we have introduced in Chapter 2. A generalization from MPS to TNS can be understood by using the concept of higher order SVD from the mathematical point of view.

In recent years, various TNS methods have been applied in ab initio quantum chemistry, including the complete-graph tensor network (Marti et al., 2010), tree TNS (TTNS) (Murg et al., 2010; Murg et al., 2015; Nakatani and Chan, 2013), self-adaptive TNS (Kovyrshin and Reiher, 2017), and three-legged tree TNS (Gunst et al., 2018; Gunst et al., 2019), as well as comb TNS (CTNS) (Li, 2021). Fig. 4.8 shows an example of CTNS topology for the large CAS model (113e, 76o) of the FeMoco (M-cluster) in nitrogenase, grouping the d orbitals within each transition metal atom and active orbitals of each sulfur or carbon atom respectively. In TNS implementations, the TNS is usually mapped onto an MPS, and then the iterative optimization step can be executed

(A) P-cluster and FeMoco (M-cluster) in nitrogenase

(B) Right canonical form of a CTNS for the FeMoco
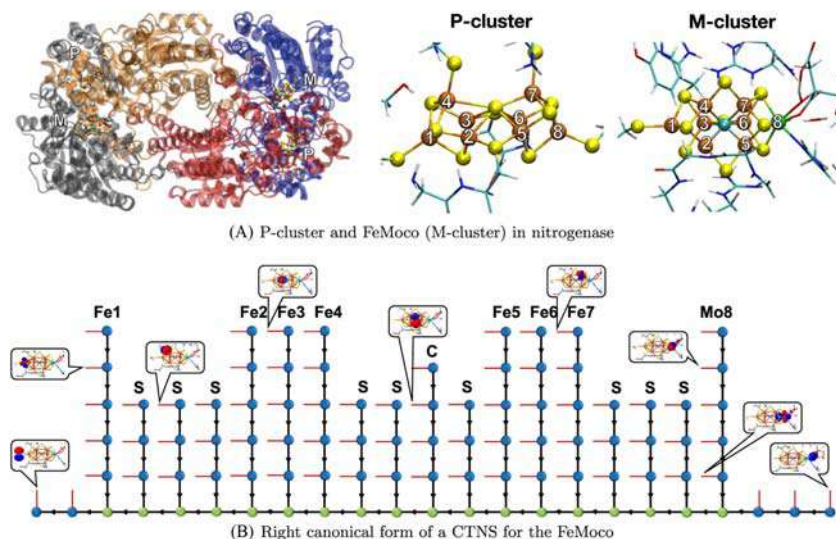
FIGURE 4.8 (A) The P-cluster and the FeMo-cofactor (M-cluster) in nitrogenase (Protein Data Bank (PDB) ID: 3U7Q). Color legend: Fe, orange; Mo, green; S, yellow; C, cyan; O, red; N, blue; H, white. The labels in the two complexes index the Fe/Mo atoms in the later figures. (B) The right canonical form of an CTNS for the active space model [CAS (113e, 76o)] of the FeMoco. The sites in blue represent physical sites associated with spatial orbitals, while the sites in green represent internal sites without physical index (*red lines*). Some selected MOs are also illustrated. *CTNS*, Comb tensor network state; *MOs*, Molecular orbitals. *Reproduced from Li, Z., 2021. Expressibility of comb tensor network states (CTNS) for the P-cluster and the FeMo-cofactor of nitrogenase. Electron. Struct. 3, 014001. https://doi.org/10.1088/2516-1075/abe192, with permission from Institute of Physics.*

in a DMRG-like variational way. High computational accuracy and efficiency for molecules of organic polyatomic radicals and polynuclear transition metal compounds have been illustrated in these works. In TTNS, the orbital optimization by canonical transformations has also been explored. (Murg et al., 2010)

In principle, the ab initio quantum chemistry Hamiltonian can be formulated in the tensor network operator language, similar to that of MPO. However, no such works have been reported due to its great complexity, and accordingly, most of the current TNS quantum chemical calculations still use the formulation of renormalized operators. Unlike MPS, the underlying chain topology of which is unique, there can be different topology shapes for TNS calculations of a given molecule. Therefore the optimization of the parameters for a high-dimensional tensor network becomes highly nontrivial and is of much higher numerical cost. In addition, one has to keep it in mind that the computational scaling of TNS is still worse than that of traditional DMRG, because of TNS's higher-dimensional nature. For these reasons, there is ample opportunity for quantum chemists and theoretical physicists to make valuable algorithmic contributions toward the quest for useful TNS quantum chemical computation.

References

Baiardi, A., Reiher, M., 2020. The density matrix renormalization group in chemistry and molecular physics: Recent developments and new challenges. J. Chem. Phys. 152, 040903. Available from: https://doi.org/10.1063/1.5129672.

Barcza, G., Legeza, Ö., Marti, K.H., Reiher, M., 2011. Quantum-information analysis of electronic states of different molecular structures. Phys. Rev. A 83, 012508. Available from: https://doi.org/10.1103/physreva.83.012508.

Barcza, G., Ivady, V., Szilvasi, T., Voros, M., Veis, L., Gali, A., et al., 2021. DMRG on top of plane-wave Kohn − Sham Orbitals: a case study of defected boron nitride. J. Chem. Theory Comput. 17, 1143−1154. Available from: https://doi.org/10.1021/acs.jctc.0c00809.

Battaglia, S., Keller, S., Knecht, S., 2018. Efficient relativistic density-matrix renormalization group implementation in a matrix-product formulation. J. Chem. Theory Comput. 14, 2353−2369. Available from: https://doi.org/10.1021/acs.jctc.7b01065.

Boguslawski, K., Marti, K.H., Reiher, M., 2011. Construction of CASCI-type wave functions for very large active spaces. J. Chem. Phys. 134, 224101. Available from: https://doi.org/10.1063/1.3596482.

Boguslawski, K., Marti, K.H., Legeza, Ö., Reiher, M., 2012a. Accurate ab initio spin densities. J. Chem. Theory Comput. 8, 1970−1982. Available from: https://doi.org/10.1021/ct300211j.

Boguslawski, K., Tecmer, P., Legeza, Ö., Reiher, M., 2012b. Entanglement measures for single- and multireference correlation effects. J. Phys. Chem. Lett. 3, 3129−3135. Available from: https://doi.org/10.1021/jz301319v.

Brabec, J., Brandejs, J., Kowalski, K., Xantheas, S., Legeza, Ö., Veis, L., 2020. Massively parallel quantum chemical density matrix renormalization group method. J. Comput. Chem. 42, 534−544. Available from: https://doi.org/10.1002/jcc.26476.

Brandejs, J., Višňák, J., Veis, L., Maté, M., Legeza, Ö., Pittner, J., 2020. Toward DMRG-tailored coupled cluster method in the 4c-relativistic domain. J. Chem. Phys. 152, 174107. Available from: https://doi.org/10.1063/1.5144974.

Chan, G.K.-L., 2004. An algorithm for large scale density matrix renormalization group calculations. J. Chem. Phys. 120, 3172−3178. Available from: https://doi.org/10.1063/1.1638734.

Chan, G.K.-L., Head-Gordon, M., 2002. Highly correlated calculations with a polynomial cost algorithm: A study of the density matrix renormalization group. J. Chem. Phys. 116, 4462−4476. Available from: https://doi.org/10.1063/1.1449459.

Chan, G.K.-L., Head-Gordon, M., 2003. Exact solution (within a triple-zeta, double polarization basis set) of the electronic Schrödinger equation for water. J. Chem. Phys. 118, 8551−8554. Available from: https://doi.org/10.1063/1.1574318.

Chan, G.K.-L., Sharma, S., 2011. The density matrix renormalization group in quantum chemistry. Annu. Rev. Phys. Chem. 62, 465−481. Available from: https://doi.org/10.1146/annurev-physchem-032210-103338.

Chan, G.K.-L., Keselman, A., Nakatani, N., Li, Z., White, S.R., 2016. Matrix product operators, matrix product states, and *ab initio* density matrix renormalization group algorithms. J. Chem. Phys. 145, 014102. Available from: https://doi.org/10.1063/1.4955108.

Chen, F.-Z., Cheng, C., Luo, H.-G., 2020. Improved hybrid parallel strategy for density matrix renormalization group method. Chin. Phys. B 29, 070202. Available from: https://doi.org/10.1088/1674-1056/ab8a42.

Chen, F.-Z., Cheng, C., Luo, H.-G., 2021. Real-space parallel density matrix renormalization group with adaptive boundaries. Chin. Phys. B 30, 080202. Available from: https://doi.org/10.1088/1674-1056/abeb08.

Cuthill, E., McKee, J., 1969. Reducing the bandwidth of sparse symmetric matrices. In: Proc. 24th National Conference of the ACM. 157−172. Available from: https://doi.org/10.1145/800195.805928.

Daul, S., Ciofini, I., Daul, C., White, S.R., 2000. Full-CI quantum chemistry using the density matrix renormalization group. Int. J. Quant. Chem. 79, 331−342. http://doi.org/10.1002/1097-461X(2000)79:6 < 331::AID-QUA1 > 3.0.CO;2-Y.

Ding, L., Mardazad, S., Das, S., Szalay, S., Schollwöck, U., Zimboras, Z., et al., 2021. Concept of orbital entanglement and correlation in quantum chemistry. J. Chem. Theory Comput. 17, 79−95. Available from: https://doi.org/10.1021/acs.jctc.0c00559.

Duperrouzel, C., Tecmer, P., Boguslawski, K., Barcza, G., Legeza, Ö., Ayers, P.W., 2015. A quantum informational approach for dissecting chemical reactions. Chem. Phys. Lett. 621, 160−164. Available from: https://doi.org/10.1016/j.cplett.2015.01.005.

Fiedler, M., 1973. Algebraic connectivity of graphs. Czech. Math. J. 23, 298. Available from: https://doi.org/10.21136/CMJ.1973.101168.

Freitag, L., Reiher, M., 2021. The density matrix renormalization group for strong correlation in ground and excited states. In: González, L., Lindh, R. (Eds.), Quantum Chemistry and Dynamics of Excited States. John Wiley & Sons Ltd, Chichester, pp. 205−245.

Golub, P., Antalik, A., Veis, L., Brabec, J., 2021. Machine learning-assisted selection of active spaces for strongly correlated transition metal systems. J. Chem. Theory Comput. 17, 6053−6072. Available from: https://doi.org/10.1021/acs.jctc.1c00235.

Grimme, S., Hansen, A., 2015. A practicable real-space measure and visualization of static electron-correlation effects. Angew. Chem., Int. (Ed.) 54, 12308−12313. Available from: https://doi.org/10.1002/anie.201501887.

Gunst, K., Verstraete, F., Wouters, S., Legeza, Ö., Van Neck, D., 2018. T3NS: three-legged tree tensor network states. J. Chem. Theory Comput. 14, 2026−2033. Available from: https://doi.org/10.1021/acs.jctc.8b00098.

Gunst, K., Verstraete, F., Van Neck, D., 2019. Three-legged tree tensor networks with SU(2) and molecular point group symmetry. J. Chem. Theory Comput. 15, 2996−3007. Available from: https://doi.org/10.1021/acs.jctc.9b00071.

Guo, S., Li, Z., Chan, G.K.-L., 2018a. A perturbative density matrix renormalization group algorithm for large active spaces. J. Chem. Theory Comput. 14, 4063−4071. Available from: https://doi.org/10.1021/acs.jctc.8b00273.

Guo, S., Li, Z., Chan, G.K.-L., 2018b. Communication: an efficient stochastic algorithm for the perturbative density matrix renormalization group in large active spaces. J. Chem. Phys. 148, 221104. Available from: https://doi.org/10.1063/1.5031140.

Hachmann, J., Cardoen, W., Chan, G.K.-L., 2006. Multireference correlation in long molecules with the quadratic scaling density matrix renormalization group. J. Chem. Phys. 125, 144101. Available from: https://doi.org/10.1063/1.2345196.

Hager, G., Jeckelmann, E., Fehske, H., Wellein, G., 2004. Parallelization strategies for density matrix renormalization group algorithms on shared-memory systems. J. Comput. Phys. 194, 795−808. Available from: https://doi.org/10.1016/j.jcp.2003.09.018.

Henderson, L., Vedral, V., 2000. Information, relative entropy of entanglement, and irreversibility. Phys. Rev. Lett. 84, 2263. Available from: https://doi.org/10.1103/PhysRevLett.84.2263.

Hopcroft, J.E., Karp, R.M., 1973. An $n^{5/2}$ algorithm for maximum matchings in bipartite graphs. SIAM J. Comput. 2, 225−231. Available from: https://doi.org/10.1137/0202019.

Hu, W., Qin, X., Jiang, Q., Chen, J., An, H., Jia, W., et al., 2021. High performance computing of DGDFT for tens of thousands of atoms using millions of cores on Sunway TaihuLight. Sci. Bull. 66, 111. Available from: https://doi.org/10.1016/j.scib.2020.06.025.

Hubig, C., McCulloch, I.P., Schollwöck, U., 2017. Generic construction of efficient matrix product operators. Phys. Rev. B 95, 035129. Available from: https://doi.org/10.1103/physrevb.95.035129.

Jeong, W., Stoneburner, S.J., King, D., Li, R., Walker, A., Lindh, R., et al., 2020. Automation of active space selection for multireference methods via machine learning on chemical bond dissociation. J. Chem. Theory Comput. 16, 2389−2399. Available from: https://doi.org/10.1021/acs.jctc.9b01297.

Keller, S., Reiher, M., 2016. Spin-adapted matrix product states and operators. J. Chem. Phys. 144, 134101. Available from: https://doi.org/10.1063/1.4944921.

Keller, S., Boguslawski, K., Janowski, T., Reiher, M., Pulay, P., 2015a. Selection of active spaces for multiconfigurational wave functions. J. Chem. Phys. 142, 244104. Available from: https://doi.org/10.1063/1.4922352.

Keller, S., Dolfi, M., Troyer, M., Reiher, M., 2015b. An efficient matrix product operator representation of the quantum chemical Hamiltonian. J. Chem. Phys. 143, 244118. Available from: https://doi.org/10.1063/1.4939000.

Khedkar, A., Roemelt, M., 2019. Active space selection based on natural orbital occupation numbers from n-electron valence perturbation theory. J. Chem. Theory Comput. 15, 3522−3536. Available from: https://doi.org/10.1021/acs.jctc.8b01293.

Khedkar, A., Roemelt, M., 2020. Extending the ASS1ST active space selection scheme to large molecules and excited states. J. Chem. Theory Comput. 16, 4993−5005. Available from: https://doi.org/10.1021/acs.jctc.0c00332.

King, D.S., Gagliardi, L., 2021. A ranked-orbital approach to select active spaces for high-throughput multireference computation. J. Chem. Theory Comput. 17, 2817−2831. Available from: https://doi.org/10.1021/acs.jctc.1c00037.

Knecht, S., Legeza, Ö., Reiher, M., 2014. Four-component density matrix renormalization group. J. Chem. Phys. 140, 041101. Available from: https://doi.org/10.1063/1.4862495.

Knecht, S., Keller, S., Autschbach, J., Reiher, M., 2016. A nonorthogonal state-interaction approach for matrix product state wave functions. J. Chem. Theory Comput. 12, 5881−5894. Available from: https://doi.org/10.1021/acs.jctc.6b00889.

König, D., 1931. Graphok és matrixok. Mat. Fiz. Lapok 38, 116−119.

Kovyrshin, A., Reiher, M., 2017. Self-adaptive tensor network states with multi-site correlators. J. Chem. Phys. 147, 214111. Available from: https://doi.org/10.1063/1.5004693.

Kuhn, H.W., 1955. The Hungarian method for the assignment problem. Nav. Res. Logist. 2, 83−97. Available from: https://doi.org/10.1002/nav.3800020109.

Kurashige, Y., 2014. Multireference electron correlation methods with density matrix renormalisation group reference functions. Mol. Phys. 112, 1485−1494. Available from: https://doi.org/10.1080/00268976.2013.843730.

Kurashige, Y., Yanai, T., 2009. High-performance ab initio density matrix renormalization group method: Applicability to large-scale multireference problems for metal compounds. J. Chem. Phys. 130, 234114. Available from: https://doi.org/10.1063/1.3152576.

Lan, T.N., Kurashige, Y., Yanai, T., 2015. Scalar relativistic calculations of hyperfine coupling constants using ab initio density matrix renormalization group method in combination with third-order Douglas − Kroll − Hess transformation: case studies on 4d transition metals. J. Chem. Theory Comput. 11, 73−81. Available from: https://doi.org/10.1021/ct5007778.

Larsson, H.K., Jimenez-Hoyos, C.A., Chan, G.K.-L., 2020. Minimal matrix product states and generalizations of mean-field and geminal wave functions. J. Chem. Theory Comput. 16, 5057−5066. Available from: https://doi.org/10.1021/acs.jctc.0c00463.

Larsson, H.K., Zhai, H., Gunst, K., Chan, G.K.-L., 2022. Matrix product states with large sites. J. Chem. Theory Comput. 18, 749−762. Available from: https://doi.org/10.1021/acs.jctc.1c00957.

Legeza, Ö., Fáth, G., 1996. Accuracy of the density-matrix renormalization-group method. Phys. Rev. B 53, 14349−14358. Available from: https://doi.org/10.1103/physrevb.53.14349.

Legeza, Ö., Sólyom, J., 2003. Optimizing the density-matrix renormalization group method using quantum information entropy. Phys. Rev. B 68, 195116. Available from: https://doi.org/10.1103/physrevb.68.195116.

Legeza, Ö., Sólyom, J., 2004. Quantum data compression, quantum information generation, and the density-matrix renormalization-group method. Phys. Rev. B 70, 205118. Available from: https://doi.org/10.1103/PhysRevB.70.205118.

Legeza, Ö., Röder, J., Hess, B.A., 2003a. QC-DMRG study of the ionic-neutral curve crossing of LiF. Mol. Phys. 101, 2019−2028. Available from: https://doi.org/10.1080/0026897031000155625.

Legeza, Ö., Röder, J., Hess, B.A., 2003b. Controlling the accuracy of the density-matrix renormalization-group method: The dynamical block state selection approach. Phys. Rev. B 67, 125114. Available from: https://doi.org/10.1103/PhysRevB.67.125114.

Lei, Y., Suo, B., Liu, W., 2021. iCAS: imposed automatic selection and localization of complete active spaces. J. Chem. Theory Comput. 17, 4846−4859. Available from: https://doi.org/10.1021/acs.jctc.1c00456.

Levy, R., Solomonik, E., Clark, B.K., 2020. Distributed-memory DMRG via sparse and dense parallel tensor contractions. In: SC '20: Proc. of the International Conference for High Performance Computing, Networking, Storage and Analysis. Available from 10.5555/3433701.3433732.

Li, Z., 2021. Expressibility of comb tensor network states (CTNS) for the P-cluster and the FeMo-cofactor of nitrogenase. Electron. Struct. 3, 014001. Available from: https://doi.org/10.1088/2516-1075/abe192.

Li, Z., Chan, G.K.-L., 2017. Spin-projected matrix product states: versatile tool for strongly correlated systems. J. Chem. Theory Comput. 13, 2681−2695. Available from: https://doi.org/10.1021/acs.jctc.7b00270.

Li, W., Ren, J., Shuai, Z., 2020. Numerical assessment for accuracy and GPU acceleration of TD-DMRG time evolution schemes. J. Chem. Phys. 152, 024127. Available from: https://doi.org/10.1063/1.5135363.

Liu, W., 2016. Big picture of relativistic molecular quantum mechanics. Natl. Sci. Rev. 3, 204−221. Available from: https://doi.org/10.1093/nsr/nwv081.

Liu, W. (Ed.), 2017. Handbook of Relativistic Quantum Chemistry. Springer, Berlin, Heidelberg. Available from: http://doi.org/10.1007/978-3-642-40766-6.

Liu, W., 2020. Essentials of relativistic quantum chemistry. J. Chem. Phys. 152, 180901. Available from: https://doi.org/10.1063/5.0008432.

Luo, Z., Ma, Y., Liu, C., Ma, H., 2017. Efficient reconstruction of CAS-CI-Type wave functions for a DMRG state using quantum information theory and a genetic algorithm. J. Chem. Theory Comput. 13, 4699−4710. Available from: https://doi.org/10.1021/acs.jctc.7b00439.

Ma, Y., Ma, H., 2013. Assessment of various natural orbitals as the basis of large active space density-matrix renormalization group calculations. J. Chem. Phys. 138, 224105. Available from: https://doi.org/10.1063/1.4809682.

Ma, Y., Wen, J., Ma, H., 2015. Density-matrix renormalization group algorithm with multilevel active space. J. Chem. Phys. 143, 034105. Available from: https://doi.org/10.1063/1.4926833.

Marti, K.H., Reiher, M., 2010. DMRG control using an automated Richardson-type error protocol. Mol. Phys. 108, 501−512. Available from: https://doi.org/10.1080/00268971003657078.

Marti, K.H., Bauer, B., Reiher, M., Troyer, M., Verstraete, F., 2010. Complete-graph tensor network states: a new fermionic wave function ansatz for molecules. N. J. Phys. 12, 103008. Available from: https://doi.org/10.1088/1367-2630/12/10/103008.

McCulloch, I.P., Gulácsi, M., 2000. Density matrix renormalisation group method and symmetries of the Hamiltonian. Aust. J. Phys. 53, 597−612. Available from: https://doi.org/10.1071/PH00023.

McCulloch, I.P., Gulácsi, M., 2002. The non-Abelian density matrix renormalization group algorithm. Europhys. Lett. 57, 852−858. Available from: https://doi.org/10.1209/epl/i2002-00393-0.

Mitrushenkov, A.O., Fano, G., Ortolani, F., Linguerri, R., Palmieri, P., 2001. Quantum chemistry using the density matrix renormalization group. J. Chem. Phys. 115, 6815−6821. Available from: https://doi.org/10.1063/1.1389475.

Mitrushenkov, A.O., Linguerri, R., Palmieri, P., Fano, G., 2003. Quantum chemistry using the density matrix renormalization group II. J. Chem. Phys. 119, 4148−4158. Available from: https://doi.org/10.1063/1.1593627.

Moritz, G., Reiher, M., 2007. Decomposition of density matrix renormalization group states into a Slater determinant basis. J. Chem. Phys. 126, 244109. Available from: https://doi.org/10.1063/1.2741527.

Moritz, G., Hess, B.A., Reiher, M., 2005a. Convergence behavior of the density-matrix renormalization group algorithm for optimized orbital orderings. J. Chem. Phys. 122, 024107. Available from: https://doi.org/10.1063/1.1824891.

Moritz, G., Wolf, A., Reiher, M., 2005b. Relativistic DMRG calculations on the curve crossing of cesium hydride. J. Chem. Phys. 123, 184105. Available from: https://doi.org/10.1063/1.2104447.

Murg, V., Verstraete, F., Legeza, Ö., Noack, R.M., 2010. Simulating strongly correlated quantum systems with tree tensor networks. Phys. Rev. B 82, 205105. Available from: https://doi.org/10.1103/physrevb.82.205105.

Murg, V., Verstraete, F., Schneider, R., Nagy, P.R., Legeza, Ö., 2015. Tree tensor network state with variable tensor order: an efficient multireference method for strongly correlated systems. J. Chem. Theory Comput. 11, 1027−1036. Available from: https://doi.org/10.1021/ct501187j.

Nakatani, N., Chan, G.K.-L., 2013. Efficient tree tensor network states (TTNS) for quantum chemistry: generalizations of the density matrix renormalization group algorithm. J. Chem. Phys. 138, 134113. Available from: https://doi.org/10.1063/1.4798639.

Nemes, C., Barcza, G., Nagya, Z., Legeza, Ö., Szolgay, P., 2014. The density matrix renormalization group algorithm on kilo-processor architectures: implementation and trade-offs. Comput. Phys. Commun. 185, 1570. Available from: https://doi.org/10.1016/j.cpc.2014.02.021.

Olivares-Amaya, R., Hu, W., Nakatani, N., Sharma, S., Yang, J., Chan, G.K.-L., 2015. The ab-initio density matrix renormalization group in practice. J. Chem. Phys. 142, 034102. Available from: https://doi.org/10.1063/1.4905329.

Parker, S.M., Shiozaki, T., 2014. Communication: active space decomposition with multiple sites: density matrix renormalization group algorithm. J. Chem. Phys. 141, 211102. Available from: https://doi.org/10.1063/1.4902991.

Parker, S.M., Seideman, T., Ratner, M.A., Shiozaki, T., 2013. Communication: active-space decomposition for molecular dimers. J. Chem. Phys. 139, 021108. Available from: https://doi.org/10.1063/1.4813827.

Percus, J.K., Rotenberg, A., 1962. Exact eigenfunctions of angular momentum by rotational projection. J. Math. Phys. 3, 928−932. Available from: https://doi.org/10.1063/1.1724308.

Reiher, M., Wolf, A., 2014. Relativistic Quantum Chemistry: The Fundamental Theory of Molecular Science, 2nd Edition Wiley-VCH, Weinheim.

Ren, J., Yi, Y., Shuai, Z., 2016. Inner space perturbation theory in matrix product states: replacing expensive iterative diagonalization. J. Chem. Theory Comput. 12, 4871−4878. Available from: https://doi.org/10.1021/acs.jctc.6b00696.

Ren, J., Li, W., Jiang, T., Shuai, Z., 2020. A general automatic method for optimal construction of matrix product operators using bipartite graph theory. J. Chem. Phys. 153, 084118. Available from: https://doi.org/10.1063/5.0018149.

Ren, J., Wang, Y., Li, W., Jiang, T., Shuai, Z., 2021. Time-dependent density matrix renormalization group coupled with n-mode representation potentials for the excited state radiationless decay rate: Formalism and application to azulene. Chin. J. Chem. Phys. 34, 565−582. Available from: https://doi.org/10.1063/1674-0068/cjcp2108138.

Rissler, J., Noack, R.M., White, S.R., 2006. Measuring orbital interaction using quantum information theory. Chem. Phys. 323, 519−531. Available from: https://doi.org/10.1016/j.chemphys.2005.10.018.

Saitow, M., Kurashige, Y., Yanai, T., 2013. Multireference configuration interaction theory using cumulant reconstruction with internal contraction of density matrix renormalization group wave function. J. Chem. Phys. 139, 044118. Available from: https://doi.org/10.1063/1.4816627.

Sayfutyarova, E.R., Chan, G.K.-L., 2018. Electron paramagnetic resonance g-tensors from state interaction spin-orbit coupling density matrix renormalization group. J. Chem. Phys. 148, 184103. Available from: https://doi.org/10.1063/1.5020079.

Sayfutyarova, E.R., Hammes-Schiffer, S., 2019. Constructing molecular π-orbital active spaces for multireference calculations of conjugated systems. J. Chem. Theory Comput. 15, 1679−1689. Available from: https://doi.org/10.1021/acs.jctc.8b01196.

Sayfutyarova, E.R., Sun, Q., Chan, G.K.-L., Knizia, G., 2017. Automated construction of molecular active spaces from atomic valence orbitals. J. Chem. Theory Comput. 13, 4063−4078. Available from: https://doi.org/10.1021/acs.jctc.7b00128.

Secular, P., Gourianov, N., Lubasch, M., Dolgov, S., Clark, S.R., Jaksch, D., 2020. Parallel time-dependent variational principle algorithm for matrix product states. Phys. Rev. B 101, 235123. Available from: https://doi.org/10.1103/PhysRevB.101.235123.

Sharma, S., 2015. A general non-Abelian density matrix renormalization group algorithm with application to the C_2 dimer. J. Chem. Phys. 142, 024107. Available from: https://doi.org/10.1063/1.4905237.

Sharma, S., Chan, G.K.-L., 2012. Spin-adapted density matrix renormalization group algorithms for quantum chemistry. J. Chem. Phys. 136, 124121. Available from: https://doi.org/10.1063/1.3695642.

Sharma, S., Chan, G.K.-L., 2014. A flexible multi-reference perturbation theory by minimizing the Hylleraas functional with matrix product states. J. Chem. Phys. 141, 111101. Available from: https://doi.org/10.1063/1.4895977.

Stein, C.J., Reiher, M., 2016. Automated selection of active orbital spaces. J. Chem. Theory Comput. 12, 1760−1771. Available from: https://doi.org/10.1021/acs.jctc.6b00156.

Stein, C.J., Reiher, M., 2019. AutoCAS: a program for fully automated multiconfigurational calculations. J. Comput. Chem. 40, 2216−2226. Available from: https://doi.org/10.1002/jcc.25869.

Stoudenmire, E.M., White, S.R., 2010. Minimally entangled typical thermal state algorithms. N. J. Phys. 12, 055026. Available from: https://doi.org/10.1088/1367-2630/12/5/055026.

Stoudenmire, E.M., White, S.R., 2013. Real-space parallel density matrix renormalization group. Phys. Rev. B 87, 155137. Available from: https://doi.org/10.1103/PhysRevB.87.155137.

Tatsuaki, W., 2000. Interaction-round-a-face density-matrix renormalization-group method applied to rotational-invariant quantum spin chains. Phys. Rev. E 61, 3199. Available from: https://doi.org/10.1103/physreve.61.3199.

Wang, T., Ma, Y., Zhao, L., Jiang, J., 2020. Portably parallel construction of a configuration-interaction wave function from a matrix−product state using the Charm++ framework. J. Comput. Chem. 41, 2707−2721. Available from: https://doi.org/10.1002/jcc.26424.

White, S.R., 2009. Minimally entangled typical quantum states at finite temperature. Phys. Rev. Lett. 102, 190601. Available from: https://doi.org/10.1103/PhysRevLett.102.190601.

White, S.R., Martin, R.L., 1999. Ab initio quantum chemistry using the density matrix renormalization group. J. Chem. Phys. 110, 4127−4130. Available from: https://doi.org/10.1063/1.478295.

Wouters, S., Limacher, P.A., Van Neck, D., Ayers, P.W., 2012. Longitudinal static optical properties of hydrogen chains: Finite field extrapolations of matrix product state calculations. J. Chem. Phys. 136, 134110. Available from: https://doi.org/10.1063/1.3700087.

Wouters, S., Van Neck, D., 2014. The density matrix renormalization group for ab initio quantum chemistry. Eur. Phys. J. D 68, 272. Available from: https://doi.org/10.1140/epjd/e2014-50500-1.

Xiang, T., 1996. Density-matrix renormalization-group method in momentum space. Phys. Rev. B 53, 10445−10448. Available from: https://doi.org/10.1103/physrevb.53.r10445.

Zgid, D., Nooijen, M., 2008a. On the spin and symmetry adaptation of the density matrix renormalization group method. J. Chem. Phys. 128, 014107. Available from: https://doi.org/10.1063/1.2814150.

Zgid, D., Nooijen, M., 2008b. Obtaining the two-body density matrix in the density matrix renormalization group method. J. Chem. Phys. 128, 144115. Available from: https://doi.org/10.1063/1.2883980.

Zhai, H., Chan, G.K.-L., 2021. Low communication high performance ab initio density matrix renormalization group algorithms. J. Chem. Phys. 154, 224116. Available from: https://doi.org/10.1063/5.0050902.

Zou, J., Niu, K., Ma, H., Li, S., Fang, W., 2020. Automatic selection of active orbitals from generalized valence bond orbitals. J. Phys. Chem. A 124, 8321−8329. Available from: https://doi.org/10.1021/acs.jpca.0c05216.

Chapter 5

Density matrix renormalization group with orbital optimization

In Chapter 4, we have shown that how the density matrix renormalization group (DMRG) method can be used as an excellent substitute to traditional full configuration interaction (FCI) or complete active space configuration interaction (CASCI) method in large active spaces composed of up to ~ 100 orbitals (Hachmann et al., 2006; Zhai and Chan, 2021). Since the multiconfigurational wave functions depend greatly on the choice of selected molecular orbitals (MOs) in an active space with a given size, multiconfigurational self-consistent field (MCSCF) calculation is usually performed, in which both configuration interaction (CI) coefficients and MOs are variationally optimized. Under those circumstances, qualitatively correct electronic structures for both the ground and excited states are obtained. Dynamic correlation effects not described by the MCSCF wave function can be generally recovered by subsequent multireference CI, perturbation theory (PT), or coupled cluster treatments that use the MCSCF wave function as zeroth-order approximation (see Chapter 6).

In this chapter, we will introduce the basic algorithms of MCSCF and its implementation in DMRG-SCF for orbital optimization, as well as their applications in geometry optimization, calculations of excited states, molecular spectra, and non-Born−Oppenheimer effects.

5.1 Orbital rotation

Since we need to optimize the MOs to minimize the total energy in the MCSCF method, first we briefly provide basic notions on the MOs and the one- and two-electron integrals. In quantum chemistry, MOs $\{\phi_i\}$ are usually expressed as linear combinations of atomic orbitals (AOs) $\{\chi_\mu\}$ by (Lennard-Jones, 1929)

$$\phi_i = \sum_{\mu=1}^{m} C_\mu^i \chi_\mu \tag{5.1}$$

149

which can be written in matrix form as

$$
\begin{pmatrix} \phi_1 & \phi_2 & \cdots & \phi_m \end{pmatrix} = \begin{pmatrix} \chi_1 & \chi_2 & \cdots & \chi_m \end{pmatrix} \begin{pmatrix} C_1^1 & C_1^2 & \cdots & C_1^m \\ C_2^1 & C_2^2 & \cdots & C_2^m \\ \vdots & \vdots & \ddots & \vdots \\ C_m^1 & C_m^2 & \cdots & C_m^m \end{pmatrix}.
$$
(5.2)

Here $\left\{ C_\mu^i \right\}$ are MO coefficients. In most wave function theory methods, one generally makes the MOs orthogonal to each other for convenience. For example, one can obtain a set of canonical MOs from Hartree−Fock (HF) self-consistent field (SCF) calculations, in which all orbitals are orthonormalized as

$$
\begin{aligned}
\langle \phi_i | \phi_j \rangle &= \begin{pmatrix} C_1^{i*} & C_2^{i*} & \cdots & C_m^{i*} \end{pmatrix} \begin{pmatrix} \chi_1^* \\ \chi_2^* \\ \vdots \\ \chi_m^* \end{pmatrix} \begin{pmatrix} \chi_1 & \chi_2 & \cdots & \chi_m \end{pmatrix} \begin{pmatrix} C_1^j \\ C_2^j \\ \vdots \\ C_m^j \end{pmatrix} \\
&= \boldsymbol{C}^{i*} \boldsymbol{S} \boldsymbol{C}^j \\
&= \delta_{ij}
\end{aligned}
$$
(5.3)

in which

$$
S_{\mu\nu} = \left\langle \chi_\mu | \chi_\nu \right\rangle
$$
(5.4)

is the overlap matrix element of the AOs. If the MOs $\{\phi_i\}$ need to be updated during the optimization iteration, one can easily construct a new MO coefficient matrix $\boldsymbol{C}$ by performing a unitary transformation on the original MO coefficient matrix $\boldsymbol{C}_0$, as

$$
\tilde{\boldsymbol{C}} = \boldsymbol{C}_0 \boldsymbol{U},
$$
(5.5)

in which $\boldsymbol{U}$ is a unitary transformation matrix. The above equation is equivalent to

$$
\tilde{\phi}_{i'} = \sum_i U_{ii'} \phi_i.
$$
(5.6)

Once the MOs are updated, one has to update the one- and two-electron MO integrals with the fixed AO integrals and the updated MO coefficients $\tilde{\boldsymbol{C}}$, alternatively one can directly refresh the MO integrals by updating the old integrals with the unitary transformation matrix $\boldsymbol{U}$ as

$$
\tilde{t}_{i'j'} = \sum_{ij} U_{ii'} U_{jj'} t_{ij}
$$
(5.7)

$$
\tilde{g}_{i'j'k'l'} = \sum_{ijkl} U_{ii'} U_{jj'} U_{kk'} U_{ll'} g_{ijkl}.
$$
(5.8)

The full transformation of the two-electron integrals in Eq. 5.8 costs $O(N^8)$ for N orbitals. As the computational cost is excessive, a cheaper and widely used technique is to perform four $O(N^5)$ steps to respectively handle the four indices i', j', k', and l', as

$$g_{i'jkl} = \sum_i U_{ii'} g_{ijkl}, \tag{5.9}$$

$$g_{i'j'kl} = \sum_j U_{jj'} g_{i'jkl}, \tag{5.10}$$

$$g_{i'j'k'l} = \sum_k U_{kk'} g_{i'j'kl}, \tag{5.11}$$

$$g_{i'j'k'l'} = \sum_l U_{ll'} g_{i'j'k'l}. \tag{5.12}$$

With the updated one- and two-electron integrals by U, one can rebuild the many-electron electronic Hamiltonian in Eq. 4.1 and solve it by exact or approximate FCI methods, to obtain the new multiconfigurational wave function along with new expansion configuration coefficients. Thereby, the goal of the orbital optimization is to find an appropriate unitary matrix U to minimize the total energy of the system. To reduce computational costs for optimizing U, a widely used technique is to expand the unitary matrix U into a progression as

$$U = \exp(R) = 1 + R + \frac{1}{2}RR + \cdots \tag{5.13}$$

in which R is an anti-Hermitian matrix containing all the orbital rotation parameters. Since we use real functions to represent orbitals and rotations, the matrix R is real and antisymmetric, which means

$$R_{rs} = -R_{sr}. \tag{5.14}$$

Therefore we only need to optimize the elements in the upper (or lower) triangle of the matrix R. In practice, it usually requires more than 100 leading terms of R expansion series, in order to construct the unitary matrix U with a satisfactory numerical accuracy. In addition, many elements in the matrix R are redundant, therefore can be safely ignored. We will explain in detail in the next section how to perform orbital optimizations by transforming the matrix R or U.

As it has been mentioned in Section 4.6 (CAS model), the entire MO space is usually divided into three subspaces: core, active, and external, as shown in Fig. 4.2. Henceforth (unless otherwise noted), the indices k, l will refer to internal orbitals; indices a, b will indicate external orbitals; r, s, p, q will represent any generic orbitals. The internal orbital space is further

divided into core and active subspaces, in which the MOs are labeled with indices i, j and t, u, v, w, respectively.

We have discussed at the beginning of this section that only those elements in the upper (or lower) triangle of the matrix $\boldsymbol{R}$ are used in orbital optimizations because $\boldsymbol{R}$ is antisymmetric. By splitting the orbital space into three subspaces, the number of orbital rotation parameters $\{R_{rs}\}$ can be reduced one step further. Some of the parameters R_{rs} may be redundant, that is, they do not influence the energy to first-order. This happens if the orbitals ϕ_i and ϕ_j have the same occupation number in all electronic configurations or the same spatial point group symmetry. An R_{rs} is also redundant if the same first-order energy change can be achieved by a variation of the CI coefficients. Since redundant variables influence the energy in higher order, they must be set to zero in order to avoid convergence difficulties. (Werner, 1987) Thus, in the complete active space SCF (CASSCF) method in which one performs exact FCI calculation within the active space, all rotations between the orbitals in the same subspace are redundant and must be set to zero. However, in other MCSCF implementations with truncated CI instead of the FCI in the active space, such as the restricted active space SCF and the DMRG methods with small m values, the rotations between active orbitals are not redundant because the CI basis functions are not complete in these cases. In this chapter, we are mainly focusing on the common and popular CASSCF implementation, whereas all active−active rotations are omitted.

5.2 The multiconfigurational self-consistent field methods

5.2.1 Energy, gradient, and Hessian

The second-quantized ab initio quantum chemistry Hamiltonian in CAS model is

$$\hat{H} = \sum_{tu,\sigma} F_{tu}^{c} \hat{a}_{t\sigma}^{\dagger} \hat{a}_{u\sigma} + \frac{1}{2} \sum_{tuvw,\sigma\tau} g_{tuvw} \hat{a}_{t\sigma}^{\dagger} \hat{a}_{v\tau}^{\dagger} \hat{a}_{w\tau} \hat{a}_{u\sigma} + E_{c} \qquad (5.15)$$

in which the core energy E_c and the closed-shell Fock matrix F_{rs}^c can be evaluated as

$$E_{c} = \sum_{j} \left(t_{jj} + F_{jj}^{c} \right) + E_{\text{nuc}}, \qquad (5.16)$$

$$F_{rs}^{c} = t_{rs} + \sum_{j} \left(2g_{rsjj} - g_{rjjs} \right). \qquad (5.17)$$

E_{nuc} is the repulsion energy between nuclei. The total energy can be directly obtained by applying the Hamiltonian $\hat{H}$ on the many-electron wave

function $|\psi\rangle$, as

$$E = \langle\psi|\hat{H}|\psi\rangle$$

$$= \sum_{tu} F_{tu}^{c} \sum_{\sigma} \langle\psi|\hat{a}_{t\sigma}^{\dagger}\hat{a}_{u\sigma}|\psi\rangle + \frac{1}{2}\sum_{tuvw} g_{tuvw} \sum_{\sigma\tau} \langle\psi|\hat{a}_{t\sigma}^{\dagger}\hat{a}_{v\tau}^{\dagger}\hat{a}_{w\tau}\hat{a}_{u\sigma}|\psi\rangle + E_{c}$$

$$= \sum_{tu} F_{tu}^{c} D_{u}^{t} + \frac{1}{2}\sum_{tuvw} g_{tuvw} D_{uw}^{tv} + E_{c}. \tag{5.18}$$

in which the one- and two-electron reduced density matrices (1-RDM and 2-RDM) D_{u}^{t} and D_{uw}^{tv} are defined as in Section 4.5. The core energy E_c is a constant in Eq. 5.16, because it is totally independent from the active orbitals. Thus the total energy E depends entirely on the RDMs and the MO integrals in the active space and can be expressed as a function of the CI coefficients c and the MO transformation matrix R (or U), as

$$E = E(c, R). \tag{5.19}$$

Once the total energy is minimized, there must be: (1) the energy gradient (first derivative) equals to zero, that is,

$$\begin{cases} \dfrac{\partial}{\partial c_I} E(c, R) = 0 \\ \dfrac{\partial}{\partial R_{rs}} E(c, R) = 0 \end{cases} \tag{5.20}$$

for arbitrary electronic configurations $|\Phi_I\rangle$ and orbitals r, s; (2) the energy Hessian (second derivative) matrix is positive definite. It can be easily derived that minimizing the total energy $E(c, R)$ with respect to the CI coefficients c leads to standard CI calculations. By introducing the operator,

$$\hat{S} = \sum_{k\neq 0} S_k \hat{S}_k = \sum_{k\neq 0} S_k \left(|\psi_k\rangle\langle\psi_0| - |\psi_0\rangle\langle\psi_k| \right), \tag{5.21}$$

where $|\psi_k\rangle$ represents a complement state orthogonal to the target state $|\psi_0\rangle$. Then the variations of the CI wave function can be written as

$$|\psi\rangle = \exp(\hat{S})|\psi_0\rangle. \tag{5.22}$$

Note that the operator $\hat{S}$ is anti-Hermitian. The CI energy can be written as a function of the variational parameters as

$$E = \langle\psi|\hat{H}|\psi\rangle = \left\langle \psi_0 \middle| e^{-\hat{S}}\hat{H}e^{\hat{S}} \middle| \psi_0 \right\rangle, \tag{5.23}$$

which can be expanded to second order according to the Baker−Campbell−Hausdorff expansion

$$E = \langle\psi_0|\hat{H}|\psi_0\rangle + \langle\psi_0|[\hat{H},\hat{S}]|\psi_0\rangle + \frac{1}{2}\langle\psi_0|[[\hat{H},\hat{S}],\hat{S}]|\psi_0\rangle. \tag{5.24}$$

Here the first term is the zeroth-order energy (E_0), also known as the reference energy; the second term denotes the first differential with respect to the CI coefficients; the third term contains the second differential. The first and the second derivative terms are also known as the gradient and the Hessian, respectively. The first-order gradient derivative $g_k'(\boldsymbol{c})$ with respect to the CI coefficients is obtained by

$$\langle\psi_0|[\hat{H},\hat{S}]|\psi_0\rangle = \sum_{k\neq0} S_k\big(\langle\psi_0|\hat{H}|\psi_k\rangle + \langle\psi_k|\hat{H}|\psi_0\rangle\big), \tag{5.25}$$

which can be reduced, because the wave functions are real and the element $\langle\psi_0|\hat{H}|\psi_k\rangle$ is thus symmetric, as

$$g_k'(\boldsymbol{c}) = 2\langle\psi_0|\hat{H}|\psi_k\rangle. \tag{5.26}$$

The Hessian elements $H_{kl}''(\boldsymbol{c})$ can be evaluated in a similar way, as

$$\langle\psi_0|[[\hat{H},\hat{S}_k],\hat{S}_l],|\psi_0\rangle = 2S_kS_l\langle\psi_k|(\hat{H}-E_0)|\psi_l\rangle, \tag{5.27}$$

and accordingly,

$$H_{kl}''(\boldsymbol{c}) = 2\langle\psi_k|(\hat{H}-E_0)|\psi_l\rangle. \tag{5.28}$$

To optimize MOs, one also needs the first and second derivatives of the energy respecting to the orbital rotations. The anti-Hermitian operator

$$\hat{R} = \sum_{rs} R_{rs}\hat{a}_r^\dagger\hat{a}_s \tag{5.29}$$

can be introduced to transform each spin-orbital ϕ_s of the original wave function into a new spin-orbital ϕ_s, as

$$\tilde{\phi}_s = \sum_r e^{R_{rs}}\phi_r. \tag{5.30}$$

The matrix $\boldsymbol{R}$ in Eq. 5.29 has been introduced in the last section. As the MOs are real, the operator $\hat{R}$ takes the compact form

$$\hat{R} = \sum_{r>s}\hat{R}_{rs} = \sum_{r>s} R_{rs}(\hat{E}_{rs}-\hat{E}_{sr}), \tag{5.31}$$

in which $\hat{E}_{rs} = \sum_{\sigma} \hat{a}_{r\sigma}^{\dagger} \hat{a}_{s\sigma}$ is a single-excitation operator. Thus applying the unitary transformation of $\exp(\hat{R})$ to the reference wave function $|\psi_0\rangle$ leads to

$$|\psi\rangle = \exp(\hat{R})|\psi_0\rangle, \tag{5.32}$$

and the energy in this situation becomes

$$E = \langle \psi | \hat{H} | \psi \rangle = \left\langle \psi_0 | e^{-\hat{R}} \hat{H} e^{\hat{R}} | \psi_0 \right\rangle. \tag{5.33}$$

We can use the Baker−Campbell−Hausdorff expansion to second order again with respect to orbital rotations as

$$E = \langle \psi_0 | \hat{H} | \psi_0 \rangle + \langle \psi_0 | [\hat{H}, \hat{R}] | \psi_0 \rangle + \frac{1}{2} \langle \psi_0 | [[\hat{H}, \hat{R}], \hat{R}] | \psi_0 \rangle. \tag{5.34}$$

Here

$$\langle \psi_0 | [\hat{H}, \hat{R}] | \psi_0 \rangle = \sum_{r > s} R_{rs} \langle \psi_0 | [\hat{H}, (\hat{E}_{rs} - \hat{E}_{sr})] | \psi_0 \rangle, \tag{5.35}$$

which gives the first-order derivative

$$g'_{rs}(\boldsymbol{R}) = \langle \psi_0 | [\hat{H}, (\hat{E}_{rs} - \hat{E}_{sr})] | \psi_0 \rangle. \tag{5.36}$$

Similarly,

$$\begin{aligned}
&\langle \psi_0 | [[\hat{H}, \hat{R}], \hat{R}] | \psi_0 \rangle \\
&= R_{rs} R_{pq} \langle \psi_0 | [[\hat{H}, \hat{e}_{rs}], \hat{e}_{pq}] | \psi_0 \rangle, \\
&\hat{e}_{ij} = \hat{E}_{ij} - \hat{E}_{ji}.
\end{aligned} \tag{5.37}$$

which gives the second-order derivative

$$H''_{rs,pq}(\boldsymbol{R}) = \langle \psi_0 | [[\hat{H}, \hat{e}_{rs}], \hat{e}_{pq}] | \psi_0 \rangle. \tag{5.38}$$

Besides, the full Hessian matrix involves the coupling between CI coefficients and orbital rotations. Therefore a naive idea of the MCSCF method is to perform CI calculations and MO optimizations iteratively, as an uncoupled scheme. Taking the CI-orbital coupling term into direct consideration leads to the coupled approach. The former one usually results in slower convergence and reduced computational costs, while the latter has faster convergence at higher computational costs.

According to the different strategies in their orbital optimization algorithms, current MCSCF methods can be categorized in two classes: (1) methods based on the generalized Brillouin's theorem (Levy and Berthier, 1968), and (2) methods based on the direct minimization of the energy. We will introduce these two approaches in the following subsections.

5.2.2 Super-configuration interaction method: a first-order multiconfigurational self-consistent field implementation

The super-configuration interaction (CI) method was firstly proposed by Grein and coworkers (Grein and Chang, 1971; Grein and Banerjee, 1975). After that, Roos and coworkers immensely contributed to the development of the method and software. (Roos et al., 1980; Roos, 1980; Siegbahn et al., 1980; Siegbahn et al., 1981; Malmqvist et al., 1990) The Super-CI method is based on the generalized Brillouin's theorem (Levy and Berthier, 1968), which states that for optimized MOs the ground-state wave function $|\psi_0\rangle$ satisfies

$$\langle \psi_0 | \hat{H} | rk \rangle = 0, \tag{5.39}$$

where $|rk\rangle = (\hat{E}_{rk} - \hat{E}_{kr})|\psi_0\rangle$ are the so-called Brillouin states, which are internally contracted singly excited configurations (see Section 6.1). Eq. 5.39 can be easily derived from the stationary point condition of

$$g'_{rk}(\boldsymbol{R}) = \langle \psi_0 | [\hat{H}, (\hat{E}_{rk} - \hat{E}_{kr})] | \psi_0 \rangle = 0. \tag{5.40}$$

The Super-CI wave function $|\psi\rangle$ can be obtained by performing unitary transformation on the reference wave function $|\psi_0\rangle$, as shown in Eq. 5.32. Expanding the exponential function in Eq. 5.32 to the first-order leads to the definition of the Super-CI wave function

$$|\psi\rangle = (1 + \hat{R})|\psi_0\rangle = |\psi_0\rangle + \sum_{r > k} R_{rk}|rk\rangle. \tag{5.41}$$

The coefficients $\{R_{rk}\}$ are determined by solving coupled Eq. 5.39 for different r and k indices. These equations represent the necessary and sufficient condition for optimized orbitals at each MCSCF macroiteration. In practice, the Super-CI Hamiltonian matrix is built and diagonalized. Because the Brillouin states $|rk\rangle$ and $|sl\rangle$ are usually nonorthogonal to each other, this corresponds to generalized eigenvalue equations.

Hamiltonian matrix elements between the reference state and the Brillouin states, $\langle \psi_0 | \hat{H} | rk \rangle$, as well as the coupling terms between Brillouin states, $\langle rk | \hat{H} | sl \rangle$, are required when solving the Super-CI eigenvalue problem, which are expensive because of the requirement for the three-body RDMs. In order to avoid their expensive computations and to achieve lower order scaling, the terms $\langle rk | \hat{H} | sl \rangle$ can be approximated by $\langle rk | \hat{H}^{\text{eff}} | sl \rangle$, (Roos, 1980; Malmqvist et al., 1990), where

$$\hat{H}^{\text{eff}} = \sum_{pq} \left(F^{\text{c}}_{pq} + F^{\text{a}}_{pq} \right) \hat{E}_{pq}. \tag{5.42}$$

The closed-shell Fock matrix $\boldsymbol{F}^{\text{c}}$ has been introduced in Eq. 5.17, while the active Fock matrix $\boldsymbol{F}^{\text{a}}$ can be obtained by

$$F^{\text{a}}_{rs} = \sum_{tu} D^t_u \left(g_{rstu} - \frac{1}{2} g_{rtsu} \right). \tag{5.43}$$

In fact, Super-CI using the generalized Brillouin theorem is also equivalent to running a perturbative treatment of $|\psi_0\rangle$ by considering the single excitations $|rk\rangle$ as Eq. 5.41. According to Rayleigh–Schrödinger PT (see Section 6.3.1), the Hylleraas functional for the Super-CI first-order wavefunction can be easily derived (summation over repeated indices implied)

$$\epsilon = 2R_{rk}\langle rk|\hat{H}|\psi_0\rangle + R_{rk}\langle rk|\hat{H} - E_0|sl\rangle R_{sl}. \tag{5.44}$$

Therefore orbital rotation parameters R_{ri} can be obtained through the minimization of ϵ.

The couplings between CI coefficients and orbital rotations are completely omitted in the Super-CI method. Each iteration of the Super-CI method starts with a closed-shell update for computing the closed-shell Fock matrix and two-electron MO integrals, followed by a CASCI calculation. From the CASCI calculation, the 1-RDM, 2-RDM as well as the Fock matrix for the active space are obtained. Finally, the orbital rotation parameters $\{R_{rk}\}$ are determined by solving the Super-CI eigenvalue problem. The computational effort of the Super-CI method scales as $O(N_{AO}^3 N_{int})$, in which N_{AO} and N_{int} are, respectively, the number of atomic and internal MOs. This scaling is smaller than the second-order methods described later. However, convergence acceleration techniques such as the Broyden–Fletcher–Goldfarb–Shanno (BFGS) method are vital for a robust convergence. Even with these acceleration methods, the Super-CI method may still show a slow convergence in some cases (Chang and Schwarz, 1977).

5.2.3 Second-order multiconfigurational self-consistent field method

In second-order MCSCF methods, both the gradient g and the Hessian matrix H of the orbital rotation parameters $\{R_{rk}\}$ are computed. The optimized orbital rotation parameters can be obtained via the Newton–Raphson (NR) method, by expanding the energy to the second-order of R

$$E = E_0(x) + g^\dagger x + \frac{1}{2}x^\dagger H x, \tag{5.45}$$

in which x contains all nonredundant parameters in the matrix ΔR. To improve the speed and robustness of convergence, the augmented Hessian (AH) method (Yarkony, 1981) is usually employed, which determines the step x by solving the eigenvalue problem

$$\begin{pmatrix} 0 & g^\dagger \\ g & H/\lambda \end{pmatrix} \begin{pmatrix} 1/\lambda \\ x \end{pmatrix} = \epsilon \begin{pmatrix} 1/\lambda \\ x \end{pmatrix}, \tag{5.46}$$

where λ is a damping parameter to keep the solution x within a trust radius. Solving the AH eigen problem is equivalent to solving the NR equations

with an adaptive shift ϵ of the diagonal elements of the Hessian matrix

$$(\boldsymbol{H} - \epsilon\boldsymbol{1})\boldsymbol{x} + \boldsymbol{g} = 0 \tag{5.47}$$

with

$$\epsilon = \lambda\boldsymbol{g}^\dagger\boldsymbol{x}. \tag{5.48}$$

$\boldsymbol{1}$ denotes a unit matrix with the same size of the Hessian matrix $\boldsymbol{H}$. Introducing the ϵ value keeps the shifted Hessian $\boldsymbol{H} - \epsilon\boldsymbol{1}$ staying positive definite for $\lambda \geq 1$, therefore convergence toward an energy minimum can always be enforced by a sufficiently large value of λ.

A more efficient implementation was proposed by Werner, Meyer, and Knowles (Werner and Meyer, 1980; Knowles and Werner, 1985; Werner and Knowles, 1985; Kreplin et al., 2019), and denoted in this book as the WMK method. Instead of expanding the total energy E to the second-order of the orbital rotation matrix $\boldsymbol{R}$, in the WMK method, the energy E is expanded to the second-order of the unitary matrix $\boldsymbol{U}$, which is equal to the infinite order of the matrix $\boldsymbol{R}$, as

$$
\begin{aligned}
E^{(2)} &= E_0 + 2\sum_{kl}\langle\Delta k|\hat{h}|l\rangle D_l^k + \sum_{kl}\langle\Delta k|\hat{h}|\Delta l\rangle D_l^k + 2\sum_{klmn}(\Delta kl|mn)D_{ln}^{km} \\
&= \sum_{klmn}(\Delta k\Delta l|mn)D_{ln}^{km} + 2\sum_{klmn}(\Delta km|n\Delta l)D_{ln}^{km},
\end{aligned}
\tag{5.49}
$$

in which k, l, m, n are internal orbitals and $(kl|mn) = g_{klmn}$ is the two-electron MO integral. This equation can be easily derived from Eq. 5.18. As the essence of orbital optimization is to get a new set of MOs via linear transformation, as shown in Eq. 5.6, the first derivatives of the one-electron MO integrals in Eq. 5.49 can be evaluated as

$$\left\langle\Delta r|\hat{h}|s\right\rangle = \sum_{r\neq p} U_{rp}\left\langle p|\hat{h}|s\right\rangle, \tag{5.50}$$

which can be simplified by introducing an auxiliary matrix $\boldsymbol{T}$

$$\boldsymbol{T} = \boldsymbol{U} - \boldsymbol{1} = \exp(\boldsymbol{R}) - \boldsymbol{1} = \boldsymbol{R} + \frac{1}{2}\boldsymbol{RR} + \cdots. \tag{5.51}$$

Thus the first and second derivatives of the one- and two-electron MO integrals can be obtained by

$$\left\langle\Delta r|\hat{h}|s\right\rangle = \sum_p T_{pr}^*\left\langle p|\hat{h}|s\right\rangle \Rightarrow \boldsymbol{T}^\dagger\boldsymbol{h}, \tag{5.52}$$

$$\left\langle\Delta r|\hat{h}|\Delta s\right\rangle = \sum_{pq} T_{pr}^* T_{qs}\left\langle p|\hat{h}|q\right\rangle \Rightarrow \boldsymbol{T}^\dagger\boldsymbol{h}\boldsymbol{T}, \tag{5.53}$$

$$(\Delta rs|kl) = \sum_p T^*_{pr} g_{pskl} \Rightarrow \boldsymbol{T}^\dagger \boldsymbol{J}^{kl}, \tag{5.54}$$

$$(\Delta r \Delta s|kl) = \sum_{pq} T^*_{pr} T_{qs} g_{pqkl} \Rightarrow \boldsymbol{T}^\dagger \boldsymbol{J}^{kl} \boldsymbol{T}, \tag{5.55}$$

$$(\Delta rk|l\Delta s) = \sum_{pq} T^*_{pr} T_{qs} g_{pklq} \Rightarrow \boldsymbol{T}^\dagger \boldsymbol{K}^{kl} \boldsymbol{T}, \tag{5.56}$$

where the matrix product expressions of these transformations lie on the right side of the arrows. Note that J^{kl} and K^{kl} are respectively the Coulomb and the exchange operators, and defined as

$$\langle r|J^{kl}|s \rangle = g_{rskl}, \tag{5.57}$$

$$\langle r|K^{kl}|s \rangle = g_{rkls}. \tag{5.58}$$

The evaluation of the second-order energy $E^{(2)}$ in Eq. 5.49 can be simplified as

$$E^{(2)}(\boldsymbol{T}) = E_0 + \sum_{rk} T_{rk} \left(2A_{rk} + \sum_{sl} G^{kl}_{rs} T_{sl} \right), \tag{5.59}$$

with

$$A_{ri} = 2F_{ri}, \tag{5.60}$$

$$A_{ru} = \sum_t F^c_{rt} D^t_u + \sum_{tvw} g_{rtvw} D^{tv}_{uw}, \tag{5.61}$$

$$A_{ra} = 0, \tag{5.62}$$

$$G^{ij}_{rs} = 2 \left(F_{rs} \delta_{ij} + L^{ij}_{rs} \right), \tag{5.63}$$

$$G^{tj}_{rs} = \sum_v D^t_v L^{vj}_{rs} = G^{jt}_{sr}, \tag{5.64}$$

$$G^{tu}_{rs} = F^c_{rs} D^t_u + \sum_{vw} \left(J^{vw}_{rs} D^{tv}_{uw} + 2K^{vw}_{rs} D^{tu}_{vw} \right). \tag{5.65}$$

The auxiliary rank-4 tensor $\boldsymbol{L}$ and the Fock matrix $\boldsymbol{F}$ which respectively are defined as

$$L^{kj}_{rs} = 4K^{kj}_{rs} - K^{kj}_{sr} - J^{kj}_{rs}, \tag{5.66}$$

$$F_{rs} = F^c_{rs} + \sum_{tu} D^t_u \left(J^{tu}_{rs} - \frac{1}{2} K^{tu}_{rs} \right). \tag{5.67}$$

Note that the Fock matrix F has been introduced in the first-order Super-CI method, as shown in Eq. 5.43.

Now one has to minimize the energy with respect to T with the constraint $U^\dagger U = 1$ because the matrix U must be unitary. This problem can be solved by introducing the Lagrangian multipliers $\{\varepsilon_{pq}\}$, as

$$\frac{\partial}{\partial T_{rk}}\left(E^{(2)} - \sum_{pq}\varepsilon_{pq}\left[\left(U^\dagger U\right)_{pq} - \delta_{pq}\right]\right) = 0. \tag{5.68}$$

Inserting Eq. 5.59 into Eq. 5.68 leads to the stationary condition

$$U^\dagger B - B^\dagger U = 0 \tag{5.69}$$

with

$$B_{rk} = A_{rk} + \sum_{sl}G^{kl}_{rs}T_{sl},\ B_{ra} = 0. \tag{5.70}$$

For the fully optimized orbitals, the solution of Eq. 5.69 must be $U = 1$. Since these matrices are real, the variational conditions are

$$A_{ak} = 0 \tag{5.71}$$

and

$$A_{kl} - A_{lk} = 0. \tag{5.72}$$

For a given $U = 1 + T$, the Hamiltonian can be expanded as

$$\hat{H}^{(2)} = \sum_{tu,\sigma}F^{c(2)}_{tu}\hat{a}^\dagger_{t\sigma}\hat{a}_{u\sigma} + \frac{1}{2}\sum_{tuvw,\sigma\tau}g^{(2)}_{tuvw}\hat{a}^\dagger_{t\sigma}\hat{a}^\dagger_{v\tau}\hat{a}_{w\tau}\hat{a}_{u\sigma} + E^{(2)}_c \tag{5.73}$$

with the second-order expansions of the integrals and closed-shell energy

$$F^{c(2)}_{tu} = \left(U^\dagger F^c U\right)_{tu} + 2\sum_i\left(U^\dagger J^{tu}U - J^{tu}\right)_{ii} - \sum_i\left(U^\dagger K^{tu}U - K^{tu}\right)_{ii}$$
$$+ \sum_i\left(T^\dagger L^{ui}T\right)_{ti} + \sum_i\left(T^\dagger L^{ti}T\right)_{ui}, \tag{5.74}$$

$$g^{(2)}_{tuvw} = -g_{tuvw} + \left(U^\dagger J^{vw}U\right)_{tu} + \left(U^\dagger J^{tu}U\right)_{vw}$$
$$+ (1 + \tau_{tu})(1 + \tau_{vw})\left(T^\dagger K^{tv}T\right)_{uw}, \tag{5.75}$$

$$E^{(2)}_c = E_c + 4\sum_i(F^c T)_{ii} + 2\sum_{ij}\left[T^\dagger\left(F^c\delta_{ij} + L^{ij}\right)T\right]_{ij}, \tag{5.76}$$

in which τ_{tu} permutes the two indices t and u. The second energy can be accordingly evaluated in the alternative form

$$E^{(2)}(T) = \left\langle\psi\left|\hat{H}^{(2)}\right|\psi\right\rangle, \tag{5.77}$$

which is equivalent to Eq. 5.59 and can be simplified by using the 1-RDM and 2-RDM.

One can see from Eq. 5.70 that the computation of the matrix $\boldsymbol{B}$ requires the unitary matrix $\boldsymbol{U}$, which suggests that SCF iterations are essential to solve the nonlinear Eq. 5.69. An update $\boldsymbol{T}(\boldsymbol{R} + \Delta \boldsymbol{R})$ is defined as

$$\boldsymbol{T}(\boldsymbol{R} + \Delta \boldsymbol{R}) = \boldsymbol{T}(\boldsymbol{R}) + \boldsymbol{U}(\boldsymbol{R})\left(\Delta \boldsymbol{R} + \frac{1}{2}\Delta \boldsymbol{R} \Delta \boldsymbol{R} + \cdots\right). \tag{5.78}$$

To address the nonconvex problem, a second-order technique with good robustness is required to determine the step $\Delta \boldsymbol{R}$ at the expansion point $E^{(2)}(\boldsymbol{T})$. Usually, the AH method is employed. In this case, the gradient $\boldsymbol{g}$ and the Hessian $\boldsymbol{H}$ for a fixed $\boldsymbol{U} = \boldsymbol{1} + \boldsymbol{T}$ can be derived by inserting Eq. 5.78 into Eq. 5.59, differentiating with respect to ΔR_{rk}, and evaluating the derivatives at $\Delta \boldsymbol{R} = 0$, which yields

$$\tilde{g}_{rk} = \left(\tilde{A}_{rk} - \tilde{A}_{kr}\right), \tag{5.79}$$

$$\tilde{H}_{rk,sl} = (1 - \tau_{rk})(1 - \tau_{sl})\left[\tilde{G}_{rs}^{kl} - \frac{1}{2}\delta_{kl}\left(\tilde{A}_{rs} + \tilde{A}_{sr}\right)\right], \tag{5.80}$$

with

$$\tilde{A}_{rk} = \left(\boldsymbol{U}^{\dagger}\boldsymbol{B}\right)_{rk}, \quad \tilde{A}_{ra} = 0, \tag{5.81}$$

$$\tilde{G}_{rs}^{kl} = \left(\boldsymbol{U}^{\dagger}\boldsymbol{G}^{kl}\boldsymbol{U}\right)_{rs}. \tag{5.82}$$

Note that $rk(r > k)$ and $sl(s > l)$ are considered as composite indices of the gradient vector $\tilde{\boldsymbol{g}}$ and the Hessian matrix $\tilde{\boldsymbol{H}}$. The tilde indicates that the gradient and the Hessian are evaluated for a given unitary matrix $\boldsymbol{U}$. Each time the AH eigenvalue equation is solved iteratively and an update $\Delta \boldsymbol{R}$ is obtained, the matrix $\boldsymbol{T}$ is updated according to Eq. 5.78 and the unitary matrix $\boldsymbol{U}$ can be easily updated since $\boldsymbol{U} = \boldsymbol{1} + \boldsymbol{T}$. This process is repeated until the convergence criterion in Eq. 5.69 is reached. The orbital optimization iterations are denoted as the microiterations. After the microiterations are converged, a new set of MOs can be constructed with the updated matrix $\boldsymbol{U}$ and the minimum energy is found for the current CI coefficients. Thence, a new macroiteration is performed, starting with a full integral transformation followed by a CI calculation and a new set of microiterations. The uncoupled WMK method is concluded in Algorithm 5.1. As $E^{(2)}(\boldsymbol{T})$ is used as the approximate energy functional rather than $E^{(2)}(\boldsymbol{R})$, the WMK method has a much larger radius of convergence than other second-order MCSCF approaches. (Werner, 1987)

Algorithm 5.1: The uncoupled second-order WMK method.

1: Set $U = 1$, $T = 0$ as initial guess
2: **procedure** Prepare(coordination, basis, . . .)
   t_{pq}, $\{g_{pqrs}\}$ ←
4:    Calculate F^c, E_c **//** see Eqs. 5.16−5.17
5:    **return** $\{t_{pq}\}$, $\{g_{pqrs}\}$, F^c and E_c
6: **end procedure**
7: **procedure** RunCASCI(F^c, $\{g_{pqrs}\}$, E_c)
8:    E_0, $\{D_u^t\}$, $\{D_{uw}^{tv}\}$ ← Do FCI in active space
9:    **return** E_0, $\{D_u^t\}$, $\{D_{uw}^{tv}\}$
10: **end procedure**
11: **procedure** PrepareMicroIteration(E_0, $\{F_{rs}^c\}$, $\{g_{pqrs}\}$, $\{D_u^t\}$, $\{D_{uw}^{tv}\}$, T, U)
12:    Calculate A, G using Eqs. 5.60−5.65
13:    $E^{(2)}$ ← Calculate second order energy(A, T, G, E_0) **//** see Eq. 5.59
14:    B ← Generate matrix $B(A, T)$ **//** see Eq. 5.70
15:    **return** A, G, $E^{(2)}$ and B
16: **end procedure**
17: **procedure** UncoupledMicroIteration (B, T, U)
18:    $\{\tilde{g}_{rk}\}$, $\{\tilde{H}_{rk,sl}\}$ **//** see Eqs. 5.79−5.82
19:    ΔR ← Solve for ΔR with AH method
20:    U, T ← Update matrix T and U **//** see Eq. 5.78
21:    B ← Generate matrix $B(A, T)$
22:    **if** $U^{\dagger}B - B^{\dagger}U \neq 0$ **then**
23:       Go back to step 18 with updated B, T, U
24:    **end if**
25:    **return** U
26: **end procedure**
27: **procedure** CheckEnergyConvergency(U)
28:    **if** $\delta E^{(2)} \neq 0$ **then**
29:       Transform $\{t_{pq}\}$, $\{g_{pqrs}\}$ with converged U **//** see Eqs. 5.7−5.12
30:       Calculate F^c, E_c
31:       Go back to step 7 with updated F^c, $\{g_{pqrs}\}$, E_c
32:    **end if**
33:    $C = C_0 U$
34:    **return** E_0, $\tilde{C}$
35: **end procedure**

5.2.4   Simultaneous optimization of configuration interaction coefficients and orbital rotations

In the above description of the second-order WMK method, the coupling of the orbital rotations and CI coefficients is still omitted, thus CI coefficients and orbital rotation parameters are optimized individually in iterative steps. Such kind of two-step optimization scheme is also known as the uncoupled MCSCF method. Although the uncoupled WMK method is efficient in most cases, it is still necessary to improve the convergence of the MCSCF method

by taking the coupling term into consideration, and optimize CI coefficients c and orbital rotation parameters R simultaneously. This leads to the coupled MCSCF method. Note that there are different implementations (Werner and Meyer, 1980, 1981; Knowles and Werner, 1985; Kreplin et al., 2019; Kreplin et al., 2020) of the coupled MCSCF method, and in some of them the coupling terms are evaluated explicitly while in others are not.

Once the coupling terms are evaluated, the second-order energy expansion in the changes of the orbitals and CI coefficients can be written as

$$E^{(2)} = E_0 + \frac{1}{2}\text{Tr}\{T^\dagger(A^0 + B^0)\} + 2\sum_I (c_I - c_I^0)\text{Tr}\{T^\dagger A^I\}, \qquad (5.83)$$

in which $\{c_I^0\}$ are the initial CI coefficients, and A^0, B^0 denote, respectively, the matrices calculated using these coefficients according to Eqs. 5.60−5.62, and 5.70. The derivative matrices A^I are defined with the same formulae as the matrix A and A^0, while the RDMs in the definition are replaced by the derivatives

$$D_u^t(I) = \sum_{J,\sigma} c_J^0\langle\Psi_I|\hat{a}_{t\sigma}^\dagger\hat{a}_{u\sigma}|\Psi_J\rangle, \qquad (5.84)$$

$$D_{uw}^{tv}(I) = \sum_{J,\sigma\tau} c_J^0\langle\Psi_I|\hat{a}_{t\sigma}^\dagger\hat{a}_{v\tau}^\dagger\hat{a}_{w\tau}\hat{a}_{u\sigma}|\Psi_J\rangle. \qquad (5.85)$$

The CI vector c and the orbital rotation parameters R can be simultaneously optimized via coupled NR equations

$$\begin{pmatrix} H_{RR} & H_{Rc} \\ H_{cR} & H_{cc} \end{pmatrix}\begin{pmatrix} R \\ c \end{pmatrix} + \begin{pmatrix} g_R \\ g_c \end{pmatrix} = \begin{pmatrix} 0 \\ 0 \end{pmatrix}. \qquad (5.86)$$

The orbital gradient g_R and Hessian H_{RR} can be computed with the same techniques used in the uncoupled WMK method, while the CI gradient g_c and Hessian H_{cc} can be easily derived from the second-order Hamiltonian in Eq. 5.73. The coupling term can be evaluated as

$$H_{R_{rk},c_I} = \frac{\partial^2 E^{(2)}}{\partial R_{rk}\partial c_I} = 2(1 - \tau_{rk})(A_{rk}^I - c_I^0 A_{rk}). \qquad (5.87)$$

Therefore only the additional calculations of the matrices $\{A^I\}$ are required to optimize the orbital rotations and CI coefficients simultaneously. The robustness of the coupled MCSCF approach can be improved by solving the changes of the orbitals and CI coefficients in the same one AH eigen equation, as shown in Sun et al. (2017). The algorithm is similar to the uncoupled case, except that the CI gradients, Hessian and the coupling terms must be evaluated before entering the AH procedure.

However, sometimes the explicit evaluation of the coupling terms is too expensive. In those cases, an implicit variant can be used, by performing a

second-order transformation of the MO integrals in the active space according to Eqs. 5.74 and 5.75, and then employing some cheap and coarse CI iterations to update the RDMs. We will give a deeper introduction about this approach in the next section.

5.3 Density matrix renormalization group self-consistent field methods

Since the DMRG method could be an efficient substitute for the traditional FCI and CASCI methods in large active spaces, one can naturally introduce the DMRG method into the CASSCF framework and implement the so-called DMRG-SCF method. From the discussion in the last section, we can see that the differences between the traditional CASSCF method and the DMRG-SCF method are:

1. The active−active orbital rotations must be taken into consideration when using an approximated FCI solver such as the DMRG, because the first-order energy change cannot be achieved by a variation of the incomplete CI basis functions. This problem can be solved by explicitly evaluating all active−active rotation parameters $R_{tu}(t > u)$ as well as the related gradients and Hessian elements, which must be set to zero in traditional CASSCF implementations.
2. The ab initio DMRG method works with large active spaces, but the costs are still substantial. Besides, as the full transformation of two-electron MO integrals costs $O(N^5)$ time and $O(N^4)$ storage for N MOs, it is extremely expensive to perform such full transformations in large molecules with $N \sim 10^{2-3}$. Therefore it is important to reduce the number of macroiterations in DMRG-SCF calculations, because in each macroiteration a full transformation of all the one- and two-electron MO integrals is required, followed by a costly DMRG calculation.
3. It is difficult to optimize the orbital rotation parameters and the CI coefficients simultaneously in a coupled MCSCF approach by explicitly evaluating the coupling terms and solving an extended AH eigen problem in ab initio DMRG, because the number of CI basis functions is too large to be handled in any existing eigen-solver. It is more realistic to make use of coupling items implicitly.
4. The construction of 1-RDM and 2-RDM is more complicated than in traditional ways. This issue has been already discussed in detail in Section 4.4.

The DMRG-SCF method was first exploited by Zgid and Nooijen (2008) and Ghosh et al. (2008) in its AH/NR-based implementations, respectively. Both implementations followed the principles of first-order approaches, transforming the wave function with rotated orbitals according to Eq. 5.35. Besides, Luo et al. (2010) proposed a method to minimize the DMRG energy

by swapping the orbitals inside and outside the active space, which is essentially also a kind of first-order approach. The first-order Super-CI method was introduced into the multilevel DMRG calculations by Ma et al. (2015). A second-order implementation was proposed by Yanai et al. (2009), in which the total energy was expanded to the second order of the matrix R and the direct inversion of iterative subspace method (Pulay, 1980) was introduced to reduce the number of macroiterations. A similar implementation was proposed by Wouters et al. (2014). Note that in all of these implementations, the coupling between the orbital rotations and CI coefficients is completely omitted. Recently, Sun et al. (2017) developed a coupled second-order DMRG-SCF method by expanding the energy to the second order of the matrix R.

As the WMK method is considered to have advantages in robustness and convergence over other second-order MCSCF implementations, Ma et al. (2017a) introduced the WMK method into DMRG-SCF calculations. The coupling between the orbital rotations and CI coefficients was evaluated implicitly as we have discussed in the last section. Their second-order DMRG-SCF implementation showed a high computational efficiency when applied to the Cr_2, $CuCl_2$, and trioxytriangulene molecules.

5.4 Excited state calculation

Understanding the fundamental physics and chemistry in photochemical reactions, optoelectronic materials as well as biological photosynthesis, is relying on an accurate electronic structure characterization of the excited states. However, as the original DMRG algorithm is designed for optimizing the ground-state wave function, extending DMRG to target the excited states efficiently is highly nontrivial.

Similar to the scheme in state-specific (SS) CASSCF, a straightforward DMRG way in calculating excited states is to still target the states of interests, respectively, by using different renormalized bases. Note that this SS-DMRG approach has the similar shortcomings of SS-CASSCF, that is, the nonorthogonality and root-flipping. The occurrence of nonorthogonality between wave functions of different electronic states is because the truncated renormalized bases of the ground and excited states become nonorthonormal now. To resolve this nonorthogonality issue, the excited states have to be optimized with a standard DMRG variation in the space orthogonal to the already optimized matrix product states (MPSs) of the lower-lying states. Therefore all lower-lying wave functions need to be calculated and sufficiently converged in order to optimize a given excited state. The root-flipping between different excited states occurs when the approximate wave function leaves the convergence basin of the target excited state and enters that of a different excited state.

In order to improve the stability of the nonlinear optimization and to prevent root flipping, the state-averaged (SA) scheme in CASSCF can be seemly adopted in DMRG.

In SA-CASSCF, one needs to solve for multiple eigenvectors ranging from the ground state to the excited state of interest, thus the averaged RDMs can be evaluated as

$$D_j^i = \sum_k w_k D_j^i(k), \tag{5.88}$$

$$D_{jl}^{ik} = \sum_k w_k D_{jl}^{ik}(k), \tag{5.89}$$

in which $D_j^i(k)$ and $D_{jl}^{ik}(k)$ are respectively the one- and two-electron RDMs computed with the multiconfigurational wave function $\left|\psi^k\right\rangle$ of the kth state

$$\left|\psi^k\right\rangle = \sum_I c_I^k |\Psi_I\rangle, \tag{5.90}$$

and w_k $(0 < w_k \leq 1)$ is its weight. Note that the weights $\{w_k\}$ must be normalized to make sure that

$$\sum_k w_k = 1. \tag{5.91}$$

There is no known optimal choice for w_k, but empirically it seems to be most reasonable to weigh states roughly equally. Consequently, one can use the averaged RDMs in MCSCF calculations to get a set of orbitals that works well with all of the states.

Instead of constructing the SA 1-RDM and 2-RDM in SA-CASSCF, SA-DMRG builds an SA RDM for the subsystem L (R) by

$$\hat{\rho}_S = \mathrm{Tr}_E \sum_k w_k \left|\psi^k\right\rangle\left\langle\psi^k\right|. \tag{5.92}$$

It is worth to clarify that, SA in DMRG is different from SA in CASSCF, although they are quite similar from a mathematic perspective. The former is used for the optimization of one MPS basis set for various states and the latter is used for obtaining one set of optimized MOs for different states. Therefore SA-DMRG and SA-CASSCF can be implemented separately or synergistically.

Targeting high-lying excited states in DMRG is even more challenging. Prominent examples include simulating X-ray photoelectron and absorption spectra as well as identifying dense vibrational spectroscopy levels. Conventional excited state approaches discussed above require solving all the eigenvectors with energies lower than the target state sequentially, which is usually computationally prohibitive. To overcome this limitation, various energy-specific diagonalization algorithms can be utilized in DMRG.

In ab initio DMRG, Dorando et al. (2007) employed a harmonic Davidson (HD) algorithm (Sleijpen and Van der Vorst, 2000), in which a shift-and-invert operator $\hat{\Omega}_\omega$ is introduced as

$$\hat{\Omega}_\omega = \hat{H}_\omega^{-1} = \left(\omega - \hat{H}\right)^{-1}, \tag{5.93}$$

to directly calculate harmonic Ritz approximations to excited eigenvalues and eigenvectors without the expensive costs to calculate all states between the ground state and excited state of interest. Here ω is an energy shift and $\hat{H}$ is the Hamiltonian in the same basis set. The operator $\hat{\Omega}_\omega$ maps the target excited state of the Hamiltonian $\hat{H}$ onto its ground state, as

$$|\psi\rangle = \sum_i c_i \big|\hat{H}_\omega \Phi_i\big\rangle. \tag{5.94}$$

Left projection with $\big\langle \Phi_j \hat{H}_\omega \big|$ yields a generalized eigenvalue problem,

$$\big\langle \Phi_j \hat{H}_\omega \big| \left(\hat{H}_\omega^{-1} - E_\omega^{-1}\right) \big| \hat{H}_\omega \Phi_i \big\rangle c_i = 0, \tag{5.95}$$

where E_ω^{-1} is the current approximation to $(\omega - E)^{-1}$. E_ω is known as a harmonic Ritz approximation to the corresponding eigenvalue of $\hat{H}_\omega$. The above equation can be simplified as

$$\sum_i \left[\langle \Phi_i | \hat{H}_\omega | \Phi_i \rangle - E_\omega^{-1} \langle \Phi_j \hat{H}_\omega | \hat{H}_\omega \Phi_i \rangle \right] c_i = 0. \tag{5.96}$$

Thus, instead of computing with the inverted operator, one can easily solve the eigenvalue equation for the noninverted operator $\hat{H}_\omega$ with a trial vector expanded in the basis $\{|\Phi_i\rangle\}$. The ground state of the operator $\hat{H}_\omega$ is the targeted excited state of the Hamiltonian $\hat{H}$. One may notice that the evaluation of matrix elements of $\big\langle \Phi_j \hat{H}_\omega | \hat{H}_\omega \Phi_i \big\rangle$ is exactly equivalent to the computation of $\big\langle \Phi_j \big| \hat{H}_\omega^2 \big| \Phi_i \big\rangle$. Dorando et al. (2007) also combined the HD procedure with state-averaging over nearby states in the spectrum and then assessed their numerical accuracy and convergence stability in DMRG-SCF calculations, on the low-lying excited states in oligoacenes ranging from naphthalene to pentacene. Results indicated that such a HD algorithm is particularly efficient for low-lying states; however, it is not stable in regions with a high density of states (Baiardi et al., 2019). The reason for this shortcoming lays in the fact that the HD algorithm introduces an approximation, specifically in the representation of the squared value of the Hamiltonian ($\hat{H}_\omega^2$) during the application of the shift-and-invert transformation to the local representation of the Hamiltonian.

To obtain a more robust convergence, the folded spectrum approach in conjunction with root-homing algorithms was implemented by Baiardi et al.

(2019) for targeting directly specific energy regions and therefore highly excited states in DMRG calculations. In the folded DMRG method, an alternative auxiliary operator $\hat{\Omega}_{\omega}^{\mathrm{F}}$ is introduced, as

$$\hat{\Omega}_{\omega}^{\mathrm{F}} = \left(\omega - \hat{H}\right)^{2}. \tag{5.97}$$

The lowest eigenvalue of the folded operator $\hat{\Omega}_{\omega}^{\mathrm{F}}$ is the eigenvalue of the Hamiltonian $\hat{H}$, which is closest to ω. The main advantage of $\hat{\Omega}_{\omega}^{\mathrm{F}}$ over $\hat{\Omega}_{\omega}$ is that, in $\hat{\Omega}_{\omega}^{\mathrm{F}}$ case, the spectral transformation is applied to the full Hamiltonian operator $\hat{H}$. The resulting modified operator is only later projected in the renormalized basis once, and, therefore, an additional spectral transformation of its renormalized representation is not required. This advantage increases the accuracy of the evaluation of the squared value of the Hamiltonian and accordingly the diagonalization convergence. It must be noticed that, the spectral range (i.e., the difference between the smallest and the largest eigenvalues) of the squared Hamiltonian is larger than the one of the original, non−squared Hamiltonian. This slows down the convergence of iterative diagonalization schemes. However, in regions with a high density of states, even if slower, the folded DMRG ensures a much smoother convergence of the energy of the target state. The robustness of this approach can be further increased by combination with a root-homing algorithm (Butscher and Kammer, 1976) to consistently follow the correct root during the optimization. Baiardi et al. (2019) illustrated their energy-specific variant of DMRG with a vibrational Hamiltonian that allows one to target highly excited states, with energies above $3000 \; \mathrm{cm}^{-1}$ in ethylene and to the dipeptide SarGly^{+}. Recently, Baiardi et al. (2022) also applied FEAST algorithm (Polizzi, 2009) to DMRG and showed that DMRG[FEAST] enables the stable optimization of both low- and high-energy vibrationally excited states without the necessity of estimating a priori the energy of the target excited states and calculating powers of the Hamiltonian.

In addition to solve the time-independent Schrödinger equation by DMRG to obtain the eigenvalues and eigenvectors, it is also possible to obtain the excited state information by calculating the spectral functions directly in the frequency domain or performing Fourier transformations of the time correlation functions from a solution of time-dependent Schrödinger equation. The principles and progresses of DMRG in frequency space- and time-dependent DMRG (TD-DMRG) will be in detail discussed in Chapter 7 and Chapter 8, respectively.

5.5   Analytic gradient and geometry optimization

All the methods and implementations that we have discussed so far are appropriated to fixed molecular geometries. In practical chemical researches,

these geometries are often stable equilibrium structures with the lowest energy or saddle-point structures in transition states of chemical reactions in a potential energy surface (PES). Therefore one of the important tasks of quantum chemistry methods is to optimize the geometry of molecules to find those stationary structures with

$$\frac{\partial E}{\partial a_i} = 0, \tag{5.98}$$

in which $\{a_i\}$ are nuclear coordinates given that nuclei make up the skeleton of molecules. The energy gradients with respect to nuclear coordinates can be computed numerically or analytically. Numerical gradients are available for any quantum chemistry method as long as a set of energies and corresponding geometries are presented. At the same time, although preferred owing to their low computational cost and numerical stability, analytic energy gradients introduced by Pulay (1969) are only available in some methods.

In this section, we are focusing on the evaluation of analytic energy gradients in DMRG methods and the optimization of molecular geometries. As the energy E can be computed with the 1- and 2-RDMs as well as MO integrals, as shown in Eq. 5.18, the first derivative can be evaluated by

$$\frac{\partial E}{\partial a} = \sum_{kl} \frac{\partial D_l^k}{\partial a} h_{kl} + \sum_{kl} D_l^k \frac{\partial h_{kl}}{\partial a} + \frac{1}{2} \sum_{klmn} \frac{\partial D_{ln}^{km}}{\partial a} g_{klmn} + \frac{1}{2} \sum_{klmn} D_{ln}^{km} \frac{\partial g_{klmn}}{\partial a}, \tag{5.99}$$

in which the derivative of the core energy is trivial and thus omitted. It is clear that the CI coefficients as well as the RDMs do not depend on the geometry of molecules, thus the first and third terms in Eq. 5.99 vanish according to Hellmann−Feynman theorem. Therefore Eq. 5.99 can be simplified as

$$\frac{\partial E}{\partial a} = \sum_{kl} D_l^k \frac{\partial h_{kl}}{\partial a} + \frac{1}{2} \sum_{klmn} D_{ln}^{km} \frac{\partial g_{klmn}}{\partial a}, \tag{5.100}$$

which states that we have to compute the first derivatives of one- and two-electron MO integrals. Since the MOs are linear combinations of AOs, as we have introduced in the first section of this chapter, the one- and two-electron MO integrals can be obtained, respectively, by

$$h_{kl} = \sum_{\mu\nu} C_\mu^k C_\nu^l h_{\mu\nu}, \tag{5.101}$$

$$g_{klmn} = \sum_{\mu\nu\rho\sigma} C_\mu^k C_\nu^l C_\rho^m C_\sigma^n g_{\mu\nu\rho\sigma}. \tag{5.102}$$

Note that the indices k, l, m, n denote MOs while the Greek characters μ, ν, ρ, σ denote atomic orbitals. The first derivative of one-electron MO integrals can be evaluated as

$$\frac{\partial h_{kl}}{\partial a} = \frac{\partial}{\partial a} \sum_{\mu\nu} C_\mu^k C_\nu^l h_{\mu\nu} = \sum_{\mu\nu} \left(\frac{\partial C_\mu^k}{\partial a} C_\nu^l h_{\mu\nu} + C_\mu^k \frac{\partial C_\nu^l}{\partial a} h_{\mu\nu} + C_\mu^k C_\nu^l \frac{\partial h_{\mu\nu}}{\partial a} \right),$$

(5.103)

in which the derivative of MO coefficients $\left\{ C_\mu^k \right\}$ can be computed by

$$\frac{\mathrm{d}C_\mu^k}{\mathrm{d}a} = \sum_r U_{rk} C_\mu^r.$$

(5.104)

Thus Eq. 5.103 can be simplified as

$$\frac{\partial h_{kl}}{\partial a} = \sum_{\mu\nu} \sum_r \left(U_{rk} C_\mu^r C_\nu^l h_{\mu\nu} + U_{rl} C_\mu^k C_\nu^r h_{\mu\nu} \right) + \sum_{\mu\nu} C_\mu^k C_\nu^l \frac{\partial h_{\mu\nu}}{\partial a}$$
$$= \sum_r (U_{rk} h_{rl} + U_{rl} h_{kr}) + \sum_{\mu\nu} C_\mu^k C_\nu^l \frac{\partial h_{\mu\nu}}{\partial a},$$

(5.105)

in which the first derivatives of one-electron AO integrals $\left\{ \partial h_{\mu\nu}/\partial a \right\}$ can be computed analytically, because the AO are usually represented with Gaussian primitive functions. Similarly, we can compute the first derivatives of two-electron MO integrals, as

$$\frac{\partial g_{klmn}}{\partial a} = \sum_r (U_{rk} g_{rlmn} + U_{rl} g_{krmn} + U_{rm} g_{klrn} + U_{rn} g_{klmr})$$
$$+ \sum_{\mu\nu\rho\sigma} C_\mu^k C_\nu^l C_\rho^m C_\sigma^n \frac{\partial g_{\mu\nu\rho\sigma}}{\partial a}.$$

(5.106)

Inserting Eqs. 5.105 and 5.106 into Eq. 5.100 yields (Yamaguchi et al., 1994)

$$\frac{\partial E}{\partial a} = \sum_{\mu\nu} D_\nu^\mu \frac{\partial h_{\mu\nu}}{\partial a} + \sum_{\mu\nu\rho\sigma} D_{\nu\sigma}^{\mu\rho} \frac{\partial g_{\mu\nu\rho\sigma}}{\partial a}$$
$$- 2 \sum_{\mu\nu} \sum_{k \geq l} \left(1 - \frac{\delta_{kl}}{2} \right) C_\mu^k C_\nu^l X_k^l \frac{\partial S_{\mu\nu}}{\partial a} + 2 \sum_{k \geq l} U_{kl} \left(X_l^k - X_k^l \right),$$

(5.107)

in which

$$X_l^k = \sum_r h_{kr} D_l^r + \sum_{rsp} g_{krsp} D_{rp}^{ls}$$

(5.108)

is the Lagrangian matrix in the generalized Brillouin's theorem (Levy and Berthier, 1968), and

$$S_{kl} = \langle k|l \rangle = \sum_{\mu\nu} C_\mu^k S_{\mu\nu} C_\nu^l \qquad (5.109)$$

is the overlap matrix of the MOs k and l. Note that the orthonormality condition

$$U_{kl} + U_{lk} + S_{kl} = 0 \qquad (5.110)$$

is used to derive Eq. 5.107. The evaluation of the matrix U in Eq. 5.107 takes more effort. The matrix U is actually the first-order orbital response. Generally, it can be computed with the coupled-perturbed HF method (Gerratt and Mills, 1968). However, in MCSCF calculations, the correlated wave function energy itself is stationary with respect to orbital variations, which leads to

$$X_l^k - X_k^l = 0, \qquad (5.111)$$

which makes that the matrix U can be safely ignored. Therefore the analytic energy gradients in MCSCF methods (including the DMRG-SCF) can be evaluated by

$$\frac{\partial E}{\partial a} = \sum_{\mu\nu} D_\nu^\mu \frac{\partial h_{\mu\nu}}{\partial a} + \sum_{\mu\nu\rho\sigma} D_{\nu\sigma}^{\mu\rho} \frac{\partial g_{\mu\nu\rho\sigma}}{\partial a} - 2 \sum_{\mu\nu} \sum_{k \geq l} \left(1 - \frac{\delta_{kl}}{2}\right) C_\mu^k C_\nu^l X_k^l \frac{\partial S_{\mu\nu}}{\partial a}. \qquad (5.112)$$

The above scheme was employed in SS-DMRG-CI, SS-DMRG-SCF, and SS-DMRG-CASPT2 calculations (Hu and Chan, 2015; Nakatani and Guo, 2017). Thence, an approximate SA approach was proposed by Freitag et al. (2019). In the SA case, the SA energy is defined as

$$E^{\text{SA}} = \sum_k w_k E_k = \sum_k w_k \langle \psi_k | \hat{H} | \psi_k \rangle. \qquad (5.113)$$

The optimization procedure in SA-CASSCF ensures that the SA energy, but not the individual SS energies, is variational with respect to both orbital rotations and CI coefficients. After that, the gradient with respect to nuclear coordinates for a specific state Θ can be evaluated as (Snyder Jr et al., 2015; Snyder Jr et al., 2017)

$$\frac{\partial E^\Theta}{\partial a} = \sum_{kl} D_l^k(\Theta)^e \frac{\partial h_{kl}}{\partial a} + \sum_{klmn} D_{klmn}^{\Theta,e} \frac{\partial g_{klmn}}{\partial a} - \sum_{kl} X_l^k(\Theta)^e \frac{\partial S_{kl}}{\partial a}, \qquad (5.114)$$

where the effective 1- and 2-RDMs are, respectively, defined as

$$D_l^k(\Theta)^e = D_l^k(\Theta) + \tilde{D}_l^k + \overline{D}_l^k, \qquad (5.115)$$

$$D_{ln}^{km}(\Theta)^e = D_{ln}^{km}(\Theta) + \tilde{D}_{ln}^{km} + \overline{D}_{ln}^{km}, \quad (5.116)$$

and the quantities with tildes and bars are respectively the orbital and CI contributions to the RDMs. All of these quantities as well as $X_l^k(\Theta)^e$ are obtained in the coupled optimization of orbital rotations and CI coefficients.

Evaluating energy gradients is a prerequisite for geometry optimization. To optimize the geometry of molecules within the DMRG-SCF method, one can construct the related matrices and quantities in Eqs. 5.112 or 5.114 after the optimized wave function and MOs are obtained from a DMRG-SCF calculation and subsequently minimize the energy E with respect to the nuclear coordinates $\{a\}$ to make $\partial E/\partial a = 0$. Thenceforth, the geometry of the molecule is updated, one has to reconstruct the one- and two-electron AO integrals and start a new DMRG-SCF calculation. Obviously, optimizing molecular geometries with DMRG-SCF method is extremely expensive, therefore few but significant applications (Liu et al., 2013; Ma, 2020) have been reported.

5.6   Molecular spectra

Molecular spectra result from either the absorption or the emission of electro-magnetic radiation as a molecule undergoes transition from one quantized energy state to another. There are two primary sets of interactions that contribute to observed molecular spectra. The first involves the internal motions of the nuclear framework of the molecule and the electrostatic forces among the nuclei and electrons, resulting in three categories of molecular energy levels with a decreasing order of magnitude: electronic, vibrational, and rotational. The interaction of electromagnetic radiation with these quantum energy levels constitutes the basis for electron spectroscopy, visible, infrared and ultraviolet (UV) spectroscopies, Raman spectroscopy, gas-phase microwave spectroscopy, etc. The second encompasses the interactions of nuclear magnetic and electro-static moments with the electrons and with each other, forming the basis for nuclear magnetic resonance spectroscopy, electron spin resonance (ESR) spectroscopy, nuclear quadrupole resonance spectroscopy, etc.

As ab initio DMRG and DMRG-SCF have been shown to be able to give accurate characterizations of the electronic structures of the ground and excited states in strongly correlated systems, it is straightforward to apply them to investigate the molecules' low-energy electronic spectrum. For example, Sharma et al. (2014) computed the individual ground- and excited-state energy levels of [2Fe−2S] and [4Fe−4S] clusters by DMRG calculations with up to 36 active orbitals, suggesting the low-energy spectrum is dense due to the presence of a large number of $d - d$ excited states arising from both orbital transitions and spin recouplings. This finding was later supported by indirect experimental measurements from iron L-edge $2p3d$

resonant inelastic X-ray scattering (Van Kuiken et al., 2018). Cho et al. (2019) further computed the UV absorption spectra and the stimulated X-ray Raman spectroscopy (SXRS) for [2Fe − 2S] complexes, which complement each other by accessing different parts of the electronic spectrum and together can effectively probe the dense $d - d$ electronic states in the Fe − S clusters. The simulated spectra presented clear signatures of the theoretically predicted dense low-lying excited states within the $d - d$ manifold. Furthermore, the difference in spectral intensity between the absorption-active and Raman-active states provides a potential mechanism to selectively excite states by a proper tuning of the excitation pump, to access the electronic dynamics within this manifold. In Cho et al. (2019)'s work, the UV absorption spectrum intensity $S_L(\omega)$ was calculated from the transition dipole moment $\boldsymbol{\mu}_{eg}$ between the ground state (g) and the excited state (e), transition frequency ω_{eg}, and a dephasing rate $\Gamma_{eg} = 0.014$ eV (Fig. 5.1).

$$S_L(\omega) = \sum_e \frac{\left|\boldsymbol{\mu}_{eg}\right|^2 \Gamma_{eg}}{\left(\omega - \omega_{eg}\right)^2 + \Gamma_{eg}^2}. \tag{5.117}$$
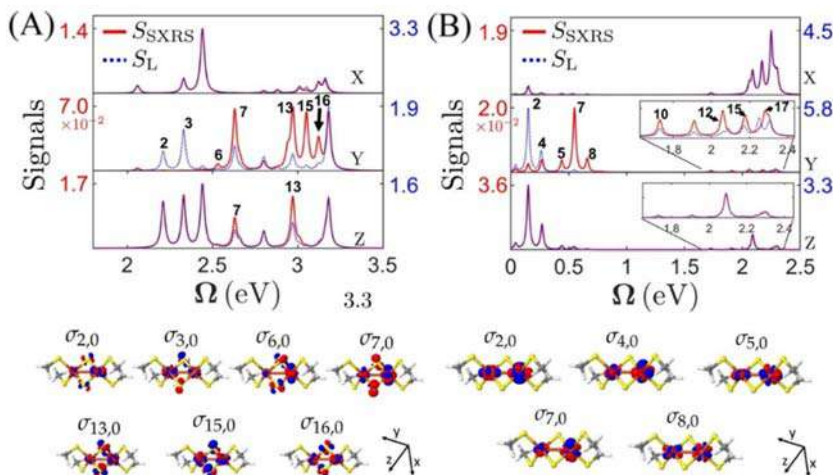
FIGURE 5.1 (A) SXRS spectra S_{SXRS} (solid line) and absorption spectra S_L (dashed line) of (A) Fe(III)−Fe(III) and (B) Fe(III)−Fe(II) dimers. (Top) Calculated spectra from X, Y, and Z polarized light. [See bottom of (B) for the axes]. (Bottom) Selected the TCDs are shown. $\Gamma_{eg} = 0.014$ eV for all states. Note that the absorption and SXRS spectra are normalized. Consequently, the strength of each spectroscopy in different directions can be compared, but SXRS and absorption strengths cannot be directly compared. *SXRS*, stimulated X-ray Raman spectroscopy; *TCDs*, Transition charge densities. *Reproduced from Cho, D., Rouxel, J. R., Mukamel, S., Chan, G. K.-L., Li, Z., 2019. Stimulated X-ray Raman and absorption spectroscopy of iron−sulfur dimers. J. Phys. Chem. Lett. 10, 6664−6671. https://doi.org/10.1021/acs.jpclett.9b02414, with permission from American Chemical Society.*

Moreover, the excited state calculations can be also extended to the simulation of molecule's photoelectron spectra. Pham and Nguyen (2018) used restricted active-space second-order PT and DMRG-CASPT2 in conjunction with density functional theory calculations to simulate the photoelectron spectra of the anion $Cr_2O_2^{-}$. Transitions from the anionic ground state $^{10}A_g$ was found to cause most of visible bands in the photoelectron spectra, while the first band with low intensity was determined to arise from a transition starting from the nearly degenerate state $^{10}B_{2g}$.

DMRG can be also used for simulating vibrational spectroscopies by treating a vibrational Hamiltonian. Rakhuba and Oseledets (2016) computed the vibrational spectra (84 states) of acetonitrile molecule CH_3CN by using DMRG in the discrete variable representation scheme with a quarticly coupled 12-dimensional vibrational Hamiltonian. Baiardi et al. (2017) further proposed to exploit vibrational DMRG (vDMRG) to optimize vibrational wave functions expressed as MPS to show the complete fingerprint region of the sarcosyn-glycin dipeptide. In this work, the authors used an approximate form of the Watson Hamiltonian, in which only the second-order Coriolis terms are included and higher order terms in the expansion of the inertia tensor are neglected.

$$
\begin{aligned}
\hat{H}_{\text{vib}} = & \sum_{i=1}^{L} \omega_i \left(\hat{b}_i^\dagger \hat{b}_i + \frac{1}{2} \right) \\
& + \frac{1}{12\sqrt{2}} \sum_{ijk=1}^{L} \Phi_{ijk} \left(\hat{b}_i^\dagger + \hat{b}_i \right) \left(\hat{b}_j^\dagger + \hat{b}_j \right) \left(\hat{b}_k^\dagger + \hat{b}_k \right) \\
& + \frac{1}{96} \sum_{ijkl=1}^{L} \Phi_{ijkl} \left(\hat{b}_i^{\ \dagger} + \hat{b}_i \right) \left(\hat{b}_j^\dagger + \hat{b}_j \right) \left(\hat{b}_k^\dagger + \hat{b}_k \right) \left(\hat{b}_l^\dagger + \hat{b}_l \right) \\
& + \sum_{ijkl=1}^{L} \sum_{\tau}^{x,y,z} B^\tau \zeta_{ij}^\tau \zeta_{kl}^\tau \sqrt{\frac{\omega_j \omega_l}{\omega_i \omega_k}} \left(\hat{b}_i^{\ \dagger} + \hat{b}_i \right) \left(\hat{b}_i^\dagger - \hat{b}_j \right) \left(\hat{b}_k^\dagger + \hat{b}_k \right) \left(\hat{b}_l^\dagger - \hat{b}_l \right)
\end{aligned}
$$

(5.118)

Here, ω_i is the harmonic frequency for the ith vibrational normal mode, while $\hat{b}_i$ and $\hat{b}_i^\dagger$ are the bosonic annihilation and creation operators for this mode. B^τ give the rotational constants and ζ_{ij}^τ indicate the Coriolis coupling constants. In a fourth-order (quartic) Taylor expansion of the potential, Φ_{ijk} and Φ_{ijkl} are the third- and fourth-order reduced force constants, respectively. Those can be defined in terms of the third- and fourth-order partial derivatives, k_{ijk} and k_{ijkl}, of the PES,

$$
\Phi_{ijk} = \frac{k_{ijk}}{\sqrt{\omega_i \omega_j \omega_k}}, \quad \Phi_{ijkl} = \frac{k_{ijkl}}{\sqrt{\omega_i \omega_j \omega_k \omega_l}}.
$$

(5.119)
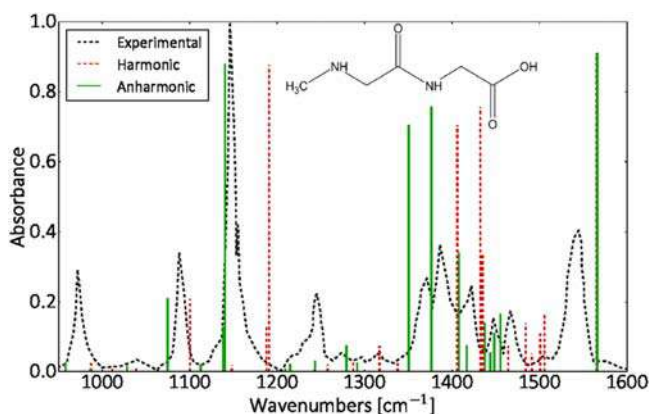
FIGURE 5.2 Experimental and theoretical infrared spectrum of SarGly$^+$ computed from harmonic (*red dashed lines*) and anharmonic vDMRG frequencies (*green solid lines*). *Reproduced from Baiardi, A., Stein, C. J., Barone, V., Reiher, M., 2017. Vibrational density matrix renormalization group. J. Chem. Theory Comput. 13, 3764−3777. https://doi.org/10.1021/acs. jctc.7b00329, with permission from American Chemical Society.*

As a generalization to support also higher order terms is straightforward, calculations with fifth- and sixth-order potentials are also presented in this work. By virtue of representing this Hamiltonian compactly as an MPO, highly accurate, converged results can be obtained with vDMRG and a moderate number m of renormalized block states, as shown in Fig. 5.2.

Later Baiardi et al. (2019) further extended vDMRG to highly excited vibrational states of ethylene via the shift-and-invert and folded auxiliary operator techniques (see Section 5.4), in order to target specific energy regions and therefore highly excited states. It was also demonstrated that one can accurately calculate prominent spectral features of large molecules such as the sarcosine-glycine dipeptide. At the same time, the computation of vibrational spectrum of acetonitrile (CH_3CN) with tree tensor network states (TTNSs) was also reported by Larsson (2019). This approach showed much faster convergences in TTNS, than for multilayer multiconfiguration time-dependent Hartree (ML-MCTDH)-based optimization and found no major advantage of the more general TTNS over MPS in this case.

Resonance Raman (RR) spectroscopy is a powerful and versatile technique for the study of both vibrational and electronic structures of chromophoric molecular systems. RR can enhance the Raman scattering intensity by a factor of 10^2-10^6 and improves signal-to-noise ratio. The enhanced Raman scattering means shorter exposure times can be used, allowing much faster spectral acquisition times. In addition, samples at extremely low concentrations can easily be studied. Ma et al. (2017b) presented a RR spectroscopy simulation of the nucleobase uracil by means of DMRG-SCF. The relative intensity for the fundamental transition of the jth normal mode

$I_j^{1 \leftarrow 0}(\omega_s)$ is given by

$$I_j^{1 \leftarrow 0}(\omega_s) = \omega_L \omega_s{}^3 \left| \boldsymbol{\mu}_{0n}^{\mathrm{el}} \right|^4 \left(\frac{\Delta_j{}^2}{2} \right) \left| \Phi(\omega_L) - \Phi(\omega_s) \right|^2. \qquad (5.120)$$

Here ω_L represents the laser excitation frequency and $\omega_s = \omega_L - \Omega_j$ indicates the frequency of the scattered light, where Ω_j is the harmonic vibrational frequency of the jth normal mode. $\boldsymbol{\mu}_{0n}^{\mathrm{el}}$ expresses the electronic transition dipole moment to the nth excited state, and $\Phi(\omega)$ gives a complex function containing the information about the intensity shift function and its Kramers−Kronig transform. (Neugebauer and Hess, 2004) Δ_j is the normal-mode displacement in the excited-state equilibrium structure, which can be calculated by taking the partial derivative of the excited-state electronic energy $E_{\mathrm{el}}^{\mathrm{ex}}$ with respect to a dimensionless ground-state normal coordinate q_j at the ground-state equilibrium position,

$$\left(\frac{\partial E_{\mathrm{el}}^{\mathrm{ex}}}{\partial q_j} \right)_{q_j=0} = \Omega_j \left(q_j - \Delta_j \right)|_{q_j=0} = -\Omega_j \Delta_j. \qquad (5.121)$$

In this work, Ma et al. calculated the excited-state energy derivatives with respect to the ground-state normal modes for the S_2 state from analytic Cartesian gradients that are subsequently transformed into the basis of normal coordinates (Fig. 5.3).

Recently, ab initio DMRG calculations were also applied to the simulation of electron paramagnetic resonance (EPR) spectra, sometimes also known as ESR, which is a central spectroscopic tool in the study of paramagnetic (unpaired electron) compounds. Electrons, like nuclei, have charge and spin, therefore have a magnetic moment, which make them susceptible to a magnetic field. An important parameter in interpreting EPR spectra is the hyperfine coupling A-tensor, which measures the hyperfine interactions between the electron and nuclear spin magnetic moments. Lan et al. (2014, 2015) applied DMRG-SCF to the accurate prediction of the isotropic hyperfine coupling constant (HFCC) of a series of diatomic $^2\Sigma$ radicals (BO, CO^+, CN, and AlO), vinyl (C_2H_3) radical, and a set of $4d$ transition-metal radicals consisting of Ag atom, PdH, and RhH_2. For the scalar-relativistic effects therein, they initially derived and implemented the Douglas−Kroll−Hess (DKH) hyperfine coupling operators up to the third order (DKH3) by using the direct transformation scheme. Good agreement between their calculated isotropic HFCC values and experiment was achieved.

Another important parameter in describing EPR spectra is the proportionality between the effective magnetic moment of the unpaired electron and its spin, namely, the g-tensor, reporting on the electronic environment of the electron. Knecht et al. (2016) presented a state-interaction (SI) approach for MPS wave functions in a nonorthogonal MO basis, allowing to calculate spin − orbit coupling (SOC) matrix elements between arbitrary electronic
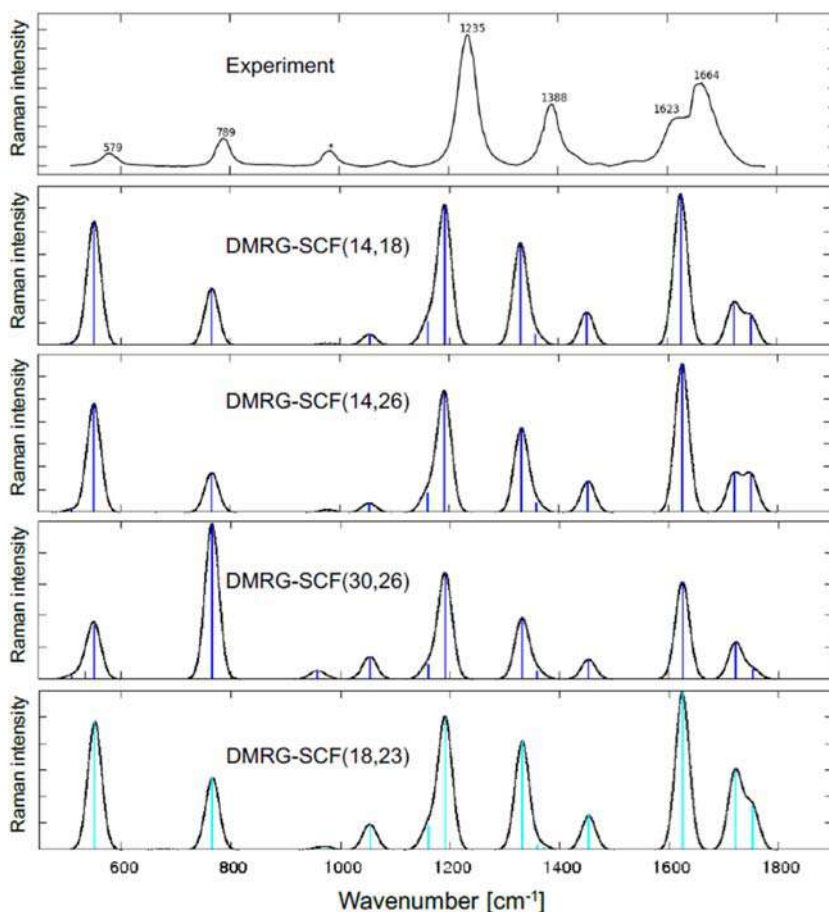
FIGURE 5.3 RR spectra of uracil in the gas phase. Intensities are given in arbitrary units. *RR*, Resonance Raman. *Reproduced from Ma, Y., Knecht, S., Reiher, M., 2017b. Multiconfigurational effects in theoretical resonance Raman spectra. ChemPhysChem, 18, 384. https://doi.org/10.1002/cphc.201601072, with permission from Chemistry Europe.*

states, provided that they share the same one-electron basis functions and size of the active orbital space, respectively. Based on the eigenstates of the SOC operator, it becomes straightforward to compute properties such as g-factors, as numerical calculations have shown in the case of g-factors for f^1- and f^2-type actinide complexes were presented. Sayfutyarova and Chan (2018) later presented a related DMRG implementation to obtain g-tensors based on a SI spin−orbit (SISO) coupling DMRG formalism. Its numerical tests were demonstrated on the TiF_3 and $CuCl_4^{2-}$ complexes, a [2Fe− 2S] model of the active center of ferredoxins, and a Mn_4CaO_5 model of the S_2 state of the oxygen evolving complex, enlightening the prospects of

determining g-tensors in multireference calculations with many open shell orbitals. Recently, Freitag et al. (2021) further presented two modifications to the original formulation of the MPS-SI method, that is, the omission of the quadratic term in the operator for counterrotating the MPS and decreasing the maximum bond dimension of the intermediate and the final counterrotated MPS. For an example of a platinum azide complex, the approximations resulted in a 63-fold reduction in computational time compared to the original method for wavefunction overlaps and SOCs, while still maintaining numerical accuracy.

As we mentioned at the end of Section 5.4, instead of using DMRG, it is also possible to describe the dynamical response properties and molecular spectra by implementing DMRG calculations in frequency space or TD-DMRG simulations in time space. Principles of those methods are properly discussed in Chapter 7 and Chapter 8, respectively. A few successful numerical examples by these methods for realistic chemical systems include the vibrationally resolved vibronic absorption and fluorescence spectrum of pyrazine (Baiardi and Reiher, 2019), covalently linked tetracene dimer (Mardazad et al., 2021), distyrylbenzenes (DSB) H-aggregate (Ren et al., 2018), and perylene bisimide (PBI) J-aggregate (Jiang et al., 2020), as well as the two-dimensional ultrafast Fourier transform electronic spectroscopy of an oligothiophene/fullerene hetero-junction (Yao et al., 2018).

5.7 Beyond Born−Oppenheimer approximation

The Born−Oppenheimer approximation (BOA) is one of the basic concepts underlying the description of the quantum states of molecules. This approximation makes it possible to separate the motion of the nuclei and the motion of the electrons, and forms the basis for most electronic structure methods. However, this approximation breaks down when the considered two or more excited electronic states are energetically close or have nonnegligible nonadiabatic couplings (NACs) at some points. Going beyond BOA to describe the properties of non-Born − Oppenheimer (also called nonadiabatic) processes requires a quantum mechanical description of the nuclei at a full quantum, mixed quantum-classical, quasi-classical, or semi-classical level.

Nonadiabatic dynamics can be simulated quantum mechanically in the electronically adiabatic representation or in a diabatic representation. Adiabatic electronic wave functions are eigenstate solutions of the electronic Schrödinger equation with BOA. In an adiabatic representation, electronic states are coupled by the action of the nuclear momentum and nuclear kinetic energy operators acting on the electronic wave functions; in approximate treatments, one usually keeps only the nuclear momentum coupling, and the resulting vector coupling matrix elements, also called NACs. For two electronic eigenstates

Θ and Λ, the NAC can be evaluated as

$$g = \left\langle \Theta \left| \frac{\partial}{\partial x} \right| \Lambda \right\rangle, \qquad (5.122)$$

which is similar to the computation of geometrical gradients (see Section 5.5). Freitag et al. (2019) proposed an approximate scheme for calculating analytical gradients and NACs for SA DMRG-SCF wave functions. They demonstrated the feasibility of this method on performing a conical intersection optimization of 1,2-dioxetanone, providing a basis for future approximate nonadiabatic dynamics studies where NACs require large active space electronic structure description.

For describing systems with strong nuclear quantum effect, multicomponent quantum chemical methods attempt to solve the full time-independent Schrödinger equation for electrons and specified nuclei (typically hydrogen nuclei) without invoking the BOA (Pavošević et al., 2020). Considering both fermionic (e.g., electrons and protons) and bosonic (e.g., He^4 nuclei) particles may be treated at the same level, the second-quantization form of a general nonrelativistic Schrödinger Hamiltonian in multicomponent quantum chemistry can be written as (Muolo et al., 2020):

$$
\begin{aligned}
\hat{H} = & \sum_i \sum_{\mu\nu\sigma} t^{(i)}_{\mu\nu} \hat{a}^\dagger_{i\mu\sigma} \hat{a}_{i\nu\sigma} + \sum_i \sum_{\mu\nu} t^{(i)}_{\mu\nu} \hat{b}^\dagger_{i\mu} \hat{b}_{i\nu} \\
& + \frac{1}{2} \sum_{ij} \sum_{\mu\nu\sigma} \sum_{\kappa\lambda\tau} \left(V^{(ij)}_{\mu\kappa\nu\lambda} + T^{(ij)}_{\mu\kappa\nu\lambda} \right) \hat{a}^\dagger_{i\mu\sigma} \hat{a}^\dagger_{j\nu\tau} \hat{a}_{j\lambda\tau} \hat{a}_{i\kappa\sigma} \\
& + \frac{1}{2} \sum_{ij} \sum_{\mu\nu} \sum_{\kappa\lambda} \left(V^{(ij)}_{\mu\kappa\nu\lambda} + T^{(ij)}_{\mu\kappa\nu\lambda} \right) \hat{b}^\dagger_{i\mu} \hat{b}^\dagger_{j\nu} \hat{b}_{j\lambda} \hat{b}_{i\kappa} \\
& + \sum_{ij} \sum_{\mu\nu\sigma} \sum_{\kappa\lambda} \left(V^{(ij)}_{\mu\kappa\nu\lambda} + T^{(ij)}_{\mu\kappa\nu\lambda} \right) \hat{a}^\dagger_{i\mu\sigma} \hat{b}^\dagger_{j\nu} \hat{b}_{j\lambda} \hat{a}_{i\kappa\sigma}.
\end{aligned}
\qquad (5.123)
$$

The indices i and j denote fermionic or bosonic particles and μ, $\upsilon, \kappa,$ and λ are for the orbital basis. $\hat{a}^\dagger (\hat{b}^\dagger)$ and $\hat{a}$ $(\hat{b})$ represent the creation and annihilation operators for the fermions (bosons), respectively, while $\sigma(\tau)$ denotes different spin-up and spin-down states. $t^{(i)}_{\mu\nu}$, $T^{(ij)}_{\mu\kappa\nu\lambda}$, and $V^{(ij)}_{\mu\kappa\nu\lambda}$ express the one-body kinetic energy of a particle of type i minus the one-body part of the kinetic energy of the center-of-mass (COM), the matrix elements of the two-body part of the kinetic energy operator of the COM and the integrals of the Coulomb interaction between particles of two types i and j calculated for the orbitals $\phi_{i\mu}$ and $\phi_{i\kappa}$ for particle type i, and $\phi_{j\nu}$ and $\phi_{j\lambda}$ for particle type j, respectively.

Yang and White (2019) presented a first multicomponent DMRG study of 1D diatomic molecule aggregates where a parametrized "Coulomb" interaction model potential was used. They found that 1D diatomic molecules with spin-1/2
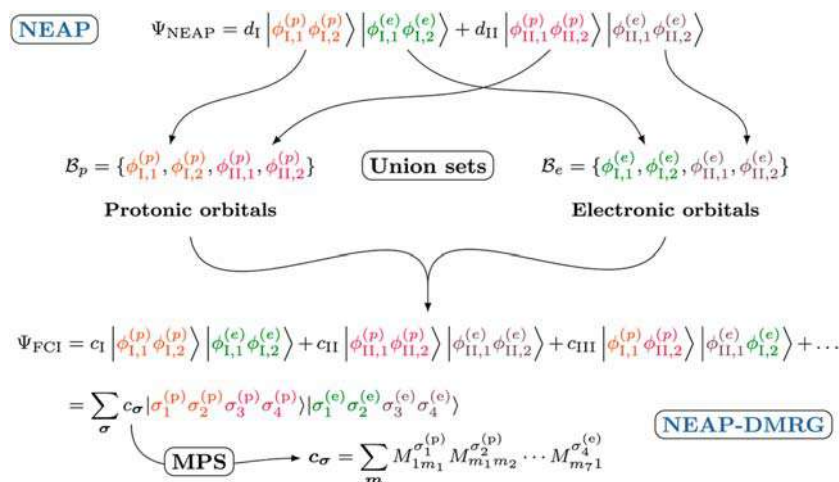
FIGURE 5.4 Schematic definition of the NEAP-DMRG wave function for the $H_2 = \{e^-, e^-,$ $p^+, p^+\}$ molecular system in terms of the nonorthogonal stochastically optimized NEAP orbitals. A generalized CI expansion (top of the figure) is considered to define the orbital union sets for each particle type. An FCI expansion is defined in the basis of these union sets and then expressed as an MPS (bottom of the figure). *CI*, Configuration interaction; *FCI*, full configuration interaction; *MPS*, matrix product state; *NEAP-DMRG*, nuclear-electronic all-particle DMRG. *Reproduced from Muolo, A., Baiardi, A., Feldmann, R., Reiher, M., 2020. Nuclear-electronic all-particle density matrix renormalization group. J. Chem. Phys. 152, 204103. https://doi.org/10.1063/5.0007166, with permission from American Institute of Physics.*

nuclei in the spin triplet state will unbind when the mass of the nuclei reduces to only a few times larger than the electron mass, while the molecule with nuclei in the singlet state always binds. Later, Muolo et al. (2020) introduced the nuclear-electronic all-particle DMRG (NEAP-DMRG) method at ab initio level for the first time (Fig. 5.4). Their efficient parameterization of the total wave function as an MPS enables NEAP-DMRG to accurately approximate the FCI energies of molecular systems (H_2, H_3^+, and BH_3) with more than three nuclei and 12 particles in total, which is currently a major challenge for other multi-component approaches. The NEAP algorithm relies on a fully stochastic optimization of all wave function parameters, a task that becomes challenging for large basis sets. Recently, Feldmann et al. (2022)'s multicomponent DMRG calculations adopted MOs which are expressed as a linear combination of preoptimized basis sets and optimized by nuclear-electronic HF (NEHF) (Pettitt, 1986). This scheme makes the computational less demanding. They demonstrated that NEHF-DMRG reproduced the reference ground-state total energy and proton density of the $HeHHe^+$ molecular ion. In addition, for the hydrogen cyanide (HCN) system, more accurate ground-state energy and proton density than state-of-the-art results were also obtained with larger basis sets were obtained.

5.8 Applications

Ab initio DMRG and DMRG-SCF methods together with post-DMRG treatments to further account for dynamic and/or environmental effect(s) (see Chapter 6) provide new powerful tools in multiconfigurational quantum chemistry. In recent years, they have been successfully applied to the electronic structure studies in various strongly correlated molecular systems with large active spaces, ranging from quasi-1D π-conjugated oligomers (polyene, polyacene, polyphenylenecarbenes, graphene nanoribbon) and transition metal complexes to heavy element chemistry and photochemistry. To the best of our knowledge, the currently largest solved CASs for DMRG-CASCI, DMRG-SCF, and post-DMRG are (30e, 108o) for a benzene molecule (Zhai and Chan, 2021), (120e, 77o) for $[Fe_8S_7]$ P-cluster (Li et al., 2019), and (42e, 42o) for an 8×8 hydrogen square lattice (Song et al., 2020), respectively. A complete overview of these numerous applications is certainly out of the scope of the present section; our aim is rather to show the potential and applicability of ab initio DMRG. Below we show two representative application examples, the electronic landscape of the P-cluster of nitrogenase (Li et al., 2019) and mechanism for photochromic ring-opening reaction of spiropyran (Liu et al., 2013).

5.8.1 Electronic landscape of the P-cluster of nitrogenase

The Fe$-$S clusters of nitrogenase, namely, the $[Fe_4S_4]$ Fe cluster of the Fe protein, and the $[Fe_8S_7]$ P-cluster and $[MoFe_7S_9C]$ FeMo cofactor of the MoFe protein, are revealed to work as the active sites for electron transfer and reduction in biological nitrogen fixation. Although the atomic structure of the P-cluster has been experimentally resolved, relating the structure to the chemical function requires electronic structure knowledge about the basic oxidation, spin states, and interpretation of the experimental spectra (particularly in magnetic spectroscopies such as EPR) that also requires microscopic models of the low-energy, spin-coupled, many-electron quantum states and their spin and charge distributions. By implementing DMRG calculations using active spaces with up to 77 orbitals, Li et al. (2019) presented the first ab initio electronic structure characterization of the P-cluster of nitrogenase at the many-electron level that can qualitatively capture the richness of the low-energy landscape. They reported on a plethora of low-energy states across the resting state (P^N), the one-electron oxidized state (P^{1+}), and the two-electron oxidized state (P^{OX}) clusters and their composition in terms of the local atomic configurations, spins, and spin-couplings. The clusters were found to exist in quantum superpositions of spin configurations with nonclassical spin correlations, complicating interpretation of magnetic spectroscopies, whereas the charges are
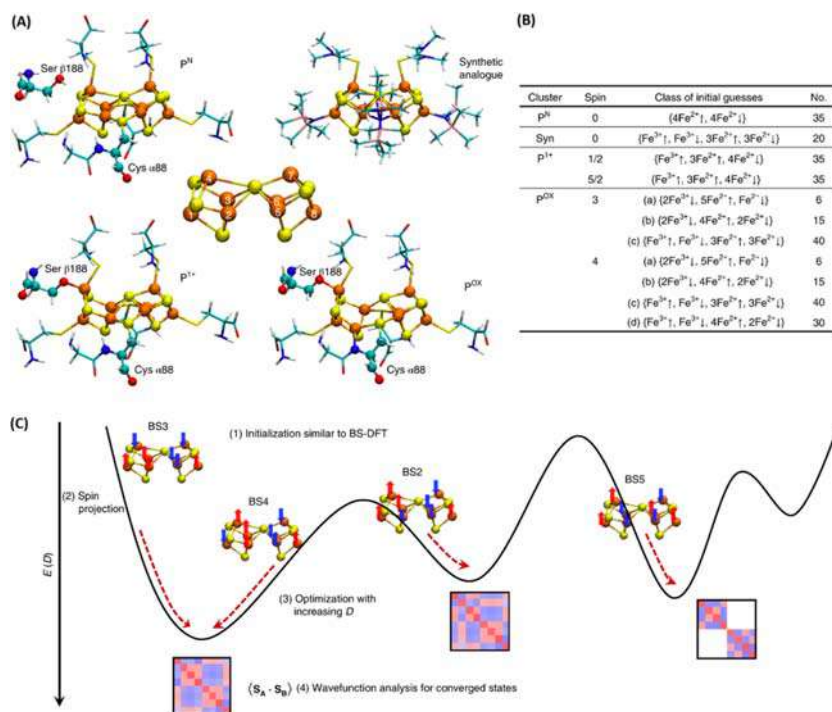
FIGURE 5.5 (A), The [Fe_8S_7] P-cluster models (PDB ID 3MIN for PN; 6CDK for P1 + and 2MIN for POX) and the synthetic analog of the P^N cluster. The redox-dependent structural rearrangements across P^N, P^{1+}, and P^{OX} that involve Ser β188 and Cys α88 are highlighted. Fe, orange; S, yellow; C, cyan; O, red; N, blue; H, white; Si, pink. (B) A table of initial guesses (broken-symmetry product states) that were obtained by distributing different states of Fe across the eight atoms. For spin states of P^{OX}, different classes of initial guesses are labeled by (a), (b), (c), and (d). (C) A schematic illustration of the change of energy in the DMRG optimization process as a function of the bond dimension (D), starting from different broken-symmetry initial guesses. The local minima in the parameter space represent (approximate) eigenstates of the many-electron Schrödinger equation within the active space. They are characterized by the spin−spin correlation functions $\langle S_A \cdot S_B \rangle$ among eight Fe atoms (red, positive; blue, negative) shown by the square graphs. *Reproduced from Li, Z., Guo, S., Sun, Q., Chan, G. K.-L., 2019. Electronic landscape of the P-cluster of nitrogenase as revealed through many-electron quantum wavefunction simulations. Nat. Chem. 11, 1026−1033. https://doi.org/10.1038/s41557-019-0337-3, with permission from Springer Nature.*

mostly localized from reorganization of the cluster and its surroundings. On oxidation, the opening of the P-cluster substantially increases the density of states, which is intriguing, given its proposed role in electron transfer. These results paved the way for obtaining a thorough microscopic understanding of the electronic structure of the nitrogenase cofactors (Fig. 5.5).

5.8.2 Mechanism for photochromic ring-opening reaction of spiropyran

Remarkable changes in structures and physical/chemical properties between spiropyran (SP) and merocyanine (MC, TCC) upon photoisomerization make the system an excellent candidate for use in optical molecular devices, such as light-driven molecular switches. Therefore its reaction channels on the multistate PESs, as well as the overall reaction mechanism, have drawn a lot of attention. By performing DMRG-SCF and DMRG-CASPT2 with a (22e, 20o) active space, Liu et al. (2013) revisited the photochromic ring-opening reaction of SP. In this work, the capability of the DMRG-SCF method in the optimization of molecular geometry was demonstrated for the first time. Compared with previous multiconfigurational studies with smaller active space, this work pointed out a more important role by the hydrogen-out-of-plane valleys near the $C-O$ S_1-minimum energy path (MEP) and the minimal-energy conical intersection (MECI) along the S_1-MEPs in the radiationless $S_1 \rightarrow S_0$ transitions, whereas the transition along the $C-N$ bond dissociation path is less favorable, because of a barrier on the S_1-MEP$_{CN}$ (Fig. 5.6).
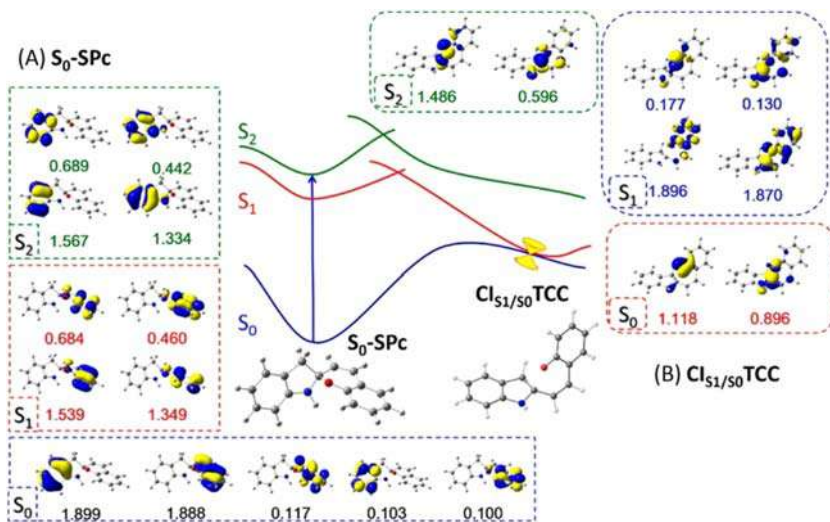
FIGURE 5.6 Schematic energy profile along the S_1-MEPt [FC(S_0-SPc) $\rightarrow$ CI$_{S1/S0}$TCC]. (Here, FC stands for Franck $-$ Condon) The most relevant nature orbitals of the S_0, S_1, and S_2 states with occupation numbers between 1.8 and 0.2, except for the S_0 state of S_0-SPc (between 1.9 and 0.1) are shown at the geometries of (a) S_0-SPc and (b) CI$_{S1/S0}$TCC. *Reproduced from Liu, F., Kurashige, Y., Yanai, T., Morokuma, K., 2013. Multireference ab Initio density matrix renormalization group (DMRG)-CASSCF and DMRG-CASPT2 study on the photochromic ring opening of spiropyran. J. Chem. Theory Comput. 9, 4462−4469. https://doi.org/10.1021/ct400707k, with permission from American Chemical Society.*

References

Baiardi, A., Reiher, M., 2019. Large-scale quantum dynamics with matrix product states. J. Chem. Theory Comput. 15, 3481−3498. Available from: https://doi.org/10.1021/acs.jctc.9b00301.

Baiardi, A., Stein, C.J., Barone, V., Reiher, M., 2017. Vibrational density matrix renormalization group. J. Chem. Theory Comput. 13, 3764−3777. Available from: https://doi.org/10.1021/acs.jctc.7b00329.

Baiardi, A., Stein, C.J., Barone, V., Reiher, M., 2019. Optimization of highly excited matrix product states with an application to vibrational spectroscopy. J. Chem. Phys. 150, 094113. Available from: https://doi.org/10.1063/1.5068747.

Baiardi, A., Kelemen, A.K., Reiher, M., 2022. Excited-state DMRG made simple with FEAST. J. Chem. Theory Comput. 18, 415−430. Available from: https://doi.org/10.1021/acs.jctc.1c00984.

Butscher, W., Kammer, W., 1976. Modification of Davidson's method for the calculation of eigenvalues and eigenvectors of large real-symmetric matrices: Root-homing procedure. J. Comput. Phys. 20, 313−325. Available from: https://doi.org/10.1016/0021-9991(76)90084-X.

Chang, T.C., Schwarz, W.H.E., 1977. Generalized brillouin theorem multiconfiguration method for excited states. Theor. Chim. Acta. 44, 45−59. Available from: https://doi.org/10.1007/BF00548028.

Cho, D., Rouxel, J.R., Mukamel, S., Chan, G.K.-L., Li, Z., 2019. Stimulated X-ray Raman and absorption spectroscopy of iron−sulfur dimers. J. Phys. Chem. Lett. 10, 6664−6671. Available from: https://doi.org/10.1021/acs.jpclett.9b02414.

Dorando, J.J., Hachmann, J., Chan, G.K.-L., 2007. Targeted excited state algorithms. J. Chem. Phys. 127, 084109. Available from: https://doi.org/10.1063/1.2768360.

Feldmann, R., Muolo, A., Baiardi, A., Reiher, M., 2022. Quantum proton effects from density matrix renormalization group calculations. J. Chem. Theory Comput. 18, 234−250. Available from: https://doi.org/10.1021/acs.jctc.1c00913.

Freitag, L., Ma, Y., Baiardi, A., Knecht, S., Reiher, M., 2019. Approximate analytical gradients and nonadiabatic couplings for the state-average density matrix renormalization group self-consistent-field method. J. Chem. Theory Comput. 15, 6724−6737. Available from: https://doi.org/10.1021/acs.jctc.9b00969.

Freitag, L., Baiardi, A., Knecht, S., González, L., 2021. Simplified state interaction for matrix product state wave functions. J. Chem. Theory Comput. 17, 7477−7485. Available from: https://doi.org/10.1021/acs.jctc.1c00674.

Gerratt, J., Mills, I.M., 1968. Force constants and dipole-moment derivatives of molecules from perturbed Hartree−Fock calculations. I. J. Chem. Phys. 49, 1719−1729. Available from: https://doi.org/10.1063/1.1670299.

Ghosh, D., Hachmann, J., Yanai, T., Chan, G.K.-L., 2008. Orbital optimization in the density matrix renormalization group, with applications to polyenes and β-carotene. J. Chem. Phys. 128, 144117. Available from: https://doi.org/10.1063/1.2883976.

Grein, F., Chang, T.C., 1971. Multiconfiguration wavefunctions obtained by application of the generalized Brillouin theorem. Chem. Phys. Lett. 12, 44−48. Available from: https://doi.org/10.1016/0009-2614(71)80612-7.

Grein, F., Banerjee, A., 1975. A multiconfiguration method for excited states of atoms and molecules. Int. J. Quantum Chem. 9, 147−154. Available from: https://doi.org/10.1002/qua.560090821.

Hachmann, J., Cardoen, W., Chan, G.K.-L., 2006. Multireference correlation in long molecules with the quadratic scaling density matrix renormalization group. J. Chem. Phys. 125, 144101. Available from: https://doi.org/10.1063/1.2345196.

Hu, W., Chan, G.K.-L., 2015. Excited-state geometry optimization with the density matrix renormalization group, as applied to polyenes. J. Chem. Theory Comput. 11, 3000−3009. Available from: https://doi.org/10.1021/acs.jctc.5b00174.

Jiang, T., Li, W., Ren, J., Shuai, Z., 2020. Finite temperature dynamical density matrix renormalization group for spectroscopy in frequency domain. J. Phys. Chem. Lett. 11, 3761−3768. Available from: https://doi.org/10.1021/acs.jpclett.0c00905.

Knecht, S., Keller, S., Autschbach, J., Reiher, M., 2016. A nonorthogonal state-interaction approach for matrix product state wave functions. J. Chem. Theory Comput. 12, 5881−5894. Available from: https://doi.org/10.1021/acs.jctc.6b00889.

Knowles, P.J., Werner, H.-J., 1985. An efficient second-order MC SCF method for long configuration expansions. Chem. Phys. Lett. 115, 259−267. Available from: https://doi.org/10.1016/0009-2614(85)80025-7.

Kreplin, D.A., Knowles, P.J., Werner, H.-J., 2019. Second-order MCSCF optimization revisited. I. Improved algorithms for fast and robust second-order CASSCF convergence. J. Chem. Phys. 150, 194106. Available from: https://doi.org/10.1063/1.5094644.

Kreplin, D.A., Knowles, P.J., Werner, H.-J., 2020. MCSCF optimization revisited. II. Combined first- and second-order orbital optimization for large molecules. J. Chem. Phys. 152, 074102. Available from: https://doi.org/10.1063/1.5142241.

Lan, T.N., Kurashige, Y., Yanai, T., 2014. Toward reliable prediction of hyperfine coupling constants using ab initio density matrix renormalization group method: diatomic $^2\Sigma$ and vinyl radicals as test cases. J. Chem. Theory Comput. 10, 1953−1967. Available from: https://doi.org/10.1021/ct400978j.

Lan, T.N., Kurashige, Y., Yanai, T., 2015. Scalar relativistic calculations of hyperfine coupling constants using ab initio density matrix renormalization group method in combination with third-order Douglas−Kroll−Hess transformation: case studies on 4d transition metals. J. Chem. Theory Comput. 11, 73−81. Available from: https://doi.org/10.1021/ct5007778.

Larsson, H.R., 2019. Computing vibrational eigenstates with tree tensor network states (TTNS). J. Chem. Phys. 151, 204102. Available from: https://doi.org/10.1063/1.5130390.

Lennard-Jones, J.E., 1929. The electronic structure of some diatomic molecules. Trans. Faraday Soc. 25, 668−686. Available from: https://doi.org/10.1039/TF9292500668.

Levy, B., Berthier, G., 1968. Generalized Brillouin theorem for multiconfigurational SCF theories. Int. J. Quantum Chem. 2, 307−319. Available from: https://doi.org/10.1002/qua.560020210.

Li, Z., Guo, S., Sun, Q., Chan, G.K.-L., 2019. Electronic landscape of the P-cluster of nitrogenase as revealed through many-electron quantum wavefunction simulations. Nat. Chem. 11, 1026−1033. Available from: https://doi.org/10.1038/s41557-019-0337-3.

Liu, F., Kurashige, Y., Yanai, T., Morokuma, K., 2013. Multireference Ab Initio density matrix renormalization group (DMRG)-CASSCF and DMRG-CASPT2 study on the photochromic ring opening of spiropyran. J. Chem. Theory Comput. 9, 4462−4469. Available from: https://doi.org/10.1021/ct400707k.

Luo, H.-G., Qin, M.-P., Xiang, T., 2010. Optimizing Hartree-Fock orbitals by the density-matrix renormalization group. Phys. Rev. B 81, 235129. Available from: https://doi.org/10.1103/PhysRevB.81.235129.

Ma, Y., 2020. Elucidating the multi-configurational character of the firefly dioxetanone anion and its prototypes in the biradical region using full valence active spaces. Phys. Chem. Chem. Phys. 22, 4957−4966. Available from: https://doi.org/10.1039/C9CP06417F.

Ma, Y., Wen, J., Ma, H., 2015. Density-matrix renormalization group algorithm with multi-level active space. J. Chem. Phys. 143, 034105. Available from: https://doi.org/10.1063/1.4926833.

Ma, Y., Knecht, S., Keller, S., Reiher, M., 2017a. Second-order self-consistent-field density-matrix renormalization group. J. Chem. Theory Comput. 13, 2533−2549. Available from: https://doi.org/10.1021/acs.jctc.6b01118.

Ma, Y., Knecht, S., Reiher, M., 2017b. Multiconfigurational effects in theoretical resonance Raman spectra. ChemPhysChem 18, 384. Available from: https://doi.org/10.1002/cphc.201601072.

Malmqvist, P.Å., Rendell, A., Roos, B.O., 1990. The restricted active space self-consistent-field method, implemented with a split graph unitary group approach. J. Phys. Chem. 94, 5477−5482. Available from: https://doi.org/10.1021/j100377a011.

Mardazad, S., Xu, Y., Yang, X., Grundner, M., Schollwöck, U., Ma, H., et al., 2021. Quantum dynamics simulation of intramolecular singlet fission in covalently linked tetracene dimer. J. Chem. Phys. 155, 194101. Available from: https://doi.org/10.1063/5.0068292.

Muolo, A., Baiardi, A., Feldmann, R., Reiher, M., 2020. Nuclear-electronic all-particle density matrix renormalization group. J. Chem. Phys. 152, 204103. Available from: https://doi.org/10.1063/5.0007166.

Nakatani, N., Guo, S., 2017. Density matrix renormalization group (DMRG) method as a common tool for large active-space CASSCF/CASPT2 calculations. J. Chem. Phys. 146, 094102. Available from: https://doi.org/10.1063/1.4976644.

Neugebauer, J., Hess, B.A., 2004. Resonance Raman spectra of uracil based on Kramers−Kronig relations using time-dependent density functional calculations and multireference perturbation theory. J. Chem. Phys. 120, 11564. Available from: https://doi.org/10.1063/1.1697371.

Pavošević, F., Culpitt, T., Hammes-Schiffer, S., 2020. Multicomponent quantum chemistry: integrating electronic and nuclear quantum effects via the nuclear−electronic orbital method. Chem. Rev. 120, 4222−4253. Available from: https://doi.org/10.1021/acs.chemrev.9b00798.

Pettitt, B.A., 1986. Hartree-Fock theory of proton states in hydrides. Chem. Phys. Lett. 130, 399−402. Available from: https://doi.org/10.1016/0009-2614(86)80493-6.

Pham, L.N., Nguyen, M.T., 2018. Another look at photoelectron spectra of the anion Cr^2O^{2-}: multireference character and energetic degeneracy. J. Chem. Theory Comput. 14, 4833−4843. Available from: https://doi.org/10.1021/acs.jctc.8b00412.

Polizzi, E., 2009. Density-matrix-based algorithm for solving eigenvalue problems. Phys. Rev. B 79, 115112. Available from: https://doi.org/10.1103/PhysRevB.79.115112.

Pulay, P., 1969. Ab initio calculation of force constants and equilibrium geometries in polyatomic molecules: I. Theory. Mol. Phys. 17, 197−204. Available from: https://doi.org/10.1080/00268976900100941.

Pulay, P., 1980. Convergence acceleration of iterative sequences. The case of SCF iteration. Chem. Phys. Lett. 73, 393−398. Available from: https://doi.org/10.1016/0009-2614(80)80396-4.

Rakhuba, M., Oseledets, I., 2016. Calculating vibrational spectra of molecules using tensor train decomposition. J. Chem. Phys. 145, 124101. Available from: https://doi.org/10.1063/1.4962420.

Ren, J., Shuai, Z., Chan, G.K.-L., 2018. Time-dependent density matrix renormalization group algorithms for nearly exact absorption and fluorescence spectra of molecular aggregates at both zero and finite temperature. J. Chem. Theory Comput. 14, 5027−5039. Available from: https://doi.org/10.1021/acs.jctc.8b00628.

Roos, B.O., 1980. The complete active space SCF method in a fock-matrix-based super-CI formulation. Int. J. Quantum Chem. 18, 175−189. Available from: https://doi.org/10.1002/qua.560180822.

Roos, B.O., Taylor, P.R., Sigbahn, P.E., 1980. A complete active space SCF method (CASSCF) using a density matrix formulated super-CI approach. Chem. Phys. 48, 157−173. Available from: https://doi.org/10.1016/0301-0104(80)80045-0.

Sayfutyarova, E.R., Chan, G.K.-L., 2018. Electron paramagnetic resonance g-tensors from state interaction spin-orbit coupling density matrix renormalization group. J. Chem. Phys. 148, 184103. Available from: https://doi.org/10.1063/1.5020079.

Sharma, S., Sivalingam, K., Neese, F., Chan, G.K.-L., 2014. Low-energy spectrum of iron−sulfur clusters directly from many-particle quantum mechanics. Nat. Chem. 6, 927−933. Available from: https://doi.org/10.1038/nchem.2041.

Siegbahn, P., Heiberg, A., Roos, B., Levy, B., 1980. A comparison of the super-CI and the Newton-Raphson scheme in the complete active space SCF method. Phys. Scr. 21, 323. Available from: https://doi.org/10.1088/0031-8949/21/3-4/014.

Siegbahn, P.E.M., Almlöf, J., Heiberg, A., Roos, B.O., 1981. The complete active space SCF (CASSCF) method in a Newton−Raphson formulation with application to the HNO molecule. J. Chem. Phys. 74, 2384−2396. Available from: https://doi.org/10.1063/1.441359.

Sleijpen, G.L., Van der Vorst, H.A., 2000. A Jacobi-Davidson iteration method for linear eigenvalue problems. SIAM Rev. 42, 267−293. Available from: https://doi.org/10.1137/S0036144599363084.

Snyder Jr, J.W., Hohenstein, E.G., Luehr, N., Martínez, T.J., 2015. An atomic orbital-based formulation of analytical gradients and nonadiabatic coupling vector elements for the state-averaged complete active space self-consistent field method on graphical processing units. J. Chem. Phys. 143, 154107. Available from: https://doi.org/10.1063/1.4932613.

Snyder Jr, J.W., Fales, B.S., Hohenstein, E.G., Levine, B.G., Martínez, T.J., 2017. A direct-compatible formulation of the coupled perturbed complete active space self-consistent field equations on graphical processing units. J. Chem. Phys. 146, 174113. Available from: https://doi.org/10.1063/1.4979844.

Song, Y., Cheng, Y., Ma, Y., Ma, H., 2020. Multi-reference Epstein-Nesbet Perturbation Theory with density matrix renormalization group reference wavefunction. Electron. Struct. 2, 014002. Available from: https://doi.org/10.1088/2516-1075/ab72db.

Sun, Q., Yang, J., Chan, G.K.-L., 2017. A general second order complete active space self-consistent-field solver for large-scale systems. Chem. Phys. Lett. 683, 291−299. Available from: https://doi.org/10.1016/j.cplett.2017.03.004.

Van Kuiken, B.E., Hahn, A.W., Nayyar, B., Schiewer, C.E., Lee, S.C., Meyer, F., et al., 2018. Electronic spectra of iron − sulfur complexes measured by 2p3d RIXS spectroscopy. Inorg. Chem. 57, 7355−7361. Available from: https://doi.org/10.1021/acs.inorgchem.8b01010.

Werner, H.-J., 1987. Matrix-formulated direct multiconfiguration self-consistent field and multi-configuration reference configuration interaction methods. In: Lawley, K.P. (Ed.), Ab Initio Methods in Quantum Chemistry, Part II. John Wiley & Sons Ltd, Chichester, pp. 1−62.

Werner, H.-J., Knowles, P.J., 1985. A second order multiconfiguration SCF procedure with optimum convergence. J. Chem. Phys. 82, 5053−5063. Available from: https://doi.org/10.1063/1.448627.

Werner, H.-J., Meyer, W., 1980. A quadratically convergent multiconfiguration−self-consistent field method with simultaneous optimization of orbitals and CI coefficients. J. Chem. Phys. 73, 2342−2356. Available from: https://doi.org/10.1063/1.440384.

Werner, H.-J., Meyer, W., 1981. A quadratically convergent MCSCF method for the simultaneous optimization of several states. J. Chem. Phys. 74, 5794−5801. Available from: https://doi.org/10.1063/1.440892.

Wouters, S., Bogaerts, T., Van Der Voort, P., Van Speybroeck, V., Van Neck, D., 2014. Communication: DMRG-SCF study of the singlet, triplet, and quintet states of oxo-Mn (Salen). J. Chem. Phys. 140, 241103. Available from: https://doi.org/10.1063/1.4885815.

Yamaguchi, Y., Osamura, Y., Goddard, J.D., Schaefer, H.F., 1994. A New Dimension to Quantum Chemistry: Analytic Derivative Methods in Ab Initio Molecular Electronic Structure Theory. Oxford University Press.

Yanai, T., Kurashige, Y., Ghosh, D., Chan, G.K.-L., 2009. Accelerating convergence in iterative solution for large-scale complete active space self-consistent-field calculations. Int. J. Quantum Chem. 109, 2178−2190. Available from: https://doi.org/10.1002/qua.22099.

Yang, M., White, S.R., 2019. Density-matrix-renormalization-group study of a one-dimensional diatomic molecule beyond the Born-Oppenheimer approximation. Phys. Rev. A 99, 022509. Available from: https://doi.org/10.1103/PhysRevA.99.022509.

Yao, Y., Sun, K.-W., Luo, Z., Ma, H., 2018. Full quantum dynamics simulation of a realistic molecular system using the adaptive time-dependent density matrix renormalization group method. J. Phys. Chem. Lett. 2018 (9), 413−419. Available from: https://doi.org/10.1021/acs.jpclett.7b03224.

Yarkony, D.R., 1981. Comment on the use of the augmented matrix in MCSCF theory. Chem. Phys. Lett. 77, 634−635. Available from: https://doi.org/10.1016/0009-2614(81)85223-2.

Zgid, D., Nooijen, M., 2008. The density matrix renormalization group self-consistent field method: Orbital optimization with the density matrix renormalization group method in the active space. J. Chem. Phys. 128, 144116. Available from: https://doi.org/10.1063/1.2883981.

Zhai, H., Chan, G.K.-L., 2021. Low communication high performance ab initio density matrix renormalization group algorithms. J. Chem. Phys. 154, 224116. Available from: https://doi.org/10.1063/5.0050902.

Chapter 6

Post-density matrix renormalization group

Previous chapters have illustrated how ab initio density matrix renormalization group (DMRG) and DMRG self-consistent field (DMRG-SCF) serve as efficient and computationally accurate methods, for describing electronic structure properties of strongly correlated systems that require large complete active spaces (CAS) composed of up to ∼100 active orbitals (Hachmann et al., 2006; Zhai and Chan, 2021), which are not accessible by conventional quantum chemistry methods. However, to achieve a high quantitative accuracy for practical molecular systems, it is still desirable to include the electron correlations between CAS and all other (∼a few hundreds or thousands of) core and external orbitals, that is, dynamic correlation. These systems tend to be computationally prohibitive for pure DMRG calculations. In the last decade, aiming at computations of the missing dynamic correlation within DMRG, several methods have been proposed. Given methods rely on the combination of DMRG with other quantum chemistry methods such as multireference (MR) configuration interaction (CI), perturbation theory (PT), and coupled cluster (CC). This category of approaches is commonly known in the DMRG community as ab initio post-DMRG. Another inevitable issue when applying ab initio DMRG and post-DMRG methods to the "real-world" chemistry problems is the proper description of the strongly correlated subsystem's chemical environment (e.g., a solvent environment or biological metalloenzyme's backbone). In this chapter, we will introduce the recently developed post-DMRG approaches to account for the dynamic electronic correlation and embedded chemical environment.

6.1 Fundamentals for multireference quantum chemical calculations

In order to give a pedagogical description of post-DMRG approaches, here we first review several important and fundamental concepts in traditional MR quantum chemical calculations.

6.1.1 Static and dynamic electron correlation

It is well known that the single-electron mean-field Hartree−Fock (HF) theory is usually the base for the other advanced wave function theory (WFT) quantum chemistry methods. In HF theory, a single Slater determinant (SD) is optimized by finding the set of molecular orbitals (MOs) which minimize its ground-state energy expectation value. However, the exact ground state of the many-electron Schrödinger equation is a linear combination over all possible SDs. The difference in energy between the HF solution and the exact ground state is the electron correlation energy. This energy is often (somewhat ambiguously) divided into two contributions: static and dynamic correlation.

In many chemical problems such as bond breaking/formation in chemical reactions and transition metal catalysis in biological photosynthesis, there are a considerable number of energetically near-degenerate frontier MOs that make it impossible to approximate the zeroth-order wave function by using only one leading configuration. Under such situations, it is said that the system exhibits static electron correlation (sometimes also-called nondynamic electron correlation or strong electron correlation). At the same time, the Coulomb repulsion caused by the instantaneous movement of the electrons contributes to the dynamic electron correlation, and it constitutes the remainder of the energy difference.

The presence of the static electron correlation is generally unavoidable when considering the molecule's entire potential energy surface. The most successful and widely used model for dealing with the static correlation is the CAS model, where a set of MOs are divided into active and inactive orbitals (see Section 4.6 and Figure 4.2). Therein, the electron occupancy numbers on each core, active, and external orbital are 2, 0/1/2, and 0, respectively. To avoid any possible ambiguities, the notations used in this chapter are clarified as follows. Core orbitals are labeled i, j, k, l, while active orbitals are t, u, v, w and external orbitals have the labels a, b, c, d. Orbital labels p, q, r, s represent general orbitals. Both the core orbitals and active orbitals can be referred to as internal orbitals, labeled m, n, whereas both the core and external orbitals can be denoted as inactive orbitals, labeled x, y. We also note that all $|\phi\rangle$ in the following part represent the single determinant or configuration state function (CSF), while $|\psi\rangle$ is a quantum superposition state which is the linear combination of various configurations.

In the CAS model, the static correlation is adequately described because an exact Hamiltonian diagonalization will be performed with the consideration of all possible electronic configurations within the active space. It is obvious that the number of CAS configurations grows exponentially with the increasing active space size. This results in an upper limit for the computational capability of conventional CAS methods, for example, nowadays the largest exactly solvable active space is (18e, 18o) for most computers, although (22e, 22o) has been achieved using massive parallelization

(Vogiatzis et al., 2017). Usually, the static correlation contributes to a large proportion of the correlation energy; however, it does not mean the dynamic correlation is negligible. For example, it has been shown that it is impossible to qualitatively describe the bonding and dissociation behaviors of the diatomic molecule Cr_2, even when the static correlations are being well accounted by DMRG using a large active space of (12e, 42o) with all $3d$, $4s$, $4p$, $4d$, and $4f$ orbitals. (Luo et al., 2018) Therefore, to capture the remaining dynamic electron correlation from the otherwise neglected external orbitals, theories of CI, PT, as well as CC are often implemented on top of a reasonable zeroth-order approximated reference wave function. Either an HF determinant in single-reference (SR) calculations for weakly correlated systems, or a CAS wave function in MR calculations for strongly correlated systems can be used as the reference.

6.1.2 Contraction approximations

Here we take a MR CI singles and doubles (MRCISD) as an example to introduce some basic concepts in MR calculations. The MRCISD wave function $|\psi\rangle$ can be written as:

$$|\psi\rangle = \sum_I c(I)|\phi(I)\rangle + \sum_I \sum_{m,e} c_m^e(I)|\phi_m^e(I)\rangle + \sum_I \sum_{mn,ef} c_{mn}^{ef}(I)\big|\phi_{mn}^{ef}(I)\rangle, \quad (6.1)$$

where $c(I), c_m^e(I)$, and $c_{mn}^{ef}(I)$ are multireference configuration interaction (MRCI) coefficients. Here, e, and f are the external or active orbital labels. $\{|\phi(I)\rangle\}$ give reference configurations generated in the active space, and $\{\big|\phi_m^e(I)\rangle\}$ and $\{\big|\phi_{mn}^{ef}(I)\rangle\}$ represent singly and doubly excited configurations from the reference configuration $|\phi(I)\rangle$ respectively, as

$$\big|\phi_m^e(I)\rangle = \hat{E}_m^e\big|\phi(I)\rangle \qquad (6.2)$$

and

$$\big|\phi_{mn}^{ef}(I)\rangle = \hat{E}_{mn}^{ef}\big|\phi(I)\rangle \qquad (6.3)$$

Here the spin-free single and double excitation operators are defined as $\hat{E}_q^p \equiv \sum_\sigma \hat{a}_{p\sigma}^\dagger \hat{a}_{q\sigma}$ and $\hat{E}_{rs}^{pq} \equiv \sum_{\sigma\tau} \hat{a}_{p\sigma}^\dagger \hat{a}_{q\tau}^\dagger \hat{a}_{s\tau} \hat{a}_{r\sigma}$. In some cases, a same excited configuration can be generated by two different excitation patterns from distinct reference configurations, that is, $\big|\phi_m^e(I)\rangle = \big|\phi_{m'}^{e'}(J)\rangle$. Consequently, special treatments must be adopted to find and eliminate the redundant configurations in Eq. 6.1.

A key concept in practical MR calculations is to classify the possible excitations in the "first-order-interacting space" (FOIS), introduced by McLean and Liu (1973). The FOIS consists of SDs or CSFs that can directly couple to the reference wave function via the Hamiltonian. According to the number of excited electrons in the external space, we can sort the eight

groups of single and double excited configurations given in the Eq. 6.1 into three sets: internal $\left|\phi_{it}^{uv}\right\rangle$, $\left|\phi_{ij}^{tu}\right\rangle$, semi-internal $\left|\phi_{ij}^{ta}\right\rangle$, $\{\left|\phi_{it}^{ua}\right\rangle, \left|\phi_{ti}^{ua}\right\rangle\}$, $\left|\phi_{tu}^{va}\right\rangle$, and external $\left|\phi_{ij}^{ab}\right\rangle$, $\left|\phi_{it}^{ab}\right\rangle$, $\left|\phi_{tu}^{ab}\right\rangle$ (see Table 6.1). Although we have discarded numerous configurations by constraining the excitation patterns to contain only single and double excitations, the number of configurations in a MRCISD calculation is still "astronomical" for most molecular systems, which results in the common bottleneck of all MR methods. For reducing the number of variational parameters in MRCI wave function, *contraction* approximations are often used. To appropriately distinguish the methods in MRCI, we will refer to the conventional MRCI without contraction approximations as uncontracted MRCI (uc-MRCI) in the following sections.

Generally, there are two widely used contraction schemes, the internal contraction (ic) and the external contraction (ec), which will be discussed below. For simplicity, we will not consider the excitations from core orbitals in the following discussions, nonetheless readers can easily perform extensions for them.

6.1.2.1   Internally contracted approximations

The "internally" contracted MRCI was first discussed by Meyer (1977) and Siegbahn (1980) and worked out in detail by Werner and Reinsch (1982). For an "internally" contracted MRCI, the reference configurations in active space are contracted as one term, whereas the excited configurations are generated by simply applying pair excitation operators on the contracted reference state.

The internally contracted MRCISD wave function is written as:

$$|\psi^{\text{ic}}\rangle = \tilde{c}_0|\psi_0\rangle + \sum_{tuv,a} \tilde{c}_{tu}^{va}|\psi_{tu}^{va}\rangle + \sum_{tu,ab} \tilde{c}_{tu}^{ab}|\psi_{tu}^{ab}\rangle, \tag{6.4}$$

with $\left|\psi_{tu}^{va}\right\rangle \equiv \hat{E}_{tu}^{va}|\psi_0\rangle = \sum_I c(I)\left|\phi_{tu}^{va}(I)\right\rangle$ and $\left|\psi_{tu}^{ab}\right\rangle \equiv \hat{E}_{tu}^{ab}|\psi_0\rangle$ $= \sum_I c(I)\left|\phi_{tu}^{ab}(I)\right\rangle$. $|\psi_0\rangle = \sum_I c(I)|\phi(I)\rangle$ gives the reference wave function obtained from a preliminary CASCI or CASSCF calculation. $\tilde{c}$ represents the variational MRCI coefficient, while c is the contraction coefficient determined in $|\psi_0\rangle$.
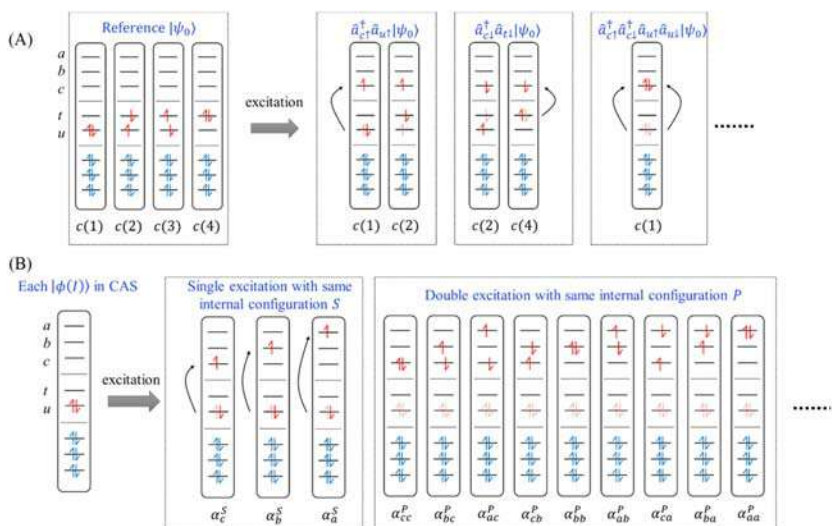
Just as Fig. 6.1 shows, all configurations that have the same excitation pattern from the reference wave function are combined together in an internal contraction approximation. Thus ic-MRCI can break through the "exponential wall" and treat a larger active space than the uc-MRCI, since the contracted terms in Eq. 6.4 are independent of the number of reference configurations. The number of contracted internal states only depends on the number of active orbitals (n_a), where at most n_a^3 contracted internal

TABLE 6.1 List of contraction schemes of ic-MRCI ansatz. The schemes are categorized by the basis representation of the reference $|\psi_0\rangle$, internal, semi-internal, and external excitation classes. Each of the classes is represented with either contracted (C) or uncontracted (U) basis.

Ansatz	Internal excitation			Semi-internal excitation		External excitation
	$\left|\psi_0\right\rangle$	$\left|\psi_{it}^{uv}\right\rangle$	$\left|\psi_{ij}^{tu}\right\rangle$	$\left|\psi_{ij}^{ta}\right\rangle/\left|\psi_{it}^{ua}\right\rangle/\left|\psi_{ti}^{ua}\right\rangle$	$\left|\psi_{tu}^{va}\right\rangle$	$\left|\psi_{ij}^{ab}\right\rangle/\left|\psi_{it}^{ab}\right\rangle/\left|\psi_{tu}^{ab}\right\rangle$
FIC-MRCI	C	C	C	C	C	C
WK-MRCI	U	U	U	U	U	C
CW-MRCI	U	U	C	C	U	C
SC-MRCI	C	C	C	C	C	C

FIGURE 6.1 Schematic illustration of (A) internal contraction and (B) external contraction approximations. Each dashed box represents a contracted state with the contraction coefficient displayed under each contracted configuration.

(N-1)-electron states $\left(\hat{a}_v^\dagger \hat{a}_t \hat{a}_u |\psi_0\rangle\right)$ are needed by applying two annihilations and one creation, and n_a^2 contracted internal (N-2)-electron states $\hat{a}_t \hat{a}_u |\psi_0\rangle$ by two annihilations (N is the number of electrons in original internal space). Because all terms in the wave function are contracted in this ic-ansatz, we referred to this as "fully internally contracted" (FIC), although in some literatures, this is referred to as WR-ansatz (Werner and Reinsch, 1982).

In order to avoid the computation of duplicate terms in ic-MRCI Hamiltonian matrix, one can utilize the reduced density matrices (RDMs) within the active space. For example, when calculating two different Hamiltonian elements:

$$
\begin{aligned}
\langle\psi_0|\hat{H}|\psi_w^a\rangle &= \langle\psi_0|\left(\sum_{psqr} g_{prqs}\hat{E}_{rs}^{pq}\right)\hat{E}_w^a|\psi_0\rangle \\
&= \sum_{ta'uv} g_{tvua'}\left\langle\psi_0\left|\hat{E}_{vw}^{tu}\right|\psi_0\right\rangle\delta_{aa'} + \dots
\end{aligned}
\tag{6.5}
$$

and

$$
\begin{aligned}
\langle\psi_0|\hat{H}|\psi_w^b\rangle &= \langle\psi_0|\left(\sum_{psqr} g_{prqs}\hat{E}_{rs}^{pq}\right)\hat{E}_w^b|\psi_0\rangle \\
&= \sum_{tb'uv} g_{tvub'}\left\langle\psi_0\left|\hat{E}_{vw}^{tu}\right|\psi_0\right\rangle\delta_{bb'} + \dots
\end{aligned}
\tag{6.6}
$$

where g_{prqs} is two-electron integral (see Eq. 4.3), the two-rank RDM $D_{wv}^{tu} = \langle \psi_0 | \hat{E}_{wv}^{tu} | \psi_0 \rangle$ shows up twice. Thus, if we calculate and store these RDMs beforehand, numerous reduplicated calculations can be avoided, and accordingly the ic-MRCI computational efficiency can be greatly improved.

However, this FIC scheme brings with it two shortcomings: (1) the contracted states in ic-MRCI are nonorthogonal and (2) the required high-order RDMs of the active space may be computationally challenging. The first point requires solving a generalized eigenequation instead of a normal eigenvalue problem, and it is usually overcome by explicitly diagonalizing the overlap matrix and discarding the zero-eigenvectors. As for the second one, this is one of the major problems in MR dynamic correlation methods, and many schemes have been proposed to address this issue. The reason lies in the fact that the highest rank RDM appearing in FIC-MRCISD Hamiltonian computation is 5-rank $\langle \psi_0 | \hat{E}_{tut'u't''}^{vwv'w'v''} | \psi_0 \rangle$, the computation cost of which is $O(n_a^{10})$. Even though 5-RDMs have been proved to be able to be canceled out by expressing the Hamiltonian matrix using commutators (Dyall, 1995; Angeli et al., 2001), the computation and storage of the highest rank 4-RDMs $\left(O(n_a^8) \right)$ are still a big challenge for large active space.

Here, we give a brief explanation about why 5-RDMs can be annihilated by using the commutator without any approximation. First, let us consider the Hamiltonian matrix elements between two singly excited states:

$$\langle \psi_0 | \hat{E}_{v'a'}^{t'u'} \hat{H} \hat{E}_{t''u''}^{v''a''} | \psi_0 \rangle, \tag{6.7}$$

which can be written as follows:

$$\langle \psi_0 | \hat{E}_{v'a'}^{t'u'} \hat{H} \hat{E}_{t''u''}^{v''a''} | \psi_0 \rangle = \langle \psi_0 | \hat{E}_{v'a'}^{t'u'} \left[\hat{H}, \hat{E}_{t''u''}^{v''a''} \right] | \psi_0 \rangle \\ + \langle \psi_0 | \hat{E}_{v'a'}^{t'u'} \hat{E}_{t''u''}^{v''a''} \hat{H} | \psi_0 \rangle. \tag{6.8}$$

Given the CAS nature of $|\psi_0\rangle$, the above equation can be transferred to:

$$\langle \psi_0 | \hat{E}_{v'a'}^{t'u'} \hat{H} \hat{E}_{t''u''}^{v''a''} | \psi_0 \rangle = \langle \psi_0 | \hat{E}_{v'a'}^{t'u'} \left[\hat{H}, \hat{E}_{t''u''}^{v''a''} \right] | \psi_0 \rangle \\ + \langle E_0 \psi_0 | \hat{E}_{v'a'}^{t'u'} \hat{E}_{t''u''}^{v''a''} | \psi_0 \rangle. \tag{6.9}$$

Considering the anticommutation property of the fermions:

$$\hat{a}_{p\sigma}^+ \hat{a}_{q\tau} + \hat{a}_{q\tau} \hat{a}_{p\sigma}^+ = \delta_{pq} \delta_{\sigma\tau}, \tag{6.10}$$

it can be deduced that the first term in right part of Eq. 6.9 does not contain RDMs with ranks larger than 4. Under those circumstances, the 5-RDMs are canceled out by commutators when calculating the Hamiltonian matrix elements in FIC-MRCI.

Besides the FIC-ansatz, there are also two widely used internal contraction schemes, which are so-called "partially contraction" (pc) and "strongly contraction" (sc). The "partially contraction" means some excitation classes are left uncontracted, and its motivation is to circumvent the use of high-order RDMs. A popular pc scheme (Werner and Knowles, 1988; Knowles and Werner, 1988) is the so-called WK-ansatz, in which only the double external excitation terms are contracted and the other configurations are left uncontracted:

$$|\Psi^{\text{WK}}\rangle = \sum_I \tilde{c}(I)|\phi(I)\rangle + \sum_I \sum_{t,a} \tilde{c}_t^a(I)|\phi_t^a(I)\rangle + \sum_{tu,ab} \tilde{c}_{tu}^{ab}|\psi_{tu}^{ab}\rangle. \qquad (6.11)$$

An improved variant of the WK-ansatz, which introduced additional ic bases associated with excitation from core orbitals, was also proposed by the same group and called CW scheme (Celani and Werner, 2000). Both ansatzes perform remarkably well for small active spaces, nonetheless their computational scaling still increases exponentially with respect to the molecular sizes for the uncontracted configurations.

As for the "strongly contracted" (sc) scheme, the subspaces in FIC-MRCI are further contracted by electron integrals such that there are not any active labels in the wave function of sc-MRCI. Here, we follow the notation introduced by Angeli et al. (2001) and let $S_l^{(k)}$ denotes the subspace in sc-MRCI. k refers to the change in the number of active electrons ($-2 \le k \le 2$), while l specifies the configuration of electrons in the inactive space. In the strong contraction scheme, only a single state $\left|\psi_l^{(k)}\right\rangle$ from each $S_l^{(k)}$ is used, which can be obtained by:

$$\left|\psi_l^{(k)}\right\rangle = \hat{P}_l^{(k)} \hat{H}|\psi_0\rangle, \qquad (6.12)$$

where $\hat{P}_l^{(k)}$ is the projector onto the $S_l^{(k)}$ space. For example, the configurations with one unoccupied core orbital i and two occupied external orbitals a and b span the $S_{i,ab}^{(-1)}$ space. The $\left|\psi_{i,ab}^{(-1)}\right\rangle$ is then formalized as:

$$\left|\psi_{i,ab}^{(-1)}\right\rangle = \sum_t (g_{aibt} - g_{atbi}) \hat{E}_{it}^{ab}|\psi_0\rangle, \qquad (6.13)$$

where g_{aibt} is the two-electron integral. This scheme leads to a more compact representation of the FOIS by tracing out the active indexes. Its another big advantage is that the resulted contracted states form an orthonormal set and accordingly no problems arise from near linear dependencies.

6.1.2.2 Externally contracted approximations

The "externally" contracted MRCI concept was first suggested by Siegbahn (1983). By grouping together configurations with the same internal parts and freezing their relative weights as:

$$|\psi_S\rangle = \sum_a \alpha_a^S(I)|\phi_S^a(I)\rangle = \sum_a \alpha_t^a(I)|\phi_t^a(I)\rangle,$$
$$|\psi_P\rangle = \sum_{ab} \alpha_{ab}^P(I)|\phi_P^{ab}(I)\rangle = \sum_{ab} \alpha_{tu}^{ab}(I)|\phi_{tu}^{ab}(I)\rangle. \tag{6.14}$$

With the ec contraction, α coefficients are determined from first-order PT

$$\alpha_a^S(I) = \frac{\langle\psi_0|\hat{H}|\phi_S^a(I)\rangle}{E_0 - \langle\phi_S^a(I)|\hat{H}|\phi_S^a(I)\rangle}, \ \alpha_{ab}^P(I) = \frac{\langle\psi_0|\hat{H}|\phi_P^{ab}(I)\rangle}{E_0 - \langle\phi_P^{ab}(I)|\hat{H}|\phi_P^{ab}(I)\rangle}. \tag{6.15}$$

$|\psi_0\rangle = \sum_I c(I)|\phi(I)\rangle$ is the reference wave function and E_0 indicates the corresponding reference energy, and every S/P denotes a particular internal $(N-1)$- $/(N-2)$-electron configuration.

As a result, the externally contracted MRCI (ec-MRCI) wave function is formalized as:

$$|\psi^{ec}\rangle = \sum_I \tilde{c}(I)|\phi(I)\rangle + \sum_S \tilde{c}^S|\psi_S\rangle + \sum_P \tilde{c}^P|\psi_P\rangle. \tag{6.16}$$

As all external configurations with a same internal "kernel" are merged into one term in ec-MRCI, as Fig. 6.1 shows, the number of configurations in the external space does not affect the size of the ec-MRCI matrix. As a result, the ec-MRCI method is particularly suitable for calculations using large basis sets, if the number of reference configurations is not excessively large. Unlike the internally contracted method, the ec-MRCI cost depends directly on the dimension of the reference space. Therefore it can hardly deal with systems that possess large active space, unless only a limited number of reference configurations are considered by using the idea of selected-CI. Due to the contraction errors in the external space, ec-MRCI results may be inaccurate for higher lying excited states with significant external orbital occupations.

It can be noticed that the traditional FIC-MRCI and sc-MRCI belong to "Static-Then-Dynamic" class of MR methods, whilst ec-MRCI belongs to "Static-Dynamic-Static" family. Because the former employs the fixed contraction coefficients $c(I)$ of the reference states $|\psi_0\rangle$ by CASCI or CASSCF, whereas the latter only uses them to evaluate the external contraction coefficients and consequently allows them to fully relax in the final "Static" procedure. The relaxation of the reference coefficients has been found to be a main contributor to the energy difference between FIC-MRCI and uc-MRCI. (Sivalingam et al., 2016) At the same time, the WK-MRCI and CW-MRCI approaches account for reference relaxation as both employ a decontracted reference space from the start. However, a simultaneous optimization of

reference coefficients and contraction coefficients in FIC- and sc-MR calculations is also possible to be achieved in a spirit similar to the simultaneous optimization of configuration and orbital coefficients in CASSCF (see Section 5.1). Hanauer and Köhn (2011) reported such an implementation in the context of internally contracted MRCC theory. Similarly, a full optimization could be included into FIC-MRCI and sc-MRCI, which would reclassify them into "Static-Dynamic-Static" family.

6.2 Density matrix renormalization group-multireference configuration interaction

6.2.1 Density matrix renormalization group-fully internally contracted-multireference configuration interaction

As we introduced in Section 4.5, quantum chemists have developed efficient algorithms to compute the n-RDMs ($n = 1,2,3,4$) in DMRG active space (with up to 30 active orbitals), which can avoid the explicit and computationally prohibitive transformation between CAS-type wave function and matrix product state (MPS) formulation. Therefore a straightforward conclusion is to combine DMRG with FIC-MRCI, which requires only RDMs in the active space. Saitow et al. (2013) first reported DMRG-MRCI built on the FIC scheme for the compact reference treatment and on the cumulant approximation for the treatment of the 4-RDMs and named this scheme as DMRG-cu (4)-MRCI. Later Saitow et al. (2015) further developed an extended optimization of the tensor contractions by explicitly incorporating the rank reduction of the decomposed form of the cumulant-approximated 4-RDMs into the factorization. The new DMRG-MRCI implementation has been successfully applied to the determination of the stability of the iron(IV)-oxo porphyrin relative to the iron(V) electronic isomer (electromer), using the active space (29e, 29o) (including four second d-shell orbitals of iron) with triple-ζ-quality atomic orbital basis sets.

Moreover, to overcome the deficiency of size-inconsistency in truncated CI methods including MRCI, a *posteriori* Davidson correction (Langhoff and Davidson, 1974; Butscher et al., 1977) can be adopted to add into the final MRCI energy. The correction energy can be computed by

$$E_{\text{Davidson}} = \left(1 - \tilde{c}_0{}^2\right)(E_{\text{MRCISD}} - E_0), \qquad (6.17)$$

where $\tilde{c}_0$ is the coefficient of the reference $|\psi_0\rangle$ in the FIC-MRCISD wave function. E_{MRCISD} represents the energy of non-corrected MRCISD calculation, and E_0 gives the energy of the reference state. Of course, some other correction schemes (Luken, 1978; Davidson and Silver, 1977; Siegbahn, 1978; Pople et al., 1977; Meissner, 1988; Duch and Diercksen, 1994) have been suggested over the years and can be used as well.

It should be noticed that the cumulant approximation brings not only a lot of computational benefits but also the nonphysical interactions in the

Hamiltonian matrix, which results in the loss of the variational nature of ic-MRCI. Recently, various techniques have been proposed in order to remedy this problematic behavior, for example, truncating the IC basis with small eigenvalue ϵ_P in the overlap matrix S (Saitow et al., 2013).

Algorithm 6.1: FIC-MRCI based on a DMRG reference wave function. *DMRG*, density matrix renormalization group; *FIC*, fully internally contracted; *MRCI*, multireference configuration interaction.

1: **procedure** DMRG **//** refer to Algorithm 4.1 or 4.2
2:    **return** MPS $|\psi_0\rangle$ **//** only in active space
3: **end procedure**
4: **procedure** PrecalculateRDMs **//** refer to Algorithm 4.3
5:    **return** 1-,2-,3-RDMs **//** $D_{ij\ldots}^{kl\ldots} = \left\langle \psi_0 \left| \hat{E}_{ij\ldots}^{kl\ldots} \right| \psi_0 \right\rangle$
6: **end procedure**
7: **procedure** GeneralizeOverlapMatrix S
8:    $S_{\mu\nu} \leftarrow$ Use precalculated RDMs $D_{ij\ldots}^{kl\ldots}$ **//** $\psi_0 \left| \hat{E}_{v'a'}^{t'u'} \hat{E}_{t''u''}^{v''a''} \right| \psi_0 = D_{v't''u''}^{t'u'v''} \delta_{a'a''}$
9:    $V_{n \times n}$ eigenvectors$\{v_0, v_1, \ldots, v_n\}, \{\epsilon_n\} \leftarrow$ Diagonalize S
10:    $V'_{n \times k} \{v_0, v_1, \ldots, v_k\}, \epsilon' \leftarrow$ Discard zero-eigenvectors $\{v_{k+1}, v_{k+2}, \ldots, v_n\}$
11:    **return** $V'_{n \times k}, \epsilon'$
12: **end procedure**
13: **procedure** SolveGeneralizedEigenequation $HC = SCE$
14:    $H \leftarrow$ Calculate cumulant-approximated 4-RDMs on the fly **//** refer to Algorithm 4.3
15:    $H'C' = C'E \leftarrow HC = SCE$ **//** $H' = \left(\epsilon'^{-\frac{1}{2}} V'^T \right) H \left(V' \epsilon'^{-\frac{1}{2}} \right)$
16:    $E, C' \leftarrow$ Diagonalize H'
17:    **return** $E, C \left(= V' \epsilon'^{-\frac{1}{2}} C' \right)$
18: **end procedure**

6.2.2 Density matrix renormalization group-externally contracted-multireference configuration interaction

To deal with larger active spaces with more than 30 active orbitals via bypassing the use of high-order RDMs, Luo et al. (2018) suggested to combine DMRG with ec-MRCI. In this implementation, DMRG wave function is first converted to the CASCI-type wave function by using the entanglement-driving genetic algorithm (EDGA) (Luo et al., 2017), as introduced in Section 4.8. A selected-CI calculation is then performed by using only the leading configurations in the reconstructed CASCI-type wave function and the ground-state eigenvalue is taken as zeroth-order energy E_0. Of course, this incorporates a meager inaccuracy for neglecting unimportant configurations (e.g., with their weights smaller than 10^{-4}), but in exchange one obtains a sharp drop in the number of reference configurations ($10^4 \sim 10^5$) as a benefit to make the further ec-MRCI feasible. Through integrating selected-CI with ec-MRCI, it bypasses

the bottleneck of computing the high-order RDMs. By virtue of using this approach, post-DMRG was applied to larger active spaces with more than 40 active orbitals for the first time (Luo et al., 2018). The capability of the DMRG-ec-MRCI method was benchmarked against calculations of the potential energy curve of Cr_2 with active spaces up to (12e, 42o), singlet-triplet gaps of higher n-acene molecules with active spaces up to (38e, 38o), and the energy of the Eu-BTBP$(NO_3)_3$ complex with active space of (38e, 36o).

It must be mentioned that the current bottleneck of DMRG-ec-MRCI is that whether a limited number (less than 10^5) of important reference SDs or CSFs for a large active space or extremely strongly correlated systems can be selected out. Also, how to efficiently select the 10^5 important configurations is another difficulty.

Algorithm 6.2: DMRG-ec-MRCI. *DMRG*, Density matrix renormalization group; *ec*, externally contracted; *MRCI*, multireference configuration interaction.

1: **procedure** DMRG // refer to Algorithm 4.1 or 4.2
2:    **return** MPS $|\psi_0\rangle_{DMRG}$ // only in active space
3: **end procedure**
4: **procedure** EDGA // refer to Algorithm 4.4
5:    **return** collected configurations $\{|\phi_0\rangle, |\phi_1\rangle, \ldots, |\phi_n\rangle\}$
6: **end procedure**
7: **procedure** Obtain Reference Wave function $|\psi_0\rangle$ and Energy E_0
8:    $\boldsymbol{H} \leftarrow$ basis: $\{|\phi_0\rangle, \ldots, |\phi_n\rangle\}$
9:    $|\psi_0\rangle$, $E_0 \leftarrow$ Diagonalize $\boldsymbol{H}$
10: **end procedure**
11: **procedure** Form Contracted Singly and Doubly Excited Terms
12: $\left\{|\phi_S^a\rangle, |\phi_P^{ab}\rangle\right\} \leftarrow$ Generate singly and doubly excited configurations based on $\{|\phi_0\rangle, |\phi_1\rangle, \ldots, |\phi_n\rangle\}$
13: $\{|\psi_S\rangle, |\psi_P\rangle\} \leftarrow$ Contract $\left\{|\phi_S^a\rangle, |\phi_P^{ab}\rangle\right\}$ using Eq. 6.15
14: **end procedure**
15: **procedure** Compute Final Energy
16: $\boldsymbol{H}_{ec-MRCI} \leftarrow$ basis: $\{|\phi_0\rangle, \ldots, |\phi_n\rangle, |\psi_S\rangle, |\psi_P\rangle\}$
17: $|\psi_0\rangle^{ec}$, $E_0^{ec} \leftarrow$ Diagonalize $\boldsymbol{H}_{ec-MRCI}$
18: $E_{Davidson} \leftarrow$ Compute Davidson correction energy
19: **return** $E_0^{ec} + E_{Davidson}$
20: **end procedure**

6.2.3   Uncontracted matrix product state-multireference configuration interaction

Recently, Larsson et al. (2022) implemented uncontracted MRCISD and MRCISDT calculations on top of MPS reference wavefunctions. This is achieved by using the cluster MPS formulation (see Section 4.10) which

groups clusters of related orbitals into large "sites." In Larsson et al. (2022)'s implementation, the core orbitals and external orbitals were grouped to two large sites locating at the two ends of the MPS chain respectively, that is,

$$|\psi\rangle = \sum_n \boldsymbol{A}^{n_{\text{core}}} \boldsymbol{A}^{n_{K_{\text{core}}+1}} \boldsymbol{A}^{n_{K_{\text{core}}+2}} \dots \boldsymbol{A}^{n_{K_{\text{core}}+K_{\text{act}}}} \boldsymbol{A}^{n_{\text{ext}}}. \tag{6.18}$$

K_{core}, K_{act}, and K_{ext} are the numbers of core, active, and external orbitals, respectively, and n_{core} and n_{ext} label the Hilbert space of the coarse-grained core and external sites, of dimension P_{core} and P_{ext}. Then it becomes feasible to incorporate standard DMRG sweeps to optimize this cluster MPS to approach the uc-MRCI ansatzes by restricting the electron numbers in the three subspaces (e.g., $\{N_{\text{el}}, N_{\text{el}} - 1, N_{\text{el}} - 2\}$ in core and active sites and $\{0, 1, 2\}$ in the external site for MRCISD, where N_{el} is the total number of electrons in the molecule). Because the degrees of freedom in all three subspaces can be fully relaxed variationally, here no contraction approximations are imposed. Therefore this kind of MPS-MRCI corresponds to the uc-MRCI ansatz. However, we can easily notice that P_{core} and P_{ext} will be generally very large (roughly proportional to K_{core}^2 and K_{ext}^2). Therefore this usually requires a much larger bond dimension in MPS-MRCI than that in traditional DMRG, contributing to very expensive computational costs. Larsson et al. (2022) illustrated the capability of MPS-MRCI for active spaces with up to 30 electrons and 30 orbitals with up to triple excitations in the external space (in case of the benzene molecule with only 78 external orbitals), and with up to 280 external orbitals (in case of the chromium dimer for a small active space of 12 electrons in 12 orbitals). But it was shown that the energy results for both MPS-MRCISD and MPS-MRCISDT calculations of the benzene molecule still did not converge at $m = 9000$. Therefore it remains highly challenging to generalize MPS-MRCI calculations to larger active spaces and larger basis sets.

6.3 Density matrix renormalization group-multireference perturbation theory

In this section we will focus on the discussion of the basic ideas in MRPT theory and its combination with DMRG.

6.3.1 Recapitulation of multireference perturbation theory

6.3.1.1 Rayleigh−Schrödinger perturbation theory

Time-independent PT was first introduced by Schrödinger (1926), in which he referred to an earlier work by Rayleigh (1894). Consequently, PT as known nowadays is often named Rayleigh−Schrödinger PT (RSPT).

RSPT starts with the decomposition of Hamiltonian:

$$\hat{H} = \hat{H}_0 + \lambda \hat{V}, \tag{6.19}$$

where $\hat{H}_0$ is an unperturbed Hamiltonian with the known energies and eigenvectors, that is, $\hat{H}_0|\psi_n^{(0)}\rangle = E_n^{(0)}|\psi_n^{(0)}\rangle$ ($n = 1, 2, 3, \ldots$). $\hat{V}$ indicates the perturbed term representing a weak physical disturbance and λ gives a dimensionless parameter used for derivation. Thus the Schrödinger equation becomes:

$$\left(\hat{H}_0 + \lambda\hat{V}\right)|\psi_n\rangle = E_n|\psi_n\rangle. \tag{6.20}$$

The energy and wave function can also be decomposed as expansions:

$$|\psi_n\rangle = |\psi_n^{(0)}\rangle + \lambda|\psi_n^{(1)}\rangle + \lambda^2|\psi_n^{(2)}\rangle + \ldots \tag{6.21}$$

$$E_n = E_n^{(0)} + \lambda E_n^{(1)} + \lambda^2 E_n^{(2)} + \ldots. \tag{6.22}$$

which results in

$$\left(\hat{H}_0 + \lambda\hat{V}\right)\left(|\psi_n^{(0)}\rangle + \lambda|\psi_n^{(1)}\rangle + \ldots\right) = \left(E_n^{(0)} + \lambda E_n^{(1)} + \ldots\right)\left(|\psi_n^{(0)}\rangle + \lambda|\psi_n^{(1)}\rangle + \ldots\right). \tag{6.23}$$

By matching the coefficients of each power of λ, we can get the equations of different order wave functions and energies. Usually, we only consider up to second-order perturbative energy correction. The first-order wave function and one- and two-order energy equations can be written as:

$$E_n^{(1)} = \langle\psi_n^{(0)}|\hat{V}|\psi_n^{(0)}\rangle, \tag{6.24}$$

$$\left(\hat{H}_0 - E_n^{(0)}\right)|\psi_n^{(1)}\rangle = \left(E_n^{(1)} - \hat{V}\right)|\psi_n^{(0)}\rangle, \tag{6.25}$$

$$E_n^{(2)} = \langle\psi_n^{(0)}|\hat{V}|\psi_n^{(1)}\rangle = \sum_{m\neq n}\frac{\langle\psi_n^{(0)}|\hat{V}|\psi_m^{(0)}\rangle^2}{E_n^{(0)} - E_m^{(0)}}. \tag{6.26}$$

Note that the scalar product of $|\psi_n^{(1)}\rangle$'s Eq. 6.25 with $|\psi_n^{(1)}\rangle$ yields:

$$\langle\psi_n^{(1)}|\hat{H}_0 - E_n^{(0)}|\psi_n^{(1)}\rangle = -\langle\psi_n^{(1)}|\hat{V}|\psi_n^{(0)}\rangle, \tag{6.27}$$

and adding it with $E_n^{(2)} = \langle\psi_n^{(0)}|\hat{V}|\psi_n^{(1)}\rangle$, one can get:

$$E_n^{(2)} = \langle\psi_n^{(1)}|\hat{H}_0 - E_n^{(0)}|\psi_n^{(1)}\rangle + 2\langle\psi_n^{(1)}|\hat{V}|\psi_n^{(0)}\rangle, \tag{6.28}$$

which can be called Hylleraas functional $H[\psi_n^{(1)}]$ (Hylleraas, 1930). This implies that the second-order energy corrections can be also determined in a variational way by minimizing the Hylleraas functional, therefore given perturbation scheme is referred to as Hylleraas variational PT (VPT).

Here we only focus on the ground state's property, so we will later refer to $|\psi_0^{(0)}\rangle, |\psi_0^{(1)}\rangle, E_0^{(2)}$ as $|\psi_0\rangle$(or$|0\rangle, |\psi^{(0)}\rangle), |\psi_1\rangle$(or $|1\rangle, |\psi^{(1)}\rangle)$ and E_2 for simplicity.

6.3.1.2 Different perturbation theory partitions

It is obvious that the performance of a PT theory is highly dependent on the choice of the zeroth-order Hamiltonian $\hat{H}_0$, which is also denoted as PT partition. Because there exist different PT partitions, there are numerous MRPT theories proposed within the framework of RSPT. Here, we just introduce a part of them, which have been used in the combination of DMRG and MRPT.

6.3.1.2.1 Complete active space with second-order perturbation theory

The CAS with second-order PT (CASPT2) was first proposed by Roos et al. (1982) and later improved by Andersson et al. (1990, 1992). It can be seen as the generalized extension of Møller−Plesset (MP) partition (Møller and Plesset, 1934) from SR situation to MR cases and employs the one-electron generalized Fock operator as the zeroth-order Hamiltonian:

$$\hat{H}_0^{\text{caspt2}} = \hat{P}_0 \hat{F} \hat{P}_0 + \hat{P}_K \hat{F} \hat{P}_K + \hat{P}_{SD} \hat{F} \hat{P}_{SD} + \hat{P}_{TQ\ldots} \hat{F} \hat{P}_{TQ\ldots}, \qquad (6.29)$$

where $\hat{F}$ is the generalized Fock operator:

$$\hat{F} = \sum_{pq} f_{pq} \hat{E}_q^p, \qquad (6.30)$$

and f_{pq} is $\hat{F}'s$ representation in the MO basis:

$$f_{pq} = \frac{1}{2} \sum_{\sigma} \left\langle 0 \middle| \hat{a}_{p\sigma} \left[\hat{H}, \hat{a}_{q\sigma}^\dagger \right] + \hat{a}_{p\sigma}^\dagger \left[\hat{H}, \hat{a}_{q\sigma} \right] \middle| 0 \right\rangle, \qquad (6.31)$$

$\hat{P}_{\ldots}$ is the projector onto the corresponding space $\hat{V}_{\ldots}$. And $\hat{V}_0$ is $\{|\psi_0\rangle\}$; $\hat{V}_K$ represents the internal excitation space; $\hat{V}_{SD}$ indicates single and double excitation space; and $\hat{V}_{TQ\ldots}$ gives the space which contains all higher order excitations not included in the other three spaces. Note that the terms in $\hat{V}_K$ and $\hat{V}_{TQ\ldots}$ do not interact with $|0\rangle$ via the total Hamiltonian, so the first-order wave function is in $\hat{V}_{SD}$ which can be divided into eight groups as we showed in Table 6.1:

$$\begin{aligned} &\text{i) } \hat{E}_i^t \hat{E}_v^u |0\rangle, \quad \text{ii) } \hat{E}_i^t \hat{E}_j^u |0\rangle, \quad \text{iii) } \hat{E}_t^a \hat{E}_v^u |0\rangle, \quad \text{iv) } \hat{E}_i^a \hat{E}_u^t |0\rangle, \ \hat{E}_i^t \hat{E}_u^a |0\rangle, \\ &\text{v) } \hat{E}_j^t \hat{E}_j^a |0\rangle, \quad \text{vi) } \hat{E}_t^a \hat{E}_u^b |0\rangle, \quad \text{vii) } \hat{E}_i^a \hat{E}_t^b |0\rangle, \quad \text{and} \quad \text{viii) } \hat{E}_i^a \hat{E}_j^b |0\rangle. \end{aligned} \qquad (6.32)$$

After the definition of $\hat{H}_0^{\text{caspt2}}$, the first-order equation set can be written out as

$$\sum_{\nu} \left[F_{\mu\nu} - E_0 S_{\mu\nu} \right] c_\nu = - V_\mu, \qquad (6.33)$$

where $F_{\mu\nu} = \langle \mu | \hat{H}_0 | \nu \rangle$, $S_{\mu\nu} = \langle \mu | \nu \rangle$, $V_\mu = \langle \mu | \hat{H} | 0 \rangle$ and μ, ν represent the different excitation configurations from the reference function $|0\rangle$, that is,

$|\mu\rangle = \hat{E}_{ij}^{ab}|0\rangle$, $|v\rangle = \hat{E}_{i'j'}^{a'b'}|0\rangle$. The solution c_v of this linear equation set is the coefficient of the excited configuration in the first-order wave function, that is, $|1\rangle = \sum_v c_v|v\rangle$. The second-order energy correction is then determined to be

$$E_0^{(2)} = \langle 0|H|1\rangle = \sum_\mu V_\mu c_\mu. \tag{6.34}$$

Although CASPT2 method provides a surprisingly accurate value of energy for a reasonable cost, CASPT2 suffers from the intruder state problem, due to the choice of one-electron Fock operator as $\hat{H}_0$ for a many-electron calculation, that is, the denominator in second-order energy would be zero when the energies of orbitals are degenerate or quasi-degenerate (QD). Thus a level-shift correction (Roos and Andersson, 1995; Forsberg and Malmqvist, 1997) usually has to be incorporated.

6.3.1.2.2 ENPT2

Different from using one-electron Fock operator in MP partition, Epstein−Nesbet partition (Epstein, 1926; Nesbet and Hartree, 1955) can provide a computationally simpler MRPT solution by partitioning the full configurational space into a variational space and an outer space. The simplicity of only having diagonal elements in the outer space for the zeroth-order Hamiltonian in ENPT makes it an attractive alternative to other MRPT methods, since no diagonalization or solving linear equation set is required. Here the zeroth-order Hamiltonian is defined as:

$$\hat{H}_0^{\text{ENPT}} = \sum_{IJ}^{\text{active}} \langle\phi_I|\hat{H}|\phi_J\rangle|\phi_I\rangle\langle\phi_J| + \sum_K^{\text{inactive}} \langle\phi_K|\hat{H}|\phi_K\rangle|\phi_K\rangle\langle\phi_K|. \tag{6.35}$$

where $|\phi_I\rangle$ and $|\phi_J\rangle$ are the configurations in active space and $|\phi_K\rangle$ represents the configuration in the rest of the space. The second-order energy correction is written as:

$$E_m^{(2)} = \sum_K \frac{\left(\langle\phi_K|\hat{H}|\psi_m^{(0)}\rangle\right)^2}{E_m^{(0)} - \langle\phi_K|\hat{H}_0|\phi_K\rangle}, \tag{6.36}$$

where $|\psi_m^{(0)}\rangle$ is the reference wave function for the mth eigenstate and $E_m^{(0)}$ introduces the corresponding reference energy.

Note that ENPT2 is generally exempted from the intruder state problem and has a closer similarity with the true electronic Hamiltonian. However, it has been proved that for SR problems, MP partition is preferred over EN partition, and the ENPT2 is generally less accurate than second-order MPPT (MP2) and lacks several important properties such as size extensivity and orbital rotation invariance. As for the MR situation, if a sufficiently large active space is used, ENPT2's disadvantages may be partly alleviated, since

the essential part of static correlation has been well described and the rotation among the active orbitals does not affect the reference energy.

6.3.1.2.3 Second-order N-electron valence state perturbation theory

Second-order N-electron valence state PT (NEVPT2) was proposed by Angeli et al. (2001, 2002) about 10 years after the formulation of CASPT2. Its uncontracted version has been rarely used in practical applications, because of the high computational cost. Instead, its two latter variants, the pc-NEVPT2 and the sc-NEVPT2 are commonly used. Hence, here we will only introduce its simplest version, sc-NEVPT2.

In sc-NEVPT2, the many-electron Dyall's Hamiltonian (Dyall, 1995) is used as a substitute for the generalized one-electron Fock operator in CASPT2 to define the zeroth-order Hamiltonian, which can be written as:

$$\hat{H}^{\text{Dyall}} = \hat{H}_{\text{c}} + \hat{H}_{\text{v}} + C. \tag{6.37}$$

Here, $\hat{H}_{\text{c}}$ is a one-electron (diagonal) operator in the inactive space:

$$\hat{H}_{\text{c}} = \sum_{i,\sigma} \varepsilon_i \hat{a}^+_{i,\sigma} \hat{a}_{i,\sigma} + \sum_{a,\sigma} \varepsilon_a \hat{a}^+_{a,\sigma} \hat{a}_{a,\sigma}, \tag{6.38}$$

and ε expresses the orbital energy. $\hat{H}_{\text{v}}$ represents a two-electron operator in the active space:

$$\hat{H}_{\text{v}} = \sum_{tu,\sigma} h^{\text{eff}}_{tu} \hat{a}^+_{t,\sigma} \hat{a}_{u,\sigma} + \sum_{tuvw,\sigma\tau} g_{twuv} \hat{a}^+_{t,\sigma} \hat{a}^+_{u,\tau} \hat{a}_{v,\tau} \hat{a}_{w,\sigma}, \tag{6.39}$$

where g_{twuv} is two-electron integral. The matrix element of closed shell Fock operator $\left(h^{\text{eff}}_{tu}\right)$ is defined as:

$$h^{\text{eff}}_{tu} = h_{tu} + \sum_i (2g_{abii} - g_{aibi}), \tag{6.40}$$

where h_{tu} indicates the one-electron integral and C introduces a constant defined as:

$$C = 2\sum_i h_{ii} + \sum_{ij} \left(2g_{iijj} - g_{ijij}\right) - 2\sum_i \varepsilon_i, \tag{6.41}$$

to ensure that $\hat{H}^{\text{Dyall}}$ is equivalent to the full Hamiltonian within the CAS space.

As we can see, the Dyall Hamiltonian can be considered as a hybrid of the zeroth-order Hamiltonians in CASPT2 and ENPT2, where the projection of Hamiltonian in inactive space is represented by generalized Fock operator, and in active space by the bielectronic Hamiltonian. The second-order correction is thus given by:

$$E^{(2)}_m = -\sum_K \frac{\left(\langle \psi_K | \hat{H} | \psi^{(0)}_m \rangle\right)^2}{\langle \psi_K | \hat{H}^{\text{Dyall}} | \psi_K \rangle - E_0}, \tag{6.42}$$

where $|\psi_K\rangle$ represents the singly and doubly excited perturber functions from the internal space to the active space or external space.

6.3.1.2.4 Linearized coupled cluster doubles

Linearized CC (LCC) was formally derived by Fink (2006), where the LCC can be interpreted as a PT using Fink's Hamiltonian. This theory is sometimes called retaining the excitation degree-PT (REPT), and it is straightforwardly extended to MR cases, resulting in a MRLCC theory (Fink, 2009).

Fink proposed to set $\hat{H}_0$ to all terms of the full Hamiltonian, which retain the excitation degree (i.e., do not change the number of electrons in any of the core, active, or external spaces):

$$\hat{H}_0^{\text{Fink}} = \sum_{pq, \triangle n = 0} \sum_{\sigma} h_{pq} \hat{a}_{p\sigma}^\dagger \hat{a}_{q\sigma} + \sum_{pqrs, \triangle n = 0} \sum_{\sigma\tau} \frac{1}{2} g_{psqr} \hat{a}_{p\sigma}^\dagger \hat{a}_{q\tau}^\dagger \hat{a}_{r\tau} \hat{a}_{s\sigma}, \quad (6.43)$$

where $\triangle n = 0$ signifies that all terms which would change the total number of electrons in the core, active, or external spaces are removed.

The first-order wave function equation is then written as:

$$\langle \phi_{tu}^{ab} | \hat{H}_0 - E_0 | \psi^{(1)} \rangle = - \langle \phi_{tu}^{ab} | \hat{V} | \phi_0 \rangle, \quad (6.44)$$

$$\sum_{vwcd} \langle \phi_{tu}^{ab} | \hat{H}_0 - E_0 | \phi_{vw}^{cd} \rangle c_{vw}^{cd} = - \langle \phi_{tu}^{ab} | \hat{V} | \phi_0 \rangle. \quad (6.45)$$

For $\hat{H}_0 = \hat{H}_0^{\text{Fink}}$, this can be rewritten as:

$$\sum_{vwcd} \langle \phi_{tu}^{ab} | \hat{H} | \phi_0 + \phi_{vw}^{cd} c_{vw}^{cd} \rangle = E_0 c_{vw}^{ab}, \quad (6.46)$$

which is also well known as the amplitude equation of the LCC doubles method.

In order to conclude this subsection, in Fig. 6.2, we offer a schematic diagram of the different $\hat{H}_0$ partition schemes within MRPT. This efficiently illustrates matrix participating elements in practical calculations.

6.3.2 Density matrix renormalization group-complete active space with second-order perturbation theory

As we can see, in CASPT2 calculation of first-order wave function and second-order energy, the central complexity arises in the computation of the matrix elements

$$F_{\mu\nu} = \sum_{tu} f_{tu} \langle \mu | \hat{E}_t^u | \nu \rangle = \sum_{tu} f_{tu} \left\langle 0 \left| \hat{E}_{v'a}^{t'u'} \hat{E}_t^u \hat{E}_{t''u''}^{v''b} \right| 0 \right\rangle. \quad (6.47)$$

Here, μ, ν represent the different excitation configuration from the reference function $|0\rangle$: $|\mu\rangle = \hat{E}_{v'a}^{t'u'} |0\rangle$, $|\nu\rangle = \hat{E}_{t''u''}^{v''b} |0\rangle$. The coupling term $\langle 0 | \ldots | 0 \rangle$ can
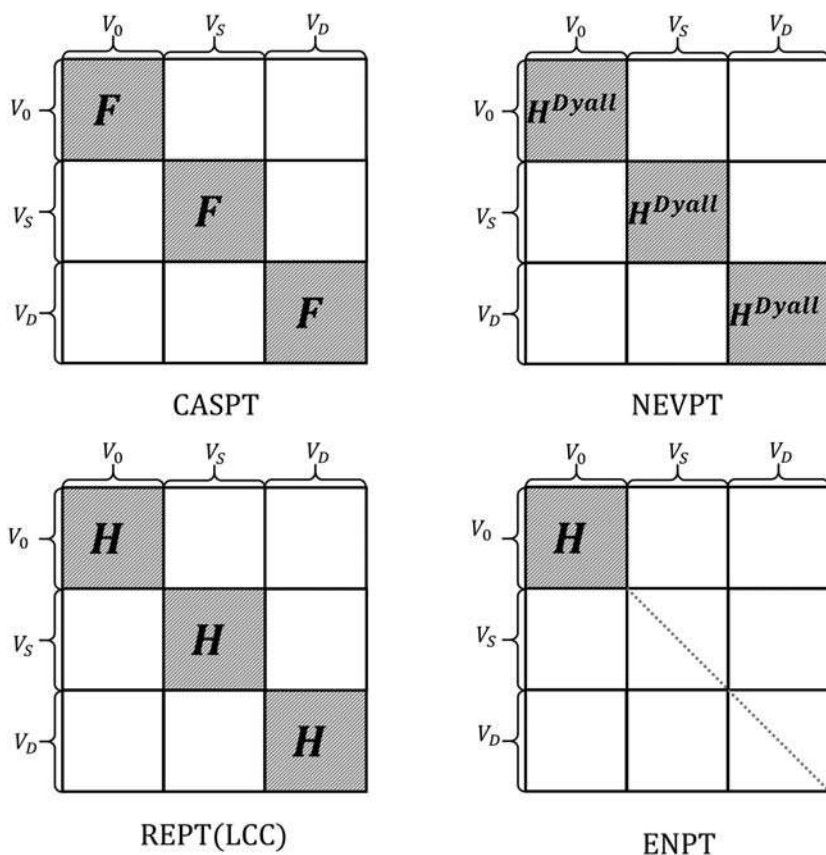
FIGURE 6.2 Schematic illustration of zeroth-order Hamiltonians $\hat{H}_0$ in different partitions of MRPT. Here, V_0 is the CAS space; V_S and V_D represent the single and double excitation spaces, respectively. The zero elements are shown in blank blocks and the nonzero elements are displayed with shadow background or dashed lines. *MRPT*, Multireference perturbation theory.

be evaluated from the n-RDMs ($n = 1, 2, 3, 4$), while $F_{\mu\nu}$ is further computed from their contractions with f_{tu} which are referred to as contracted RDMs (Cn-RDMs). It has been proved that Cn-RDMs can be computed with the same computation cost as n-RDMs for any used MOs. Kurashige and Yanai (2011) illustrated the first implementation of CASPT2 on top of the DMRG wave function, and its capability was demonstrated with the calculation of the potential energy curve of the chromium dimer with a large ($3d$ double-shell) active space consisting of 28 orbitals. Just like the cumulant approximation methods used in the combination of DMRG with MRCI, the cumulant versions of DMRG-CASPT2 were also later proposed (Kurashige et al., 2014; Nakatani and Guo, 2017). Such a DMRG-cu(4)-CASPT2

approach has been successfully applied to calculate the longitudinal static second hyperpolarizability of all-trans polyenes $C_{2n}H_{2n+2}$ ($n = 4-12$) (Wouters et al., 2016) and investigate the mechanism of various photochemistry systems (Liu et al., 2013; Shirai et al., 2016; Yanai et al., 2017) as well as characterize the low-lying excited states in chloro-ligated iron(IV)-oxo porphyrin and other mono- and di-nuclear metal complexes (Phung et al., 2016; Phung and Pierloot, 2019; Phung et al., 2021; Tran, 2021).

Algorithm 6.3: DMRG-cu(4)-FIC-CASPT2.

1: **procedure** DMRG // refer to Algorithm 4.1 or 4.2
2:    **return** $E_0, |\psi_0\rangle$ // only in active space
3: **end procedure**
4: **procedure** PrecalculateRDMs // refer to Algorithm 4.3
5:    **return** 1-,2-,3-RDMs // $D_{ij\dots}^{kl\dots} = \left\langle \psi_0 \left| \hat{E}_{ij\dots}^{kl\dots} \right| \psi_0 \right\rangle$
6: **end procedure**
7: **procedure** GeneralizeOverlapMatrix S
8:    $S_{\mu\nu} \leftarrow$ Use precalculated RDMs $D_{ij\dots}^{kl\dots} // \left\langle \psi_0 \left| \hat{E}_{v'a'}^{t'u'} \hat{E}_{t'u'}^{v'a'} \right| \psi_0 \right\rangle = D_{v't'u'}^{t'u'v''} \delta_{a'a''}$
9:    $V_{n \times n}$ eigenvectors $\{v_0, v_1, \dots, v_n\}$, $\{\epsilon_n\} \leftarrow$ Diagonalize S
10:    $V_{n \times k}'$ $\{v_0, v_1, \dots, v_k\}, \epsilon' \leftarrow$ Discard zero-eigenvectors $\{v_{k+1}, v_{k+2}, \dots, v_n\}$
11:    **return** $V_{n \times k}', \epsilon'$
12: **end procedure**
13: **procedure** SolveLinearizedEquation $(F - E_0 S)C = -V$
14:    $V \leftarrow$ 1-,2-,3-RDMs
15:    $F \leftarrow$ Calculate cumulant-approximated 4-RDMs on the fly // refer to Algorithm 4.3
16:    $(F' - E_0)C' = -V' \leftarrow (F - E_0 S)C = -V // H' = \left(\epsilon'^{-\frac{1}{2}} V'^T\right) H \left(V' \epsilon'^{-\frac{1}{2}}\right)$
17:    $C' \longleftarrow$ Solve linearized Equation
18:    **return** $|\psi_1\rangle \left(= \sum_\mu c_\mu |\mu\rangle\right) // C\{c_\mu\} \left(= V' \epsilon'^{-\frac{1}{2}} C'\right)$
19: **end procedure**
20: **procedure** CalculateSecondOrderEnergy
21:    $E_0^{(2)} = \langle \psi_0 | H | \psi_1 \rangle = \sum_\mu V_\mu c_\mu$
22:    **return** $E_0 + E_0^{(2)}$
23: **end procedure**

6.3.3 Density matrix renormalization group-second-order N-electron valence state perturbation theory

The cumulant approximation version for the combination of DMRG and sc-NEVPT2 was firstly implemented by Guo et al. (2016). Besides, a projection approximation scheme (Roemelt et al., 2016) was further incorporated to reduce the cost of evaluating the norm and energy expectation value for the most expensive classes of perturber functions, which requires 3-RDMs

and 4-RDMs in DMRG-sc-NEVPT2. Later, a Cholesky decomposition of the two-electron repulsion integrals was also exploited in DMRG-sc-NEVPT2 by Freitag et al. (2017) to efficiently describe static and dynamic correlation in spin-crossover complexes involving calculations with more than 1000 atomic basis functions. Recently, DMRG-sc-NEVPT2 was successfully applied to the investigation of magnetic exchange couplings in bis-μ-oxo/μ-acetato Mn(III,IV) dimer (Roemelt et al., 2018), intra- and inter-molecular singlet fission (Taffet and Scholes, 2018; Walia et al., 2021), as well as carotenoid nuclear reorganization (Taffet et al., 2019). It may be also noted that, a recent benchmark comparison for approximations of RDMs in NEVPT2 by Guo et al. (2021) indicated that the cumulant approximation always leads to intruder states, while the prescreening approximation produces stable results with modest computational savings.

Algorithm 6.4: DMRG-cu(4)-sc-NEVPT2.

1: **procedure** DMRG **//** refer to Algorithm 4.1 or 4.2
2:   **return** $E_0, |\psi_0\rangle$ **//** only in active space
3: **end procedure**
4: **procedure** PrecalculateRDMs **//** refer to algorithm 4.3
5:   **return** 1-,2-,3-RDMs **//** $D_{ij\ldots}^{kl\ldots} = \left\langle \psi_0 \left| \hat{E}_{ij\ldots}^{kl\ldots} \right| \psi_0 \right\rangle$
6: **end procedure**
7: **procedure** CalculateSecondOrderEnergy
8:   Calculate $N_l^{(k)}$ **//** $N_l^{(k)} = \langle \psi_l^k | \psi_l^k \rangle = \langle \psi_l^k | \hat{H} | \psi_m^{(0)} \rangle$ using $D_{ij\ldots}^{kl\ldots}$
9:   $\left\langle \psi_K \left| \hat{H}^D \right| \psi_K \right\rangle \leftarrow$ Calculate cu(4)-RDMs **//** refer to Angeli et al. (2002)
10:   Calculate $E_m^{(2)}$ using Eq. 6.42
11:   **return** $E_0 + E_0^{(2)}$
12: **end procedure**

The time-dependent formulation of the second-order N-electron valence PT (t-NEVPT2) (Sokolov and Chan, 2016) was also incorporated by Sokolov et al. (2017) to use in conjugation with a MPS reference wave function. This (t-MPS-NEVPT2) allowed to compute uncontracted dynamic correlation energies for large active spaces and basis sets, by using the time-dependent density matrix renormalization group (TD-DMRG, see Chapter 8) algorithm. It avoids the computation of expensive 4-RDMs. The active-space wave function is represented in terms of compact time-dependent quantities (active-space imaginary-time Green's functions), and numerical tests with up to 24 active orbitals show that the resulting t-MPS-NEVPT2 approach can get results equivalent to the fully uncontracted NEVPT2, but with a smaller computational cost.

6.3.4 Density matrix renormalization group-ENPT2

The combination of DMRG and MR-ENPT2 was first presented by Song et al. (2020) along with a selected-CI approximation. They suggested to use EDGA (Luo et al., 2017) to sample the most important CASCI-type configurations in a DMRG/MPS wave function and then perform selected-CI calculations, by constructing the Hamiltonian with the selected small number ($10^2 \sim 10^5$) of important configurations as the basis. The solution of a selected-CI calculation with the sampled important configurations will be then used for the zeroth-order wave function $|\psi_0\rangle$ and the zeroth-order energy E_0 in ENPT2 calculation. By avoiding the computation of n-RDMs, DMRG-ENPT2 allows to efficiently calculate systems with large active space beyond 40 orbitals, for example, a (42e, 42o) active space for a strongly correlated 8×8 Hydrogen square lattice. It should be noted that although ENPT2 suffers from two well-known deficiencies, size extensivity and orbital rotation variance, MR dynamic correlation calculations are heavily dependent on the quality of the reference wave function. By using a highly accurate DMRG wave function with a sufficiently large active space and a sufficiently large number m of preserved renormalized basis, DMRG-ENPT2 can be expected to greatly reduce the negative influences of the above mentioned two deficiencies in ENPT2. Similar to DMRG-ec-MRCI, DMRG-ENPT2 has the bottleneck of finding a limited number (less than 10^5) of important reference configurations for a large active space or extremely strongly correlated systems.

Algorithm 6.5: DMRG-ENPT2. *DMRG*, Density matrix renormalization group.

1: **procedure** DMRG **//** refer to Algorithm 4.1 or 4.2
2:　**return** MPS $|\psi_0\rangle_{\text{DMRG}}$ **//** only in active space
3: **end procedure**
4: **procedure** EDGA **//** refer to Algorithm 4.4
5:　**return** collected configurations $\{|\phi_0\rangle, |\phi_1\rangle, \ldots, |\phi_n\rangle\}$
6: **end procedure**
7: **procedure** Obtain Reference Wave function $|\psi_0\rangle$ and Energy E_0
8:　$\boldsymbol{H} \leftarrow$ basis: $\{|\phi_0\rangle, |\phi_1\rangle, \ldots, |\phi_n\rangle\}$
9:　$|\psi_0\rangle$, $E_0 \leftarrow$ Diagonalize $\boldsymbol{H}$
10: **end procedure**
11: **procedure** Compute 2-order Energy Contribution
12:　$\left\{ |\phi_S^a\rangle, |\phi_P^{ab}\rangle \right\} \leftarrow$ Generate singly and doubly excited configurations based on $\{|\phi_0\rangle, |\phi_1\rangle, \ldots, |\phi_n\rangle\}$
13:　$E_0^{(2)} = \sum_{S,a} \frac{\left(\langle \phi_S^a|\hat{H}|\psi_0\rangle\right)^2}{E_0 - \langle \phi_S^a|\hat{H}_0|\phi_S^a\rangle} + \sum_{P,a,b} \frac{\left(\langle \phi_P^{ab}|\hat{H}|\psi_0\rangle\right)^2}{E_0 - \langle \phi_P^{ab}|\hat{H}_0|\phi_P^{ab}\rangle}$
14:　**return** $E_0 + E_0^{(2)}$
15: **end procedure**

6.3.5 Matrix product states-perturbation theory

Instead of solving the first-order PT equations directly, Sharma and Chan (2014) proposed MPS-PT, in which the second-order energy was obtained by minimizing the Hylleraas functional in the space of MPS variationally. As we have introduced in Section 6.3.1, for the second-order energy, the variational functional of the Hylleraas functional $H[\psi_1]$ can be written as:

$$
\begin{aligned}
H[\psi_1] &= \langle\psi_1|\hat{H}_0 - E_0|\psi_1\rangle + 2\langle\psi_1|\hat{Q}\hat{V}|\psi_0\rangle \\
&= \langle\psi_1|\hat{H}_0 - E_0|\psi_1\rangle + 2\langle\psi_1|\hat{V}|\psi_0\rangle - 2\langle\psi_1|\psi_0\rangle\langle\psi_0|\hat{V}|\psi_0\rangle,
\end{aligned}
\tag{6.48}
$$

where $\hat{Q}$ is the projector onto the space orthogonal to $|\psi_0\rangle$ (equals $\hat{I}$ when $\langle\psi_1|\psi_0\rangle = 0$). In Sharma and Chan (2014)'s implementation (Fig. 6.3), the $\hat{H}_0$ was chosen as Dyall's Hamiltonian, the same as in sc-NEVPT2.

Thus $|\psi_1\rangle$ can be optimized by a sweep algorithm analogous to that in the DMRG, and overlaps and transition operator elements can be obtained easily by the efficient product operations between two MPSs and one MPO. However, it also means we have to do another sweep procedure, including the construction of MPOs besides the DMRG sweep, and the two sweeps have to be performed over the whole space (not only active orbitals).

Under this scheme, RDMs are no longer needed and the zeroth-order Hamiltonian $\hat{H}_0$ can be decided arbitrarily. Later, Sharma et al. (2016) further generalize MPS-PT for calculating energies of excited states by using QDPT. Another advantage of MPS-PT is its ability to recover the exact uncontracted MRPT energies in the limit of large MPS bond dimension. However, a standard DMRG-like sweep over the entire orbital set will become prohibitively expensive when working with a few hundred external orbitals. Sharma et al. (2017) further proposed to solve this problem by parametrizing the perturbed wave function using a mixture of CW partial

$$\partial\langle\Psi_1|H_0 - E_0|\Psi_1\rangle/\partial A^{n_{i_l}}_{i_{l-1}i_l} \qquad 2\partial\langle\Psi_1|V|\Psi_0\rangle/\partial A^{n_{i_l}}_{i_{l-1}i_l}$$

$$+$$

$$2\partial\langle\Psi_1|\Psi_0\rangle\langle\Psi_0|V|\Psi_0\rangle/\partial A^{n_{i_l}}_{i_{l-1}i_l} \qquad = 0$$
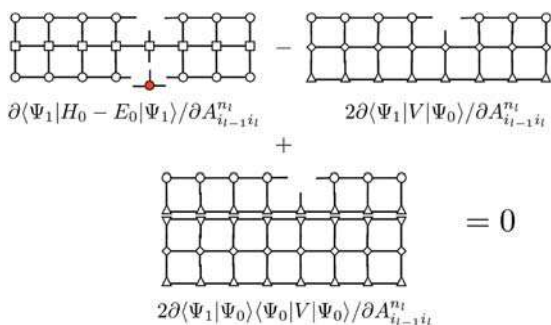
FIGURE 6.3 Schematic illustration of the optimization of $A^{n_{i_l}}_{i_{l-1}i_l}$ in $|\psi_1\rangle$. The red tensor is the quantity being solved for. *Reproduced from Sharma, S., Chan, G.K.-L., 2014. A flexible multireference perturbation theory by minimizing the Hylleraas functional with matrix product states. J. Chem. Phys. 141, 111101. https://doi.org/10.1063/1.4895977, with permission from American Institute of Physics.*

internal contraction and MPS-PT. All terms (i and iii in Eq. 6.32) that require 4-RDMs (internally contracted states with three active space indices and one external or core index) are treated fully uncontracted by MPS-PT, and the rest of the terms, requiring three-body or lower-order RDMs, are treated using internal contraction, for example,

$$\left(\hat{H}_0 - E_0\right)\left|\psi_1^{\text{iv}}\right\rangle = -\hat{V}^{\text{iv}}\left|\psi_0\right\rangle, \tag{6.49}$$

where $\left|\psi_1^{\text{iv}}\right\rangle$ and $\hat{V}^{\text{iv}}$ are respectively the space iv's contribution in $\left|\psi_1\right\rangle$ and $\hat{V}$, the space partition refers to Eq. 6.32. Now in MPS-PT, the first-order state has a maximum of a single electron in the external space, therefore the maximum bond dimension required for the tensors on external orbitals is only n_v, the number of external orbitals, which is much less than a typical m value of a few thousand that is routinely used in DMRG calculations. Recently, Khokhlov and Belov (2020) successfully applied the NEVPT2 under this combination framework (ic-MPS-NEVPT2) to study the low-lying excited states of polyenes containing from 8 to 13 conjugated double bonds, which serve as a model for natural carotenoids. With relaxed geometries of the excited states, absorption and transient absorption spectra were also calculated within the Franck − Condon approximation bridging the gap between experimental spectroscopic data and computational results.

6.3.5.1 Matrix product states-linearized coupled cluster

Sharma and Alavi (2015) proposed a new size-extensive MRLCC theory using matrix product states (MPS-LCC), which provides remarkably accurate ground-state energies for a wide variety of electronic Hamiltonians. As we introduced and proposed by Fink (2009), MRLCC can be reformulated as MR-REPT. Under this framework, an MPS-LCC scheme can be worked out as the extension of the MPS-PT algorithm.

In LCC ansatz, the Baker−Campbell−Hausdorff (BCH) expansion is truncated at the first order, that is, $e^{-\hat{T}}\hat{H}e^{\hat{T}} = \hat{H} + [\hat{H}, \hat{T}]$, which yields the governing equations of the SRLCC theory:

$$E = \left\langle\phi_0\middle|\hat{H}\middle|\phi_0\right\rangle + \left\langle\phi_0\middle|\hat{H}\middle|\psi_1\right\rangle, \tag{6.50}$$

$$0 = \left\langle\phi_{ij\cdots}^{ab\cdots}\middle|\hat{H}\middle|\phi_0\right\rangle + \left\langle\phi_{ij\cdots}^{ab\cdots}\middle|\hat{H} - E_0\middle|\psi_1\right\rangle. \tag{6.51}$$

Here, $\left|\psi_1\right\rangle \equiv \hat{T}\left|\phi_0\right\rangle$ is defined as the correction to wave function consisting of only single and double excitations, that is, $\hat{T} = \hat{T}_1 + \hat{T}_2$.

The MRLCC method can be achieved by replacing the HF determinant $\left|\phi_0\right\rangle$ with the many-electron wave function of CASCI or CASSCF $\left|\psi^{(0)}\right\rangle$.

By utilizing the PT and the projector approximation, the governing equation of $|\Psi^{(n)}\rangle$, which is the nth-order correction of the ground state wave function $|\Psi\rangle$ of the full Hamiltonian, is written as:

$$\left(\hat{H}_0 - E^{(0)}\right)|\psi^{(n)}\rangle = \hat{Q}\left(-\hat{V}|\psi^{(n-1)}\rangle + \sum_{k=1}^{n} E^{(k)}|\psi^{(n-k)}\rangle\right), \qquad (6.52)$$

where $\hat{H}_0$ gives Fink Hamiltonian, $\hat{Q} = 1 - |\psi^{(0)}\rangle\langle\psi^{(0)}|$, and $\hat{V}$ represents the perturbative operator. Therefore, using the variational principle for the PT, the Hylleraas functional can be written as:

$$H\left[\psi^{(n)}\right] = \langle\psi^{(n)}|\hat{H}_0 - E^{(0)}|\psi^{(n)}\rangle$$

$$- \left(\langle\psi^{(n)}|\hat{V}|\psi^{(n-1)}\rangle - \sum_{k=1}^{n} E^{(k)}\langle\psi^{(n)}|\psi^{(n-k)}\rangle\right)$$

$$+ \langle\psi^{(n)}|\psi^{(0)}\rangle\left(\langle\psi^{(0)}|\hat{V}|\psi^{(n-1)}\rangle - \sum_{k=1}^{n} E^{(k)}\langle\psi^{(0)}|\psi^{(n-k)}\rangle\right).$$

$$(6.53)$$

The remaining part of this approach is to evaluate the MPS-LCC wave function by minimizing the Hylleraas functional using the sweep algorithm, which is totally equivalent to the MPS-PT method.

Algorithm 6.6: MPS-PT (not in combination with ic-ansatz). *MPS*, Matrix product states; *PT*, perturbation theory.

1: **procedure** DMRG **//** refer to Algorithm 4.1 or 4.2
2:    **return** $E_0, |\psi_0\rangle$ **//** in the active space
3: **end procedure**
4: **procedure** Optimize first-order wave function $|\psi_1\rangle$
5:    $\hat{H}_0$, $\hat{V}$ $\longleftarrow$ Construct needed MPO **//** in the whole orbital space
6:    Generate Hylleraas functional $H(|\psi_1\rangle)$ **//** refer to Fig. 6.3
7:    optimized $|\psi_1\rangle \longleftarrow$ Optimize each site MPS in $|\psi_1\rangle$ by sweeping through whole space
8:    **return** $|\psi_1\rangle$
9: **end procedure**
10: **procedure** Compute 2-order Energy Contribution
11:    $E_0^{(2)} = \langle\psi_0|\hat{V}|\psi_1\rangle$
12:    **return** $E_0 + E_0^{(2)}$
13: **end procedure**

Algorithm 6.7: MPS-PT in combination with ic-ansatz. *MPS*, matrix product states; *PT*, perturbation theory.

1: **procedure** DMRG // refer to Algorithm 4.1 or 4.2
2:   **return** $E_0, |\psi_0\rangle$ // in the active space
3: **end procedure**
4: **procedure** Optimize $|\psi_1^i\rangle$ and $|\psi_1^{iii}\rangle$ // refer to Eq. 6.32
5:   $\hat{H}_0, \hat{V}^i, \hat{V}^{iii}$ $\longleftarrow$ Construct needed MPO // in the whole orbital space
6:   Generate Hylleraas functional $H[|\psi_1^i\rangle], H[|\psi_1^{iii}\rangle]$ according to Eq. 6.49
7:   **return** optimized $|\psi_1^i\rangle, |\psi_1^{iii}\rangle$ // refer to Algorithm 6.6
8: **end procedure**
9: **procedure** Optimize other space contribution in $|\psi_1\rangle$
10:   $\sum_\nu \left((H_0)_{\mu\nu} - E_0 S_{\mu\nu} \right) c_\nu = -V_\mu \leftarrow \langle\mu|\hat{H}_0 - E_0|\psi_1^{ii,iv,\cdots}\rangle = -\langle\mu|\hat{V}|\psi_0\rangle$
11:   c_ν $\longleftarrow$ Solve linearized equation // refer to Algorithm 6.3
12:   **return** $|\psi_1^{ii,iv,\cdots}\rangle$
13: **end procedure**
14: **procedure** Compute 2-order Energy Contribution
15:   $\begin{aligned} E_0^{(2)} &= \langle\psi_0|\hat{V}|\psi_1\rangle \\ &= \langle\psi_0|\hat{V}^{i,iii}|\psi_1^{i,iii}\rangle + \langle\psi_0|\hat{V}^{ii,iv,\cdots}|\psi_1^{ii,iv,\cdots}\rangle \end{aligned}$
16:   **return** $E_0 + E_0^{(2)}$
17: **end procedure**

6.3.6   Other variants

Besides the aforementioned DMRG-MRPT approaches, there are also many other DMRG-MRPT variants. For example, DMRG was suggested to be followed by the second-order perturbative version (DSRG-MRPT2) of driven similarity renormalization group (DSRG) by Khokhlov and Belov (2021), and the hybridization between DMRG and blocked correlated second-order PT (BCPT2) was implemented based on the generalized valence bond (GVB) reference by Xu et al. (2015).

DSRG introduced by Evangelista (2014) is an alternative approach to treat dynamic correlation effects in many-body theories. It is based on a series of infinitesimal unitary transformations of the Hamiltonian to decouple the reference wave function from its excited configurations.

$$\hat{H} \rightarrow \overline{H}(s) = \hat{U}^\dagger(s)\hat{H}\hat{U}(s), \tag{6.54}$$

where $\overline{H}(s)$ is the transformed Hamiltonian and $\hat{U}(s)$ gives a unitary operator that depends on a time-like parameter s defined in the range $(0, \infty)$. Both DSRG and its second-order perturbative version, DSRG-MRPT2, (Li and Evangelista, 2015) are inherently intruder free by suppressing those excitations that correspond to a denominator smaller than an energy cutoff $\left(\Lambda = s^{-1/2}\right)$. Another advantage of DSRG-MRPT2 is that it only requires

RDMs up to the third order. Recently, Khokhlov and Belov (2021) applied ab initio DMRG and DMRG-SCF calculations followed by DSRG-MRPT2 for the calculation of vertical and adiabatic excitation energies into the $2A_g^-$, $1B_u^-$, and $1B_u^+$ electronic states of polyenes, which contains from 8 to 13 conjugating double bonds acting as a model for natural carotenoids. The calculated adiabatic excitation energies deviated less than $1000\,\mathrm{cm}^{-1}$ from the experimental data for the $2A_g^-$ state and less than $3000\,\mathrm{cm}^{-1}$ for the $1B_u^-$ and $1B_u^+$ states. Given results can be considered as a fine agreement, when compared with the accuracy of ic-MPS-NEVPT2 reported by the same authors (Khokhlov and Belov, 2020) earlier.

Instead of applying MRPT theories on the DMRG reference wave functions or their RDMs, Xu et al. (2015) proposed to include the dynamic correlation as a simple energy correction calculated at an independent and lower MR quantum chemistry level, that is, GVB-BCPT2 in this work. The basic idea is to approximate the DMRG reference and excited functions as the GVB reference and the corresponding excited functions and simplify the zeroth-order Hamiltonian as $\hat{H}_0^{\mathrm{GVB}}$ in computing the dynamic correlation term. Therefore the total energy of this hybridized method (DMRG-BCPT2/GVB) can be written as

$$E_{\mathrm{DMRG-BCPT2/GVB}} = E_{\mathrm{DMRG}} + \sum_{u\neq 0} \frac{\left|\left\langle \psi_0^{\mathrm{GVB}} \middle| \hat{H} - \hat{H}_0^{\mathrm{GVB}} \middle| \psi_u^{\mathrm{GVB}} \right\rangle\right|^2}{E_0^{\mathrm{GVB}} - E_u^{\mathrm{GVB}}}, \qquad (6.55)$$

where E_0^{GVB} (E_u^{GVB}) and $|\psi_0^{\mathrm{GVB}}\rangle$ ($|\psi_u^{\mathrm{GVB}}\rangle$) are the ground (excited) state energy and wave function, respectively. Xu et al. (2015) applied DMRG-BCPT2/GVB to investigate the bond-breaking potential energy surfaces in *n*-butane and the spectroscopic constants of Cr_2. However, when the molecules are extremely strongly correlated, the GVB approximation for the DMRG reference may break down and accordingly the performance of the DMRG-BCPT2/GVB method becomes less satisfactory.

6.4 Density matrix renormalization group-coupled cluster theory

In this section, we first give a brief recapitulation about CC theory, followed by an introduction to the recently proposed combination schemes of DMRG with different CC approaches.

6.4.1 Recapitulation of coupled cluster theory

The wave function of traditional SRCC theory is written as an exponential ansatz:

$$|\psi\rangle = e^{\hat{T}}|\phi_0\rangle = \left(1 + \hat{T} + \frac{\hat{T}^2}{2!} + \frac{\hat{T}^3}{3!} + \dots\right)|\phi_0\rangle. \qquad (6.56)$$

where $|\phi_0\rangle$ is the SD (e.g., the HF determinant), and $\hat{T}$ is an excitation operator which contains a set of excitation terms at the different levels:

$$\hat{T} = \hat{T}_1 + \hat{T}_2 + \hat{T}_3 + \dots,$$

$$\hat{T}_1 = \sum_{i,a} t_i^a \hat{a}_a^\dagger \hat{a}_i = \sum_{i,a} t_i^a \hat{E}_i^a,$$

$$\hat{T}_2 = \sum_{i>j,a>b} t_{ij}^{ab} \hat{a}_a^\dagger \hat{a}_i \hat{a}_b^\dagger \hat{a}_j = \frac{1}{4} \sum_{ij,ab} t_{ij}^{ab} \hat{E}_{ij}^{ab}, \tag{6.57}$$

Here, $i, j, \dots$ label occupied orbitals and $a, b, \dots$ label unoccupied orbitals. t_i^a and t_{ij}^{ab} are excitation amplitudes.

Due to the exponential ansatz, the standard CC wave function that contains all determinants in FCI space obtains several significant properties (Crawford and Schaefer, 2000) such as *size extensivity* and *size consistency* provided that the reference function adopts a direct-product form in the noninteracting separated limit. The CC Schrödinger equation is written like:

$$\hat{H}|\psi\rangle = \hat{H}e^{\hat{T}}|\phi_0\rangle = E_{CC}e^{\hat{T}}|\phi_0\rangle. \tag{6.58}$$

We may left-multiply it by $\langle\phi_0|e^{-\hat{T}}$ or $\langle\phi_{ij\dots}^{ab\dots}|e^{-\hat{T}}$ to achieve:

$$\left\langle \phi_0 \middle| e^{-\hat{T}}\hat{H}e^{\hat{T}} \middle| \phi_0 \right\rangle = E_{CC}, \tag{6.59}$$

$$\left\langle \phi_{ij\dots}^{ab\dots} \middle| e^{-\hat{T}}\hat{H}e^{\hat{T}} \middle| \phi_0 \right\rangle = 0. \tag{6.60}$$

The similarity transformed Hamiltonian ($\hat{H}^T$) is non-Hermitian and may be expressed through the BCH expansion:

$$\begin{aligned}
\hat{H}^T &= e^{-\hat{T}}\hat{H}e^{\hat{T}} \\
&= \hat{H} + [\hat{H}, \hat{T}] + \frac{1}{2!}\left[[\hat{H}, \hat{T}], \hat{T}\right] + \frac{1}{3!}\left[\left[[\hat{H}, \hat{T}], \hat{T}\right], \hat{T}\right] + \dots
\end{aligned} \tag{6.61}$$

Thus we can obtain the energy from Eq. 6.59, while the amplitudes come from Eq. 6.60. Because the energy is given by an expectation value of the non-Hermitian $\hat{H}^T$, it is not guaranteed to obey the variational theorem. For practical uses, different truncations of the excitation operator $\hat{T}$ define the CC methods at different levels. If the cluster operator only contains double excitation, that is, $\hat{T} \approx \hat{T}_2$, then it is the simplest CC method, generally denoted as CCD, and if single excitation is also included, thence CCSD method will be obtained, etc.

Just like CISD or MP2 method, the CC theory is still an SR method, even though the exponential CC wave function is defined in the entire

Hilbert space. Thus SRCC fails in describing MR chemical systems, which encouraged the extension of the CC formalism to produce an efficient multireference CC (MRCC) method applicable to a wider class of interesting problems. Theoretically, MRCC (Lyakh et al., 2012; Evangelista, 2018) can be obtained through substituting the SD by a multiconfigurational reference wave function (e.g., the CASSCF wave function).

It can be easily derived that, in SRCC, higher than fourfold commutators cannot appear in Eq. 6.61, because of the two-body nature of the Hamiltonian and commutativity of all components in $\hat{T}$. However, in most cases of MRCC, the excitation and deexcitation coupling between the active indexes leads to an unterminated BCH expansion due to the noncommutativity of the excitation operators that constitute $\hat{T}$, leading to more complex equations as compared to SRCC. Recent advances in MRCC theory seem to have opened new frontiers for simplier implementations. Generally, the MRCC algorithms can be categorized into two sets. The first one is called "genuine" MRCC scheme, where a true multiconfigurational reference wave function is used, and the second one is named alternative MRCC, which simply adjusts the conventional CC formalism to MR problems. For details about MRCC theory, the readers may refer to the reviews by Lyakh et al. (2012) and Köhn et al. (2013) or the book by Kowalski et al. (2013) as well as the references therein.

6.4.2 Density matrix renormalization group-alternative-multireference coupled cluster

Since practical MRCC methods are limited, works on the combination of CC theory and DMRG are significantly fewer compared with those for the MRCI or MRPT methods. However, there are still several impressive attempts in combining the alternative MRCC schemes with DMRG.

Since 2016 the combination of tailored CC (TCC), one of the alternative MRCC schemes, with DMRG has been extensively investigated (Veis et al., 2016; Faulstich et al., 2019; Antalík et al., 2019; Lang et al., 2020). The general TCC (Kinoshita et al., 2005) wave function employs the following split-amplitude ansatz

$$\left|\psi_{\mathrm{TCC}}\right\rangle = e^{\hat{T}}\left|\phi_0\right\rangle = e^{\hat{T}_{\mathrm{ext}}+\hat{T}_{\mathrm{cas}}}\left|\phi_0\right\rangle = e^{\hat{T}_{\mathrm{ext}}}e^{\hat{T}_{\mathrm{cas}}}\left|\phi_0\right\rangle, \tag{6.62}$$

where $\left|\phi_0\right\rangle$ is the single determinant reference wave function, and the cluster operator $\hat{T}$ is divided into two parts: $\hat{T}_{\mathrm{cas}}$ represents the amplitudes corresponding to the active space and $\hat{T}_{\mathrm{ext}}$ is the rest of the cluster operator, that is, the amplitudes with at least one index outside the active space. The active part ($\hat{T}_{\mathrm{cas}}$) is obtained from a precomputed CAS wave function and keeps fixed during the calculation, while the external amplitudes ($\hat{T}_{\mathrm{ext}}$) are iterated using the standard CC framework. Note that $\left|\phi_0\right\rangle$ is the single determinant wave function, so $\hat{T}_{\mathrm{cas}}$ and $\hat{T}_{\mathrm{ext}}$ commute naturally.

As we mentioned before, the MPS-type wave function:

$$|\psi_{MPS}\rangle = \sum_{\{\sigma_i\}} A^{\sigma_1} A^{\sigma_2} \ldots A^{\sigma_n} |\sigma_1 \sigma_2 \ldots \sigma_n\rangle, \tag{6.63}$$

can be transformed into the CAS-type wave function:

$$|\psi\rangle = \sum_{\{\sigma_i\}} c_{\sigma_1 \ldots \sigma_n} |\sigma_1 \sigma_2 \ldots \sigma_n\rangle, \tag{6.64}$$

where the MPS matrices A^{σ_i} are contracted to obtain the CI coefficients $c_{\sigma_1 \ldots \sigma_n}$. Using the relations between CI and CC expansions

$$T_1 = C_1, \tag{6.65}$$

$$T_2 = C_2 - \frac{1}{2}(C_1)^2, \tag{6.66}$$

the CC amplitudes in active space can be acquired by DMRG procedure, which are kept frozen during the calculation. Thus the $\hat{T}_{cas}$ can be seen as the static correlation to the HF reference function. As for the amplitudes in $\hat{T}_{ext}$, they are optimized by treating the equations:

$$\left\langle \phi_{ij\ldots}^{ab\ldots} \left| e^{-\hat{T}_{ext}} \left(e^{-\hat{T}_{cas}} \hat{H} e^{\hat{T}_{cas}} \right) e^{\hat{T}_{ext}} \right| \phi_0 \right\rangle = 0 \tag{6.67}$$

which is analogous to the standard CC method and corresponds to the dynamic correlation.

Algorithm 6.8: DMRG-TCCSD. *DMRG*, Density matrix renormalization group. *TCCSD*, tailored coupled cluster singles and doubles.

1: **procedure** DMRG // refer to Algorithm 4.1 or 4.2
2:   **return** MPS $|\psi_0\rangle$ // only in active space
3: **end procedure**
4: **procedure** Calculate $\hat{T}_{cas}^{(1)}$ and $\hat{T}_{cas}^{(2)}$
5:   Choose the single-configurational reference wave function $|\phi_0\rangle$ (usually HF determinant)
6:   $\{c_t^u\}, \{c_{tu}^{vw}\} \longleftarrow$ extract the coefficients of singly and doubly excited configurations corresponding to $|\phi_0\rangle$ from $|\psi_0\rangle$ using Eq. 4.101: Obtain the CC amplitudes in active space from $\{c_t^u\}, \{c_{tu}^{vw}\}$ using Eqs. 6.65/6.66
8:   **return** $\hat{T}_{cas}^{(1)}$ and $\hat{T}_{cas}^{(2)}$
9: end procedure
10: procedure Calculate $\hat{T}_{ext}^{(1)}$ and $\hat{T}_{ext}^{(2)}$
11:   $\hat{T}_{ext}^{(1)}$ and $\hat{T}_{ext}^{(2)} \longleftarrow$ solve CC amplitude equations // see Eq. 6.67
12:   **return** $\hat{T}_{ext}^{(1)}$ and $\hat{T}_{ext}^{(2)}$
13: **end procedure**
14: **procedure** Compute CC energy
15:   Solve the CC energy equation // see Eq. 6.59
16:   **return** E_{CC}
17:   **end procedure**

DMRG-TCC does not require the computation of the high-rank RDMs, since the reference function is a single determinant, which, on the other hand, limits its accuracy for systems displaying strong static correlation, where the efficiency of DMRG is maximal in contrast. Recently, scrutinization of the performance of various CC methods tailored by electronic wave functions, including the DMRG, was given by Leszczyk et al. (2022). It was shown that, by restricting the cluster operator to at most double excitations, the studied tailored CC methods were not able to treat very challenging systems such as predicting the correct barrier height for the automerization of cyclobutadiene, or reliably describing the complete potential energy surface of the chromium dimer.

On contrary to tailored CC, the externally corrected CC (ecCC) method (Li et al., 1997) extracts static correlation from a MR method, by using the MR wave function as an "external" source of higher order CC amplitudes. For example, in the externally corrected coupled cluster singles and doubles (ecCCSD), the $\hat{T}_3$ and $\hat{T}_4$ amplitudes are extracted from the external source

$$T_3 = C_3 - C_1 C_2 + \frac{C_1^3}{3},$$

$$T_4 = C_4 - C_1 C_3 - \frac{C_2^2}{2} + C_1^2 C_2 - \frac{C_1^4}{4},$$

(6.68)

and accordingly, a new set of $\hat{T}_1$ and $\hat{T}_2$ amplitudes are computed in their presence. The concept is that a *priori* exact $\hat{T}_3$ and $\hat{T}_4$ clusters, can yield the exact $\hat{T}_1$ and $\hat{T}_2$ clusters and as a result the exact final energy. Therefore, using an approximate many-electron wave function obtained by a low-level multiconfigurational calculation, one can fix the amplitudes in $\hat{T}_3$ and $\hat{T}_4$ and employ them in the CC chain:

$$\hat{T} = \hat{T}_1 + \hat{T}_2 + \hat{T}_3' + \hat{T}_4'$$

(6.69)

where $\hat{T}_3', \hat{T}_4'$ indicate they are approximated clusters. It has been shown that the $\hat{T}_3', \hat{T}_4'$ obtained from a partially converged FCIQMC calculation already provides nearly accurate FCI energy (Deustua et al., 2018). Thus a partially converged MPS with a small bond dimension can also be coupled with this theory and gives an exceptional combination scheme for DMRG and CC (Lee et al., 2021).

Algorithm 6.9: DMRG-ecCCSD(T).

1: **procedure** DMRG // refer to Algorithm 4.1 or 4.2
2:   Large CAS with small m or small CAS with large m // m is bond dimension
3:   **return** approximate $|\psi_0\rangle'$
4: **end procedure**
5: **procedure** Calculate $\hat{T}_3'$ and $\hat{T}_4'$
6:   Choose the single-configurational reference wave function $|\phi_0\rangle$ (usually HF determinant)
7:   $C_1', C_2', C_3', C_4' \leftarrow$ extract the coefficients of singly to quadruply excited configurations corresponding to $|\phi_0\rangle$ from $|\psi_0\rangle'$ using Eq. 4.101:   Choose the triply and quadruply excited configurations with large coefficients
// set the threshold according to Lee et al. (2021)
9:   Obtain the CC amplitudes of selected configurations using Eq. 6.68
10:   **return** $\hat{T}_3'$ and $\hat{T}_4'$
11: **end procedure**
12: **procedure** Calculate $\hat{T}_1$ and $\hat{T}_2$
13:   $\hat{T}_1$ and $\hat{T}_2 \leftarrow$ solve CC amplitude equations // see Eq. 6.60
14:   **return** $\hat{T}_1$ and $\hat{T}_2$
15: **end procedure**
16: **procedure** Compute total energy
17:   Solve the CC energy equation // see Eq. 6.59
18:   Add perturbative triples correction // refer to Lee et al. (2021)
19:   **return** $E_{\mathrm{CC}} + \delta^{\mathrm{ecCCSD(T)}}$
20: **end procedure**

6.4.3   Density matrix renormalization group-canonical transformation

Yanai, Chan and their coworkers have developed the so-called canonical transformation (CT) theory (Yanai and Chan, 2006; Neuscamman et al., 2010a), an elaborated theory seeking feasible alternatives to the "genuine" CC method. Its combination with DMRG has also been discussed in the subsequent literatures (Neuscamman et al., 2009; Yanai et al., 2010).

In common with CC methods, CT theory is also based on an exponential ansatz

$$|\psi\rangle = e^{\hat{A}}|\psi_0\rangle. \tag{6.70}$$

However, $\hat{A}$ is an anti-Hermitian operator, that is, $\hat{A} = \sum_\mu A_\mu \left(\hat{O}_\mu - \hat{O}_\mu^\dagger\right)$, which makes $e^{\hat{A}}$ a unitary transformation, and $|\psi_0\rangle$ is a reference wave function.

At the singles and doubles (CTSD) level of theory, the full set of possible excitations are given by the following:

$$
\begin{aligned}
\hat{A} = &\sum_{ij,tu} A_{ij}^{tu}\left(\hat{E}_{ij}^{tu} - \hat{E}_{tu}^{ij}\right) + \sum_{i,tuv} A_{iv}^{tu}\left(\hat{E}_{iv}^{tu} - \hat{E}_{tu}^{iv}\right) + \sum_{i,t} A_{i}^{t}\left(\hat{E}_{i}^{t} - \hat{E}_{t}^{i}\right) \\
&+ \sum_{tu,ab} A_{tu}^{ab}\left(\hat{E}_{tu}^{ab} - \hat{E}_{ab}^{tu}\right) + \sum_{tuv,a} A_{tu}^{va}\left(\hat{E}_{tu}^{va} - \hat{E}_{va}^{tu}\right) + \sum_{t,a} A_{t}^{a}\left(\hat{E}_{t}^{a} - \hat{E}_{a}^{t}\right) \\
&+ \sum_{i,tu,a} A_{it}^{ua}\left(\hat{E}_{it}^{ua} - \hat{E}_{ua}^{it}\right) + \sum_{i,t,ab} A_{it}^{ab}\left(\hat{E}_{it}^{ab} - \hat{E}_{ab}^{it}\right) + \sum_{ij,t,a} A_{ij}^{ta}\left(\hat{E}_{ij}^{ta} - \hat{E}_{ta}^{ij}\right) \\
&+ \sum_{ij,ab} A_{ij}^{ab}\left(\hat{E}_{ij}^{ab} - \hat{E}_{ab}^{ij}\right) + \sum_{i,a} A_{i}^{a}\left(\hat{E}_{i}^{a} - \hat{E}_{a}^{i}\right),
\end{aligned}
\tag{6.71}
$$

where the indices obey the rules that we mentioned in Section 6.1.1.

Given that $e^{\hat{A}}$ is a unitary transformation, the effective Schrödinger equation in CT method is written as:

$$
\widehat{\overline{H}}\left|\psi_0\right\rangle = E\left|\psi_0\right\rangle,
\tag{6.71}
$$

where the effective Hamiltonian is obtained by $\widehat{\overline{H}} = e^{-\hat{A}}\hat{H}e^{\hat{A}}$. Therefore the energy and amplitude equations are formalized as:

$$
E_{\mathrm{CT}} = \left\langle\psi_0\left|\widehat{\overline{H}}\right|\psi_0\right\rangle,
\tag{6.72}
$$

$$
0 = \left\langle\psi_0\left|\left[\widehat{\overline{H}},\hat{A}\right]\right|\psi_0\right\rangle.
\tag{6.73}
$$

If $\left|\psi_0\right\rangle$ is a multiconfigurational reference wave function, the CT ansatz aforementioned becomes the same as that used in an internally contracted MR unitary CC theory (ic-MRUCC) (Chen and Hoffmann, 2012), except the fact that the CT method further applies operator decompositions to avoid the high computational costs in ic-MRUCC theories.

As we can see, after the canonical transformation of the Hamiltonian, the complexity of wave function is transferred to the Hamiltonian operator

$$
\widehat{\overline{H}} = e^{-\hat{A}}\hat{H}e^{\hat{A}} = \hat{H} + \left[\hat{H},\hat{A}\right] + \frac{1}{2!}\left[\left[\hat{H},\hat{A}\right],\hat{A}\right] + \ldots
\tag{6.74}
$$

Here over two-particle-rank operators appear, for example, $\left[\hat{H},\hat{A}\right]$ gives out $a_{p_1}^{\dagger}a_{p_2}^{\dagger}a_{p_3}^{\dagger}a_{q_1}a_{q_2}a_{q_3}$ terms which are not included in an electronic Hamiltonian. In order to avoid the unlimited expansion of the transformed Hamiltonian, the three- and higher-body interactions (operators) are approximated by the products of one- and two-body interactions,

$$
\widehat{\overline{H}}_{1,2} = \hat{H} + \left[\hat{H},\hat{A}\right]_{1,2} + \frac{1}{2!}\left[\left[\hat{H},\hat{A}\right]_{1,2},\hat{A}\right]_{1,2} + \ldots
\tag{6.75}
$$

where the notation $\left[\hat{H},\hat{A}\right]_{1,2}$ indicates that a combination of one- and two-body operators is used as an approximation. Note that the quadratic term in Eq. 6.75 could also be approximated by applying the decomposition once $\frac{1}{2!}\left[\left[\hat{H},\hat{A}\right],\hat{A}\right]_{1,2}$ rather than applying it twice $\frac{1}{2!}\left[\left[\hat{H},\hat{A}\right]_{1,2},\hat{A}\right]_{1,2}$.

Using the formalism of extended normal ordering (ENO) operators suggested by Kutzelnigg and Mukherjee (1997), one can employ the operator approximation by neglecting any resulting three-body ENO operators. The one-, two-, and three-body ENO operators are defined as

$$\tilde{\hat{E}}_{q_1}^{p_1} = \hat{E}_{q_1}^{p_1} - D_{q_1}^{p_1},$$

$$\tilde{\hat{E}}_{q_1 q_2}^{p_1 p_2} = \hat{E}_{q_1 q_2}^{p_1 p_2} - \sum^{P}\left(-\frac{1}{2}\right) D_{q_1}^{p_1}\tilde{\hat{E}}_{q_2}^{p_2} - D_{q_1 q_2}^{p_1 p_2},$$

$$\tilde{\hat{E}}_{q_1 q_2 q_3}^{p_1 p_2 p_3} = \hat{E}_{q_1 q_2 q_3}^{p_1 p_2 p_3} - \sum^{P}\left(-\frac{1}{2}\right) D_{q_1}^{p_1}\tilde{\hat{E}}_{q_2 q_3}^{p_2 p_3} - \sum^{P}\left(-\frac{1}{2}\right) D_{q_1 q_2}^{p_1 p_2}\tilde{\hat{E}}_{q_3}^{p_3} - D_{q_1 q_2 q_3}^{p_1 p_2 p_3},$$

$$(6.76)$$

where D represents the reference function's RDMs (see Section 4.6) and the summation runs over all possible permutations among $\{p_1, p_2, p_3\}$ and $\{q_1, q_2, q_3\}$ respectively. For each permutation operation of the indices from their original positions, a factor of $\left(-\frac{1}{2}\right)$ is applied. As a result, the three-body operators in $\left[\hat{H},\hat{A}\right]$ can be approximated by the combination of one- and two-body operators with the n-RDMs ($n = 1, 2, 3$),

$$\hat{E}_{q_1 q_2 q_3}^{p_1 p_2 p_3} \Rightarrow \sum^{P}\left(-\frac{1}{2}\right) D_{q_1}^{p_1}\tilde{\hat{E}}_{q_2 q_3}^{p_2 p_3} + \sum^{P}\left(-\frac{1}{2}\right) D_{q_1 q_2}^{p_1 p_2}\tilde{\hat{E}}_{q_3}^{p_3} + D_{q_1 q_2 q_3}^{p_1 p_2 p_3}. \qquad (6.77)$$

The energy and amplitude equations can be formalized using only the one- and two-body operators of the electronic Hamiltonian:

$$E_{\text{CT}} = \left\langle \psi_0 \left| \widehat{\overline{H}}_{1,2} \right| \psi_0 \right\rangle, \qquad (6.78)$$

$$0 = \left\langle \psi_0 \left| \left[\widehat{\overline{H}}_{1,2},\hat{A}\right]_{1,2} \right| \psi_0 \right\rangle. \qquad (6.79)$$

So far, the operator approximation eliminates all three- or higher body interactions in the expansion of the Hamiltonian, while requires the use of the reference function's 3-RDMs. In order to avoid calculating 3-RDMs, the cumulant approximation that we discussed before is utilized to decompose the 3-RDMs into its 1-RDMs and 2-RDMs approximations in CT method. Consequently, the final CT method only needs the 1-RDMs and 2-RDMs from the active space, which is easily obtained from the DMRG procedure.

A strongly contracted CT (sc-CT) theory has also been proposed (Neuscamman et al., 2010b). In this, the operators in $\hat{A}$ are written as the strongly contracted excitation operators, that is,

$$\hat{A} = \sum_{\mu} C_{\mu} \hat{o}_{\mu}. \tag{6.80}$$

Here $\hat{o}_{\mu}$ is a strongly contracted operator, for example,

$$\hat{o}^{a_1 a_2} = \sum_{t_1 t_2} g_{a_1 t_1 a_2 t_2} \left(\hat{E}_{t_1 t_2}^{a_1 a_2} - \hat{E}_{a_1 a_2}^{t_1 t_2} \right), \tag{6.81}$$

where $g_{a_1 t_1 a_2 t_2}$ is the two-electron integral appearing in the Hamiltonian.

Though the CT scheme slowly scales in the function of the system size, it introduces the intruder state problems, which are caused by the cumulant and operator decomposition approximations. These intruder states can be circumvented by the overlap truncation, the use of strongly contracted excitation operators or the level-shifted condition (Yanai et al., 2012). Unfortunately, those countermeasures now disrupt the size consistency of CT theory.

Algorithm 6.10: DMRG-CT. *DMRG*, Density matrix renormalization group; *CT*, canonical transformation.

1: **procedure** DMRG // refer to Algorithm 4.1or 4.2
2:   **return** $|\psi_0\rangle$ // only in active space
3: **end procedure**
4: **procedure** PrecalculateRDMs // refer to Algorithm 4.3
5:   Calculate cumulant-approximated 3-RDMs
6:   **return** 1-, 2-RDMs and cumulant approximated 3-RDMs
7: **end procedure**
8: **procedure** Calculate amplitudes of $\hat{A}$
9:   generate amplitude equations using the one- and two-body operators with 1-, 2-RDMs and cumulant approximated 3-RDMs // see Eqs. 6.76/6.77
10:   Solve amplitude equations // see Eq. 6.79
11:   **return** $\hat{A}$
12: **end procedure**
13: **procedure** Compute final energy
14:   Generate $\widehat{\overline{H}}_{1,2}$ // see Eq. 6.75
15:   Solve the energy equation (Eq. 6.78).
16:   **return** E_{CT}
17: **end procedure**

6.5 Hybridization of density matrix renormalization group with density functional theory

A computationally cheap alternative to obtain dynamic correlation with multi-configurational wave functions is to combine these with a density functional,

thereby exploiting the efficiency of density functional theory (DFT), while maintaining a correct description of multiconfigurational systems. In turn, the combination can also correct the errors observed in current DFT approximations, namely, the delocalization error and static correlation error (Cohen et al., 2008). In this section we will introduce several schemes for combining DMRG with DFT.

6.5.1 Recapitulation of density functional theory

DFT is probably the most widely used electronic structure method in solid-state physics, computational material science, and quantum chemistry. The principle behind DFT is that the ground-state density uniquely determines the external potential, and for this reason all properties of the system, including the energy and many-body wave function. In other words, the ground-state energy is a functional of the electron density (ρ):

$$E_{\text{DFT}} = E(\rho) = T(\rho) + V_{\text{ext}}(\rho) + U(\rho), \tag{6.83}$$

where T is the kinetic energy, V_{ext} expresses the potential energy from the external field (the attraction to the nuclei) and U represents the electron-electron energy. Assuming we can minimize this functional with respect to ρ, we will obtain the ground-state energy and electron density ρ with all other ground-state observables. In the framework of Kohn and Sham (1965), they mapped the interacting electronic system to a fake noninteracting system with the same density ρ, where every electron is treated as formally independent particles in the mean field of all other electrons, this results in a new functional of the energy:

$$E_{\text{KS-DFT}} = T_s(\rho) + V_s(\rho) = T_s(\rho) + V_{\text{ext}}(\rho) + E_H(\rho) + E_{xc}(\rho). \tag{6.84}$$

Here, $T_s(\rho)$ gives the kinetic energy and $V_s(\rho)$ is the external potential of one electron in the noninteracting system. $V_s(\rho)$ consists of three ingredients, the attraction to the nuclei ($V_{\text{ext}}(\rho)$), the Coulomb repulsion of electrons ($E_H(\rho)$), and all the rest things in the exchange-correlation term ($E_{xc}(\rho)$). Based on the expression of $E_{\text{KS-DFT}}$, Kohn–Sham (KS) equations of this auxiliary noninteracting system can be derived:

$$\left[-\frac{\hbar^2}{2m} \nabla^2 + \hat{V}_s \right] \phi_i = \varepsilon_i \phi_i. \tag{6.85}$$

By solving the KS equations, one can obtain the KS orbitals $\{\phi_i\}$ and reproduce the density ρ of the original interacting electronic system

$$\rho = \sum_{i=1}^{N} |\phi_i|^2. \tag{6.86}$$

Notwithstanding its simplicity, in the KS formulation the $\hat{V}_s$ depends on the ρ, that at the same time depends on $\{\phi_i\}$, which in turn depend on $\hat{V}_s$. The problem of solving KS equation can be fixed by the self-consistent method.

Note that although DFT is a single determinant method, we can obtain the exact energy and wave function by solving the KS equation if we have an ideally exact $E_{xc}(\rho)$. However, except for the free-electron gas, the exact functionals for exchange and correlation are unknown, approximations must be adopted to generate the $E_{xc}(\rho)$, such as local density approximation (LDA), generalized gradient approximation (GGA), hybrid functionals, and so on. (Cohen et al., 2012; Zhang and Xu, 2021)

6.5.2 Density matrix renormalization group-short-range density functional theory

The combination of multiconfigurational WFT and DFT is not straightforward, since static and dynamic correlation are merely phenomenological terms and cannot be strictly separated. A small part of static correlation is therefore already included in DFT calculations, implicitly by an empirical functional, leading to double-counting of correlation effects if no special precautions are taken.

To avoid the double-counting issue, Savin and Flad (1995) proposed multiconfigurational ranged-separated short-range DFT (MC-srDFT) method, where the two-electron operator are separated into long-range and short-range components,

$$\hat{g}(1,2) = \hat{g}^{\mu,\text{lr}}(1,2) + \hat{g}^{\mu,\text{sr}}(1,2). \tag{6.87}$$

The exact definition of $\hat{g}^{\mu,\text{lr}}(1,2)$ and $\hat{g}^{\mu,\text{sr}}(1,2)$ can differ by virtue of tuning the error function

$$\hat{g}^{\mu,\text{lr}}(1,2) = \frac{\text{erf}(\mu|\boldsymbol{r}_1 - \boldsymbol{r}_2|)}{|\boldsymbol{r}_1 - \boldsymbol{r}_2|}, \hat{g}^{\mu,\text{sr}}(1,2) = \frac{1 - \text{erf}(\mu|\boldsymbol{r}_1 - \boldsymbol{r}_2|)}{|\boldsymbol{r}_1 - \boldsymbol{r}_2|}, \tag{6.88}$$

which involves a range-separation parameter μ. Calibration studies suggest that μ values in the interval between 0.33 and 0.5 a.u. are optimal.

The short-range part of the electron interaction is henceforth treated by DFT, while the long-range part is assigned to the WFT approach. Accordingly, the ground-state energy expression of MC-srDFT can be written as:

$$E = \min_{\psi \to \rho} \left\{ \langle \psi | \hat{T} + \hat{g}^{\mu,\text{lr}} | \psi \rangle + E_{\text{Hxc}}^{\mu,\text{sr}} \left(\rho_\psi \right) + \int \rho_\psi(\boldsymbol{r}) V_{\text{ext}}(\boldsymbol{r}) d\boldsymbol{r} \right\}, \tag{6.89}$$

where $E_{\text{Hxc}}^{\mu,\text{sr}}\left(\rho_\psi\right)$ indicates the short-range Hartree-exchange-correlation functional and ρ_ψ is the density coming from the wave function ψ, that is,

$\rho_\psi = \langle\psi|\hat{\rho}|\psi\rangle = \sum_{pq}\langle\psi|\Omega_{pq}\hat{E}_q^p|\psi\rangle = \sum_{pq}\Omega_{pq}D_q^p$, where $\hat{\rho}$ represents the density operator and $\Omega_{pq} = \phi_p^*\phi_q$ is the overlap matrix of MOs. The minimizing wave function $|\psi_\mu\rangle$ from Eq. 6.89 can be given by the Euler−Lagrange equation:

$$\left[\hat{T} + \hat{g}^{\mu,\mathrm{lr}} + \hat{V}_{\mathrm{ext}} + v_{\mathrm{Hxc}}^{\mu,\mathrm{sr}}\left(\rho_{\psi_\mu}\right)\right]|\psi_\mu\rangle = \varepsilon_\mu|\psi_\mu\rangle, \tag{6.90}$$

where $v_{\mathrm{Hxc}}^{\mu,\mathrm{sr}}\left(\rho_{\psi_\mu}\right) = \delta E_{\mathrm{Hxc}}^{\mu,\mathrm{sr}}\left(\rho_\psi\right)/\delta\rho(\boldsymbol{r})$.

As we can see, MC-srDFT requires new short-range exchange-correlation functionals ($E_{\mathrm{Hxc}}^{\mu,\mathrm{sr}}$), because the standard functionals which were designed to capture all electron correlation are not suitable for it. Thus srLDA, srGGA, and *meta*-srGGA variants have been developed. Once the approximation is chosen for $E_{\mathrm{Hxc}}^{\mu,\mathrm{sr}}$, the wave function $|\psi_\mu\rangle$ can be computed by solving self-consistently Eq. 6.63 using wave function theories. As a result, the electron density ρ_ψ can be obtained and the total energy is calculated according to the Eq. 6.62.

Following the range-separation approach, Hedegård et al. (2015) proposed the combination of DMRG with DFT, so-called DMRG-srDFT. In this work, range-separation parameter μ is chosen to be 0.4 a.u., and the energy expression is written as:

$$\mathrm{E}_{\mathrm{DMRG}}^{\mathrm{srDFT}} = E_C^{\mathrm{lr}} + E_A^{\mathrm{lr}} + E_{\mathrm{Hxc}}^{\mathrm{sr}}(\rho), \tag{6.91}$$

where E_C^{lr}, E_A^{lr} are the core energy and active energy obtained by the WFT, and the regular two-electron integrals are replaced by the long-range two-electron integrals, that is $g_{pqrs} \rightarrow g_{pqrs}^{\mathrm{lr}}$.

Since $E_{\mathrm{Hxc}}^{\mathrm{sr}}(\rho)$ is nonlinear in 1-RDMs, an exact DMRG-srDFT expression is state specific (SS). In order to formulate the DMRG-srDFT energy to be linear with the density matrix, a reference density is introduced. This results in a more complicated energy expression as (a detailed derivation can be referred to works of Pedersen, 2004 and Hedegård et al., 2015):

$$E_{\mathrm{DMRG}}^{\mathrm{srDFT}} = E_C^{\mathrm{srDFT}} + E_A^{\mathrm{srDFT}}, \tag{6.92}$$

where the core part becomes

$$\begin{aligned}
E_C^{\mathrm{srDFT}} = E_C^{\mathrm{lr}} &+ \frac{1}{2}\sum_{ij} j_{ij}^{\mathrm{C,sr}}\left(D_j^i\right)^C - \frac{1}{2}\sum_{tu} j_{tu}^{\mathrm{A,ref,sr}}\left(D_u^t\right)^{\mathrm{A,ref}} \\
&+ E_{\mathrm{xc}}^{\mathrm{sr}}\left(\rho^{\mathrm{ref}}\right) - \sum_{tu} v_{xc,tu}^{\mathrm{ref,sr}}\left(D_u^t\right)^{\mathrm{A,ref}}
\end{aligned} \tag{6.93}$$

and the active part is

$$E_A^{\mathrm{srDFT}} = E_A^{\mathrm{lr}} + \sum_{tu}\left(j_{tu}^{\mathrm{C,sr}} + j_{tu}^{\mathrm{A,ref,sr}} + v_{xc,tu}^{\mathrm{ref,sr}}\right)\left(D_u^t\right)^{\mathrm{A}} \tag{6.94}$$

$$E_A^{\text{srDFT}} = \sum_{tu} \left(f_{tu}^{\text{C,lr}} + j_{tu}^{\text{C,sr}} + j_{tu}^{\text{A,ref,sr}} + v_{\text{xc},tu}^{\text{ref,sr}} \right) \left(D_u^t \right)^A + \frac{1}{2} \sum_{tuvw} g_{tuvw}^{\text{lr}} \left(D_{wu}^{tv} \right)^A.$$

(6.95)

Here, j_{pq}^{sr} are the matrix elements of the short-range two-electron Coulomb operator,

$$j_{pq}^{\text{sr}} = \left\langle \phi_p \left| \frac{\delta E_{\text{H}}^{\text{sr}}}{\delta \rho(\boldsymbol{r})} \right| \phi_q \right\rangle = \sum_{rs} g_{pqrs}^{\text{sr}} D_s^r$$

(6.96)

and $v_{\text{xc},pq}^{\text{sr}}$ are the matrix elements of the short-range exchange-correlation potential,

$$v_{\text{xc},pq}^{\text{sr}} = \left\langle \phi_p \left| \frac{\delta E_{\text{H}}^{\text{sr}}}{\delta \rho(\boldsymbol{r})} \right| \phi_q \right\rangle.$$

(6.97)

$f_{pq} = h_{pq} + \sum_k (2g_{pqkk} - g_{pkqk})$ are the elements in generalized Fock matrix, and D_q^p, D_{rs}^{pq} denote 1-RDM and 2-RDM. Note that $\left(D_j^i \right)^C = 2\delta_{ij}$, since core orbitals are all doubly occupied, therefore only the density matrices in active space $\left(\left(D_u^t \right)^A, \left(D_{wu}^{tv} \right)^A \right)$ are needed in the energy expression.

In this formulation, a "DMRG macro iterations" can be made, where we rerun the DMRG-srDFT with an updated reference density, as Algorithm 6.11 shows. Note that the density matrices in every macro iteration are utilized as the reference density matrix in the next iteration, and only $j_{tu}^{\text{A,ref,sr}}$ and $v_{\text{xc},tu}^{\text{ref,sr}}$ need to be recalculated in each macro iteration. Thus, by adding them to the core Fock matrix, that is, $f_{tu}^{\text{C,lr}} + j_{tu}^{\text{C,sr}} + j_{tu}^{\text{A,ref,sr}} + v_{\text{xc},tu}^{\text{ref,sr}}$ in Eq. 6.95, the density matrices can influence $j_{tu}^{\text{A,ref,sr}}$ and $v_{\text{xc},tu}^{\text{ref,sr}}$, which in turn influence the newly obtained density matrices from DMRG. The macro iterations can therefore be continued until getting self-consistently converged DMRG-srDFT density matrices.

In practice, DMRG calculation is implemented on a CAS with a limited size instead of the full MO space. Therefore the long-range dynamic correlation energy is missing, which may be recovered by the recently proposed long-range-corrected multiconfiguration density functional with the on-top pair density based on adiabatic connection (AC) formalism (Hapka et al., 2020).

As an alternative to range-separated methods, the combination of CI methods with orbital occupation functionals has been also explored, at the formal level through the separation of correlation effects in the orbital space by Fromager (2015), and its combination with DMRG has been applied to treat the uniform one-dimensional Hubbard model (Senjean et al., 2018).

The lack of well-established algorithms for the design of new functionals has limited the applications of this approach to only model Hamiltonians.

Algorithm 6.11: DMRG-srDFT. *DMRG*, Density matrix renormalization group; *srDFT*, short-range density functional theory.

1: **procedure** Calculate Pre-Requisites
2:   Calculate lr/sr integrals and $\{f^{C,lr}\}$
3:   $\{j^{C,sr}\}, E_C^{lr} \longleftarrow$ integrals and $\{f^{C,lr}\}$
4:   $\left\{\left(D_u^t\right)^A\right\}, \left\{\left(D_{wu}^{tv}\right)^A\right\} \longleftarrow$ Run DMRG
5: **end procedure**
6: **procedure** Calculate Modified One-Electron Integrals
7:   $\rho^{ref} \longleftarrow \left\{\left(D_u^t\right)^A\right\}$ as reference density matrices $\left\{\left(D_u^t\right)^{A,ref}\right\}$
8:   $j^{A,ref,sr}, E_{xc}^{sr}(\rho^{ref}), v_{xc}^{ref,sr} \longleftarrow \rho^{ref}, \left\{\left(D_u^t\right)^{A,ref}\right\}$
9:   **return** $\{f_{tu}^{C,lr} + j_{tu}^{C,sr} + j_{tu}^{A,ref,sr} + v_{xc,tu}^{ref,sr}\}$
10: **end procedure**
11: **procedure** Run DMRG with Modified One-Electron Integrals and lr Integrals
12:   $\left\{\left(D_u^t\right)^A\right\}, \left\{\left(D_{wu}^{tv}\right)^A\right\}, E_A^{srDFT} \longleftarrow \{f_{tu}^{C,lr} + j_{tu}^{C,sr} + j_{tu}^{A,ref,sr} + v_{xc,tu}^{ref,sr}\}$ and g_{tuvw}^{lr}
13:   **if** D^A not converged **then**
14:     Go back to step 7 with updated $\left\{\left(D_u^t\right)^{A,ref}\right\}$
15:   **end if**
16:   **return** converged $\left\{\left(D_u^t\right)^A\right\}, \left\{\left(D_{wu}^{tv}\right)^A\right\}$ and E_A^{srDFT}
17: **end procedure**
18: **procedure** Calculate Total Energy
19:   Calculate E_C^{srDFT} using Eq. 6.93
20:   **return** $E_C^{srDFT} + E_A^{srDFT}$
21: **end procedure**

6.5.3 Density matrix renormalization group-pair density functional theory

Treatment of open-shell systems by conventional DFT models relies on utilizing unphysical ρ_α and ρ_β densities obtained from unrestricted (i.e., spin-polarized) SDs with broken spin symmetry. This is incompatible with the retained spin symmetry in multiconfigurational wave functions, which are eigenfunction of $\hat{S}^2$ as well as $\hat{S}_Z$ (S is total electron spin). Therefore Li Manni et al. (2014) proposed a multiconfigurational pair-DFT (MC-PDFT) to correct the multiconfigurational WFT for dynamic correlations. In this method, the functional is expressed in terms of not only the total density ρ, but also on-top pair density Π (Perdew et al., 1995).

The combination of DMRG with MC-PDFT (DMRG-PDFT) was later implemented by Sharma et al. (2019), in which DMRG is used as a substitute for the MCSCF method to calculate the kinetic energy and the Coulomb

energy. Here, we utilize the DMRG-PDFT to explain this scheme. It is important to mention that all equations hold for the other variants.

In the CAS model, the electronic energy for a multiconfigurational eigenstate $|\psi\rangle$ is expressed as:

$$E = \langle \psi | \hat{H} | \psi \rangle = \sum_{pq} h_{pq} D_q^p + \frac{1}{2} \sum_{pqrs} g_{pqrs} D_{qs}^{pr} + V_{nn} \qquad (6.98)$$

$$E = \sum_{i} (h_{ii} + f_{ii}) + \sum_{tu} f_{tu} D_u^t + \frac{1}{2} \sum_{tuvw} g_{tuvw} D_{uw}^{tv} + V_{nn}. \qquad (6.99)$$

In order to properly correct the energy for the dynamic correlation, the new MC-PDFT method calculates the energy via

$$E^{\text{MC-PDFT}} = \sum_{pq} h_{pq} D_q^p + \frac{1}{2} \sum_{pqrs} g_{pqrs} D_q^p D_s^r + E_{\text{ot}}(\rho, \Pi) + V_{NN} \qquad (6.100)$$

$$E^{\text{MC-PDFT}} = V_{NN} + 2 \sum_{i} h_{ii} + 2 \sum_{ij} g_{iijj} + \sum_{tu} h_{tu} D_u^t + 2 \sum_{i,tu} g_{iitu} D_u^t$$
$$+ \frac{1}{2} \sum_{tuvw} g_{tuvw} D_u^t D_w^v + E_{\text{ot}}(\rho, \Pi) \qquad (6.101)$$

where the 2-RDM (D_{sq}^{pr}) in Eq. 6.98 is replaced by the product of two 1-RDMs ($D_q^p D_s^r$), and the neglected exchange contributions are now included in the new-added on-top density functional $E_{\text{ot}}(\rho, \Pi)$. Note that in the MC-PDFT calculation, only the kinetic energy and the Coulomb energy are calculated from the MCSCF wave function, whereas all exchange and correlation contributions are evaluated by the density functional, and accordingly this results in the elimination of the double-counting errors that we mentioned before. The density and on-top pair density in $E_{\text{ot}}(\rho, \Pi)$ are calculated according to:

$$\rho = \sum_{ij} D_i^i \phi_i(\boldsymbol{r}) \phi_i(\boldsymbol{r}) + \sum_{tu} D_u^t \phi_t(\boldsymbol{r}) \phi_u(\boldsymbol{r}), \qquad (6.102)$$

$$\Pi = \sum_{ij} D_i^i D_j^j \phi_i(\boldsymbol{r}) \phi_j(\boldsymbol{r}) \phi_i(\boldsymbol{r}) \phi_j(\boldsymbol{r}) + \sum_{iitu} D_i^i D_u^t \phi_i(\boldsymbol{r}) \phi_i(\boldsymbol{r}) \phi_t(\boldsymbol{r}) \phi_u(\boldsymbol{r})$$
$$+ \sum_{tu} D_{wu}^{tv} \phi_t(\boldsymbol{r}) \phi_u(\boldsymbol{r}) \phi_v(\boldsymbol{r}) \phi_w(\boldsymbol{r}), \qquad (6.103)$$

Therefore the density functional correction can be evaluated only once, directly from the 1-RDMs and 2-RDMs obtained from DMRG. Evaluating the functional only once indicates that DMRG-PDFT has a computational advantage over DMRG-sr-DFT, since no self-consistent iterations between the DMRG and DFT parts are needed (only need one DMRG procedure).

Algorithm 6.12: DMRG-PDFT. *DMRG-PDFT*, Density matrix renormalization group-pair density functional theory.

1: **procedure** DMRG // refer to Algorithm 4.1 or 4.2
2:   **return** $E_0, |\psi_0\rangle$
3: **end procedure**
4: **procedure** PrecalculateRDMs
5:   **return** 1-,2-RDMs
6: **end procedure**
7: **procedure** Calculate on-top density functional $E_{ot}(\rho, \Pi)$
8:   $\rho, \Pi \leftarrow$ 1-,2-RDMs
9:   **return** $E_{ot}(\rho, \Pi)$
10: **end procedure**
11: **procedure** Calculate Total Energy // see Eq. 6.101
12:   **return** $E^{MC-PDFT}$ // V_{NN} is obtained in procedure "Prepare" of Algorithm 4.1 or 4.2
13: **end procedure**

6.6 Density matrix renormalization group-adiabatic connection

Recently, Beran et al. (2021) presented a new post-DMRG approach to include the dynamic correlation via the AC technique (Pernal, 2018; Pastorczak and Pernal, 2018a,b), which requires only up to two-body active space RDMs. They reported encouraging results of this approach on typical candidates for DMRG computations, namely, the n-acenes ($n = 2 \rightarrow 7$), Fe (II)-porphyrin, and Fe_3S_4 cluster.

The AC theory is a general approach to the correlation energy calculation, which can be applied to a broad class of multireference wave functions. The DMRG-AC recovers the correlation energy missing in the underlying DMRG model and the total electronic energy follows as the sum

$$E = E^{DMRG} + E_{corr}^{AC}. \qquad (6.104)$$

Given approach is based on the partitioning of the Hamiltonian $\hat{H} = \hat{H}^{(0)} + \hat{H}'$, where $\hat{H}^{(0)}$ comprises only two terms, one corresponding to the doubly occupied (inactive) part and other corresponding to the active orbitals. The AC formula defines the AC Hamiltonian by linearly interpolating between the zeroth-order Hamiltonian $\hat{H}^{(0)}$ and the exact one $\hat{H}$

$$\hat{H}^\alpha = \hat{H}^{(0)} + \alpha \hat{H}', \qquad (6.105)$$

with the coupling parameter α ranging from 0 to 1. By exploiting the Hellmann−Feynman theorem, a general AC correlation energy formula can be expressed as

$$E_{corr}^{AC} = \int_0^1 W^\alpha d\alpha, \qquad (6.106)$$

where the AC integrand reads

$$W^{\alpha} = \frac{1}{2}\sum_{pqrs} g_{rpsq} \sum_{\upsilon} D_r^p(\alpha,\nu) D_q^s(\alpha,\nu) + \frac{1}{2}\sum_{pqrs} g_{rpsq}\left(n_p + 1\right) n_q \delta_{rq}\delta_{ps},$$

$$(6.107)$$

with exclusion of terms involving all four indices *pqrs* belonging to a set of either active or inactive orbitals. Here n_p and n_q are occupation numbers of MOs p and q. $D_r^p(\alpha,\nu)$ and $D_q^s(\alpha,\nu)$ are transition 1-RDMs between the ground and νth eigenstates of the AC Hamiltonian $\hat{H}^{\alpha}$, which can be approximately obtained by employing extended random phase approximation (ERPA) equations (Chatterjee and Pernal, 2012), which require 1-RDMs and 2-RDMs from DMRG reference wave functions.

Based on the observation that the AC integral is typically nearly linear, the missing correlation energy has been further approximated using the first-order expansion of W^{α} at $\alpha = 0$, that is, $W^{\alpha} = W^{(0)} + \alpha W^{(1)}$. By noticing that $W^{(0)} = 0$, the AC0 approximation has been derived as

$$E_{\text{corr}}^{\text{AC0}} = \frac{W^{(1)}}{2}.$$

$$(6.108)$$

Beran et al. (2021) combined the DMRG-SCF and AC0 methods to describe the dynamic correlation outside the large CAS. 1-RDMs and 2-RDMs obtained from the DMRG-SCF calculation were employed to construct one-body transition RDMs in conjunction with the solutions of the ERPA equations and subsequently evaluate the AC0 energy correction. The final electronic energy of DMRG-SCF-AC0 is then expressed as

$$E^{\text{DMRG}-\text{SCF}-\text{AC0}} = E^{\text{DMRG}-\text{SCF}} + E_{\text{corr}}^{\text{AC0}}.$$

$$(6.109)$$

It is worth to note that the derivation of Eq. 6.106 assumed that a 1-RDM stays constant along the AC path, which is approximately valid in DMRG-AC calculations, because a major part of the static correlation would be already accounted for at $\alpha = 0$ in DMRG reference wave function with a large CAS. One limitation in the AC theory lies in the fact that only singly excited configurations are considered in ERPA, while double (and higher) excitations are completely neglected. Given restriction hampers its applicability as double excitations may play a key role in photophysics and photochemistry processes.

6.7 Embedding density matrix renormalization group in environments

Chemical reactions and molecular spectroscopy are usually local phenomena, which in principle can be well described with a small cluster model by using a quantum mechanics (QM) method at a sufficiently high level of theory.

However, an important aspect for the theoretical simulation of a molecular system is the reasonable treatment of its complex environment, which might be a solution, molecular matrices, or a biological protein. The direct incorporation of the environment into QM part will make the calculation infeasible, primarily due to the large number of nuclear and electronic degrees of freedom. Nowadays, many theoretical chemistry approaches have been proposed for describing the electronic structure of solvated molecules in environments. Solvation models can be classified into two main categories, depending on the way the environmental molecules are treated, that is, explicitly or implicitly. To describe the solvents explicitly with an affordable computational cost, quantum embedding schemes are often used with a division of the entire system into smaller less costly subsystems, usually a chemically active part requiring higher QM level description and its environment described by a more approximate theory, at either a classical molecule mechanics (MM) or lower QM level. On the other hand, on the basis of the traditional non-equilibrium solvation theory in continuum models, the solvent environmental effect can be described with an implicit solvation model with cheaper computational costs. In recent years, various combinations of DMRG with different solvation models have been explored. This enables accurate calculations on large systems with strong electron correlations embedded in realistic complex environments.

6.7.1 Density matrix renormalization group-in-density functional theory

Dresselhaus et al. (2015) presented the first implementation of DMRG embedded in a DFT environment (DMRG-in-DFT) by utilizing the frozen density embedding (FDE) scheme (Wesolowski and Warshel, 1993). In FDE, a specific subsystem DFT method, a subsystem is calculated in a KS approach by adding an effective potential to the KS potential of the isolated subsystem, assuming a constant (frozen) environmental electron density. The FDE framework also allows for treating one active subsystem with a correlated WFT method and the rest of the system with DFT, namely, WFT-in-DFT embedding. Here we briefly review the theoretical framework of Dresselhaus et al. (2015)'s implementation.

In WFT-in-DFT scheme, the total electronic energy E_{tot} can be calculated in the following way:

$$E_{\text{tot}} = E_{\text{act}}^{\text{WFT}} + E_{\text{env}}^{\text{KS−DFT}} + E_{\text{int}}^{\text{OF−DFT}}. \tag{6.110}$$

Here $E_{\text{act}}^{\text{WFT}}$, $E_{\text{env}}^{\text{KS−DFT}}$, and $E_{\text{int}}^{\text{OF−DFT}}$ are the energy of the active subsystem by WFT, the KS energy evaluated for the environmental electron density, and the system−environment interaction energy, respectively. $E_{\text{act}}^{\text{WFT}}$ gives the expected value of $\langle \psi^{\text{act}} | \hat{H}_{\text{act}} | \psi^{\text{act}} \rangle$ with $\hat{H}_{\text{act}}$ being the Hamiltonian of the

isolated active subsystem. To account for the polarization effect by the environment, the wave function $|\psi^{act}\rangle$ is expected to be fully relaxed with respect to the environment. For describing the inter-subsystem interactions, an effective embedding potential, the functional derivative of E_{int}^{OF-DFT} over a subsystem density, will be applied on each subsystem. For the active subsystem, this reads as

$$
\begin{aligned}
v_{emb}^{act}\left[\rho_{act}, \rho_{env}\right](\boldsymbol{r}) = {} & v_{kin}\left[\rho_{act} + \rho_{env}\right](\boldsymbol{r}) - v_{kin}\left[\rho_{act}\right](\boldsymbol{r}) \\
& + v_{xc}\left[\rho_{act} + \rho_{env}\right](\boldsymbol{r}) - v_{xc}\left[\rho_{act}\right](\boldsymbol{r}) \\
& + \int \frac{\rho_{env}(\boldsymbol{r}_2)}{|\boldsymbol{r} - \boldsymbol{r}_2|} \mathrm{d}r_2 + v_{ext}^{env}(\boldsymbol{r}).
\end{aligned}
\tag{6.111}
$$

Here v_{kin} is the functional derivative of the noninteracting kinetic energy and v_{xc} indicates the exchange-correlation energy. v_{ext}^{env} gives the potential caused by the nuclei of environmental subsystems. Therefore, to relax $|\psi^{act}\rangle$ with respect to the environment requires a solution of the Hamiltonian

$$
\hat{H}_{act}' = \hat{H}_{act} + \sum_{i=1}^{n_{act}} v_{emb}^{act}\left[\rho_{act}, \rho_{env}\right](\boldsymbol{r}_i),
\tag{6.112}
$$

where n_{act} is the number of electrons in the active subsystem. To solve the Hamiltonian of Eq. 6.112 by multiconfigurational WFT methods, one can add the extra potential $v_{emb}^{act}\left[\rho_{act}, \rho_{env}\right](\boldsymbol{r})$ onto the one-electron part of the Fock operator. Consequently, the eigenvectors of the modified Fock operator are used as new MO basis, and accordingly the one- and two-electron MO integrals are updated for later electron correlation WFT calculations. To achieve an accurate and self-consistent description for the mutual polarization between the system and surrounding environment, an iterative procedure (known as freeze-and-thaw cycle) is usually implemented, in which the role of system and environment is interchanged for the subsystems until convergence is reached.

In Dresselhaus et al. (2015)'s work, WFT-in-DFT is extended to DMRG-in-DFT by using DMRG-SCF as the WFT solver for the active subsystem.

6.7.2 Polarizable embedding density matrix renormalization group

Hybrid QM/MM framework, in which the most important part of the problem is treated by QM and the surrounding environment is described by an empirical force field for discrete solvent molecules, is another widely used explicit solvation model. Therein, the system−environment interactions are usually approximated by electrostatic embedding (EE) or polarizable embedding (PE) potentials. The EE potential, only accounting for the permanent charge distribution of the environment, is represented by a multicenter multipole expansion and accordingly neglects the QM part's polarization effect on

the environment. In order to account for many-body induction effects, that is, the polarization of the environment both internally and by the QM core, Olsen et al. (2010) suggested a PE scheme, in which the interaction with the surrounding environment is modeled through an effective operator. This effective operator represents the environment by multipoles [e.g., charges $q(\mathbf{r}_i)$, dipole moment $\mu_\alpha(\mathbf{r}_i)$, quadruple moment $Q_{\alpha\beta}(\mathbf{r}_i)$] and polarizabilities ($\alpha_i$) for each atomic center (and bond midpoint) i derived from QM calculations (usually with DFT) on subsystems of the environment.

In PE scheme, the interaction energy of environment and embedded system $\left(E^{\mathrm{PE}}\right)$ have both electrostatic and polarization contributions, E^{es} and E^{pol}, respectively.

$$E^{\mathrm{PE}} = E^{\mathrm{es}} + E^{\mathrm{pol}}. \tag{6.113}$$

E^{es} contains the interaction of all electrons in the QM region with the electrostatic environment via a multicenter multipole expansion of the environmental electrostatic quantities and the interaction of all multipoles within the environment. E^{pol} describes the interaction of all electrons in the QM region with the polarization of the environment by using distributed anisotropic polarizability tensors α_i on the environmental sites. The induced dipole moments are updated in each SCF iteration, thus leading to a fully self-consistent treatment of the polarization.

Hedegård and Reiher (2016) implemented the coupling of the PE approach with DMRG as well as DMRG-sr-DFT. The developed PE-DMRG and PE-DMRG-sr-DFT were then successfully applied for the study of the first excited state of water and a retinylidene Schiff base within a channelrhodopsin protein.

6.7.3   Combining density matrix renormalization group with reference interaction site model

Compared with the explicit counterparties, implicit solvation models provide an efficient means to estimate solvation energies without the necessity to calculate the solvent molecules explicitly and sample costly molecular dynamics trajectories. For example, dielectric continuum models along with parametrized terms are commonly used to obtain the long-range electrostatic interactions, in order to partially include in some average manner short-range interactions such as dispersion and exchange. However, such methods are well known to be infeasible to illustrate local solvation structures such as hydrogen bonding well. The reference interaction site model (RISM) (Chandler and Andersen, 1972) is another representative implicit solvation model based on integral equation theory for liquids. This method determines the electronic structure of a solute molecule and the statistical solvent distribution around the solute in a self-consistent manner. Recently, the combination between DMRG approaches with RISM has been successfully illustrated

by Shimizu et al. (2018), providing a new tool for calculating the photochemical properties of near-infrared molecules in solution.

The RISM method is a solvation theory of a statistical mechanical approach, in which the solvation structure is represented by the spatial correlation functions. In RISM, the total free energy $\mathcal{A}$ of the solvation system is defined as the sum of the electronic energy of the solute (E_{solute}) and the solvation free energy ($\Delta\mu$),

$$\mathcal{A} = E_{\text{solute}} + \Delta\mu. \tag{6.114}$$

The Fock operator for the solvated solute $\left(\hat{F}^{\text{solv}}\right)$ contains a solvent-specific term $\left(\hat{V}\right)$,

$$\hat{F}^{\text{solv}} = \hat{F}^{\text{gas}} + \hat{V}, \tag{6.115}$$

where $\hat{V}$ expresses the solvent reaction field in RISM as

$$\hat{V} = \rho \sum_{\lambda\alpha} \hat{b}_\lambda q_\alpha \int 4\pi r^2 \frac{g_{\lambda,\alpha}(r)}{r} dr. \tag{6.116}$$

Here ρ is the number density of the solvent, $\hat{b}_\lambda$ indicates a population operator of the solute, and q_α points the partial charge on the solvent site. $g_{\lambda,\alpha}(r)$ expresses a spatial pair correlation function between λ (solute) and α (solvent) with an inter-site distance of r, obtained by solving RISM equations. Thence, the combination of a WFT method with RISM is just modifying the one-electron integrals through replacing the original Fock operator by Eq. 6.115. The sketch of Shimizu et al. (2018)'s implementation of the RISM-DMRG-CASPT2 method in a SS fashion is depicted in Fig. 6.4. For the ground-state calculation, first the ground-SS (DMRG-)CASCI and orbital optimization are performed, and consequently the obtained 1-RDMs are passed to the RISM code for computing the electrostatic potential $\hat{V}$ induced by the solvents. These electrostatic potentials are used to construct the solvated Hamiltonian for the successive iteration. Once the wave function converges, the obtained solvated Hamiltonian is used in ground-state (DMRG-)CASPT2 to apply perturbation in solution. While computing the electronic absorption energy, the potentials obtained from the ground-state calculation are used to construct the solvated Hamiltonian for determining the excited state; this corresponds to the calculation of the excited state with the solvation structure fixed at the ground state. Finally, perturbation is applied in solution for the excited state via SS (DMRG-)CASPT2 with the obtained solvated Hamiltonian.

As it is well-known, and in the present book highlighted in Section 5.4, the SSCAS treatment for the excited state typically suffers from the root-flipping issue, which occurs when the approximate wave function leaves the convergence basin of the target excited state and enters that of a different excited state. To improve the convergence of the calculation under
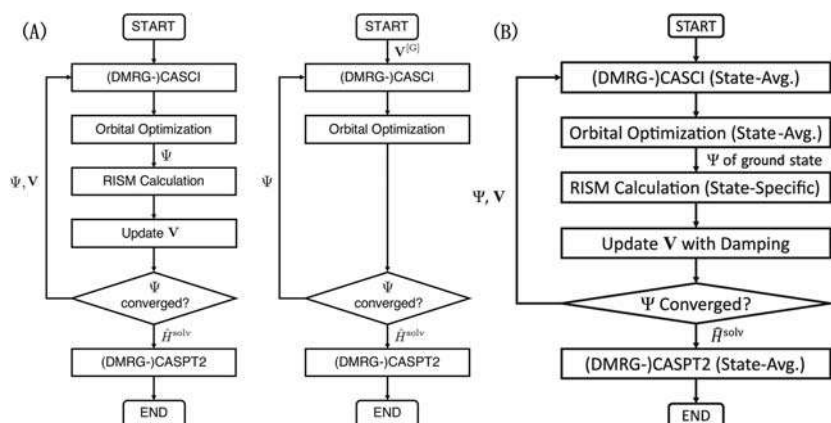
FIGURE 6.4 (A) Flowchart of the state-specific RISM-CASPT2 method for the ground (left) and excited (right) state in calculating absorption energies. (B) Flowchart of the state-average and damping procedure of the RISM-CASPT2 calculation. *CASPT2*, Complete active space with second-order perturbation theory; *RISM*, reference interaction site model. *Reproduced from Shimizu, R.Y., Yanai, T., Kurashige, Y., Yokogawa, D., 2018. Electronically Excited Solute Described by RISM Approach Coupled with Multireference Perturbation Theory: Vertical Excitation Energies of Bioimaging Probes. J. Chem. Theory Comput. 14, 5673−5679. https:// doi.org/10.1021/acs.jctc.8b00599; Shimizu, R.Y., Yanai, T., Yokogawa, D., 2020. Improved RISM-CASSCF Optimization via State-Average Treatment and Damping for Characterizing Excited Molecules in Solution with Multireference Perturbation Theory. J. Chem. Theory Comput. 16, 4865−4873. https://doi.org/10.1021/acs.jctc.9b01289, with permission from American Chemical Society.*

reasonable computational cost, Shimizu et al. (2020) later proposed a state-average (SA) version of RISM-DMRG-CASPT2 method with damping treatment for solvation, making feasible the analysis of a wider variety of solvated molecules. Given method is expected to boost and benefit fundamental research, for example providing complementary information of near-infrared molecular excitation and enabling the rational design of bioimaging probes, where the possibly preferable SS treatment is intractable.

6.8 Summary and outlook

The quantitatively accurate computation of the electronic structure of large and strongly correlated molecules and materials requires a balanced description of both static and dynamic electron correlations. In this chapter, we briefly overview the recent efforts of developing post-DMRG methods toward this aim which are usually based on the combination of DMRG and other inexpensive MR quantum chemical methods or DFT. Although the number of these developing methods is increasing quickly, by considering the nontrivial treatment of high-order n-RDMs ($n = 3, 4$), ab initio post-DMRG methods can be characterized into two main categories, depending
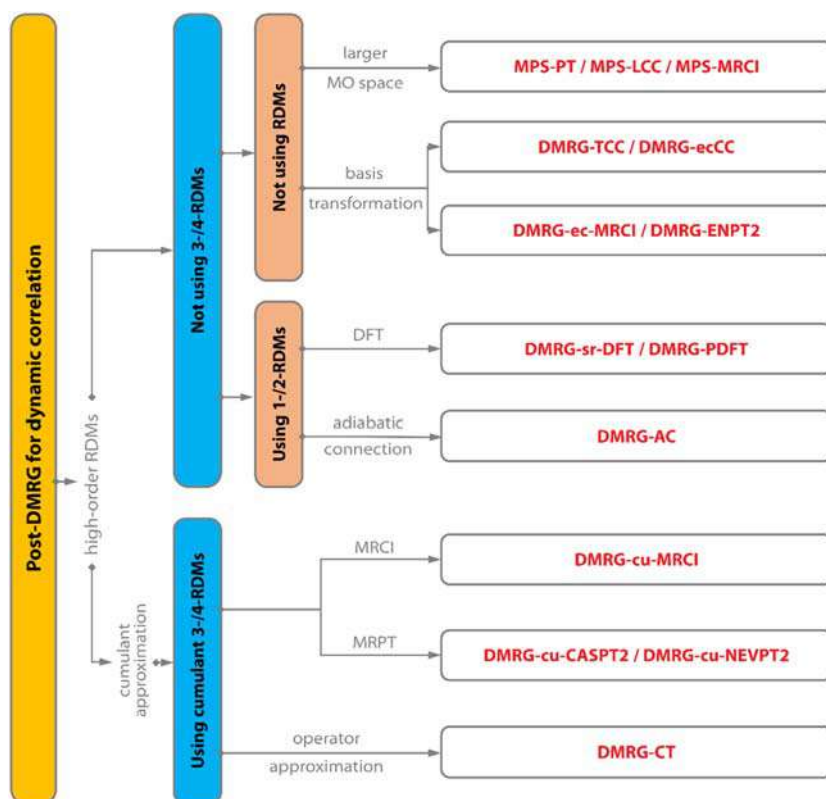
FIGURE 6.5 Schematic classification of post-DMRG methods according to the treatment for *n*-RDMs (Cheng et al., 2022). *DMRG*, Density matrix renormalization group. *Reproduced from Cheng, Y., Xie, Z., Ma, H., 2022. Post Density-matrix Renormalization-group for Describing Dynamic Electron Correlation with Large Active Spaces. J. Phys. Chem. Lett. 13, 904−915. https://doi.org/10.1021/acs.jpclett.1c04078, with permission from American Chemical Society.*

on whether high-order *n*-RDMs are used (as the Fig. 6.5 shows). These diverse and fruitful progresses provide powerful new tools for treating dynamic correlation with a large active space, which is infeasible by using traditional quantum chemistry methods. However, the popularization of post-DMRG is far from being satisfactory, quite different from the situation in ab initio DMRG, because post-DMRG's efficient implementation in popular quantum chemistry codes is still quite rare and its power in computing the molecular gradients and response properties hasn't been illustrated. Moreover, new post-DMRG schemes are still greatly desired when treating extremely strongly correlated systems.

The proper description of the strongly correlated subsystem's chemical environment is another important issue when applying ab initio DMRG and post-DMRG methods to the "real-world" chemistry problems. In this chapter,

we also introduce the recent progresses of DMRG-in-DFT and PE-DMRG using the quantum embedding schemes to describe the environment explicitly as well as the combination of DMRG and RISM solvation model which treats the environment molecules implicitly. These efforts for describing the strongly correlated subsystem's chemical environment, together with post-DMRG's progresses of simultaneously treating the static and dynamic electron correlations, are going to make the highly accurate characterization of the electronic structures in realistic strongly correlated systems possible. This can be expected to greatly promote the theoretical studies of strongly correlated materials in various fields, ranging from multicenter spin coupling in spintronic devices to transition metal catalysis in biological photosynthesis.

References

Andersson, K., Malmqvist, P.A., Roos, B.O., Sadlej, A.J., Wolinski, K., 1990. Second-order perturbation theory with a CASSCF reference function. J. Phys. Chem. 94, 5483−5488. Available from: https://doi.org/10.1021/j100377a012.

Andersson, K., Malmqvist, P., Roos, B.O., 1992. Second-order perturbation theory with a complete active space self-consistent field reference function. J. Chem. Phys. 96, 1218−1226. Available from: https://doi.org/10.1063/1.462209.

Angeli, C., Cimiraglia, R., Malrieu, J.-P., 2001. N-electron valence state perturbation theory: a fast implementation of the strongly contracted variant. Chem. Phys. Lett. 350, 297−305. Available from: https://doi.org/10.1016/S0009-2614(01)01303-3.

Angeli, C., Cimiraglia, R., Malrieu, J.-P., 2002. N-electron valence state perturbation theory: A spinless formulation and an efficient implementation of the strongly contracted and of the partially contracted variants. J. Chem. Phys. 117, 9138−9153. Available from: https://doi.org/10.1063/1.1515317.

Antalík, A., Veis, L., Brabec, J., Demel, O., Legeza, Ö., Pittner, J., 2019. Toward the efficient local tailored coupled cluster approximation and the peculiar case of oxo-Mn(Salen). J. Chem. Phys. 151, 084112. Available from: https://doi.org/10.1063/1.5110477.

Beran, P., Matoušek, M., Hapka, M., Pernal, K., Veis, L., 2021. Density matrix renormalization group with dynamical correlation via adiabatic connection. J. Chem. Theory Comput. 17, 7575−7585. Available from: https://doi.org/10.1021/acs.jctc.1c00896.

Butscher, W., Shih, S.-K., Buenker, R.J., Peyerimhoff, S.D., 1977. Configuration interaction calculations for the N2 molecule and its three lowest dissociation limits. Chem. Phys. Lett. 52, 457−462. Available from: https://doi.org/10.1016/0009-2614(77)80485-5.

Celani, P., Werner, H.-J., 2000. Multireference perturbation theory for large restricted and selected active space reference wave functions. J. Chem. Phys. 112, 5546−5557. Available from: https://doi.org/10.1063/1.481132.

Chandler, D., Andersen, H.C., 1972. Optimized cluster expansions for classical fluids. II. Theory of molecular liquids. J. Chem. Phys. 57, 1930−1937. Available from: https://doi.org/10.1063/1.1678513.

Chatterjee, K., Pernal, K., 2012. Excitation energies from extended random phase approximation employed with approximate one-and two-electron reduced density matrices. J. Chem. Phys. 137, 204109. Available from: https://doi.org/10.1063/1.4766934.

Chen, Z., Hoffmann, M.R., 2012. Orbitally invariant internally contracted multireference unitary coupled cluster theory and its perturbative approximation: Theory and test calculations of

second-order approximation. J. Chem. Phys. 137, 014108. Available from: https://doi.org/10.1063/1.4731634.

Cheng, Y., Xie, Z., Ma, H., 2022. Post density-matrix renormalization-group for describing dynamic electron correlation with large active spaces. J. Phys. Chem. Lett. 13, 904−915. Available from: https://doi.org/10.1021/acs.jpclett.1c04078.

Cohen, A.J., Mori-Sánchez, P., Yang, W., 2008. Insights into current limitations of density functional theory. Science 321, 792−794. Available from: https://doi.org/10.1126/science.1158722.

Cohen, A.J., Mori-Sánchez, P., Yang, W., 2012. Challenges for density functional theory. Chem. Rev. 112, 289−320. Available from: https://doi.org/10.1021/cr200107z.

Crawford, T.D., Schaefer, H.F., 2000. An introduction to coupled cluster theory for computational chemists. Reviews in Computational Chemistry. John Wiley & Sons, Ltd, pp. 33−136. Available from: http://doi.og/10.1002/9780470125915.ch2.

Davidson, E.R., Silver, D.W., 1977. Size consistency in the dilute helium gas electronic structure. Chem. Phys. Lett. 52, 403−406. Available from: https://doi.org/10.1016/0009-2614(77)80475-2.

Deustua, J.E., Magoulas, I., Shen, J., Piecuch, P., 2018. Communication: Approaching exact quantum chemistry by cluster analysis of full configuration interaction quantum Monte Carlo wave functions. J. Chem. Phys. 149, 151101. Available from: https://doi.org/10.1063/1.5055769.

Dresselhaus, T., Neugebauer, J., Knecht, S., Keller, S., Ma, Y., Reiher, M., 2015. Self-consistent embedding of density-matrix renormalization group wavefunctions in a density functional environment. J. Chem. Phys. 142, 044111. Available from: https://doi.org/10.1063/1.4906152.

Duch, W., Diercksen, G.H.F., 1994. Size-extensivity corrections in configuration interaction methods. J. Chem. Phys. 101, 3018−3030. Available from: https://doi.org/10.1063/1.467615.

Dyall, K.G., 1995. The choice of a zeroth-order Hamiltonian for second-order perturbation theory with a complete active space self-consistent-field reference function. J. Chem. Phys. 102, 4909−4918. Available from: https://doi.org/10.1063/1.469539.

Epstein, P.S., 1926. The Stark effect from the point of view of Schroedinger's quantum theory. Phys. Rev. 28, 695−710. Available from: https://doi.org/10.1103/PhysRev.28.695.

Evangelista, F.A., 2014. A driven similarity renormalization group approach to quantum many-body problems. J. Chem. Phys. 141, 054109. Available from: https://doi.org/10.1063/1.4890660.

Evangelista, F.A., 2018. Perspective: multireference coupled cluster theories of dynamical electron correlation. J. Chem. Phys. 149, 030901. Available from: https://doi.org/10.1063/1.5039496.

Faulstich, F.M., Máté, M., Laestadius, A., Csirik, M.A., Veis, L., Antalik, A., et al., 2019. Numerical and theoretical aspects of the DMRG-TCC method exemplified by the nitrogen dimer. J. Chem. Theory Comput. 15, 2206−2220. Available from: https://doi.org/10.1021/acs.jctc.8b00960.

Fink, R.F., 2006. Two new unitary-invariant and size-consistent perturbation theoretical approaches to the electron correlation energy. Chem. Phys. Lett. 428, 461−466. Available from: https://doi.org/10.1016/j.cplett.2006.07.081.

Fink, R.F., 2009. The multi-reference retaining the excitation degree perturbation theory: a size-consistent, unitary invariant, and rapidly convergent wavefunction based ab initio approach. Chem. Phys. 356, 39−46. Available from: https://doi.org/10.1016/j.chemphys.2008.10.004.

Forsberg, N., Malmqvist, P.-Å., 1997. Multiconfiguration perturbation theory with imaginary level shift. Chem. Phys. Lett. 274, 196−204. Available from: https://doi.org/10.1016/S0009-2614(97)00669-6.

Freitag, L., Knecht, S., Angeli, C., Reiher, M., 2017. Multireference Perturbation theory with Cholesky decomposition for the density matrix renormalization group. J. Chem. Theory Comput. 13, 451−459. Available from: https://doi.org/10.1021/acs.jctc.6b00778.

Fromager, E., 2015. On the exact formulation of multi-configuration density-functional theory: electron density vs orbitals occupation. Mol. Phys. 113, 419−434. Available from: https://doi.org/10.1080/00268976.2014.993342.

Guo, S., Watson, M.A., Hu, W., Sun, Q., Chan, G.K.-L., 2016. N-electron valence state perturbation theory based on a density matrix renormalization group reference function, with applications to the chromium dimer and a trimer model of poly(p-phenylenevinylene). J. Chem. Theory Comput. 12, 1583−1591. Available from: https://doi.org/10.1021/acs.jctc.5b01225.

Guo, Y., Sivalingam, K., Neese, F., 2021. Approximations of density matrices in N-electron valence state second-order perturbation theory (NEVPT2). I. Revisiting the NEVPT2 construction. J. Chem. Phys. 154, 214111. Available from: https://doi.org/10.1063/5.0051211.

Hachmann, J., Cardoen, W., Chan, G.K.-L., 2006. Multireference correlation in long molecules with the quadratic scaling density matrix renormalization group. J. Chem. Phys. 125, 144101. Available from: https://doi.org/10.1063/1.2345196.

Hanauer, M., Köhn, A., 2011. Pilot applications of internally contracted multireference coupled cluster theory, and how to choose the cluster operator properly. J. Chem. Phys. 134, 204111. Available from: https://doi.org/10.1063/1.3592786.

Hapka, M., Pastorczak, E., Krzemińska, A., Pernal, K., 2020. Long-range-corrected multiconfiguration density functional with the on-top pair density. J. Chem. Phys. 152, 094102. Available from: https://doi.org/10.1063/1.5138980.

Hedegård, E.D., Reiher, M., 2016. Polarizable embedding density matrix renormalization group. J. Chem. Theory Comput. 12, 4242−4253. Available from: https://doi.org/10.1021/acs.jctc.6b00476.

Hedegård, E.D., Knecht, S., Kielberg, J.S., Jensen, H.J.A., Reiher, M., 2015. Density matrix renormalization group with efficient dynamical electron correlation through range separation. J. Chem. Phys. 142, 224108. Available from: https://doi.org/10.1063/1.4922295.

Hylleraas, E.A., 1930. Über den Grundterm der Zweielektronenprobleme von H −, He, Li +, Be++ usw. Z. Für Phys 65, 209−225. Available from: https://doi.org/10.1007/BF01397032.

Khokhlov, D., Belov, A., 2020. Ab initio study of low-lying excited states of carotenoid-derived polyenes. J. Phys. Chem. A 124, 5790−5803. Available from: https://doi.org/10.1021/acs.jpca.0c01678.

Khokhlov, D., Belov, A., 2021. Toward an accurate ab initio description of low-lying singlet excited states of polyenes. J. Chem. Theory Comput. 17, 4301−4315. Available from: https://doi.org/10.1021/acs.jctc.0c01293.

Kinoshita, T., Hino, O., Bartlett, R.J., 2005. Coupled-cluster method tailored by configuration interaction. J. Chem. Phys. 123, 074106. Available from: https://doi.org/10.1063/1.2000251.

Knowles, P.J., Werner, H.-J., 1988. An efficient method for the evaluation of coupling coefficients in configuration interaction calculations. Chem. Phys. Lett. 145, 514−522. Available from: https://doi.org/10.1016/0009-2614(88)87412-8.

Köhn, A., Hanauer, M., Mück, L.A., Jagau, T.-C., Gauss, J., 2013. State-specific multireference coupled-cluster theory. WIREs Comput. Mol. Sci. 3, 176−197. Available from: https://doi.org/10.1002/wcms.1120.

Kohn, W., Sham, L.J., 1965. Self-consistent equations including exchange and correlation effects. Phys. Rev. 140, A1133−A1138. Available from: https://doi.org/10.1103/PhysRev.140.A1133.

Kowalski, K., Bhaskaran-Nair, K., Brabec, J., Pittner, J., 2013. Coupled cluster theories for strongly correlated molecular systems. In: Avella, A., Mancini, F. (Eds.), Strongly Correlated Systems: Numerical Methods. Springer, Berlin, Heidelberg, pp. 237−271. Springer Series in Solid-State Sciences. Available from: http://doi.org/10.1007/978-3-642-35106-8_9.

Kurashige, Y., Yanai, T., 2011. Second-order perturbation theory with a density matrix renormalization group self-consistent field reference function: theory and application to the study of chromium dimer. J. Chem. Phys. 135, 094104. Available from: https://doi.org/10.1063/1.3629454.

Kurashige, Y., Chalupský, J., Lan, T.N., Yanai, T., 2014. Complete active space second-order perturbation theory with cumulant approximation for extended active-space wavefunction from density matrix renormalization group. J. Chem. Phys. 141, 174111. Available from: https://doi.org/10.1063/1.4900878.

Kutzelnigg, W., Mukherjee, D., 1997. Normal order and extended Wick theorem for a multiconfiguration reference wave function. J. Chem. Phys. 107, 432. Available from: https://doi.org/10.1063/1.474405.

Lang, J., Antalík, A., Veis, L., Brandejs, J., Brabec, J., Legeza, Ö., et al., 2020. Near-linear scaling in DMRG-based tailored coupled clusters: an implementation of DLPNO-TCCSD and DLPNO-TCCSD(T). J. Chem. Theory Comput. 16, 3028−3040. Available from: https://doi.org/10.1021/acs.jctc.0c00065.

Langhoff, S.R., Davidson, E.R., 1974. Configuration interaction calculations on the nitrogen molecule. Int. J. Quantum Chem. 8, 61−72. Available from: https://doi.org/10.1002/qua.560080106.

Larsson, H.K., Zhai, H., Gunst, K., Chan, G.K.-L., 2022. Matrix product states with large sites. J. Chem. Theory Comput. 18, 749−762. Available from: https://doi.org/10.1021/acs.jctc.1c00957.

Lee, S., Zhai, H., Sharma, S., Umrigar, C.J., Chan, G.K.-L., 2021. Externally corrected CCSD with renormalized perturbative triples (R-ecCCSD(T)) and density matrix renormalization group and selected configuration interaction external sources. J. Chem. Theory Comput. 17, 3414−3425. Available from: https://doi.org/10.1021/acs.jctc.1c00205.

Leszczyk, A., Máté, M., Legeza, Ö., Boguslawski, K., 2022. Assessing the accuracy of tailored coupled cluster methods corrected by electronic wave functions of polynomial cost. J. Chem. Theory Comput. 18, 96−117. Available from: https://doi.org/10.1021/acs.jctc.1c00284.

Li Manni, G., Carlson, R.K., Luo, S., Ma, D., Olsen, J., Truhlar, D.G., et al., 2014. Multiconfiguration pair-density functional theory. J. Chem. Theory Comput. 10, 3669−3680. Available from: https://doi.org/10.1021/ct500483t.

Li, C., Evangelista, F.A., 2015. Multireference driven similarity renormalization group: a second-order perturbative analysis. J. Chem. Theory Comput. 11, 2097−2108. Available from: https://doi.org/10.1021/acs.jctc.5b00134.

Li, X., Peris, G., Planelles, J., Rajadall, F., Paldus, J., 1997. Externally corrected singles and doubles coupled cluster methods for open-shell systems. J. Chem. Phys. 107, 90−98. Available from: https://doi.org/10.1063/1.474355.

Liu, F., Kurashige, Y., Yanai, T., Morokuma, K., 2013. Multireference ab initio density matrix renormalization group (DMRG)-CASSCF and DMRG-CASPT2 study on the photochromic ring opening of spiropyran. J. Chem. Theory Comput. 9, 4462−4469. Available from: https://doi.org/10.1021/ct400707k.

Luken, W.L., 1978. Unlinked cluster corrections for configuration interaction calculations. Chem. Phys. Lett. 58, 421−424. Available from: https://doi.org/10.1016/0009-2614(78)85066-0.

Luo, Z., Ma, Y., Liu, C., Ma, H., 2017. Efficient reconstruction of CAS-CI-type wave functions for a DMRG state using quantum information theory and a genetic algorithm. J. Chem. Theory Comput. 13, 4699−4710. Available from: https://doi.org/10.1021/acs.jctc.7b00439.

Luo, Z., Ma, Y., Wang, X., Ma, H., 2018. Externally-contracted multireference configuration interaction method using a DMRG reference wave function. J. Chem. Theory Comput. 14, 4747−4755. Available from: https://doi.org/10.1021/acs.jctc.8b00613.

Lyakh, D.I., Musiał, M., Lotrich, V.F., Bartlett, R.J., 2012. Multireference nature of chemistry: the coupled-cluster view. Chem. Rev. 112, 182−243. Available from: https://doi.org/10.1021/cr2001417.

McLean, A.D., Liu, B., 1973. Classification of configurations and the determination of interacting and noninteracting spaces in configuration interaction. J. Chem. Phys. 58, 1066−1078. Available from: https://doi.org/10.1063/1.1679288.

Meissner, L., 1988. Size-consistency corrections for configuration interaction calculations. Chem. Phys. Lett. 146, 204−210. Available from: https://doi.org/10.1016/0009-2614(88)87431-1.

Meyer, W., 1977. Configuration expansion by means of pseudonatural orbitals. In: Schaefer III, H.F. (Ed.), Methods of Electronic Structure Theory, Modern Theoretical Chemistry. Springer, New York, pp. 413−446. Available from: http://doi.org/10.1007/978-1-4757-0887-5.

Møller, Chr, Plesset, M.S., 1934. Note on an approximation treatment for many-electron systems. Phys. Rev. 46, 618−622. Available from: https://doi.org/10.1103/PhysRev.46.618.

Nakatani, N., Guo, S., 2017. Density matrix renormalization group (DMRG) method as a common tool for large active-space CASSCF/CASPT2 calculations. J. Chem. Phys. 146, 094102. Available from: https://doi.org/10.1063/1.4976644.

Nesbet, R.K., Hartree, D.R., 1955. Configuration interaction in orbital theories. Proc. R. Soc. Lond. Ser. Math. Phys. Sci. 230, 312−321. Available from: https://doi.org/10.1098/rspa.1955.0134.

Neuscamman, E., Yanai, T., Chan, G.K.-L., 2009. Quadratic canonical transformation theory and higher order density matrices. J. Chem. Phys. 130, 124102. Available from: https://doi.org/10.1063/1.3086932.

Neuscamman, E., Yanai, T., Chan, G.K.-L., 2010a. A review of canonical transformation theory. Int. Rev. Phys. Chem. 29, 231−271. Available from: https://doi.org/10.1080/01442351003620540.

Neuscamman, E., Yanai, T., Chan, G.K.-L., 2010b. Strongly contracted canonical transformation theory. J. Chem. Phys. 132, 024106. Available from: https://doi.org/10.1063/1.3274822.

Olsen, J.M., Aidas, K., Kongsted, J., 2010. Excited States in Solution through Polarizable Embedding. J. Chem. Theory Comput. 6, 3721−3734. Available from: https://doi.org/10.1021/ct1003803.

Pastorczak, E., Pernal, K., 2018a. Correlation energy from the adiabatic connection formalism for complete active space wave functions. J. Chem. Theory Comput. 14, 3493−3503. Available from: https://doi.org/10.1021/acs.jctc.8b00213.

Pastorczak, E., Pernal, K., 2018b. Electronic excited states from the adiabatic-connection formalism with complete active space wave functions. J. Phys. Chem. Lett. 9, 5534−5538. Available from: https://doi.org/10.1021/acs.jpclett.8b02391.

Pedersen, J. K., 2004. Description of Correlation and Relativistic Effects in Calculations of Molecular Properties[D] (Ph. D. thesis). University of Southern Denmark.

Perdew, J.P., Savin, A., Burke, K., 1995. Escaping the symmetry dilemma through a pair-density interpretation of spin-density functional theory. Phys. Rev. A 51, 4531−4541. Available from: https://doi.org/10.1103/PhysRevA.51.4531.

Pernal, K., 2018. Electron correlation from the adiabatic connection for multireference wave functions. Phys. Rev. Lett. 120, 013001. Available from: https://doi.org/10.1103/PhysRevLett.120.013001.

Phung, Q.M., Pierloot, K., 2019. Low-Lying electromeric states in chloro-ligated iron(IV)-oxo porphyrin as a model for compound i, studied with second-order perturbation theory based on density matrix renormalization group. J. Chem. Theory Comput. 15, 3033−3043. Available from: https://doi.org/10.1021/acs.jctc.9b00166.

Phung, Q.M., Wouters, S., Pierloot, K., 2016. Cumulant approximated second-order perturbation theory based on the density matrix renormalization group for transition metal complexes: a benchmark study. J. Chem. Theory Comput. 12, 4352−4361. Available from: https://doi.org/10.1021/acs.jctc.6b00714.

Phung, Q.M., Muchammad, Y., Yanai, T., Ghosh, A., 2021. A DMRG/CASPT2 investigation of metallocorroles: quantifying ligand noninnocence in archetypal 3d and 4d element derivatives. JACS Au 1, 2303−2314. Available from: https://doi.org/10.1021/jacsau.1c00417.

Pople, J.A., Seeger, R., Krishnan, R., 1977. Variational configuration interaction methods and comparison with perturbation theory. Int. J. Quantum Chem. 12, 149−163. Available from: https://doi.org/10.1002/qua.560120820.

Rayleigh, J.W.S.B., 1894. The Theory of Sound. Macmillan.

Roemelt, M., Guo, S., Chan, G.K.-L., 2016. A projected approximation to strongly contracted N-electron valence perturbation theory for DMRG wavefunctions. J. Chem. Phys. 144, 204113. Available from: https://doi.org/10.1063/1.4950757.

Roemelt, M., Krewald, V., Pantazis, D.A., 2018. Exchange coupling interactions from the density matrix renormalization group and n-electron valence perturbation theory: application to a biomimetic mixed-valence manganese complex. J. Chem. Theory Comput. 14, 166−179. Available from: https://doi.org/10.1021/acs.jctc.7b01035.

Roos, B.O., Andersson, K., 1995. Multiconfigurational perturbation theory with level shift—the Cr2 potential revisited. Chem. Phys. Lett. 245, 215−223. Available from: https://doi.org/10.1016/0009-2614(95)01010-7.

Roos, B.O., Linse, P., Siegbahn, P.E.M., Blomberg, M.R.A., 1982. A simple method for the evaluation of the second-order-perturbation energy from external double-excitations with a CASSCF reference wavefunction. Chem. Phys. 66, 197−207. Available from: https://doi.org/10.1016/0301-0104(82)88019-1.

Saitow, M., Kurashige, Y., Yanai, T., 2013. Multireference configuration interaction theory using cumulant reconstruction with internal contraction of density matrix renormalization group wave function. J. Chem. Phys. 139, 044118. Available from: https://doi.org/10.1063/1.4816627.

Saitow, M., Kurashige, Y., Yanai, T., 2015. Fully internally contracted multireference configuration interaction theory using density matrix renormalization group: a reduced-scaling implementation derived by computer-aided tensor factorization. J. Chem. Theory Comput. 11, 5120−5131. Available from: https://doi.org/10.1021/acs.jctc.5b00270.

Savin, A., Flad, H.-J., 1995. Density functionals for the Yukawa electron-electron interaction. Int. J. Quantum Chem. 56, 327−332. Available from: https://doi.org/10.1002/qua.560560417.

Schrödinger, E., 1926. Quantisierung als eigenwertproblem. III. Ann. Phys. 80, 437−490.

Senjean, B., Nakatani, N., Tsuchiizu, M., Fromager, E., 2018. Site-occupation embedding theory using Bethe ansatz local density approximations. Phys. Rev. B 97, 235105. Available from: https://doi.org/10.1103/PhysRevB.97.235105.

Sharma, S., Alavi, A., 2015. Multireference linearized coupled cluster theory for strongly correlated systems using matrix product states. J. Chem. Phys. 143, 102815. Available from: https://doi.org/10.1063/1.4928643.

Sharma, S., Chan, G.K.-L., 2014. A flexible multi-reference perturbation theory by minimizing the Hylleraas functional with matrix product states. J. Chem. Phys. 141, 111101. Available from: https://doi.org/10.1063/1.4895977.

Sharma, S., Jeanmairet, G., Alavi, A., 2016. Quasi-degenerate perturbation theory using matrix product states. J. Chem. Phys. 144, 034103. Available from: https://doi.org/10.1063/1.4939752.

Sharma, S., Knizia, G., Guo, S., Alavi, A., 2017. Combining internally contracted states and matrix product states to perform multireference perturbation theory. J. Chem. Theory Comput. 13, 488−498. Available from: https://doi.org/10.1021/acs.jctc.6b00898.

Sharma, P., Bernales, V., Knecht, S., Truhlar, D.G., Gagliardi, L., 2019. Density matrix renormalization group pair-density functional theory (DMRG-PDFT): singlet−triplet gaps in polyacenes and polyacetylenes. Chem. Sci. 10, 1716−1723. Available from: https://doi.org/10.1039/c8sc03569e.

Shimizu, R.Y., Yanai, T., Kurashige, Y., Yokogawa, D., 2018. Electronically excited solute described by rism approach coupled with multireference perturbation theory: vertical excitation energies of bioimaging probes. J. Chem. Theory Comput. 14, 5673−5679. Available from: https://doi.org/10.1021/acs.jctc.8b00599.

Shimizu, R.Y., Yanai, T., Yokogawa, D., 2020. Improved RISM-CASSCF optimization via state-average treatment and damping for characterizing excited molecules in solution with multireference perturbation theory. J. Chem. Theory Comput. 16, 4865−4873. Available from: https://doi.org/10.1021/acs.jctc.9b01289.

Shirai, S., Kurashige, Y., Yanai, T., 2016. Computational evidence of inversion of ^1L_a and ^1L_b-derived excited states in naphthalene excimer formation from ab initio multireference theory with large active space: DMRG-CASPT2 study. J. Chem. Theory Comput. 12, 2366−2372. Available from: https://doi.org/10.1021/acs.jctc.6b00210.

Siegbahn, P.E.M., 1978. Multiple substitution effects in configuration interaction calculations. Chem. Phys. Lett. 55, 386−394. Available from: https://doi.org/10.1016/0009-2614(78)87046-8.

Siegbahn, P.E.M., 1980. Direct configuration interaction with a reference state composed of many reference configurations. Int. J. Quantum Chem. 18, 1229−1242. Available from: https://doi.org/10.1002/qua.560180510.

Siegbahn, P.E.M., 1983. The externally contracted CI method applied to N_2. Int. J. Quantum Chem. 23, 1869−1889. Available from: https://doi.org/10.1002/qua.560230602.

Sivalingam, K., Krupicka, M., Auer, A.A., Neese, F., 2016. Comparison of fully internally and strongly contracted multireference configuration interaction procedures. J. Chem. Phys. 145, 054104. Available from: https://doi.org/10.1063/1.4959029.

Sokolov, A.Y., Chan, G.K.-L., 2016. A time-dependent formulation of multi-reference perturbation theory. J. Chem. Phys. 144, 064102. Available from: https://doi.org/10.1063/1.4941606.

Sokolov, A.Y., Guo, S., Ronca, E., Chan, G.K.-L., 2017. Time-dependent N-electron valence perturbation theory with matrix product state reference wavefunctions for large active spaces and basis sets: applications to the chromium dimer and all-trans polyenes. J. Chem. Phys. 146. Available from: https://doi.org/10.1063/1.4986975.

Song, Y., Cheng, Y., Ma, Y., Ma, H., 2020. Multi-reference Epstein-Nesbet perturbation theory with density matrix renormalization group reference wavefunction. Electron. Struct. 2, 014002. Available from: https://doi.org/10.1088/2516-1075/ab72db.

Taffet, E.J., Scholes, G.D., 2018. Peridinin torsional distortion and bond-length alternation introduce intramolecular charge-transfer and correlated triplet pair intermediate excited states. J. Phys. Chem. B 122, 5835−5844. Available from: https://doi.org/10.1021/acs.jpcb.8b02504.

Taffet, E.J., Lee, B.G., Toa, Z.S.D., Pace, N., Rumbles, G., Southall, J., et al., 2019. Carotenoid nuclear reorganization and interplay of bright and dark excited states. J. Phys. Chem. B 123, 8628−8643. Available from: https://doi.org/10.1021/acs.jpcb.9b04027.

Tran, V.T., 2021. Electronic States of $CoSi_n^{-/0/+}$ ($n = 1−3$) clusters from density matrix renormalization group-CASPT2 calculations. J. Phys. Chem. A 125, 5800−5810. Available from: https://doi.org/10.1021/acs.jpca.1c04469.

Veis, L., Antalík, A., Brabec, J., Neese, F., Legeza, Ö., Pittner, J., 2016. Coupled cluster method with single and double excitations tailored by matrix product state wave functions. J. Phys. Chem. Lett. 7, 4072−4078. Available from: https://doi.org/10.1021/acs.jpclett.6b01908.

Vogiatzis, K.D., Ma, D., Olsen, J., Gagliardi, L., de Jong, W.A., 2017. Pushing configuration-interaction to the limit: Towards massively parallel MCSCF calculations. J. Chem. Phys. 147, 184111. Available from: https://doi.org/10.1063/1.4989858.

Walia, R., Deng, Z., Yang, J., 2021. Towards multistate multimode landscapes in singlet fission of pentacene: the dual role of charge-transfer states. Chem. Sci. 12, 12928−12938. Available from: https://doi.org/10.1039/d1sc01703a.

Werner, H., Knowles, P.J., 1988. An efficient internally contracted multiconfiguration−reference configuration interaction method. J. Chem. Phys. 89, 5803−5814. Available from: https://doi.org/10.1063/1.455556.

Werner, H., Reinsch, E., 1982. The self-consistent electron pairs method for multiconfiguration reference state functions. J. Chem. Phys. 76, 3144−3156. Available from: https://doi.org/10.1063/1.443357.

Wesolowski, T.A., Warshel, A., 1993. Frozen density functional approach for ab initio calculations of solvated molecules. J. Phys. Chem. 97, 8050−8053. Available from: https://doi.org/10.1021/j100132a040.

Wouters, S., Van Speybroeck, V., Van Neck, D., 2016. DMRG-CASPT2 study of the longitudinal static second hyperpolarizability of all-trans polyenes. J. Chem. Phys. 145, 054120. Available from: https://doi.org/10.1063/1.4959817.

Xu, E., Zhao, D., Li, S., 2015. Multireference second-order perturbation theory with a simplified treatment of dynamical correlation. J. Chem. Theory Comput. 11, 4634−4643. Available from: https://doi.org/10.1021/acs.jctc.5b00495.

Yanai, T., Chan, G.K.-L., 2006. Canonical transformation theory for multireference problems. J. Chem. Phys. 124, 194106. Available from: https://doi.org/10.1063/1.2196410.

Yanai, T., Kurashige, Y., Neuscamman, E., Chan, G.K.-L., 2010. Multireference quantum chemistry through a joint density matrix renormalization group and canonical transformation theory. J. Chem. Phys. 132, 024105. Available from: https://doi.org/10.1063/1.3275806.

Yanai, T., Kurashige, Y., Neuscamman, E., Chan, G.K.-L., 2012. Extended implementation of canonical transformation theory: parallelization and a new level-shifted condition. Phys. Chem. Chem. Phys. 14, 7809−7820. Available from: https://doi.org/10.1039/C2CP23767A.

Yanai, T., Saitow, M., Xiong, X.-G., Chalupský, J., Kurashige, Y., Guo, S., et al., 2017. Multistate complete-active-space second-order perturbation theory based on density matrix renormalization group reference states. J. Chem. Theory Comput. 13, 4829−4840. Available from: https://doi.org/10.1021/acs.jctc.7b00735.

Zhai, H., Chan, G.K.-L., 2021. Low communication high performance ab initio density matrix renormalization group algorithms. J. Chem. Phys. 154, 224116. Available from: https://doi.org/10.1063/5.0050902.

Zhang, I.Y., Xu, X., 2021. On the top Rung of Jacob's ladder of density functional theory: toward resolving the dilemma of SIE and NCE. WIREs Comput. Mol. Sci. 11, e1490. Available from: https://doi.org/10.1002/wcms.1490.

Chapter 7

DMRG in frequency space

7.1 Introduction

Calculating spectral function is of central importance in both quantum chemistry and condensed matter physics, which describes many frequency-dependent dynamical properties that can be probed experimentally, including linear absorption and emission spectroscopy, photoelectron spectroscopy, optical conductivity, etc. When a physical quantity $\hat{O}$ of an equilibrium system at zero temperature is perturbed by external perturbation, the spectral function that describes the response is given by

$$S(\omega) = \left\langle 0 \left| \hat{O}^{\dagger} \delta(\omega - \hat{H}_0 + E_0) \hat{O} \right| 0 \right\rangle \tag{7.1}$$

where $\hat{H}_0$ is the Hamiltonian of the system at equilibrium, E_0 and $|0\rangle$ are the ground-state energy and wavefunction. The Dirac δ function describes the energy resonance condition between the external field and states transition.

The spectral function can also be obtained by the Fourier transform of time correlation function $\left\langle 0 \left| \hat{O}^{\dagger}(t)\hat{O}(0) \right| 0 \right\rangle$ (up to a constant prefactor $1/2\pi$). Therefore two different roads are paved for the calculation of the spectral function: the frequency-domain methods and the time-domain methods. The former directly calculates the frequency-dependent function (Eq. 7.1) and the latter performs real-time evolutions to obtain the time correlation function $\left\langle 0 \left| \hat{O}^{\dagger}(t)\hat{O}(0) \right| 0 \right\rangle$ and then performs Fourier transform.

Density matrix renormalization group (DMRG) was initially developed to study the equilibrium properties of many-body systems, and it was gradually developed for dynamical quantity calculation. The earliest attempts in extending it to study the dynamical properties started from the frequency domain. In this chapter, we will present a pedagogical introduction of the frequency-domain DMRG, including its theoretical foundation, algorithms, and several applications adapted to different problems, and the next chapter will introduce the time-dependent methods.

The pioneering work of frequency-domain DMRG originated from the Lanczos algorithm, which is widely used to solve the linear equation and the eigenvalue problem of large sparse Hermitian matrices. Gagliano and

Balseiro (1987) first used the Lanczos algorithm to calculate the ground-state wavefunction and spectral function at zero temperature. Soon after the invention of DMRG (White, 1992, 1993), Hallberg (1995) proposed the Lanczos DMRG method by combining DMRG with the Lanczos algorithm, which was easy to implement and numerically economic but limited to calculating discrete spectral function made of only the first several low-lying states (Kühner and White, 1999). Later, based on the correction vector (CV) method, Ramasesha et al. (1997) and Pati et al. (1999) proposed the CV-DMRG. The CV method was originally combined with the valence bond theory by Soos and Ramasesha (1989) to study the nonlinear optical properties of the π electron conjugated systems, which was accurate but only applicable to small systems. CV-DMRG expanded the research scope to more complex systems and exhibited very high accuracy. Based on the essential working equations of CV-DMRG, Jeckelmann (2002) proposed a more elegant method that works in a variational manner, called the dynamical DMRG (DDMRG), and to date, it is regarded as the method of choice for high precision calculations of spectral functions (Dorando et al., 2009; Ronca et al., 2017). However, DDMRG is usually computationally expensive since the time cost of DDMRG relies on the number of frequencies that need to be calculated because the response at each frequency is calculated independently. Similar to the Lanczos algorithm, the Chebyshev polynomial expansion method also employs a recursive manner to expand the dynamical correlation function, and it has been successfully applied to the calculation of optical absorption, conductivity, and other response properties of spin, phonon, and impurity models (Silver and Röder, 1994; Wang, 1994; Weisse, 2004; Weiße et al., 2006). Holzner et al. (2011) combined the matrix product state (MPS) with the Chebyshev polynomial expansion and proposed the Chebyshev MPS (CheMPS) method, which gained good compromise between the accuracy and numerical cost when applied to the isotropic Heisenberg model. The resolution was increased by employing the effective band with the energy truncation procedure (Holzner et al., 2011) and employing the linear prediction (Ganahl et al., 2014) techniques for extrapolation in some cases. Inspired by the linear response theories of conventional quantum chemistry methods, the analytic linear response DMRG (Dorando et al., 2009; Haegeman et al., 2013; Nakatani et al., 2014; Wouters et al., 2013) was proposed by combining the time-dependent perturbation theory with the tangent space of DMRG wavefunction to calculate the dynamical quantities and achieved comparable accuracy with DDMRG (Dorando et al., 2009).

Some of the algorithms have also been extended to finite temperature to tackle the thermal effects on the dynamical quantities of many-body systems. Kokalj and Prelovšek (2009) extended the Lanczos DMRG to finite temperature by sampling the initial state to approximate the thermal equilibrium density matrix. Using the quantum mechanical technique of thermal field

dynamics which is also called purification, Tiegel et al. (2014) presented the finite temperature algorithms for CheMPS, and Jiang et al. (2020a) extended DDMRG to finite temperature to study the thermal effects on the electron−phonon coupled systems such as organic molecular aggregates.

In the following sections, we first recap the linear response theory and give the formulation of spectral function. Next we pay attention to the algorithm details at zero and finite temperature. Then we introduce several representative applications in electron−electron/electron−phonon correlated systems. Finally, we summarize and give further outlooks.

7.2 Spectral function in linear response regime

In this section, we briefly describe the linear response theory and give the formulation of spectral function at zero and finite temperature. Unless stated otherwise, the atomic unit will be used.

Considering a canonical ensemble described by Hamiltonian $\hat{H}_0$ at thermal equilibrium of temperature T, the density matrix is written as $\rho_\beta = e^{-\beta \hat{H}_0}/Z(\beta)$, where $Z(\beta) = \mathrm{Tr}(e^{-\beta \hat{H}_0})$ and $\beta = 1/k_B T$ (k_B is the Boltzmann constant). When the system is perturbed by a time-dependent external field $f(t)\hat{V}$, the Hamiltonian is written as

$$\hat{H}(t) = \hat{H}_0 + f(t)\hat{V}, \tag{7.2}$$

where $f(t)$ represents the strength of the external field, and $\hat{V}$ is the observable of the system that obeys $\hat{V} = \hat{V}^\dagger$. The system will respond to the perturbation, and according to the linear response theory, the thermal expectation value of the observable $\hat{O}$ at time t is,

$$\left\langle \hat{O}(t) \right\rangle_{\rho_\beta} = \left\langle \hat{O}(0) \right\rangle_{\rho_\beta} + \int_{-\infty}^{t} \chi(t-t')f(t')dt', \tag{7.3}$$

where $\hat{O}(\tau) = e^{i\hat{H}_0\tau}\hat{O}e^{-i\hat{H}_0\tau}$ and $\langle \cdot \rangle_{\rho_\beta}$ denotes the expectation with respect to the density matrix ρ_β. The equation is also called the Kubo formula (Kubo, 1957) and $\chi(t-t')$ is the retarded Green function (other names are dynamical correlation function and susceptibility, etc.) that is nonzero only if $t > t'$:

$$\chi(t-t') = -i\theta(t-t')\left\langle \left[\hat{O}(t-t'), \hat{V}(0)\right] \right\rangle_{\rho_\beta} \tag{7.4}$$

where $\theta(t-t')$ is the Heaviside step function and $[\cdot,\cdot]$ is the anticommutator with $[\hat{A}, \hat{B}] = \hat{A}\hat{B} - \hat{B}\hat{A}$. The retarded Green function in frequency domain can be obtained by the Fourier transform $G(\omega) = \int_{-\infty}^{\infty} d\tau e^{i\omega\tau}\chi(\tau)$, leading to

$$G(\omega) = G^{(1)}(\omega) - G^{(2)}(\omega) \tag{7.5}$$

$$G^{(1)}(\omega) = \lim_{\eta \to 0^+} \sum_{m,n} \frac{e^{-\beta E_n}}{Z(\beta)} \frac{\langle n|\hat{O}|m\rangle\langle m|\hat{V}|n\rangle}{\omega - (E_m - E_n) + i\eta} \tag{7.6}$$

$$G^{(2)}(\omega) = \lim_{\eta \to 0^+} \sum_{m,n} \frac{e^{-\beta E_m}}{Z(\beta)} \frac{\langle n|\hat{O}|m\rangle\langle m|\hat{V}|n\rangle}{\omega - (E_m - E_n) + i\eta} \qquad (7.7)$$

which are expanded with the eigenstates of $\hat{H}_0$. The operator-based formulation can be written as:

$$G(\omega) = \lim_{\eta \to 0^+} \mathrm{Tr}\left(\hat{O}\frac{1}{\omega - \mathcal{L} + i\eta}\hat{V}\rho_\beta\right) - \mathrm{Tr}\left(\hat{V}\frac{1}{\omega + \mathcal{L} + i\eta}\hat{O}\rho_\beta\right) \qquad (7.8)$$

where $\mathcal{L} = [\hat{H}_0, \cdot]$ acts as a Liouville superoperator, the eigenvalues of which correspond to the difference between the eigenvalues of $\hat{H}_0$. These two terms follow the relation of $G^{(1)}(-\omega)^* = -G^{(2)}(\omega)$; hence, only the calculation of the first term will be calculated. The second term can be dropped in some cases, as will be described below. The imaginary part of $G(\omega)$ is called the spectral function which is proportional to the rate of absorbing energy from the external field (Mahan, 2013),

$$S_{\hat{O},\hat{V}}(\omega) = -\frac{1}{\pi}\mathbf{Im}\chi_{\hat{O},\hat{V}}(\omega). \qquad (7.9)$$

At zero temperature, $\mathbf{Im}G^{(2)}(\omega > 0) = 0$, we have

$$S_{\hat{O},\hat{V}}(\omega > 0)_{\mathrm{ZT}} = -\frac{1}{\pi}\mathbf{Im}\lim_{\eta \to 0^+}\left\langle 0\left|\hat{O}\frac{1}{\omega - \hat{H}_0 + E_0 + i\eta}\hat{V}\right|0\right\rangle \qquad (7.10)$$

$$= \langle 0|\hat{O}\delta(\omega - \hat{H}_0 + E_0)\hat{V}|0\rangle.$$

At finite temperature, when the energy gap for excitation is large compared to the thermal energy $k_\mathrm{B}T$, $\mathbf{Im}G^{(2)}(\omega)$ can also be safely neglected.

Several examples are given as follows. When $\hat{O} = \hat{V} = \hat{\mu}$ ($\hat{\mu}$ is the dipole operator), $S_{\hat{\mu},\hat{\mu}}(\omega)$ is proportional to the linear absorption cross section, and $\mathbf{Im}G^{(1)}(\omega)$, $\mathbf{Im}G^{(2)}(\omega)$ represent the stimulated absorption and stimulated emission respectively, the latter of which can be safely neglected for the absorption in the visible and ultraviolet region at ambient temperature. The correlation function of current−current operator corresponds to the transport properties. As noted above, the operator $\hat{O}$ and $\hat{V}$ are both Hermitian observables. In the case of non-Hermitian single creation or annihilation operator, $G(\omega)$ is also called the single-particle Green function, and $G(\omega) = G^{(1)}(\omega) \pm G^{(2)}(\omega)$ where the upper sign is for fermions and the lower sign is for bosons (Mahan, 2013). When $\hat{V}/\hat{O} = a_j^\dagger/a_i$ where $a_{i(j)}^{(\dagger)}$ is the fermion annihilation (creation) operator of the $i(j)$th orbital, $\mathbf{Im}G^{(1)}(\omega)$ and $\mathbf{Im}G^{(2)}(\omega)$ describe the electron affinity and ionization of the photoelectron spectroscopy separately.

7.3   Algorithms at zero temperature

7.3.1   Lanczos density matrix renormalization group

To illustrate the algorithms at zero temperature, we use the single-particle spectral function for simplicity, which writes

$$
\begin{aligned}
S(\omega) &= -\frac{1}{\pi} \mathbf{Im} \lim_{\eta \to 0^+} \left\langle 0 \left| \hat{O}^\dagger \frac{1}{\omega - \hat{H}_0 + E_0 + i\eta} \hat{O} \right| 0 \right\rangle \\
&= \sum_n \left| \langle n | \hat{O} | 0 \rangle \right|^2 \delta(\omega - E_n + E_0).
\end{aligned}
\tag{7.11}
$$

The second type of expansion is written in the Lehmann representation. The Lanczos algorithm is the symmetric matrix version of the Arnoldi method, the logic of which is projecting the primitive large sparse matrix into the Krylov subspace spanned by the so-called Lanczos vectors. The Lanczos DMRG method combines Lanczos algorithm with DMRG to calculate the dynamical correlation function (Hallberg, 1995) by projecting the Hamiltonian which is numerically inaccessible for exact diagonalization to a tridiagonalized matrix $\mathbf{H}_{\mathrm{eff}}$ in the Krylov subspace,

$$
\mathbf{H}_{\mathrm{eff}} = \begin{pmatrix}
a_0 & b_1 & 0 & \dots & 0 \\
b_1 & a_1 & b_2 & \ddots & \vdots \\
0 & b_2 & \ddots & \ddots & 0 \\
\vdots & \ddots & \ddots & \ddots & b_{n-1} \\
0 & \dots & 0 & b_{n-1} & a_{n-1}
\end{pmatrix}
\tag{7.12}
$$

the eigenvalues and eigenvectors of which can then be obtained by direct diagonalization and then be substituted back to Eq. 7.11 for the final result of response. The Krylov space is generated by the Lanczos iteration procedure starting from the initial Lanczos vectors $|f_{-1}\rangle = 0$ and $|f_0\rangle = \hat{O}|0\rangle / \left\langle 0 \left| \hat{O}^\dagger \hat{O} \right| 0 \right\rangle$. The rest of Lanczos vectors follow a three-term recurrence relation:

$$
|f_{n+1}\rangle = \hat{H}_0 |f_n\rangle - a_n |f_n\rangle - b_n^2 |f_{n-1}\rangle
$$

$$
a_n = \frac{\langle f_n | \hat{H}_0 | f_n \rangle}{\langle f_n | f_n \rangle}, \; b_{n+1}^2 = \frac{\langle f_{n+1} | f_{n+1} \rangle}{\langle f_n | f_n \rangle}
\tag{7.13}
$$

In addition to directly diagonalizing $\mathbf{H}_{\mathrm{eff}}$, a smooth spectral lineshape with a Lorentzian broadening width η can also be obtained by the continued fraction expansion,

$$
S(\omega) = -\frac{1}{\pi} \mathrm{Im} \frac{\left\langle 0 \left| \hat{O}^\dagger \hat{O} \right| 0 \right\rangle}{z - a_0 - \cfrac{b_1^2}{z - a_1 - \cfrac{b_2^2}{z - \dots}}}
\tag{7.14}
$$

which is subjected to a finite Lorentzian broadening width η with $z = E_0 + \omega + i\eta$.

The algorithms of Lanczos DMRG can be roughly categorized into the multi-targeting scheme and the adaptive scheme which are based on the first-generation DMRG with renormalized operator, and the modern scheme employing MPS and matrix product operators (MPO).

7.3.1.1 The multi-targeting scheme and adaptive scheme

The reason for employing the so-called targeting arises from the fact that $\hat{H}_0^{\,n}|0\rangle$ brings increasing errors for increasing n since $\hat{H}_0$ is approximated in the form of renormalized operator. Therefore one makes compromise by constructing the reduced density matrix that suits only the first several vectors as possible, which is called multi-targeting. Generation of Lanczos vectors starts from the ground state $|0\rangle$ optimized by targeting the ground state itself and the other Lanczos vectors simultaneously to construct the reduced density matrix $\hat{\rho} = \sum_i c_i |f_i\rangle\langle f_i|$ where i is the index of the targeted vectors and $\sum c_i = 1$. The reduced density matrix is expected to well describe both the ground state and the targeted excited states, which on the other hand reminds us that the increasing number of targeted vectors leads to decreasing accuracy for each vector. Therefore only the first few Lanczos vectors are involved in the construction of the reduced density matrix, with which the following higher excited states are usually not described well, making this scheme restricted to calculate the discrete spectra made of the first low-lying excited state (Kühner and White, 1999). On the other hand, the loss of orthogonality between Lanczos vectors because of the error accumulation of the successive compressions further restricts the precision for higher excited states' calculations. It was proposed to monitor $\langle f_0|f_n\rangle$ to decide whether the iteration should be stopped (Kühner and White, 1999).

As for the adaptive scheme, the idea of multi-targeting is kept but only the last three vectors are targeted at one time, that is to say, the basis changes adaptively as the recursion moves forward, through which the accuracy is greatly enhanced (Dargel et al., 2011). However, the reorthogonalization of Lanczos vectors (as will be stated below) is not easy to be performed in this scheme.

7.3.1.2 The matrix product states/matrix product operators scheme

Within the modern framework of MPS/MPO, each vector is independently represented in the form of MPS, and the Hamiltonian will be precisely represented in the form of MPO. Then the Lanczos DMRG can be implemented by conducting the elementary operations of MPO/MPS (Schollwöck, 2011), including the application of MPO onto MPS ($\hat{H}_0|f_i\rangle$) where $\hat{H}_0$ is precisely represented, and the summation between MPSs, and the following compressions for controlling the bond dimension which is the only approximation made in this scheme. Because of the accumulated errors by the successive compressions for new Lanczos vectors, the three-term Lanczos recurrence relation will be broken and introduces nonorthogonalities. The nonorthogonality

can be mended by employing a post-treatment for the primitive Lanczos vectors, for example, the Gram−Schmidt reorthogonalization (Dargel et al., 2012). The reorthogonalized vectors are expressed as

$$|\phi_n\rangle = c_n \left(1 - \sum_{m<n} |\phi_m\rangle\langle\phi_m| \right) |f_n\rangle, \langle\phi_m|\phi_n\rangle = \delta_{mn} \qquad (7.15)$$

where c_n is the normalization constant. The reorthogonalization cannot be carried out directly, otherwise it involves adding a sequence of MPS that brings errors arising from MPS compressions. The reothogonalization is achieved by assuming that $|\phi_n\rangle = \sum_{i=0}^{n} C_{in}|f_i\rangle$, and by putting it into the Gram−Schmidt orthogonalization formula, the coefficient matrix C can be calculated in a recursive style (Dargel et al., 2012) which uses the inner products $W_{ij} = \langle f_i|f_j\rangle$. After the reorthogonalization is complete, an effective Hamiltonian in the Krylov space is constructed by,

$$H_{\text{eff},mn} = \langle\phi_m|\hat{H}_0|\phi_n\rangle = \sum_{i,j=0}^{n,m} C_{in}C_{jm}\langle f_i|\hat{H}_0|f_j\rangle \qquad (7.16)$$

The effective Hamiltonian matrix can be directly diagonalized for the excited states and the corresponding transition amplitudes, with which the spectral functions can be calculated.

$$\mathbf{H}_{\text{eff}}|n\rangle = \lambda_n|n\rangle. \qquad (7.17)$$

$$S(\omega) = c_0^{-1} \sum_n \left|\langle n|\phi_0\rangle\right|^2 \delta(\omega - \lambda_n + E_0). \qquad (7.18)$$

We outline the procedure in Algorithm 7.1.

Algorithm 7.1: Lanczos MPS with reorthogonalization. *MPS*, Matrix product state.

1: **prepare** operater $\hat{H}_0$, $\hat{O}$, and ground state $|0\rangle$.
2: **generate** first two Lanczos vector $|f_0\rangle$, $|f_1\rangle$
3: **initialize** $W_{ij} = \langle f_i|f_j\rangle$, $F_{ij} = \langle f_i|\hat{H}_0|f_j\rangle$ for $i,j \in [0,1]$
4: **procedure** vector generation
5:   **for** $n = 1$ **to** $n = N - 1$ **do**
6:     $|f_{n+1}\rangle \leftarrow \min:||f_{n+1}\rangle - (\hat{H}_0 - a_n)|f_n\rangle - b_n^2|f_{n-1}\rangle|^2$
7:     $a_n \leftarrow \langle f_n|\hat{H}_0|f_n\rangle/\langle f_n|f_n\rangle$, $b_{n+1}^2 \leftarrow \langle f_{n+1}|f_{n+1}\rangle/\langle f_n|f_n\rangle$
8:     **for** $j = 0$ **to** $j = n$ **do**
9:       $W_{jn} = W_{nj} \leftarrow \langle f_j|f_n\rangle$, $F_{jn} = F_{nj} \leftarrow \langle f_j|\hat{H}_0|f_n\rangle$
10:     **end for**
11:   **end for**
12: **end procedure**
13: **procedure** reorthogonalization
14:   $C \leftarrow RecursiveGramSchmidt(W)$
15:   $\mathbf{H}_{\text{eff}} \leftarrow MatrixMultiply(C^T, F, C)$
16:   $\lambda_n, |n\rangle \leftarrow Diag(\mathbf{H}_{\text{eff}})$
17: **end procedure**

7.3.2   Correction vector density matrix renormalization group

To solve the spectral function (Eq. 7.11) at a fixed frequency ω, one can introduce the CV (Soos and Ramasesha, 1989),

$$\big|C(\omega)\big\rangle = \frac{1}{\omega - \hat{H}_0 + E_0 + i\eta}|O\rangle, \tag{7.19}$$

where $|O\rangle = \hat{O}|0\rangle$. It is straightforward to get the following linear equation of $|C(\omega)\rangle$,

$$\big(\omega - \hat{H}_0 + E_0 + i\eta\big)\big|C(\omega)\big\rangle = |O\rangle, \tag{7.20}$$

and by only solving for $|C(\omega)\rangle$, the spectral function is directly obtained,

$$S(\omega) = -\frac{1}{\pi}\mathbf{Im}\langle O|C(\omega)\rangle. \tag{7.21}$$

Because $(\omega - \hat{H}_0 + E_0 + i\eta)$ is non-Hermitian, the above equation is typically not solved directly. Instead, the common treatment is multiplying both sides of the linear equation by $(\omega - \hat{H}_0 + E_0 - i\eta)$ and splitting $|C(\omega)\rangle$ into the real and imaginary part, and the latter one satisfies a real symmetric and positive definite linear equation,

$$\big[(\omega - H_0 + E_0)^2 + \eta^2\big]\mathbf{Im}\big|C(\omega)\big\rangle = -\eta|O\rangle \tag{7.22}$$

$$\mathbf{Re}|C(\omega)\rangle = \frac{\hat{H}_0 - \omega - E_0}{\eta}\mathbf{Im}\big|C(\omega)\big\rangle. \tag{7.23}$$

Since the spectral function merely relates to the imaginary part $\mathbf{Im}|C(\omega)\rangle$, CV-DMRG aims at Eq. 7.22, which can be solved by a sweeping manner in the local renormalized basis using the conjugate gradient method. During the process of sweeping, the reduced density matrix is averaged over $|0\rangle$, $|O\rangle$, and $\mathbf{Im}|C(\omega)\rangle$ $\big(\rho = \sum_s c_s \rho_s,\ \sum c_s = 1\big)$, in order to optimize a single set of renormalized basis for all of them. In addition, a sightly improvement can be made by also including $\mathbf{Re}|C(\omega)\rangle$ in the averaged reduced density matrix, which ensures minimal truncation error when calculating $\hat{H}_0\mathbf{Im}|C(\omega)\rangle$ (Schollwöck, 2005), although $\mathbf{Re}|C(\omega)\rangle$ is not explicitly needed to calculate Eq. 7.21.

The main approximation made within the representation of renormalized basis is that the projected Hamiltonian of the ith site is represented as $\hat{H}_{0i} = \hat{P}_i\hat{H}_0\hat{P}_i$, where $\hat{P}_i = \sum_{a_{i-1},\sigma_i,a_i}|l_{a_{i-1}}\sigma_i r_{a_i}\rangle\langle l_{a_{i-1}}\sigma_i r_{a_i}|$ is made of a mixed canonical MPS (for the graphical representation, see also Fig. 7.1). As a consequence, $\hat{P}_i\hat{H}_0^2\hat{P}_i$ cannot be precisely given but only be approximated by $(\hat{P}_i\hat{H}_0\hat{P}_i)^2$. This approximation becomes rigorously accurate when the bond dimension $m \to +\infty$, which means extra error for a finite m. This drawback
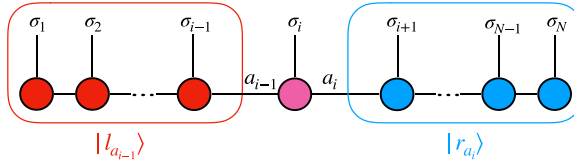
FIGURE 7.1 The mixed canonical representation of wavefunction composed of left-canonicalized matrix product, canonical center and right-canonicalized matrix product.

can be mended by employing the MPO representation of $\hat{H}_0$, as will be introduced in the next section. Moreover, the introduction of $\hat{H}_0^2$ in Eq. 7.22 leads to a roughly squared condition number, and when the Lorentzian broadening width η is small, the equation becomes quasi-singular at the resonance position of ω and $\hat{H}_0 - E_0$. The preconditioned treatment such as using the solution relating to the matrix composed of only the diagonal elements is often employed to improve the convergence.

Compared to Lanczos DMRG in the previous section that employs one set of renormalized basis for the responses of all frequencies, one unique set of basis is tailored for each frequency in the procedure of CV-DMRG, leading to much improved accuracy. In principle, CV-DMRG possesses the flexibility of arbitrarily choosing the artificial broadening width and the number of frequency points to obtain a spectrum with desired resolution, while in practice the numerical cost shall be taken into consideration. Higher resolution usually means smaller broadening width and more dense frequency points to be computed, which accordingly requires higher numerical resources: on the one hand, a large amount of frequencies need to be calculated independently, although this drawback allows for natural paralleled computations at the same time. The converged CV can be used as the initial guess for the adjacent frequency for apparent accelerations; on the other hand, a smaller η in Eq. 7.22 increases the condition number thus the difficulty of solving the equation, so there are trade-offs to be made. Kühner and White (1999) mentioned that considering the large amount of computations, a dense set of frequencies is not necessarily computed using CV-DMRG, and as for the calculation within the region of $[\omega_1, \omega_2]$, when $\eta \sim \omega_2 - \omega_1$, one can only calculate the CV at ω_1 and ω_2, and the response of those frequencies inside this interval can be calculated using the more economic Lanczos DMRG by providing a better basis that employs $|0\rangle$, $|O\rangle$ together with the CV of both ω_1 and ω_2 for approximating Hamiltonian. One shall keep in mind that this is under the assumption that the CV of ω_1 and ω_2 can fairly reflect the responses near to them.

Recently, Nocera and Alvarez (2016) proposed a method that employed the Lanczos method for solving the CV $|C(\omega)\rangle$: when optimizing a local site

during the sweeping process, the effective Hamiltonian is transformed into a tridiagonalized matrix through the Lanczos algorithm: $\hat{H}_0 = V^\dagger TV$, and the the T matrix is directly diagonalized by $T = S^\dagger DS$ where D is the diagonal matrix made of the eigenvalues of the T matrix:

$$\left|C(\omega)\right\rangle = V^\dagger S^\dagger \frac{1}{E_0 + \omega - D + i\eta} SV|O\rangle. \tag{7.24}$$

This method is essentially different from the Lanczos DMRG, and the Lanczos method here serves as an alternative solver for CV, which avoids directly solving ill-conditioned linear equations. The reduced density matrix for Lanczos recurrence considers the contribution of $|C(\omega)\rangle$ compared to the original Lanczos DMRG, namely, it still employs different renormalized basis for different frequency points.

7.3.3   Dynamical density matrix renormalization group

More frequently used CV approach is the DDMRG, which is a reformulation of CV-DMRG in terms of the variational principle (Jeckelmann, 2002). DDMRG transforms the task of solving the Eq. 7.22 for CV to a minimization problem for functional F,

$$F = \langle X(\omega)|\left(\omega - \hat{H}_0 + E_0\right)^2 + \eta^2|X(\omega)\rangle + 2\eta\langle O|X(\omega)\rangle. \tag{7.25}$$

F finds its minimum when $|X(\omega)\rangle = \mathbf{Im}|C(\omega)\rangle$, and one important feature is that the spectral function $S(\omega)$ in Eq. 7.21 equals $-F_{\min}/\pi\eta$, which means the explicit use of CV is not necessary for obtaining $S(\omega)$, and this leads to increased accuracy: the numerical error of $S(\omega)$ drops from $O(\varepsilon)$ to $O(\varepsilon^2)$, if the error of the obtained $|X(\omega)\rangle$ is $O(\varepsilon)$ by adopting the minimization procedure. The problem now turns into calculating F_{min}. The minimization of F employs a variational manner, and the working equation for a local site i comes from the variational treatment of the local site matrix A^{σ_i} while keeping the rest of matrices fixed,

$$\frac{\partial F[X(\omega)]}{\partial A^{\sigma_i}} = 2\langle X(\omega)|\left(\omega - \hat{H}_0 + E_0\right)^2 + \eta^2|\frac{\partial}{\partial A^{\sigma_i}}X(\omega)\rangle + 2\eta\langle O|\frac{\partial}{\partial A^{\sigma_i}}X(\omega)\rangle = 0. \tag{7.26}$$

For clear demonstration, we graphically illustrate Eq. 7.26 that is formulated with the structure of MPS/MPO (Jiang et al., 2020a), see Fig. 7.2. Here, the MPS provides a mathematical ansatz for the CV.

This linear equation can be solved via standard iterative methods such as the conjugate gradient method. Eq. 7.26 and Fig. 7.2 describe the "single-site" algorithm that optimizes one local matrix at a time, and the procedure is outlined in Algorithm 7.2.
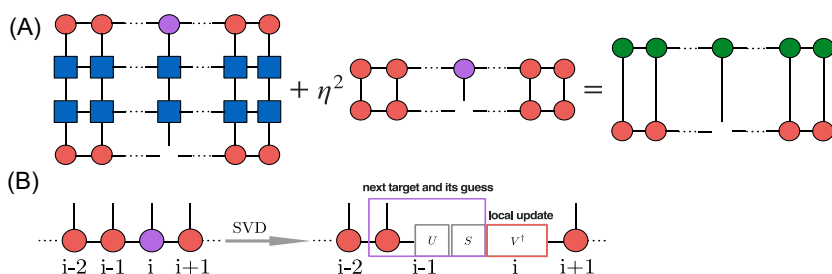
FIGURE 7.2 (A) The linear equation problem for optimizing A^{σ_i}; (B) when sweep from right to left, perform the SVD of A^{σ_i} each time after solving the local linear equation and update the local site A^{σ_i} and meanwhile obtain the guess for $A^{\sigma_{i-1}}$. *SVD*, Singular value decomposition. *Reproduced from Jiang, T., Li, W., Ren, J., Shuai, Z., 2020a. Finite temperature dynamical density matrix renormalization group for spectroscopy in frequency domain. J. Phys. Chem. Lett. 11, 3761−3768.* https://doi.org/10.1021/acs.jpclett.0c00905, *with permission from American Chemical Society.*

Algorithm 7.2: Single-site dynamical DMRG. *DMRG*, Density matrix renormalization group.

1: **prepare** operater $\hat{H}_0$ and $\hat{O}$, ground state $|0\rangle$.
2: **generate** initial guess of left canonical $|X\rangle = \sum_{\{\sigma_i\}} A^{\sigma_0} A^{\sigma_1} \cdots A^{\sigma_{N-1}}$.
3: **for** $j = 0$ **to** $j = $ max_iter **do**
4:      **if** j **is** even:
5:          **procedure** *right_to_left_sweep*
6:              **for** $i = N - 1$ **to** $i = 1$ **do**
7:                  $\frac{\partial}{\partial A^{\sigma_i}} F_j[X(\omega)] = 0$
8:                  $U, S, V^{\mathsf{T}} \leftarrow \text{SVD}(A^{\sigma_i})$
9:                  update $A^{\sigma_i} \leftarrow V^{\mathsf{T}}$, $A^{\sigma_{i-1}} \leftarrow A^{\sigma_{i-1}} US$
10:             **end for**
11:         **end procedure**
12:         **if** $(F_j - F_{j-1})/F_j < \epsilon$ **break**
13:     **elif** j **is** odd:
14:         **procedure** *left_to_right_sweep*
15:             **for** $i = 0$ **to** $i = N - 2$ **do**
16:                 $\frac{\partial}{\partial A^{\sigma_i}} F_j[X(\omega)] = 0$
17:                 $U, S, V^{\mathsf{T}} \leftarrow \text{SVD}(A^{\sigma_i})$
18:                 update $A^{\sigma_i} \leftarrow U$, $A^{\sigma_{i+1}} \leftarrow SV^{\mathsf{T}} A^{\sigma_{i+1}}$
19:             **end for**
20:         **end procedure**
21:         **if** $(F_j - F_{j-1})/F_j < \epsilon$ **break**
22: **end for**

Similar to the difference between the "single-site" and "two-site" ground-state optimization, the extension to the "two-site" algorithm is fairly straightforward. The "two-site" algorithm is numerically more expensive but can prevent from being trapped to a local minimum. In the first-generation

DMRG in terms of renormalized operator, the implementation is the same as CV-DMRG with the targeting state $|X(\omega)\rangle$, the ground-state wavefuction $|0\rangle$ and $|O\rangle$. The targeting states share one set of renormalized basis by state averaging (Jeckelmann, 2002). In contrast, here all of them are accurately represented by independent MPSs, which enables increased accuracy. Meanwhile, the local effective Hamiltonian is based on the renormalized basis in the traditional DDMRG (see discussion for CV in the previous sub-section), so those moments with higher order such as $\left\langle X^{\dagger}\left|(\omega-\hat{H}_0)^2\right|\frac{\partial}{\partial A^{\sigma_i}}X\right\rangle$ are approximated (see discussion in Section 7.3.2), while the use of MPO allows precise representation of all operators appeared in Eq. 7.26.

7.3.4 Chebyshev matrix product states

The CheMPS (Holzner et al., 2011) addresses the δ function formulation of the spectral function:

$$S(\omega) = \left\langle 0\left|\hat{O}^{\dagger}\delta(\omega - \hat{H}_0 + E_0)\hat{O}\right|0\right\rangle. \tag{7.27}$$

CheMPS combined the kernel polynomial expansion (Weiße et al., 2006) with MPS to approximate the δ function. A general function $f(x)$ can be expanded by the Chebyshev polynomials,

$$f(x) = \frac{1}{\pi\sqrt{1\text{-}x^2}}\left(\int_{-1}^{1}dxf(x)T_0(x) + 2\sum_{n=1}^{\infty}T_n(x)\int_{-1}^{1}dxf(x)T_n(x)\right)$$

where $T_n(x)$ follows the recurrence relation:

$$\begin{aligned} T_0(x) &= 1, \\ T_1(x) &= x, \\ T_n(x) &= 2xT_{n-1}(x) - T_{n-2}(x), n = 2, 3, \cdots. \end{aligned} \tag{7.29}$$

The expansion only holds when $x \in [-1, 1]$ out of which the norm of polynomial will diverge. When dealing with the δ function in Eq. 7.27, one should rescale and shift the frequency ω and (the eigenvalues of) $\hat{H}_0 - E_0$ into $[-1, 1]$ (in practice into $[-W', W']$ where W' is slightly smaller than 1 to ensure the numerical stability). The rescale and shift operation is defined by a function $\omega' = f(\omega')$ and $\hat{H}_0 = f(\hat{H}_0 - E_0)$ where $f(x) = \frac{x - E_{\min}}{a} - W'$, $a = (E_{\max} - E_{\min})/2W'$, and $E_{\max(\min)}$ correspond to the largest (smallest) transition energy. The ground state of $\hat{H}_0$ and $-\hat{H}_0$ can be calculated for the lowest and highest energy of the system and then the transition energy can be determined. Sometimes, not all states are involved in the transitions, depending on the problems investigated, the quantum number (qn) constraints can be used to extract the energy window that involves energy transition. A smaller value of $E_{\max} - E_{\min}$ speeds up the convergence rate of Chebyshev expansion. For instance, for linear optical absorption or emission

spectroscopy of exciton models, the transitions happen between spaces with $qn = 0$ and $qn = 1$, where qn denotes the number of exciton, and thus we can only calculate the transition energies between these two spaces to determine E_{max} and E_{min}.

The δ function is approximated by

$$\delta\left(\omega - \hat{H}_0 + E_0\right) = a^{-1}\delta\left(\omega' - \hat{H}_0'\right) \approx \frac{1}{a\pi\sqrt{1 - \omega'^2}} \left(g_0 + 2 \sum_{n=1}^{N-1} g_n T_n\left(\hat{H}_0'\right) T_n(\omega') \right) \tag{7.30}$$

The approximation in Eq. 7.30 becomes exact in the limit of the expansion order of $N \to \infty$. Otherwise, the damping factor g_n should be used. A finite N without using g_n leads to the so-called Gibbs oscillation (Holzner et al., 2011). The introduction of g_n let the spectral function become smooth, for instance, the most commonly used Jackson kernel with the damping factor (Eq. 7.31) mimics the effect of frequency-dependent Gaussian broadening with width η (Weiße et al., 2006).

$$g_n^J = \frac{(N - n + 1)\cos\frac{\pi n}{N+1} + \sin\frac{\pi n}{N+1}\cot\frac{\pi}{N+1}}{N + 1} \tag{7.31}$$

$$\eta' = \sqrt{1 - \omega'^2}\frac{\pi}{N}, \eta = a\eta' \tag{7.32}$$

Substitute Eq. 7.30 back to Eq. 7.27, then

$$S(\omega) = \frac{1}{a\pi\sqrt{1 - \omega'^2}} \left[g_0\mu_0 + 2 \sum_{n=1}^{N-1} g_n\mu_n T_n(\omega') \right], \tag{7.33}$$

where $\mu_n = \langle t_n | t_0 \rangle$ is called the Chebyshev moments. Following the three-term recurrence relation of Chebyshev polynomials, the Chebyshev vector $|t_n\rangle$ satisfies the recurrence relation,

$$|t_n\rangle = 2\hat{H}_0'|t_{n-1}\rangle - |t_{n-2}\rangle, \tag{7.34}$$

with $|t_0\rangle = \hat{O}|0\rangle$ and $|t_1\rangle = \hat{H}_0'|t_0\rangle$.

The rescaled $\hat{H}_0'$ is represented as an MPO and the generated Chebyshev vectors are each represented by an MPS. To prevent the exponential growth of the bond dimension of Chebyshev vectors, $|t_n\rangle$ is approximated by $\left|t_n^m\right\rangle$ in terms of a MPS with a fixed virtual bond dimension m by the variational compression called "recurrence fitting" which minimizes

$$\Delta_{fit} = \left\| |t_n\rangle - 2\hat{H}_0'|t_{n-1}\rangle + |t_{n-2}\rangle \right\|^2. \tag{7.35}$$

$$\frac{\partial\Delta_{fit}}{\partial X_i} = 0 \to 2\langle t_{n-1}|\hat{H}_0'\frac{\partial|t_n^m\rangle}{\partial X_i} - \langle t_{n-2}|\frac{\partial|t_n^m\rangle}{\partial X_i} = X_i \tag{7.36}$$
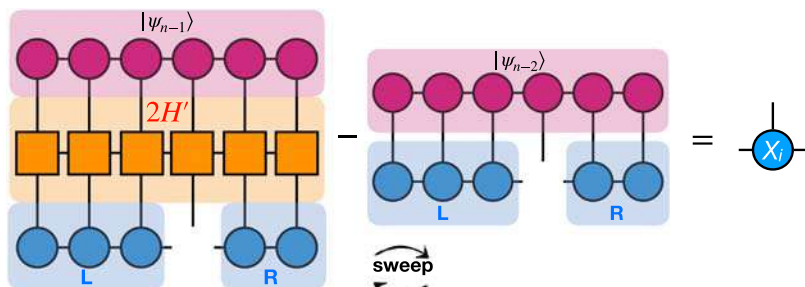
FIGURE 7.3 Graphical representation of the single-site variational optimization of Chebyshev vector $|t_n^m\rangle$. L (R) denotes left (right) canonical matrices. *Reproduced from Jiang, T., Ren, J., Shuai, Z., 2021. Chebyshev matrix product states with canonical orthogonalization for spectral functions of many-body systems. J. Phys. Chem. Lett. 12, 9344–9352.* https://doi.org/10.1021/acs.jpclett.1c02688, *with permission from American Chemical Society.*

where X_i is the canonical center of the MPS $|t_n^m\rangle$. The minimization is graphically represented in Fig. 7.3. Eq. 7.35 can also be minimized with two-site algorithm which avoids local minimum but is more expensive. We outline the procedure of Chebyshev MPS in Algorithm 7.3.

Algorithm 7.3: Chebyshev MPS. *MPS, Matrix product states.*

1: **prepare** operater $\hat{H}_0$, $\hat{O}$, and ground state $|0\rangle$.
2: **procedure** rescale Hamiltonian
3:    **calculate** minimal and maximal transition energy $E_{\min}$ and $E_{\max}$.
4:    $\hat{H}_0' \leftarrow Rescale(\hat{H}_0, E_{\min}, E_{\max})$
5: **end procedure**
6: **generate** first two Chebyshev MPS $|t_0\rangle \leftarrow \hat{O}|0\rangle, |t_1\rangle \leftarrow \hat{H}_0'|t_0\rangle$
7: **procedure** vector generation
8:    **for** $n = 1$ **to** $n = N - 1$ **do**
9:      $|t_{n+1}\rangle \leftarrow \min: \left| |t_{n+1}\rangle - \left(2\hat{H}_0'|t_{n-1}\rangle - |t_{n-2}\rangle\right) \right|^2$
10:     $\mu[n] \leftarrow \langle t_n|t_0\rangle \times g[n]$
11:   **end for**
12: **end procedure**
13: **procedure** calculate spectral function
14:   **for** $\omega = \omega_0$ **to** $\omega = \omega_{K-1}$ **do**
15:     $\omega' \leftarrow Rescale(\omega, E_{min}, E_{max})$
16:     $T[0:N-1] \leftarrow ChebyshevRecurrence(\omega')$
17:     $S[\omega] \leftarrow \left(\mu[0] + 2\mu T^T\right) \times \text{coeff}(\omega')$
18:   **end for**
19: **end procedure**

According to Eq. 7.32, the spectral function is obtained with the frequency-dependent resolution which is proportional to $1/N$ and $E_{\max} - E_{\min}$. Considering the fact that the frequency range with a finite dynamical response called the spectral width (W_S) is often significantly narrower than the full many-body bandwidth $W = E_{\max} - E_{\min}$, an effective

bandwidth W^* smaller than W can be adopted in the rescaling implementation to increase the resolution. However, if doing so, an additional higher-energy truncation procedure has to be included to throw away the higher-energy components coming from the eigenstates of $\hat{H}_0'$ that fall outside of $[-1, 1]$. Otherwise, the newly generated Chebyshev vectors diverge rapidly. Each time after compressing the newly generated Chebyshev vector, the truncation is implemented in the traditional DMRG-like sweeping procedure by first constructing a Krylov space of the local site and then project out the higher-energy components. Nevertheless, the energy truncation procedure cannot be formulated in a variational way as the ground-state calculation, that is, there is no criterion to decide when to stop the sweep process and how large the Krylov space should be constructed for the local site, so one should assess the accuracy of using different combinations of parameters before the real calculation. It was also shown that the energy truncation increases the entanglement (bond entropy) (Holzner et al., 2011). All these facts stated in this paragraph complicate the application of CheMPS to those systems having especially broad full many-body bandwidth but narrow spectral width such as the electron−phonon systems.

There is another approach to increase the resolution. The idea is behind the fact that the damping factor is used to cure the Gibbs oscillation because of finite expansions, which also leads to the reduction of the resolution. The linear prediction which makes predictions by the extrapolation of the previous data points was proposed to monitor the decay of the Chebyshev moments so as to discard the Gibbs oscillation in the absence of damping factor (Ganahl et al., 2014).

Similar to the Lanczos MPS method, CheMPS follows a three-term recurrence relation that proceeds by variational compression of new vectors using Eq. 7.35, which is the primary approximation made in CheMPS. Therefore the recurrence relation will be broken because of accumulated errors, a post-treatment by orthogonalizing the primitive Chebyshev vectors and constructing a Krylov space (Xie et al., 2018) (similar to what was used in Lanczos MPS, see Algorithm 7.1), in which the three-term recurrence relation can be strictly preserved, and the accuracy and efficiency will be effectively increased. Sometimes, the linear dependency between the Chebyshev vectors makes the Gram−Schmidt orthogonalization numerically unstable. A numerically stable canonical orthogonalization approach (inspired by Lowdin's orthogonalization in electronic structure calculation) was later presented and significantly increased the accuracy of CheMPS (Jiang et al., 2021).

The canonical orthogonalization assumes the orthogonal vectors are linearly combined by the primitive N vectors,

$$\left|\phi_n\right\rangle = \sum_{i=0}^{N-1} C_{in}|t_i\rangle, \ \left\langle\phi_m|\phi_n\right\rangle = \delta_{mn} \tag{7.37}$$

The C matrix is obtained by first diagonalizing the overlap matrix S of the primitive Chebyshev vectors $\left(S_{ij} = \langle t_i|t_j\rangle\right)$ by $S = U^{\mathrm{T}}DU$, where D is diagonal with elements being the eigenvalues of S. Then we have $C = UD^{-1/2}$. The effective Hamiltonian matrix in the Krylov subspace spanned by the new orthogonal vectors is,

$$\mathrm{H}_{\mathrm{eff},mn} = \langle\phi_m|\hat{H}_0'|\phi_n\rangle = \sum_{i,j=0}^{N-1} C_{im}C_{jn}\langle t_i|\hat{H}_0'|t_j\rangle \tag{7.38}$$

$$\mathrm{H}_{\mathrm{eff}}|n\rangle = \lambda_n'|n\rangle \tag{7.39}$$

Finally the spectral function is calculated by

$$S(\omega) = a^{-1}\sum_n\left|\langle n|t_0^*\rangle\right|^2\delta(\omega'-\lambda_n') = a^{-1}\sum_n\Omega_n\delta(\omega'-\lambda_n') \tag{7.40}$$

where $\left|t_0^*\right\rangle$ is the first Chebyshev vector that represented in the new basis set by $\left|t_0^*\right\rangle = \sum_{ij=0}^{N-1}C_{ij}\langle t_0|t_i\rangle|j\rangle$. We outline the procedure of CheMPS with canonical orthogonalization in Algorithm 7.4.

Algorithm 7.4: Chebyshev MPS with canonical orthogonalization. *MPS*, Matrix product states.

1: **prepare** operater $\hat{H}_0$, $\hat{O}$, and ground state $|0\rangle$.
2: **procedure** rescale Hamiltonian
3:     **calculate** minimal and maximal transition energy $E_{\min}$ and $E_{\max}$.
4:     $\hat{H}_0' \leftarrow Rescale(\hat{H}_0, E_{\min}, E_{\max})$
5: **end procedure**
6: **generate** first two Chebyshev MPS $|t_0\rangle \leftarrow \hat{O}|0\rangle, |t_1\rangle \leftarrow \hat{H}_0'|t_0\rangle$
7: **initialize** $W_{ij} = \langle t_i|t_j\rangle$, $F_{ij} = \left\langle t_i|\hat{H}_0'|t_j\right\rangle$ for $i, j \in [0, 1]$
8: **procedure** vector generation
9:     **for** $n = 1$ **to** $n = N - 1$ **do**
10:       $|t_{n+1}\rangle \leftarrow min:\left|\left|t_{n+1}\rangle - \left(2\hat{H}_0'|t_{n-1}\rangle - |t_{n-2}\rangle\right)\right|\right|^2$
11:       **for** $j = 0$ **to** $j = n$ **do**
12:         $W_{jn} = W_{nj} \leftarrow \langle f_j|f_n\rangle$, $F_{jn} = F_{nj} \leftarrow \left\langle f_j|\hat{H}_0'|f_n\right\rangle$
13:       end for
14:     **end for**
15: **end procedure**
16: **procedure** reorthogonalization
17:     $C \leftarrow CanonicalOrtho(W)$
18:     $H_{\mathrm{eff}} \leftarrow MatrixMultiply(C^T, F, C)$
19:     $\lambda_n, |n\rangle \leftarrow Diag(H_{\mathrm{eff}}), n = 0, 1, \cdots, N - 1$
20:     $\left|t_0^*\right\rangle \leftarrow MatrixMultiply(C^T, W[0, :])$
21:     **for** $n = 1$ **to** $n = N - 1$ **do**
22:       $\Omega_n \leftarrow \left|\langle n|t_0^*\rangle\right|^2$
23:     **end for**
24: **end procedure**

7.3.5 Analytic linear response density matrix renormalization group

We may as well group those algorithms (Lanczos DMRG, CV-DMRG, DDMRG, and CheMPS) stated above into one category since all of them are incorporating the independently existed method (Lanczos method, CV method, and Chebyshev polynomial expansion method) with DMRG or MPS/MPO as the supporter to calculate the spectral function. In contrast, the analytic linear response DMRG that will be introduced in this section is inspired by the linear response theories of conventional quantum chemistry methods (Dorando et al., 2009; Wouters et al., 2013; Haegeman et al., 2013; Nakatani et al., 2014).

First, we briefly review the canonical representation of the wavefunction (also see Fig. 7.1),

$$|\psi\rangle = \sum_{\{i\}} L_1^{(0)} \cdots L_{i-1}^{(0)} C_i^{(0)} R_{i+1}^{(0)} \cdots R_N^{(0)} |\sigma_1 \cdots \sigma_i \cdots \sigma_N\rangle \qquad (7.41)$$

where the right superscripts represent that the system is unperturbed. When the system is perturbed by the external electromagnetic field $V(t) = V e^{i\omega t} + V^* e^{-i\omega t}$, the local site matrix responses,

$$L_i(t) = \left(L_i^{(0)} + L_i^{(1)}(t) + \cdots \right) e^{-iE_0 t}$$

$$C_i(t) = \left(C_i^{(0)} + C_i^{(1)}(t) + \cdots \right) e^{-iE_0 t} \qquad (7.42)$$

$$R_i(t) = \left(R_i^{(0)} + R_i^{(1)}(t) + \cdots \right) e^{-iE_0 t}$$

Substitute Eqs. 7.41 and 7.42 into the time-dependent Schrödinger equation $i\partial_t C_i(t) = H_i(t) C_i(t)$ and maintain the first-order terms, the linear response matrix of the ith site $C_i^{(1)}(\omega)$, $C_i^{(1)}(-\omega)$ satisfies

$$\left(H_i^{(0)} - (E_0 + \omega)I \right) C_i^{(1)}(\omega) = -Q\left(\Delta H_i^{(1)}(\omega) + V_i^{(1)} \right) C_i^{(0)} \qquad (7.43)$$

$$\left(H_i^{(0)} - (E_0 - \omega)I \right) C_i^{(1)}(-\omega) = -Q\left(\Delta H_i^{(1)}(-\omega) + V_i^{(1)*} \right) C_i^{(0)} \qquad (7.44)$$

where $Q = 1 - C_i^{(0)} C_i^{(0)\dagger}$ assumes the intermediate normalization condition. $\Delta H_i^{(1)}(\pm\omega)$ is the linear response of the effective Hamiltonian of the ith site, which in turn relies on $C_i^{(1)}(\pm\omega)$, and therefore Eqs. 7.43 and 7.44 should be solved iteratively. The entire linear response is obtained by a sweeping manner: when sweeping from left to right, after solving for $C_i^{(1)}$, $L_i^{(1)}$ needs to be updated, and one can solve the equation of its column vector $l_p^{(1)}$,

$$\left(D_L^{(0)} - \sigma_p \right) l_p^{(1)} = -Q_i^L D_L^{(1)} l_p^{(0)} \qquad (7.45)$$

where the projection operator $Q_i^L = 1 - L_i^{(0)} L_i^{(0)\dagger}$. The zeroth and first-order response density matrix of the ith site are defined as,

$$D_L^{(0)} = C_i^{(0)} C_i^{(0)\dagger} \tag{7.46}$$

$$D_L^{(1)} = C^{(0)} C^{(1)\dagger} + C^{(1)} C^{(0)\dagger}, \tag{7.47}$$

and then move to the $(i + 1)$th site to get $C_{i+1}^{(1)}$.

The polarizability ($\omega > 0$) can be obtained after having the converged linear response wavefunction:

$$G^1(\omega) = C^{(0)\dagger} \mu_i^{(0)} C^{(1)}(\omega) + C^{(1)\dagger}(\omega) \mu_i^{[0]} C^{(0)} + C^{(0)\dagger} \mu_i^{(1)}(\omega) C^{(0)} \tag{7.48}$$

where $\mu_i^{(0)}$ is the projection of the dipole operator at the renormalized basis of the ith site, and $C^{(1)}(\omega)$ is the linear response wavefunction at ω after the perturbation from external field.

7.4 Finite temperature algorithms

7.4.1 Lanczos density matrix renormalization group

The calculation of spectral function at finite temperature relies on getting the thermal equilibrium density matrix, with which the algorithms at zero temperature can be slightly modified for the finite temperature case. The density matrix of thermal equilibrium mixed state at $T > 0$ can be represented by

$$\hat{\rho} = \frac{1}{Z} e^{-\beta \hat{H}_0} = \frac{1}{Z} \sum_{n=1}^{N} |n\rangle e^{-\beta E_n} \langle n|, \ \beta = 1/k_B T \tag{7.49}$$

where Z is the partition function. Note that all notations are identical to those in Section 7.2. By sampling R normalized states $|r\rangle$ with random amplitudes, the thermal density matrix $\hat{\rho}$ can be approximated as

$$\hat{\rho} \sim \frac{N}{ZR} \sum_{r=1}^{R} e^{-\frac{\beta \hat{H}_0}{2}} |r\rangle \langle r| e^{-\frac{\beta \hat{H}_0}{2}}, \ |r\rangle = \sum_n c_{rn} |n\rangle \tag{7.50}$$

With the random sampling treatment of the initial state, Kokalj and Prelovšek (2009) extended the Lanczos DMRG to finite temperature. A tridiagonalized matrix $\mathbf{H}_{\text{eff}}$ can be obtained by performing the Lanczos iteration on $|r\rangle$, then $\mathbf{H}_{\text{eff}}$ is diagonalized to obtain a set of eigenvectors $|\psi_i^r\rangle$ and the corresponding eigenvalues $\epsilon_i^r (i = 1, 2, \cdots, M)$. Therefore $e^{-\beta \hat{H}_0/2} |r\rangle$ can be approximated as

$$|\tilde{\psi}_r\rangle = \sum_{i=1}^{M} e^{-\frac{\beta \epsilon_i^r}{2}} |\psi_i^r\rangle \langle \psi_i^r | r\rangle, \tag{7.51}$$

then the density matrix is approximated as

$$\hat{\rho} \sim \frac{N}{ZR} \sum_{r=1}^{R} |\tilde{\psi}_r\rangle\langle\tilde{\psi}_r|, \ Z = \frac{N}{R} \sum_{r=1}^{R} \sum_{j=1}^{M} e^{-\beta\varepsilon_j^r} |\langle r|\psi_j^r\rangle|^2 \tag{7.52}$$

For the spectral function,

$$G^{(1)}(\omega) = \frac{1}{Z} \sum_n e^{-\beta E_n} \left\langle n|\hat{O}^\dagger \frac{1}{\omega - (\hat{H}_0 - E_n) + i\eta} \hat{O}|n \right\rangle, \tag{7.53}$$

use the approximation of random sampling,

$$G^{(1)}(\omega) \approx \frac{N}{ZR} \sum_{r=1}^{R} \sum_{i,j=1}^{M} e^{-\beta\epsilon_i^r} \frac{1}{\omega - \left(\epsilon_j^{Or} - \epsilon_i^r\right) + i\eta} \\ \times \langle r|\psi_i^r\rangle \left\langle \psi_i^r \left| \hat{O}^\dagger \right| \psi_j^{Or} \right\rangle \left\langle \psi_j^{Or}|\hat{O}|r \right\rangle \tag{7.54}$$

where $\left|\psi_j^{Or}\right\rangle$ and ϵ_j^{Or} are the Lanczos vectors and the corresponding eigenvalues by using $\hat{O}|r\rangle$ as the initial state to perform the Lanczos iteration.

The accuracy of this method relies on the number of states being sampled for the construction of density matrix, indicating the suitability for situations with relatively low temperature. However, it often requires a large number of states to be sampled for high temperatures. As will be introduced in Chapter 8, a more rigorous approach using the imaginary time evolution for the thermal density matrix has become more popular for obtaining the thermal density matrix.

7.4.2 Dynamical density matrix renormalization group

The response function $S(\omega)$ at finite temperature (see Section 7.2) reads

$$S(\omega) = -\frac{1}{\pi} \lim_{\eta \to 0^+} \mathbf{Im}\mathrm{Tr}\left\{ \hat{O}^\dagger \frac{1}{\omega - \mathcal{L} + i\eta} \hat{O}\hat{\rho}_\beta \right\} \tag{7.55}$$

Jiang et al. (2020a) extended the DDMRG method to finite temperature with the help of the purification technique that provides the thermal equilibrium. Accordingly, they defined the CV at finite temperature as

$$C(\omega) = \frac{1}{(\omega - \mathcal{L} + i\eta)} \hat{\mu}\hat{\rho}_\beta^{1/2}, \tag{7.56}$$

where $\hat{\rho}_\beta^{1/2}$ can be obtained by the imaginary time evolution (see Chapter 8 for details), and $C(\omega)$ is in the form of MPO, whose imaginary part $X(\omega)$ satisfies the following real symmetric and positive definite equation:
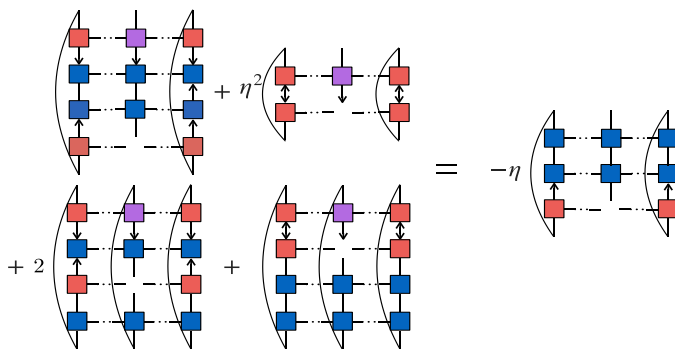
FIGURE 7.4 Graphical representation of DDMRG's working equation for optimizing single local site at finite temperature. DDMRG, Dynamical density matrix renormalization group; *MPO*, matrix product operator. *Reproduced from Jiang, T., Li, W., Ren, J., Shuai, Z., 2020a. Finite temperature dynamical density matrix renormalization group for spectroscopy in frequency domain. J. Phys. Chem. Lett. 11, 3761−3768. https://doi.org/10.1021/acs.jpclett.0c00905. With permission from American Chemical Society.*

$$\left((\omega - \mathcal{L})^2 + \eta^2\right)X(\omega) = -\eta \hat{O}\hat{\rho}_\beta^{1/2}, \tag{7.57}$$

basing upon which the functional F is constructed,

$$F = \mathrm{Tr}\left\{X^\dagger\left((\omega - \mathcal{L})^2 + \eta^2\right)X + 2\eta X^\dagger \hat{O}\hat{\rho}_\beta^{1/2}\right\} \tag{7.58}$$

Similar to the zero-temperature case, F finds its minimum where $X(\omega)$ satisfies Eq. 7.57, and $S(\omega) = -F_{\min}/\pi\eta$. $X(\omega)$ can be obtained by solving the equation $\partial F/\partial A^{\sigma_i}_{a_{i-1}a_i} = 0$ iteratively in a variational way (Schollwöck, 2011), which is graphically represented in Fig. 7.4.

$$\frac{\partial F}{\partial A^{\sigma_i}} =$$

$$\mathrm{Tr}\left\{X^\dagger\left[(\omega - \hat{H}_0)^2 + \eta^2\right]\frac{\partial X}{\partial A^{\sigma_i}} + 2X^\dagger(\omega - \hat{H}_0)\frac{\partial X}{\partial A^{\sigma_i}}\hat{H}_0 + X^\dagger\frac{\partial X}{\partial A^{\sigma_i}}\hat{H}_0^2 + \eta\rho_\beta^{1/2}\hat{\mu}\frac{\partial X}{\partial A^{\sigma_i}}\right\} = 0. \tag{7.59}$$

The complexity for solving the linear equation at finite temperature is $\mathcal{O}(m^4 p^4)$, compared with $\mathcal{O}(m^4 p^2)$ at zero temperature, which could be a vast increase of numerical resources especially for the electron−phonon systems that typically possess a large physical bond dimension p (tens or hundreds) of the local phonon mode.

7.4.3 Chebyshev matrix product state

In Section 7.3.4, we introduced the CheMPS method at zero temperature. Tiegel et al. (2014) combined it with the purification technique to calculate the spectral function at finite temperature.

$$S(\omega) = \text{Tr}\left\{\hat{\rho}_\beta^{1/2} \hat{O}^\dagger \delta(\omega - \mathcal{L}) \hat{O} \hat{\rho}_\beta^{1/2}\right\} \tag{7.60}$$

Similar to the procedure at zero temperature in Section 7.3.4, ω and the operator $\mathcal{L}$ should be rescaled first. Considering the case of frequency lying in the full many-body band $[E_{\min}, E_{\max}]$, the projection works as follows,

$$\omega' = \frac{\omega - E_{\min}}{a} - W', \mathcal{L}' = \frac{\mathcal{L} - E_{\min}}{a} - W', \tag{7.61}$$

the δ function is rewritten as

$$\delta(\omega - \mathcal{L}) = \frac{1}{a}\delta(\omega' - \mathcal{L}')$$

$$\approx \frac{1}{a\pi\sqrt{1 - \omega'^2}}\left(g_0 + 2\sum_{n=1}^{N-1} g_n T_n(\mathcal{L}')T_n(\omega')\right) \tag{7.62}$$

this equation is substituted back to Eq. 7.60, and a formula same as the zero-temperature case is obtained, see Eq. 7.33, where the Chebyshev moments $\mu_n = \text{Tr}\{\hat{t}_n \hat{t}_0\}$, and $\hat{t}_n$ satisfied the following recurrence relation,

$$\hat{t}_n = 2\mathcal{L}'\hat{t}_{n-1} - \hat{t}_{n-2}, \tag{7.63}$$

with the initial vectors $\hat{t}_0 = \hat{O}\hat{\rho}_\beta^{1/2}$, $\hat{t}_1 = \mathcal{L}'\hat{t}_0$.

7.5 Applications

With all these efforts, the DMRG methods in frequency space discussed in the previous sections have been extensively applied in calculating the dynamical properties of electron systems, electron−phonon systems, spin systems, etc. Some representative applications that study the dynamical quantities of many-body systems or examine/benchmark the performance of numerical methods will be presented in this section.

7.5.1 Electron system

The frequency space DMRG methods have been used to study the dynamical quantities of many-body electron systems, including the Hubbard model and its extensions, the Anderson impurity model, and ab initio quantum chemistry Hamiltonian. Earlier applications were applied to study the optical properties of conjugated polymer described by the (extended) Hubbard lattice model (Chapter 3 discussed the electronic structure investigations using DMRG). In organic semiconductors, the electron/hole pair of an exciton is bounded locally compared to the inorganic counterparts. The inorganic semiconductors typically have a large dielectric constant $\varepsilon > 10$ so that the Coulombic interaction is well screened, and, hence, the single-electron band model is often appropriate. However, as for the organic semiconductors, the
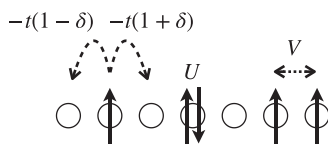
FIGURE 7.5 The graphical representation of the extended Hubbard−Peierls model.

intermolecular interaction is dominated by relatively small van der Waals force and the typically small dielectric constant $\varepsilon \sim 2-4$ cannot exhibit well screening effect. The binding energy of the electron−hole pair generated by the photon excitation is greater than the bandwidth of single electron band, thus the electron and hole are generally bounded. The extended Hubbard−Peierls model is a simple treatment to consider the attractive potential of the electron−hole pair,

$$\hat{H} = -\sum_i t\left[1 + (-1)^i \delta\right]\left(\hat{c}_{i\sigma}^\dagger \hat{c}_{i+1\sigma} + h.c.\right) + U\sum_i \hat{n}_{i\uparrow}\hat{n}_{i\downarrow} + V\sum_i (\hat{n}_i - 1)(\hat{n}_{i+1} - 1)$$

(7.64)

where t is the nearest hopping integral, δ is the parameter for adjusting the bond length, U is the on-site Coulombic repulsion, and V is the nearest Coulombic potential. A graphical representation is shown in Fig. 7.5.

With this Hamiltonian, Pati et al. (1999) investigated the third-order polarizability of different length, see Fig. 7.6. In Section 7.2.2, we only introduced how to calculate the linear response function using CV-DMRG, although the nonlinear response has a more complicated form, it can be calculated using CV-DMRG within the same framework (Ramasesha et al., 1997; Pati et al., 1999), see the third-order polarizability shown in Chapter 3.

Jeckelmann (2002) applied DDMRG to calculate the current−current correlation function of the extended Hubbard−Peierls model ($V = 0$) to obtain the optical conductivity, see Fig. 7.7. If the Hubbard term ($U = 0$) in Eq. 7.64 is again neglected, the Hamiltonian describes the free electron system, the optical conductivity of which is exactly solvable, which is regarded as one criteria to test the accuracy of DDMRG, and according to Fig. 7.7, the DDMRG result rigorously overlaps with the exact result.

Dorando et al. (2009) developed the analytic linear response DMRG method and applied it to calculate the polarizability of oligodiacetylenes (ODAs) and the result is compared with the DDMRG result. It was found that for relatively smaller m (e.g., $m = 25$), DDMRG gave poor polarizabilities in some cases, and some of the relative errors even reach 50%. By contrast, the results from the analytic linear response DMRG are more reasonable than DDMRG. This was explained that DDMRG suffers from using one set of DMRG basis to represent both the zeroth and response vectors, and we anticipate the improved accuracy if adopting different MPSs to represent the zeroth and response vector separately, as stated in Section 7.3.3. With the increase of
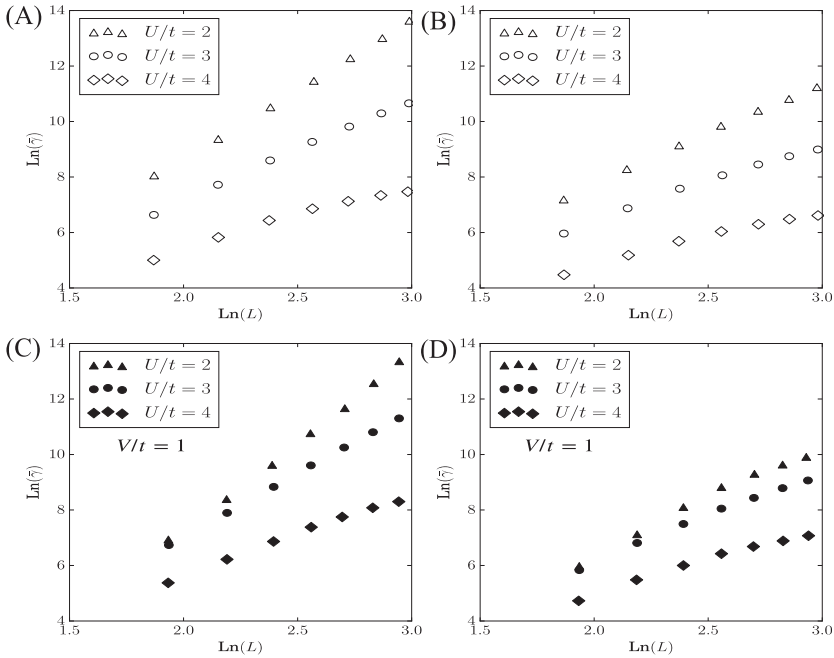
FIGURE 7.6 Plot of the log of average third-order polarizability $\tilde{\gamma}$ versus log of the chain length, L. Hubbard chain with three different values of U/t for $\delta = 0$ (A) and $\delta = 0.09$ (B); Hubbard−Peierls chain with three different values of U/t and $V/t = 1$ for $\delta = 0$ (C) and $\delta = 0.09$ (D). *Reproduced from Pati, S.K., Ramasesha, S., Shuai, Z., Brédas, J.-L., 1999. Dynamical nonlinear optical coefficients from the symmetrized density-matrix renormalization-group method. Phys. Rev. B. 59, 14827. https://doi.org/10.1103/PhysRevB.59.14827, with permission from American Physical Society.*
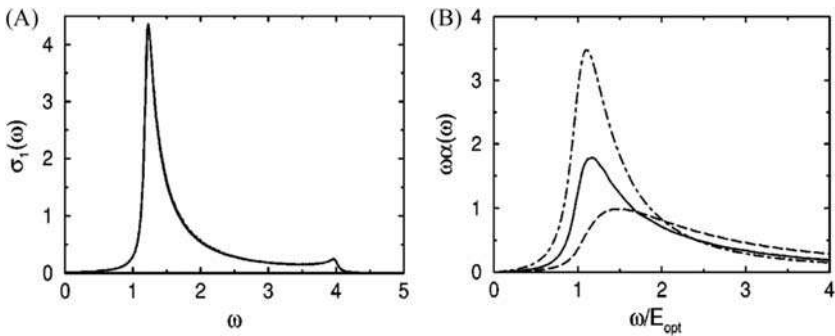
FIGURE 7.7 (A) Peierls insulator with $U = 0$ and $\delta = 0.3$, both DDMRG result for a 128-site chain and the exact result in the thermodynamic limit are shown (broadening width $\eta = 0.05t$); (B) optical conductivity on a 128-site chain for: Mott−Hubbard insulator with $U = 3t, \delta = 0$ (dashed), Peierls insulator with $U = 0, \delta = 0.15$ (dot dashed), and Hubbard−Peierls insulator with $U = 2.3t, \delta = 0.075$ (solid), broadening width $\eta = 0.1t$. *Reproduced from Jeckelmann, E., 2002. Dynamical density-matrix renormalization-group method. Phys. Rev. B. 66, 045114. https://doi.org/10.1103/PhysRevB.66.045114, with permission from American Physical Society.*

m, both methods converge gradually, and when $m = 250$, the results from DDMRG are a little bit better than the analytic linear response DMRG. Ronca et al. (2017) also applied DDMRG to calculate the single-electron Green function to obtain the photoelectron spectrum of quantum chemical systems with ab initio Hamiltonian, and the full configuration interaction results are used as the benchmarking results to compare the performance of DDMRG and time-dependent DMRG (TD-DMRG). Apart from this, they also applied DDMRG to precisely calculate the core ionization energy of the O 1s orbital of water molecule.

Jiang et al. (2021) combined CheMPS with canonical orthogonalization (coCheMPS), and applied it to calculate the photoelectron spectra of ab inito Hamiltonian. The coCheMPS exhibited both high accuracy and efficiency as compared with other state-of-the-art DMRG methods, as shown in Fig. 7.8. Such system is with relatively discrete density of states; however, the application to electron−phonon systems with dense states should be cautioned (as shown by Fig. 7.12). The algorithm did not adopt the spin adaptation with which the performance can be further increased (Ronca et al., 2017).
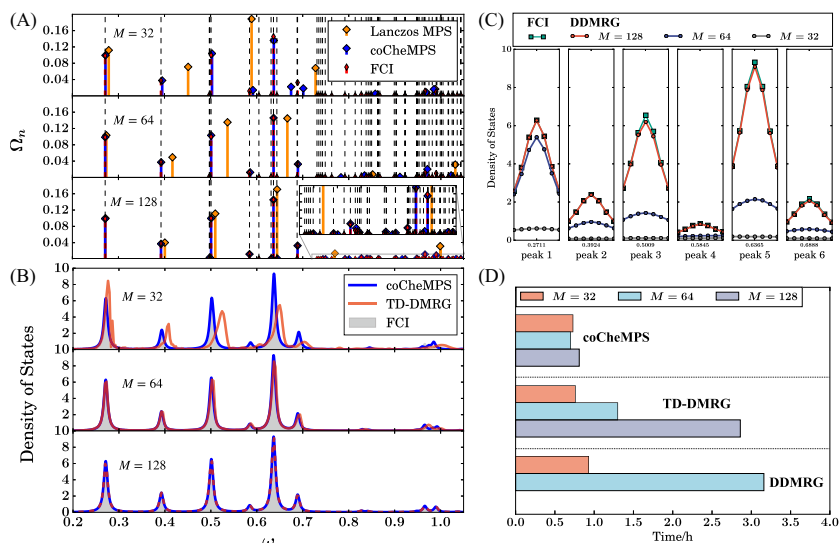
FIGURE 7.8 (A) The transition amplitude and transition energy (in unit of a.u.) computed by Lanczos MPS, CheMPS (both with canonical orthogonalization) with different bond dimension. (B) Density of states computed by coCheMPS and TD-DMRG. (C) The first six peaks using DDMRG. (D) Time cost for obtaining whole spectral functions using TD-DMRG and coCheMPS and the averaged time for one frequency using DDMRG. coCheMPS, CheMPS with canonical orthogonalization; *DDMRG*, dynamical density matrix renormalization group; *TD-DMRG*, time-dependent density matrix renormalization group. *Reproduced from Jiang, T., Ren, J., Shuai, Z., 2021. Chebyshev matrix product states with canonical orthogonalization for spectral functions of many-body systems. J. Phys. Chem. Lett. 12, 9344−9352. https://doi.org/10.1021/acs.jpclett.1c02688, with permission from American Chemical Society.*
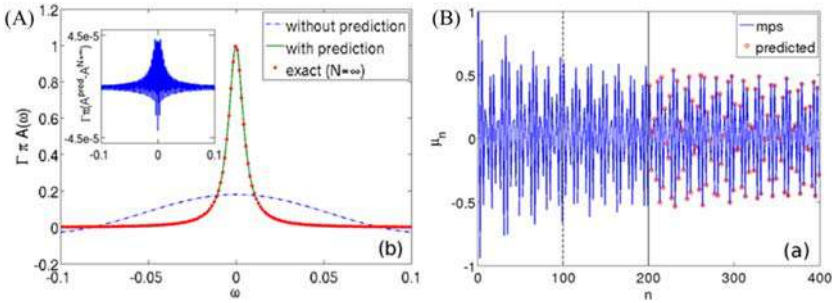
FIGURE 7.9 The application of CheMPS with the linear prediction technique to the SIAM model: (A) spectral function of the 100-site SIAM model in the noninteracting limit (U = 0) without (*dash-dotted blue line*, using 200 moments) and with (*solid green line*) linear prediction by using the CheMPS method as well as the exact results for the infinite system (*red dots*). The difference is shown in the inset. (B) Linear prediction of MPS-computed Chebyshev moments for the SIAM model with finite interaction strength: moments data in the left of the black dashed line are used as input and those between the black dashed and solid line are used as training data to make predictions. *CheMPS*, Chebyshev matrix product states; *MPS*, matrix product states; *SIAM*, Single-impurity Anderson model. *Reproduced from Ganahl, M., Thunström, P., Verstraete, F., Held, K., Evertz, H.G., 2014. Chebyshev expansion for impurity models using matrix product states. Phys. Rev. B. 90, 045144. https://doi.org/10.1103/PhysRevB.90.045144, with permission from American Physical Society.*

Ganahl et al. (2014) applied the CheMPS method with the linear prediction technique to the single-impurity Anderson model (SIAM) The method was benchmarked with the exactly solvable noninteracting SIAM which is equivalent to the spinless fermion model which is a nontrivial case for the MPS-based method, as shown in Fig. 7.9A, and the linear prediction dramatically increases the resolution of the spectral function and leads to great overlap with the exact results. As for the SIAM model with finite interaction strength, in Fig. 7.9B the trained MPS-based Chebyshev moments using the first 200 moments for training prediction are well overlapped with those without linear prediction.

7.5.2 Electron−phonon system

The Holstein model represents the most often studied object relating to electron−phonon coupled systems. Using the Lanczos DMRG, Zhang et al. (1999) studied the spectral functions and the optical conductivity of Holstein model with noninteracting electrons coupled to dispersionless phonons,

$$\hat{H} = \Omega \sum_i \hat{b}_i^\dagger \hat{b}_i - \gamma \sum_i \left(\hat{b}_i^\dagger + \hat{b}_i \right) \hat{n}_i - t \sum_{i\sigma} \left(\hat{c}_{i+1\sigma}^\dagger \hat{c}_{i\sigma} + \hat{c}_{i\sigma}^\dagger \hat{c}_{i+1\sigma} \right), \quad (7.65)$$

where $\hat{c}_{i\sigma}^\dagger(\hat{c}_{i\sigma})$ is the creation (annihilation) operator of electron with spin σ on site i, $\hat{n}_i$ is the number of electrons on site i, $\hat{b}_i^\dagger(\hat{b}_i)$ is the creation (annihilation) operator of local phonon mode. γ is the electron−phonon coupling
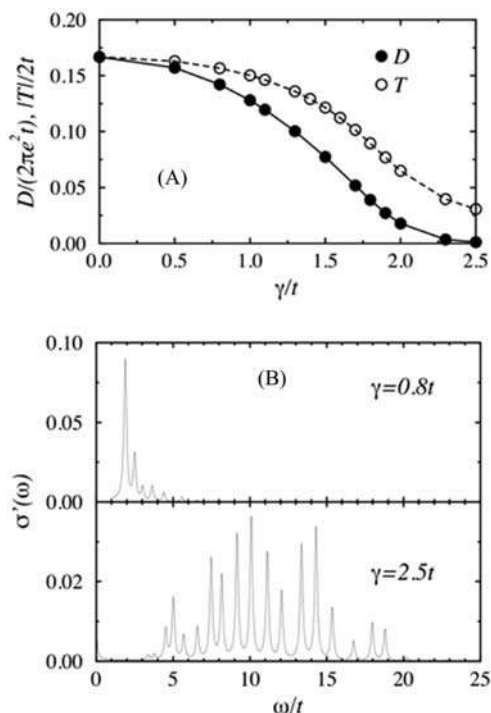
FIGURE 7.10 (A) Drude weight D and the kinetic energy per site T as a function of the electron−phonon coupling γ; (B) the incoherent part of the optical conductivity $\sigma'(\omega)$ in the quasi-free electron regime ($\gamma = 0.8t$) and in the small polaron regime ($\gamma = 2.5t$). *Reproduced from Zhang, C., Jeckelmann, E., White, S.R., 1999. Dynamical properties of the one-dimensional Holstein model. Phys. Rev. B. 60, 14092. https://doi.org/10.1103/PhysRevB.60.14092, with permission from American Physical Society.*

strength of the ith lattice site, and t is the hopping integral of the nearest lattice sites.

Fig. 7.10 presents the change of physical quantities related to the optical conductivity with the changes of the electron−phonon coupling strength γ. The optical conductivity $\sigma(\omega) = D\delta(\omega) + \sigma'(\omega)$ and D is the Drude peak corresponding to the weight of the coherent part, and $\sigma'(\omega)$ corresponds to the weight of the incoherent part. In Fig. 7.10A, T is the kinetic energy per site and follows the relation with $\sigma(\omega)$ that $\int_0^{\infty} \sigma(\omega)d\omega = \frac{\pi e^2}{2}(-T)$, namely, T gives the total weight of the optical conductivity. In the absence of the electron−phonon coupling ($\gamma = 0$), the incoherent part $\sigma'(\omega)$ contributes nothing to the optical conductivity, and one has the relation that $D = T$, corresponding to the noninteracted free electron system. With the increase of γ, both D and T decrease, and D deceases faster and becomes very small when $\gamma > 2t$. The decrease of the ratio D/T implies the more contribution of the incoherent part, and this corresponds to the polaronic behavior in the strong electron−phonon coupling. It is also observed that $\sigma'(\omega)$ becomes more complex in the polaronic regime. When

the electron−phonon coupling is weak, the picture of a nearly free electron slightly dressed by the phonon cloud is appropriate, and when the electron−phonon coupling is strong, the distortion of lattice acts as a trap of electron to form a quasi-particle called polaron.

The Holstein model is widely used to study the nonadiabatic quantum dynamics of π electron conjugated organic aggregates and polymers, where the excitation energy and charge transfer are usually accompanied by the nuclear motion and hence the interaction between electron and nuclear motion (electron−phonon coupling) has a crucial impact on the dynamical properties of the excited states. Considering the comparable magnitude of the intermolecular coupling and the electron−vibrational (electron−phonon) coupling, the perturbation treatment often fails and DMRG methods will be used to treat them on equal footing. Jiang et al. (2020a) presented the MPS/MPO formulation of the DDMRG algorithm at finite temperature (code can be found in Further reading). The absorption and emission spectra of one-dimensional molecular aggregates are studied by calculating the dipole−dipole correlation function. The Hamiltonian is

$$\hat{H} = \sum_i \varepsilon_i \hat{a}_i^\dagger \hat{a}_i + \sum_{ij} J_{ij}\hat{a}_i^\dagger \hat{a}_j + \sum_{in} \omega_{in}\hat{b}_{in}^\dagger \hat{b}_{in} + \sum_{in} \omega_{in}g_{in}\hat{a}_i^\dagger \hat{a}_i \left(\hat{b}_{in}^\dagger + \hat{b}_{in} \right) \quad (7.66)$$

where ε_i is the adiabatic transition energy of the ith molecular, J_{ij} is the intermolecular excitonic coupling between the ith and jth molecules, and ω_{in} and g_{in} is the vibrational frequency and the corresponding electron−phonon coupling constant belonging to the nth vibrational mode of the $i-$th molecule.

Fig. 7.11 compared DDMRG (Jiang et al., 2020a) with TD-DMRG (Ren et al., 2018) by calculating the absorption spectra. The dimer model contains
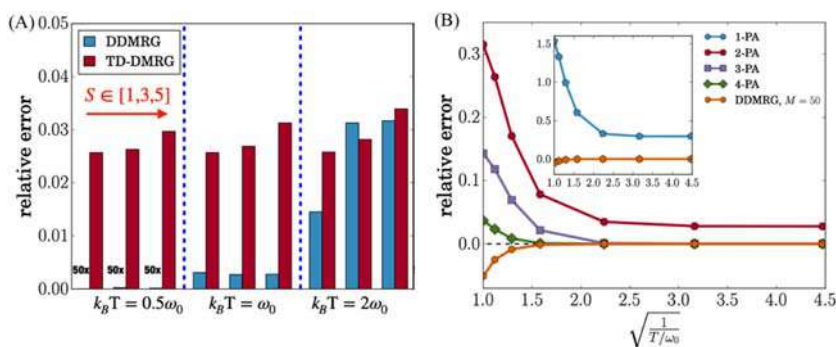
FIGURE 7.11 (A) Relative error for the absorption spectra of J-aggregated dimer with different Huang−Rhys factor S across different temperatures (Jiang, et al., 2020a). The error of DDMRG at $k_{\rm B}T = 0.5\omega_0$ is magnified by 50 times to make it clearly visible. (B) Relative error of $0-0$ emission strength of an open boundary 5-site system using n-particle approximation and DDMRG. *DDMRG,* Dynamical density matrix renormalization group. *Reproduced from Jiang, T., Li, W., Ren, J., Shuai, Z., 2020a. Finite temperature dynamical density matrix renormalization group for spectroscopy in frequency domain. J. Phys. Chem. Lett. 11, 3761−3768. https:// doi.org/10.1021/acs.jpclett.0c00905, with permission from American Chemical Society.*

one vibration mode with frequency of ω_0 for each molecule and covers the parameter space of different Huang−Rhys factor ($S = g^2$) and temperature $k_B T \in [\omega_0, 2\omega_0, 4\omega_0]$. Keeping the fixed $m = 120$, DDMRG is generally more accurate than TD-DMRG within the parameters space studied, and in particular accurate at low temperature regime with a nearly exact result, but it exhibits growing error with increased temperature, because more transition pairs exist at higher temperature, which requires a large bond dimension m to maintain the accuracy. Therefore DDMRG is more suitable to calculate the response properties at low temperature. In fact, large amounts of organic conjugated molecules have the vibronic progression of $\omega_0 = 1400\text{cm}^{-1}$, which lies at region of $k_B T \leq \omega_0$ for ambient temperature. Fig. 7.11b also compared DDMRG with the n-particle approximation, which is a truncated configuration interaction method that was popularly applied in studying the spectra of organic molecular aggregates. It turned out that DDMRG is able to achieve the precision of up to 4-PA with a relatively small bond dimension.

The coCheMPS method was applied to the emission spectrum of molecular aggregates with electron−phonon coupling at finite temperature. It was found that the canonical orthogonalization can greatly improve the accuracy; however, coCheMPS may not be very well suited to study the spectral function of complex electron−phonon systems, which requires more Chebyshev
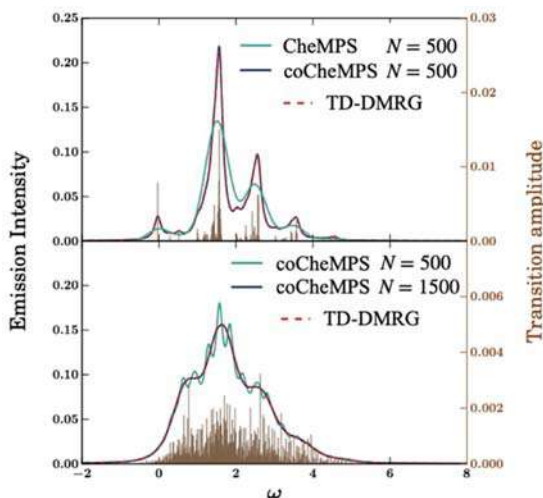
FIGURE 7.12 Emission spectra of 10-site molecular aggregates at 298K using $m = 32$. The upper panel belongs to a system with one fast mode for each molecule and the lower panel belongs to a system with one fast mode and one slow mode for each molecule. The frequency axis is in units of 1400cm^{-1}. The stemmed lines are discrete transition amplitudes calculated by coCheMPS ($N = 500$ for the upper panel and $N = 1500$ for the lower panel). *Reproduced from Jiang, T., Ren, J., Shuai, Z., 2021. Chebyshev matrix product states with canonical orthogonalization for spectral functions of many-body systems. J. Phys. Chem. Lett. 12, 9344−9352. https:// doi.org/10.1021/acs.jpclett.1c02688, with permission from American Chemical Society.*

vectors since the involvement of slow modes makes the density of states larger. Besides, the spectral window shown in Fig. 7.12 constitutes very little part of the full many-body frequency window ($\sim 8\%$). It was also suggested to rescale the effective energy window rather than the full window to $[-1, 1]$ (Holzner et al., 2011) since the rest frequencies have near zero response. However, the energy truncation leads to increased entanglement (Holzner et al., 2011) and the parameters for additional energy truncation is quite empirical (Jiang et al., 2020b). All in all, the application of CheMPS method to electron−phonon coupled systems deserves further investigations.

7.6 Summary and outlook

DMRG was initially proposed as a powerful technique to study the equilibrium properties of the strongly correlated system and has gradually been developed to accurately calculate the dynamical response properties of large systems. One can obtain the response properties by two schemes: one is directly solving the response function in frequency space and another is by performing the Fourier transform of the time correlation function computed in the time domain. This chapter elaborated the methods in frequency space and introduced some of their applications.

Although we focus on introducing the frequency domain methods, we find it necessary to leave some comments on the TD-DMRG (also serves as an introduction for Chapter 8), which helps for a more comprehensive understanding of the frequency domain method. TD-DMRG has been extensively applied to the simulation of the ultrafast dynamics, and compared with the frequency-domain algorithms, it gives the information of the real-time dynamics, as will be introduced. The weakness of TD-DMRG is that the accumulated error and the increased entanglement with the time evolution require the larger bond dimension and hence lead to great challenges to the long-time evolution (Barthel et al., 2009; Gobert et al., 2005; Kloss et al., 2018). The frequency-domain algorithm can avoid this issue and is promising to give more accurate results. As for the frequency-domain algorithms, both CV-DMRG and DDMRG need separate calculations for different frequencies and have high accuracy but low efficiency. They become the choice of methods when only the dynamical quantities of several important frequencies are needed. Technically speaking, the naturally paralleled character of them and the powerful GPU acceleration (Jiang et al., 2020a) can drastically reduce the computing time. CheMPS is a newly proposed method that is promising to have a balance between accuracy and numerical cost, the introduction of post-orthogonalization significantly increases both the accuracy and efficiency of traditional CheMPS method, especially for system with discrete states; however, its application in complex electron−phonon systems still waits for more comprehensive and systematic explorations.

Originated from the zero-temperature case, the ability of the frequency-domain DMRG methods are naturally extended to finite temperature after obtaining the thermal equilibrium density matrix with the help of techniques such as the thermal field dynamics (the purification method). The purification is conducted by evolving the maximally entangled state at infinite high temperature along the imaginary time axis. Hence, more evolution steps are needed to get access to the thermal density matrix at low temperature, and the minimally entangled typical thermal state (METTS) method (White, 2009) may be explored as a powerful complement at the low-temperature regime.

The frequency-domain DMRG methods and their MPS/MPO formulation have achieved excellent applications for the dynamical quantities and spectroscopy, and there are still lots of space to be explored considering more broad application cases, method development as well as assessment.

References

Barthel, T., Schollwöck, U., White, S.R., 2009. Spectral functions in one-dimensional quantum systems at finite temperature using the density matrix renormalization group. Phys. Rev. B. 79, 245101. Available from: https://doi.org/10.1103/PhysRevB.79.245101.

Dargel, P.E., Honecker, A., Peters, R., Noack, R.M., Pruschke, T., 2011. Adaptive lanczos-vector method for dynamic properties within the density matrix renormalization group. Phys. Rev. B 83, 161104. Available from: https://doi.org/10.1103/PhysRevB.83.161104.

Dargel, P.E., Wöllert, A., Honecker, A., McCulloch, I.P., Schollwöck, U., Pruschke, T., 2012. Lanczos algorithm with matrix product states for dynamical correlation functions. Phys. Rev. B 85, 205119. Available from: https://doi.org/10.1103/PhysRevB.85.205119.

Dorando, J.J., Hachmann, J., Chan, G.K.-L., 2009. Analytic response theory for the density matrix renormalization group. J. Chem. Phys. 130, 184111. Available from: https://doi.org/10.1063/1.3121422.

Gagliano, E.R., Balseiro, C.A., 1987. Dynamical properties of quantum many-body systems at zero temperature. Phys. Rev. letters 59, 2999. Available from: https://doi.org/10.1103/PhysRevLett.59.2999.

Ganahl, M., Thunström, P., Verstraete, F., Held, K., Evertz, H.G., 2014. Chebyshev expansion for impurity models using matrix product states. Phys. Rev. B 90, 045144. Available from: https://doi.org/10.1103/PhysRevB.90.045144.

Gobert, D., Kollath, C., Schollwöck, U., Schütz, G., 2005. Real-time dynamics in spin-1/2 chains with adaptive time-dependent density matrix renormalization group. Phys. Rev. E. 71, 036102. Available from: https://doi.org/10.1103/PhysRevE.71.036102.

Haegeman, J., Osborne, T.J., Verstraete, F., 2013. Post-matrix product state methods: to tangent space and beyond. Phys. Rev. B 88, 075133. Available from: https://doi.org/10.1103/PhysRevB.88.075133.

Hallberg, K.A., 1995. Density-matrix algorithm for the calculation of dynamical properties of low-dimensional systems. Phys. Rev. B 52, R9827. Available from: https://doi.org/10.1103/PhysRevB.52.R9827.

Holzner, A., Weichselbaum, A., McCulloch, I.P., Schollwöck, U., von Delft, J., 2011. Chebyshev matrix product state approach for spectral functions. Phys. Rev. B 83, 195115. Available from: https://doi.org/10.1103/PhysRevB.83.195115.

Jeckelmann, E., 2002. Dynamical density-matrix renormalization-group method. Phys. Rev. B 66, 045114. Available from: https://doi.org/10.1103/PhysRevB.66.045114.

Jiang, T., Li, W., Ren, J., Shuai, Z., 2020a. Finite temperature dynamical density matrix renormalization group for spectroscopy in frequency domain. J. Phys. Chem. Lett. 11, 3761−3768. Available from: https://doi.org/10.1021/acs.jpclett.0c00905.

Jiang, T., Ren, J., Shuai, Z., 2021. Chebyshev matrix product states with canonical orthogonalization for spectral functions of many-body systems. J. Phys. Chem. Lett. 12, 9344−9352. Available from: https://doi.org/10.1021/acs.jpclett.1c02688.

Jiang, T., Ren, J., Shuai, Z., 2020b. Frequency domain density matrix renormalization group. Chem. J. Chinese. U 41, 2610−2628.

Kloss, B., Lev, Y.B., Reichman, D., 2018. Time-dependent variational principle in matrix-product state manifolds: pitfalls and potential. Phys. Rev. B 97, 024307. Available from: https://doi.org/10.1103/PhysRevB.97.024307.

Kokalj, J., Prelovšek, P., 2009. Finite-temperature dynamics with the density-matrix renormalization group method. Phys. Rev. B 80, 205117. Available from: https://doi.org/10.1103/PhysRevB.80.205117.

Kubo, R., 1957. Statistical-mechanical theory of irreversible processes. I. General theory and simple applications to magnetic and conduction problems. J. Phys. Soc. Jpn. 12, 570−586. Available from: https://doi.org/10.1143/JPSJ.12.570.

Kühner, T.D., White, S.R., 1999. Dynamical correlation functions using the density matrix renormalization group. Phys. Rev. B 60, 335. Available from: https://doi.org/10.1103/PhysRevB.60.335.

Mahan, G.D., 2013. Many-Particle Physics. Springer Science & Business Media.

Nakatani, N., Wouters, S., Van Neck, D., Chan, G.K.-L., 2014. Linear response theory for the density matrix renormalization group: Efficient algorithms for strongly correlated excited states. J. Chem. Phys. 140, 024108. Available from: https://doi.org/10.1063/1.4860375.

Nocera, A., Alvarez, G., 2016. Spectral functions with the density matrix renormalization group: Krylov-space approach for correction vectors. Phys. Rev. E 94, 053308. Available from: https://doi.org/10.1103/PhysRevE.94.053308.

Pati, S.K., Ramasesha, S., Shuai, Z., Brédas, J.-L., 1999. Dynamical nonlinear optical coefficients from the symmetrized density-matrix renormalization-group method. Phys. Rev. B 59, 14827. Available from: https://doi.org/10.1103/PhysRevB.59.14827.

Ramasesha, S., Pati, S.K., Krishnamurthy, H.R., Shuai, Z., Brédas, J.L., 1997. Low-lying electronic excitations and nonlinear optic properties of polymers via symmetrized density matrix renormalization group method. Synthetic. Met 85, 1019−1022. Available from: https://doi.org/10.1016/S0379-6779(97)80136-1.

Ren, J., Shuai, Z., Kin-Lic Chan, G., 2018. Time-dependent density matrix renormalization group algorithms for nearly exact absorption and fluorescence spectra of molecular aggregates at both zero and finite temperature. J. Chem. Theory. Comput. 14, 5027−5039. Available from: https://doi.org/10.1021/acs.jctc.8b00628.

Ronca, E., Li, Z., Jimenez-Hoyos, C.A., Chan, G.K.-L., 2017. Time-step targeting time-dependent and dynamical density matrix renormalization group algorithms with ab initio Hamiltonians. J. Chem. Theory. Comput. 13, 5560−5571. Available from: https://doi.org/10.1021/acs.jctc.7b00682.

Schollwöck, U., 2011. The density-matrix renormalization group in the age of matrix product states. Ann. Phys. 326, 96−192. Available from: https://doi.org/10.1016/j.aop.2010.09.012.

Schollwöck, U., 2005. The density-matrix renormalization group. Rev. Mod. Phys. 77, 259. Available from: https://doi.org/10.1103/RevModPhys.77.259.

Silver, R.N., Röder, H., 1994. Densities of states of mega-dimensional Hamiltonian matrices. Int. J. Mod. Phys. C. 5, 735−753. Available from: https://doi.org/10.1142/S0129183194000842.

Soos, Z.G., Ramasesha, S., 1989. Valence bond approach to exact nonlinear optical properties of conjugated systems. J. Chem. Phys. 90, 1067−1076. Available from: https://doi.org/10.1063/1.456160.

Tiegel, A.C., Manmana, S.R., Pruschke, T., Honecker, A., 2014. Matrix product state formulation of frequency-space dynamics at finite temperatures. Phys. Rev. B 90, 060406. Available from: https://doi.org/10.1103/PhysRevB.90.060406.

Wang, L.-W., 1994. Calculating the density of states and optical-absorption spectra of large quantum systems by the plane-wave moments method. Phys. Rev. B. 49, 10154. Available from: https://doi.org/10.1103/PhysRevB.49.10154.

Weisse, A., 2004. Chebyshev expansion approach to the AC conductivity of the Anderson model. Eur. Phys. J. B 40, 125−128. Available from: https://doi.org/10.1140/epjb/e2004-00250-6.

Weiße, A., Wellein, G., Alvermann, A., Fehske, H., 2006. The kernel polynomial method. Reviews of modern physics 78, 275. Available from: https://doi.org/10.1103/RevModPhys.78.275.

White, S.R., 2009. Minimally entangled typical quantum states at finite temperature. Phys. Rev. letters 102, 190601. Available from: https://doi.org/10.1103/PhysRevLett.102.190601.

White, S.R., 1993. Density-matrix algorithms for quantum renormalization groups. Phys. Rev. b. 48, 10345. Available from: https://doi.org/10.1103/PhysRevB.48.10345.

White, S.R., 1992. Density matrix formulation for quantum renormalization groups. Phys. Rev. letters 69, 2863. Available from: https://doi.org/10.1103/PhysRevLett.69.2863.

Wouters, S., Nakatani, N., Van Neck, D., Chan, G.K.-L., 2013. Thouless theorem for matrix product states and subsequent post density matrix renormalization group methods. Phys. Rev. B 88, 075122. Available from: https://doi.org/10.1103/PhysRevB.88.075122.

Xie, H.D., Huang, R.Z., Han, X.J., Yan, X., Zhao, H.H., Xie, Z.Y., Liao, H.J., Xiang, T., 2018. Reorthonormalization of Chebyshev matrix product states for dynamical correlation functions. Phys. Rev. B 97, 075111. Available from: https://doi.org/10.1103/PhysRevB.97.075111.

Zhang, C., Jeckelmann, E., White, S.R., 1999. Dynamical properties of the one-dimensional Holstein model. Phys. Rev. B 60, 14092. Available from: https://doi.org/10.1103/PhysRevB.60.14092.

Further reading

Renormalizer. (n.d.). https://github.com/shuaigroup/Renormalizer.

Chapter 8

Time-dependent density matrix renormalization group

8.1 Overview

8.1.1 Time-dependent density matrix renormalization group and nonadiabatic dynamics

The time evolution algorithms for density matrix renormalization group (DMRG) are initially proposed around 2002 (Cazalilla and Marston, 2002; Daley et al., 2004; Luo et al., 2003; Vidal, 2004; White and Feiguin, 2004) and have developed rapidly ever since, enabled by the establishment of the relation between DMRG and the matrix product states ansatz. These algorithms offer a numerically exact solution to the time-dependent Schrödinger equation of complex many-body systems, provided that the bond dimension or the number of variational parameters is large enough. Although the time evolution algorithms have become an indispensable part of DMRG, there has not been a unified terminology or abbreviation for time-dependent DMRG in the literature, and in this chapter we choose to use TD-DMRG at our discretion.

Unlike in the realm of physics where most often DMRG as well as TD-DMRG are utilized to tackle spin problems, the application of TD-DMRG in chemistry is primarily focused on electron-vibration coupled models, also known as vibronic models. These models are fundamental for the study of chemical reactions, photochemical, or photophysical phenomena in (bio-) molecules and transport properties in solids. For example, TD-DMRG has been successfully used to study exciton dissociation in donor/acceptor heterojunction (Yao et al., 2018, 2016), absorption and fluorescence spectra of molecular aggregates (Baiardi and Reiher, 2019; Ren et al., 2018), and carrier mobility in organic semiconductors (Li et al., 2020b). More details on the applications will be elaborated in Section 8.4,

Actually, vibronic problems are so prevalent and important in chemistry that even before DMRG is invented theoretical chemists have already developed a full set of tools for them, named as nonadiabatic dynamics, whose purpose is to describe the simultaneous motion of electrons and nuclei (Crespo-Otero and Barbatti, 2018; Yarkony, 2012). The numerous nonadiabatic dynamics

methodologies can be roughly divided into two categories. The first category, usually termed quantum dynamics, includes the methodologies that treat the nuclear motion quantum mechanically and the advantage is that the zero-point energy and tunneling effect of the nuclei can be correctly accounted for. In the second category, usually termed mixed quantum-classical dynamics, the nuclear motion is approximated by classical or semi-classical mechanics, and the advantage is the possibility to study larger systems with more degrees of freedom over a longer timescale. For vibronic models TD-DMRG describes the state of the nuclei with wavefunctions, and thus it falls into the category of quantum dynamics, whose representative method is multiconfiguration time-dependent Hartree (MCTDH) (Beck et al., 2000; Meyer et al., 1990) and its multilayer extension (ML-MCTDH) (Wang, 2015; Wang and Thoss, 2003). (ML-) MCTDH has achieved great success in the past years and is implemented in the famous Heidelberg MCTDH package (Vendrell and Meyer, 2011). TD-DMRG and (ML-)MCTDH target similar problems in nonadiabatic dynamics and their formulations share a lot in common. We shall discuss the relation between TD-DMRG and ML-MCTDH in the next subsection.

The materials of the chapter are organized with a special focus on the applicability of TD-DMRG to vibronic problems. For example, in Section 8.3 we will introduce several algorithms that enable TD-DMRG to capture the finite temperature effect, significant for nuclear degrees of freedom but not much for electron motion in molecules. However, it is important to note that TD-DMRG cannot be simply understood as one of the emerging methodologies in nonadiabatic dynamics and serves as an alternative to (ML-)MCTDH, since DMRG and TD-DMRG are general methods that are not limited to specific models. Leaving the various models conquered with TD-DMRG in physics aside, several recent studies in chemistry have revealed the potential of using TD-DMRG to investigate the dynamics of electronic degrees of freedom based on ab initio Hamiltonian (Baiardi, 2021; Frahm and Pfannkuche, 2019; Ronca et al., 2017). Although these reports, for the time being, only make up a relatively small portion of all the literature regarding TD-DMRG in chemistry, we believe that the spectrum of its application will continue to expand.

8.1.2   Relation between time-dependent density matrix renormalization group and multilayer multiconfiguration time-dependent Hartree

MCTDH and ML-MCTDH are the de-facto reference method for nonadiabatic dynamics and have gained great popularity (Beck et al., 2000; Wang, 2015). The starting points of TD-DMRG and ML-MCTDH resemble each other, which are approximating system wavefunction with low-rank tensors. The ML-MCTDH ansatz is formally known as hierarchical Tucker tensor decomposition. A typical two-layer ML-MCTDH wavefunction can be

expressed using graphical notations similar to those used in MPS to describe the ML-MCTDH ansatz:

$$(8.1)$$

Adopting ML-MCTDH notation (Wang, 2015), the two-layer wavefunction for Eq. (8.1) reads:

$$|\Psi\rangle = \sum_{j_1} \cdots \sum_{j_p} A_{j_1 \cdots j_p} \prod_{\kappa}^{p} \left| \varphi_{j_\kappa}^{(\kappa)} \right\rangle$$

$$\left| \varphi_{j_\kappa}^{(\kappa)} \right\rangle = \sum_{i_1} \cdots \sum_{i_{Q(\kappa)}} B_{i_1 \cdots i_{Q(\kappa)}}^{\kappa, j_\kappa} \prod_{q}^{Q(\kappa)} \left| v_{i_q}^{(\kappa,q)} \right\rangle \qquad (8.2)$$

where A is the coefficient matrix at layer 0 with indices j_1 to j_p, p is the total number of nodes in layer 1 or the number of the children of the node at layer 0, B^{κ,j_κ} is the coefficient matrix of j_κth single-particle function of the κ node at layer 1 with indices i_1 to $i_{Q(\kappa)}$, $Q(\kappa)$ is the number of the children of the κth node at layer 1, and $|v_{i_q}^{(\kappa,q)}\rangle$ is a time-dependent linear combination of the corresponding time-independent primitive basis $|\sigma_i\rangle$. The ML-MCTDH wavefunction with arbitrary layers can be defined recursively in a similar way. The same as MPS, ML-MCTDH belongs to tensor networks. Their difference is that ML-MCTDH adopts a tree-like structure, while MPS is linear. At the first glance, ML-MCTDH seems to be identical to tree tensor networks (Orús, 2019). Nevertheless, for typical tree tensor networks, each node can have its physical bond, while in ML-MCTDH only nodes at the top layer have physical bond. Note that the top layer in Eq. (8.1) is actually the bottom layer by ML-MCTDH convention. Eq. (8.2) and its recursive extension indicate that the ML-MCTDH wavefunction is rather flexible. In fact, MPS can be viewed as a very special case of ML-MCTDH, in which the tree is extremely unbalanced and reduces to a linear chain (Grasedyck, 2010):

$$(8.3)$$

In this case, the number of layers in ML-MCTDH is identical to the number of sites in MPS. It can be shown that, both derived from time-dependent variational principle (TDVP), the equations of motion (EOM) for MPS is identical to the EOM of ML-MCTDH with this extremely imbalanced architecture. However, to the best of our knowledge, in practical ML-MCTDH computations, the number of layers never exceeds 10, so the "unification" here is purely conceptual.

Although ML-MCTDH is a more general and flexible ansatz, the specific structure restriction on MPS actually gives it an advantage over ML-MCTDH, which is the possibility of flexible quantum state manipulation with the help of MPOs. If a quantum state $|\Psi\rangle$ represented by an MPS is applied by an operator $\hat{O}$ represented by an MPO, the resulting state $\hat{O}|\Psi\rangle$ trivially retains the MPS structure, with an enlarged bond dimension. On the contrary, after being applied by an MPO, the tree structure of the ML-MCTDH ansatz with an enlarged bond dimension cannot be easily restored:

$$\hat{O}\,|\Psi\rangle = \qquad\qquad\qquad\qquad\overset{?}{=} \qquad\qquad\qquad\qquad\qquad (8.4)$$

To design an operator which is able to retain the ML-MCTDH tree structure, the operator should also adopt the tree topology. Such design is more complicated than MPO and has not been reported yet. Thus, in the MCTDH community, the idea of MPO is never used and quantum state manipulation is limited to relatively simple cases. The fact that universal operator application can be straightforwardly implemented for MPS lays the foundation of a whole class of time evolution algorithms and enables the calculation of general correlation functions such as current-current correlation function.

Interestingly, the similarities between TD-DMRG and (ML-)MCTDH have boosted the development of the two methodologies with ideas originating from each other. For instance, in Section 8.2, we shall discuss MPS time evolution algorithms that are inspired by (ML-)MCTDH, and the projector splitting algorithm originally designed for MPS has also been successfully migrated to (ML-)MCTDH (Bonfanti and Burghardt, 2018; Kloss et al., 2017; Lubich, 2015). Besides, the idea of MPS has enabled a variant of the MCTDH ansatz (Kurashige, 2018), and the resulting methodology is very similar to the optimized boson basis technique for MPS (Guo et al., 2012). Also, both MPS and (ML-)MCTDH can be integrated with hierarchical equations of motion (HEOM) for efficient propagation of the reduced density operators (Shi et al., 2018; Yan et al., 2021).

8.1.3 Reviews, software, and other resources

In this chapter, we aim to provide a pedagogical view of TD-DMRG with a flavor of our understanding and due to length limitation several topics are not discussed in detail. These topics include but are not limited to the historical development of TD-DMRG, rigorous derivations of several conclusions and formulas, scaling analysis of the algorithms, and numerical evidence for the performance of the algorithms over a variety of computational examples. Readers are referred to several excellent reviews on TD-DMRG for more information (Ma et al., 2018; Paeckel et al., 2019; Ren et al., 2022).

There also exist a number of packages that implements the algorithms introduced in the chapter. Some of the packages are well-documented with high-level interfaces that can be put into production out of the box. In Table 8.1, we provide a non-exhaustive list of the packages. To focus on the topic of the chapter, general tensor network packages or DMRG packages focused on ground state properties that do not process full-fledged time-evolution algorithm are not listed. Apart from kln-X, SymMPS, and SyTen, all packages in Table 8.1 are open source software with source code hosted on public websites such as GitHub, where readers can easily find runnable code for most of the formulas and algorithms introduced in the chapter.

TABLE 8.1 An incomplete list of available TD-DMRG packages in alphabetical order.

Name	Feature
evoMPS (Milsted et al., 2013)	Nonuniform dynamics in the thermodynamic limit
Itensor/TDVP (Yang and White, 2020)	Global subspace expansion algorithm for TDVP
kln-X (Xu et al., 2021)	Stochastically adaptive single-site TDVP
OSMPS (Jaschke et al., 2018)	Excited state search and parallelization over MPI
pytenet (Mendl, 2018)	Light weight and compact implementation
Renormalizer (Ren et al., 2021)	Optimal MPO construction and GPU acceleration
SymMPS (Paeckel and Köhler, 2021)	Projected purification for large local Hilbert space
SyTen (Hubig, 2017; Hubig et al., 2021)	Local basis optimization and exploitation of symmetry
TeNPy (Hauschild and Pollmann, 2018)	Disentanglers for purification and active community

The packages listed are quite unique and it's almost impossible to give a proper summary of their features in just a few words. Detailed descriptions on these packages can be found at their respective websites. Most of the package websites also contain an abundant amount of introductory information on (TD-)DMRG, which may serve as complementary resources to the reviews mentioned above and the contents of the chapter.

8.2   Time evolution algorithms

The available time evolution algorithms for TD-DMRG could be roughly classified into three groups. The first group is based on globally approximating the formal time evolution operator $e^{-i\hat{H}t}$ or $e^{-i\hat{H}t}|\Psi\rangle$, including Runge-Kutta (García-Ripoll, 2006; Ren et al., 2018), time-evolving block decimation (TEBD) (Daley et al., 2004; Vidal, 2004; White and Feiguin, 2004), $W^{I, II}$ (Zaletel et al., 2015), Krylov subspace (García-Ripoll, 2006; Wall and Carr, 2012) methods, Chebyshev expansion (Halimeh et al., 2015), and split operator method on the grid basis (Greene and Batista, 2017). The same feature shared in these schemes is that in each time step the wavefunction is firstly propagated as a whole globally, usually through MPO/MPS multiplication, resulting in an MPS with increased bond dimension, and then compressed to the original bond dimension or according to truncation threshold. The second group is based on the TDVP (Dirac, 1930). Depending on the different ways to derive the EOMs, this group includes the original method with fixed gauge freedom (Haegeman et al., 2011) and the more recent projector splitting (PS) method (Haegeman et al., 2016). The third group is more inspired by the original DMRG, which is formulated in the local renormalized space and the basis is adapted by the averaged reduced density matrix. The representatives are the time step targeting method (TST) (Feiguin and White, 2005b) and some related variants (Dutta and Ramasesha, 2010; Ronca et al., 2017). Among the above evolution schemes, all schemes can be directly applied to models with long-range interactions except TEBD, which requires modifications such as unitary transformation of the Hamiltonian in the system-reservoir quantum models (Prior et al., 2010) and the introduction of swap gates (Stoudenmire and White, 2010). In addition, the global evolution scheme is the most straightforward one when the modern framework of matrix product state / matrix product operator (MPS/MPO) is investigated, while the PS scheme seems to have become the most popular choice as it has been widely employed in the recent articles (Baiardi and Reiher, 2019; Borrelli and Gelin, 2017; Kloss et al., 2019; Li et al., 2020b, 2021; Xie et al., 2019).

Computationally, all of the time evolution algorithms involve intensive tensor multiplications, which can be effectively accelerated by GPUs (Li et al., 2020a). Particularly high acceleration ratio is achieved for algorithms that do not require the compression of the MPS (which are primarily

TDVP based algorithms) because matrix decompositions are not the strong point of GPUs.

8.2.1 Propagation and compression

One of the most intuitive way to study the dynamics of an initial state $|\Psi\rangle(t = 0)$ under Hamiltonian $\hat{H}$ is to numerically integrate the time-dependent Schrödinger equation:

$$\frac{\partial|\Psi(t)\rangle}{\partial t} = -i\hat{H}|\Psi(t)\rangle \tag{8.5}$$

$\hbar$ is set to 1 hereinafter. Based on the simplest forward-Euler scheme, for each integration step τ the $|\Psi\rangle$ should be propagated as:

$$|\Psi(t+\tau)\rangle = |\Psi(t)\rangle - i\hat{H}\tau|\Psi(t)\rangle + \mathcal{O}(\tau^2) \tag{8.6}$$

Since MPO/MPS multiplication and MPS/MPS addition are routine operations, the equation can be translated into TD-DMRG algorithm with ease (Algorithm 1). The resulting state $|\Psi(t+\tau)\rangle$ typically has a much larger bond dimension than $|\Psi(t)\rangle$, and thus it is usually compressed before the next iteration. This two-step scheme is therefore summarized as propagation and compression (P&C).

Algorithm 1: Forward-Euler P&C time evolution

    input : System wavefunction at time t in MPS representation $|\Psi(t)\rangle$, system Hamiltonian
           in MPO representation $\hat{H}$

    output: System wavefunction at time $t + \tau$ in MPS representation $|\Psi(t+\tau)\rangle$

1 $\hat{H}|\Psi(t)\rangle$ = ApplyMPOtoMPS $(\hat{H}, |\Psi(t)\rangle)$

2 $-i\hat{H}\tau|\Psi(t)\rangle$ = ScaleMPS $(\hat{H}|\Psi(t)\rangle, -i\tau)$

3 $|\Phi\rangle$ = CompressMPS$(-i\hat{H}\tau|\Psi\rangle)$

4 $|\Psi(t)\rangle - i\hat{H}\tau|\Psi(t)\rangle$ = AddMPS$(|\Psi(t)\rangle, |\Phi\rangle)$

5 $|\Psi(t+\tau)\rangle$ = CompressMPS$(|\Psi(t)\rangle - i\hat{H}\tau|\Psi(t)\rangle)$

A straightforward improvement for the simple scheme is to replace the first-order forward-Euler integration scheme with the classical 4th-order Runge-Kutta (RK4) integration scheme (García-Ripoll, 2006; Ren et al., 2018):

$$
\begin{aligned}
|k_1\rangle &= -i\hat{H}(t)|\Psi(t)\rangle \\[2pt]
|k_2\rangle &= -i\hat{H}\left(t+\tau/2\right)\left(|\Psi(t)\rangle + \frac{1}{2}\tau|k_1\rangle\right) \\[2pt]
|k_3\rangle &= -i\hat{H}\left(t+\tau/2\right)\left(|\Psi(t)\rangle + \frac{1}{2}\tau|k_2\rangle\right) \\[2pt]
|k_4\rangle &= -i\hat{H}(t+\tau)(|\Psi(t)\rangle + \tau|k_3\rangle) \\[2pt]
|\Psi(t+\tau)\rangle &= |\Psi(t)\rangle + \frac{1}{6}\tau(|k_1\rangle + 2|k_2\rangle + 2|k_3\rangle + |k_4\rangle) + \mathcal{O}(\tau^5)
\end{aligned}
\tag{8.7}
$$

For time-independent Hamiltonian, the RK4 algorithm is nothing more than a fourth-order Taylor expansion of the formal time evolution operator $e^{-i\hat{H}\tau}$:

$$|\Psi(t + \tau)\rangle = \sum_{n=0}^{4} \frac{1}{n!}(-i\hat{H}\tau)^n |\Psi(t)\rangle + O(\tau^5) \qquad (8.8)$$

Thus, the n-th order term $(-i\hat{H}\tau)^n |\Psi(t)\rangle$ could be calculated based on the $(n-1)$-th order term one by one from $|\Psi(t)\rangle$.

The mathematical foundation of the P&C schemes is quite different, but they can be translated to similar TD-DMRG algorithms. The most well-known P&C time evolution scheme in physics is probably TEBD (Daley et al., 2004; Vidal, 2004; White and Feiguin, 2004) which is efficient and easy to implement. However, the algorithm cannot be directly applied to models with long-range interactions, thus it is rarely used in chemistry problems. For any nearest-neighbor Hamiltonian with $2N$ DoFs:

$$\hat{H} = \sum_{j==1}^{2N-1} \hat{h}_{j,j+1} \qquad (8.9)$$

where $\hat{h}_{j,j+1}$ acts on the jth DoF and the $(j+1)$th DoF, it is observed that the Hamiltonian can be decomposed into two parts $\hat{H} = \hat{H}_1 + \hat{H}_2$:

$$\begin{aligned}
\hat{H}_1 &= \sum_{j=1}^{N} \hat{h}_{2j-1,2j} \\
\hat{H}_2 &= \sum_{j=1}^{N-1} \hat{h}_{2j,2j+1}
\end{aligned} \qquad (8.10)$$

$e^{-i\hat{H}\tau}$ can be decomposed into two parts by first-order Trotter decomposition:

$$\begin{aligned}
e^{-i\hat{H}\tau} &= e^{-i\hat{H}_1\tau} e^{-i\hat{H}_2\tau} e^{-i\tau^2[\hat{H}_1,\hat{H}_2]} \\
&= e^{-i\hat{H}_1\tau} e^{-i\hat{H}_2\tau} + \mathcal{O}(\tau^2)
\end{aligned} \qquad (8.11)$$

Although $\hat{H}_1$ and $\hat{H}_2$ do not commute with each other, all terms within $\hat{H}_1$ and $\hat{H}_2$ commute. In other words:

$$\begin{aligned}
e^{-i\hat{H}_1\tau} &= \prod_{j=1}^{N} e^{-i\hat{h}_{2j-1,2j}\tau} \\
e^{-i\hat{H}_2\tau} &= \prod_{j=1}^{N-1} e^{-i\hat{h}_{2j,2j+1}\tau}
\end{aligned} \qquad (8.12)$$

Both $e^{-i\hat{H}_1\tau}$ and $e^{-i\hat{H}_2\tau}$ can be efficiently expressed as MPO with two sites. Applying the operators onto $|\Psi\rangle$ and then compressing it constitute one

step of time evolution. A second-order decomposition can be constructed by symmetrizing the decomposition:

$$e^{-i\hat{H}\tau} = e^{-i\hat{H}_1\tau/2}e^{-i\hat{H}_2\tau}e^{-i\hat{H}_1\tau/2} + \mathcal{O}(\tau^3) \tag{8.13}$$

For models with long-range interactions, TEBD must be combined with additional techniques such as unitary transformation of the Hamiltonian in the system-reservoir quantum models (Prior et al., 2010) and the introduction of swap gates (Stoudenmire and White, 2010).

Interestingly, it's possible to combine the Trotter decomposition with the Taylor expansion of time evolution operator scheme described above (Greene and Batista, 2017). The idea is to split the kinetic part out of the Hamiltonian so that the MPO in the time evolution operator has a smaller bond dimension.

The $W^{I, II}$ method (Zaletel et al., 2015) aims to explicitly approximate the time evolution operator $e^{-i\hat{H}\tau}$ as an MPO to the first order, based on the form of the Hamiltonian $\hat{H}$. The advantage of the method against RK integrator is that integration error per site is constant.

The Krylov subspace method (also known as the Lanczos method) instead is an efficient algorithm for approximating $e^{-i\hat{H}\tau}|\Psi\rangle$ (García-Ripoll, 2006; Wall and Carr, 2012). The Krylov subspace is defined as the space spanned by $\{|\Psi\rangle, \hat{H}|\Psi\rangle, \cdots, \hat{H}^{N-1}|\Psi\rangle\}$ with dimension N. For numerical convenience the vectors are orthonormalized to give Krylov vectors $\{k_0, k_1, \cdots, k_{N-1}\}$. The overall goal of the method is to find the best approximate for $e^{-i\hat{H}\tau}|\Psi\rangle$ in the Krylov subspace. Although the exact limit is achieved when N is equal to the dimension of the original Hilbert space for $|\Psi\rangle$, in practice usually a few Krylov vectors are sufficient for decent accuracy. Define the projector to the Krylov subspace:

$$\hat{P} = \sum_{i=0}^{N-1} |k_i\rangle\langle k_i| \tag{8.14}$$

The approximate solution for $|\Psi(t+\tau)\rangle$ is given by:

$$|\Psi(t+\tau)\rangle = e^{-i\hat{H}\tau}|\Psi(t)\rangle \approx \hat{P}^\dagger e^{-i\hat{H}\tau}\hat{P}|\Psi(t)\rangle \tag{8.15}$$

Note that the dimension for $\langle k_i|\hat{H}|k_j\rangle$ is N and the matrix can be diagonalized with negligible computational effort. The Krylov subspace method is typically a much more efficient way to approximate $e^{-i\hat{H}\tau}|\Psi\rangle$ than simple Tayler expansion such as Eq. (8.8); however, due to truncation error caused by MPS compression, it is difficult to fulfill the orthonormal condition of the Krylov vectors, which can severely deteriorate the quality of the outcome (Frahm and Pfannkuche, 2019).

The Chebyshev expansion method expands $e^{-i\hat{H}t}$ with Chebyshev polynomials and calculates Chebyshev vectors according to the recursive relation (Halimeh et al., 2015):

$$
\begin{aligned}
|t_0\rangle &= \Psi(t = 0) \\
|t_1\rangle &= \hat{H}'|t_0\rangle \\
|t_n\rangle &= 2\hat{H}'|t_{n-1}\rangle - |t_{n-2}\rangle
\end{aligned}
\tag{8.16}
$$

here $\hat{H}' = \frac{\hat{H} - b}{a}$ is the rescaled Hamiltonian so that the eigenspectrum falls within $(-1, 1)$. For a Hamiltonian with ground state energy E_g and highest excited state energy E_s, $a = E_s - E_g$ and $b = \frac{E_g + E_s}{2}$ can be adopted. In practical computation, allowing a few eigenvalues of the rescaled Hamiltonian to exceed $(-1, 1)$ may improve computational efficiency. After the Chebyshev vectors are obtained, propagated wavefunction is given by:

$$
\left|\Psi(t)\right\rangle = e^{-ibt} \sum_{n=0}^{N-1} \phi_n(t)|t_n\rangle
\tag{8.17}
$$

where $\phi_0(t) = c_0(t)$ and $\phi_{n>0} = 2c_n(t)$ with $c_n(t)$ defined as

$$
c_n(t) = (-i)^n J_n(at)
\tag{8.18}
$$

where J_n is the Bessel function of the first kind.

Of all the P&C time evolution methods, Taylor expansion of $e^{-i\hat{H}\tau}$, TEBD, and Krylov subspace method is the most popular. For Hamiltonian which processes only nearest-neighbor interaction or can be transformed to a form with only nearest-neighbor interaction, TEBD strikes a balance between easy to implement and high accuracy (Chin et al., 2013; Ma and Schollwöck, 2008; Mannouch et al., 2018; Xie et al., 2019).

8.2.2 Time-dependent variational principle

The Rayleigh-Ritz variational principle is widely used in finding an approximate ground state in time-independent Schrödinger equation. Similarly, TDVP also provides a strong tool to find an optimal time-dependent wavefunction if the wavefunction ansatz and the initial state are known. The Dirac-Frenkel TDVP is (Dirac, 1930; Gatti et al., 2017)

$$
\langle \delta\Psi| i\frac{\partial}{\partial t} - \hat{H}|\Psi\rangle = 0
\tag{8.19}
$$

It has been proved that TDVP could strictly conserve the norm of the wavefunction and the total energy in the real-time propagation (Gatti et al., 2017), which is essential for long-time dynamics. In a geometric fashion, TDVP could be understood as an orthogonal projection of $-i\hat{H}|\Psi\rangle$ onto the tangent space of $|\Psi(t)\rangle$ at the current time:

$$\frac{\partial|\Psi\rangle}{\partial t} = -i\hat{P}\hat{H}|\Psi\rangle \tag{8.20}$$

where $\hat{P}$ is the projector constructed by the orthonormal vectors in the tangent space. For a general MPS:

$$|\Psi\rangle = \sum_{\{a\},\{\sigma\}} A_{a_1}^{\sigma_1} A_{a_1 a_2}^{\sigma_2} \cdots A_{a_{N-1}}^{\sigma_N} |\sigma_1 \sigma_2 \cdots \sigma_N\rangle \tag{8.21}$$

the tangent space projector is defined as:

$$\hat{P} = \sum_{i=1}^{N} \hat{P}[1:i-1] \otimes \hat{I}_i \otimes \hat{P}[i+1:N] - \sum_{i=1}^{N-1} \hat{P}[1:i] \otimes \hat{P}[i+1:N] \tag{8.22}$$

where

$$\hat{P}[1:i] = \sum_{a_i,a_{i'}} |a_i'[1:i]\rangle S[1:i]_{a_i' a_i}^{-1} \langle a_i[1:i]| \tag{8.23}$$

$$\hat{P}[i+1:N] = \sum_{a_i,a_{i'}} |a_i'[i+1:N]\rangle S[i+1:N]_{a_i' a_i}^{-1} \langle a_i[i+1:N]| \tag{8.24}$$

$$|a_i[1:i]\rangle = \sum_{\{a\},\{\sigma\}} A_{a_1}^{\sigma_1} A_{a_1 a_2}^{\sigma_2} \cdots A_{a_{i-1} a_i}^{\sigma_i} |\sigma_1 \cdots \sigma_i\rangle \tag{8.25}$$

$$|a_j[j+1:N]\rangle = \sum_{\{a\},\{\sigma\}} A_{a_j a_{j+1}}^{\sigma_{j+1}} \cdots A_{a_{N-1}}^{\sigma_N} |\sigma_{j+1} \cdots \sigma_N\rangle \tag{8.26}$$

$$S[1:i]_{a_i a_i'} = \langle a_i[1:i]|a_i'[1:i]\rangle \tag{8.27}$$

$$S[j+1:N]_{a_j a_j'} = \langle a_j[j+1:N]|a_j'[j+1:N]\rangle \tag{8.28}$$

$$\hat{I}_i = \sum_{\sigma_i'} |\sigma_i\rangle\langle\sigma_i| \tag{8.29}$$

$$\hat{P}[1:0] = \hat{P}[N+1:N] = 1 \tag{8.30}$$

or graphically:

$$(8.31)$$

The inversion of the overlap matrix S^{-1} accounts for the non-orthogonality of the renormalized basis and the "-" terms are to eliminate the parameterization redundancy (Haegeman et al., 2011; Wouters et al., 2013). In the literature, there are two different time evolution schemes based on TDVP. They differ in choosing the specific gauge condition of the MPS and in solving Eq. (8.20), which will be discussed in detail in the following.

In the first TDVP evolution scheme, the gauge freedom of MPS is fixed. For convenience, the projector in Eq. (8.22) could be transformed to Eq. (8.32) by combining the neighboring "+" term and "-" term together except one "+" term with $i = n$:

$$
\begin{aligned}
\hat{P} = {} & \hat{P}[1{:}n-1] \otimes \hat{I}_n \otimes \hat{P}[n+1{:}N] \\
& + \sum_{i=1}^{n-1} \hat{Q}[1{:}i] \otimes \hat{P}[i+1{:}N] + \sum_{i=n+1}^{N} \hat{P}[1{:}i-1] \otimes \hat{Q}[i{:}N]
\end{aligned}
\tag{8.32}
$$

where

$$
\hat{Q}[1{:}i] = \sum_{a_{i-1},a_{i-1}',\sigma_i,\sigma_i'} |a_{i-1}'[1{:}i-1]\sigma_i'\rangle \langle a_{i-1}[1{:}i-1]\sigma_i|
$$

$$
\cdot \left(S[1{:}i-1]^{-1}_{a_{i-1}'a_{i-1}} \delta_{\sigma_i'\sigma_i} - \sum_{a_i',a_i} A^{\sigma_i'}_{a_{i-1}'a_i'} S[1{:}i]^{-1}_{a_i'a_i} A^{\sigma_i *}_{a_{i-1}a_i} \right)
\tag{8.33}
$$

$$
\hat{Q}[i{:}N] = \sum_{a_i,a_i',\sigma_i,\sigma_i'} |a_i'[i+1{:}N]\sigma_i'\rangle \langle a_i[i+1{:}N]\sigma_i|
$$

$$
\cdot \left(S[i+1{:}N]^{-1}_{a_i'a_i} \delta_{\sigma_i'\sigma_i} - \sum_{a_{i-1}',a_{i-1}} A^{\sigma_i'}_{a_{i-1}'a_i'} S[i{:}N]^{-1}_{a_{i-1}'a_{i-1}} A^{\sigma_i *}_{a_{i-1}a_i} \right)
\tag{8.34}
$$

This type of projector or the corresponding tangent space vectors was firstly proposed by Haegeman et al. (2011) for uniform MPS and restated by Wouters et al. (2013) to derive several post-DMRG methods for the ground state and excited states.

Eqs. (8.33) and (8.34) could be further simplified by adopting a specific gauge condition, and then some overlap matrices turn to identity. Assuming that the MPS is left-canonical with gauge center at site N, $S[1:i]$ is reduced to I and it is most convenient to set $n = N$ in Eq. (8.32). Inserting the simplified projector into Eq. (8.20) yields:

$$i \frac{\partial C_{l'_{N-1}}^{\sigma'_N}}{\partial t} = \sum_{\sigma''_N, l''_{N-1}} H[N]_{l'_{N-1}\sigma'_N, l''_{N-1}\sigma''_N} C_{l''_{N-1}}^{\sigma''_N} \tag{8.35}$$

$$i \frac{\partial L_{l'_{i-1}l'_i}^{\sigma'_i}}{\partial t} = \sum_{l_{i-1},\sigma_i} (\delta_{l'_{i-1}l_{i-1}} \delta_{\sigma'_i\sigma_i} - p[i]_{l'_{i-1}\sigma'_i,l_{i-1}\sigma_i}) \sum_{l_i} S[i+1:N]_{l'_i l_i}^{-1}$$

$$\sum_{l''_{i-1},\sigma''_i,l''_i} H[i]_{l_{i-1}\sigma_i l_i, l''_{i-1}\sigma''_i l''_i} L_{l''_{i-1}l''_i}^{\sigma''_i} \tag{8.36}$$

where

$$H[i]_{l'_{i-1}\sigma'_i l'_i, l_{i-1}\sigma_i l_i} = \sum_{\{w\}} h[1:i-1]_{\{l',w,l\}_{i-1}} W_{w_{i-1}w_i}^{\sigma'_i,\sigma_i} h[i+1:N]_{\{l',w,l\}_i} \tag{8.37}$$

$$h[1:i-1]_{\{l',w,l\}_{i-1}} = \sum_{\{l'\},\{w\},\{l\}} h[1]_{\{l',w,l\}_1} \cdots h[i-1]_{\{l',w,l\}_{i-2},\{l',w,l\}_{i-1}} \tag{8.38}$$

$$h[i+1:N]_{\{l',w,l\}_i} = \sum_{\{l'\},\{w\},\{l\}} h[i+1]_{\{l',w,l\}_i,\{l',w,l\}_{i+1}} \cdots h[N]_{\{l',w,l\}_{N-1}} \tag{8.39}$$

$$h[i]_{\{l',w,l\}_{i-1},\{l',w,l\}_i} = \sum_{\sigma_i,\sigma'_i} A_{l'_{i-1}l'_i}^{\sigma'^*_i} W_{w_{i-1}w_i}^{\sigma'_i,\sigma_i} A_{l_{i-1}l_i}^{\sigma_i} \quad (A = L \text{ or } C) \tag{8.40}$$

$$p[i]_{l'_{i-1}\sigma'_i,l_{i-1}\sigma_i} = \sum_{l_i} L_{l'_{i-1}l_i}^{\sigma'_i} L_{l_{i-1}l_i}^{\sigma_i *} \tag{8.41}$$

Eqs. (8.35) and (8.36) together form a set of coupled nonlinear equations that are very similar to the standard EOMs of (ML-)MCTDH (Beck et al., 2000; Meyer et al., 1990; Wang and Thoss, 2003), and ideas from the MCTDH community called variable mean field (VMF) and constant mean field (CMF) can be borrowed to integrate these equations (Li et al., 2020a). VMF regards the time evolution as an initial value problem for all individual MPS parameters and employs an all-purpose solver such as forward-Euler to directly solve the coupled equations, as demonstrated when TDVP is firstly

proposed for MPS (Haegeman et al., 2011). In CMF, it is assumed that $H[i]$ and $S[i + 1:N]$ generally change much slower in time than the local matrices C^{σ_N} and L^{σ_i}. As a result, during the integration of Eqs. (8.35) and (8.36) one may hold the so-called mean field $H[i]$ and $S[i + 1:N]$ constant for τ and evolve only the local matrix with time step smaller than τ. Hence, CMF can be regarded as an approximation of VMF. We outline the TDVP-VMF procedure for left-canonical MPS in Algorithm 2.2.

Algorithm 2: TDVP-VMF time evolution for left-canonical MPS

input : System wavefunction $|\Psi(t)\rangle$ in left-canonical MPS representation $\{L[i]\}$ and C, system Hamiltonian $\hat{H}$ in MPO representation $\{W[i]\}$

output: Time evolved system wavefunction $|\Psi(t + \tau)\rangle$ in left-canonical MPS representation $\{L'[i]\}$ and C'

1 **procedure** CalculateDerivative($\{L[i]\}$, C, $\{W[i]\}$)

    /* Setting up intermediate variables with dynamic programming   */

2     $h[1:0] = 1$

3   **for** $i = 1$ **to** $i = N - 1$ **do**

4         $h[1:i] \leftarrow h[1:i-1], A[i], W[i]$ /* Eq. 38 */

5   **end**

6     $h[N+1:N] = 1$

7     $S[N+1:N] = 1$

8   **for** $i = N$ **to** $i = 2$ **do**

9         $h[i:N] \leftarrow h[i+1:N], A[i], W[i]$ /* Eq. 39 */

10         $S[i:N] \leftarrow S[i+1:N], A[i]$ /* Eq. 28 */

11   **end**

    /* Calculate time derivatives based on Eq. 35 and Eq. 36   */

12     $\frac{\partial C}{\partial t} \leftarrow h[1:N-1], C, W[N]$ /* Eq. 35 */

13   **for** $i = 1$ **to** $i = N - 1$ **do**

14         $p[i] \leftarrow L[i]$ /* Eq. 41 */

15         $\frac{\partial L[i]}{\partial t} \leftarrow h[1:i-1], h[i+1:N], S[i+1:N], L[i], W[i], p[i]$ /* Eq. 36 */

16   **end**

17   **return** $\frac{\partial C}{\partial t}, \{\frac{\partial L[i]}{\partial t}\}$

18 **end procedure**

19 $\{L'[i]\}, C' = $ SolveIVP(CalculateDerivative, $[\{L[i]\}, C, \{W[i]\}], \tau$)

Another aspect should be concerned is that the inversion of S would be unstable numerically if some eigenvalues of S are very small. This problem will be severe when the state is weakly correlated (such as a Hartree product state which is usually an initial state) and the bond dimension is much larger than what is required. To some extent, this instability problem makes this evolution scheme paradoxical in that a large bond dimension should in principle push the result to a numerically exact limit but in fact deteriorates it if the time step is hold as constant. The same problem also arises in (ML)-MCTDH, where in order to make the EOMs more well-behaved, S is usually replaced with a regularized overlap matrix $\tilde{S}$ (Beck et al., 2000):

$$\tilde{S} = S + \varepsilon e^{-S/\varepsilon} \tag{8.42}$$

Here ε is a small scalar commonly from 10^{-8} to 10^{-14}. More recently, an improved regularization scheme based on the matrix unfolding (MU) of the coefficient matrix by SVD in (ML-)MCTDH is proposed by Meyer and

Wang, which has been proved to make the time integration more accurate and robust (Meyer and Wang, 2018; Wang and Meyer, 2018). The same idea can be adopted to integrate Eq. (8.36), giving the name of the scheme "TDVP-MU." When calculating the overlap matrix $S[i+1:N]_{a'_i a_i}^{-1}$, a copy of the current MPS is made and the gauge center of the copy is moved to the $(i+1)$ th site and the matrix at this site is further decomposed by SVD:

$$\left|l_i[i+1:N]\right\rangle = \sum_{\{l\},\{\sigma\}} L_{l_i l_{i+1}}^{\sigma_{i+1}} \cdots L_{l_{N-2} l_{N-1}}^{\sigma_{N-1}} C_{l_{N-1}}^{\sigma_N} \left|\sigma_{i+1}\cdots\sigma_N\right\rangle$$

$$= \sum_{\{r\},\{\sigma\}} U_{l_i r_i} \Lambda_{r_i r_i} R_{r_i r_{i+1}}^{\sigma_{i+1}} \cdots R_{r_{N-2} r_{N-1}}^{\sigma_{N-1}} R_{r_{N-1}}^{\sigma_N} \left|\sigma_{i+1}\cdots\sigma_N\right\rangle \quad (8.43)$$

where $|r_i|$ equals $|l_i|$ (the symbol $|\cdot|$ denotes the size of the given index). Thus, the overlap matrix $S[i+1:N]$ and its inversion could be expressed as $U^*\Lambda^2 U^T$ and $U^*\Lambda^{-2}U^T$, respectively. The Hamiltonian matrix in Eq. (8.37) is also reconstructed. For site from $i+1$ to N the matrix A^{σ_i} in Eq. (8.40) is replaced with matrix R^{σ_i} in Eq. (8.43) and then Eq. (8.36) with MU algorithm becomes:

$$i\frac{\partial L_{l'_{i-1} l'_i}^{\sigma'_i}}{\partial t} = \sum_{l_{i-1},\sigma_i} (\delta_{l'_{i-1} l_{i-1}} \delta_{\sigma'_i \sigma_i} - p[i]_{l'_{i-1}\sigma'_i, l_{i-1}\sigma_i}) \sum_{r_i, r'_i, l_i} [U^*_{l'_i r'_i} \Lambda^{-1}_{r'_i r'_i} \underline{\Lambda^{-1}_{r'_i r_i} U^T_{r'_i l_i}}] U^*_{l_i r_i} \Lambda_{r_i r_i}$$

$$\sum_{l''_{i-1},\sigma''_i, l''_i, r''_i} H[i]_{l_{i-1}\sigma_i r_i, l''_{i-1}\sigma''_i r''_i} \Lambda_{r''_i r''_i} U^T_{r''_i l''_i} L_{l''_{i-1} l''_i}^{\sigma''_i}$$

$$(8.44)$$

The expression inside "$[\cdots]$" is $S[i+1:N]^{-1}$. The key point of this new regularization scheme is that the underlined part could be contracted first, which is $\delta_{r'_i r_i}$. Thus, only the singular matrix $\Lambda_{r'_i r'_i}$ instead of $\Lambda^2_{r'_i r'_i}$ should be regularized:

$$\tilde{\Lambda}_{r'_i r'_i} = \Lambda_{r'_i r'_i} + \varepsilon^{1/2} e^{-\Lambda_{r'_i r'_i}/\varepsilon^{1/2}} \quad (8.45)$$

The power $1/2$ here is for consistency with the original regularization scheme Eq. (8.42) and $\Lambda_{r'_i r'_i}$ in Eq. (8.44) is untouched in order to be minimally invasive as stated in the MCTDH literatures (Meyer and Wang, 2018; Wang and Meyer, 2018). Although in the MU scheme, it is necessary to perform canonicalization on the environmental part $\left|l_i[i+1:N]\right\rangle$, the gauge condition of the MPS that is evolved remains unchanged.

The second evolution scheme based on TDVP is called PS. The idea of PS is that the tangent space projector in Eq. (8.22) is invariant under different gauge conditions. More specifically, after canonicalization of a general MPS in Eq. (8.21) from site N to $i+1$, $|r_i[i+1:N]\rangle$ becomes the right-hand orthonormal renormalized basis, which is related to $|a_i[i+1:N]\rangle$ by:

$$|a_i[i+1:N]\rangle = \sum_{r_i} D_{a_i r_i} |r_i[i+1:N]\rangle \quad (8.46)$$

The matrix D is an upper triangular matrix in RQ decomposition. Therefore, the overlap matrix $S[i + 1:N]$ equals D^*D^T and the projector $\hat{P}[i + 1:N]$ in Eq. (8.24) defined for a general non-canonical MPS is transformed to:

$$\hat{P}[i + 1:N] = \sum_{r_i',r_i} |r_i'[i + 1:N]\rangle \underbrace{\left[\sum_{a_i',a_i} D_{r_i'a_i'}^T (D^*D^T)_{a_i'a_i}^{-1} D_{a_i r_i}^* \right]}_{=\delta_{r_i'r_i}} \langle r_i[i + 1:N]|$$

$$= \sum_{r_i} |r_i[i + 1:N]\rangle \langle r_i[i + 1:N]| \tag{8.47}$$

Similar result can be obtained for $\hat{P}[1:i]$:

$$\hat{P}[1:i] = \sum_{l_i} |l_i[1:i]\rangle \langle l_i[1:i]| \tag{8.48}$$

This definition of the tangent space projector does not contain any inversion operations of the overlap matrix, which seems to be a remarkable improvement over the first definition in Eqs. (8.23) and (8.24). However, since the gauge is not fixed in different terms of this projector, the VMF and CMF integration algorithm described above could not be directly applied. Lubich and Haegeman et al. proposed to use a symmetric second-order Trotter decomposition to split the formal time evolution operator into the individual terms (Haegeman et al., 2016; Lubich et al., 2015):

$$e^{-i\hat{P}\hat{H}\tau} = \left[\prod_{i=N}^{2} e^{-i\hat{P}[1:i-1]\otimes\hat{I}_i\otimes\hat{P}[i+1:N]\hat{H}\tau/2} \cdot e^{i\hat{P}[1:i-1]\otimes\hat{P}[i:N]\hat{H}\tau/2} \right] \cdot e^{-i\hat{I}_1\otimes\hat{P}[2:N]\hat{H}\tau}$$

$$\cdot \left[\prod_{i=2}^{N} e^{i\hat{P}[1:i-1]\otimes\hat{P}[i:N]\hat{H}\tau/2} \cdot e^{-i\hat{P}[1:i-1]\otimes\hat{I}_i\otimes\hat{P}[i+1:N]\hat{H}\tau/2} \right] + \mathcal{O}(\tau^3)$$

$$\tag{8.49}$$

Based on the time evolution operator in Eq. (8.49), a single step of time evolution consists of a right-to-left sweep and a subsequent left-to-right sweep each with step size $\tau/2$. Taking left-to-right sweep as an example, the matrix at the gauge center $C_{l_{i-1}r_i}^{\sigma_i}$ is firstly evolved forward in time by applying the projector $\hat{P}[1:i-1] \otimes \hat{I}_i \otimes \hat{P}[i+1:N]$:

$$i\frac{\partial C_{l_{i-1}'r_i'}^{\sigma_i'}}{\partial t} = \sum_{l_{i-1},\sigma_i,r_i} H[i]_{l_{i-1}'\sigma_i'r_i',l_{i-1}\sigma_i r_i} C_{l_{i-1}r_i}^{\sigma_i} \tag{8.50}$$

where $H[i]$ and the ingredients $h[1:i-1]$, $h[i+1:N]$, $h[i]$ all have the same definitions as in Eqs. (8.37)−(8.40) except that the A^{σ_i} in Eq. (8.40) is replaced with L^{σ_i} or R^{σ_i} accordingly. Then, the evolved matrix $C_{l_{i-1}r_i}^{\sigma_i}$ is decomposed by QR to obtain the left-canonical matrix $L_{l_{i-1}l_i}^{\sigma_i}$ and the coefficient matrix $D_{l_ir_i}$. $D_{l_ir_i}$ is evolved backward in time by applying the projector $\hat{P}[1:i] \otimes \hat{P}[i+1:N]$:

$$i\frac{\partial D_{l_i'r_i'}}{\partial t} = \sum_{l_i,w_i,r_i} h[1:i]_{\{l',w,l\}_i} h[i+1:N]_{\{r',w,r\}_i} D_{l_ir_i} \tag{8.51}$$

Afterwards, the gauge center is moved to site $i+1$ by contracting the evolved $D_{l_i r_i}$ and $R_{r_i r_{i+1}}^{\sigma_{i+1}}$ together to obtain $C_{l_i r_{i+1}}^{\sigma_{i+1}} = \sum_{r_i} D_{l_i r_i} R_{r_i r_{i+1}}^{\sigma_{i+1}}$. Following the procedure above, the sweep continues until all the individual projectors in Eq. (8.49) are applied. The Krylov subspace method is preferred over other general-purpose integrator for solving Eqs. (8.50) and (8.51) since they are linear equations. The procedure for one time step of the TDVP-PS time evolution is listed in Algorithm 3.

Algorithm 3: TDVP-PS time evolution for left-canonical MPS

input : System wavefunction $|\Psi(t)\rangle$ in left-canonical MPS representation $\{L[i]\}$ and C, system Hamiltonian H in MPO representation $\{W[i]\}$

output: Time evolved system wavefunction $|\Psi(t+\tau)\rangle$ in left-canonical MPS representation $\{L'[i]\}$ and C'

```
    /* Right to left sweep                                              */
 1  h[1 : N − 2] ← {L[i]}, {W[i]}                             /* Eq. 38 */
 2  h[N + 1 : N] = 1
 3  for i = N to i = 1 do
 4  |   procedure CalculateDerivativeC(C)
 5  |   |   ∂C/∂t ← h[1 : i − 1], h[i + 1 : N], W[i], C        /* Eq. 50 */
 6  |   |   return ∂C/∂t
 7  |   end procedure
 8  |   C = Krylov(CalculateDerivativeC, C, τ/2)
 9  |   if i = 1 then break
10  |   D, R[i] = QR(C)
11  |   h[i : N] ← h[i + 1 : N], R[i], W[i]                    /* Eq. 39 */
12  |   procedure CalculateDerivativeD(D)
13  |   |   ∂D/∂t ← h[1 : i − 1], h[i : N], D                  /* Eq. 51 */
14  |   |   return ∂D/∂t
15  |   end procedure
16  |   D = Krylov(CalculateDerivativeD, D, −τ/2)
17  |   C ← L[i − 1], D
18  end
    /* Left to right sweep                                              */
19  for i = 1 to i = N do
20  |   procedure CalculateDerivativeC(C)
21  |   |   ∂C/∂t ← h[1 : i − 1], h[i + 1 : N], W[i], C        /* Eq. 50 */
22  |   |   return ∂C/∂t
23  |   end procedure
24  |   C = Krylov(CalculateDerivativeC, C, τ/2)
25  |   if i = N then break
26  |   L[i], D = QR(C)
27  |   h[1 : i] ← h[1 : i − 1], L[i], W[i]                    /* Eq. 38 */
28  |   procedure CalculateDerivativeD(D)
29  |   |   ∂D/∂t ← h[1 : i], h[i + 1 : N], D                  /* Eq. 51 */
30  |   |   return ∂D/∂t
31  |   end procedure
32  |   D = Krylov(CalculateDerivativeD, D, −τ/2)
33  |   C ← D, R[i + 1]
34  end
    /* Now C and {L[i]} have been updated to represent |Ψ(t + τ)⟩       */
35  C' = C, {L'[i]} = {L[i]}
```

Similar to the original two-site DMRG algorithm, it is also possible to formulate TDVP-PS into a two-site algorithm so that the bond dimension

could grow up adaptively (Haegeman et al., 2016; Xie et al., 2019). The two-site algorithm is found to be more numerically stable than the single-site algorithm (Paeckel et al., 2019; Xie et al., 2019). However, just as the ground state algorithm, the two-site algorithm is much more expensive than the single-site algorithm both in the tensor contraction and QR decomposition.

In summary, since TDVP-MU and TDVP-PS are both based on the TDVP, $\left|\Psi(t)\right\rangle$ should be the same if not considering the numerical error. In contrast to the P&C scheme discussed in the last section, TDVP-MU and single-site TDVP-PS schemes both require to define a fixed bond dimension a priori, and additional renormalized basis should be constructed smartly to complement the empty MPS space if the initial state is weakly correlated. Two-site TDVP-PS usually do not need to construct additional renormalized basis, because SVD decomposition of the two-site matrices allows adaptive adjustment of the bond dimension. The main difference between TDVP-MU and TDVP-PS lies in that TDVP-MU would introduce a minor artificial regularization, while TDVP-PS is inherently free of it. It is worth noting that TDVP provides a deterministic wavefunction path during the time evolution determined by tangent space projections with infinitesimal time step, which is locally optimal. As discussed in a recent review (Paeckel et al., 2019), the TDVP path suffers from the projection error due to the restricted bond dimension and it may not be the globally optimal path in some models.

8.2.3 Time step targeting

The time step targeting algorithm is inspired by the state-averaged DMRG for the ground state and low-lying excited states. Its mathematical foundation is not as rigorous as other algorithms introduced in this section (Feiguin and White, 2005b; Paeckel et al., 2019). Here we only provide a hand-waving explanation on the basic idea of the time step targeting algorithm due to limited length.

At each time step, the matrix at the gauge center $C_{l_{i-1}r_i}^{\sigma_i}(t)$ is evolved based on Eq. (8.50), yielding $C_{l_{i-1}r_i}^{\sigma_i}(t+\frac{1}{3}\tau)$, $C_{l_{i-1}r_i}^{\sigma_i}(t+\frac{2}{3}\tau)$ and $C_{l_{i-1}r_i}^{\sigma_i}(t+\tau)$ (the time steps here are arbitrary). However, $C_{l_{i-1}r_i}^{\sigma_i}(t)$ is not replaced by $C_{l_{i-1}r_i}^{\sigma_i}(t+\tau)$ immediately. Rather, $C_{l_{i-1}r_i}^{\sigma_i}(t)$ is replaced by the eigenvectors $L_{l_{i-1}l_i}^{\sigma_i}$ of the state-averaged reduced density matrix, constructed from the above four $C_{l_{i-1}r_i}^{\sigma_i}$ matrices at different time steps with empirically determined weights. Then, the eigenvectors $L_{l_{i-1}r_i}^{\sigma_i}$ and $C_{l_{i-1}r_i}^{\sigma_i}$ are contracted with $R_{r_ir_{i+1}}^{\sigma_{i+1}}$ to move the gauge center into the next site.

$$C_{l_ir_{i+1}}^{\sigma_{i+1}} = \sum_{l_{i-1},\sigma_i,r_i} L_{l_{i-1}l_i}^{\sigma_i*} C_{l_{i-1}r_i}^{\sigma_i} R_{r_ir_{i+1}}^{\sigma_{i+1}} \tag{8.52}$$

At this stage, the MPS still represents the wavefunction at time t, yet the basis is updated to adapt the next time step. We note that this update is not

rigorous and an error is introduced into the current MPS. The iterative sweep continues until convergence, at which point it is assumed that the basis for the MPS has transformed to best describe both $\left|\Psi(t)\right\rangle$ and $\left|\Psi(t+\tau)\right\rangle$. After that, the actual time evolution over the current gauge center takes place and finishes one step of the time evolution.

8.3   Finite temperature algorithms

The effect of temperature plays an indispensable role in a large fraction of vibronic models in chemistry. There are in general two methods to incorporate temperature effect in TD-DMRG. The first method is called the purification or ancilla method or thermal field dynamics, well suited for high and intermediate temperature (Feiguin and White, 2005a; Verstraete et al., 2004), and the second method is called the minimally entangled typical thermal state (METTS) method, particularly effective at low temperature (Stoudenmire and White, 2010; White, 2009). A purification-METTS hybrid algorithm has also been proposed (Chen and Stoudenmire, 2020). Neither of the two approaches are specially designed for MPS or tensor network states and they can be applied to any wavefunction-based methodologies. In the chemistry regime, the purification method is used most often.

8.3.1   Purification in an enlarged Hilbert space

The essence of the purification method is to express mixed states (density matrices) as pure states (wavefunctions) in an enlarged Hilbert space (Feiguin and White, 2005a; Takahashi and Umezawa, 1996; Verstraete et al., 2004). For any physical observable $\hat{O}$, the finite temperature expectation can be expressed as:

$$\left\langle \hat{O} \right\rangle = \sum_n \left\langle n|\hat{O}|n \right\rangle e^{-\beta E_n}/Z = \mathrm{Tr}\{\hat{O}\rho\} \qquad (8.53)$$

where $|n\rangle$ is a set of orthonormal basis in energy representation with eigenenergy E_n, $Z = \sum_n e^{-\beta E_n}$ is the partition function, and ρ is the density matrix. Suppose the space in which we build the physical model and make observation is called the physical space P, it can be proven that for general cases there does not exist a wavefunction in the P space $|\Psi\rangle$ that fulfills (Takahashi and Umezawa, 1996):

$$\left\langle \Psi|\hat{O}|\Psi \right\rangle = \sum_n \left\langle n|\hat{O}|n \right\rangle e^{-\beta E_n}/Z \qquad (8.54)$$

and that's exactly why density matrices should be introduced to describe the temperature effect. Since MPS is an ansatz for wavefunction, it would be ideal if we can avoid density matrix and find a pure state that produces the correct formula for the expectation Eq. (8.54). This goal can be achieved by adding an auxiliary space Q to the P space and working in the resulting

$P \otimes Q$ space. The Q space is chosen as a copy of the P space in terms of states and operators. If the energy eigenstate in the Q space is labeled with a tilde $|\tilde{m}\rangle$, the basis for the enlarged Hilbert space can be expressed as $|n, \tilde{m}\rangle$. Define wavefunction $|\Psi\rangle_{PQ}$ in the enlarged space:

$$|\Psi\rangle_{PQ} = \sum_n e^{-\beta E_n/2} |n, \tilde{n}\rangle / Z^{\frac{1}{2}} \qquad (8.55)$$

By noting that $\hat{O}$ only acts on the P space, it is straightforward to prove that $|\Psi\rangle_{PQ}$ fulfills Eq. (8.54). If desired, the thermal equilibrium density matrix can be explicitly constructed by partial trace (or partial inner product) over the Q space:

$$\rho = \text{Tr}_Q |\Psi\rangle_{PQ} \quad _{PQ}\langle\Psi| \qquad (8.56)$$

$|\Psi\rangle_{PQ}$ can be calculated by TD-DMRG via imaginary time evolution from the identity state in P and Q space:

$$|I\rangle = \sum_n |n, \tilde{n}\rangle \qquad (8.57)$$

$|I\rangle$ is also called a maximally entangled state in the sense that the P and Q space are maximally entangled. Imaginary time evolution from $|I\rangle$ yields the thermal state $|\Psi\rangle_{PQ}$:

$$|\Psi\rangle_{PQ} = e^{-\beta \hat{H}/2} |I\rangle / Z^{\frac{1}{2}} \qquad (8.58)$$

Note that $|I\rangle$ is invariant under basis transformation so usually an appropriate set of basis is chosen for computational convenience and it's not necessary to calculate $|n\rangle$. The partition function $Z^{\frac{1}{2}}$ typically does not need to be calculated in practice either, because it can be viewed as the normalization factor for $|\Psi\rangle_{PQ}$. Further real time evolution may be performed on $|\Psi\rangle_{PQ}$ to obtain time-dependent properties.

In the context of TD-DMRG, the fact that the initial state for the imaginary time evolution $|I\rangle$ is maximally entangled is quite alarming, since the larger the entanglement, the larger the required bond dimension and computational cost. Indeed, finite temperature calculation is typically much more time-consuming than that of zero temperature, particularly when vibrational DoFs are involved, not only because the number of the DoFs is doubled, but also because the bond dimension required during imaginary and real time evolution is much larger than that of zero temperature. For example, suppose there are two uncoupled harmonic vibration DoFs in the system termed λ_1 and λ_2 with occupation number basis $|n_1\rangle$ and $|n_2\rangle$. At zero temperature, the ground state $|00\rangle$ can be trivially described by an MPS with bond dimension 1 because λ_1 and λ_2 are not entangled. Yet at finite temperature β, the thermal state in P and Q space reads:

$$|\Psi\rangle_{PQ}(\beta) = \sum_{n_1} e^{-\beta n_1 \omega/2} |n_1, \tilde{n}_1\rangle \sum_{n_2} e^{-\beta n_2 \omega/2} |n_2, \tilde{n}_2\rangle / Z^{\frac{1}{2}} \qquad (8.59)$$

While the entanglement entropy between $(\lambda_1, \tilde{\lambda}_1)$ and $(\lambda_2, \tilde{\lambda}_2)$ is still zero due to their uncoupled nature, the entanglement entropy between λ_1 (λ_2) and $\tilde{\lambda}_1$ ($\tilde{\lambda}_2$) is $\frac{\beta\omega}{e^{\beta\omega}-1} - \ln(1 - e^{-\beta\omega})$, which is only zero when $\beta\omega \to \infty$. If the state is represented by an MPS:

$$|\Psi\rangle_{PQ}(\beta) = \underset{\lambda_1 \quad\quad \tilde{\lambda}_1 \quad\quad \lambda_2 \quad\quad \tilde{\lambda}_2}{\bigcirc\!\!-\!\!\bigcirc\!\!-\!\!\bigcirc\!\!-\!\!\bigcirc} \tag{8.60}$$

Then the bond dimension between $\tilde{\lambda}_1$ and λ_2 is 1 as expected from the uncoupled model, whereas the bond dimension between λ_1 (λ_2) and $\tilde{\lambda}_1$ ($\tilde{\lambda}_2$) is in general much larger than 1. In view of the strong entanglement between the P space and the Q space at finite temperature, in practical implementation sometimes it is desirable to merge the P space and the Q space of each DoF into the same site:

$$|\Psi\rangle_{PQ}(\beta) = \underset{\tilde{\lambda}_1 \quad\quad \tilde{\lambda}_2}{\overset{\lambda_1 \quad\quad \lambda_2}{\bigcirc\!\!-\!\!\bigcirc}} \tag{8.61}$$

In this case, the strong entanglement between the P space and Q space seems to be eliminated. However, adding another physical index into each site results in an unfavorable computational scaling and the overall computational cost is hardly reduced. Although the form of Eq. (8.61) closely resembles an MPO and it is tempting to recognize Eq. (8.61) as a density matrix, according to Eq. (8.56), the density matrix is only constructed after contracting out the Q space:

$$\rho = \underset{\lambda_1 \quad\quad \lambda_2}{\overset{\lambda_1 \quad\quad \lambda_2}{\boxed{}}} \tag{8.62}$$

Eq. (8.61) is a more efficient representation of the thermal state than directly expressing the density matrix as an MPO (Feiguin and White, 2005a; Zwolak and Vidal, 2004) because Eq. (8.62) guarantees that ρ is positive semi-definite and Hermitian. A more intuitive viewpoint is to note that if the bond dimension for Eq. (8.61) is M then the bond dimension of the corresponding density matrix in Eq. (8.62) is M^2.

The fact that the Q space is traced out before physical observables are extracted from the MPS leaves the room for arbitrary unitary transformation over the Q space. This opportunity has been exploited to reduce the entanglement growth of purified states during real time evolution (Karrasch et al., 2012, 2013). The transformation applied to the Q space is simply the "backward time evolution" $e^{i\hat{H}t}$, which hopefully should reverse the growth of entanglement caused by the forward time evolution in the P space. Recently an algorithm for finding the purification with minimal entanglement is proposed and has proven more effective in reducing entanglement entropy than the "backward time evolution" method (Hauschild et al., 2018).

For a number of vibronic models that frequently appear in chemistry, it is possible to perform a basis transformation known as Bogoliubov transformation over the PQ space so as to truly eliminate the entanglement between them (Borrelli and Gelin, 2016, 2021; de Vega and Bañuls, 2015). In these models, the vibrations are described by harmonic oscillators, and the non-equilibrium dynamics starts with an electronic excitation from the thermal equilibrium state in which electron and phonon parts are not correlated. Suppose that the initial electronic ground state is $|g\rangle$ and the vibrations are at thermal equilibrium, the total thermal density matrix of the system is:

$$\rho_{e,\lambda} = |g\rangle\langle g|\rho_\lambda \tag{8.63}$$

The setup is common in chemistry since usually the gap between $|g\rangle$ and its excited state is much larger than the thermal energy. The thermal equilibrium density matrix Eq. (8.63) can be constructed as an MPS through the purification method. Unfortunately, due to the reasons mentioned above, the entanglement entropy in this seemingly trivial model is actually quite large. Suppose the Hamiltonian of the harmonic vibrations is

$$\hat{H}_\lambda = \sum_\lambda \omega_\lambda \hat{b}_\lambda^\dagger \hat{b}_\lambda \tag{8.64}$$

Mathematically, it can be proven that the purified thermal state Eq. (8.55) is identical to a unitary transformation over the ground state (Takahashi and Umezawa, 1996):

$$\prod_\lambda \sum_n e^{-\beta n_\lambda \omega_\lambda/2}|n_\lambda, \tilde{n}_\lambda\rangle/Z^{\frac{1}{2}} = e^{-i\hat{G}}\prod_\lambda|0_\lambda, \tilde{0}_\lambda\rangle \tag{8.65}$$

where $\hat{G}$ takes the form:

$$G = -i\sum_\lambda \theta_\lambda\left(\hat{b}_\lambda\hat{\tilde{b}}_\lambda - \hat{b}_\lambda^\dagger\hat{\tilde{b}}_\lambda^\dagger\right)\theta_\lambda = \text{arctanh}\left(e^{-\beta\omega_\lambda/2}\right) \tag{8.66}$$

The state $\prod_\lambda|0_\lambda, \tilde{0}_\lambda\rangle$ is completely not entangled and can be efficiently represented by an MPS with bond dimension 1, so it is an ideal initial state for the study of non-equilibrium dynamics. To use $\prod_\lambda|0_\lambda, \tilde{0}_\lambda\rangle$ as the initial

state, it is necessary to deduce the form of the operators such as the Hamiltonian after the transformation:

$$\hat{H}_\theta = e^{i\hat{G}}\hat{H}e^{-i\hat{G}} \tag{8.67}$$

Take the Holstein-Peierls Hamiltonian as an example:

$$\hat{H} = \sum_{mn}\varepsilon_{mn}\hat{a}_m^\dagger\hat{a}_n + \sum_\lambda \omega_\lambda \hat{b}_\lambda^\dagger\hat{b}_\lambda + \sum_{mn\lambda}g_\lambda\omega_\lambda\hat{a}_m^\dagger\hat{a}_n(\hat{b}_\lambda^\dagger + \hat{b}_\lambda) \tag{8.68}$$

The transformed Hamiltonian is

$$\hat{H}_\theta = e^{i\hat{G}}(\hat{H} - \sum_\lambda \omega_\lambda \hat{\tilde{b}}_\lambda^\dagger\hat{\tilde{b}}_\lambda)e^{-i\hat{G}}$$

$$= \sum_{mn}\varepsilon_{mn}\hat{a}_m^\dagger\hat{a}_n + \sum_\lambda\omega_\lambda(\hat{b}_\lambda^\dagger\hat{b}_\lambda - \hat{\tilde{b}}_\lambda^\dagger\hat{\tilde{b}}_\lambda)$$

$$+ \sum_{mn\lambda}\cosh(\theta_k)g_\lambda\omega_\lambda\hat{a}_m^\dagger\hat{a}_n(\hat{b}_\lambda^\dagger + \hat{b}_\lambda)$$

$$+ \sum_{mn\lambda}\sinh(\theta_k)g_\lambda\omega_\lambda\hat{a}_m^\dagger\hat{a}_n(\hat{\tilde{b}}_\lambda^\dagger + \hat{\tilde{b}}_\lambda) \tag{8.69}$$

The additional term added to the Hamiltonian $\sum_\lambda\omega_\lambda\hat{\tilde{b}}_\lambda^\dagger\hat{\tilde{b}}_\lambda$ is only for computational convenience because it acts on the Q space and thus does not affect the time evolution of physical observables. In the transformed Hamiltonian, the vibrations in the Q space have negative frequency and the electron-phonon coupling strengths are renormalized by the inverse temperature β. To summarize, the finite temperature dynamics is reduced to zero temperature dynamics with temperature-dependent Hamiltonian. We note that similar idea (extending phonon bath spectral density to negative frequency domain for finite temperature properties) has been proposed through the equivalence of phonon correlation function (Tamascelli et al., 2019).

8.3.2 Minimally entangled typical thermal states

At low temperature, the purification method becomes less effective for TD-DMRG. In the $\beta \to \infty$ limit, the thermal state is actually the ground state, so the Q space introduced by the purification method becomes a burden for the MPS representation. On the other hand, the fact $\beta \to \infty$ itself implies infinite steps of imaginary time evolution (Schollwöck, 2011). The METTS method avoids the purification by sampling and is more efficient at the low temperature limit (Stoudenmire and White, 2010; White, 2009).

The starting point of METTS is the introduction of typical thermal states. Eq. (8.53) expresses the finite temperature physical expectation $\langle \hat{O} \rangle$ in energy basis. For any complete orthonormal basis $|j\rangle$, the expectation can be written as:

$$\langle \hat{O} \rangle = \sum_j \langle j | e^{-\beta\hat{H}/2} \hat{O} e^{-\beta\hat{H}/2} | j \rangle / Z = \sum_j p_j(\beta) \langle \phi_j(\beta) | \hat{O} | \phi_j(\beta) \rangle / Z \quad (8.70)$$

where $|\phi_j(\beta)\rangle$ is defined as a set of normalized typical thermal states (while the energy eigenbasis is argued to be "not typical" (White, 2009)):

$$|\phi_j(\beta)\rangle = p_j(\beta)^{-(1/2)} e^{-\beta\hat{H}/2} |j\rangle$$
$$p_j(\beta) = \langle j | e^{-\beta\hat{H}} | j \rangle \quad (8.71)$$

By noting that $\sum_j p_j(\beta)/Z = 1$, Eq. (8.70) can be viewed as the statistical average of the typical thermal states. The problems now are how to choose $|j\rangle$ and how to calculate $p_j(\beta)/Z$ efficiently (if necessary).

For TD-DMRG, an ideal choice of $|j\rangle$ is to let $|\phi_j(\beta)\rangle$ minimally entangled. Although this is a non-trivial task, an intuitive attempt is to use Hartree product states for $|j\rangle$:

$$|j\rangle = \prod_n |j_n\rangle \quad (8.72)$$

Here n denotes different DoFs. The hope is that if the initial state $|j\rangle$ is minimally entangled, the typical thermal state $|\phi_j(\beta)\rangle$ is also minimally entangled. The METTSs can be sampled efficiently through a Markov chain of states without the calculation of $p_j(\beta)/Z$. The probability of transition from $|\phi_j(\beta)\rangle$ to $|\phi_{j'}(\beta)\rangle$ is simply $|\langle j' | \phi_j(\beta) \rangle|^2$. Suppose that in one step of the Markov sampling, all states $|\phi_j(\beta)\rangle$ are already correctly sampled with probability $p_j(\beta)/Z$, then for the next step the probability of transition to a particular state $|\phi_{j'}(\beta)\rangle$ is

$$p = \sum_j \frac{p_j(\beta)}{Z} |\langle j' | \phi_j(\beta) \rangle|^2 = \sum_j \frac{1}{Z} \langle j' | e^{-\beta\hat{H}/2} | j \rangle \langle j | e^{-\beta\hat{H}/2} | j' \rangle = \frac{P_{j'}(\beta)}{Z} \quad (8.73)$$

which is exactly the desired probability. The existence of a fixed point indicates that after enough steps the Markov sampling should converge to the correct probability. An additional trick for efficient sampling with MPS is carrying out the "collapse" from $|\phi_j(\beta)\rangle$ to $|j'\rangle$ by taking local measurements site-by-site.

8.4 Applications

In this section, we describe several groups of scientific problems in chemistry that TD-DMRG has been successfully applied to. We shall firstly focus

on nonadiabatic dynamics with vibronic models and then move on to electron dynamics based on ab initio Hamiltonian.

8.4.1 Exciton and charge transfer dynamics

Exciton dynamics and charge transfer dynamics are of great significance for the energy and charge transfer in bio-molecules and novel materials, which are usually modeled by Frenkel-Holstein Hamiltonian and its variants. In the photosynthesis process, ambient photons are absorbed by optically active molecules, leading to the formation of molecular excitons. The molecular excitons transfer the solar energy received to the reaction center in an efficient manner, and the study toward its mechanism can provide helpful information on the design of artificial light-harvesting system. Chin et al. (Chin et al., 2013). used TD-DMRG to study the exciton dynamics in pigment-protein complexes exemplified by the Fenna−Matthew−Olson complex. The authors used a two-pigment model and the Hamiltonian can be transformed to an equivalent Hamiltonian with only nearest interactions such that the TEBD time evolution algorithm can be efficiently applied (Prior et al., 2010). Subsequently, Gelin and Borrelli extended the study to seven-pigment model as well as electron transfer model in reaction center via the TDVP-PS algorithm (Borrelli, 2018; Borrelli and Gelin, 2017). The finite temperature effect is also taken into consideration using the purification method coupled with Bogoliubov transformation. Later, with the aid of TD-DMRG, they also demonstrated that the long-time exciton dynamics of identical pigments with static disorder is dominated by vibrational dynamics (Gelin et al., 2019).

Similar simulations can be carried out for the ultrafast exciton dissociation at donor/acceptor interface in organic solar cells (Yao et al., 2018, 2016). These models include both exciton and charge transfer states as well as electron-phonon couplings. Yao et al. (Yao et al., 2016) reported the evolution of the charge density of the hole in the donor part and the electron in the acceptor part obtained by TD-DMRG at different electron-phonon coupling strength α. The electron-phonon coupling is characterized by the phonon spectral density function $J(\omega)$

$$J(\omega) = 2\pi\alpha\omega_c^{\frac{1}{2}}\omega^{\frac{1}{2}}e^{-\omega/\omega_c} \tag{8.74}$$

where ω_c is the cutoff frequency. The results are shown in Fig. 8.1. It is found that ultrafast long-range charge separation in organic photovoltaics devices should be ascribed to the quantum resonance between local Frenkel excited states and a broad array of long-range charge transfer states assisted by the moderate off-diagonal vibronic couplings. There are also reports on the ultrafast relaxation, decoherence, and localization of excitons in
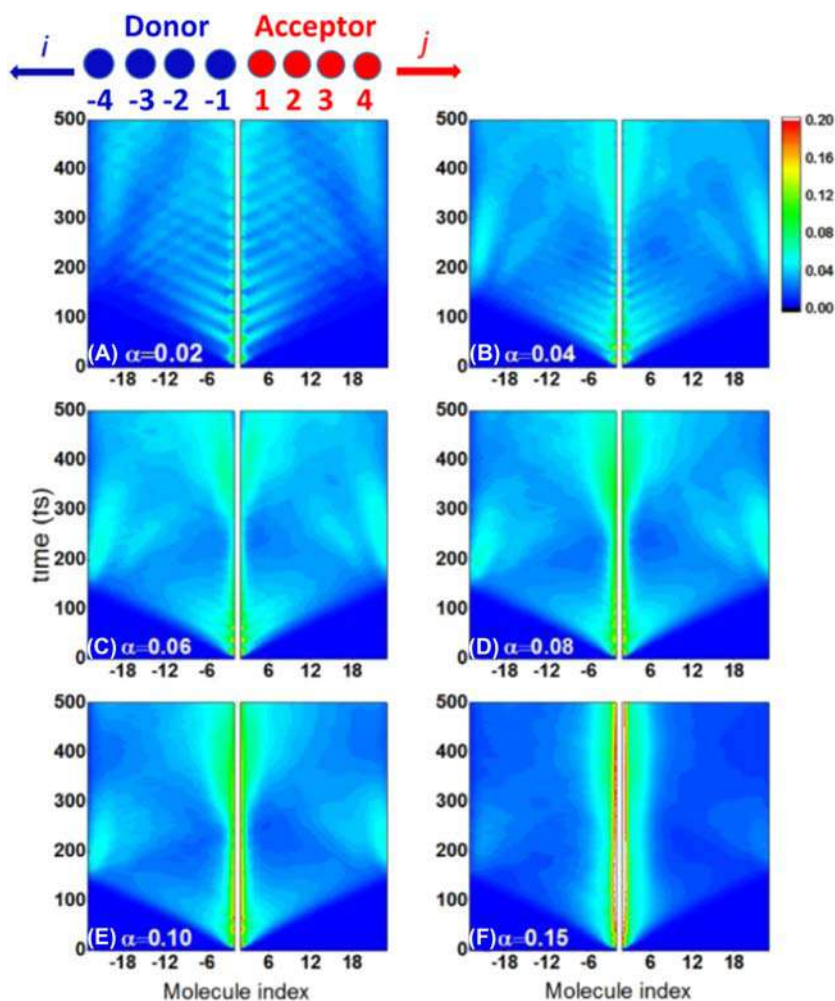
FIGURE 8.1 Charge density evolution of hole in the donor part and electron in the acceptor part with different α values where α is the electron-phonon coupling strength. *Reproduced from Yao, Y., Xie, X., Ma, H., 2016. Ultrafast long-range charge separation in organic photovoltaics: promotion by off-diagonal vibronic couplings and entropy increase. J. Phys. Chem. Lett., 7, 4830–4835. https://doi.org/10.1021/acs.jpclett.6b02400, with permission from American Chemical Society.*

π-conjugated polymers such as poly(para-phenylene) and poly(p-phenylene-vinylene) (Barford and Mannouch, 2018; Mannouch et al., 2018). By adding triplet pair state to the electronic basis, TD-DMRG can be applied to study the singlet fission of an exciton based on three-state or more complex models as well (Xie et al., 2019; Yao, 2016).

The typical workflow for the simulation of exciton dynamics (or charge transfer dynamics) is quite straightforward. Firstly, the zero temperature pure state or thermal equilibrium ground state without excitons (or charges) are prepared as an MPS, which are usually uncorrelated. After that, an exciton (or a charge) is injected into the appropriate molecule(s) in the system by applying the creation operator to the MPS, and then the out-of-equilibrium state is evolved according to an appropriate time evolution algorithm and interested quantities such as elements of the electronic reduced density matrix are computed along the way. It should be pointed out that the dynamics of the vertical Franck-Condon excitation mentioned above could be significantly different from the dynamics of vibrationally relaxed excitations according to a recent TD-DMRG study (Kloss et al., 2019). Lastly, we note that as long as the vibrations are described as harmonic oscillators and additionally the initial electronic and vibrational parts are uncorrelated, the finite temperature effect is probably best treated by the Bogoliubov transformation (Borrelli, 2018; Borrelli and Gelin, 2017).

8.4.2 Excited state dynamics and spectra

The excited state dynamics is closely connected to exciton dynamics described in the last subsection, however in this subsection we concentrate on the dynamics that involves complex potential energy surface and/or application to molecular spectra. An exemplary case is the S_1/S_2 interconversion dynamics of pyrazine after UV photoexcitation to the S_2 state, which is already explored in detail by a number of methods including MCTDH (Raab et al., 1999; Worth et al., 1996). Pyrazine features a conical intersection between the S_1 and the S_2 states and strong vibronic couplings with 24 vibration modes. Thus, the molecule serves as a rigorous benchmark platform for quantum dynamics methodologies. The absorption spectra $I(\omega)$ is calculated via the Fourier transformation of dipole−dipole correlation function $C(t)$ by virtue of linear response theory:

$$
\begin{aligned}
I(\omega) &\propto \int_{-\infty}^{\infty} e^{i\omega t} C(t) dt \\
C(t) &= \left\langle \hat{\mu}(t)\hat{\mu}(0) \right\rangle_g
\end{aligned}
\tag{8.75}
$$

Here μ is the dipole operator and the subscript g denotes the ground state. At zero temperature, the calculation of $C(t)$ reduces to the calculation of the overlap between the time evolved wavefunction $\Psi(t)$ and the initial S_2 wavefunction $\Psi(0)$:

$$
\left\langle \hat{\mu}(t)\hat{\mu}(0) \right\rangle_g = \left\langle e^{i\hat{H}t} \hat{\mu} e^{-i\hat{H}t} \hat{\mu} \right\rangle_g = e^{iE_g t} \left\langle \hat{\mu} e^{-i\hat{H}t} \hat{\mu} \right\rangle_g \propto \left\langle \Psi(0)|\Psi(t) \right\rangle
\tag{8.76}
$$

Here E_g is the ground state energy which can be set to 0 when defining the Hamiltonian. Both the P&C and TDVP time evolution schemes have been applied to tackle the problem (Baiardi and Reiher, 2019; Greene and

Batista, 2017; Xie et al., 2019). Coupled with ab initio parameters from highly accurate electronic structure methods, the calculated spectra coincides with experimental spectra remarkably well.

The same formulation can be extended to the spectra of molecular aggregates such as perylene bisimide dyes (PBI), also pioneered by MCTDH (Ambrosek et al., 2012; Baiardi and Reiher, 2019; Ren et al., 2018). With slight modification, the finite temperature spectra can also be obtained (Ren et al., 2018). The key ingredient is to perform two sets of time evolution simultaneously over the purified finite temperature state $|\Psi\rangle_{PQ}$ for the evaluation of $C(t)$:

$$C(t) = {}_{PQ}\langle\Psi|e^{i\hat{H}t}\hat{\mu}e^{-i\hat{H}t}\hat{\mu}|\Psi\rangle_{PQ} \qquad (8.77)$$

with the first time evolution being $e^{-i\hat{H}t}\hat{\mu}|\Psi\rangle_{PQ}$ starting from $\hat{\mu}|\Psi\rangle_{PQ}$ and the second time evolution being $e^{-i\hat{H}t}|\Psi\rangle_{PQ}$ starting from $|\Psi\rangle_{PQ}$. Benchmarks at zero temperature indicates that the results by TD-DMRG are in exact accordance with ML-MCTDH. Fig. 8.2 shows the absorption and emission spectra of PBI dimer at 298 K calculated by TD-DMRG. It is observed that the fine spectra are in agreement with experimentally determined broad peaks. Besides, the results derived from TD-DMRG are more accurate than the results by the popular n-particle approximation (Ren et al., 2018). Furthermore, the two-dimensional electronic spectra can be simulated by TD-DMRG through calculating the third-order nonlinear response function (Yao et al., 2018).
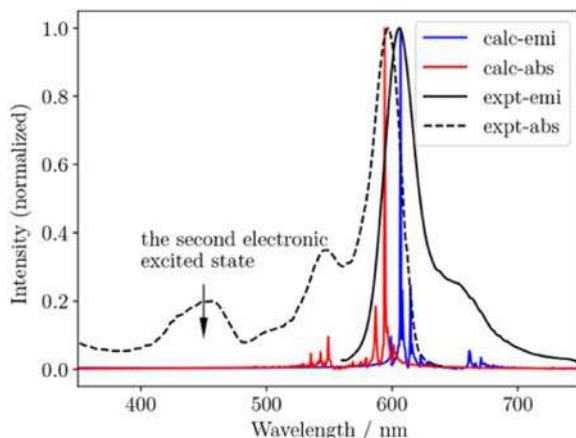
FIGURE 8.2 Calculated absorption and fluorescence spectra of PBI dimer at 298K from finite temperature TD-DMR, with comparison to experiments. Please check the online version to view the color image of the figure. *Reproduced from Ren, J., Shuai, Z., Chan, G.K., 2018. Time-dependent density matrix renormalization group algorithms for nearly exact absorption and fluorescence spectra of molecular aggregates at both zero and finite temperature. J. Chem. Theory Comput., 14, 5027−5039. doi: 10/gpggr5, with permission from American Chemical Society.*

8.4.3 Charge transport

Charge transport properties in conjugated polymers are one of the first applications of TD-DMRG in chemistry (Ma and Schollwöck, 2008, 2009; Zhao et al., 2009, 2008). In these works, while the electron motion is simulated with high precision by TD-DMRG, the nuclear motion is approximated by classical dynamics, forming a hybrid TD-DMRG/Ehrenfest time evolution scheme. More recently, the finite temperature carrier mobility for organic semiconductors is calculated by TD-DMRG through the Kubo formula:

$$\mu = \frac{1}{2k_B T e_0} \int_{-\infty}^{\infty} \left\langle \hat{j}(t)\hat{j}(0) \right\rangle dt \tag{8.78}$$

where $\hat{j}$ is the current operator represented analytically by an MPO (Li et al., 2020b). The calculated mobility based on ab initio parameters correctly reproduces the experimental mobility-temperature relationship and further confirms the negative isotope effect for mobility. Later, the study is extended to include the effect of nonlocal electron-phonon coupling and a general charge transport picture unifying previously contradicting theories (Fig. 8.3) is presented (Li et al., 2021). We note that (ML)-MCTDH will struggle for the very same task because the effect of applying $\hat{j}$ to a quantum state is difficult to model without MPO.

8.4.4 Electron dynamics

Although in a large number of literatures TD-DMRG is targeted to vibronic problems, pure electronic dynamics also emerges in recent literatures, owing to the general nature of TD-DMRG. Ronca et al. (Ronca et al., 2017).
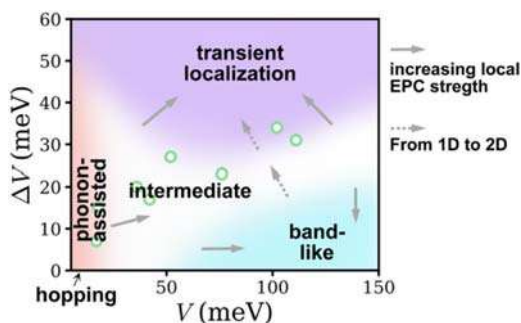
FIGURE 8.3 A schematic regime diagram determined by TD-DMRG showing different charge transport regimes according to the transfer integral V and its room temperature thermal variation ΔV for the charge transport of the Holstein-Peierls model. *Reproduced from Li, W., Ren, J., Shuai, Z., 2021. A general charge transport picture for organic semiconductors with nonlocal electron-phonon couplings. Nat. Commun., 12, 4260.* https://doi.org/10.1038/s41467-021-24520-y, *with permission from Springer Nature.*
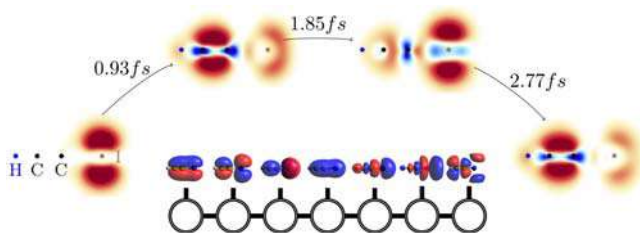
FIGURE 8.4 Hole density of the iodoacetylene molecule at four different points in time. *Reproduced from Frahm, L.-H., Pfannkuche, D., 2019. Ultrafast ab initio quantum chemistry using matrix product states. J. Chem. Theory Comput., 15, 2154−2165. https://doi.org/10.1021/acs.jctc.8b01291, with permission from American Chemical Society.*

TD-DMRG to study the oxygen core-excitation energy in the water and dynamical properties of hydrogen chain with an improved version of the time step targeting algorithm. Coupled with frequency domain algorithms, they were able to extract density of states and complex polarization function from the ab initio system Hamiltonian, as indicators for the metallicity and delocalization at different bond lengths. Frahm & Pfannkuche (Frahm and Pfannkuche, 2019) simulated the ultrafast charge migration dynamics in the iodoacetylene molecule with TD-DMRG (Fig. 8.4) and their result is in direct agreement with experiments. Very recently, Baiardi (Baiardi, 2021) applies TD-DMRG to the calculation of molecular (hyper)polarizabilities, electronic absorption spectra, and ultrafast ionization dynamics.

8.5 Summary and outlook

In this chapter, we introduce several key algorithms for TD-DMRG and some of their recent applications to chemistry problems. Owing to the delicate and compact mathematical structure of MPS, a variety of time evolution schemes have been invented for TD-DMRG. The schemes have distinct features and almost all schemes are under active usage in the community. It is common practice to choose the appropriate scheme according to the scientific problem at hand. Furthermore, in Section 8.3, we introduced several formulations that enable TD-DMRG to capture the finite temperature effect, which makes TD-DMRG an even powerful tool in modeling realistic systems.

As demonstrated in Section 8.4, with the state-of-the-art algorithms, TD-DMRG is able to simulate a wide range of dynamic processes with nearly exact accuracy. Its applications include exciton dynamics in various systems, singlet fission, 1D and 2D spectra of small molecules and aggregates, charge transport in organic semiconductors, and electronic dynamics at ab initio level. For some of the cases such as exciton dynamics, TD-DMRG serves as an alternative to (ML)-MCTDH, while in other cases such as charge

transport, TD-DMRG has emerged as the most accurate methodology for complex systems. In near future, we expect TD-DMRG to be applied to the dynamics of more realistic systems, probably combined with ab initio potential energy surfaces. Moreover, it is natural to generalize the charge transport formalism to study heat transport, spin transport, thermoelectric effect, and so on. Nevertheless, to go beyond one-dimensional models is still one of the major challenges of simulating transport phenomenon in bulk materials for TD-DMRG. As high dimensional models are much more computationally demanding than the one-dimensional models, efficient simulation still requires further development of the TD-DMRG methodology.

One possible approach for larger scale TD-DMRG calculation is to adopt more flexible tensor network structure, such as tree tensor networks (Larsson, 2019; Nakatani et al., 2014). In tree tensor networks, the average distance in terms of virtual bonds between two DoFs is $\mathcal{O}(\log N)$ instead of $\mathcal{O}(N)$ in MPS. Therefore, with the same bond dimension tree tensor networks should in principle be more accurate than MPS to approximate a general state. Besides, it is possible to overcome the formally higher scaling of tree tensor networks by separating the nodes with physical bond from the nodes with only three virtual bonds (Gunst et al., 2018). Compared to even more powerful loop-containing tensor networks, there are no fundamental difficulties regarding porting existing MPS algorithms to tree tensor networks, however, reports on the application of tree tensor networks to time-dependent chemical problems are so far rather limited (Schröder et al., 2019).

Before closing the chapter, we would like to discuss a notable drawback of TD-DMRG, which is the limitation on the computationally reachable evolution time. In almost all time evolution scenarios relevant to chemistry as discussed in Section 8.4, the bipartite entanglement entropy of the system S grows linearly with time: $S \propto t$ (Calabrese and Cardy, 2005; Žnidarič, 2020). The situation is similar for imaginary time evolution (Dubail, 2017). The consequence of this seemingly arcane assertion is that the required bond dimension for numerically exact time evolution grows exponentially with time: $M \propto e^t$, according to the relation between the upper bound of entanglement entropy for an MPS and the corresponding bond dimension(M) $S = \ln M$. In other words, for a fixed bond dimension, the time evolution error grows exponentially (Schollwöck, 2011). Thus, in general, TD-DMRG is not a suitable tool to study the long time limit behavior. However, as have shown in Section 8.4, in many cases the state-of-the-art TD-DMRG algorithms are well capable of offering a reliable solution to the time-dependent Schrödinger equation up to a decent time scale. And a helpful strategy to bypass the limitation of evolution time is to compute the interested physical observable through time correlation function, which for most realistic chemistry systems should decay to zero at long time limit. Another strategy is to use frequency-domain DMRG algorithm instead, which is discussed in

[Chapter 7](#) of this book. Techniques to overcome the entanglement barrier directly are hitherto under development ([Rams and Zwolak, 2020](#)).

References

Ambrosek, D., Köhn, A., Schulze, J., Kühn, O., 2012. Quantum chemical parametrization and spectroscopic characterization of the Frenkel exciton Hamiltonian for a j-aggregate forming perylene bisimide dye. J. Phys. Chem. A 116, 11451−11458. Available from: https://doi.org/10.1021/jp3069706.

Baiardi, A., 2021. Electron dynamics with the time-dependent density matrix renormalization group. J. Chem. Theory Comput. 17, 3320−3334. Available from: https://doi.org/10.1021/acs.jctc.0c01048.

Baiardi, A., Reiher, M., 2019. Large-scale quantum dynamics with matrix product states. J. Chem. Theory Comput. 15, 3481−3498. Available from: https://doi.org/10.1021/acs.jctc.9b00301.

Barford, W., Mannouch, J.R., 2018. Torsionally induced exciton localization and decoherence in ∏-Conjugated polymers. J. Chem. Phys. 149, 214107. Available from: https://doi.org/10.1063/1.5054176.

Beck, M.H., Jäckle, A., Worth, G.A., Meyer, H.-D., 2000. The multiconfiguration time-dependent hartree (MCTDH) method: a highly efficient algorithm for propagating wave-packets. Phys. Rep. 324, 1−105.

Bonfanti, M., Burghardt, I., 2018. Tangent space formulation of the multi-configuration time-dependent hartree equations of motion: The Projector−Splitting algorithm revisited. Chem. Phys. 515, 252−261. Available from: https://doi.org/10.1016/j.chemphys.2018.05.029.

Borrelli, R., 2018. Theoretical study of charge-transfer processes at finite temperature using a novel thermal Schrödinger equation. Chem. Phys. 515, 236−241. Available from: https://doi.org/10.1016/j.chemphys.2018.06.005.

Borrelli, R., Gelin, M.F., 2016. Quantum electron-vibrational dynamics at finite temperature: Thermo field dynamics approach. J. Chem. Phys. 145, 224101. Available from: https://doi.org/10.1063/1.4971211.

Borrelli, R., Gelin, M.F., 2017. Simulation of quantum dynamics of excitonic systems at finite temperature: An efficient method based on thermo field dynamics. Sci. Rep. 7, 9127. Available from: https://doi.org/10.1038/s41598-017-08901-2.

Borrelli, R., Gelin, M.F., 2021. Finite temperature quantum dynamics of complex systems: Integrating thermo-field theories and tensor-train methods. Wiley Interdiscip. Rev. Comput. Mol. Sci. 11, e1539. Available from: https://doi.org/10.1002/wcms.1539arXiv. Available from: https://wires.onlinelibrary.wiley.com/doi/pdf/10.1002/wcms.1539.

Calabrese, P., Cardy, J., 2005. Evolution of entanglement entropy in one-dimensional systems. J. Stat. Mech. Theory Exp. 2005, P04010. Available from: https://doi.org/10.1088/1742-5468/2005/04/P04010.

Cazalilla, M., Marston, J., 2002. Time-dependent density-matrix renormalization group: a systematic method for the study of quantum many-body out-of-equilibrium systems. Phys. Rev. Lett. 88, 256403. Available from: https://doi.org/10.1103/PhysRevLett.88.256403.

Chen, J., Stoudenmire, E.M., 2020. Hybrid purification and sampling approach for thermal quantum systems. Phys. Rev. B 101, 195119. Available from: https://doi.org/10.1103/PhysRevB.101.195119.

Chin, A.W., Prior, J., Rosenbach, R., Caycedo-Soler, F., Huelga, S., Plenio, M., 2013. The role of non-equilibrium vibrational structures in electronic coherence and recoherence in pigment-protein complexes. Nat. Phys. 9, 113−118. 10/f4n85q.

Crespo-Otero, R., Barbatti, M., 2018. Recent advances and perspectives on nonadiabatic mixed Quantum−Classical dynamics. Chem. Rev. 118, 7026−7068. 10/gjg5dn.

Daley, A.J., Kollath, C., Schollwöck, U., Vidal, G., 2004. Time-dependent density-matrix renormalization-group using adaptive effective Hilbert spaces. J. Stat. Mech.: Theory Exp. 2004, P04005. Available from: https://doi.org/10.1088/1742-5468/2004/04/P04005.

de Vega, I., Bañuls, M.-C., 2015. Thermofield-based chain-mapping approach for open quantum systems. Phys. Rev. A 92, 052116. Available from: https://doi.org/10.1103/PhysRevA.92.052116.

Dirac, P.A.M., 1930. Note on exchange phenomena in the Thomas atom. Math. Proc. Camb. Philos. Soc. 26, 376−385.

Dubail, J., 2017. Entanglement scaling of operators: a conformal field theory approach, with a glimpse of simulability of long-time dynamics in $1 + 1$d. J. Phys. A Math. Theor. 50, 234001. Available from: https://doi.org/10.1088/1751-8121/aa6f38.

Dutta, T., Ramasesha, S., 2010. Double time window targeting technique: real-time DMRG dynamics in the Pariser-Parr-Pople model. Phys. Rev. B 82, 035115. Available from: https://doi.org/10.1103/PhysRevB.82.035115.

Feiguin, A.E., White, S.R., 2005a. Finite-temperature density matrix renormalization using an enlarged Hilbert space. Phys. Rev. B 72, 220401. Available from: https://doi.org/10.1103/PhysRevB.72.220401.

Feiguin, A.E., White, S.R., 2005b. Time-step targeting methods for real-time dynamics using the density matrix renormalization group. Phys. Rev. B 72, 020404. Available from: https://doi.org/10.1103/PhysRevB.72.020404.

Frahm, L.-H., Pfannkuche, D., 2019. Ultrafast ab initio quantum chemistry using matrix product states. J. Chem. Theory Comput. 15, 2154−2165. Available from: https://doi.org/10.1021/acs.jctc.8b01291.

García-Ripoll, J.J., 2006. Time evolution of matrix product states. N. J. Phys. 8, 305. Available from: https://doi.org/10.1088/1367-2630/8/12/305.

Gatti, F., Lasorne, B., Meyer, H.-D., Nauts, A., 2017. Applications of Quantum Dynamics in Chemistry. Springer.

Gelin, M.F., Borrelli, R., Domcke, W., 2019. Origin of unexpectedly simple oscillatory responses in the excited-state dynamics of disordered molecular aggregates. J. Phys. Chem. Lett. 10, 2806−2810. Available from: https://doi.org/10.1021/acs.jpclett.9b00840.

Grasedyck, L., 2010. Hierarchical singular value decomposition of tensors. SIAM J. Matrix Anal. Appl. 31, 2029−2054. Available from: https://doi.org/10.1137/090764189.

Greene, S.M., Batista, V.S., 2017. Tensor-train split-operator Fourier transform (TT-SOFT) method: Multidimensional nonadiabatic quantum dynamics. J. Chem. Theory Comput. 13, 4034−4042. Available from: https://doi.org/10.1021/acs.jctc.7b00608.

Gunst, K., Verstraete, F., Wouters, S., Legeza, Ö., Van Neck, D., 2018. T3NS: Three-legged tree tensor network states. J. Chem. Theory Comput. 14, 2026−2033. Available from: https://doi.org/10.1021/acs.jctc.8b00098.

Guo, C., Weichselbaum, A., von Delft, J., Vojta, M., 2012. Critical and strong-coupling phases in one- and two-bath spin-boson models. Phys. Rev. Lett. 108, 160401. Available from: https://doi.org/10.1103/PhysRevLett.108.160401.

Haegeman, J., Cirac, J.I., Osborne, T.J., Pižorn, I., Verschelde, H., Verstraete, F., 2011. Time-dependent variational principle for quantum lattices. Phys. Rev. Lett. 107, 070601. Available from: https://doi.org/10.1103/PhysRevLett.107.070601.

Haegeman, J., Lubich, C., Oseledets, I., Vandereycken, B., Verstraete, F., 2016. Unifying time evolution and optimization with matrix product states. Phys. Rev. B 94, 165116. Available from: https://doi.org/10.1103/PhysRevB.94.165116.

Halimeh, J.C., Kolley, F., McCulloch, I.P., 2015. Chebyshev matrix product state approach for time evolution. Phys. Rev. B 92, 115130. Available from: https://doi.org/10.1103/PhysRevB.92.115130.

Hauschild, J., Pollmann, F., 2018. Efficient numerical simulations with tensor networks: Tensor network python (TeNPy). SciPost Phys. Lect. Notes (p. 5), . Available from: https://doi.org/10.21468/SciPostPhysLectNotes.5.

Hauschild, J., Leviatan, E., Bardarson, J.H., Altman, E., Zaletel, M.P., Pollmann, F., 2018. Finding purifications with minimal entanglement. Phys. Rev. B 98, 235163. Available from: https://doi.org/10.1103/PhysRevB.98.235163.

Hubig, C., 2017. Symmetry-Protected Tensor Networks (Ph.D. thesis). LMU München.

Hubig, C., Lachenmaier, F., Linden, N.-O., Reinhard, T., Stenzel, L., Swoboda, A., et al., 2021. The SyTen Toolkit. <https://syten.eu>.

Jaschke, D., Wall, M.L., Carr, L.D., 2018. Open source matrix product states: opening ways to simulate entangled many-body quantum systems in one dimension. Comput. Phys. Commun. 225, 59−91. Available from: https://doi.org/10.1016/j.cpc.2017.12.015.

Karrasch, C., Bardarson, J.H., Moore, J.E., 2012. Finite-temperature dynamical density matrix renormalization group and the drude weight of spin-1/2 chains. Phys. Rev. Lett. 108, 227206. Available from: https://doi.org/10.1103/PhysRevLett.108.227206.

Karrasch, C., Bardarson, J.H., Moore, J.E., 2013. Reducing the numerical effort of finite-temperature density matrix renormalization group calculations. N. J. Phys. 15, 083031. Available from: https://doi.org/10.1088/1367-2630/15/8/083031.

Kloss, B., Burghardt, I., Lubich, C., 2017. Implementation of a novel projector-splitting integrator for the multi-configurational time-dependent hartree approach. J. Chem. Phys. 146, 174107. Available from: https://doi.org/10.1063/1.4982065.

Kloss, B., Reichman, D.R., Tempelaar, R., 2019. Multiset matrix product state calculations reveal mobile Franck-condon excitations under strong Holstein-type coupling. Phys. Rev. Lett. 123, 126601. Available from: https://doi.org/10.1103/PhysRevLett.123.126601.

Kurashige, Y., 2018. Matrix product state formulation of the multiconfiguration time-dependent hartree theory. J. Chem. Phys. 149, 194114. Available from: https://doi.org/10.1063/1.5051498.

Larsson, H.R., 2019. Computing vibrational eigenstates with tree tensor network states (TTNS). J. Chem. Phys. 151, 204102. Available from: https://doi.org/10.1063/1.5130390.

Li, W., Ren, J., Shuai, Z., 2020a. Numerical assessment for accuracy and GPU acceleration of TD-DMRG time evolution schemes. J. Chem. Phys. 152, 024127. Available from: https://doi.org/10.1063/1.5135363.

Li, W., Ren, J., Shuai, Z., 2020b. Finite-temperature TD-DMRG for the carrier mobility of organic semiconductors. J. Phys. Chem. Lett. 11, 4930−4936. Available from: https://doi.org/10.1021/acs.jpclett.0c01072.

Li, W., Ren, J., Shuai, Z., 2021. A general charge transport picture for organic semiconductors with nonlocal electron-phonon couplings. Nat. Commun. 12, 4260. Available from: https://doi.org/10.1038/s41467-021-24520-y.

Lubich, C., 2015. Time integration in the multiconfiguration time-dependent hartree method of molecular quantum dynamics. Appl. Math. Res. Express 2015, 311−328. 10/gpggr4.

Lubich, C., Oseledets, I., Vandereycken, B., 2015. Time integration of tensor trains. SIAM J. Numer. Anal. 53, 917−941. 10/f6969d.

Luo, H., Xiang, T., Wang, X., 2003. Comment on time-dependent density-matrix renormalization group: a systematic method for the study of quantum many-body out-of-equilibrium

systems. Phys. Rev. Lett. 91, 049701. Available from: https://doi.org/10.1103/PhysRevLett.91.049701.

Ma, H., Schollwöck, U., 2008. Dynamical simulations of charged soliton transport in conjugated polymers with the inclusion of electron-electron interactions. J. Chem. Phys. 129, 244705. Available from: https://doi.org/10.1063/1.3046738.

Ma, H., Schollwöck, U., 2009. Dynamical simulations of polaron transport in conjugated polymers with the inclusion of electron-electron interactions. J. Phys. Chem. A 113, 1360−1367. Available from: https://doi.org/10.1021/jp809045r.

Ma, H., Luo, Z., Yao, Y., 2018. The time-dependent density matrix renormalisation group method. Mol. Phys. 116, 854−868. 10/gpggr6.

Mannouch, J.R., Barford, W., Al-Assam, S., 2018. Ultra-fast relaxation, decoherence, and localization of photoexcited states in ∏-Conjugated polymers. J. Chem. Phys. 148, 034901. Available from: https://doi.org/10.1063/1.5009393.

Mendl, C.B., 2018. PyTeNet: A concise python implementation of quantum tensor network algorithms. J. Open. Source Softw. 3, 948. Available from: https://doi.org/10.21105/joss.00948.

Meyer, H.-D., Wang, H., 2018. On regularizing the MCTDH equations of motion. J. Chem. Phys. 148, 124105. Available from: https://doi.org/10.1063/1.5024859.

Meyer, H.-D., Manthe, U., Cederbaum, L., 1990. The multi-configurational time-dependent hartree approach. Chem. Phys. Lett. 165, 73−78. Available from: https://doi.org/10.1016/0009-2614(90)87014-I.

Milsted, A., Haegeman, J., Osborne, T.J., Verstraete, F., 2013. Variational matrix product ansatz for nonuniform dynamics in the thermodynamic limit. Phys. Rev. B 88, 155116. 10/f3svvc.

Nakatani, N., Wouters, S., Van Neck, D., Chan, G.K.-L., 2014. Linear response theory for the density matrix renormalization group: Efficient algorithms for strongly correlated excited states. J. Chem. Phys. 140, 024108. Available from: https://doi.org/10.1063/1.4860375.

Orús, R., 2019. Tensor networks for complex quantum systems. Nat. Rev. Phys. 1, 538−550. Available from: https://doi.org/10.1038/s42254-019-0086-7.

Paeckel, S., Köhler, T., 2021. The SymMPS Toolkit. <https://symmps.eu>.

Paeckel, S., Köhler, T., Swoboda, A., Manmana, S.R., Schollwöck, U., Hubig, C., 2019. Time-evolution methods for matrix-product states. Ann. Phys. 411, 167998. Available from: https://doi.org/10.1016/j.aop.2019.167998.

Prior, J., Chin, A.W., Huelga, S.F., Plenio, M.B., 2010. Efficient simulation of strong system-environment interactions. Phys. Rev. Lett. 105, 050404. Available from: https://doi.org/10.1103/PhysRevLett.105.050404.

Raab, A., Worth, G.A., Meyer, H.-D., Cederbaum, L.S., 1999. Molecular dynamics of pyrazine after excitation to the S2 electronic state using a realistic 24-Mode model Hamiltonian. J. Chem. Phys. 110, 936−946. Available from: https://doi.org/10.1063/1.478061.

Rams, M.M., Zwolak, M., 2020. Breaking the entanglement barrier: Tensor network simulation of quantum transport. Phys. Rev. Lett. 124, 137701. Available from: https://doi.org/10.1103/PhysRevLett.124.137701.

Ren, J., Li, W., Jiang, T., Wang, Y., Shuai, Z., 2022. Time-dependent density matrix renormalization group method for quantum dynamics in complex systems. Wiley Interdiscip. Rev. Comput. Mol. Sci. e1614. Available from: https://doi.org/10.1002/wcms.1614.

Ren, J., Shuai, Z., Chan, G.K., 2018. Time-dependent density matrix renormalization group algorithms for nearly exact absorption and fluorescence spectra of molecular aggregates at both zero and finite temperature. J. Chem. Theory Comput. 14, 5027−5039.

Ren, J., Li, W., Jiang, T., Wang, Y., Zhigang, S., 2021. The Renormalizer Package. <https://github.com/shuaigroup/Renormalizer>.

Ronca, E., Li, Z., Jimenez-Hoyos, C.A., Chan, G.K.-L., 2017. Time-step targeting time-dependent and dynamical density matrix renormalization group algorithms with ab initio Hamiltonians. J. Chem. Theory Comput. 13, 5560−5571. Available from: https://doi.org/10.1021/acs.jctc.7b00682.

Schollwöck, U., 2011. The density-matrix renormalization group in the age of matrix product states. Ann. Phys. 326, 96−192. Available from: https://doi.org/10.1016/j.aop.2010.09.012.

Schröder, F.A.Y.N., Turban, D.H.P., Musser, A., Hine, N., Chin, A.W., 2019. Tensor network simulation of multi-environmental open quantum dynamics via machine learning and entanglement renormalisation. Nat. Commun. 10, 1062. Available from: https://doi.org/10.1038/s41467-019-09039-7.

Shi, Q., Xu, Y., Yan, Y., Xu, M., 2018. Efficient propagation of the hierarchical equations of motion using the matrix product state method. J. Chem. Phys. 148, 174102. Available from: https://doi.org/10.1063/1.5026753.

Stoudenmire, E.M., White, S.R., 2010. Minimally entangled typical thermal state algorithms. New. J. Phys. 12, 055026. 10/czp6sh.

Takahashi, Y., Umezawa, H., 1996. Thermo field dynamics. Int. J. Mod. Phys. B 10, 1755−1805. Available from: https://doi.org/10.1142/S0217979296000817.

Tamascelli, D., Smirne, A., Lim, J., Huelga, S.F., Plenio, M.B., 2019. Efficient simulation of finite-temperature open quantum systems. Phys. Rev. Lett. 123, 090402. Available from: https://doi.org/10.1103/PhysRevLett.123.090402.

Vendrell, O., Meyer, H.-D., 2011. Multilayer multiconfiguration time-dependent Hartree method: Implementation and applications to a Henon−Heiles Hamiltonian and to pyrazine. J. Chem. Phys. 134, 044135. 10/cbmwsc.

Verstraete, F., Garcia-Ripoll, J.J., Cirac, J.I., 2004. Matrix product density operators: Simulation of finite-temperature and dissipative systems. Phys. Rev. Lett. 93, 207204. Available from: https://doi.org/10.1103/PhysRevLett.93.207204.

Vidal, G., 2004. Efficient simulation of one-dimensional quantum many-body systems. Phys. Rev. Lett. 93, 040502. Available from: https://doi.org/10.1103/PhysRevLett.93.040502.

Wall, M.L., Carr, L.D., 2012. Out-of-equilibrium dynamics with matrix product states. N. J. Phys. 14, 125015. Available from: https://doi.org/10.1088/1367-2630/14/12/125015.

Wang, H., 2015. Multilayer multiconfiguration time-dependent hartree theory. J. Phys. Chem. A 119, 7951−7965. 10/f7m282.

Wang, H., Meyer, H.-D., 2018. On regularizing the ML-MCTDH equations of motion. J. Chem. Phys. 149, 044119. Available from: https://doi.org/10.1063/1.5042776.

Wang, H., Thoss, M., 2003. Multilayer formulation of the multiconfiguration time-dependent hartree theory. J. Chem. Phys. 119, 1289−1299. Available from: https://doi.org/10.1063/1.1580111.

White, S.R., 2009. Minimally entangled typical quantum states at finite temperature. Phys. Rev. Lett. 102, 190601. Available from: https://doi.org/10.1103/PhysRevLett.102.190601.

White, S.R., Feiguin, A.E., 2004. Real-time evolution using the density matrix renormalization group. Phys. Rev. Lett. 93, 076401. Available from: https://doi.org/10.1103/PhysRevLett.93.076401.

Worth, G.A., Meyer, H.-D., Cederbaum, L.S., 1996. The effect of a model environment on the S2 absorption spectrum of pyrazine: A wave packet study treating all 24 vibrational modes. J. Chem. Phys. 105, 4412−4426. Available from: https://doi.org/10.1063/1.472327.

Wouters, S., Nakatani, N., Van Neck, D., Chan, G.K.-L., 2013. Thouless theorem for matrix product states and subsequent post density matrix renormalization group methods. Phys. Rev. B 88, 075122. Available from: https://doi.org/10.1103/PhysRevB.88.075122.

Xie, X., Liu, Y., Yao, Y., Schollwöck, U., Liu, C., Ma, H., 2019. Time-dependent density matrix renormalization group quantum dynamics for realistic chemical systems. J. Chem. Phys. 151, 224101. 10/gpggr3.

Xu, Y., Xie, Z., Ma, H., 2021. The kln-X Package. <https://kylin-qc.com>.

Yan, Y., Xu, M., Li, T., Shi, Q., 2021. Efficient propagation of the hierarchical equations of motion using the Tucker and hierarchical Tucker tensors. J. Chem. Phys. 154, 194104. Available from: https://doi.org/10.1063/5.0050720.

Yang, M., White, S.R., 2020. Time-dependent variational principle with ancillary Krylov subspace. Phys. Rev. B 102, 094315. Available from: https://doi.org/10.1103/PhysRevB.102.094315.

Yao, Y., 2016. Coherent dynamics of singlet fission controlled by nonlocal electron-phonon coupling. Phys. Rev. B 93, 115426. Available from: https://doi.org/10.1103/PhysRevB.93.115426.

Yao, Y., Xie, X., Ma, H., 2016. Ultrafast long-range charge separation in organic photovoltaics: promotion by off-diagonal vibronic couplings and entropy increase. J. Phys. Chem. Lett. 7, 4830−4835. Available from: https://doi.org/10.1021/acs.jpclett.6b02400.

Yao, Y., Sun, K.-W., Luo, Z., Ma, H., 2018. Full quantum dynamics simulation of a realistic molecular system using the adaptive time-dependent density matrix renormalization group method. J. Phys. Chem. Lett. 9, 413−419. 10/gpggsc.

Yarkony, D.R., 2012. Nonadiabatic quantum chemistry—past, present, and future. Chem. Rev. 112, 481−498. Available from: https://doi.org/10.1021/cr2001299.

Zaletel, M.P., Mong, R.S., Karrasch, C., Moore, J.E., Pollmann, F., 2015. Time-evolving a matrix product state with long-ranged interactions. Phys. Rev. B 91, 165112. Available from: https://doi.org/10.1103/PhysRevB.91.165112.

Zhao, H., Yao, Y., An, Z., Wu, C.-Q., 2008. Dynamics of polarons in conjugated polymers: An adaptive time-dependent density-matrix renormalization-group study. Phys. Rev. B 78, 035209. Available from: https://doi.org/10.1103/PhysRevB.78.035209.

Zhao, H., Chen, Y.-G., Zhang, X.-M., An, Z., Wu, C.-Q., 2009. Correlation effects on the dynamics of bipolarons in nondegenerate conjugated polymers. J. Chem. Phys. 130, 234908. Available from: https://doi.org/10.1063/1.3155207.

Žnidarič, M., 2020. Entanglement growth in diffusive systems. Commun. Phys. 3, 100. 10/gpgg6g.

Zwolak, M., Vidal, G., 2004. Mixed-state dynamics in one-dimensional quantum lattice systems: A time-dependent superoperator renormalization algorithm. Phys. Rev. Lett. 93, 207205. Available from: https://doi.org/10.1103/PhysRevLett.93.207205.

Index

Note: Page numbers followed by "*f*" refer to figures.

DENSITY MATRIX RENORMALIZATION GROUP (DMRG)-BASED APPROACHES IN COMPUTATIONAL CHEMISTRY

Key Features

- Provides an expertly curated, consolidated overview of research in the field
- Outlines key theories and algorithms for computational chemistry applications

The simulation of strongly correlated systems is crucial for understanding varied interdisciplinary molecular science problems, ranging from bond dissociation in chemical reactions to nonadiabatic dynamics in optoelectronic materials. As a tool to tackle this challenge, the Density Matrix Renormalization Group (DMRG) theory has been one of the biggest breakthroughs in the last two decades. *Density Matrix Renormalization Group (DMRG)-based Approaches in Computational Chemistry* outlines important theories and algorithms of DMRG-based approaches and explores their use in computational chemistry.

Beginning with an introduction to DMRG and DMRG-based approaches, this book goes on to discuss the key theories and applications of DMRG, from DMRG for semiempirical and ab initio quantum chemistry, to DMRG in embedded environments, frequency spaces, and quantum dynamics.

Drawing on the experience of its expert authors, this book details recent ideas and key developments, providing an up-to-date view of current developments in the field for students and researchers in quantum chemistry.

About the Authors

Haibo Ma, *School of Chemistry and Chemical Engineering, Nanjing University*

Haibo Ma is a professor of theoretical chemistry at the Nanjing University. He has a BS and a PhD from the Nanjing University in 2002 and 2007, respectively. He has received the Humboldt Research Fellowship from the Alexander von Humboldt Foundation (2007–09) and Tang Au-Qing youth award on theoretical chemistry from Chinese Chemical Society (2018). His main research interests focus on the development of renormalization group-based quantum chemical methods for strongly correlated systems and excited-state processes.

Ulrich Schollwöck, *Department of Physics, Ludwig-Maximilian University of Munich*

Ulrich Schollwöck is a professor of theoretical physics at the Ludwig-Maximilian University of Munich. He has an MSc from Balliol College, the University of Oxford in 1991, a diploma in physics from the University of Munich in 1993, and a PhD from the French Atomic Energy Commission in 1995. His key interests are strongly correlated quantum systems with a focus on the development of new algorithms for large-scale simulations. He is a leading expert on the *DMRG* and was a pioneer in applying it to quantum systems far from equilibrium. He is a fellow of the American Physical Society (2006) and Academy of Science member in Germany (2007). He has received the Gerhard Hess Prize of the German Research Foundation (2000) and has been a fellow of the Institute of Advanced Study in Berlin (2009/2010).

Zhigang Shuai, *Department of Chemistry, Tsinghua University*

Zhigang Shuai is a professor of Changjiang Scholars at the Tsinghua University. He received BSc from the Sun Yat-sen University in 1983 and his PhD degree from the Fudan University in 1989. His research interests focus on the development of computational methodologies for modeling conjugated organic and polymeric materials. He extended the DMRG theory for investigating the excited-state structures and dynamical processes, light-emitting properties, and nonlinear optical responses for conjugated polymers since 1996. He is the Vice President of the International Academy of Quantum Molecular Science since 2018.